JAERI-Conf
2003-001

JP0350237

PROCEEDINGS OF THE 3rd INTERNATIONAL SYMPOSIUM ON MATERIAL CHEMISTRY IN NUCLEAR ENVIRONMENT (MATERIAL CHEMISTRY '02 MC '02) MARCH 13-15, 2002, TSUKUBA

March 2003

MC '02 Symposium Committee

日本原子力研究所
Japan Atomic Energy Research Institute

本レポートは、日本原子力研究所が不定期に公刊している研究報告書です。
入手の問合わせは、日本原子力研究所研究情報部研究情報課（〒319-1195 茨城県那珂郡東海村）あて、お申し越し下さい。なお、このほかに財団法人原子力弘済会資料センター（〒319-1195 茨城県那珂郡東海村日本原子力研究所内）で複写による実費頒布を行っております。

This report is issued irregularly.
Inquiries about availability of the reports should be addressed to Research Information Division, Department of Intellectual Resources, Japan Atomic Energy Research Institute, Tokai-mura, Naka-gun, Ibaraki-ken 〒319-1195, Japan.

© Japan Atomic Energy Research Institute, 2003
編集兼発行　日本原子力研究所

JAERI－Conf 2003－001

Proceedings of the 3rd International Symposium on Material Chemistry in Nuclear Environment

(MATERIAL CHEMISTRY '02 MC'02)

March 13-15, 2002, Tsukuba

MC'02 Symposium Committee

Tokai Research Establishment
Japan Atomic Energy Research Institute
Tokai-mura, Naka-gun, Ibaraki-ken

(Received January 10, 2003)

The volume contains all presented papers during the the 3rd International Symposium on Material Chemistry in Nuclear Environment: MATERIAL CHEMISTRY '02 (MC'02), held March 13-15, 2002. The purpose of this symposium is to provide an international forum for the discussion of recent progress in the field of materials chemistry in nuclear environments. This symposium intends to build on the success of the previous symposiums held in Tsukuba in 1992 and 1996. The topics discussed in the symposium MC'02 are Chemical Reaction and Thermodynamics, Degradation Phenomena, New Characterization Technology, Fabrication and New Materials, Composite Materials, Surface Modification, and Computational Science.

This report consist of 27 papers for oral session and 34 papers for poster session.

Keywords: Nuclear Environment, Materials, Chemistry, Degradation, Thermodynamics, Material Characterization, Composite Materials, Computational Science, Surface Modification

JAERI－Conf 2003－001

第３回　材料化学国際シンポジウム論文集

(MATERIAL CHEMISTRY '02　MC'02)

２００２年３月１３日～１５日、つくば市

日本原子力研究所東海研究所

MC'02 企画委員会

(2003 年 1 月 10 日受理)

第３回材料化学国際シンポジウム（Third International Symposium on Material Chemistry in Nuclear Environment, MC'02）が、平成１４年３月１３日～１５日の３日間、原子力基盤技術クロスオーバー研究の一環として、筑波研究交流センターで開催された。これまで、当該シンポジウムは原子力材料クロスオーバー研究グループが中心となって第１期（89～93)、第２期（94～98）の各節目にそれぞれ MC'92、MC'96 として開催され、今回の第３期では計算科学及び陽電子ビームクロスオーバー研究グループと合同で MC'02 として開催した。MC'02 では、特に発電炉、再処理、核融合、加速器等の原子力技術の高度化に不可欠な複合環境用材料の課題と材料開発、計算科学、環境適応性評価技術等の最新技術開発動向に関して、国際的な専門家を集めて活発な討論が行われた。

本報告書は、会議にて発表された２７の口頭発表と３４のポスターセッションの論文を取りまとめたものである。

東海研究所：　〒319-1195　茨城県那珂郡東海村白方白根 2-4

Sponsors:

Specialist Committee of Cross-over Research on Nuclear Materials, Positron Beam Technology and Computational Science

Promotion Committee of Cross-over Research

Co-sponsors:

Atomic Energy Society of Japan

Chemical Society of Japan

International Committee:

Prof. Terai, T.(The University of Tokyo, Japan; Chairperson)

Dr. Akahane, T. (NIMS, Japan)

Dr. Bastasz, R. (SNL, USA)

Dr. Futakawa, M. (JAERI, Japan)

Prof. Hara, N. (Tohoku Univ., Japan)

Dr. Himeno, R. (RIKEN, Japan)

Dr. Itoh, H. (JAERI, Japan)

Dr. Iwaki, M. (RIKEN, Japan)

Dr. Kaburaki, H. (JAERI, Japan)

Dr. Kitajima, M. (NIMS, Japan)

Dr. Kiuchi, K. (JAERI, Japan)

Dr. Kobayashi, Y. (AIST, Japan)

Dr. Konys, J. (FZK, Germany)

Dr. Mitsuhashi, T. (NIMS, Japan)

Prof. Nishijima, S. (Osaka Univ., Japan)

Dr. Sekiguchi, T. (AIST, Japan)

Dr. Saito, F. (RIKEN, Japan)

Dr. Suzuki, R. (AIST, Japan)

Dr. Tabuchi, M. (NIMS, Japan)

Prof. Taya, M. (Univ. of Washington, USA)

Local Committee:

Dr. Futakawa, M. (JAERI, Japan)

Ms. Hasegawa, N. (JAERI, Japan)

Dr. Hirata, K. (AIST, Japan)

Dr. Hishita, S. (NIMS, Japan)

Mr. Ikejima, T. (JAERI, Japan)

Dr. Ishioka, K. (NIMS, Japan)

Dr. Kawasuso, A. (JAERI, Japan)

Dr. Ohdaira, T. (AIST, Japan)

Dr. Shiga, M. (JAERI, Japan)

Secretariat

Japan Atomic Industrial Forum

Cross-Over Research Development Division

Contents

1. ORAL SESSION 1

1.1 Review 3

Chair: R. Bastasz (Sandia National Laboratories, USA)
T. Terai (The University of Tokyo, Japan)

1.1.1 Research on New Materials Development and Elucidation of Degradation Phenomena in Nuclear Environments 5
T. Terai (The University of Tokyo, Japan)

1.1.2 Surface Studies of Liquid Metals and Alloys 12
R. Bastasz (Sandia National Laboratories, USA)

1.1.3 Hierarchical Modeling of Active Materials 19
M. Taya (University of Washington, USA)

1.2 Chemical Reaction and Thermodynamic 27

Chair: J. Konys (Forschungszentrum Karlsruhe FZK, Germany)
Y. Shirai (Osaka University, Japan)

1.2.1 Corrosion and Compatibility of Structural Materials in Liquid Lead Alloys 29
J. Konys , G. Müller (Forschungszentrum Karlsruhe FZK, Germany)

1.2.2 Positron Annihilation Study of Hydrogen Storage Alloys 37
Y. Shirai, H. Araki, K. Sakaki (Osaka University, Japan)

1.2.3 High Temperature Sulfide Corrosion and Transport Properties of Transition Metal Sulfides 44
K. Przybylski, S. Mrowec (University of Mining and Metallurgy (AGH), Poland)

1.3 Degradation Phenomena 53

Chair: P. Asoka-Kumar (Lawrence Livermore National Laboratory, USA)
K. Kiuchi (Japan Atomic Energy Research Institute, Japan)

1.3.1 Positron Annihilation Studies on Bulk Metallic Glass and High Intensity Positron Beam Developments 55
P. Asoka-Kumar, W. Stoeffl (Lawrence Livermore National Laboratory, USA)

1.3.2 Liquid Metal Embrittlement: from Basic Concepts to Recent Results Related to Structural Materials for Liquid Metal Spallation Targets 63
D. Gorse, S. Goryachev, T. Auger (CNRS-CECM, France)

1.3.3 Analysis of Stress Degradation of Metals by Positron Annihilation 71
E. Kuramoto (Kyushu University, Japan)

1.3.4 Boron Content in Type 316 L Stainless Steel by Neutron Induced Autoradiography 77
J. Jang, Y. K. Kim, W. S. Ryu (KAERI, Korea-South)
Y. B. Lee (Korea University, Korea-South)
K. T. Kim (POSCO, Korea-South)

1.3.5 Corrosion Mechanism on Heat Transfer Surface of Pressure Boundary Materials Used in

Nuclear Environments ····· 84
K. Kiuchi, H. Ogawa, I. Ioka, (JAERI, Japan)
Y. Kuroda (JAPC, Japan)
T. Anegawa (TEPC, Japan)

1.4 New Characterization Technology ····· 93
Chair: T. Staab (University of Bonn, Germany)
M. Kitajima (National Institute of Materials Science, Japan)

1.4.1 Defects in Fine-grained and Porous Materials Characterized by Positron Annihilation ··· 95
T. E. M. Staab (University of Bonn, Germany)
R. Krause-Rehberg (Martin-Luther-University, Germany)
B. Kieback (Technical University, Germany)

1.4.2 Modeling of Positron States and Annihilation in Solids ····· 102
M. J. Puska (Helsinki University of Technology, Finland)

1.4.3 Study of Radiation Defects in Semiconductors by Means of Positron Annihilation ····· 114
R. Krause-Rehberg, V. Bondarenko, F. Redmann, F. Börner (University Halle, Germany)
H. Feick, E. Weber (University of California, USA)
C. D. Via (Brunel University, UK)
W. Egger, G. Kögel, P. Sperr, W. Triftshäuser (Univ. der Bundeswehr, Germany)

1.4.4 Characterization of Nanoparticle and Porous Ultra Low-K Using Positron Beam ····· 118
J. Xu, J. Moxom (Oak Ridge National Laboratory, USA)
R. Suzuki, T. Ohdaira (National Institute of Advanced Industrial Science and Technology, Japan)
A. P. Mills, Jr. (University of California, USA)

1.4.5 Time-domain Vibrational Study on Defects in Ion-irradiated Crystal ····· 127
M. Kitajima (National Institute for Materials Science, Japan)

1.5 Fabrication and New Materials ····· 135
Chair: V. Balek (Nuclear Research Institute, Czech Republic)
T. Mitsuhashi (National Institute for Materials Science, Japan)

1.5.1 Surface Modification of Ceramic Materials Induced by Irradiation of High Power Pulsed ICP ····· 137
T. Ishigaki, N. Okada, N. Ohashi, H. Hnaeda (National Institute for Materials Science, Japan)

1.5.2 Emanation Thermal Analysis for Characterization of Surface and Near Surface Layers of Advanced Materials ····· 143
V. Balek (Nuclear Research Institute, Czech Republic)
T. Mitsuhashi (National Institute for Materials Science, Japan)
J. Subrt (Institute of Inorganic Chemistry, Czech Republic)

1.5.3 Kinetic Study of Solid-state Processes ····· 149

J. Málek (University of Pardubice, Czech Republic)
T. Mitsuhashi (National Institute for Materials Research, Japan)

1.5.4 Microstructure of SiC Ceramics Fabricated by Pyrolysis of Electron Beam Irradiated Polycarbomethylsilane Containing Precursors ····· 156
Y. XU (Institute of Nuclear Physics and Chemistry, China)
S. Tanaka (Japan Atomic Energy Research Institute, Japan)

1.6 Composite Materials ····· 163
Chair: M. Hasegawa (Tohoku University, Japan)
D. Fink (Hahn-Meitner-Institut Berlin, Germany)

1.6.1 Photocontrolled Selective Isolation of Uranyl Cation From Aqueous Solution Onto a Photo-responsive Langmuir-blodgett Film ····· 165
Y. Izumi, T. Yamamoto, S. Nishijima (Osaka University, Japan)
T. Yaita, S. Tachimori (Japan Atomic Energy Research Institute, Japan)
K. Ushida (The Institute of Physical and Chemical Research, Japan)

1.6.2 Creation of Nanoscale Objects by Swift Heavy Ion Track Manipulations ····· 171
D. Fink, A. .Petrov, N. Stolterfoht, M. Wilhelm, V. Hoffmann (Hahn-Meitner-Institut, Germany)
A. Richter (Technische Fachhochschule Wildau, Germany)
M. Behar, L. Farenzena (Instituto de Física, Brazil)
R. Papaleo (Instituto de Física, Brazil)
K. Hirata (National Institute of Chemical Research, Japan)
L. T. Chadderton (ANU, Australia)
A. Schulz (SDK GmbH, Germany)
W. R. Fahrner (Institut für Elektrotechnik, Germany)

1.6.3 Plasma-polymerized SiOx Deposition on Polymer Film Surfaces for Preparation of Oxygen Gas Barrier Polymeric Films ····· 179
N. Inagaki (Shizuoka University, Japan)

1.7 Surface Modification ····· 187
Chair: T. Goto (Tohoku University, Japan)
K. Kobayashi (National Institute of Advanced Industrial Science and Technology, Japan)

1.7.1 Characterization of Surfaces and Subsurfaces by an Intense Positron Beam ····· 189
R. Suzuki, T. Ohdaira (National Institute of Advanced Industrial Science and Technology, Japan)

1.7.2 Ultra-high Temperature Oxidation Behavior of Chemical Vapor Deposited Silicon Carbide Layers ····· 195
T. Goto (Tohoku University, Japan)

1.7.3 Study of Nanoporous Structure of Sputter-deposited Silicon Oxide Thin Films by Positron Annihilation Spectroscopy in Relation to Gas Barrier Coating ····· 203
Y. Kobayashi (National Institute of Advanced Industrial Science and Technology, Japan)

1.8 Computational Science 211
Chair: D. J. Bacon (The University of Liverpool, UK)
H. Kaburaki (Japan Atomic Energy Research Institute, Japan)

1.8.1 Behavior of Cu Atoms in α-Fe Under Irradiation: a Computer Simulation Study 213
N. Soneda (Central Research Institute of Electric Power Industry, The University of Tokyo, Japan)
A. Takahashi, G. Yagawa (University of Tokyo, Japan)
S. Ishino (Tokai University, Japan)

2. POSTER SESSION 221

2.1 Effect of Ion Irradiation on Structural and Electrical Properties of BSCC Thin Films 223
S. Hishita (National Institute for Materials Science, Japan)
S. S. Kim (Sunchon National University, Korea)
J. H. Moon (Chonnam National University, Korea)

2.2 Formation Mechanism of SiC in C-Si System by Ion Irradiation 228
S. Hishita, T. Aizawa, S. Suehara, H. Haneda (National Institute for Materials Science)

2.3 Pattern-deposition of Zinc Oxide Particles Using Self-assembled Monolayer Template .. 233
N. Saito, H. Haneda (National Institute for Materials Science, Japan)
K. Koumoto (Nagoya University, Japan)

2.4 Development of Nano-composite 9Cr-ODS Martensitic Steels by Means of α to γ Phase Transformation 237
T. Kaito, S. Ukai, K. Hatakeyama (Japan Nuclear Cycle Development Institute, Japan)
M. Fujiwara (Kobelco Research Institute Inc., Japan)
T. Okuda (Kobe Special Tube Co. Ltd, Japan)
T. Kobayashi (Sumitomo Metal Technology Ltd. Japan)

2.5 Microfabrication of Crosslinked PTFE by Synchrotron Radiation 245
Y. Sato, D. Yamaguchi, A. Oshima, M. Washio (Waseda University, Japan)
T. Katoh, Y. Aoki (Sumitomo Heavy Industries Ltd., Japan)
S. Ikeda (Raytech Corporation, Japan)
S. Tanaka (Japan Atomic Energy Research Institute, Japan)
Y. Tabata (Professor Emeritus, The University of Tokyo, Japan)

2.6 Anatase Thin Film with Diverse Epitaxial Relationship Grown on Yittrum Stabilized Zirconia Substrate by Chemical Vapor Deposition 251
T. Miyagi, A. Yamazaki (National Institute for Materials Science, Waseda University, Japan)
T. Ogawa (National Institute for Materials Science , Keio-Gijuku University, Japan)
M. Kamei, Y. Wada, T. Mitsuhashi (National Institute for Materials Science, Japan)

2.7 Photoluminescence Measurements of ZnO Heterostructures 257
Y. Adachi, I. Sakaguchi, N. Ohashi, H. Haneda (National Institute for Materials Science, Japan)
H. Ryoken, T. Takenaka (Science University of Tokyo, Japan)

2.8 Characterization of SCC Crack Tip in Alloy 600 in Simulated Primary Water of PWR ·· 262
K. Fujii, K. Fukuya, N. Nakajima (Institute of Nuclear Safety System, Inc., Japan)

2.9 Vacancy Formation Energy of Metals Determined by Using Positron Age-momentum Correlation Technique ····· 270
N. Suzuki, Y. Itoh, A. Goto (The Institute of Physical and Chemical Research, Japan)
K. Manabe, T. Hyodo (The University of Tokyo, Japan)

2.10 Thermal Diffusivity and Heat Capacity Measurements of Li_2ZrO_3 and Li_2TiO_3 with the Laser-flash Method ····· 276
T. Hoshino, T. Terai, M. Yamawaki (The University of Tokyo, Japan)
Y. Takahashi (Chuo University, Japan)

2.11 Positron Annihilation Study on Defects in Ion-implanted Si ····· 282
T. Akahane (National Institute for Materials Science, Japan)
M. Fujinami, T. Sawada (The University of Tokyo, Japan)

2.12 Mechanical Characterization of Magnesium Aluminate $MgO{\cdot}nAl_2O_3$ Spinel Single Crystals Irradiated with Cu^- Ions ····· 287
T. Ohmura (National Institute for Materials Science, Japan)
Chi-Gyu Lee , N. Kishimoto (National Institute for Materials Science, Japan)

2.13 Fabrication of Ni_3Al Thin Foils by Cold Rolling and the Mechanical Properties ····· 295
T. Hirano, M. Demura, K. Kishida (National Institute for Materials Science, Japan)
Y. Suga (Nippon Cross Rolling Co., Japan)

2.14 Dynamics of Coherent Phonons in Ion-irradiated Bismuth Studied by Femtosecond Pump-probe Technique ····· 303
M. Hase, K. Ishioka, M. Kitajima (National Institute for Materials Science, Japan)
S. Hishita (National Institute for Materials Science , Japan)
K. Ushida (The Institute of Physical and Chemical Research, Japan)

2.15 Development of an Intense Pulsed Atomic Hydrogen Beam Source ····· 309
A. Kubo (National Institute for Materials Science, University of Tsukuba, Japan)
M. Kitajima (National Institute for Materials Science, Japan)

2.16 Design of a Transmission Electron-positron Microscope ····· 316
M. Doyama, M. Inoue, Y. Kogure (Teikyo University of Science and Technology, Japan)
Y. Hayashi, T. Yoshiie (Kyoto University, Japan)
T. Kurihara (High Energy Accelerator Research Organization (KEK), Japan)
K. Tsuno (JEOL, Japan)

2.17 Development of High Power Ceramic Lasers and Possible Application to Nuclear Fusion ····· 322
T. Yanagitani, H. Yagi (Konoshima Chemical Co. Ltd., Japan)
K. Ueda, J. Lu, Junhua Lu (University of Electro-Communications, Japan)
A. A. Kaminskii (Crystal Laser Physics Laboratory, Russia)

2.18 Design of a Spin Polarized Positron Beam and a Spin Rotator ····· 331
F. Saito, N. Suzuki, Y. Itoh, A. Goto (The Institute of Physical and Chemical Research, Japan)

T. Kurihara (The University of Tokyo, Japan)
Y. Nagashima, T. Hyodo (Institute of Materials Structure Science(IMMS),High Energy Accelerator Research Organization, Japan)

2.19 Computational Simulation for Creep Fracture Properties Taking Microscopic Mechanism Into Account ····· 336
M. Tabuchi (National Institute for Materials Science, Japan)

2.20 A Molecular-dynamics Simulation of Displacement Cascades in α-iron ····· 344
K. Kusunoki (National Institute for Materials Science, Japan)

2.21 Modelling for Near-surface Interaction of Lithium Ceramics and Sweep-gas by Use of Cellular Automation ····· 352
K.Shimura, T.Terai, M.Yamawaki (The University of Tokyo, Japan)
K.Yamaguchi (Japan Atomic Energy Research Institute, Japan)

2.22 Observation of Inner Surface of Flame-tower Type Reactor for Uranium Conversion···· 359
I. Amamoto (The University of Tokyo, Japan Nuclear Cycle Development Institute, Japan)
T. Terai(The University of Tokyo, Japan)
H. Umetsu (Japan Nuclear Cycle Development Institute, Japan)

2.23 Study on Synthesis Technique and Thermal Analysis of Na-Fe Complex Oxides ····· 367
F. Ono, M. Tonegawa, T. Terai and M. Yamawaki (The University of Tokyo, Japan)
T. Furukawa, F. Ueno, K. Aoto (Japan Nuclear Cycle Development Institute, Japan)

2.24 Development of SSRT Facility with Ability of In-situ Observation During SCC Test in High Temperature Water for Irradiated Materials ····· 374
J. Nakano, T. Tsukada, M. Kikuchi, Y. Kaji, H. Ugachi, Y. Miwa, H. Tsuji (Japan Atomic Energy Research Institute, Japan)
S. Terakado, T. Kohya (Japan Atomic Energy Research Institute, Japan)

2.25 Static and Dynamic Corrosion Experiments in Liquid Lead-bismuth ····· 382
Y. Kurata, K. Kikuchi, M. Futakawa, S. Saito, T. Sasa (Japan Atomic Energy Research Institute, Japan)

2.26 Two-dimensional Graphite-like Si_xC Observed by Polarization Dependence in the Near-edge X-ray Absorption Fine Structure ····· 390
Y. Baba, I. Shimoyama , T. Sekiguchi (Japan Atomic Energy Research Institute, Japan)

2.27 AFM Evaluation of Grain Boundary Corrosion Behavior on Ion Irradiated Stainless Steel ····· 397
Y. Nemoto, Y. Miwa, T. Tsukada , H. Tsuji (Japan Atomic Energy Research ..... Institute, Japan)

2.28 Effect of Helium and Hydrogen Production on Hardness of F82H Steel Irradiated by Dual/Triple Ion Beams ····· 405
Wakai, T. Sawai, H. Tanigawa, A. Naito, T. Taguchi, S. Jistukawa (Japan Atomic Energy Research Institute, Japan)

2.29 Sintering and Polytype Transformation of SiC by AlB_2 Addition ····· 413
H. Tanaka, T. Mitsuhashi (National Institute for Materials Science, Japan)
Dong-Wo Shin, Sam-Shik Park (Gyeongsank National University, Korea)

2.30 Ellipsometry Studies on Nitrogenated Diamond-like Carbon (DLC) Thin Films Produced by RF Magnetron Sputtering ····· 418

P. R. Vinod, H. Kakiuchi, T. Terai (The University of Tokyo, Japan)
A. N. Itakura, M. Kitajima (National Institute for Materials Science, Japan)
2.31 Change in Properties of $Bi_2Sr_2CaCu_2O_{8+x}$ Single Crystals Due to Neutron Irradiation Followed by Thermal Annealing ····· 424
T. Shitamichi, M. Nakano, K. Ogikubo, T. Terai, M. Yamawaki (The University of Tokyo, Japan)
T. Hoshiya (Japan Atomic Energy Research Institute, Japan)
2.32 Difference in Low Energy Plasma Excitation and Chemical Reactivity of Rare Gases ····· 429
H. Ogawa, K. Kiuchi (Japan Atomic Energy Research Institute, Japan)
2.33 Corrosion of Type 304L Stainless Steel in Boiling Dilute Neptunium Nitrate Solution ··· 439
T. Motooka, K. Kiuchi (Japan Atomic Energy Research Institute, Japan)
2.34 Effect of Triple Ion Beam Irradiation on Mechanical Properties of High Chromium Austenitic Stainless Steel ····· 445
I. Ioka, M. Futakawa, Y. Nanjyo, K. Kiuchi (Japan Atomic Energy Research Institute, Japan)
Y. Kuroda (The Japan Atomic Power Company, Japan)
T. Anegawa (Tokyo Electric Power Company, Japan)

PREFACE

Takayuki Terai
The University of Tokyo

The International Conference of Material Chemistry have been planned to introduce each research activity and to expand the international collaboration for overcoming the technological barrier on The Nuclear Materials in The Nuclear Cross-over Research. The project was started from 1987 by the advisory committee for promoting the fundamental research projects in The STA. On the first phase, new materials design and fabrication technologies for improving the compatibility to each heavily corrosive environment under irradiation were developed based on the new principles obtained from analyses of each degradation phenomenon. The research output was discussed in The First International Conference of Material Chemistry `92. In the second phase, Multi-Composite Materials (MCMs) by the advanced technological means were developed. Cladding, coating, ion implantation and/or graduated composition materials were developed by considering the practical application to the pressure boundary materials such as new reactor components, reprocessing equipment etc. The research output was also discussed in The Second International Conference of Material Chemistry `96. In the third phase, the advanced materials and monitoring technologies have been examined by the simulation tests for evaluating the reliability and for optimizing the practical components used in nuclear environments. The major objectives on The International Conference of Material Chemistry `02 were planned to discuss above important issues up to date by gathering a number of researchers with each professional research field, namely, the materials development, ultra-high resolution analyzing technologies and computer simulation methods so on. About 120 delegates were attended including 10 countries and about 100 papers were presented in oral and poster sessions.

The conference was held with the cooperation of Atomic Energy Society of Japan, Chemical Society of Japan and The Promotion Office for Cross-over Research in Nuclear Industrial Forum. The proceeding of International Conference of Material Chemistry`02 was summarized with the collaboration by the specialist committee members of cross-over research on nuclear materials, positron beam technology, computational science in JAERI.

1. Oral Session

This is a blank page.

1.1 Review

Chair: R. Bastasz

(Sandia National Laboratories, USA)

T. Terai

(The University of Tokyo, Japan)

This is a blank page.

JP0350238

1.1.1 Research on New Materials Development and Elucidation of Degradation Phenomena in Nuclear Environments

Takayuki TERAI

University of Tokyo
7-3-1, Hongo, Bunkyo-ku, Tokyo, 133-8656, Japan

ABSTRUCT

Advanced materials technologies are required to develop the pressure boundary materials used in nuclear corrosive environments under irradiation. The outline of the materials research for overcoming the requirements is described. The applicability and fusibility of new materials technology and major characteristics are shown with respect to several examples. A new-type coating method of diamond-like carbide films by using RF magnetron sputtering, mechanistic analysis on tritium release behavior from molten lithium-tin alloy in-reactor, neutron irradiation assisted change in pinning properties of Bi2Sr2CaCu2O8+x single crystals are discussed as typical outputs concerning the research.

Keywords: Nuclear environment, Advanced materials, Degradation, Defects, Irradiation

1. Introduction

The nuclear environment is characterized to be one of extremely heavily corrosive environments due to the combined effects of chemical & physical attack by environments and irradiation. Several controlling parameters are related to the degradation mechanisms. In particularly, major unknown parameters are included in the irradiation effects. The effects would be different among irradiation particles such as neutron, ion, electron, photon and the energy spectra. In the nuclear environment, the material degradation promptly proceeds with the irradiation effects. The effect of heavy neutron irradiation is to form primary knock-on atoms (PKA) and dissimilar atoms due to nuclear transmutation reaction. The micro-structural evolution is formed due to secondary defects by mutual interactions between defects and solute atoms. Finally, the characteristics required to structural materials such as mechanical properties and corrosion resistance are markedly affected by irradiation hardening, secondary phase formation and segregation of selective elements, as shown in Fig. 1.

In particular, the pressure boundary material used as a barrier between two different environments is required to have the excellent properties with respect to the corrosion resistance, creep strength and mechanical toughness under irradiation. For examples, these materials are used for the pressure vessel for nuclear reactor, reaction vessel for spent fuel reprocessing plant, nuclear fuel cladding, first wall for fusion reactor, organic insulator so on. Consequently, the reliability is limited with the degradation phenomena in relation to plant aging. The formation of deteriorated inner surface layer, environmental cracking such as SCC, shape change and change in physical properties

such as thermal conductivity would be experienced as effects due to the degradation. On the other hand, the irradiation effect and ion implantation are useful to modify the material properties and to synthesis new structural materials as shown in Fig. 2. Ion-implantation and plasma processing are possible to modify the surface characteristics by non-thermal process. Radiation damage would be possible to make several different materials functions. Nuclear transmutation reaction is one of the doping method as known NDT for modifying the semiconductor properties. Ion-implantation is useful for making semiconductor devices and compositional gradient material and so on. And plasma processing is applied to form the new surface films. And finally, laser abrasion is applied to make new materials such as atom clusters, fullerene, carbon nano-tube etc.

Based on the above background, The Crossover Research on Nuclear Materials was started since 1989, following 3 phases; up to 1993, 1994 to 1998, and 1999 to 2003 respectively. In this paper, the outlines of activities in the 3rd phase and in the research activity on the University of Tokyo are shortly introduced.

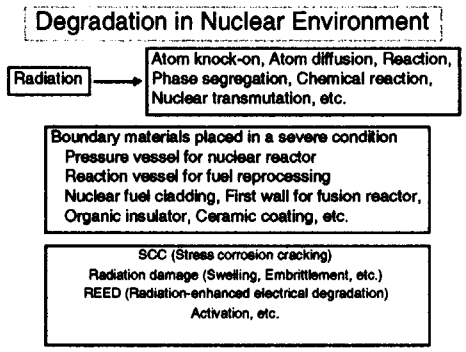


Figure 1 Degradation in nuclear environment

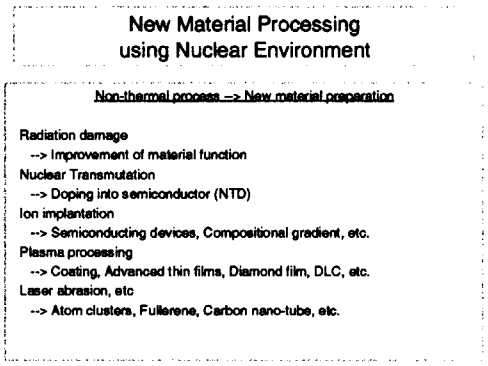


Figure 2 New material processing using nuclear environment

2. Activities in the 3rd phase for materials research

Figure 3 shows the activities in the 3rd phase for The Crossover Research for Nuclear Materials consisting of major two items. One is to evaluate the reliability of newly-developed materials on practical use by simulation tests. The other is to develop monitoring techniques and sensor applied to detect aging degradations. In particular, we are focusing on the boundary materials between two different environments as described above. For example, in the case of fuel cladding materials, each surface is faced on LWR primary coolant and nuclear fuels respectively. And in the case of 1st wall of fusion reactor blanket, it is faced to plasma and coolant respectively. In the case of reaction vessel of reprocessing plant, it is reprocessing hydrogen nitrate and steam respectively. In the case of organic insulators, it is faced on circumstance air under temperature gradient due to electrical resistance heating. The degradation of pressure boundary materials would be accelerated with synergistic effects of corrosion, stress and micro-structural change due to irradiation aging

In the 3rd phase for this research, two research items are addressed. One is to evaluate the reliability of newly developed materials by modeling the degradation

mechanism and to optimize the materials design and fabrication process, by considering the practical application to nuclear environments. The other is to develop monitoring techniques and sensor. In this scope, in-situ detection of phonon vibration under irradiation, microscopic analyses on corrosion and surface defects, positron annihilation techniques for radiation defects are examined for developing in-situ monitoring of corrosion and environmental cracking. Solid sensors which are possible to use in nuclear corrosive environments are also investigated to evaluate the applicability of newly-developed devices made of new materials.

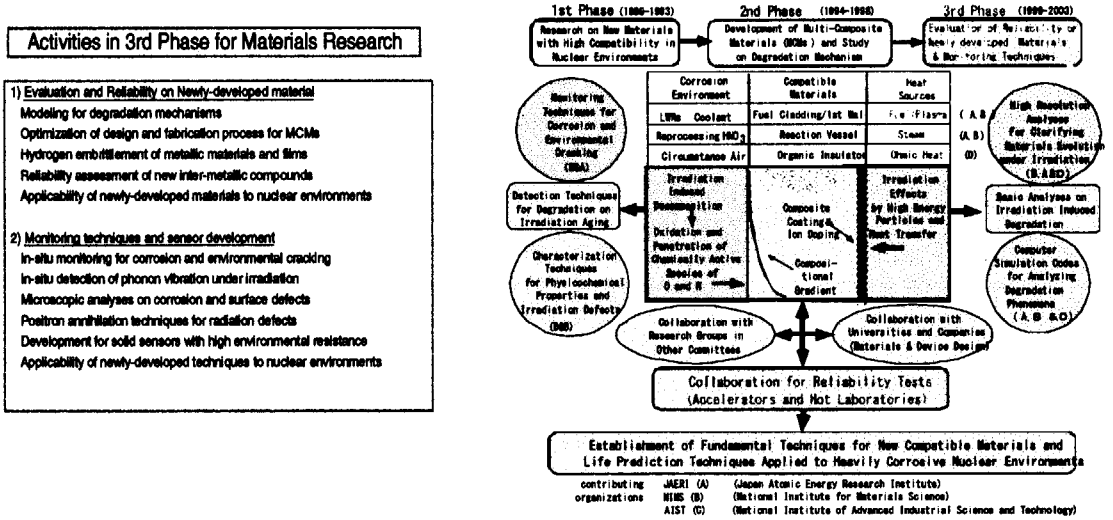


Figure 3 Research activities in 3rd Phase for Crossover Research on Nuclear Materials.

3. Activities in The University of Tokyo (Terai group)

Our research activities are divided into two research items as shown in Fig. 4. One is the change in materials properties due to irradiation on nuclear energy systems. The other is the property control and new material development. In this paper, the outlines of underlined topics were described.

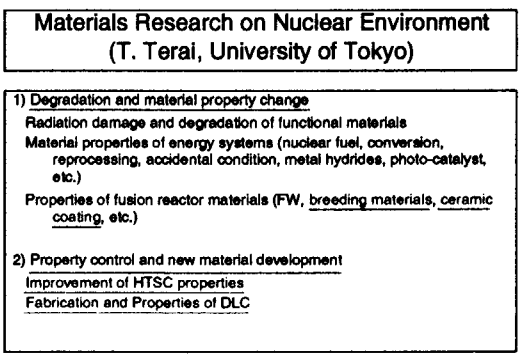


Figure 4 Materials research on nuclear environment leaded by T. Terai in the university of Tokyo.

The first is the properties of tritium breeding materials used in the fusion reactor system. Tritium is produced from Li which would be used as a nuclear fuel for D-T fusion reactors. The tritium breeding materials are divided into solid and liquid materials. The former is mainly oxide ceramic including Li_2ZrO_3, Li_2TiO_3, Li_4SiO_4 and so on. The thermal diffusivity, vapour pressure and the tritium release behavior of these materials have been investigated. The latter is metallic Li, Li alloys, LiF molten salt so called "LIFE". The

tritium release behavior from Li alloy has been studied. The compatibility between structural materials and these liquid breeders have done up to date.

Figure 5 shows the results on in-situ tritium release behavior of liquid breeding materials. It was measured in the simulation environment by using The First Neutron Source Reactor located in Tokai campus of The University of Tokyo. The chemical form of released tritium, the mass transfer coefficient of tritium from the breeder into

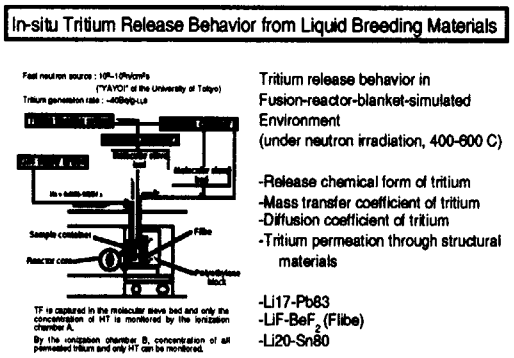


Figure 5 In-situ tritium release behavior from liquid breeding materials.

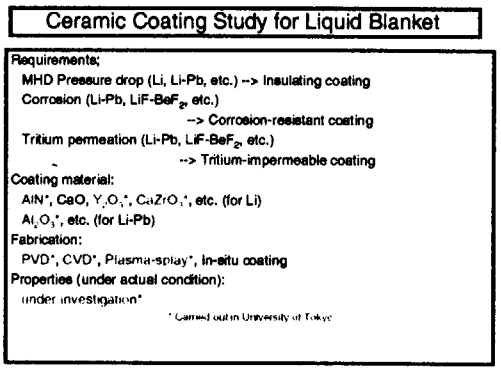


Figure 6 Ceramic coating study for liquid Blanket.

environment gas, the diffusion coefficient of tritium in breeder materials and tritium permeation rates through structural materials were evaluated. Ceramic coating is required for liquid blanket with respect to several objectives as shown in Fig.6. The first is a role as insulators for minimizing the MHD pressure drop on self-cooled liquid blanket system. The second is to improve the corrosion resistance against the severe corrosiveness of Pb-Li, LiF molten salt. The third is to minimize tritium permeability. The tritium permeation is a key issue on the application of Pb-Li and LiF molten salt blanket. According to these requirements, functional ceramic coating methods were investigated in our research group. AlN, CaO, Y_2O_3, $CaZrO_3$ are candidate coating materials for liquid Li. On the other hand, Al_2O_3 and Europe S6K are considered to be the most promising coating materials for liquid Pb-Li. The fabrication technology is also very important issue for coating the inner surface of pipes. At this moment, physical vapor deposition (PVD), chemical vapor deposition (CVD) and plasma-splay method have been evaluated for selecting the candidate of in-situ coating method.

The material properties on our developed materials have been obtained. The improvement effect on superconductor properties of HTSC ties by particle beam irradiation is shown in Fig 7. It has very high critical temperature Tc required to the practical application as high-temperature superconductors, although the low critical current density, J_c . It is needed to enhance J_c for the practical application. The magnetic flux exists as a quantized flux (fluxoid) in HTSC by forming a normal-state core. If the current flows along this direction, Fluxoid (normal electron) moves by Lorenz force and electric resistance. In that case, the superconductivity would be lost instantaneously. Therfore, fluxoid should be trapped by pinning center in a normal state area to enhance

the critical current density. To introduce the strong pinning centers is very important issue on the superconductor materials development.

There are several methods to improve the superconductor properties of HTSC. One is to form trapping defects by high energy particles irradiation as shown in Fig 7.

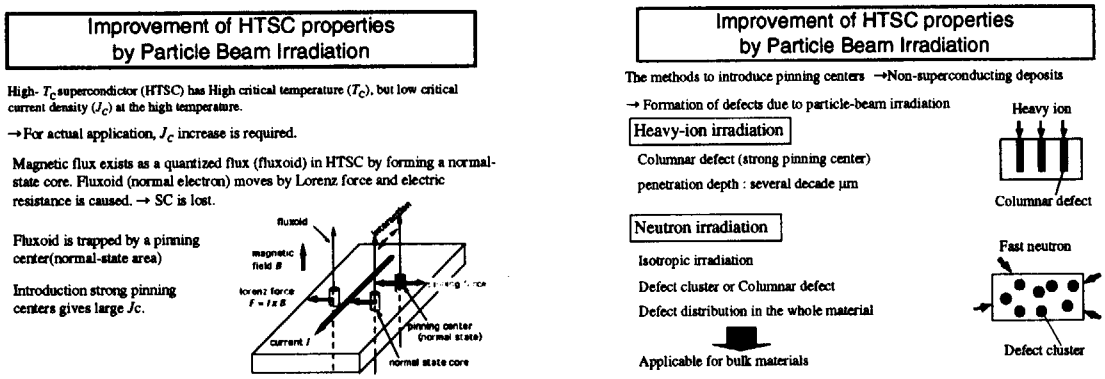


Figure 7 Improvement of super conductivity of HTSC

From our study, the formation of columnar defects in superconductor HTSC by heavy ion irradiation at high temperature, a strong pinning center was formed inside layer, although it is limited within thin surface layer of a few micrometers. On the other hand, neutron irradiation in reactors is effective means for producing uniform defect clusters in bulk materials. Threfore, we tried three methods to improve pinning property by neutron irradiation, as shown in Fig.8. The first is to use fast neutron irradiation with optimum fluence, ca. 10^{17} n/cm^2. In that case, the defect clusters will be produced in all area of the material and enhancement ratio of J_c is very high. The second is fast neutron irradiation with excess fluence followed by thermal annealing. All of the superconducting area was damaged due to the excess damage by heavy neutron irradiation, and the superconductor property is disappeared. However, it is recovered by the appropriate thermal annealing due to change of the defect characteristics such as the shape, size, and distribution. Comparing with non-irradiation materials, the superconductor current density after annealing was also markedly improved. The formation of complex defects with the appropriate size is considered to be relation to the semiconductor properties.

The third one is thermal neutron irradiation after doping with U into High-Tc superconductors. In this case, the irradiation of thermal neutron, high energy fission fragments formed by fission of U and it makes columnar defects inside/in the whole material of

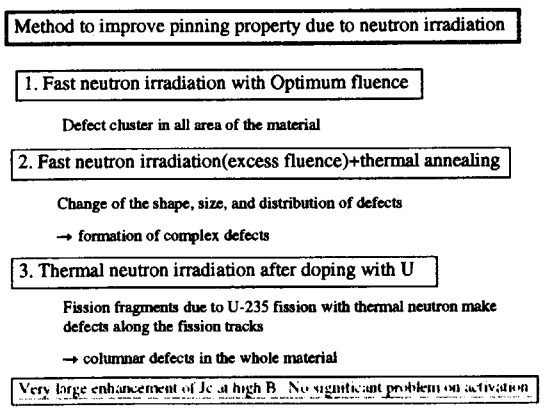


Figure 8 Method to improve property due to neutron irradiation

the specimen. From these methods, very large enhancement effect of J_c in HTSC was observed at high magnetic field and no significant problems on activation.

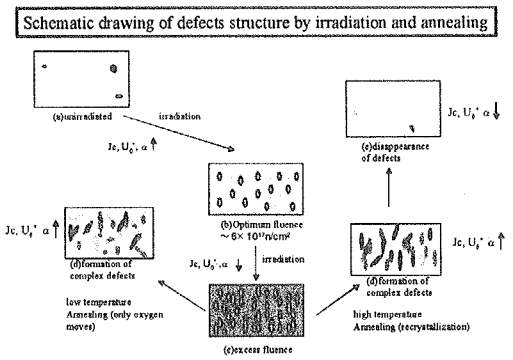


Figure 9 Defects structure by irradiation and annealing.

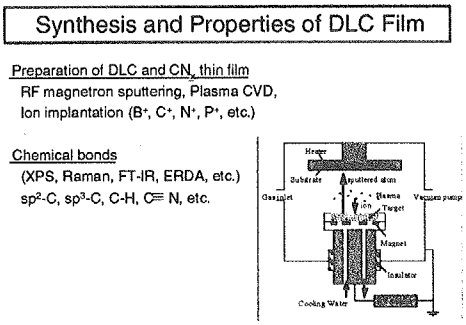


Figure 10 Synthesis and properties of DLC.

Fig. 9 shows a schematic drawing of defects structure by irradiation and annealing. Before irradiation, the specimen has some intrinsic pins in it. After neutron irradiation, there are a number of damage area produced by neutron irradiation with the optimum limit of neutron fluence of 6 x 10^{17}n/cm^2 that is not formed the large damage areas in the High-Tc Superconductors. The temperature and annealing time are very important parameters to modify the superconducting properties in this case.

The final topic is the synthesis and properties of diamond-like carbon film. DLC and CN thin films were prepared by means of magnetic sputtering and plasma CVD methods. And several ion implantation techniques were attempted to examine the characteristics of these thin films as shown in Fig.10. Characteristics of these films were examined as shown in Fig.11. The sheet resistance decreases with increasing the ratio of sp^2–C bonding. This material showed p-type semiconductor properties in some cases. The difference in electrical current with diode-like behavior on the semiconductor was observed with the direction of voltage supply as shown in Fig. 11. DLC or CN film shows very anti-reflecting properties that are dependent on the structure and impurity composition. It is possible to apply the fabrication process for the photovoltaic cell on the future. This research is carried out as a collaboration work with National Institute of Material Research Center.

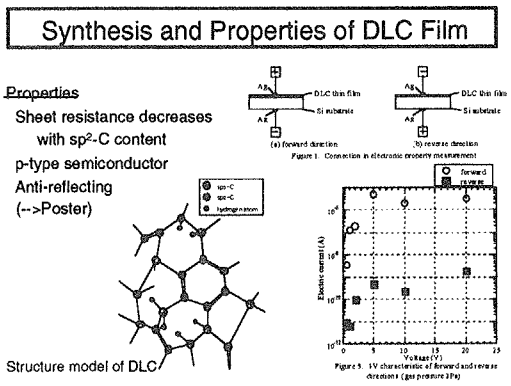


Figure 11 Synthesis and properties of DLC film

4. Summary

One of the significant technological problems on the nuclear systems is the material degradation phenomena experienced in heavily corrosive nuclear environments. On the advanced nuclear systems, to elucidate the degradation mechanism, to develop the counter-measure and monitoring techniques would be strongly required. New material processing technologies would be applied to the pressure boundary materials faced to two different environments with severe corrosiveness under irradiation. The representative techniques for surface treatments and material processing carried out in our research group were summarized as examples for expecting future progress.

JP0350239

JAERI－Conf 2003－001

1.1.2 SURFACE STUDIES OF LIQUID METALS AND ALLOYS

Robert Bastasz*
Sandia National Laboratories, Livermore, California 94551–0969, USA

Abstract

Liquid metals and alloys have been proposed for use in nuclear fusion reactors to serve as replaceable plasma-facing surfaces that remove particles and heat from reacting plasmas. Several materials are being considered for this purpose including lithium, gallium, and tin as well as some of the alloys made from these elements. In order to better understand the properties of liquid surfaces, the technique of low-energy ion scattering was used to examine the surface composition of several of these materials in vacuum as a function of temperature. Oxygen is found to rapidly segregate to the surface of several metallic liquids. The segregation process can be interpreted using a simple thermodynamic model based on Gibbs theory. In the case of an alloy of Sn and Li, Li also segregates to the liquid surface. This provides a means to produce a surface enriched in Li, which is more plasma compatible than Sn, without the need to handle large quantities of liquid Li.

Keywords: liquid metals, tin, lithium, surface segregation, low-energy ion scattering, plasma-surface interactions, magnetic fusion reactors.

1. Introduction

Liquid plasma-facing surfaces are being considered as an advanced materials option for magnetic fusion energy reactors, particularly in the divertor region where solid materials may not survive over long operating periods. Because liquid surfaces can be replenished, they offer the possibility of handling high power loads, recovering from plasma disruptions, and tolerating intense bombardment by neutrons and other plasma particles [1,2]. The low-melting temperature metals, lithium, gallium, and tin, have been selected as candidate liquid materials, based on their plasma compatibility, reactivity with fusion neutrons, and thermodynamic properties. Additionally, alloys made from these elements are also being considered, such as a binary alloy of Sn and Li.

Since the surface composition of a material can be different than its bulk composition, a question of fundamental interest is: what is the composition of a liquid plasma-facing surface? This question is of considerable practical importance for the development of fusion technology as plasma-surface interactions are necessarily influenced by surface composition. As a first step in answering this question, the surface composition of liquid lithium and a tin-lithium alloy have been examined using low-energy ion scattering (LEIS) spectroscopy. This technique can provide top-layer analysis of both solid and liquid materials, enabling the outer surface composition to be measured and distinguished from the subsurface composition. There apppear to be no previous reports of using LEIS to analyze liquid metal surfaces, although it has been used to a limited extent for surface analysis on liquid organic materials [3–6].

* Tel: +1 925 294–2013, Fax: +1 925 294-3231, E-mail: bastasz@sandia.gov

2. Experimental

2.1 Sample Preparation

Preparing clean surfaces of liquid Li and Sn-Li requires several procedures to avoid the buildup of oxide layers. For the Li measurements, high-purity (99.9%) Li foil was supplied in Ar-filled ampoules, which were opened in a dry Ar atmosphere glove box. Li disks (8 mm diameter and 50 μm thick) were cut from the foil and mounted on a sample assembly containing a resistance heater and thermocouple. The sample assembly was loaded and sealed inside a hermetic transfer canister. The canister was then transported to the analytical apparatus and attached to a load lock, which allowed the sample assembly to be installed on a manipulator inside the ultra-high vacuum (UHV) analysis chamber without air exposure. The solid sample surface was sputter cleaned using a rastered He^+ beam and then heated to the melting point of Li (180.5 °C). After several sputtering and heating cycles, the liquid Li surface appeared smooth and highly reflective.

For the Sn-Li alloy measurements, the alloy was prepared in-situ by melting a stack of high-purity Sn (99.99%) and Li metal foils. Referring to the molar volumes of Li and Sn, (13.1 and 16.3 cm^3, respectively) one finds that a 5:1 Sn-Li foil thickness ratio gives the desired alloy composition of $Sn_{0.8}Li_{0.2}$. Based on the Sn-Li binary phase diagram, this composition leads to the formation of a phase with a melting temperature near 222 °C [7]. The preparation procedure was similar to that used for pure Li. Several layers of 250 μm Sn foil and 50 μm Li foil were placed in contact and punched into 8 mm disks. The outer layers were made from Sn to reduce Li evaporation during reaction of the metals. Alloy formation was observed to be exothermic and commenced near the melting point of Li.

2.2 LEIS Measurements

Low-energy ion scattering data were obtained in a UHV apparatus with a base pressure of <90 nPa. The apparatus consists of an ion source connected to an analysis chamber, which contains a sample manipulator and a hemispherical, electrostatic, ion-energy analyzer. The ion source produces monoenergetic (ΔE <1 eV), mass-analyzed, inert-gas ion beams in the energy range between 0.1 to 3 keV. The manipulator positions the sample in front of the ion source/analyzer and provides electrical connections for temperature control and ion current monitoring. The energy analyzer is mounted on a turntable that allows the observing angle (i.e., the scattering angle) to be varied from 15° to 90°. The arrangement and the scattering process is diagrammed in Fig. 1.

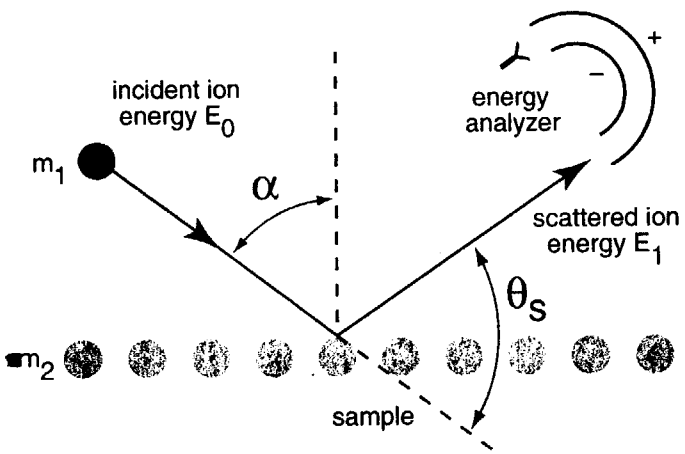


Figure 1. *Arrangement and angle definitions for LEIS measurements. The incident ion has kinetic energy E_0 initially and E_1 after scattering. α is the incidence angle, and θ_s is the scattering angle. For an incident ion with mass m_1, the surface atom mass m_2 can be determined from $m_2 = m_1(1 + E_s - 2\sqrt{E_s}\cos\theta)$ / $(1 - E_s - Q_n)$ where $E_s = E_1/E_0$ and Q_n accounts for any inelasticity in the collision.*

3. Results

3.1 Liquid Li

Energy spectra of He^+ scattering from the surface of Li in the solid and liquid phases are shown in Fig. 2. Peaks in the spectra result from the energy loss of He^+ due to quasi-elastic collisions with surface atoms of different masses, which can be identified using the kinematic relationship given in Fig. 1. For in-situ sputter-cleaned, high-purity (99.9%) Li samples, the solid surface was almost entirely composed of Li. Upon melting the clean Li sample, two effects were observed. First, the intensity of He^+ scattering from Li surface atoms increased by almost a factor of two. Second, the presence of oxygen at the liquid surface was detected. The only atom species observed at the liquid surface were Li and O. No evidence for higher atomic-number elements on the liquid surface was found. Based on the experimental data and calculated cross sections for 1 keV He^+ scattering, the estimated composition of the liquid at 300 °C was about 90% lithium and 10% oxygen, indicating a bulk-to-surface segregation ratio on the order of 100.

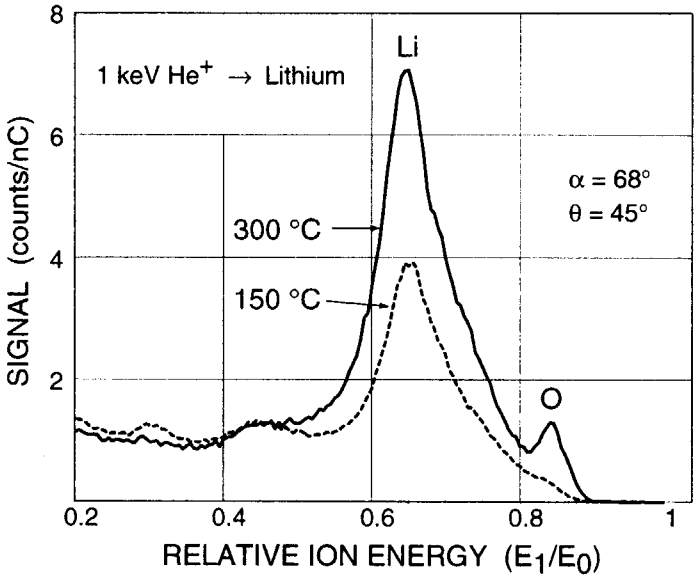


Figure 2. *LEIS energy spectra for 1 keV He^+ incident on solid (150 °C) and liquid (300 °C) Li. Upon melting the He^+ scattering intensity from Li increases and oxygen appears at the liquid Li surface. The minor peaks seen near 0.31 and 0.45 relative energy are due to recoil emission of O^+ and Li^+ ions.*

The surface composition of liquid Li was monitored as a function of temperature and the results are shown in Fig. 3. For these measurements, the sample was heated to 300 °C and then allowed to cool down across the liquid to solid phase transition with the heater switched off. This procedure prevented any perturbing effects, such as outgassing or changing electromagnetic fields, from interfering with the measurements due to the operation of the heater. The data were recorded in a multiplex mode by setting the analyzer to detect ions at a set of energies corresponding to the peaks in the ion energy spectrum. The signal at each ion energy was integrated for a short period and recorded along with the temperature of the sample. This process was repeated as the sample cooled. The results indicated that the surface oxygen level was substantially higher while the sample was in the liquid phase than in the solid phase. A sharp change in surface composition occurred near the freezing point of the Li. The Li scattering and recoil signals remained relatively constant in both phases.

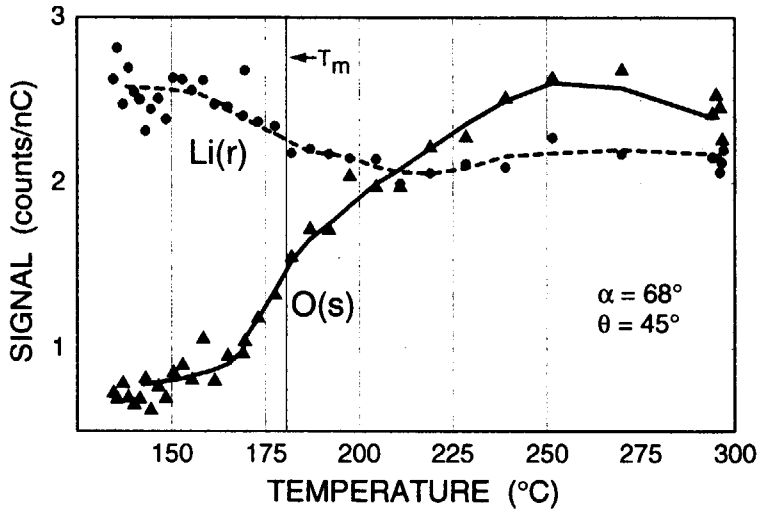


Figure 3. *Variation in oxygen coverage on a lithium surface as a function of temperature. The intensity of ion scattering from O and recoil emission from Li were monitored while the sample was bombarded with a 500 eV He^+ beam. Oxygen is more abundant on the liquid surface.*

3.2 Liquid Sn-Li

For the Sn-Li system, LEIS measurements were first made of the outer Sn layer on the stacked foil sample before melting. An ion energy spectrum of the clean Sn surface is shown in Fig. 4, along with a spectrum of pure Li. The observation angle for the measurements was chosen after taking into account the tradeoff between sensitivity and mass resolution. Scattering signals are stronger at smaller angles, since collision cross sections increase with decreasing scattering angle. In contrast, mass resolution increases with scattering angle. It was found that detecting scattered ions at an angle of 45° provided good sensitivity to Li and produced scattering peaks from Li, O, and Sn that were well separated.

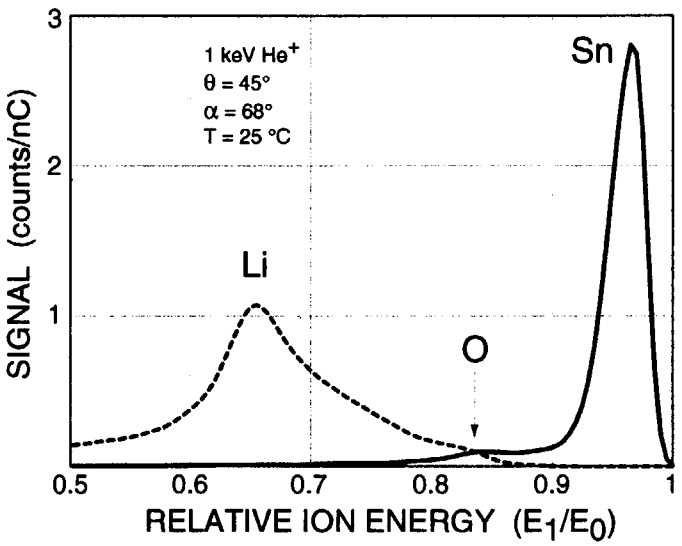


Figure 4. *LEIS energy spectra for 1 keV He^+ incident on solid, sputter-cleaned Li and Sn. The Sn signal is more intense than the Li signal due to the increase in the scattering cross section with atomic number. The position where the scattering signal from surface O occurs is indicated.*

After preparing the liquid Sn-Li alloy using the procedure described above, the surface composition of the sample completely changed. This is illustrated in Fig. 5, which shows LEIS spectra recorded before and after melting the sample. Immediately upon melting, Sn disappeared from the surface and only Li and O were detected.

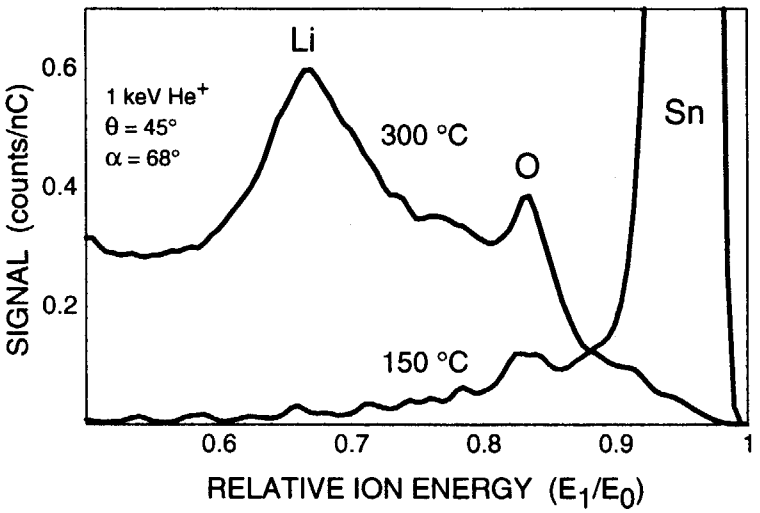


Figure 5. *LEIS spectra before (150 °C) and after (300 °C) melting the Sn-Li sample. Initially, the liquid alloy surface is entirely composed of Li and O. The peak intensity of the scattering signal from Sn on the solid sample is off-scale at 6 counts/nC.*

With time, Sn reappeared at the surface and an equilibrium was reached after about 2×10^3 s at 250 °C. Ion energy spectra were recorded after equilibration at each of several temperatures. The peak areas of the scattering signals were computed after subtraction of an inelastic scattering background and the areas were divided by the corresponding scattering cross sections, which were calculated using an appropriate screened Coulomb potential. This procedure enabled the equilibrium composition of the liquid surface to be estimated as a function of temperature. The results are shown in Fig. 6. The surface coverage of Li increased with temperature and it appeared to be the major component at temperatures from 400 °C to at least 500 °C. When the sample was briefly heated to 800 °C, significant Li evaporation occurred. Consequently, only limited LEIS measurements were made above 500 °C, which indicated that the Sn surface coverage increased at higher temperatures.

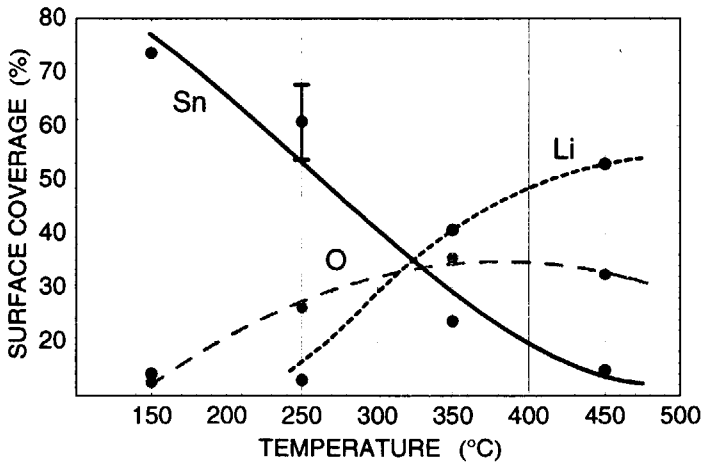


Figure 6. *Equilibrium surface composition of a Sn-Li alloy as a function of temperature as determined from LEIS spectra. The liquid surface is enriched in Li and O. The curves are guidelines only.*

4. Discussion

The liquid surfaces of Li and Sn-Li are affected by segregation of impurities, such as O, and in the case of $Sn_{0.8}Li_{0.2}$, by segregation of the minor alloy component Li. The formation of a surface layer with altered composition can be predicted by Gibbs segregation theory[7]. Species that lower the surface tension of a material tend to segregate to its surface. At equilibrium, the surface energies of the various components are balanced, leading to a surface composition that may be quite different than the bulk composition. For the materials in the present study, the surface tensions of the constituent elements as liquids are in the order O<Li<Sn, with values of 20, 390,

and 525 mN/m, respectively [9–11]. Consequently, one predicts O to segregate to the surface of Li, and O and Li to segregate to the surface of Sn, in agreement with the present results. Similar segregation effects have also been observed with X-ray reflectivity measurements on liquid Ga-In and Ga-Bi alloys [12, 13].

The rate at which segregation occurs is determined by the diffusivity of the segregating components. In a liquid, it is expected that solutes will move at least as fast as the self-diffusion rate. In liquid Li, the self-diffusivity is of the order of 10^{-4} cm^2/s at 375 °C [14]. This high value suggests that segregation occurs rapidly, on a time scale that is much shorter than that of the measurements reported here (10 s).

The composition of a liquid surface is determined not only by segregation, but also by processes that remove surface atoms. Two mechanisms by which this occurs are sputtering and evaporation. The ion beam used to analyze the surface had a small enough flux ($<10^{14}$ /cm^2-s) to not significantly alter the surface during the measurements. Surface oxide evaporation rates are rather small, but Li evaporation can be significant. At 325 °C, Li evaporates at about 1 monolayer/s (10^{15} /cm^2-s) and the evaporation rate increases strongly with temperature. At a sufficiently high temperature, the evaporation rate can exceed the segregation rate, leading to a depletion of surface Li in the Sn-Li alloy. The combined effects of segregation, sputtering, and evaporation can be modeled and for the case of Sn-Li, regimes are found in which the surface is enriched in either Li or Sn, depending on the incident particle flux and temperature [2]. Above 700 °C, a Li enriched surface will not persist.

There are several implications of these measurements in considering the use of liquid metals in a fusion environment. The following comments apply mainly to the use of liquids in the divertor region of a magnetic fusion reactor, where a flowing liquid surface would interact directly with the plasma. First, oxygen segregation and sputtering is expected to be an initial, but perhaps transient, source of plasma contamination for many, if not all, liquid systems. A conditioning procedure, such as with a He glow discharge, may be needed prior to fusion plasma operation to reduce surface oxygen content to an acceptable level. Removal of O from liquid surfaces exposed to a plasma is expected to readily occur as the O segregates and is sputtered away. If there are not additional sources of O in the liquid system or in the plasma, the liquid should become purified with continued plasma operation. Second, the surface composition of liquid Sn-Li is initially enriched in Li as well as O. This is expected to lower the flux of Sn initially sputtered from the liquid surface by plasma particles. However, at high incident particle fluxes or high surface temperatures, the segregated layer can be quickly removed through sputtering or evaporation. This may limit the allowable plasma exposure time and require a fast flow rate for a liquid Sn-Li surface, in order to preserve the Li-enriched layer.

It is possible that the segregation behavior of Li to liquid Sn surfaces could be used to advantage. Since Sn has several desirable characteristics in comparison to Li (e.g., lower chemical reactivity, lower vapor pressure, lower cost), it may be a more tractable working fluid for a divertor component. However, a significant disadvantage is the high atomic number of Sn (50), which causes it not to be tolerated in high concentrations as an impurity in fusion plasmas. By using a Sn-Li alloy or by adding small amounts of Li to pure liquid Sn, it may be possible to produce a Li-enriched plasma-facing surface with better plasma compatibility than would be achievable with Sn alone. This would reduce the need to process and handle large quantities of liquid Li in the reactor.

5. Summary

The surface composition of the liquids Li and Sn-Li, two advanced materials being considered for use inside magnetic fusion reactors, were studied using LEIS. Oxygen segregates to both Li and

Sn-Li surfaces and lithium segregates to the Sn-Li surface. The driving force for this segregation appears to be the reduction of surface energy, as expected from a consideration of the surface tension of the liquid elements. Surface oxygen is a source of plasma contamination, but the segregation of Li could be an advantageous property for the use of Sn-Li or Sn in the fusion environment.

Acknowledgments

The expert technical assistance of J. A. Whaley in performing the experiments is gratefully acknowledged. This work was supported by the US Department of Energy under contract DE-AC04-94AL85000.

References

[1] R. F. Mattas, et al., Fusion Technol. **34**, 345 (1998).
[2] R. Bastasz and W. Eckstein, J. Nucl. Mater **290-293**, 19 (2001).
[3] M. Tassotto, T. J. Gannon and P. R. Watson, J. Chem. Phys. **107**, 8899 (1997).
[4] G. Andersson and H. Morgner, Surf. Sci. **405**, 138 (1998).
[5] T. J. Gannon, M. Tassotto, and P. R. Watson, Chem. Phys. Lett. **300**, 163 (1999).
[6] G. Andersson and H. Morgner, Surf. Sci. **445**, 89 (2000).
[7] *Binary Alloy Phase Diagrams*, (Amer. Soc. Metals, Ohio, 1986) p. 1504.
[8] J. W. Gibbs, *The Scientific Papers of J. Willard Gibbs, Vol. 1*, (Longmans, New York, 1906), p. 219.
[9] C. R. Tipton, Ed., *Reactor Handbook* (Interscience, New York, 1960) ch. 49.
[10] A. Zangwill, *Physics at Surfaces* (Cambridge Univ. Press, England, 1988) p. 11.
[11] P. Dashora, P. Karnawat, and U. Parnami, Physica Scripta **64**, 554 (2001).
[12] M. J. Regan, et al., Phys. Rev. B **55**, 15874 (1997).
[13] E. DiMasi, et al., J. Phys.: Condens. Matter **12**, A209 (2000).
[14] A. Feinauer, G. Majer, and A. Seegar, Defect and Diffusion Forum **143**, 881 (1997).

JP0350240

1.1.3 HIERARCHICAL MODELING OF ACTIVE MATERIALS

Minoru Taya[1*],
Professor and Director,
Center for Intelligent Materials and Systems
Department of Mechanical Engineering
University of Washington, Box 352600
Seattle, WA 98195-2600
U.S.A

Abstract

Intelligent (or smart) materials are increasingly becoming key materials for use in actuators and sensors. If an intelligent material is used as a sensor, it can be embedded in a variety of structure functioning as a health monitoring system to make their life longer with high reliability. If an intelligent material is used as an active material in an actuator, it plays a key role of making dynamic movement of the actuator under a set of stimuli.

This talk intends to cover two different active materials in actuators, (1) piezoelectric laminate with FGM microstructure, (2) ferromagnetic shape memory alloy (FSMA). The advantage of using the FGM piezo laminate is to enhance its fatigue life while maintaining large bending displacement, while that of use in FSMA is its fast actuation while providing a large force and stroke capability.

Use of hierarchical modeling of the above active materials is a key design step in optimizing its microstructure for enhancement of their performance. I will discuss briefly hierarchical modeling of the above two active materials. For FGM piezo laminate, we will use both micromechanical model and laminate theory, while for FSMA, the modeling interfacing nano-structure, microstructure and macro-behavior is discussed.

1. Introduction

Active Materials exhibit strains or property change upon a set of stimuli, thus ideal materials for use in sensors and actuators. This talk focuses only on the actuator materials. The scale of the actuators range from robotic arms to micron-sized MEMS. Design of new actuators with unique properties must cover the material design, actuator design and system design.

Hierarchical modeling of active materials is a key step in optimization of the microstructure of the active materials toward their best performance in use environment. The active materials that

* Corresponding author. Tel: 206-685-2850 Fax: 206-685-8047
E-mail address: tayam@u.washington.edu

are reviewed in this article are FGM piezoelectric composites and ferromagnetic shape memory alloys (FSMA).

Fig.1 illustrates popular active materials where (a) and (b) denote, respectively the stress-strain, and actuation time-strain relations for piezoceramics, shape memory alloys (SMAs) and electro-active polymers. The arrow sign in Fig.1. indicates the direction of improvement needed for these active materials.

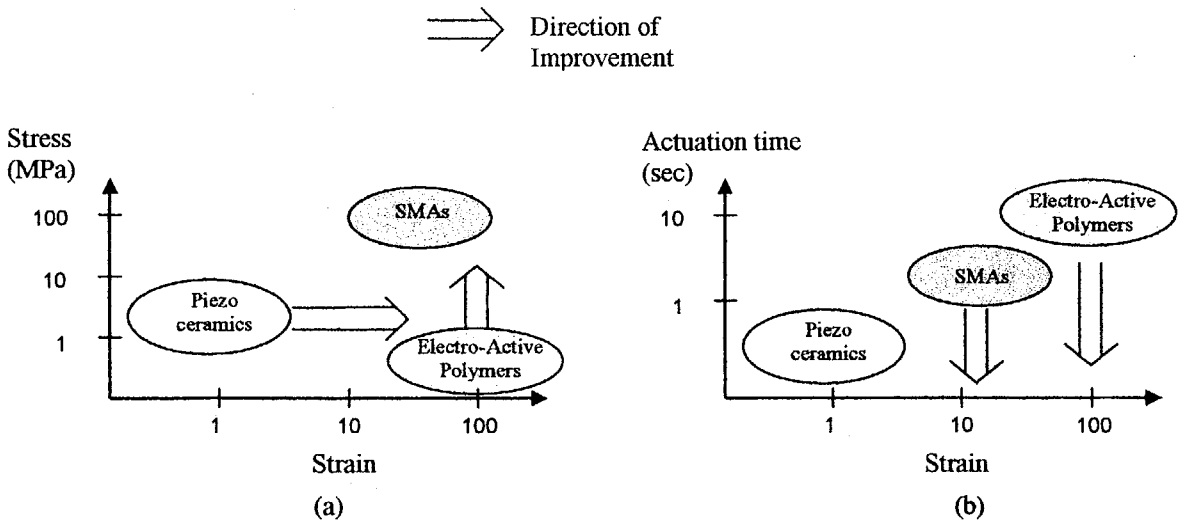


Fig. 1. Performance of three active materials, (a) range of stress and strain, (b) range of actuation speed and strain. The arrow sign denotes the direction of improvement in the performance of the active materials.

2. FGM Piezo Composites

The piezo actuators for bending mode are made of piezo monomorph bonded to a substrate, Fig. 2(a) or bimorph, Fig. 2(b) where the top and bottom piezo plate with identical piezo-elastic properties are bonded with opposite polarity such that the top expands while the bottom shrinks, thus providing bending mode displacement. Despite large bending displacement obtained by the bimorph piezo actuator, there exists a large stress field induced by the large misfit strain at the interface between the top and bottom plates, limiting the use life of the bimorph piezo actuator. The concept of functionally graded microstructure (FGM) was originally introduced to diffuse otherwise large thermal stress that exists at the interface between ceramic and metal plates which are bonded [1-3]. To reduce the induced stress field at the interface between the top and bottom plates in the bimorph piezo actuator, we proposed use of FGM [4].

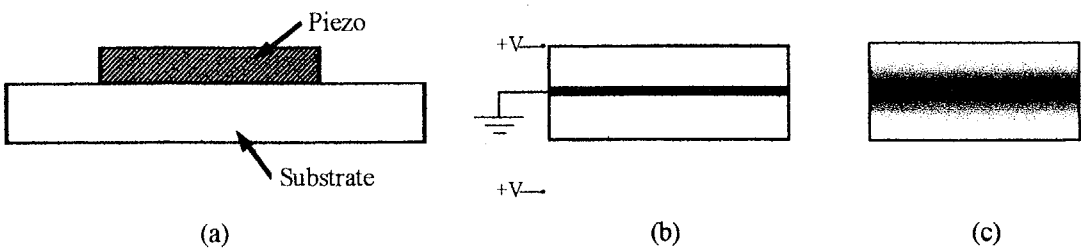


Fig. 2. Piezo actuators (a) monomorph (b) bimorph and (c) FGM bimorph

To tailor the optimum FGM layering, one needs to use a hierarchical modeling for such as FGM piezo composite actuator. The hierarchical modeling consists of (1) micromechanic model based on Eshelby's method [5, 6] and (2) laminate plate model [8, 9]. The micromechanic model is to predict the effective electroelastic properties of each lamina for a given set of constituent parameters (volume fraction of piezomaterials, their electroelastic properties, and shape). The detailed micromechanical modeling is described elsewhere [6,7] while a brief statement of the laminate plate model is given below.

The in-plane constitutive equations of a piezoelectric material of class 6mm type can be obtained from eq. (1) as

$$\begin{Bmatrix}\sigma_x\\ \sigma_y\\ \sigma_{xy}\end{Bmatrix}_i = \begin{bmatrix}\overline{Q}_{11} & \overline{Q}_{12} & 0\\ \overline{Q}_{21} & \overline{Q}_{22} & 0\\ 0 & 0 & Q_{66}\end{bmatrix}_i \begin{Bmatrix}\varepsilon_x^\circ + z\kappa_x - \alpha_{11}\Delta T\\ \varepsilon_y^\circ + z\kappa_y - \alpha_{11}\Delta T\\ \gamma_{xy}^\circ + z\kappa_{xy}\end{Bmatrix} - \begin{bmatrix}0 & 0 & \overline{e}_{31}\\ 0 & 0 & \overline{e}_{32}\\ 0 & 0 & 0\end{bmatrix}_i \begin{Bmatrix}0\\ 0\\ E_z\end{Bmatrix}_i \tag{1}$$

where

$$\begin{aligned}\overline{Q}_{ij} &= C_{ij} - \frac{C_{i3}}{C_{33}}C_{j3}\\ \overline{e}_{ij} &= \frac{C_{j3}}{C_{33}}e_{33} - e_{ij}\end{aligned} \tag{2}$$

It is noted here that $\overline{Q}_{ij}$, $\overline{e}_{ij}$ are the reduced stiffness constants and reduced piezoelectric constants that are modified by the assumption of plane stress and where $\varepsilon_x^\circ, \varepsilon_y^\circ$, and ε_{xy}° are the in-plane strain components at mid-plane, $z = 0$, κ_x, κ_y, and κ_{xy} are the curvatures of the plate.

Each piezoelectric lamina is considered a capacitor whose electric field corresponds to its dielectric constant. The electric field in each layer of multi layer FGM piezoelectric can be obtained by considering the multi layers piezoelectric FGM as a series of condensers. The relationship between the electric capacity and the voltage is given as

$$C_t = \frac{Q}{V_t} \tag{3}$$

where C_t is the capacitance, Q is the charge, and V_t is the total voltage. The total capacitance in a series of capacitance is found as

$$\frac{1}{C_t} = \sum_{i=1}^{n}\frac{1}{C_i} = \sum_{i=1}^{n}\frac{d_i}{\varepsilon_i} \tag{4}$$

where d_i is the thickness of each capacitance or lamina as in piezoelectric FGM and ε_i is the dielectric constant for each lamina. The electric capacity in each layer will then be

$$C_i = \frac{Q}{V_i} = \frac{\varepsilon_i}{d_i} \tag{5}$$

Substituting eq.(3) and (4) into eq.(5) results in

$$V_i = Q\frac{d_i}{\varepsilon_i} = V_t \frac{d_i}{\varepsilon_i \sum_{l=1}^{n} \frac{d_l}{\varepsilon_l}} \tag{6}$$

The electric field in each layer can then be

$$E_i = \frac{V_i}{d_i} = V_t \frac{1}{\varepsilon_i \sum_{l=1}^{n} \frac{h_l - h_{l-1}}{\varepsilon_l}} \tag{7}$$

In-plane stress resultants (N_x, N_y, N_{xy}) and stress couples (M_x, M_y, M_{xy}) are defined as

$$\{N,M\} = \sum_{i=1}^{n} \int_{h_{i-1}}^{h_i} \{\sigma\}(dz, zdz) \tag{8}$$

Substituting eqs. (8) into (1), we obtain

$$\begin{bmatrix} N \\ M \end{bmatrix} = \begin{bmatrix} A & B \\ B & D \end{bmatrix} \begin{Bmatrix} \varepsilon^o \\ \kappa \end{Bmatrix} - \begin{bmatrix} N^E \\ M^E \end{bmatrix} \tag{9}$$

where

$$[A,B,D] = \sum_{i=1}^{n} \int_{h_{i-1}}^{h} [\overline{Q}]_i (dz, zdz, z^2 dz) \tag{10}$$

$$[N,M]^E = \sum_{i=1}^{n} \int_{h_{i-1}}^{h_i} [\overline{e}]_i \{E\}_i (dz, zdz) \tag{11}$$

In the above derivation, we assumed that the piezoelectric laminated plate is subjected to constant temperature and constant electric field. Under the constant applied electric field ($E_x = E_y = 0$, $E_z \neq 0$) and constant temperature ($\Delta T = 0$) in the absence of applied mechanical loading, we obtain from eq.(9) the strain of the mid-plane strain curvature as

$$\begin{bmatrix} \varepsilon^0 \\ \kappa \end{bmatrix} = \begin{bmatrix} a & b \\ b & d \end{bmatrix} \begin{bmatrix} N^E \\ M^E \end{bmatrix} \tag{12}$$

where

$$\begin{bmatrix} a & b \\ b & d \end{bmatrix} = \begin{bmatrix} A & B \\ B & D \end{bmatrix}^{-1} \tag{13}$$

The numerical results of the hierarchical modeling applied to standard bimorph (Fig. 2(b)) and the bimorph FGM of type A and B, see Fig.3 are listed in Table I.

Type of FGM microstructure	Standard bimorph, C91 Figure 7.2(a)	Standard bimorph, C6, Figure 7.2(a)	Bimorph FGM, C91-C6 Type B,	Bimorph FGM, C91-C6 Type A,
Applied Voltage (V)	33	33	33	33
Laminate thickness (mm)	0.67	0.67	0.67	0.67
No. of layers	2	2	6	6
Layer thickness (mm)	0.33 Pl = 0.01	0.33 Pl = 0.01	0.11 Pl = 0.01	0.11 Pl = 0.01
Electric Field (V/mm)	100	100	100	100
Curvature (1/m)	0.152	0.102	0.143	0.112
Max. σ_x (MPa)	3.08	1.91	1.89	3.1
Deflection (μm) for plate length 50mm	47.5	31.9	44.8	29

Table I Comparison of out-of-plane displacement and in-plane stress in various types of piezo-composite plates

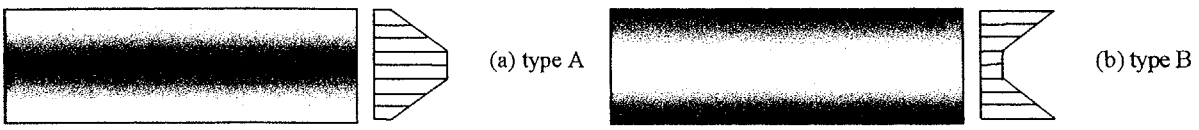


Fig. 3. Electroelastic properties distribution in FGM-bimorph

3. Hierarchical Modeling of Ferromagnetic Shape Memory Alloys (FSMA)

Since the pioneering work of Webster et al [5], there have been a number of works reported on ferromagnetic shape memory alloys (FSMA) with a promise of designing these into fast

responsive actuators. We proposed a new mechanism, "hybrid mechanism" which is a sequence of chair reaction; applied magnetic field gradient, magnetic force, stress-induced martensite phase transformation, softening of a FSMA, resulting in a large displacement [6]. We selected a polycrystalline FePd alloy as a promising FSMA as this alloy can be processed into any 3D shapes. To elucidate the proposed hybrid mechanism, we proposed a hierarchical modeling composed of nanomodel based on Bain Correspondent Varianto (BCV_s) and micromechanic model, Fig.4 [7].

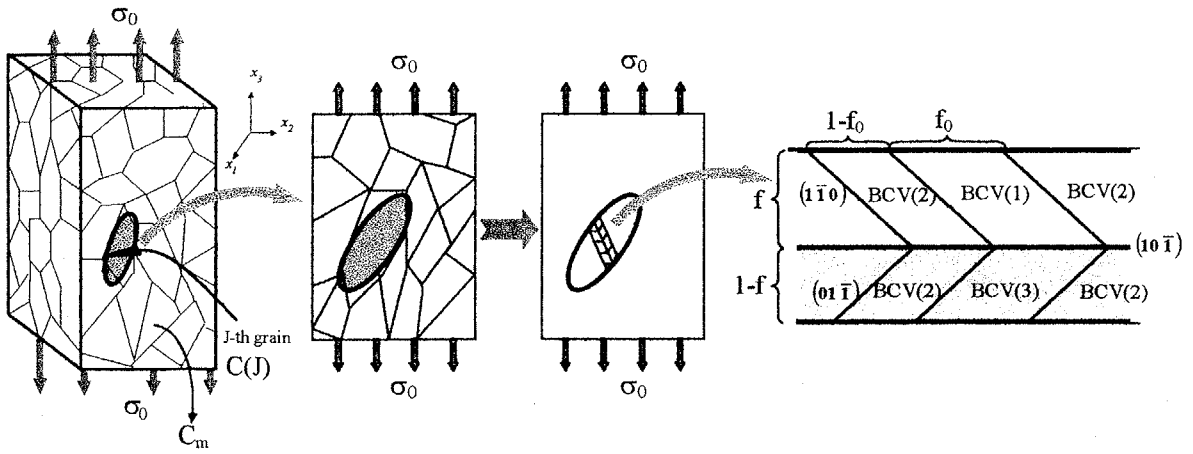


Fig.4 Hierarchical Modeling of Shape Memory Alloy (a) J-th grain embedded in a polycrystal with stiffness C_m, (b) J-th grain with C(J) converted to (c) equivalent inclusion with C_m.

The nano-model is used to explain the nano-twin structure observed in a Fe-Pd alloy, Fig.4 (a) and Fig.5 (c). While the micromechanic model based on the micro-twin structure of Fig. 4 (b)-(c) is used to predict the stress strain curve of a polycrystalline Fe-Pd, Fig.6.

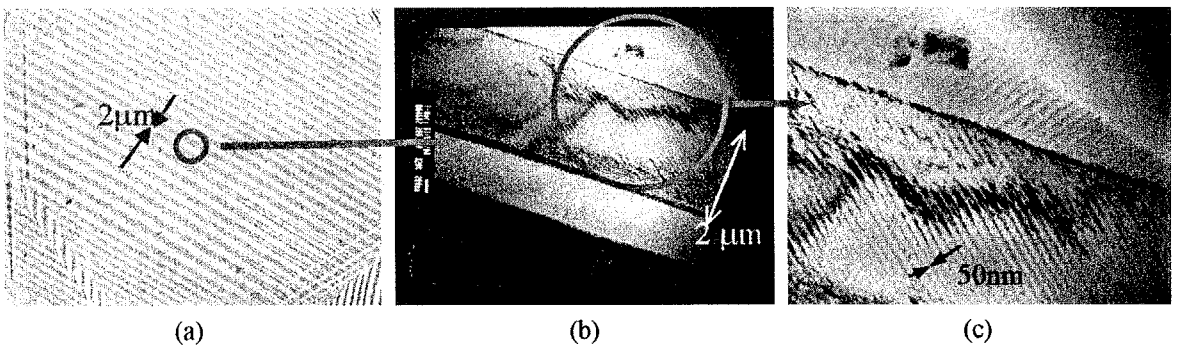


Fig.5 Structure of martensite in polycrystalline Fe-Pd (a) micro twins (b) nano twins (c)

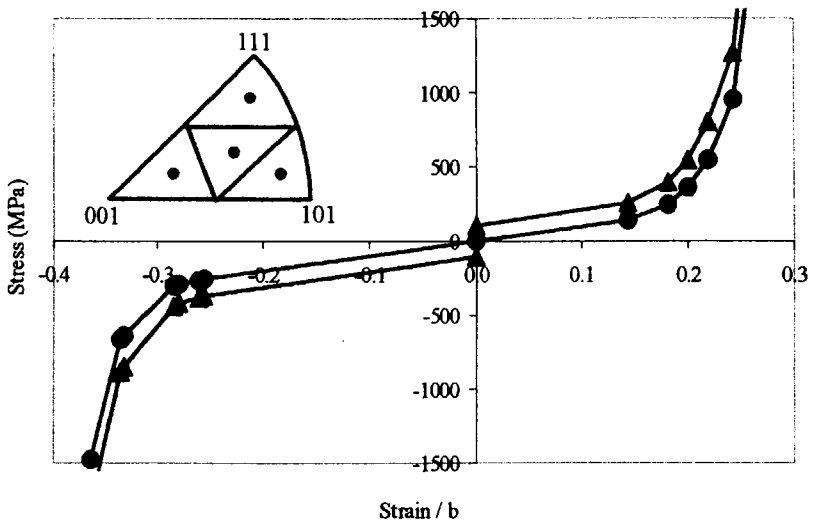


Fig. 6 Stress-strain curves of a polycrystalline Fe-Pd having 4 types of grains with (closed triangle) and without (closed circle) energy dissipation (k = 2MPa).

Acknowledgements

The author is thankful to the NEDO grant to the University of Washington on Smart Materials and Structures, and also to the Air Force Office of Scientific Research (F49620-02-1-0028).

References

[1] A. Kawasaki, R. Watanabe, J. Jpn Insti. Metal **51**, 525-529 (1987).
[2] M. Taya, J.K. Lee and T. Mori, Acta Mater., 45, 6, 2349-2356 (1997).
[3] T. Hirai, Functionally gradient materials, in : R.J. Brook (Ed.), Processing of Ceramics, Part 2, Materials Science and Technology, vol. 17B, VCH, Weinheim, 293-341 (1996).
[4] A. Almajid, M. Taya, S. Hudnut, Int. J. Solids Struct. **38**, 3377-3391 (2001).
[5] P. J. Webster, K.R.A. Zrebeck, S.L. Town and M.S. Peak, Phil. Mag. **49**, 295- (1984).
[6] H. Kato, T. Wada, T. Tagawa, Y. Liang, and M. Taya, Proceedings of the 50th Anniversary of Japan Society of Materials Science, Osaka, Japan, May 21-26, 296-305 (2001).
[7] Y. Liang, T. Wada, T. Tagawa, and M. Taya, Proceedings of SPIE Meeting, San Diego, March 17-21, 2002, in press.

This is a blank page.

1.2 Chemical Reaction and Thermodynamic

Chair: J. Konys

(Forschungszentrum Karlsruhe FZK, Germany)

Y. Shirai

(Osaka University, Japan)

This is a blank page.

JP0350241

JAERI－Conf 2003－001

1.2.1 CORROSION AND COMPATIBILITY OF STRUCTURAL MATERIALS IN LIQUID LEAD ALLOYS

Jürgen Konys, Georg Müller

Forschungszentrum Karlsruhe, P.O. Box 3640, D-76021 Karlsruhe, Germany

Abstract

The paper describes investigations of the behavior of structural materials in both eutectic lead alloys, Pb-17Li as the liquid breeder within the European WCLL-concept for Fusion Reactors and Pb-55Bi as a possible spallation target and coolant of future Accelerator Driven Systems (ADS) for the transmutation of minor actinides and long-lived fission products from nuclear waste.

Ferritic-martensitic steels of the 8-10 wt.-% Cr type are considered as structural materials for the use in liquid Pb-17Li at temperatures up to 500°C. Steels like MANET I, Optifer, F82H-mod. and EUROFER are investigated in the flowing liquid metal over a long period of time. Due to the specific physical chemistry of Pb-17Li, dissolution corrosion is the major corrosion mechanism of iron-based alloys. No oxide formation on steel surfaces can occur due to the very low oxygen potential in Pb-17Li. Therefore, only coatings could be a solution to minimize corrosion effects, at medium (500°C) and higher operational temperatures (650°C) of advanced blanket concepts.

Ferritic-martensitic and austenitic steels are considered as potential structural materials for ADS application, too. But the high nickel solubility in Pb-55Bi limits the use of unprotected austenitic steels to temperatures of about 400°C. Because of the much higher oxygen potential of Pb-55Bi, a totally different strategy of minimizing corrosion must be applied. By using active oxygen control, a desired oxygen activity (concentration) will be adjusted in the liquid metal via gas phase equilibrium. If the oxygen activity of the liquid metal is set in the right "window" of the corresponding thermodynamic properties, a controlled formation of oxide layers on the steel surfaces will be found. These in-situ formed oxides can act as corrosion barriers and make the use of high-nickel alloys possible, even at temperatures of around 600°C.

Keywords: Liquid metal corrosion, Pb-17Li, Pb-55Bi, steels, surface treatment, oxide layer

[1]1. Introduction

The application of liquid lead alloys for heat transfer purposes in energy conversion systems is based on their good heat-transfer properties. The eutectic melt with 17 at.-% lithium, which has a melting point of 235°C, is considered as an attractive breeding material for future fusion reactor concepts (water-cooled lead-lithium: WCLL). Various studies have been carried out exposing steel samples to Pb-17Li under static and dynamic conditions [1-5]. Two classes of steels have been mainly investigated: austenitic and ferritic steels. The temperatures have been varied between 400 and 550°C. Generally, no grain boundary attack was observed. It was found that austenitic steels have a poor resistance in Pb-17Li because of the high solubility of nickel in the melt [6, 7]. For ferritic steels, the corrosion after a more or

[1] Corresponding author. Tel: +49-7247-82-3720 Fax: +49-7247-82-3956
E-mail address: juergen.konys@imf.fzk.de

less pronounced incubation period is governed by uniform dissolution of iron and chromium at a rate that is distinctly less than for nickel [2, 5], as in the case of austenitic alloys. This behavior recommends ferrites as the structural material in a liquid breeder blanket design. According to the requirements to use low activation steels as structural materials, ferritic-martensitic 7-10% Cr steels were developed for the application in fusion reactors [8].

Particular nuclear properties make lead and lead alloys also very attractive for the use in accelerator driven systems (ADS) for the transmutation of plutonium, minor actinides and long-lived fission products. For this purpose protons are injected into a spallation target through a vacuum beam pipe in order to generate free neutrons by a spallation process. The spallation neutrons convert non-fissile isotopes into fissile ones (transmutation). A heavy liquid metal like lead or the eutectic lead-bismuth alloy is needed for the spallation target material to ensure efficient production of neutrons. Furthermore, the molten metal is intended to be used not only as a target but also as a coolant. It is known that the heavy metals lead and bismuth are much more corrosive than alkali metals [7, 9-10]. Corrosion effects in the 100 µm ranges are reported on ferritic Fe-Cr steels between 575 and 750°C after 3250 h of exposure to liquid lead [11]. Steel components are soluble in liquid lead in the range of $0.1 - 10^{-3}$ at.-% in this temperature region [12]. An exception exists for Ni, which has a high solubility of 2 at.-% at 600°C in lead [13]. Using the eutectic Pb-55Bi alloy instead of pure Pb increases these problems.

Experiments in Russia with liquid Pb and Pb-55Bi revealed that stable oxide scales on steel surfaces, consisting of magnetite and FeCr-spinel, prevent the dissolution attack if oxygen is dissolved in the liquid metal with a concentration of ca. 10^{-6} at.-% [14, 15]. Recent investigations of corrosion effects in stagnant liquid lead give an overview on the corrosion processes and its prevention by oxide scale formation on steel [16, 17]. The scale thickness including a magnetite layer on top and a spinel layer underneath amounts to 20 – 30 µm after 3000 h of exposure. This may impose a new problem at much longer times because the corrosion turns from dissolution attack to that of oxidation. A solution for this dilemma might be the alloying of Al into the steel surface. The incorporated Al causes formation of a thin protective alumina layer that grows very slowly and prevents also extensive oxidation of the steel.

It is well known, that active oxygen control is an effective way to reduce and control the corrosion of structural materials in pure lead and lead-bismuth [16, 18]. Due to the reaction of the dissolved oxygen with the steel surface, stable oxide layers can be formed if the oxygen potential is adjusted in a specific range. An oxygen control system in a Pb-55Bi loop requires the continuous measurement of the oxygen potential in the liquid alloy. A very suitable technique is the use of solid electrolyte oxygen sensors [19], which were developed for the use in liquid alkali metals. To prevent PbO precipitation and to support Fe_3O_4 formation, the following conditions for the oxygen potential must be established:

$$2\Delta G^0_{PbO} > RT \ln p_{O_2} > 0.5\Delta G^0_{Fe_3O_4}$$

The standard values ΔG^0 of the Gibbs energies are well known for all relevant oxides and with these values the equilibrium oxygen partial pressure region that retains the stable conditions can be calculated.

Due to the very low oxygen potential and the very low solubility of oxygen in Pb-17Li, no protecting oxides can be formed on the surface of austenitic and martensitic steels under these conditions. Hence, they are always in the "*liquid metal corrosion regime*" which results in dissolution of alloying elements into the Pb-17Li alloy. Therefore, the corrosion behavior of

steels in Pb-17Li can be considered as a "*worst case scenario*" of unprotected steels in very low oxygen-containing Pb-55Bi.

2. Experimental

2.1 Corrosion studies in Pb-17Li

For corrosion measurements in flowing Pb-17Li, the forced convection loop PICOLO is used [20]. The loop consists of a "figure-of-eight" shape with a central recuperative heat-exchanger, a test section (hot leg), a cold leg for corrosion product deposition and impurity removal, an EM-pump, flow meter, cooler and magnetic trap. Heat exchanger, main heater and the tubes of the hot section were fabricated of a ferritic 10%Cr-steel, whereas for the cold section, an austenitic CrNi-steel is used. The whole circuit is connected to a dry Ar-glove box on top of the expansion vessel. The glove box has a gas purification unit, which is able to keep the oxygen concentration below 1 vppm. The test section is a tube of 16 mm inner diameter and 440 mm in length. Cylindrical corrosion test specimens with the dimensions of 8 mm in diameter and 35 mm in length are used. They can be mounted to a stack of 16 samples, which is fixed in the central position of the test section tube. The volume flow is typically 120 l/h, which corresponds to a flow velocity of 0.3 m/s. The temperature in the test section was maintained at 480°C ± 5 K, the coldest temperature before the magnetic trap was 350°C.

2.1.1 Materials

3 ferritic-martensitic steels have been selected for corrosion testing in Pb-17Li: MANET I, F82H-mod. and Optifer IVa. The chemical composition of these steels is given in table 1. Hardening and tempering processes were carried out under vacuum. Specimens were exposed for 2000 h, 4000 h, 9000 h and 10,000 h in the eutectic melt. The corroded specimens were cut and prepared for analytical investigation by optical microscopy, SEM/EDX and line scan analysis.

2.2 Corrosion studies in Pb-55Bi

The corrosion tests in Pb-55Bi were carried out in two different non-isothermal forced convection loops at IPPE, Obninsk and at Prometey, St. Petersburg, both in Russia. The loops consist of a main heater, a cooler, a hot and a cold section, an EM-pump, a purification system, a flow meter and oxygen sensors. In the IPPE loop, two test sections are available, one at 420°C, a second one at 600°C. In case of the Prometey-loop, the experiments are performed in the hot test section at 550°C. The volume of the liquid Pb-55Bi in both loops is about 60 l. The oxygen content in the liquid Pb-55Bi of about 10^{-6} at.-% is controlled by electrochemical cells. The flow velocity of the Pb-55Bi is 2 m/s in the IPPE loop, whereas ca. 0.5 m/s are chosen in the Prometey-loop. The corrosion experiments were performed for exposure times up to 4300 h. The corroded specimens were examined by optical and scanning electron microscopy with energy dispersive x-ray analysis.

2.2.1 Materials

Materials used in the experiments are cylindrical tubes and rods of AISI 316, 1.4970 and MANET I steel of 10 mm diameter. The chemical composition of the steels is listed in table 1. A surface layer of 10 μm to 30 μm is alloyed with Al in one part of the specimens. The other part is just kept in the as fabricated state. Al alloying was achieved by wrapping Al-foil around the tube and heating at 1040°C for 0.5 h.

3. Results and discussion

3.1 Corrosion in flowing Pb-17Li

After the vacuum heat treatment before exposure to Pb-17Li, the specimens showed a chromium and manganese enrichment, which corresponds to $MnCr_2O_4$ spinel with a thickness of about 5 nm. After exposure to Pb-17Li, cross sections revealed, that the corrosive attack occurred locally, and even after longer exposure times, there were still areas without any attack. A typical corrosion pattern of the investigated steels after 6000 h is shown in fig. 1. AES investigations showed, that for areas where "no attack" occurred, a few nm thick $(Fe,Cr)_2O_3$ layer still protected the surface. After an incubation time, which can last a few thousand hours until full wetting occurs; this layer was totally dissolved into the Pb-17Li. The $MnCr_2O_4$ spinel could not be detected already after 1000 h of testing. This is due to the fact that $MnCr_2O_4$ is less protective than $(Fe,Cr)_2O_3$ [21]. Taking unattacked areas as a zero line, the metal loss could be determined on the cross sectional cuts, using optical and electron microscopy. Results of the analysis reveal an average metal loss of ca. 100 μm/a due to dissolution, whereas not much differences between the 3 steels was observed.
The cross sections of the specimens exposed up to 10,000 h looked quite similar. The surfaces are relatively smooth and show a macroscopic wave-like contour as can be seen in fig. 2 a/b. Generally, intergranular attack and formation of corrosion layers by leaching of alloying steel elements could not be detected on exposed specimens.
EPMA line scan analyses were carried out on different areas of each sample. On the surface of MANET I specimens exposed for 2000 h to Pb-17Li no enrichment of any element could be observed. On the contrary to this, an enrichment of W on top of the steel surfaces was revealed on F82H-mod. and Optifer IVa, both corroded for 2000 h. In the case of F82H-mod. the iron content decreased and the chromium content stayed relatively unchanged compared to the steel composition in this W rich region. In the case of Optifer IVa the iron content decreased as well, but the chromium content seemed to increase like the W content. After long-term exposure, the MANET I specimens tested for 9000 h did not show any enrichment of Mo, whereas for F82H-mod., a slight enrichment of W was found after 10,000 h. The thickness of the enriched layer was in the range of 7 μm, only a thick layer of solidified Pb-17Li was revealed on the steel surface. On etched specimens it was found that preferred matrix dissolution along martensitic lath boundaries occurred. It was interesting to note, that this effect was greater for MANET I than for Optifer IVa and F82H-mod.

3.2 Corrosion in flowing Pb-55Bi

The effect of liquid Pb-55Bi with 10^{-6} wt.-% of oxygen on the original AISI 316 steel specimen after 2000 h of exposure in the Pb–55Bi loop is shown in fig. 3. No attack on the surface can be seen at the SEM cross section after exposure to 420°C. The EDX analysis indicates that the steel composition is not changed in the vicinity of the surface. This points out that no dissolution took place. Probably, a thin oxide scale protects the material from dissolution attack.
During exposure to 550°C the specimen develops partly thick oxide scales consisting of a magnetite and a spinel zone underneath. The thin oxide layer observed after exposure to 420°C is maintained on some other parts of the surface. In any case no dissolution attack took place. The concentration of the steel components below the oxide layer is also not changed.
Deep liquid metal penetration and massive ablation of material by erosion is observed at 600°C on the specimen in the lower part of fig. 3. Bright inclusions consist of a Pb-55Bi alloy enriched in Bi. The penetration zone is depleted in Ni down to 1 at.-%. However, after 4000 h

severe corrosion damage is already observed at 550°C. The conclusion is, original not surface treated austenitic steel can be used as a structural material in liquid Pb-Bi only below 550°C
A completely different behavior is observed for the surface alloyed steel specimens in the loop tests. The specimens show good corrosion resistance at all temperatures. This is demonstrated by the SEM cross-sections and the overview picture for the example of AISI 316 L specimen after 2000 h of exposure in fig. 4.
The only difference between the specimens is the appearance of some pores in the NiAl interface layer between the FeAl and the Fe(Al) dissolved region of 316 L on specimens exposed to 550°C and 600°C because of outward diffusion of iron into the Fe(Al) layer. The FeAl layer on top of the specimens is maintained with the original thickness. No dissolution attack or liquid metal penetration is visible also at 600°C on both specimens. This behavior did not change at all also after 4000 h of exposure. It can be concluded since also after 4000 h of exposure no sign of attack is to be observed, surface alloying with Al can be a appropriate mean to avoid corrosion attack in liquid Pb-55Bi.

4. Conclusion

4.1 Compatibility in Pb-17Li

The corrosion mechanism of three ferritic-martensitic steels by Pb-17Li was examined. Two different processes are responsible for the corrosive attack. Firstly the passivating oxide layer on top of the steel surface is dissolved into the liquid alloy. This so-called incubation period is dependent on temperature and as well as on the flow velocity of the liquid melt. The second step is the dissolution of the steel matrix, which is characterized by a strong depletion of the steel element Fe. The remaining porous zone shows a low adherence to the steel matrix and can be easily eroded from the surface by the flowing melt. The thickness of this corrosion layer did never exceed 5 µm. Hence, no protecting character can be ascribed to the layer in which the element W is enriched.

4.2 Compatibility in Pb-55Bi

In general, the original steels without surface alloying are suitable for application in liquid Pb-55Bi below temperatures of 550°C at oxygen concentrations of $>10^{-6}$ at.-%. At higher temperatures, austenitic and ferritic-martensitic steels, surface alloyed by Al with formation of FeAl-phase at the surface have to be used. After 4000 h in Pb-55Bi, they showed no indication of any corrosion due to the protection by a thin alumina layer, which remains stable in Pb-55Bi.
In liquid Pb-55Bi the activity of Al at the surface must be low enough to minimize the solution rate of Al in Pb-55Bi and allow oxide scale formation. FeAl at the surface fulfills this requirement.

5. Acknowledgements

This work is supported by the European Community within the European Fusion Technology Programme and by the German National HGF Strategy Fund Project 01SF9926/3

6. References

[1] V. Coen, P. Fenici, Nucl. Eng. Des. / Fusion 1 (1984) 215.
[2] M. Broc, T. Flament, P. Fauvet, J. Sannier, J. Nucl. Mater. 155-157 (1988) 710.
[3] H. U. Borgstedt, H.D. Röhrig, J. Nucl. Mater. 179-181 (1991) 596.
[4] O. K. Chopra, D. L. Smith, J. Nucl. Mater. 141-143 (1986) 566.
[5] O. K. Chopra, D. L. Smith, J. Nucl. Mater. 155-157 (1988) 683

[6] C. Guminski, Zeitschrift für Metallkunde 81 (1990) 105.
[7] W.E. Berry in „Corrosion in Nuclear Applications", John Wiley and Sons, New York 1971, 308.
[8] K. Ehrlich, D.R. Harris, A. Möslang, Report FZKA 5626, Forschungszentrum Karlsruhe 1997
[9] G .M. Tolson, A. Taboada, ORNL-TM1437, April 1966.
[10] R .C. Asher, D. Davies, S.A. Beetham, Corr. Sci., 17 (1977) 545.
[11] G. Y. Lai, 'High Temperature Corrosion of Engineering Alloys', ASM Int. (1990).
[12] R. P. Elliot, 'Constitution of Binary Alloys', First Supplement, McGraw-Hill Book Company.
[13] T.B. Massalski, Editor, 'Binary Phase Diagrams' ASM Int. (1990).
[14] B.F. Gromov, Yu. I. Orlov, P. N. Martynov, K. D. Ivanov, V. A. Gulevski in 'Liquid Metal Systems', Edited by H. U. Borgstedt and G. Frees, Plenum Press (1995) 339.
[15] I.V. Gorynin, G,. P. Karzov, V. Markov, V. S. Lavrukhin, V. A. Yakovlev, Proceedings of the Conference HLMC 98, Obninsk: SSC RF – IPPE, 1999. – Volume 1, 120.
[16] G. Müller, G. Schumacher, F. Zimmermann, J. Nucl. Mater., 278 (2000) 85.
[17] G. Benamati, P. Buttol, V. Imbeni, C. Martini, G. Palombarini, J. Nucl. Mater., 278 (2000) 308.
[18] V. Markov, "Corrosion of structural materials in PbBi and Pb, Seminar on the concept of lead-cooled fast reactors, September 22-23, 1997, Cadarache, France
[19] J. Konys, H. Muscher, Z. Voß, O. Wedemeyer, J. Nucl. Mater. 296 (2001) 289
[20] G. Frees, G. Drechsler, Z. Peric, Werkstoffe und Korrosion 40 (1989) 593.
[21] F.H. Stott, F.I. Wei, C.A. Enahoro, Werkstoffe und Korrosion 40 (1989) 198.

Steel	Cr	Ni	C	Mn	V	W	Mo	Ti	Si
MANET I	10.6	0.87	0.13	0.82	0.22	-	0.77	-	0.18
F82H-mod.	7.7	0.04	0.09	0.16	0.16	1.95	-	0.01	0.13
Optifer IVa	8.5	-	0.11	0.57	0.23	1.16	-	-	-
AISI 316L	17.3	12.1	0.02	1.8	-	-	2.31	-	0.75
1.4970	16.5	13.8	0.46	1.91	-	-	0.66	0.43	0.37

Table I: Chemical composition of the investigated steels

Figures and Captions



Fig. 1: Cross section of Optifer IVa (etched), exposed for 6000 h in Pb-17Li at 480°C.

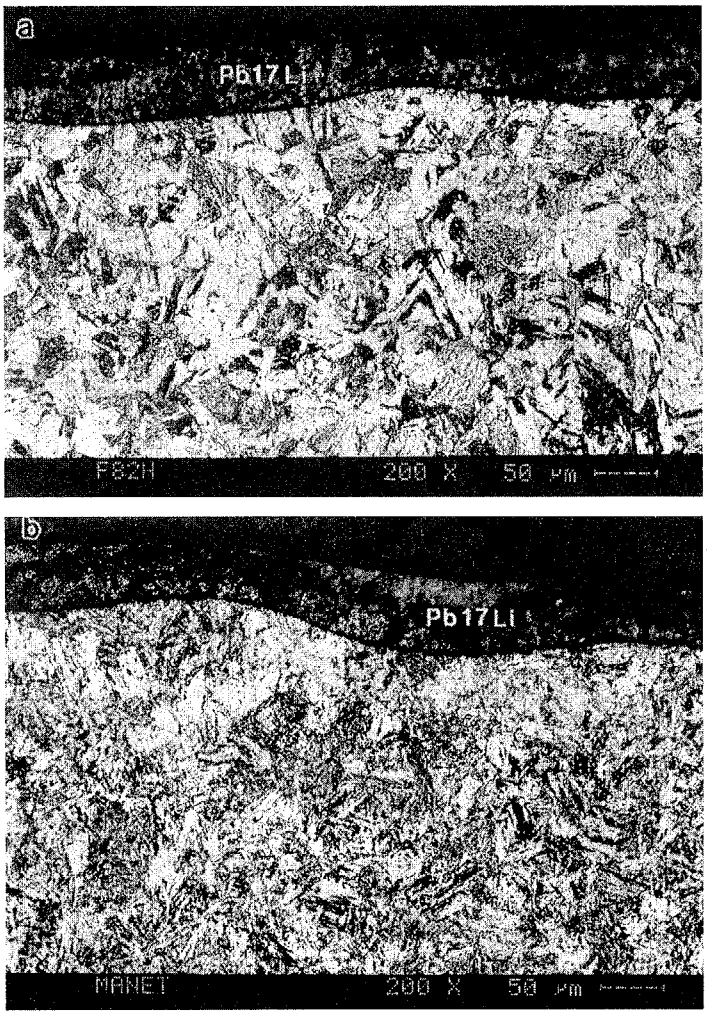


Fig. 2: Etched cross sections of a) F82H-mod. exposed for 10,000 h and b) MANET I exposed for 9000 h in Pb-17Li at 480°C

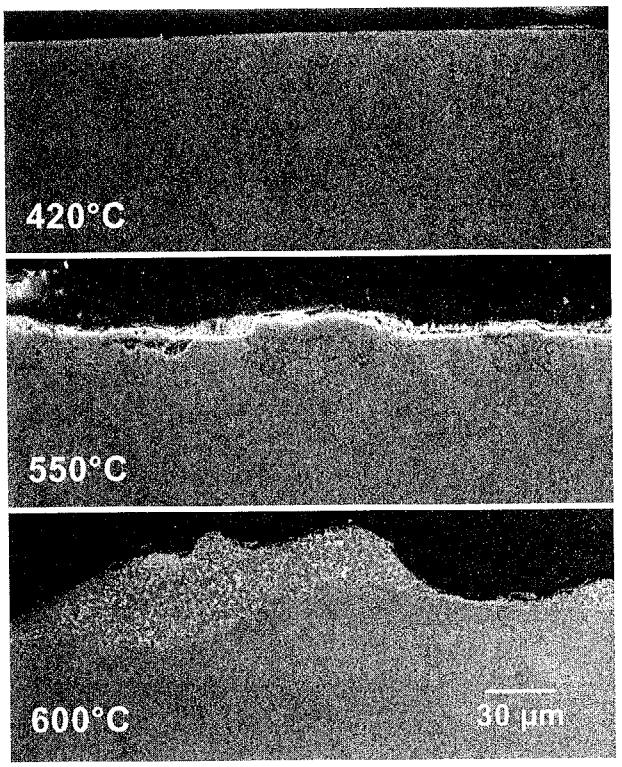


Fig. 3: Corrosion effects on AISI 316L after 2000 h in Pb-55Bi with 10^{-6} wt.-% of oxygen

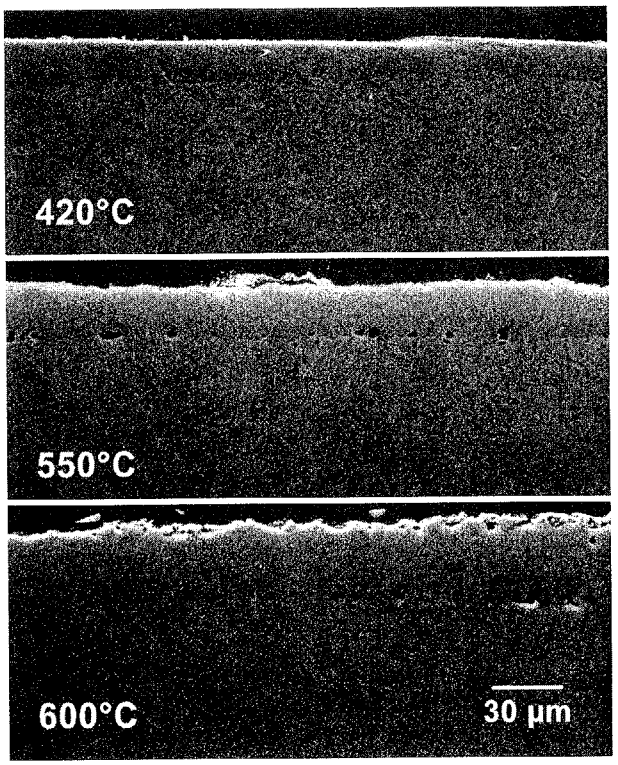


Fig. 4: Behavior of Al surface alloyed AISI 316L after 2000 h in Pb-55Bi with 10^{-6} wt.-% of oxygen

JP0350242

1.2.2 POSITRON ANNIHILATION STUDY OF HYDROGEN STORAGE ALLOYS

Yasuharu Shirai*, Hideki Araki, Kouji Sakaki
Department of Materials Science and Engineering, Osaka University, Yamada-oka 2-1,
Suita Osaka 565-0871, Japan.

Abstract

Some AB_5 and AB_2 hydrogen storage alloys have been characterized by using positron-annihilation lifetime spectroscopy. It has been shown that they contain no constitutional vacancies and that deviations from the stoichiometric compositions are all compensated by antistructure atoms. Positron lifetimes in fully-annealed $LaNi_{5-x}Al_x$ and $MmNi_{5-x}Al_x$ alloys show good correlation with their hydrogen desorption pressures. On the other hand, surprising amounts of vacancies together with dislocations have been found to be generated during the first hydrogen absorption process of $LaNi_5$ and $ZrMn_2$. These lattice defects play important role in hydrogen absorption-desorption processes of hydrogen storage alloys.

Keywords: positron annihilation, vacancy formation, $LaNi_5$, $ZrMn_2$, hydrogen storage alloys

1. Introduction

The positron is a unique probe to study the behaviour of the proton in hydrogen-absorbing matters, for both particles have the same positive elementary charge. In perfect crystals, positrons delocalise in interstitial sites and annihilate with electrons there, since positrons are strongly repelled by ion cores due to the Coulomb repulsion, as are protons. Then, positron annihilation characteristics are determined by the local electronic structure at the interstitial sites, where protons also stay stably.

When there exist vacancies, vacancy clusters or dislocations, which have lower densities of ion cores than the surroundings, positrons are trapped in such defects like protons and annihilate with electrons in the defects. Positron-annihilation characteristics in defects are unique for each kind of defects, and make it possible to identify existing defects with which protons should have strong interactions.

Thus the positron should be a quite unique probe that gives us direct information from the standpoint of the proton about hydrogen storage materials and their structural changes during hydrogen absorption and desorption processes. In this respect we have applied positron lifetime spectroscopy to study some AB_5 and AB_2 hydrogen absorbing alloys.

2. Positron Annihilation

In condensed matter, each positron annihilates with an electron, producing gamma rays, in a very short time. The annihilation rate (λ) is proportional to the electron density at the

* Corresponding author. Tel: +81-6-6879-7490 Fax: +81-6-6879-7492.
E-mail address: shirai@mat.eng.osaka-u.ac.jp (Y. Shirai).

annihilation site. Positron lifetimes τ (= λ^{-1}) in well-annealed metallic materials are characteristic of each material and in the range of 1-2 x 10^{-10}sec.

In a perfect crystal, a thermalized positron is delocalized (in a Bloch state). The density has maxima in the interstices, since a positron is strongly repelled by ion cores due to the Coulomb repulsion. When there exist vacancies, vacancy clusters or other defects that have lower densities of ion cores than the surroundings, positrons are trapped in the defects and annihilate there. In such defects, positron lifetime is longer, because electron density (both conduction and core electrons) is lower. The positron annihilation characteristics are unique for each kind of defects, and thus make us possible to identify each kind of defects.

For positrons annihilating in a perfect lattice, the decay is simple exponential; the positron lifetime spectrum $T(t)$ has the form

$$T(t) = (1/\tau_1)\exp(-t/\tau_1), \quad (1)$$

where the τ_1 is the positron lifetime in the perfect lattice. When positron-trapping centers such as vacancies exist in the lattice, some positrons are trapped and annihilate in them. According to the so-called trapping model [1-3], the positron lifetime spectrum well approximates to two discrete components:

$$T(t) = (I_0/\tau_0)\exp(-t/\tau_0) + (I_d/\tau_d)\exp(-t/\tau_d). \quad (2)$$

The second term is the defect component. The decay constant τ_d is the positron lifetime in the defect, which is characteristic of each kind of defects. The relative intensity of the defect component, I_d, increases with the defect concentration ($I_0 + I_d = 1$). The first decay constant τ_0 is always shorter than τ_1 [4,5].

Above treatment is readily extended to the cases in which more than two kinds of defects are included [4,5]. Thus, by measuring and analyzing positron lifetime spectra, information on the nature and concentration of defects can be obtained; the defect nature via τ_d and the concentration via I_d. In the case of microvoids, positron lifetime τ_d increases with the number of vacancies that constitute the microvoids, and is asymptotic to 500ps [6]. Positron lifetime at dislocations is not longer than that in monovacancies and changes with the magnitude of the Burger's vector [7].

The positron sensitivity to such defects is quite high: In the case of vacancies, a concentration of 10^{-6} in atomic fraction is enough to be detected; 10^{-4} vacancies make observed positron annihilation characteristics saturated. The sensitivity to vacancy clusters and secondary defects is even higher. This distinctive character is especially noteworthy, since the fraction of a defect's signal is equal to the defect fraction in almost all experimental methods other than positron annihilation. Positrons are able to amplify the signal of defects by a factor of order of 10^4.

We measured positron lifetime spectra in some hydrogen absorption materials using fast-fast coincidence systems. The instrumental time resolutions were 190-240ps FWHM (full width at half maximum of the resolution function). Measured lifetime spectra were analyzed, after correcting for a small source component, in terms of one, two or three components, using the computer programs Resolution [8] and Positronfit Extended [9]. Other experimental details will be published elsewhere.

3. Defect Structure in Some AB_5 and AB_2 Hydrogen Storage Intermetallics

In intermetallic compounds and ordered alloys, different atomic species occupy differently designated lattice sites and they are usually held together by strong bonds. If an intermetallic compound or an ordered alloy has an extended phase field, its nonstoichiometry may give rise to the existence of constitutional defects such as atoms occupying atomic sites of a sublattice other than its own sublattice (antisite atoms) or vacancies of deficient atomic

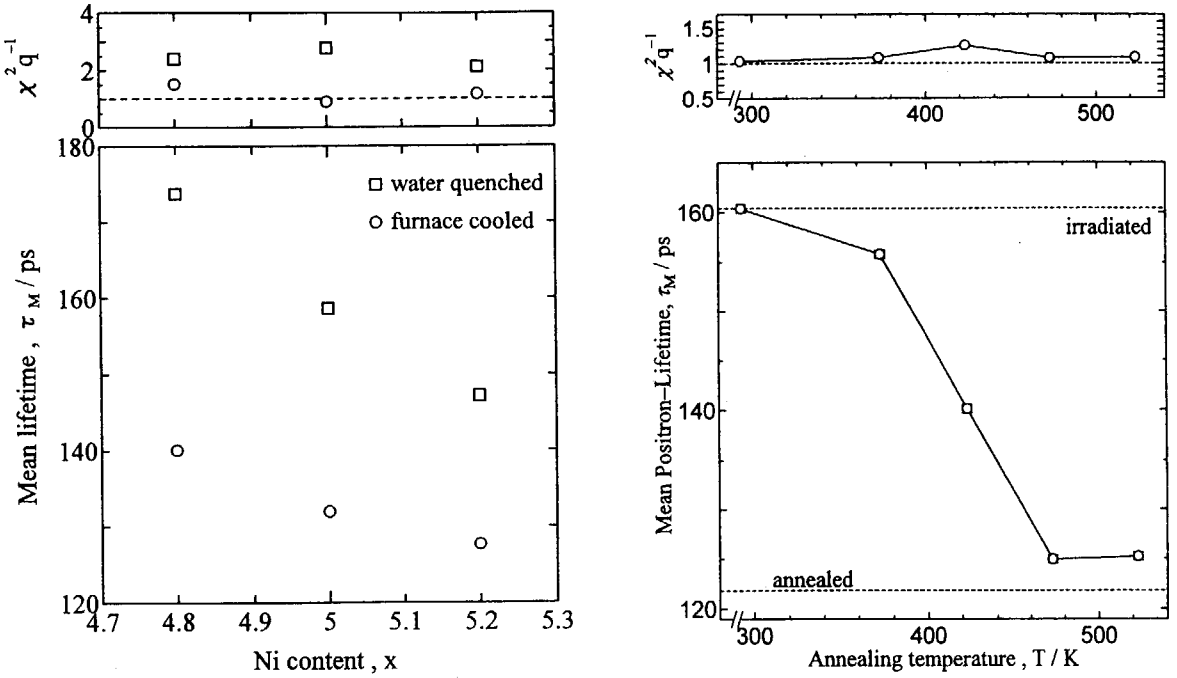


Fig. 1 Positron mean-lifetime in $LaNi_5$, $LaNi_{4.8}$ and $LaNi_{5.2}$ before and after quenching from 1473K. The variance of the fit $\chi^2 q^{-1}$ is also indicated. (Left)

Fig. 2 Recovery of vacancies in $LaNi_5$ irradiated with 8MeV electrons at ambient temperature up to 1 x 10^{17} e/cm^2. The variance of the fit $\chi^2 q^{-1}$ is also indicated.(Right)

species (constitutional vacancies). It is well known that the type and quantity of constitutional defects directly affect mechanical properties and atomic diffusion in the host ordered materials. Which of these defects dominates the defect structure of the nonstoichiometric compound depends on the crystal structure, constituent elements, and bonding nature of the compound as well as on which of the constituent elements is deficient and the amount by which the compound is non stoichiometric [10].

Which kind of constitutional defects exist in a given compound is easy to distinguish by using the positron lifetime measurement. Positron lifetime values in intermetallic compounds directly reflect their defect structures. For example, Fig.1 shows the positron lifetime resulting from a single-component analysis of experimental spectra obtained for stoichiometric $LaNi_5$, Ni-poor ($LaNi_{4.8}$) and Ni-rich ($LaNi_{5.2}$) samples (prepared by arc-melting of 3N La and Ni). Positron mean lifetime in water-quenched sample is substantially higher than that in furnace cooled sample for all compositions. This is due to the positron trapping by excess vacancies that are quenched from high temperature. In Fig. 1 the variance of the fit $\chi^2 q^{-1}$ is also shown as a measure of the fitting accuracy of the analysis; in case where the quantity of $\chi^2 q^{-1}$ is significantly larger than unity, the measured spectrum is not adequately fitted by the analysis [8,9]. Larger values of the variance for quenched samples also indicate the existence the defect component besides the matrix component.

From this measurement, we can readily conclude that there are no constitutional vacancies in stoichiometric and non-stoichiometric $LaNi_5$. This is because, if constitutional vacancies exist, all positrons are trapped in such constitutional vacancies even at low temperatures (the concentration of constitutional vacancies is generally much higher than that of thermal vacancies) and no such changes as shown in Fig. 1 should be observed. In the same manner, defect structures can be readily judged by thermal equilibrium positron lifetime measurement at high temperatures or by comparing positron lifetime before and after electron-irradiation

[11].

A $LaNi_5$ sample (purity; 99.9wt%, made by High-Purity Chemicals Co.Ltd.) was irradiated with electrons of 8MeV up to 1 x $10^{17}e/cm^2$ at ambient temperature. Positron mean lifetime was increased from 122ps to 160ps by the irradiation, which shows clearly that the $LaNi_5$ does not contain any constitutional vacancies. Fig. 2 shows the recovery of radiation-induced vacancies in $LaNi_5$ during the subsequent isochronal annealing (900s/50K) in Ar. This observation makes it clear that vacancies in $LaNi_5$ become mobile around 423K and migrate to permanent sinks such as dislocations, grain boundaries and free surfaces.

Similar results have been obtained for $LaNi_{5-x}Al_x$ (x = 0, 0.1, 0.5), $MmNi_{5-x}Al_x$ (x = 0, 0.1, 0.5), $La_{1-x}Ca_xNi_5$, $Mm_{1-x}Ca_xNi_5$, $ZrMn_2$, $ZrMn_{2-x}Co_x$, $ZrMn_{2-x}Ni_x$. All these intermetallic compounds have no constitutional vacancies. In other words, their nonstoichiometries are always compensated with anti-site atoms. Until now, B2 compounds, such as NiAl, NiGa, CoAl, CoGa, CoTi, seem to be unique examples in which the existence of vacancies compensating nonstoichiometry has been proved by using positron annihilation lifetime method [9].

4. Lattice Defects Induced by Hydrogen Absorption

Fig. 3 shows positron lifetime changes during the first hydrogen absorption process of $LaNi_5$ (purity; 99.9%, made by High-Purity Chemicals Co. Ltd.) at ambient temperature. The abscissa indicates the hydrogen content H/M. The positron lifetime increases steeply and shows a saturation behavior. This increase cannot be due to the formation of the hydride itself, but should be due to the accompanying irreversible structural change, the introduction of high density of lattice defects, since subsequent hydrogen desorption did not make the positron lifetime recover but caused a further increase.

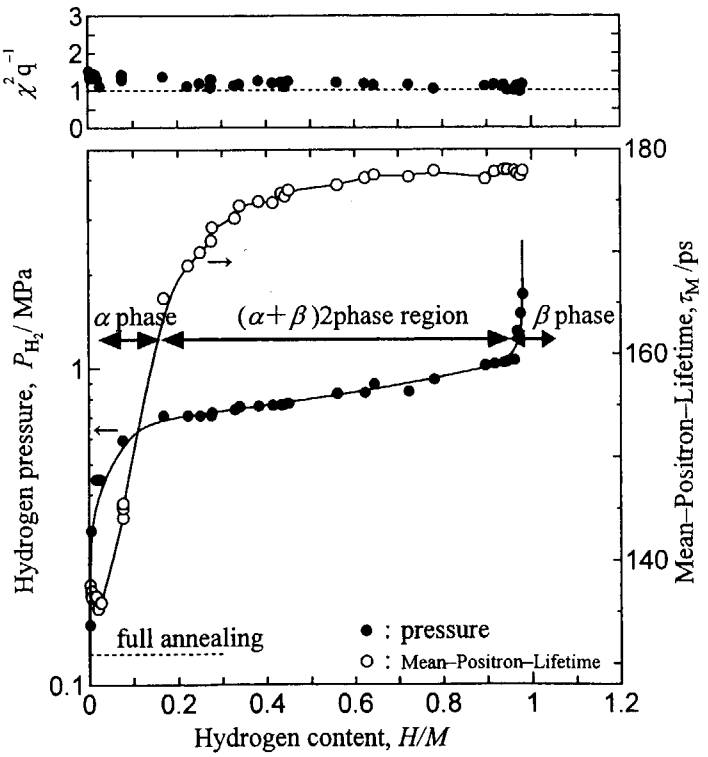
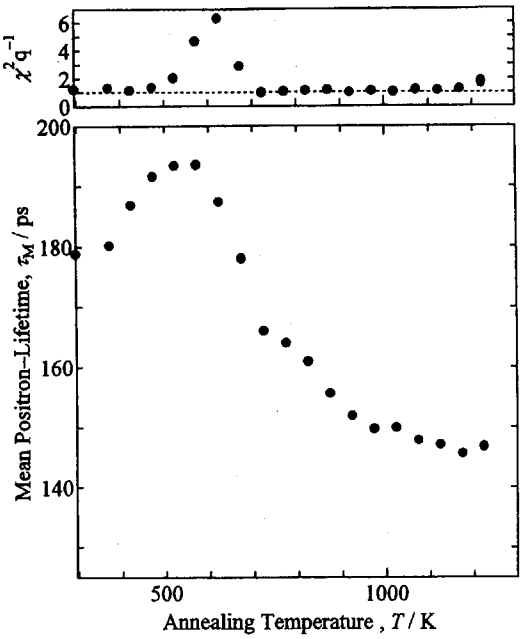


Fig. 3 Positron mean-lifetime change in $LaNi_5$ during the first hydrogen absorption at ambient temperature. The variance of the fit $\chi^2 q^{-1}$ is also indicated.



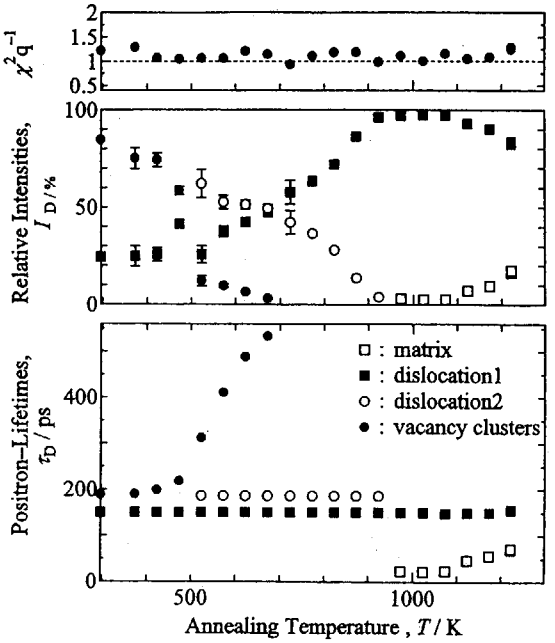


Fig. 4 Positron mean-lifetime change in $LaNi_5$ during isochronal annealing (15min / 50K) after the first hydrogen absorption-desorption cycle. The variance of the fit $\chi^2 q^{-1}$ is also indicated.(Left)

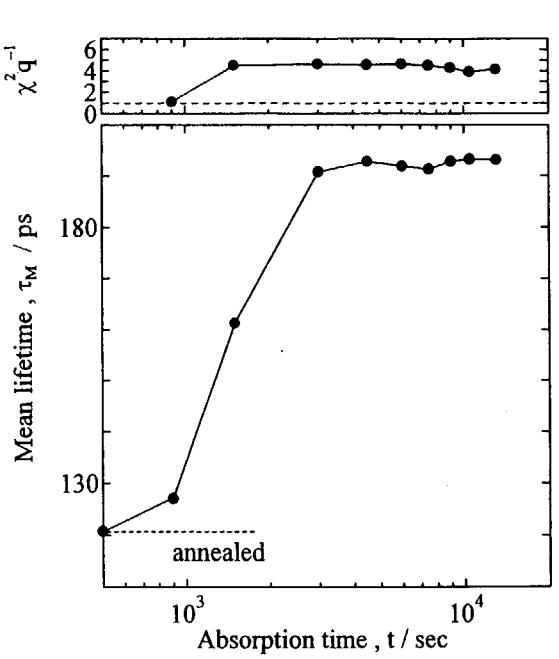
Fig. 5 Result of the component analysis of the lifetime spectra recorded during isochronal annealing of $LaNi_5$ that has undergone one absorption-desorption cycle. Positron lifetime in each component (lower part) and their relative intensities (upper part).(Right)

The annealing process of the hydrogen-induced defect was studied by positron lifetime measurements in the same specimen during isochronal annealing. The result is presented in Fig. 4. Three recovery stages can be recognized in Fig. 4, around 423K, 823K and 1123K. The most important change is the mean lifetime increase observed above 423K, because this kind of lifetime change is the typical manifestation of void formation by vacancy clustering. The increase in the variance of the fit $\chi^2 q^{-1}$ also indicate the appearance of a new defect-component whose positron lifetime is much higher than co-existing defects. This vacancy-migration temperature in $LaNi_5$ coincides well with that obtained after electron irradiation (see Fig. 2). This experiment revealed an important fact, that high numbers of excess vacancies are introduced in $LaNi_5$ by hydrogen absorption. The two other recovery stages in Fig. 4, around 823K and 1123K, are safely attributed to the recovery of two kinds of dislocations by the following multi-component analyses of positron lifetime spectra.

The positron lifetime spectra were decomposed into multicomponents. The results are shown in Fig. 5. The lower part shows positron lifetimes for vacancy clusters, dislocations and the matrix, and the upper part shows the relative intensities of the each component. In this analysis, two dislocation components are resolved.

Just after hydrogen desorption, small vacancy clusters (single vacancies and di- and tri-vacancies at most) and dislocations are observed. Above 423K the positron lifetime of the vacancy-cluster component drastically increase from 200ps to around 500ps. This is the direct evidence for the void formation by the clustering of vacancies that are generated during hydrogen absorption. On the other hand, the relative intensity of the vacancy-cluster component decreases at the same time. This behavior is quite normal since most vacancies and vacancy clusters annihilate at such permanent sinks as dislocations, grain boundaries and surfaces, whose densities are very high after a hydrogen absorption and desorption cycle.

Above 700K, relative intensity of the dislocation component becomes 100%. All positrons are trapped and annihilate at dislocations. This result clearly shows that dislocation density is



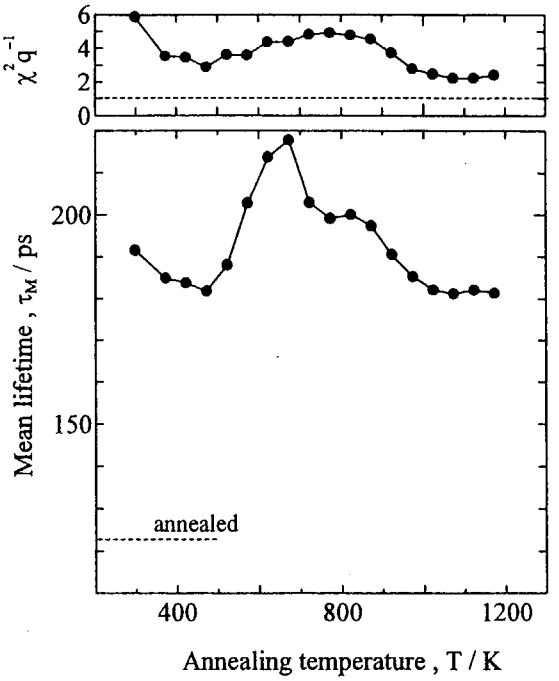


Fig. 6 Positron mean-lifetime change in $ZrMn_2$ during the first hydrogen absorption under a constant hydrogen pressure of 0.5MPa at ambient temperature. The variance of the fit $\chi^2 q^{-1}$ is also indicated.(Left)

Fig. 7 Positron mean-lifetime change in $ZrMn_2$ during isochronal annealing (15min / 50K) after the first hydrogen absorption-desorption cycle. The variance of the fit $\chi^2 q^{-1}$ is also indicated.(Right)

high enough to cause the saturation trapping of positrons even after the disappearance of vacancies and vacancy clusters. The matrix component appears above 1073K at long last. This implies that the vacancy concentration generated by hydrogen absorption is high enough to surpass even a high density of dislocations in trapping positrons. Rough estimation indicates that the vacancy concentration should amount to the order of 10^{-2}.

While there can be no doubt about the vacancy formation in $LaNi_5$ by hydrogen absorption, this leads us to the question of whether the vacancy formation by hydrogen absorption is a specific behavior of $LaNi_5$ or a more general phenomenon. In order to clarify this point we have carried out positron lifetime measurements on $ZrMn_2$ (prepared by arc-melting 99.6wt%Zr and 99.9wt%Mn). Positron lifetime change in $ZrMn_2$ during the first absorption process of hydrogen at ambient temperature under a constant hydrogen pressure of 0.5Mpa is shown in Fig. 6. Fig. 7 demonstrates the positron lifetime change during the subsequent isochronal annealing of the same specimen. All important features are quite similar to those observed in $LaNi_5$: huge numbers of defects, not only dislocations but also vacancies, are formed during hydrogen absorption. Induced vacancies agglomerate during subsequent annealing (around 500K in this compound).

It follows from the observations above that the vacancy formation during hydrogen absorption in hydrogen storage materials should be a rather general phenomenon. More detailed studies including the study of the vacancy formation mechanism are now in progress.

5. Concluding Remarks

The unique characteristics of positron annihilation have been applied to study some AB_5 and AB_2 hydrogen absorbing alloys and the following points have been revealed:

1. In $LaNi_{5\pm x}$ there are no constitutional vacancies due to deviations from the stoichiometric

compositions. The deviations are compensated by antistructure atoms in these alloys.
2. Huge numbers of excess vacancies are formed in addition to dislocations during the first hydrogen absorption process of $LaNi_5$ and $ZrMn_2$.
3. Excess vacancies introduced in the alloys by hydriding are contained in the specimen at ambient temperature, where vacancies are practically immobile.
4. Above certain temperatures, excess vacancies become mobile and form microvoids.

Hereafter, defects and their properties in many important and potential hydrogen storage materials will be clarified by using positron annihilation methods and such information will be quite useful to develop hydrogen storage materials and processing.

Acknowledgements

This work is supported partially by a Grant-in Aid for Special-Area Research from the Ministry of Education, Science and Culture, Japan.

References

[1] W. Brandt, in *Positron Annihilation*, ed. by A.T. Stewart and L.O. Roeling, Academic Press, New York, 155 (1967).

[2] B. Bergersen and M.J. Stott, *Solid State Commun.*, 7, (1969) 1203.

[3] D.C. Connors and R.N. West, *Phys. Lett.* **A30**, (1969) 24.

[4] M. Doyama, *J. Phys. Soc. Japan*, **33**, (1972) 1495.

[5] A. Seeger, *Appl. Phys.*, **4**, (1974) 183.

[6] M.J. Puska and R.M. Nieminen, J. Phys. F, **13** (1983) 333.

[7] Y. Shirai, K. Matsumoto, G. Kawaguchi, and M. Yamaguchi, Materials Science and Forum, **105-110** (1992) 1225.

[8] P. Kirkegaard and M. Eldrup, O. E. Morgensen and N. Pedersen, *Computer Phys. Commun.*, **23** (1981) 307.

[9] P. Kirkegaard and M. Eldrup, *Computer Phys. Commun.*, **3** (1972) 240; 7(1974) 401.

[10] M. Yamaguchi and Y. Shirai, in *Physical Metallurgy and Processing of Intermetallic Compounds* ed. by N.S. Stoloff and V.K. Sikka, Chapmann and Hall, New York, 3 (1995).

[11] Y. Shirai, High Temperature Materials and Processing, **17** (1998) 57-67.

JP0350243

1.2.3 HIGH TEMPERATURE SULFIDE CORROSION AND TRANSPORT PROPERTIES OF TRANSITION METAL SULFIDES

K. Przybylski*, S. Mrowec
University of Mining and Metallurgy (AGH), Faculty of Materials Science and Ceramics, Department of Solid State Chemistry, Al. Mickiewicza 30, 30-059 Kraków, Poland

Abstract

An overview is presented of the role of the defect and transport properties of transition metal sulfides on the kinetics and mechanism of high-temperature sulfide corrosion of metals and alloys. It has been shown that due to the very high concentration of defects in common metal sulfides, not only pure metals but also conventional high-temperature alloys (chromia and alumina formers) undergo very rapid degradation in highly sulfidizing environments. Refractory metals (Mo, Nb), on the other hands, are highly resistant to sulfide corrosion, their sulfidation rates being comparable with the oxidation rate of chromium. Also, alloying of common metals by niobium and molybdenum improve considerably corrosion resistance with respect to highly sulfidizing atmospheres. It has demonstrated that Al.-Mo and Al.-Mo-Si alloys shown excellent resistant to sulfidizing environments, these materials being also simultaneously oxidation resistant. Thus, new prospects have been created for the development of a new generation of coating materials, resistant to multicomponent sulfidizing-oxidizing atmospheres, often encountered in many branches of modern technology.

Keywords: sulfidation; oxidation; common and refractory metals and alloys.

1. Introduction

In many branches of modern technology metallic materials are exposed to sulfur-containing atmospheres at high temperatures [1,2]. The corrosion of common metals and conventional oxidation resistant alloys (chromia and alumina formers) undergo under these conditions very rapid, often catastrophic degradation.

The mechanism of this type of corrosion, observed in multicomponent oxidizing-sulfidizing atmospheres, is very complex and still not satisfactorily understood. Thus, many attempts have been made to improve the resistance of high-temperature alloys, against sulfide corrosion and to design novel materials resistant to such very aggressive environments.

The present paper is an attempt to discuss the role of defects and transport properties of sulfides in sulfide corrosion and to demonstrate that the resistance of metallic materials to this type of corrosion may be considerably improved by alloying of common metals by refractories and in particular by replacing of common metals by aluminum (Al-Mo, Al-Nb, Al-Mo-Si).

2. Physicochemical properties of metal sulfides

Transition-metal sulfides are less thermodynamically stable, melt generally at lower temperatures and show higher deviations from stoichiometry than the corresponding oxides (Tables I,II,III). Actually, with few exceptions only the sulfides of common metals, including

*Corresponding author. Tel: +48 (0)12-617-2469 Fax: +48 (0) 12-633-1593.
E-mail address: kaz@uci.agh.edu.pl (K. Przybylski).

Table I. Free energies of sulfide and oxide formation at 1123 K (kcal/mol S or O) [3]

Sulfide	$-\Delta G^0_{1123\,K}$	Oxide	$-\Delta G^0_{1123\,K}$
FeS	21.9	FeO	45.0
NiS	15.4	NiO	32.0
CoS	17.0	CoO	37.5
Cr_2S_3	34.9	Cr_2O_3	66.5
MnS	46.5	MnO	77.5
MoS_2	18.5	MoO_2	47.0
TiS	44.0	TiO	98.5
TiS_2	31.3	TiO_2	88.5

Table II. Melting points of some sulfides and oxides and metal-sulfide eutectics [3]

Sulfide	Melting poit, *K*	Oxide	Melting point, *K*
TiS	2373	TiO	2023
La_2S_3	2353	La_2O_3	2490
Ce_2S_3	2333	Ce_2O_3	1963
NbS_2	?	NbO_2	2353
ThS_2	2198	ThO_2	3323
US_2	2123	UO_2	3113
Y_2S_3	1873	Y_2O_3	2683
CrS	1823		
Cr_2S_3	?	Cr_2O_3	2607
MoS_2	1431	MoO_2	2200
MnS	1598	MnO	2058
FeS	1468	FeO	1697
Cu_2S	1403	Cu_2O	1515
CoS	1373	CoO	2083
Al_2S_3	1373	Al_2O_3	2319
In_2S_3	1326	In_2O_3	2273
NiS	1083	NiO	2230
Ni_3S_2	1061		
InS	965	InO	1325
M-MnS	1513		
Cu-Cu_2S	1343		
Fe-FeS	1258	Metal sulphide eutectics	
Co-Co_4S_3	1153		
Ni-Ni_3S_2	918		

Table III. Maximum deviations from stoichiometry of some metal sulfides and oxides at 1273 K [4]

Sulfide	Formula	Oxide	Formula
$Fe_{1-y}S$	$Fe_{0.85}S$	$Fe_{1-y}O$	$Fe_{0.85}O$
$Ni_{1-y}S$	$Ni_{0.91}S$	$Ni_{1-y}O$	$Ni_{0.9994}O$
$Co_{1-y}S$	$Co_{0.84}S$	$Co_{1-y}O$	$Co_{0.993}O$
$Cr_{2+y}S_3$	$Cr_{2.03}S_3$	$Cr_{2+y}O_3$	$Cr_{1.99995}O_3$
$Cu_{2-y}S$	$Cu_{1.83}S$	$Cu_{2-y}O$	$Cu_{1.998}O$

chromium sulfides, show much greater nonstoichiometry, and thereby defect concentration, than the corresponding oxides (Fig.1). On the other hand, refractory-metal sulfides seem to show very low deviations from stoichiometry, of the order of that of chromium oxide. Rau [5] has shown, for instance, that the maximum deviation from stoichiometry of molybdenum disulfide (MoS_2) at 1373 K is smaller than 8×10^{-5} mole of sulfur per mole of the sulfide.
As the matter transport in metal sulfides, like in the majority of oxides, proceeds mainly through point defects, i.e., by volume diffusion, from these short remarks it follows that transport properties of sulfide scales may roughly be described by self- and chemical-diffusion coefficients. A comparison of a self-diffusion coefficients in oxides and sulfides clearly indicates that the rate of cation self-diffusion in common-metal sulfides is generally much higher than in the corresponding oxides (Fig.2) [3,4].

The question then arises as to why self-diffusion rates of cations in the majority of sulfides are much higher than in the corresponding oxides. As the self-diffusion coefficient of

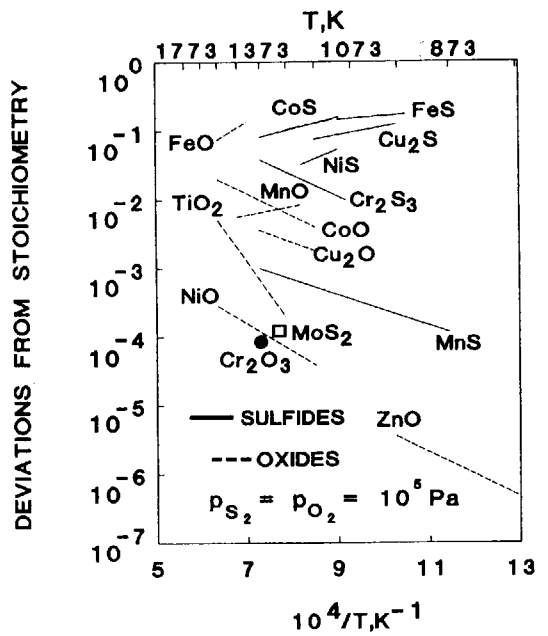


Fig.1 Collective plot of maximum nonstoichiometry in several metal sulfides and oxides as a function of temperature at constant sulfur and oxygen pressure [4]

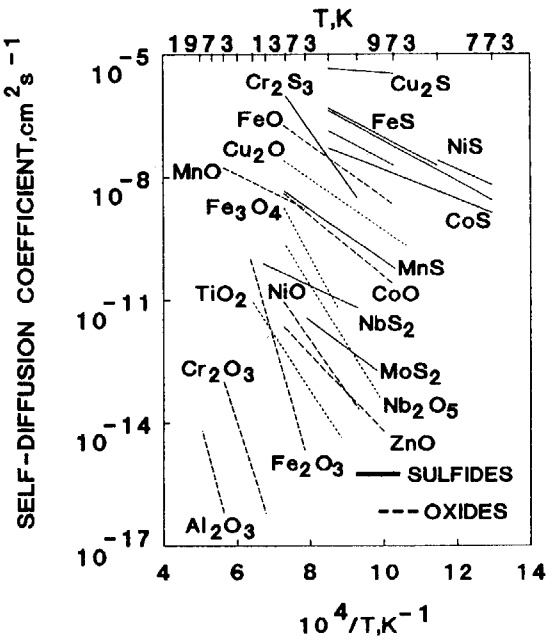


Fig.2 Comparison of self-diffusion coefficients in some metal sulfides and oxides [4]

atoms or ions in a given solid is a product of defect concentration and their mobility, deviations from stoichiometry and chemical-diffusion coefficients for both groups of these materials should be compared. As far as nonstoichiometry is concerned, it has already been pointed out that except for refractory-metal sulfides, virtually all other transition-metal sulfides show many times greater deviations from stoichiometry and thereby defect concentrations than the corresponding oxides. A comparison, in turn, of available data of chemical-diffusion coefficients shows, rather surprisingly, that the rates of this process and thereby the mobilities of defects in sulfides and oxides do not differ significantly (Fig.3) [3,4]. In fact, the rate of chemical diffusion is generally higher in sulfides, but maximum differences do not exceed one order of magnitude. It may then be concluded that significantly higher self-diffusion rates of cations in the majority of transition-metal sulfides result mainly from much higher defect concentrations and not from greater defect mobilities. However, in

the case of refractory-metal sulfides the situation may be different. In contrast, namely, to the very low defect concentration in MoS_2, niobium disulfide, NbS_2, shows rather high deviations from stoichiometry [6] and none the less the rate of niobium sulfidation is comparable with that of molybdenum. Based on detailed theoretical analysis of the defect structure of NbS_2 and the mechanism of niobium sulfidation, Gesmundo et al. [7] arrived at the conclusion that the very good protective properties of a NbS_2 scale on niobium result mainly from very low-defect mobility. This conclusion has recently been confirmed experimentally [8].

3. Sulfidation of pure metals

As the sulfide corrosion of pure metals is concerned, only the main similarities and differences between the kinetics and mechanism of sulfidation and oxidation processes will be discussed. One of the most important conclusions in this respect is, that as in the case of oxidation, sulfide scales on common metals grow by the outward diffusion of cations, and on refractory metals by the inward diffusion of anions. This is illustrated in Fig.4, showing four cross sections of sulfide and oxide scales formed on nickel, cobalt, tungsten and titanium. As

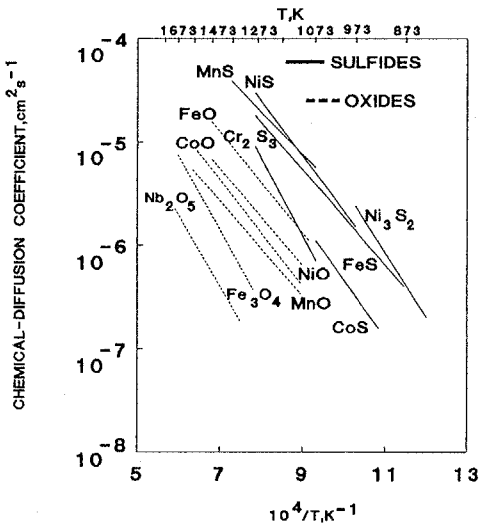


Fig.3 Comparison of chemical diffusion coefficients in some metal sulfides and oxides [3]

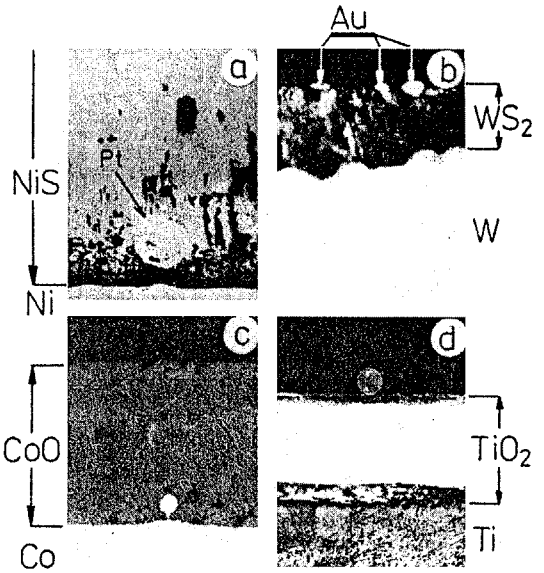


Fig.4 Cross sections of sulfide (a,b) and oxide (c,d) scales on nickel, tungsten, cobalt and titanium [9]

can be seen, inert markers located before the reaction on the surface of nickel and cobalt remained at the metal-scale interface, clearly indicating that the sulfide and oxide scales on these metals grew by the outward diffusion of cations. On the other hand, in the case of tungsten sulfidation and titanium oxidation inert markers were found on the scale surface, strongly suggesting that the WS_2 and TiO_2 scales grew by inward diffusion of anions. This important analogy in the growth mechanism of sulfide and oxide scales on metals result from the same type of predominant disorder in transition-metal sulfides and oxides.

The main difference, in turn, is observed between sulfidation and oxidation rates of these metals. In spite of compact-scale formation and the parabolic course of the reaction the rate of sulfide corrosion of such important metals as nickel, cobalt and even chromium, is many times higher than their oxidation rates. This is illustrated in Fig. 5 showing the temperature dependence of the sulfidation and oxidation rates of some metals. From this diagram it follows also that refractory metals are highly resistant to sulfide corrosion, their sulfidation rates being comparable to the oxidation rate of chromium, representing one of the most-resistant metals to oxide corrosion.

4. Sulfidation of alloys

Passing now to a short discussion of alloy sulfidation, again the similarities and differences between sulfide and oxide corrosion will be considered. As in the case of

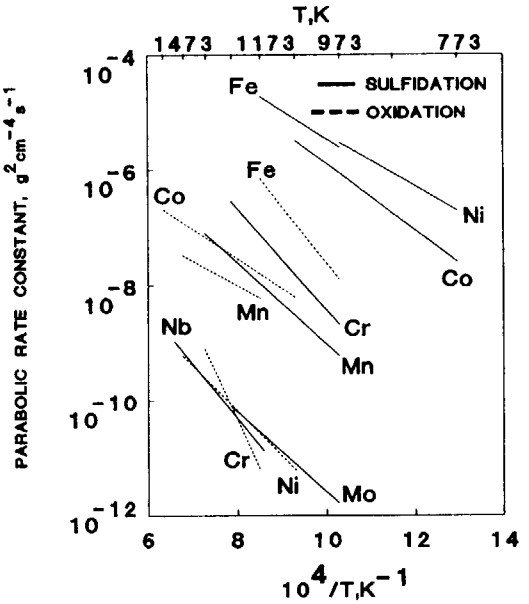


Fig.5 Collective plot of the temperature dependence of the sulfidation and oxidation rates of some metals [4]

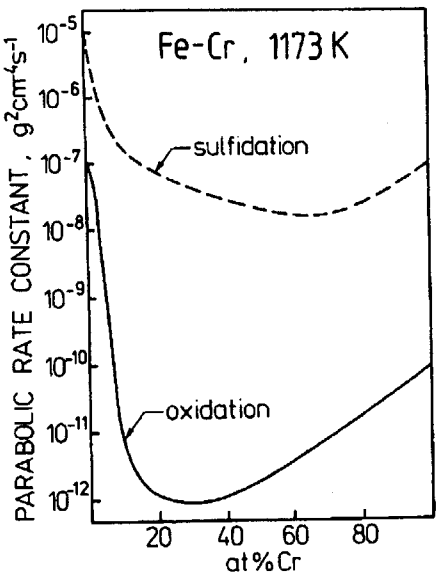


Fig.6 The dependence of the sulfidation and oxidation rates of Fe-Cr alloys on composition [9]

oxidation the sulfide scales on the binary Fe-Cr, Ni-Cr, and Co-Cr alloys grow essentially by outward diffusion of cations [3,4]. However, despite great similarities in the growth mechanism of oxide and sulfide scales, the sulfidation and oxidation rates of these alloys differ dramatically. This is illustrated in Fig.6 by the dependence of the oxidation and sulfidation rates of Fe-Cr alloys on their composition. As can be seen, the oxidation rate of chromia formers (about 40% Cr) is more than four orders of magnitude lower than the sulfidation rate of alloys, on the surface of which a homogeneous Cr_2S_3 scale is formed. Aluminum additions to the alloys under discussion improve their resistance to sulfide corrosion, but this effect is rather weak [3,10,11], not exceeding two orders of magnitude even when the concentration of aluminum reaches 20 at.%. At very low sulfur pressure only, lower than the dissociation pressure of base-metal sulfide, a highly protective scale is formed [3]. In order to illustrate the dramatic differences between sulfide and oxide corrosion of high-temperature alloys, Fig.7 shows a collective plot of the temperature dependence of the rates

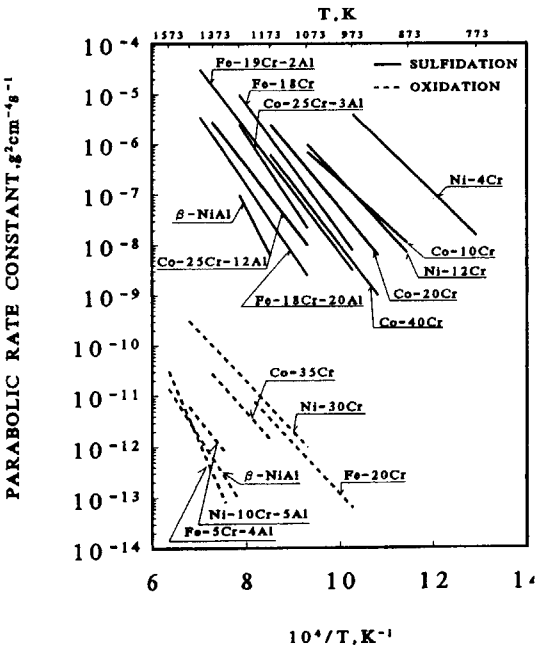


Fig.7 Collective plot of the temperature dependence of the sulfidation and oxidation rates of several binary and ternary alloys and β-NiAl intermetallic [9]

of these processes for several binary and ternary alloys and β-NiAl intermetallic compound. It is clearly seen that all oxidation resistant alloys, including the β-NiAl intermetallic compound, corrode many orders of magnitude faster in a highly sulfidizing environment than in oxygen. Such a situation results mainly from the fact that in oxidizing atmospheres highly protective chromia or alumina layers are formed on these alloys as a result of selective oxidation of chromium or aluminum. On the other hand, in sulfidizing environments even at higher concentrations of chromium, and in particular aluminum, heterogeneous scales of poor protective properties are formed, containing sulfides of all alloying components. This important difference results mainly from thermodynamic and kinetic reasons. In the case of oxidation, absolute values of free energy of formation of Cr_2O_3 and Al_2O_3 are much higher than those of base metal oxides (FeO, CoO, NiO). Consequently, about 30 wt.% of chromium and only 5-7 wt.% Al is high enough for selective oxidation of these alloying components. In addition, the growth rates of these oxide layers are so low that the rate of interdiffusion within the alloy is high enough to maintain the chromium and/or aluminum activity at the alloy-scale interface on the level sufficient for steady-state, selective oxidation.

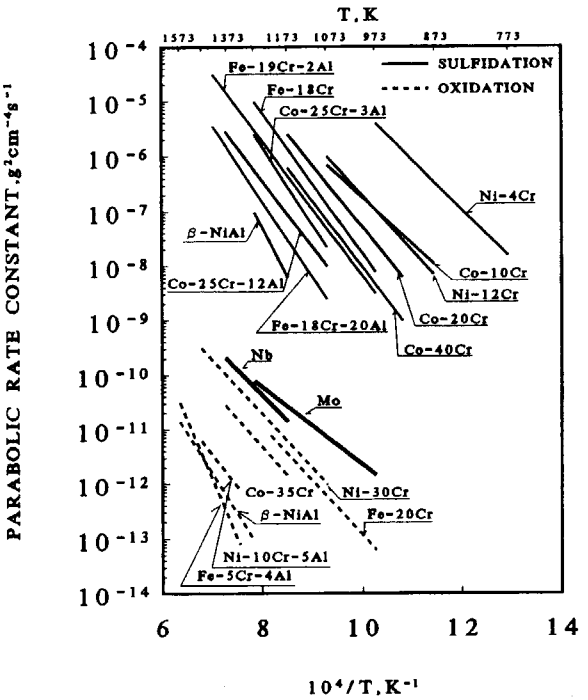


Fig.8 Collective plot of the temperature dependence of the sulfidation and oxidation rates of high-temperature alloys compared to niobium and molybdenum sulfidation (solid lines-sulfidation; dashed lines-oxidation) [9]

The situation is different in the case of sulfidation, because absolute values of free energies of formation of CrS, Cr_2S_3 and Al_2S_3 are not much higher than those of iron, cobalt and nickel sulfides. Thus, selective sulfidation of chromium and aluminum is not favored, and heterogeneous scales are formed which have poor protective properties. In addition, the very high growth rates of base-metal sulfides impede the formation of a continuous chromium sulfide or aluminum sulfide layer. Thus, from a practical point of view chromium and aluminum alone do not seem to be very promising in designing novel materials resistant to sulfide corrosion. In contract to this, refractory metals seem to be very promising as they show excellent resistance to sulfur. In order to stress this point, Fig. 8 shows once again a collective plot of the temperature dependence of the sulfidation and oxidation rates of some high-temperature alloys compared to molybdenum and niobium sulfidation. It is clearly seen, that the sulfidation rates of these refractory metals are only slightly higher than the oxidation rates of chromia formers. Douglas [12-19] has shown that combined alloying of iron with molybdenum and aluminum dramatically decreases the sulfidation rate of iron as illustrated in Fig.9. However, a pest phenomenon has been observed desintegrated the material after prolonged sulfidation. On the other hand, novel nanocrystalline Al-Mo, Al-Nb and in particular Al-Mo-Si alloys [20-23] have been found to by surprisingle high resistant not only to highly sulfidizing atmospheres but also to oxygen attack at high temperatures. This is well illustrated in Fig.10 representing the collective plot of temperature dependence of the

sulfidation (solid lines) and oxidation (dotted lines) rates of these novel materials on the background of the sulfide and oxide corrosion rates of chromia and alumina formers.

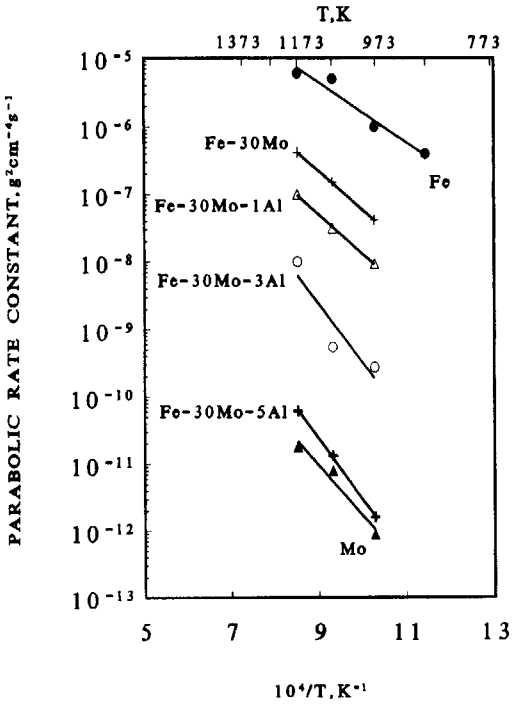


Fig.9 Temperature dependence of the sulfidation rate of Fe-30Mo and Fe-30Mo-xAl alloys compared to the sulfidation rates of pure iron and molybdenum [9]

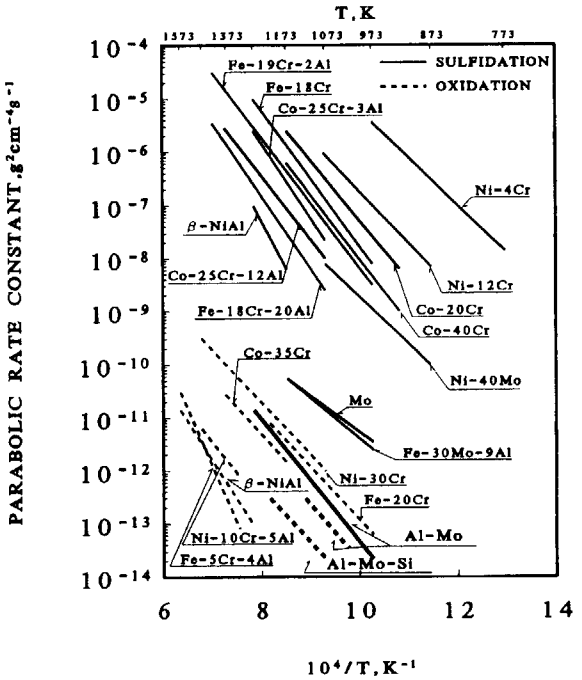


Fig.10 Collective plot of the temperature dependence of the sulfidation and oxidation rates for Al.-Mo and Al.-Mo-Si alloys, compered to a number of conventional high-temperature alloys, as well as for the sulfidation rates of pure molybdenum and Fe-30Mo-9Al alloy [9,20,22]

5. Concluding remarks

The main reason why common metals are rapidly attacked by sulfur results from the very high concentration of point defects in their sulfides. On the other hand, refractory metals are highly resistant to sulfide corrosion because of either low-defect concentration or low-defect mobility in the sulfides of these metals.

The mechanisms of sulfide and oxide corrosion of pure metals are very similar because of the same type of predominant disorder in transition-metal sulfides and oxides.

All conventional oxidation-resistant alloys (chromia and alumina formers) undergo very rapid degradation in highly sulfidizing environments because of heterogeneous-scale formation of poor protective properties.

New prospects for the development of coating materials resistant to high-temperature sulfide corrosion have been created by combined alloying of common metals with molybdenum and aluminum and in particular by the development of novel nanocrystalline aluminum based refractory metal alloys containing silicon which are highly resistant to **both** sulfidizing and oxidizing environments.

Acknowledgement

This work was supported by the Faculty of Materials Science and Ceramics of the University of Mining and Metallurgy (AGH) in Kraków under contract number 11.11.160.169

References

[1] D. B. Meadowcroft and M. J. Manning, *Corrosion Resistant Materials for Coal Gasification Systems* (Applied Science, London, 1993)
[2] P. Kofstad, *High Temperature Corrosion* (Elsevier, London and New York, 1988)
[3] S. Mrowec and K. Przybylski, High Temp. Mater. Processes **6**, 1 (1984)
[4] S. Mrowec and J. Janowski, in *Selected Topics in High Temperature Chemistry*, O. Johannesen and A. G. Andersen, eds. (Elsevier, New York, 1989), pp.55-99.
[5] H. Rau, J. Phys. Chem. Solids **41**, 765 (1980)
[6] T. Tatsaki, M. Wakihara, and M. Taniguchi, J. Less Common Metals **68**, 183 (1979)
[7] F. Gesmundo, F. Viani, and Y. Niu, Oxid. Met. **38**, 465 (1992)
[8] S. Mrowec, Z. Grzesik, J. Dąbek, Solid State Phenom. **72**, 29 (2000)
[9] S. Mrowec, Oxid. Met. **44**, 177 (1995)
[10] S. Mrowec, M. Wędrychowska, Oxid. Met. **13**, 481 (1979)
[11] T. Biegun, A. Brückman, and S. Mrowec, Oxid. Met. **12**, 157 (1978)
[12] M. F. Chen and D. L. Douglass, Oxid. Met. **32**, 185 (1989)
[13] R. V. Carter, D. L. Douglass, and F. Gesmundo, Oxid. Met. **31**, 341 (1989)
[14] B. Glesson, D. L. Douglass, and F. Gesmundo, Oxid. Met. **31**, 209 (1989)
[15] M. F. Chen, D. L. Douglass, and F. Gesmundo, Oxid. Met. **31**, 237 (1989)
[16] Ge Wang, R. V. Carter, and D. L. Douglass, Oxid. Met. **32**, 273 (1989)
[17] B. Glesson, D. L. Douglass, and F. Gesmundo, Oxid. Met. **33**, 425 (1990)
[18] Ge Wang, D. L. Douglass, and F. Gesmundo, Oxid. Met. **35**, 279 (1991)
[19] Ge Wang, D. L. Douglass, and F. Gesmundo, Oxid. Met. **35**, 349 (1991)
[20] H. Habazaki, J. Dąbek, K. Hashimoto, S. Mrowec, M. Danielewski, Corr. Sci. **34**, 183 (1993)
[21] H. Mitsui, H. Habazaki, K. Asami, K. Hashimoto, S. Mrowec, Corr. Sci. **38**, 1431 (1996)
[22] H. Habazaki, K. Hashimoto, S. Mrowec, M. Danielewski, Zairyo-to-Kankyo, **44**, 174 (1995)
[23] H. Habazaki, H. Mitsui, K. Ito, K. Asami, K. Hashimoto, S. Mrowec, Corr. Sci. **44**, 285 (2002).

This is a blank page.

1.3 Degradation Phenomena

Chair: P. Asoka-Kumar

(Lawrence Livermore National Laboratory, USA)

K. Kiuchi

(Japan Atomic Energy Research Institute, Japan)

This is a blank page.

JP0350244

JAERI－Conf 2003－001

1.3.1 POSITRON ANNIHILATION STUDIES ON BULK METALLIC GLASS AND HIGH INTENSITY POSITRON BEAM DEVELOPMENTS

P. Asoka-Kumar* and W. Stoeffl
Lawrence Livermore National Laboratory, Livermore, CA 94550 USA

Abstract

Positron annihilation spectroscopy is an ideal probe to examine atomic scale open-volume regions in materials. Below, we summarize the recent results on studies of open-volume regions of a multicomponent Zr-Ti-Ni-Cu-Be bulk metallic glass. Our studies establish two types of open-volume regions, one group that is too shallow to trap positrons at room temperature and becomes effective only at low temperatures and the other group that localizes positrons at room temperature and is large enough to accommodate hydrogen. The second half of the paper will concentrate on the high intensity positron program at Lawrence Livermore National Laboratory. A new positron production target is under development and we are constructing two experimental end stations to accommodate a pulsed positron microprobe and an experiment on positron diffraction and holography. Important design considerations of these experiments will be described.

Keywords: metallic glass, positron production, positron microprobe, positron diffraction and holography

1. Introduction

The use of positron beams in surface and materials science offers unique opportunities to obtain detailed information on defects and electronic properties of materials[1-5]. Since the initial discovery of "moderation", the process by which a small portion of positrons incident on a material with a negative positron work function is reemitted with narrow energy and angular distributions, several monoenergetic positron beam systems has been developed. At Lawrence Livermore National Laboratory, we are operating and developing several positron beam systems that are capable of examining materials at different depth scales and sampling volumes. Below, we summarize the results obtained with high-energy positron beams and new developments to build a multi-user experimental program using a high-intensity, low-energy positron beam.

A high-energy positron beam is formed using positrons emitted from a ^{22}Na source placed at the terminal of a 3 MeV electrostatic accelerator[6]. The positron beam (with a typical intensity of $5x10^5$ positrons/sec) emerging from the accelerator column is focused by a thin solenoid, exits the vacuum through a 25 μm thick Al window, and enters the specimen either directly or after passing through a 2 mm thick scintillator, that provides a start signal for positron lifetime measurements. The positron penetration depth into the test material is greater than 2-3 mm and allows us to measure bulk properties without significant contributions from the near-surface regions. The annihilation spectrum is detected with detectors positioned collinear or perpendicular to the incoming positron beam direction. A collinear geometry is often used in lifetime measurements, while a perpendicular geometry allows both lifetime and energy analysis

* Corresponding Author, E-mail Address: asoka@llnl.gov

using coincidence logic between the annihilation gamma rays. Since the beam exits the vacuum system, the setup is convenient to probe engineering materials with specialized fixtures, encapsulated samples requiring a specific environment, and liquids. Recently, we have applied this system to study diverse problems such as embrittlement in reactor pressure vessel steels[7], direct observation of carbon-decorated defects in fatigued type 304 stainless steel[8], preferential positron sampling of anions in alkali halides[9], and characterization of open-volume regions in bulk metallic glass[10-13]. In section 2, we summarize results obtained from bulk metallic glass.

The high intensity positron program is summarized in section 3. The primary source of positrons is built at the end of a 100 MeV linear accelerator, capable of delivering up to 40 kilo Watt peak power at a repetition rate of up to 1400 Hz. At present, the positron program is well integrated into the core mission of the 100 MeV accelerator and is expected to be available for positron studies and associated collaborative experiments for about 4-6 months a year.

2. Free volume characterization in bulk metallic glass

A new class of multi-component metallic glasses that can be grown in bulk form at relatively slow cooling rates have attracted considerable commercial and technological interest[14,15]. These glasses exhibit a number of attractive physical and mechanical properties, including large elastic strains to failure, high tensile strengths, and excellent wear and corrosion resistances. Open volume regions in glassy structures are known to play an important role in determining and modifying their properties when subjected to various external conditions. Positron annihilation spectroscopy is a highly sensitive, nondestructive probe to study the nature, concentration, and spatial distribution of open volume regions in materials. Positron lifetimes are influenced by the presence of these open volume regions and can be used to measure the "openness" of these frozen-in disordered regions. A number of studies in conventional rapidly quenched metallic glasses yield single-component lifetime spectrum with a decay constant indicative of open volume regions that are smaller than the vacancies found in constituent metals[16].

Electron momentum distributions in a solid can be examined using the Doppler shift of annihilation gamma rays[1]. The high momentum part of this spectrum (denoted as OEMS, Orbital Electron Momentum Spectrum) is dominated by orbital electrons that retain their atomic character and are thus elemental specific[17-19]. The elemental specificity of OEMS has been employed successfully to address many defect-related problems[20-23].

We have used positron lifetime and OEMS measurements to characterize open volume regions in two sets of Zr-based five-component alloys, $Zr_{52.5}Ti_5Al_{10}Cu_{17.9}Ni_{14.6}$ and $Zr_{41.25}Ti_{13.75}Ni_{10}Cu_{12.5}Be_{22.5}$. They yield similar lifetime values of 177±3 ps and 179.5±0.5 ps, respectively. Similar to conventional metallic glass, these lifetime values lie between those observed for bulk constituent metals and metal vacancies, suggesting positrons are sampling quenched-in open volume regions that are smaller than metal vacancies.

OEMS measurements conducted as a function of sample temperature confirm that positrons are localized at open volume regions and are not distributed throughout the alloy. Fig. 1

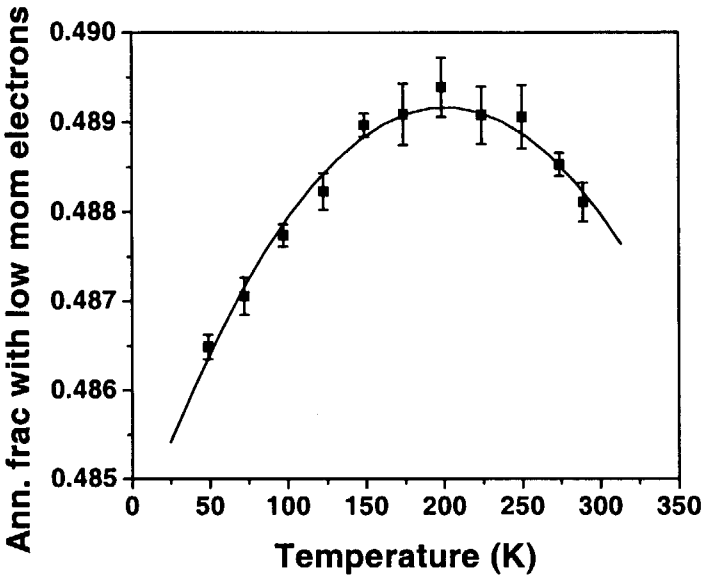


Figure 1. The plot shows the fraction of positrons annihilating with low momentum electrons (< 0.38 atomic units, with a system resolution of 0.38 atomic units) as a function of the sample temperature. The solid line through the data points is a guide to the eye.

shows the fraction of positrons annihilating with low momentum (< 0.38 atomic units, a.u.) electrons as a function of temperature. As the temperature is reduced from ambient, the fraction of positrons annihilating with low momentum electrons increases first, reaches a peak value at ~ 200 K, before decreasing and showing an opposite trend at temperatures below 200K. The positrons sample low momentum electrons more effectively when they are localized at open volume regions. These measurements suggest that there are at least two groupings of open volume sizes in these materials. The first group is more open and is barely deep enough to produce positron binding at room temperature, while the second group is shallow and binds positrons only at low temperatures. At room temperature, positron binding to open volume regions with large mean size is not complete and as the temperature approaches ~ 200 K, positron thermal energy is not sufficient to cause significant detrapping. At temperatures below 200 K, the second group with higher number density dominates the observed positron features. Similar positron measurements from samples charged with hydrogen show that open-volume regions that are localizing positrons at room temperature can also accommodate hydrogen[10].

A two-hour annealing at 650 °C (above the crystallization temperature, 470 °C) of the Al containing alloy reduced the lifetime to a value of 172±2 ps. The small changes upon annealing suggest that the crystallized sample contains many phases with a high concentration of positron localization sites, such as dislocations and grain boundaries and positrons are easily transported through the grains. A long anneal (48 hours at 500 °C) of the Be containing alloy reduced the lifetime value to 164.5±0.5 ps. However, calculated lifetime values for some of the known phases $NiZr_2$ and Zr_2Cu were 143 and 151 ps, respectively[24], significantly shorter than the experimental lifetime value, suggesting positron localization at open volume regions and not at crystallized regions.

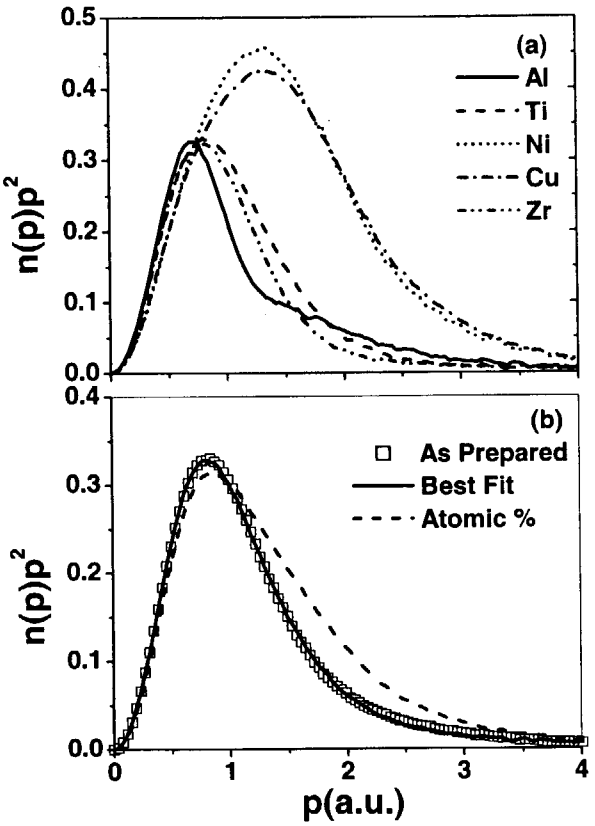


Figure 2. The top panel (a) shows the electron momentum distribution of constituent elements weighted with p^2 to enhance the features associated with orbital electrons at high momentum values. The bottom panel (b) shows the momentum distribution of $Zr_{41.25}Ti_{13.75}Ni_{10}Cu_{12.5}Be_{22.5}$. Broken line represents a perfect random distribution of elements around the positron annihilation site. The solid curve corresponds to the best fit obtained by adjusting the contributions from different elements shown in panel (a).

Detailed comparison of the OEMS spectra corresponding to the amorphous metal and metallic sub components show significant chemical ordering around open-volume regions[24]. Our results show that Ni and Cu atoms closely occupy the volume bounded by their neighboring atoms, while Be, Al, Ti, and Zr are less closely packed, and more likely to be associated with the open volume regions. Fig. 2 shows the OEMS spectra for constituent metals and best fit obtained by using a linear combination of the individual contributions. Also shown is a curve that corresponds to a linear combination in which the positron wave function is sampling a perfect random distribution of the constituents. The fitted coefficients are shown in Fig. 3. Ti contribution is enhanced to ~30% from a value of 5%. Contributions from Ni and Cu are combined and are reduced from 32.5% to 8%. Zr and Al contribution are comparable to grown-in concentration. These results show that open volume regions sampled by positrons are surrounded by atoms like Ti, Zr, and Al. Similar results are obtained in Be containing alloy where Be replaces the role of Al[12].

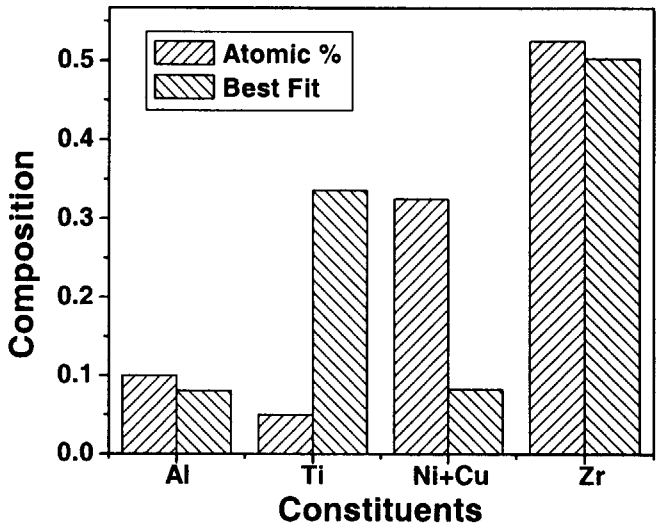


Figure 3. Composition of constituent elements as revealed by positron annihilation measurements. Compared to the grown-in concentration, Ti is enhanced at the expense of Ni and Cu.

3. High Intensity Positron Program at LLNL

A large number of experiments can benefit from a high-intensity, low-energy positron beam. At present the low energy positron beam capabilities at US National Laboratories are led by the efforts at Lawrence Livermore National Laboratory. We are building a state-of-the-art multi user experimental program to meet the needs of the scientific community. Below we summarize the design features of the positron production area and some of the experiments planned for the immediate future.

The layout of the experimental hall, positron production hall, and linear electron accelerator (linac) is shown in Fig. 4. Positrons are produced at the end of a 100 MeV linac. The linac vacuum system is not connected to the positron vacuum system and electrons exit the linac system through a thin, water-cooled window and enter the positron vacuum system. The entrance vacuum window is integrated with a well-cooled stopping target for electrons. In the previous design[25], the stopping target was outside the vacuum system and physically decoupled from the vacuum window. Thus, the vacuum window to the positron production chamber was located downstream of the Bremstrahlung shower and suffered significant degradation at high power and was not able to withstand the sustained linac operation. In addition, the close proximity of the stopping target and vacuum window caused electrical arcing during the short linac pulse cycle, causing further degradation. In our current design, the vacuum window will face the electron beam first and thus will overcome the electrical arcing problem.

Immediately following the stopping target is an option to add either a flat tungsten foil or a set of tungsten foils of different geometry (like vanes) to increase the overall positron emission area. Initial tests conducted at low power will optimize the geometry for both phase space and

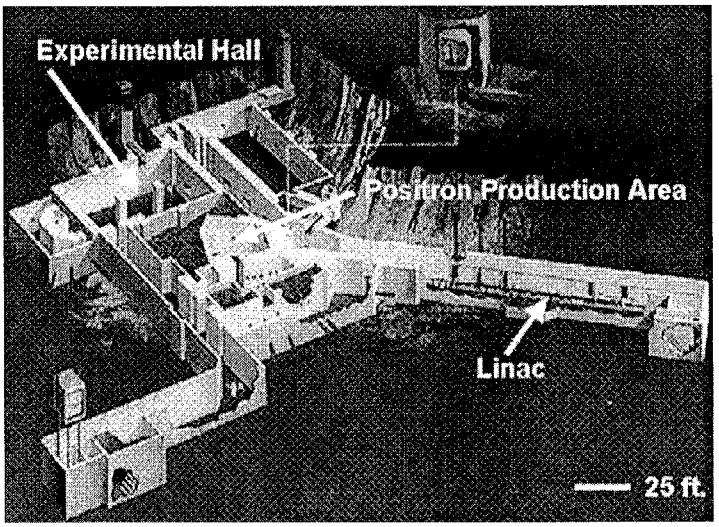


Figure 4. The layout of the intense positron beam at Lawrence Livermore National Laboratory. Positrons are produced at the end of a 100 MeV linac and transported to the experimental hall using a guiding magnetic field.

intensity. New design also allows easy interchange of the entrance window with fixtures incorporating in situ heating of the tungsten foil using direct electrical current flowing through them. We intend to study the effects of foil temperature on positron emission characteristics at low linac power to understand the relationship between the dynamic annealing of beam-induced defects and positron emission characteristics[26]. The tungsten foil temperature during a high power linac pulse is expected to be well above migration energies of simple defects in tungsten. We also have installed additional ports for introducing trace amounts of gases to study their effects on positron conversion efficiency. Another design criteria is to keep all surfaces exposed and close to the primary tungsten foil to be made out of tungsten to prevent sputter deposition of foreign elements. In our previous design, we observed significant coatings formed from sputtered aluminum and tungsten during high power linac operation.

A fraction of positrons that are slowed down near the surface of the tungsten foils will get reemitted as moderated positrons. These positrons are harvested and transported to an experimental hall with a guiding magnetic field. The beam transport system contains a curved section to prevent direct line of sight from the source region. The experimental hall and the positron production area are separated by 4.5 m of concrete shielding to ensure a low radiation background in the experimental hall. At the end of the curved section (in the positron production hall), we have also installed a ^{22}Na source (~15 mCi) and a tungsten moderator foil. This new source-moderator assembly provides a low intensity positron beam for test and setup purpose and can be withdrawn during high intensity beam operation. Both the high intensity and low intensity positron beam can be transported to the experimental hall at energies of ~ 10 eV to 10 keV.

The positron beam entering the experimental hall can be transported to multiple end stations, including positron microprobe, positron diffraction and holography, and a OEMS chamber. Some of the experiments (OEMS) will use the low intensity beam exclusively, while

the others will use the high intensity beam with further conditioning to alter their time structure and phase space properties.

The positron microprobe will produce a tunable (~ 1keV to 50 keV), time-bunched (100 ps wide, 20 MHz) positron beam with a pot size of ~ 1 μm and can be used to obtain a three dimensional maps of defects in materials. Some of the novel features associated with our microprobe design can be found elsewhere[27]. The time structure of the initial positron beam is decided by the primary electron beam and is not suited for positron microprobe since it will saturate most detector systems. Therefore positrons produced by each linac pulse are captured, time stretched, and rebunched to provide suitable time structure for the micropobe[28]. To compress the beam spot from an initial diameter of 1 cm to ~ 1 μm, we will also employ several stages of remoderation. Overall efficiency of the transport system and 3-stage remoderation stages is expected to be of the order of 10^{-3}, and hence we expect a beam intensity of more than 10^6 positrons/sec at the target.

The intense positron beam is ideal for positron diffraction and holography measurement. The advantages of a positron beam over an electron beam in terms of fewer artifacts and ambiguities in the diffraction pattern are well known[2]. However, lack of a sufficiently intense positron beam has hindered previous attempts to take full advantage of the positron diffraction for surface characterization. A serious disadvantage posed by a positron diffraction experiment over an electron diffraction experiment is the background caused by the prolific emission of positronium (a neutral bound state of an electron and a positron) from the sample surface. Since positronium is neutral it will pass through the grid system located in front of the channel plate detector system. In standard electron diffraction experiment, the grid system is used to suppress the electrons scattered inelastically and is used to perform similar functions in a positron diffraction experiment. To overcome issued associated with positronium background, we will take advantage of the pulsed nature of the positron beam. Since positronium signal will reach the channel plate at a later time compared to the elastically scattered positrons contributions arising form inelastic scattering and positronium can be discarded.

We summarized the intense positron beam development at Lawrence Livermore National Laboratory. The high flux of the LLNL beam and the assortment of spectroscopic tools being developed will enable several unique experiments.

We would like to thank R.H. Dauskardt, K.M. Flores, R. Howell, T.G. Nieh, D. Schneider, P.A. Sterne, and D. Suh for many useful discussions. This work was performed under the auspices of the U.S. Department of Energy by the University of California at Lawrence Livermore National Laboratory under contract No. W-7405-Eng-48. Part of this work was also supported by Basic Energy Research, Materials Science Division of U.S. Department of Energy.

References

1. R .Krauuse-Rehber and H.S. Leipner, *Positron Annihilation in Semi-conductors* (Springer, Berlin, 1999).
2. S.Y. Tong, H. Huang, and X.Q. Guo, Phys. Rev. Lett., **69**, 3654 (1992).
3. P. Asoka-Kumar, K.G. Lynn, and D.O. Welch, J. Appl. Phys., **76**, 4935 (1994).

4. A. David, G. Kögel, P. Sperr, and W. Triftshäuser, Phys. Rev. Lett., **87**, 067402 (2001).
5. M.J. Puska and R.M. Nieminen, Rev. Mod. Phys., **66**, 841 (1994).
6. R.H. Howell, P.A. Sterne, J. Hartley, T.E. Cowan, Appl. Surf. Sci., **149**, 103 (1999).
7. P. Asoka-Kumar, R. Howell, T.G. Nieh, P.A. Sterne, B.D. Wirth, R.H. Dauskardt, K.M. Flores, D. Suh, and G.R. Odette, Appl. Surf. Sci., in print (2002).
8. P. Asoka-Kumar, J.H. Hartley, R.H. Howell, P.A. Sterne, D. Akers, V. Shah, and A. Denison, Acta Materialia, in press (2002).
9. J.H. Hartley, P. Asoka-Kumar, R.H. Howell, P.A. Sterne, Phys. Rev, B, Submitted (2002).
10. Daewoong Suh, P. Asoka-Kumar, R.H. Dauskardt, Acta Materialia **50**, 537 (2002).
11. K.M. Flores, D. Suh, R. Howell, P. Asoka-Kumar, and R.H. Dauskardt, Materials Transaction, **42**, 619 (2001).
12. K.M. Flores, D. Suh, R.H. Dauskardt , P. Asoka-Kumar, P.A. Sterne, and R.H. Howell, J. of Material Research, in press (2002).
13. P.A. Sterne, P. Asoka-Kumar, J.H. Hartley, R.H. Howell, T.G. Nieh, K.M. Flores, D. Suh, R.H. Dauskardt, Mater. Res. Soc. Sympos. Proc., **644**, L1.3.1 (2001).
14. R.J. Gottschall, Materials Trans., **42**, 548 (2001).
15. A. Inoue, Acta Mater. **48**, 279 (2000).
16. K.P. Gopinathan and C.S. Sunder, in *Metallic Glasses – Production, Properties, and Applications*, p 115 (Trans. Tech., Aedermannsdorf, Switzerland, 1984).
17. S. Matsui, J. Phys. Soc. Japan, **61**, 187 (1992).
18. M. Alatalo, H. Kauppinen, K. Saarinen, M.J. Puska, J. Makinen, P. Hautojärvi, and R.M. Nieminen, Phys. Rev. B **51,** 4176(1995).
19. P. Asoka-Kumar, M. Alatalo, V.J. Ghosh, A.C. Kruseman, B. Nielsen, and K.G. Lynn, Phys. Rev. Lett., **77**, 2097 (1996) 2097.
20. U. Myler, P.J. Simpson, D.W. Lawther, and P.M. Rousseau, J. Vac. Sci. Technol. B **15**, 1(1997).
21. K. Saarinen, T. Laine, S. Kuisma, J. Nissilä, P. Hautojärvi, L. Dobrzynski, J.M. Baranowski, K. Pakula, R. Stepniewski, M. Wojdak, A. Wysmolek, T. Suski, M. Leszczynski, I. Grzegory, and S. Porowski, Phys. Rev. Lett., **79**, 3030 (1997).
22. J. Kuriplach, A.L. Morales, C. Dauwe, D. Sgers, M. Šob, Phys. Rev. B 58, 10475(1998).
23. M.P. Petkov, M.H. Weber, K.G. Lynn, R.S. Crandall, V.J. Ghosh, Phys. Rev. Lett., **82**, 3819(1999).
24. P. Asoka-Kumar, J. Hartley, R. Howell, P.A. Sterne, and T.G. Nieh, Appl. Phys. Lett., **77**, 1973 (2000).
25. R. Howell, R.A. Alvarez, and M. Stanek, Appl. Phys. Lett. **40**, 751 (1982).
26. R. Ley, Hyperfine Interactions, **109**, 167 (1997).
27. W. Stoeffl, P. Asoka-Kumar, R.H. Howell, Appl. Surf. Sci., **149**, 1 (1999).
28. P. Asoka-Kumar, R. Howell, W. Stoeffl, and D. Carter, *Application of Accelerators in Research and Industry*, Eds. J.L. Duggan, I.L. Morgan, (American Institute of Physics, New York 1999).

JP0350245

1.3.2 LIQUID METAL EMBRITTLEMENT: FROM BASIC CONCEPTS TO RECENT RESULTS RELATED TO STRUCTURAL MATERIALS FOR LIQUID METAL SPALLATION TARGETS

D. Gorse, S. Goryachev and T.Auger

CNRS-CECM, 15 rue Georges Urbain, F-94407, Vitry/Seine, Cedex, France

Abstract

At first, the basic features of LME are recalled (definition, characteristics, embrittling couples), together with classical experimental features and open questions. Then, a review of a few very recent results obtained on classical embrittling couples but using new powerful investigation techniques developed in France is proposed. Second we define LMC. The "LME- LMC" correlation is postulated. Then we concentrate on the LME-LMC problem related to the build-up of the Liquid Metal Spallation target in the frame of the MEGAPIE project. The Russian expertise on LME is briefly mentioned. Then we present some results obtained in the frame of the "Groupement de Recherche" GEDEON, focusing on steel grade T91 in contact with lead and lead-bismuth eutectic, in agreement with Russian literature.

Keywords: Liquid Metal Embrittlement, intergranular penetration, Liquid Metal Corrosion, Lead-Bismuth eutectic, steels, spallation target, ADS.

1. Introduction

One task is to define Liquid Metal (LM) Corrosion, another one to define LM Embrittlement, because of the intriguing synergy between the stress - strain state and the environment. One can define LME as a degradation of the mechanical properties of an otherwise ductile metal (like Cu, Al...) induced by some interaction with LM and mechanical solicitation. Since its discovery in 1874, embrittlement of structural materials by Lead-Bismuth was extensively studied, especially in Russia during the 50's for nuclear applications [1]. Model studies of model systems [2] appeared in the 70's, and continued to attract the attention of materials scientists over the past 30 years, not disconnected from basic research conducted on Grain Boundaries (GB) [3]. Now the renewed interest for LME is motivated by material research programs related to an important component of the park of nuclear reactors of new generation for the 21st century, namely accelerator driven subcritical reactors (ADS) for incineration of minor actinides [4-7].

This paper is organised as follows. In section 2, the main characteristics of LME, related to thermodynamics, morphology and kinetics aspects, are reviewed and illustrated [6-8]. Basic concepts of very recent models are presented [8-18]. Section 3 is devoted LMC, and relations with LME [19-21]. Note already that models are presented first, at purpose, since none of them takes into account the environmental effects on the SM/LM interface. In all cases, defects are only permitted in the GBs, with quasi ideal SM/LM interfaces (smooth at all scales and free from segregating metallic or metalloid impurities, except the embrittling atoms). In section 4, susceptibility to LME of iron base alloys is first shortly reviewed.

Then we come to the LME and related LMC studies carried out in the frame of the "Groupement De Recherche GEDEON" (GEstion des DEchets par des Options Nouvelles), taking into account the characteristics of the MEGAPIE spallation target [7,20-22]. We conclude briefly.

2. Liquid Metal Embrittlement

2.1 Main characteristics of LME.

Just as for Localised Corrosion (LC) or Stress Corrosion Cracking (SCC) [8], one distinguishes three phases: nucleation, subcritical growth, and propagation until final rupture with possible crack arrests. Most studies concern the phase of subcritical crack growth. The crack nucleation phase is unknown. Cracking is in general intergranular, scarcely transgranular.

Thermodynamically, LME may concern all SM/LM couples, whatever the phase diagrams (exhibiting mutual solubility or not, forming or not high temperature intermetallic compounds). There are tables collecting the most studied and considered embrittling and nonembrittling SM/LM couples, as the one proposed by Shunk and Warke [9-10]. In our opinion, the famous SM/LM « specificity » is based on non-exhaustive or inadequate criteria... Of course, the most spectacular case is the embrittling penetration of Aluminium by liquid Gallium. Nonembrittling couples can be incorrectly considered either because suitable testing and analysing conditions were not applied or are still missing or because the crack growth rate is so slow or too slow regarding the experiment duration [11].

To illustrate this important point, we reported in Figure 1 results published in 1960 by Rostoker *et Coll.*[12] It is well known that Cu is severely embrittled by Bi. Shall we conclude that Cu is rather immune against LME in Pb? Shall we not better suppose that the embrittling criteria were not fulfilled under the operating conditions of Figure 1?

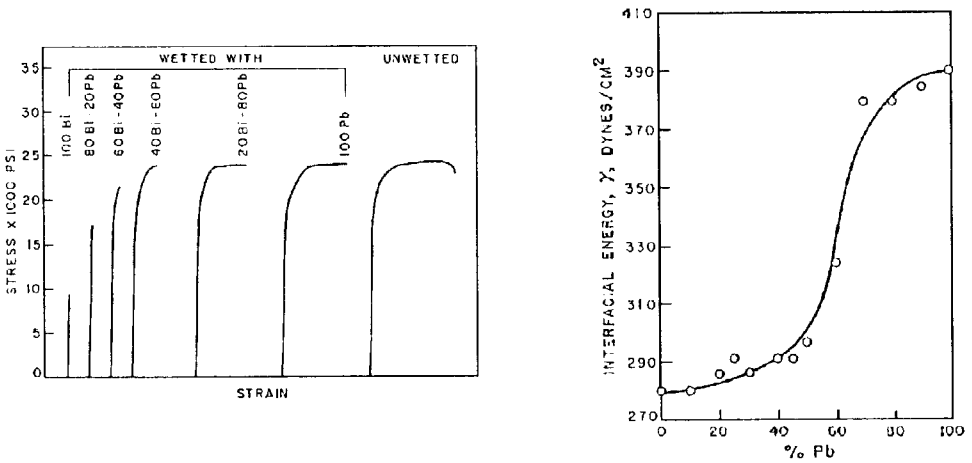
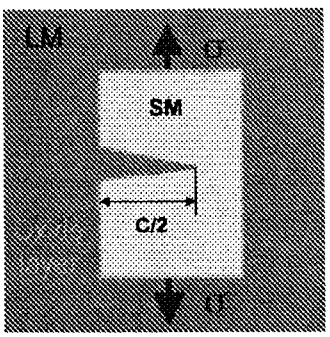


Figure 1. *Left:* stress *vs.* strain plots for cold-rolled Cu in contact with Pb_x-Bi_{1-x} alloys; *Right*: Variation of the interfacial energy $\gamma_{S/L}$ between Cu and Pb_x-Bi_{1-x} alloys at 350°C (note the reference values $\gamma_{Cu/Pb} \sim 390$ erg/cm^2 and $\gamma_{Cu/Bi} = 280$ erg/cm^2. *After W. Rostoker et Coll.* [12]

Let us note that rare gases, like Argon, can be also embrittling. The only difference is that the crack propagation rate, v_{crack}, in Cu under Argon cover gas is three orders of magnitude slower than in Bismuth!

For *real* SM/LM couples, surface heterogeneities constitute a source of crack initiation sites (as for LC!). A simple-minded scheme including parameters favouring (LM, stress σ) and hindering (oxide layer) crack propagation is shown here. Are missing the SM strain state and all chemical impurities in both phases. Rebinder first proved that the contact with LM reduces the surface energy, now $\gamma_{S/L}$ if perfect wetting.



The Griffith criterion gives the critical stress $\sigma_C = [2\,E\,\gamma_{S/L}/\pi c]^{1/2}$ for crack growth of size c/2. Using $K = [\pi c/2]^{1/2}$, we define the critical stress intensity factor $K_{IC} = [2E\gamma_{S/L}]^{1/2}$. So we justify qualitatively the huge difference in susceptibility to LME of Cu/Bi with respect to Cu/Pb.

Crack propagation gives rise to the opening of "fresh" surfaces at crack tip. The crack propagation rate is determined by the competition between the oxidation kinetics in the crack tip area and the kinetics of penetration of the embrittling (LM) atoms, once defined the metallurgical conditions (stress-strain state).

There are different crack morphologies, depending on the SM/LM system (nature and purity), environmental, metallurgical and mechanical testing conditions: Mullins grove, finger-like, or rather narrow channels as the one displayed in Figure 2 [13].

Over a depth of order 100 μm, the crack width is invaded by Bismuth, leading to a Bi film wetting the parallel channel walls. Beyond, Bi is no longer observable, while the crack becomes narrower, of submicronic, then nanometric width with approaching the crack tip area. Note that Ni is clearly embrittled far ahead of the micrometric film!

Impact broken Ni specimens were analysed *in situ* within an Auger spectrometer which allowed to reveal the presence of Bismuth on fracture surfaces and to quantify the number of Bi layers present in the GBs.

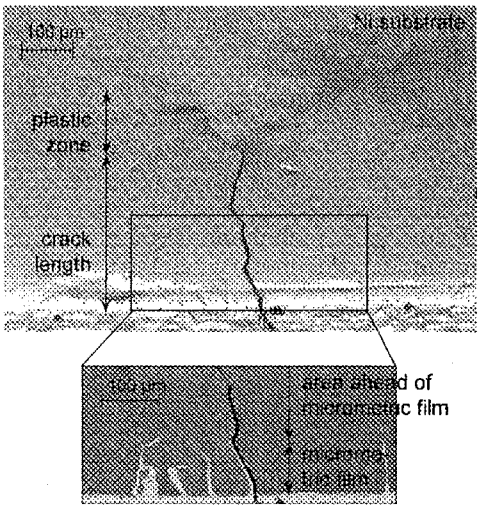


Figure 2. Metallographic observation of intergranular crack formed in polycristal Ni (100 ppm impurities) bent at room temperature after 1 h exposure to Bi vapor at 700°C. Below: SEM micrograph showing that the crack stops far ahead the region of Bi visible penetration. *After N. Marié et Coll* [13]

Rabkin addressed the question of how the embrittling atoms are supplied in the crack tip zone and beyond [14]. Writing the width of the steady-state diffusion zone ahead of crack tip as $l = D_{GB}/v_{crack}$ gives $l \approx 10^{-12}$ cm for $v_{crack} \approx 0.1$ cm/s and $D_{GB} = 10^{-14}$ cm^2/s at about 0.3 T_m (T_m designates the SM melting temperature) which is unrealistic.

To make this value acceptable, Rabkin suggested first that a tensile stress might accelerate GB diffusion. The author also assumed that the driving force for "diffusion" could be affected too.

Finally, a pre-melted GB was assumed, consistent with a sufficient diffusivity (10^{-5} cm^2/s) to supply the embrittling atoms in the GB, and allowing for intergranular cracking.

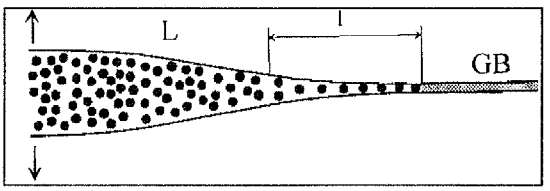


Figure 3. Gradual decohesion zone of length l separating the region "macroscopically" filled with LM from the unsegregated GB. *After E. Rabkin* [14].

The question of applied stress is also a matter of debate. Scientists studying wetting and intergranular penetration often consider tensile stress is not a prerequisite parameter for occurrence of LME. Definitions of LME can be found in the literature where σ tends to zero, the prominent role of the LM embrittling phase being emphasized. Al/Ga is the best couple to the purpose of validating such models of LME.

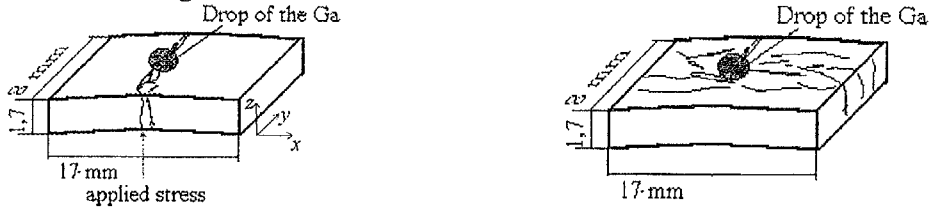


Figure 4. Geometry of fracture in case of an Al alloy (*Left*) with applied stress ; (*Right*) after plastic deformation in bending and without applied stress during the experiment of Ga penetration; *After Brechet et Coll.* [7]

*Corresponding author. Tel: 33 (1) 56 70 30 61, Fax: 33 (1) 46 75 04 33. E-mail address :gorse@glvt-cnrs.fr (D.Gorse)

Of course it is known that LME occurs at applied stress much lower than the yield stress (Fig 1). However, the above Figure 4 enlightens the important role of the stress - strain state regarding susceptibility to LME of Al put into contact with a Gallium drop. Note that the stress-strain state influences the morphology of the fracture.

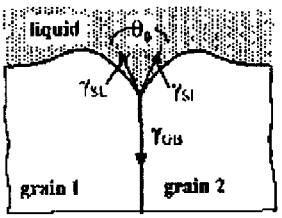
With stress, the tensile components are in the Ox direction. On the contrary after stress removal and elastic relaxation, the residual tensile stress is in the Oy direction which explains the geometry of fracture seen in Figure 4. We have also chosen to present this experiment since Al/Ga is the perfect example of embrittling couple at zero applied stress!

Powerful techniques are now available to study LME. First, synchrotron radiation X-ray microtomography recently proved to be a very useful tool for investigating propagation paths and kinetics of the "embrittling" elements in a metallic polycrystal [15]. Second, High Resolution Transmission Electron Microscopy (HRTEM) and related analysis techniques permits to attain elementary defects in GBs. It could be of great help to understand their influence on penetration of the embrittling elements and on intergranular crack advance [7].

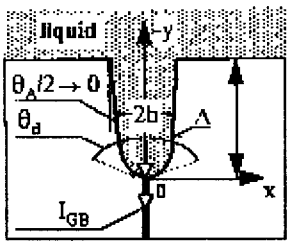
Contrary to an opinion found in recent literature [16], we would like to emphasize that LME can be observed over a wide temperature range, not determined by the melting temperature of the "embrittler" ($T_{m,E}$) and confined in a narrow range given by $T_{m,E} \pm 50°C$. This point will be confirmed in Section 4 where susceptibility to LME of steel grade T91 in Pb-Bi eutectic will be specifically treated.

Recent modeling of LME take into account some ingredients of intergranular cracking discussed above and try to explain the crack morphology and its kinetics of propagation. The role of externally applied stress is not explicitly included.

It would have been surprising that the Mullins groove requiring thermodynamic equilibrium conditions in the crack (see scheme opposite) describes satisfyingly its morphology. However, this theory of thermal grooving allows to define an equilibrium dihedral angle θ_0 using: $2\,\gamma_{SL}\cos(\theta_0/2) = \gamma_{GB}$



On can easily think how difficult to measure the dynamic wetting angles on crack walls and (θ_d) at crack tip, once remarked that an acute measurement of the time dependent curvature gradients are a key factor for modeling crack propagation.



Glickman *et Coll.*[17] proposed that the non zero dynamic concave angle that develops at crack tip is responsible for an inward driving force F:

$F \propto \gamma_{GB}\,[1 - \cos(\theta_d/2) / \cos(\theta_0/2)]$ (with the above definitions of θ_0 and θ_d)

and for the transport of "embrittling atoms ahead of crack tip, in the GB[1].

On the other hand, Chatain *et Coll.* [18] developed another approach, emphasizing the role of structural defects in the GBs, especially facets, and allowing to predict the observed linear LM penetration rate as well as the crack morphology found remarkably time-independent in the literature.

3. Liquid Metal Corrosion (LMC)

3.1 definition and application to 9%Cr martensitic steels

LMC means passive film growth (~ nm) and thickening (~ μm) on an oxidisable metallic alloy followed by generalised or localised corrosive attack. In principle, self-healing of locally depassivated area (Pits) may be obtained by active oxygen control in the LM bath.

[1] We do not develop here the arguments given by the authors to iterate the process. Neither do we comment the fact that this process implicates high stress. After Glickman, wetting induced surface roughening of GBs will make easier point defect production and decrease γ_{SL}.

Recent studies, using dedicated devices like COXCIMEL with electrochemical oxygen control in LM bath and suitable cover gas [7-19-21], have shown that over a wide range of oxygen contents going from highly reducing (~10^{-10} wt.%O_2) to highly oxidizing conditions (~10^{-4} wt.%O_2), the steel surface of the 9%Cr pre-selected steels for the MEGAPIE spallation target and future ADS is always found a priori oxidised, and poorly wettable by LM (Fig. 5), in agreement with classical thermodynamics and Ellingham Diagrams.

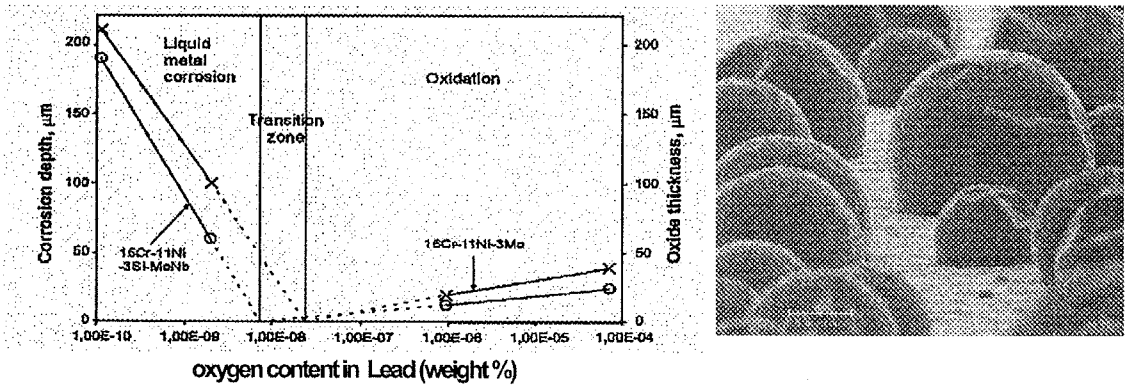


Figure 5. (*Left*) Diagram showing the oxidation conditions used in IPPE-Obninsk by Markov *et Coll.* [7] giving rise to surface oxide films, whose protectiveness and wettability by LM should be already initially function of the temperature and oxygen content. (*Right*) SEM micrograph showing a top view of oxidised T91 steel surf. after 15 days ageing above a stagnant Pb bath under highly reducing conditions in COXCIMEL set-up revealing Pb droplets *and* the bad wettability of the oxide surface film, *After V. Ghetta et Coll* [19-21]

3.2 Relation LMC – LME: case of 9%Cr martensitic steels

It was also shown that one month ageing under highly reducing conditions gives rise to surface pitting and roughening. Less known, ageing under similar conditions in LM causes also appearance of porosities in the T91 steel in bulk [7]. It is argued that pits, pores, and roughness induced by exposure of T91 steel to Lead might be very detrimental regarding susceptibility to LME. Note that such corrosive degradations do not require long-term ageing (just a few weeks !), and that exposure to lead-bismuth eutectic could possibly accelerate this ageing process and affect resistance to LME. This is pure conjecture!

According to the Kamdar criterion that intimate SM/LM contact at atomic scale is a necessary condition for occurrence of LME, it could be tempting to suppose:

- that "unaged" steel specimens, covered with an oxide film in the very initial protective stage of LMC, are not prone to LME;
- but that ageing in LM causes degradation of resistance to LMC, taking the form of "pits - pores and roughness" and thus might increase substantially the susceptibility to LME.

This is what we call the "LMC-LME" correlation. After long-term ageing in LM [21], in any case, the SM/LM contact will be macroscopically recovered possibly permitting LME.

4. Susceptibility to LME of 9%Cr martensitic steels in liquid Lead alloys

4.1 from Iron Armco to 9%Cr martensitic steels

Even a non exhaustive review of the Russian literature from the 60's gives an idea of the considerable amount of knowledge already existing as concerns susceptibility to LME of both model systems and *real* systems, like steels in contact with Lead, Bismuth and their alloys. Metallurgical and environmental criteria were already studied. This point is illustrated below.

Susceptibility to LME was known to be dependent on i) surface state, ii) metallurgical parameters like grain size, iii) environment meaning temperature and chemistry of the contacting phase. Briefly, susceptibility to LME is maximized around 350°C for polished specimens of iron or iron-base alloys of large grain size. The steel microstructure as a whole (lath structure, precipitates...) is determining. The welding effect on LME was studied.

*Corresponding author. Tel: 33 (1) 56 70 30 61, Fax: 33 (1) 46 75 04 33. E-mail address :gorse@glvt-cnrs.fr (D.Gorse)

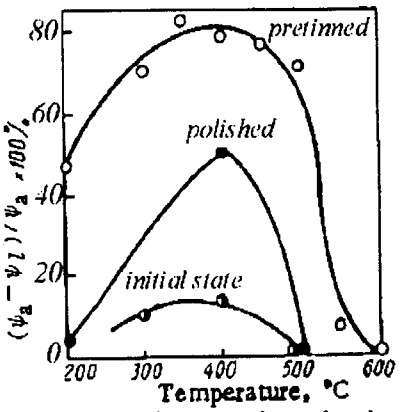


Figure 6. Relative decrease in reduction of area for a type 12KhM steel (0.12C-1Cr-1Mo) *vs.* test temperature in liquid Pb-Bi eutectic showing the influence of the surface state, *After Balandin* [1].

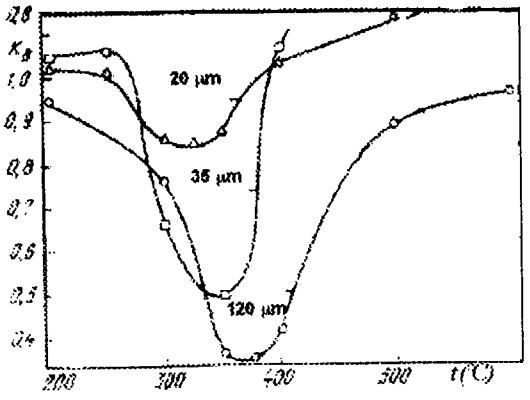


Figure 7. Relative reduction of elongation for Fe pretinned specimens *vs.* test temperature in liquid Pb-Bi eutectic showing the influence of grain size, *After Popovich* [1].

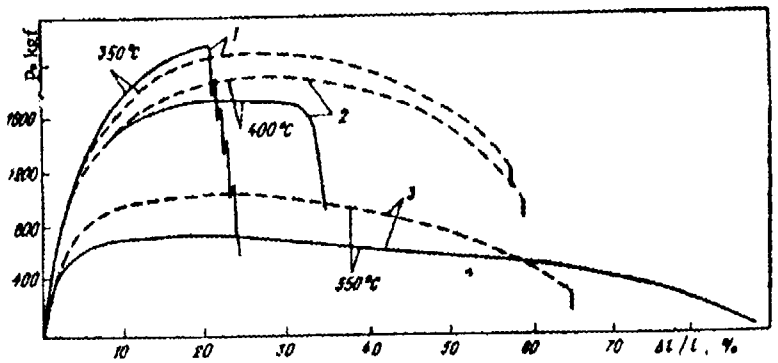


Figure 8. Stress *vs.* strain curves obtained with Armco Iron in Bismuth (continuous line) and in vacuum (dashed lines) showing the influence of the temperature, *After Popovich et Coll.* [1]

4.2 Resistance to LME of 9%Cr martensitic steels in Lead-Bismuth: some recent features

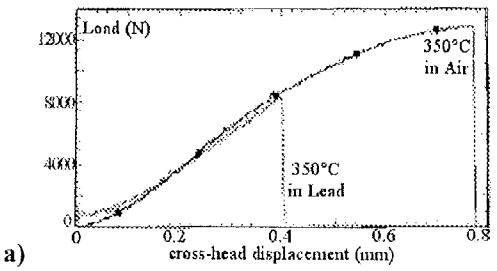
Today, 9Cr-1Mo mod. steel grade (T91) is studied in the frame of both ADS and LM spallation target projects [4,7,22]. In order to validate the "T91 steel/Pb-Bi eutectic" system for the target window and LM respectively, one has to verify the LMC and LME resistance without and under the specific irradiation conditions of the MEGAPIE spallation target. We concentrate here on some aspects of the problem without irradiation. The irradiation effects including Hydrogen and Helium effects will be the treated with LiSoR experiment and *in fine* with the MEGAPIE target.

One has to check the LME resistance under the more severe environmental conditions and damageable metallurgical conditions. From the tensile behaviour of T91 steel in LM, we deduce immediately the energy to fracture (calculated as the area under the load *vs.* cross-head displacement plots).

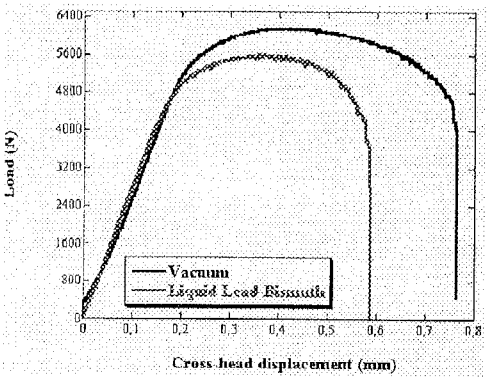
From the metallurgical point of view, one can combine suitable heat treatment and notch effect: the tensile tests are carried out in air as function of the temperature of the stagnant LM bath (Fig. 9.a). This gives the ductility trough of Fig. 9.b [7].

On the other hand, keeping the steel in its standard metallurgical state, we may vary the environmental conditions (vacuum or hydrogenated helium), temperature and mechanical test conditions. The LME effect is net by comparing the tensile behaviour of notched T91 steel specimens in Pb-Bi eutectic under hydrogenated helium with a reference in vacuum (Fig. 9.c).

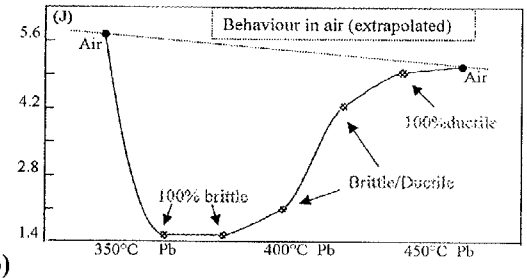
Recalling that 9%Cr martensitic steels were selected as the best compromise between fabricability and resistance to severe irradiation conditions and lead alloys environment, as stated in the GEDEON Material research program, these results are considered with special attention [4,7].



a)

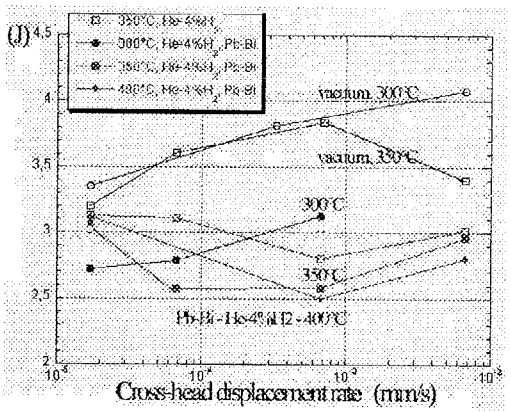


c)



b)

Figure 9. a) Exemplary load *vs.* cross-head displacement plot with heat-treated T91 steel at 350°C in air or contacting lead in air; **b)** Corresponding ductility trough for T91 steel after hardening heat treatment in [350–450°C] temperature range; *After G.Nicaise et Coll.* [7];
c) Same as in **a)** for T91 steel in standard metallurgical state exposed to vacuum and to Lead-Bismuth eutectic at 350°C under He-4%H_2. [22].



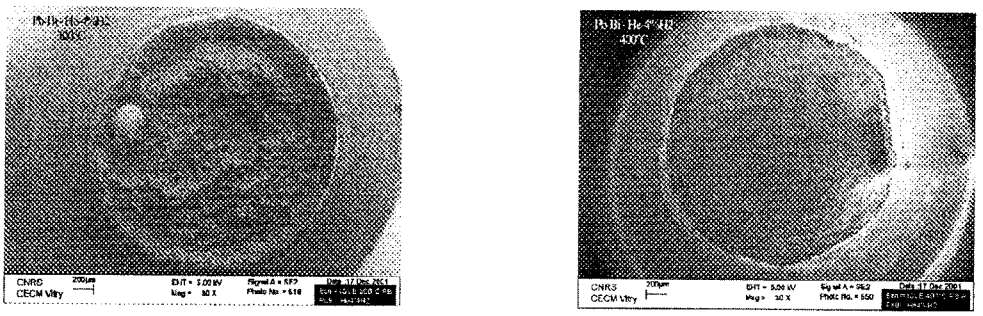


Figure 10. Energy to fracture *vs.* crosshead displacement rate for notched T91 steel (in standard metallurgical state) tested in vacuum (open symbols), under He-4%H_2 and in Pb-Bi under He-4%H_2 (full symbols) at 300°C, 350°C and 400°C. Rupture facies obtained on notched T91 steel specimens in Pb-Bi eutectic under flowing He-4%H_2 for a cross-head displacement rate of 1.6 10^{-5} mm s^{-1} at 300°C (*left*) and at 400°C (*right*).

As seen in Figure 10, resistance to LME is degraded not only by applying suitable hardening treatment but just by choosing a suitable combination of cross-head displacement rate, temperature and cover gas. Apparently, the embrittling effect of Pb-Bi is made clearer under flowing He-4%H_2. The role of hydrogen, at the SM/LM interface or in bulk steel is

*Corresponding author. Tel: 33 (1) 56 70 30 61, Fax: 33 (1) 46 75 04 33. E-mail address :gorse@glvt-cnrs.fr (D.Gorse)

outside the scope of this paper. Even at low magnification, in otherwise identical conditions, we observe a significant change in the rupture faciès with increasing temperature. At 300°C, the facies is ductile (equiaxed dimples). At 400°C, the evolution is net, crack nucleation occurred in a single area.

Other studies have shown a substantial acceleration of creep for T91 steel contacting Pb-Bi under pure H_2, not observable in the absence of the LM phase. This result suggests that the LM induced roughened surface is a perfect source for points defects (vacancies...), detrimental for both tensile and creep behaviour. From this point of view, one can conjecture that a rigorous control of the oxygen content in the spallation target should be welcome to avoid "pits, pores and roughness"!

Let us mention that we were not concerned here by the influence of radiation damage and production of spallation elements (especially helium and hydrogen) that will harden and embrittle the steel. Last, the problem of He embrittlement, of H embrittlement, of (He+H) then finally of (He+H+LM) embrittlement is evoked incidentally here. It will be a challenge for the next coming years and the new generation of nuclear reactors.

4. Conclusions

In this paper, well-known characteristics of LME and LMC are recalled. Concerning 9%Cr martensitic steels proposed for the spallation target of future ADS, we have shown that long-term exposure of metallic alloys to LM decreases the resistance to LMC, giving rise to "pits – pores" and surface roughening, and could be somehow responsible for a LME effect, not a priori expected with these steels. Work is in progress to "quantify" these preliminary results before beginning mechanical tests under irradiation in LiSoR experiment.

Acknowledgements

Financial support of French « Groupement de Recherche GEDEON », of TECLA and MEGAPIE-TEST programs founded by the EU 5th fwp are acknowledged. Thanks are due to all Colleagues of the CNRS-Dpt.SC and IN2P3 involved in these programs. DG thanks especially V. Ghetta for fruitful discussions.

References

[1] S. Goryachev, D. Gorse, *in preparation*
[2] C. Roques-Carmes, M. Aucouturier and P. Lacombe, Metal Science Journal, 7, 128 (1973).
[3] A.P. Sutton and R.W. Balluffi, Interfaces in Crystalline Materials, Clarendon Press, Oxford (1995).
[4] J.L.Boutard, D.Gorse, «Programme du GDR GEDEON sur les Matériaux des Systèmes Hybrides», ref DECM 98.078.
[5] Proceedings of the 2nd International Workshop on the Materials Technology for Spallation Neutron Source, M. Kawai and K. Kikuchi Eds., March 21-22 (2001).
[6] Proceedings of the 4th International Workshop on Spallation Materials Technology (IWSMT-4) G. S. Bauer, Y. Dai, L.K. Mansur, H. Ullmaier and S. A. Maloy Eds, J. Nucl. Mat., **296** (2001).
[7] Proceedings of the Symposium "Structural Materials for Hybrid Systems: a challenge in Metallurgy", held in Paris, October 29-31 (2001), to be published as a Thematic issue of "Annales de Chimie – Science des Matériaux", J.-L. Boutard and D. Gorse Eds. (2002).
[8] D. Gorse, in: "Multiscale phenomena in Plasticity", NATO ASI Series E, **Vol. 367**, 425 (2000).
[9] M.H.Kamdar, "Embrittlement by liquid metals" in: Prog. in Mat. Sci., Pergamon Press, **Vol. 15**, 289 (1973).
[10] F. Shunk and W. Warke, Scripta Metallurgica, **8**, 519-526 (1974).
[11] E.E.Glickman, in: "Multiscale phenomena in Plasticity", NATO ASI Series E, **Vol.367**, 383 (2000).
[12] W. Rostoker, J. Mc Caughey, H. Markus, "Embrittlement by Liquid Metals", Rheinhold Publishing Corporation, New-YorK (1960).
[13] N. Marié, K. Wolski and M. Biscondi, Scripta Mater. **43**, 943-949 (2000).
[14] E.Rabkin, in: "Multiscale phenomena in Plasticity", NATO ASI Series E, **Vol.367**, 403-413 (2000).
[15] W. Ludwig, Workshop on "Grain Boundary wetting by liquid metals", ESRF, January 14 (2000).
[16] B. Joseph, M. Picat and F. Barbier, Eur. Phys. J. AP. **5**, 19-31 (1999).
[17] E.E. Glickman and M. Nathan, J. Applied Physics, **85**, 3185-3191 (1999).
[18] D. Chatain, E. Rabkin,J. Derenne and J. Bernardini, Acta Mater. **49**, 1123-1128 (2001).
[19] V. Ghetta, J. Fouletier, M. Henault and A Lemoulec, J. Nucl. Mat. **296**, (2001).
[20] «MEGAPIE-TEST: A European Project on Spallation Target testing», J.U. Knebel, J.C.Klein, D.Gorse P.Agostini, F.Gröschel, P.Kupschus, T.Kirchner, J.Vogt. ANS Winter Meeting, Reno (2001).
[21] D. Gorse, S. Goryachev, V. Ghetta, M. Dupeux, J.-L. Pastol, S. Guerin, C. Leroux, MEGAPIE report, D22-01-02, February (2002).
[22] "CAMMEL : 1st GEDEON Workshop on Materials for Hybrid Systems", Paris, September 24 – 25 (1997).

JP0350246

1.3.3 ANALYSIS OF STRESS DEGRADATION OF METALS BY POSITRON ANNIHILATION

E. Kuramoto

Research Institute for Applied Mechanics, Kyushu University
6 – 1 Kasuga-koen, Kasuga, Fukuoka 816-8580 Japan

Abstract

Since the stress degradation of metals originates from the change of the microstructure induced by glide motion and multiplication of dislocations, fundamental features of this process have been investigated from the viewpoint of the dislocation - dislocation interaction and the consequent vacancy production by using positron technique and computer simulation. Corresponding to the positron trapping at deformation induced defects in metals such as Fe and Ni, positron lifetime calculation has been made for the configurations obtained in model Fe and Ni lattices which contain a dislocation and vacancies produced by dislocation cutting process. The important results are (i) straight dislocation lines usually behave as shallow traps for a positron and the corresponding positron lifetime is close to that at matrix, (ii) complex defects consisting of a dislocation line and vacancies usually show intermediate positron lifetimes between matrix and a single vacancy.

Vacancy production process by dislocation cutting is simulated in model Fe lattice and it has been clarified that a vacancy is produced at each step of a climbing jog dragged by a screw dislocation line on <111> atomic row in the vicinity of a jog. Another topic of vacancy production process in a small Cu precipitate cut by a gliding dislocation has also been simulated in Fe model lattice, showing a conversion from a straight dislocation line to a jogged line after cutting the Cu precipitates.

Key words: Dislocation cutting, Vacancy production, Complex defect of a dislocation and vacancies, Positron lifetime, Fe, Ni, Cu-precipitate

1. Introduction

Since the degradation of materials used under stress is a very severe problem in various fields, fundamental features in this phenomenon must be fully investigated. Dislocation multiplication and cutting between gliding dislocations are considered to be the most fundamental processes of the stress degradation of materials. It is well known that point defects such as vacancies and self-interstitial atoms (SIAs) are formed through dragging motion of jogs produced by dislocation cutting. The probability of vacancy formation is considered to be higher than that of SIAs due to the lower formation energy of a vacancy than that of a SIA. Vacancies produced usually migrate into dislocation lines or form clusters in matrix and on dislocation lines, resulting in the evolution of the complex microstructure which might cause the stress degradation of materials, e.g., the microvoid formation and coalescence of them tending to the ductile fracture of materials at the end of plastic deformation process. It is, however, not easy to observe microstructures in the

*Corresponding author: Tel: +81-92-583-7766, Fax: +81-92-583-7767
E-mail address: kuramoto@riam.kyushu-u.ac.jp

deformed specimens by the conventional microscopy. On the other hand, positron annihilation technique has become extremely powerful to preferentially detect free-volume type defects such as vacancies and dislocations. In order to identify various type defects atomic structures of them must be determined in the simulation calculation in model lattices and for the atomic structures thus obtained positron lifetime calculation must be performed. In the present study these processes will be made for typical metals such as Fe (bcc) and Ni (fcc) to obtain further understanding of the fundamental features of materials stress degraded.

2. Positron lifetime in deformed Fe and Ni

Positron lifetime measurement was made for Fe specimens deformed at low temperature (77K) and two lifetime components (short one and long one) were found (1). In this study the long one (> 300 psec) was considered to be corresponding to microvoids formed by deformation-induced vacancies and short one (~165 psec) was considered to be corresponding to dislocations. On the other hand, the positron lifetime calculation was made for a positron trapped at an edge dislocation line in Fe by using the so-called atomic superposition method developed by Puska and Nieminen (2-5) and a very short lifetime and a shallow trapping of a positron were found (6). In this calculation the atomic structure was determined before lifetime calculation in Fe model lattice constructed by Finnis-Sinclair potential (7). Lifetime calculation was also made for the complexes of a dislocation and a vacancy in Fe and an intermediate lifetime between a matrix and an isolated single vacancy was obtained, such as 140 psec. Results of these calculations are shown in Fig. 1, where short lifetimes are obtained for a straight dislocation line and a jog, and intermediate lifetimes are obtained for dislocation – vacancy complexes and long lifetimes are obtained for a vacancy and vacancy clusters.

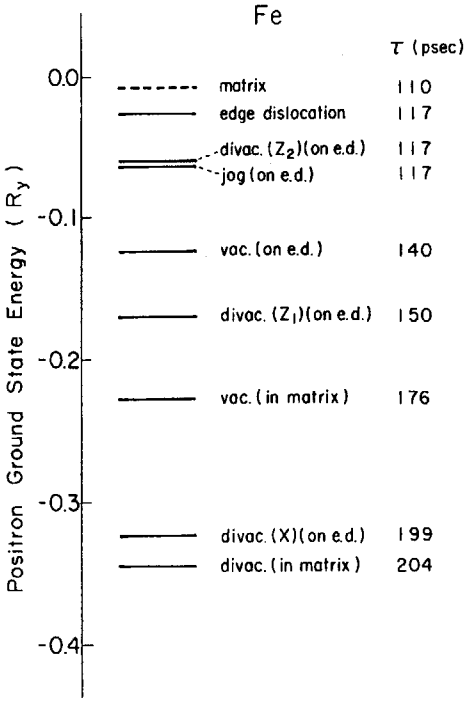


Fig. 1 Calculated results of the positron lifetime and the positron ground state energy for an edge dislocation, a jog, vacancies and dislocation–vacancy complexes in Fe.

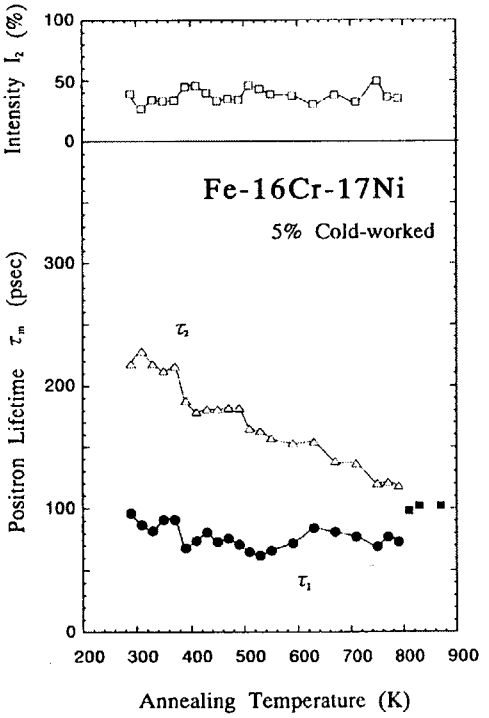


Fig. 2 Isochronal annealing result obtained by the positron lifetime measurement for Ni specimen deformed at room temperature.

In Fig. 2 the isochronal annealing behavior obtained by the positron lifetime measurement for Ni specimen deformed at room temperature is shown, where the long lifetime component decreases from about 200 psec to 130 psec with increasing annealing temperature (8,9). This suggests that the long lifetime component does not correspond to positron annihilation at the dislocation site, but at the vacancy or vacancy clusters on a dislocation line. Positron lifetime calculation was also made for a vacancy and vacancy clusters on an extended edge dislocation in Ni by using the N-body potential developed by Gao et al. (10) and the results are shown in Fig. 3, where short lifetimes are obtained for a straight dislocation line and a jog, and intermediate lifetimes are obtained for a dislocation and vacancy complexes, and long lifetimes are obtained for a vacancy and vacancy clusters. In fcc metals such as Ni stacking fault tetrahedra (SFT) are formed by agglomeration of vacancies and a wave function of a positron trapped at an SFT is shown in Fig. 4, where positron trapping mainly occurs at the corner sites of an SFT. This is the reason why the positron lifetime at an SFT is longer than that at a straight dislocation.

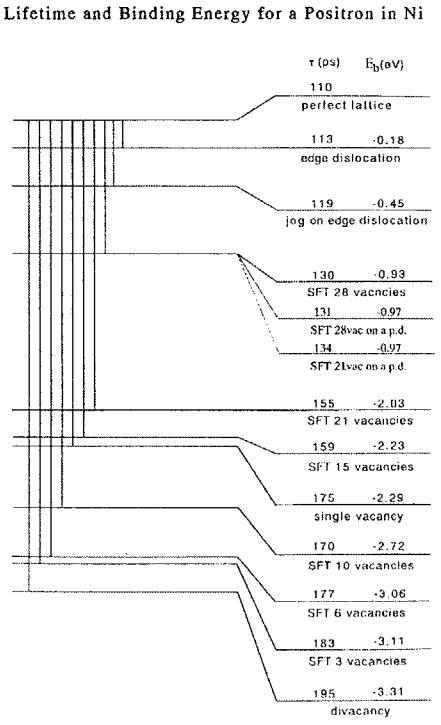
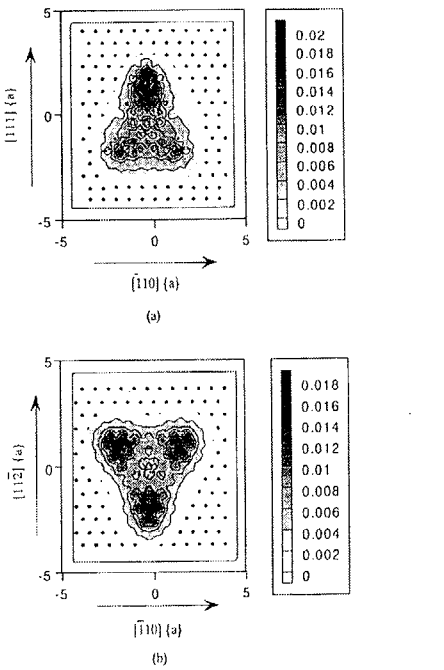


Fig. 3 Calculated results of the positron lifetime and the positron ground state energy for an extended edge dislocation, a jog, vacancies and dislocation – vacancy complexes in Ni.



Wave function of a positron trapped at vacancy clusters of V_{28} (SFT, collapsed type). (a) front view ({112} cross section), and (b) top view ({111} cross section)

Fig. 4 Calculated wave function of a positron trapped at an SFT in Ni.

From these results of positron lifetime measurements and calculations for deformed metals (Fe and Ni), it is clearly seen that positron lifetimes experimentally obtained do not necessarily correspond to that at straight dislocation lines, but that at complexes of a dislocation and vacancies. Dislocation lines give rather shallow trapping potential for a positron, and then low temperature measurements will be needed to detect this annihilation event at a dislocation line.

3. Vacancy production by dislocation cutting

It is well known that dislocation cutting produces point defects like vacancies and self-interstitial atoms (SIAs), but detailed atomistic features of this process have not been clearly studied yet. This process plays a very important role in the deformation of materials and especially in the ductile fracture at the end of deformation processes such as tensile test and creep test. Hence in the present study the model Fe lattice was constructed by using Finnis-Sinclair potential (7) and two screw dislocation lines (belonging to primary and conjugate slip systems) are introduced as shown in Fig. 5. Then the shear stress was applied to the model lattice to move the primary screw dislocation upward and make a cutting with the conjugate screw dislocation. By this cutting a jog was generated on each dislocation and the one on the primary screw dislocation was dragged. Depending upon the direction of Burgers vectors of two screw dislocations opposite jogs are formed as shown in Fig. 6. One of them (here the left one) results in the production of vacancies nearby on <111> atomic rows. In the other word, Frenkel pair was generated and an SIA was placed on the jog which enabled the jog to make a climb motion of one atomic distance and a vacancy in the pair was left in the neighborhood. Calculated behavior of jog dragging motion is shown in Fig. 7, where vacancies produced by jog dragging are aligned regularly probably due to minimization of the total energy.

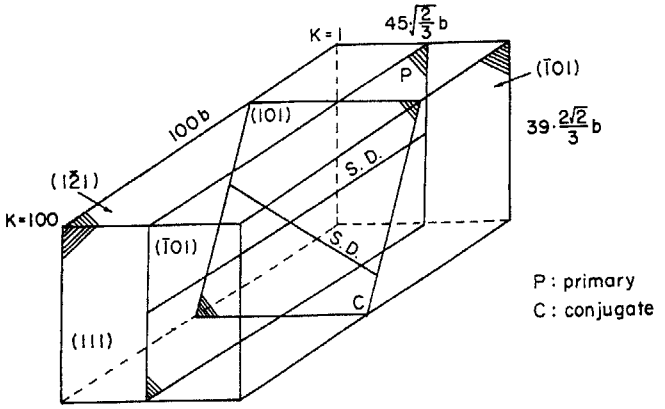


Fig. 5 Fe model lattice with two screw dislocations (belonging to primary and conjugate slip systems).

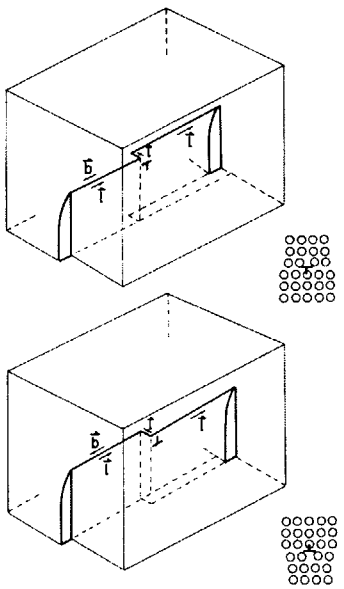


Fig. 6 Two jogged screw dislocations of opposite signs in Fe model lattice.

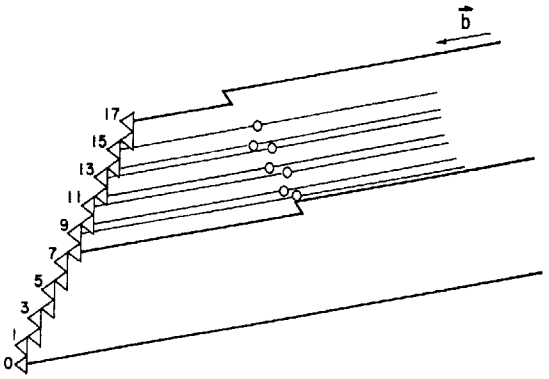


Fig. 7 Calculated behavior of jog dragging motion, where vacancies produced by jog dragging are aligned regularly.

4. Vacancy production by cutting Cu precipitates by gliding dislocation

Another case resulting in the vacancy production was found in the computer simulation which was made to reveal the atomic features of the cutting process of Cu precipitates in Fe matrix by gliding edge dislocations. This is the related problem to the embrittlement of pressure vessel steels in nuclear reactors (11). The model Fe lattice containing Cu precipitates was constructed by using the potential developed by Ackland et al. (12). It is observed in the simulation that a small round shape Cu precipitate (Cu_{15}) being cut by a gliding edge dislocation vacancies are produced in or on the periphery region of a Cu precipitate, and corresponding to this vacancy production SIAs are attached to the edge dislocation line, resulting in the conversion from a straight edge dislocation to the one with jog pairs which still can easily glide totally as shown in Fig. 8. The basic reason why vacancies are produced by dislocation passing is considered to reduce the expansion strain field which Cu precipitates form around them. In the case of larger Cu precipitates bcc structure of the precipitate seems to be disturbed by the large strain field of an edge dislocation probably due to the tendency of the conversion from bcc to fcc structure with the increase of the size of precipitates.

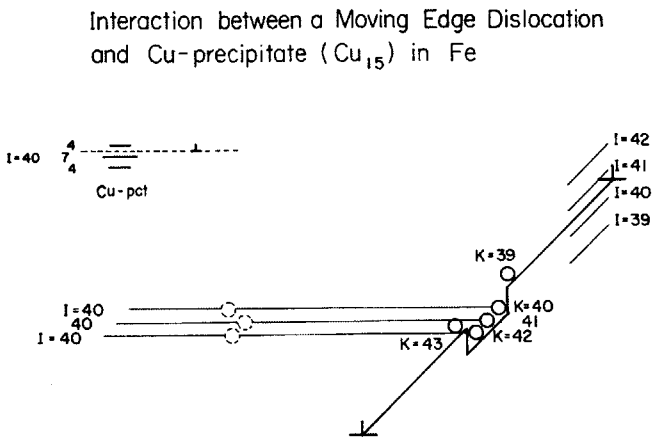


Fig. 8 Calculated behavior of the cutting process of a small round shape Cu precipitate (Cu_{15}) by a gliding edge dislocation, where vacancies are produced in or on the periphery region of a Cu precipitate, and corresponding to this vacancy production SIAs are attached to the edge dislocation line, resulting in the conversion from a straight edge dislocation to the one with jog pairs.

5. Summary

Fundamental processes of the stress degradation of metals and alloys have been discussed from the viewpoints of the dislocation – dislocation interaction, vacancy production by the jog dragging, dislocation – precipitate interaction, mainly based on the positron annihilation technique and the computer simulation. It is concluded that in the deformed state vacancies produced by dislocation cutting and jog dragging usually affect the positron trapping and annihilation behavior, and provide several intermediate positron lifetimes. Positrons are rather shallowly trapped at straight dislocation lines with short lifetimes.

Vacancy production process by dislocation cutting and jog dragging has been simulated in Fe model lattice and the atomistic feature of vacancy production was investigated. On <111> atomic row through a jog a Frenkel pair is produced and an SIA is placed on the jog resulting in climbing of one atomic distance and a vacancy is left nearby on <111> atomic row.

The simulation of the interaction between a Cu precipitate and a gliding edge dislocation in Fe matrix has shown the vacancy production in or nearby Cu precipitate probably due to reduce the strain field around the precipitate.

References

[1] P. Hautojärvi, J. Johansson, T. Judin, P. Moser, M. Puska, A. Vehanen, and J. Yli-Kauppila, Proc. 5th Int. Conf. Positron Annihilation, Lake Yamanaka (The Japan Institute for Metals, Sendai, Japan, 1979), p.737.
[2] M. J. Puska and R. M. Nieminen, J. Phys. F: Met. Phys. **13,** 333 (1983).
[3] E. Boronsky and R. M. Nieminen, Phys. Rev. B**34**, 3820 (1986).
[4] G. E. Kimball and G. H. Shortley, Phys. Rev. **45,** 815 (1934).
[5] F. Herman and S. Skillman, *Atomic Structure Calculations* (Prentice-Hall, Englewood Cliffs, NJ, 1963)
[6] Y. Kamimura, T. Tsutsumi and E. Kuramoto, Phys. Rev. B**52,** 879 (1995).
[7] M. W. Finnis and J. E. Sinclair, Phil. Mag. A**50**, (1984) 45 (erratum: Phil. Mag. A**53**, (1986) 161)
[8] K. Ueno, M. Ohmura, M. Kimura, Y. Kamimura, M. Takenaka, T. Tsutsumi, K. Ohsawa, H. Abe and E. Kuramoto, Mat. Sci. Forum, 255-257 (1997) 430.
[9] E. Kuramoto, H. Abe, M. Takenaka, F. Hori, Y. Kamimura, M. Kimura and K. Ueno, J. Nucl. Mat., 239 (1996) 54.
[10] F. Gao, D. J. Bacon, G. J. Ackland, Phil. Mag. A**67,** 275 (1993).
[11] T. Onitsuka, M. Takenaka, E. Kuramoto, Y. Nagai and M. Hasegawa, Phys. Rev. B**65**, 012204-1 (2002).
[12] G. J. Ackland, D. J. Bacon, A. F. Calder and T. Harry, Phil. Mag. A**75,** 713 (1997).

JP0350247

1.3.4 BORON CONTENT IN TYPE 316 L STAINLESS STEEL BY NEUTRON INDUCED AUTORADIOGRAPHY

Jinsung Jang*, Yong Bok Lee[1], Kwang Tae Kim[2], Yi Kyung Kim, Woo Seok Ryu
K.A.E.R.I, 150 Duckjin-dong, Yusong-gu, Daejeon, Korea (south)
[1] Korea University, 5-1 Anam-dong, Sungbuk-gu, Seoul, Korea (south)
[2] POSCO, 1 Geodong-dong, Nam-gu, Pohang, Gyeongbuk, Korea (south)

Abstract

Boron is effective to the improvement of various properties of alloys, but it is difficult to characterize its behavior during the alloy processing. Neutron induced autoradiography (or called as F.T.E: Fission Track Etching) technique was attempted to quantitatively analyze boron content in type 316 L austenitic stainless steel. Reference samples with nine different boron contents were prepared and analyzed by conventional analysis method as well as by autoradiography technique using 'HANARO', a 30 MW research reactor in K.A.E.R.I (Korea Atomic Energy Research Institute). Cd ratio of the neutron flux was about 200 and thermal neutron flux was around 2×10^{13} /cm^2/sec. A Kodak CN-85™ detector with an alloy sample was irradiated with two different thermal neutron fluences of 10^{13} and 10^{14} /cm^2. Track densities on the autoradiographs were measured using image analyzer. Within the range of 10 to 50 ppm of boron, track densities from autoradiography showed the linear relationship with results from conventional analyses. When complementarily applied with other analysis technique like E.B.S.D (Electron Backscattered Diffraction) or E.D.S (Energy Dispersive Spectroscopy) neutron induced autoradiography technique was found very useful in distinguishing and identifying phases with the different distribution coefficient of boron.

Keywords: autoradiography, fission track etching, boron, 316 L stainless steel, segregation, (n, α) reaction

1. Introduction

Boron is an important alloying element in steel-making, but it is not easy to detect due to its own lightness. It is usually added to improve hot workability, hardenability, or high temperature properties, like creep resistance, and so on [1, 2, 3]. Boron atom is prone to segregate to interface (or grain boundary) and sometimes distributed preferably into one phase than the other. Neutron induced autoradiography has been known very useful analysis technique to investigate the distribution of boron atoms, especially when applied complementarily with other analysis techniques [4]. This technique is based on ^{10}B (n,α) ^{7}Li nuclear reaction. Natural boron is composed with 19.61% of ^{10}B and 80.39% of ^{11}B isotopes and neutron cross section of ^{10}B is much greater (3836×10^{-24} cm^2) than other elements.

* jjang@kaeri.re.kr

Accordingly the probability of boron atoms to emit α particles is much higher than other elements [5].

In this study 'HANARO' - a 30 MW research reactor operated by Korea Atomic Energy Research Institute - was utilized for neutron induced autoradiography. Experimental reference samples of type 316 L austenitic stainless steel were prepared with different boron contents and the quantitative analyses were done by track density measurement on the autoradiographs. Local concentration of boron in a segregated grain boundary as well as bulk concentration was estimated by the autoradiography, and qualitative approach was also confirmed useful to investigate phase transformation of austenitic stainless steel.

2. Experimental

2. 1 Sample Preparation

Using relatively clean (99.9% or purer) raw material, nine experimental type 316 L stainless steel ingots (1.7 kg each) were prepared by V.I.M (Vacuum Induction Melting). Chemical analyses for nine ingots were done by I.C.P (Inductively Coupled Plasma)-spectrometric, and I.C.P-MS (isotope dilution) by various laboratories. For autoradiography work nine ingots were hot rolled at 1200℃ and cold rolled to 1.2 mm thickness. To distribute boron atoms uniformly cold rolled sheets were solution annealed at 1100℃ for 1 hr and water quenched. Parts of solution annealed sheets were heat treated at 650℃ for 1 hr and water quenched to investigate the segregation of boron atoms along the grain boundaries. Samples were sectioned and cold mounted with resin and followed through the routine metallographic preparation procedures. After neutron irradiation test, samples were electrolytically etched in 2% nital solution for the observation with optical microscope and scanning electron microscope.

2. 2 Neutron Irradiation and Track Density Measurement

Mirror polished samples were mechanically put together with cellulose nitrate film detector (Kodak CN-85™ ; $C_6H_8O_9N_2$) for close contact, encapsulated in polyethylene container and carried into reactor by pneumatic transfer system. Neutron fluence was calibrated by Au wire measurement for each experiment. After irradiation detector film was etched in 2.5 N NaOH solution at 50℃ for 15 minutes. Tracks on detectors were recorded by optical microscope and the densities were measured on 3 frames each by image analyzer and plotted against bulk concentration of boron from I.C.P analyses.

3. Results and Discussion

Boron contents of nine type 316 L stainless steel samples is shown in Table I.

Table I Boron concentration of nine experimental type 316 L stainless steel

No.	1	2	3	4	5	6	7	8	9
B [ppm]	< 2	< 2	2	3	5	10	20	30	51

Boron contents are, as designed, from less than 2 ppm (detection limit) to 51 ppm. All the other elements were well within the ASTM specification, and carbon and nitrogen contents were extremely low (0.003～0.014 and 0.0004～0.0088 wt % respectively).

At 1.782 × 10^{13} and 1.16 × 10^{14} /cm^2 of thermal neutron fluence track densities from solution annealed nine samples are measured and plotted against bulk concentration of boron (Figure 1). Increase of track densities according to the neutron fluence is clear as well as boron content. Track densities in the range of 10 to 50 ppm of boron in type 316 L stainless

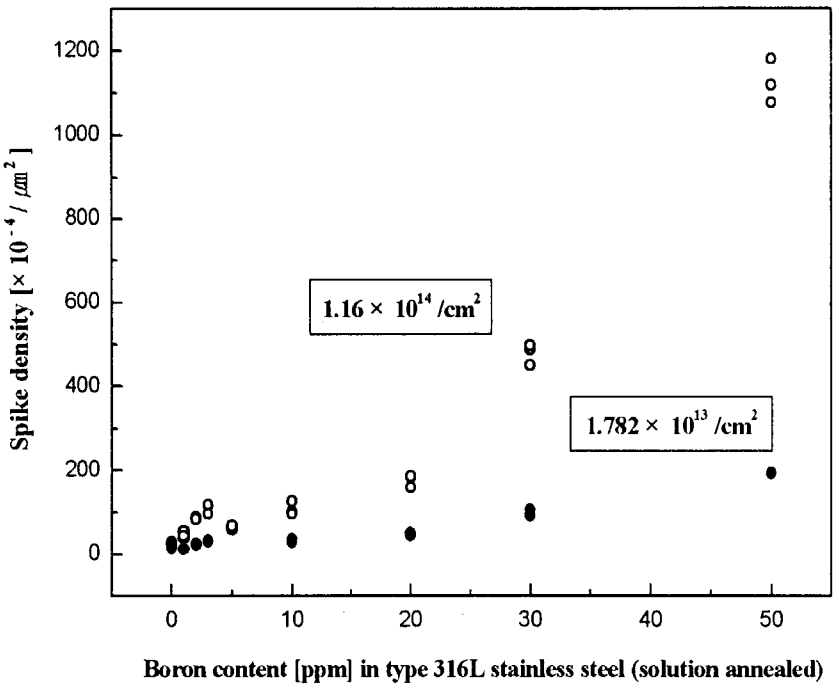


Fig. 1 Plot of measured track density vs. bulk boron content of type 316 L stainless steel samples, solution annealed

steel show linear relationship with bulk boron contents as in previous reports [6, 7]. The correlation factors were 0.97 for 1.782 × 10^{13} /cm^2 and 0.96 for 1.16 × 10^{14} /cm^2. Below 10 ppm of boron, however, track densities show irregular change along bulk concentration. It is not clear whether it is inherent characteristics of neutron induced autoradiography or statistical error.

Segregation of boron atoms along the grain boundary is clearly shown in Figure 2. The autoradiograph is from the solution annealed and heat treated (650℃/1 hr) stainless steel containing 10 ppm of boron (sample No. 7). Therefore it can be said that alloys with low amount of boron could change their grain boundary (or interface) related properties significantly by segregation. This is also confirmed on the autoradiogrphs from the samples of extremely low concentration (a few ppm) of boron. Quantitative analysis of boron concentration within grain boundary has been attempted by autoradiography technique through measuring track density along grain boundary. Tracks from segregated boron atoms

along the grain boundary have been counted within rectangular area of about 3 × 20 μm along boundary segment. In the case of sample No. 7 (e.g. Figure 2; 10 ppm of bulk concentration) boron concentration in a grain boundary segment was estimated as around 25 ppm. Definition of rectangular area along the segment should be arbitrary and measured track densities would be varied especially by the definition of the width of grain boundary (or of the width of the area). Also, in nature, the extent of segregation of boron atoms would be different boundary segment to segment according to the boundary character. To quantitatively estimate the boron concentration in the interface, standardization of measuring width of the interface on the autoradiographs is prerequisite. Linear intercept method could avoid the width variation problem in measuring the track density, but separate calibration curves established by the same intercept method would be necessary. Judgement for the compromise between the reliability of calibration curve and of local measurement on the boundary is still remained.

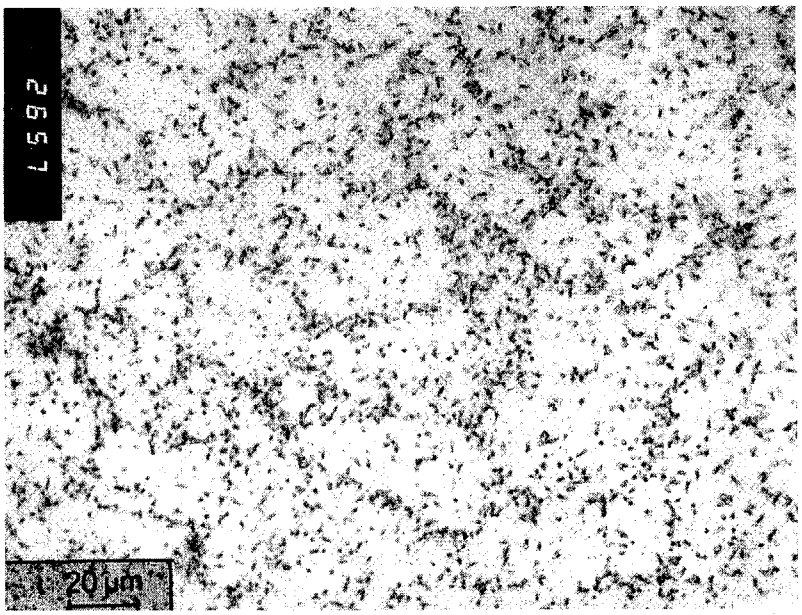
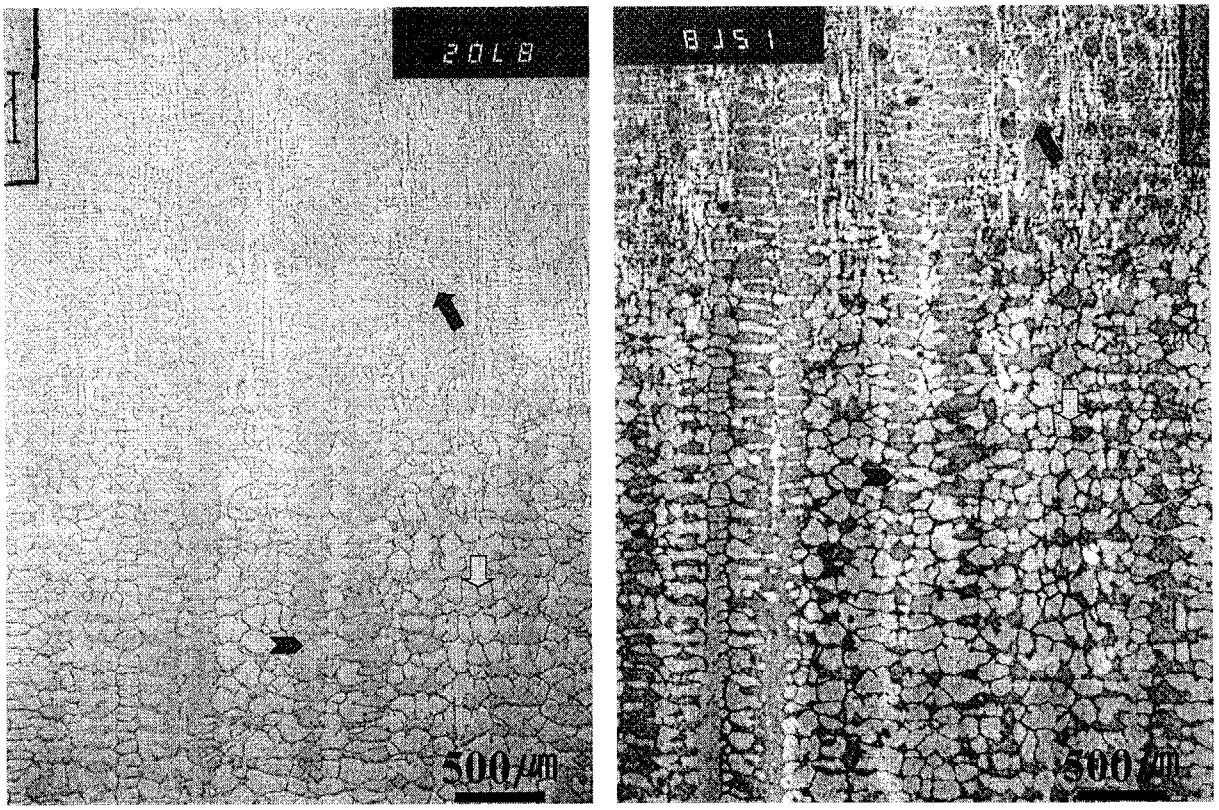


Fig. 2 Autoradiograph of type 316 L stainless steel (10 ppm of boron), solution annealed at 1100℃ for 1 hr and heat treated at 650℃ for 1hr (fluence : 1.16×10^{14} /cm^2)

Figure 3 (a) shows an optical micrograph of directionally solidified type 316 L stainless steel at just below liquid/solid interface. Sample withdrawal velocity was about 30 μm/sec, and upward directional growth of dendrite phase are observed. The corresponding autoradiograph of the same area is shown in Figure 3 (b). Three arrows indicate each corresponding local point on the micrograph. Preferential partitioning of boron atoms in a specific phase is elucidated by autoradiograph. Coarser primary dendrite phase which seems to contain most boron atoms and finer dendrite coexist. As the distance from the liquid/solid interface becomes farther (or as the local temperature decreases), fraction of the boron-free phase (bright phase on the autoradiograph) expands, consuming the other phase (or expelling



(a) (b)

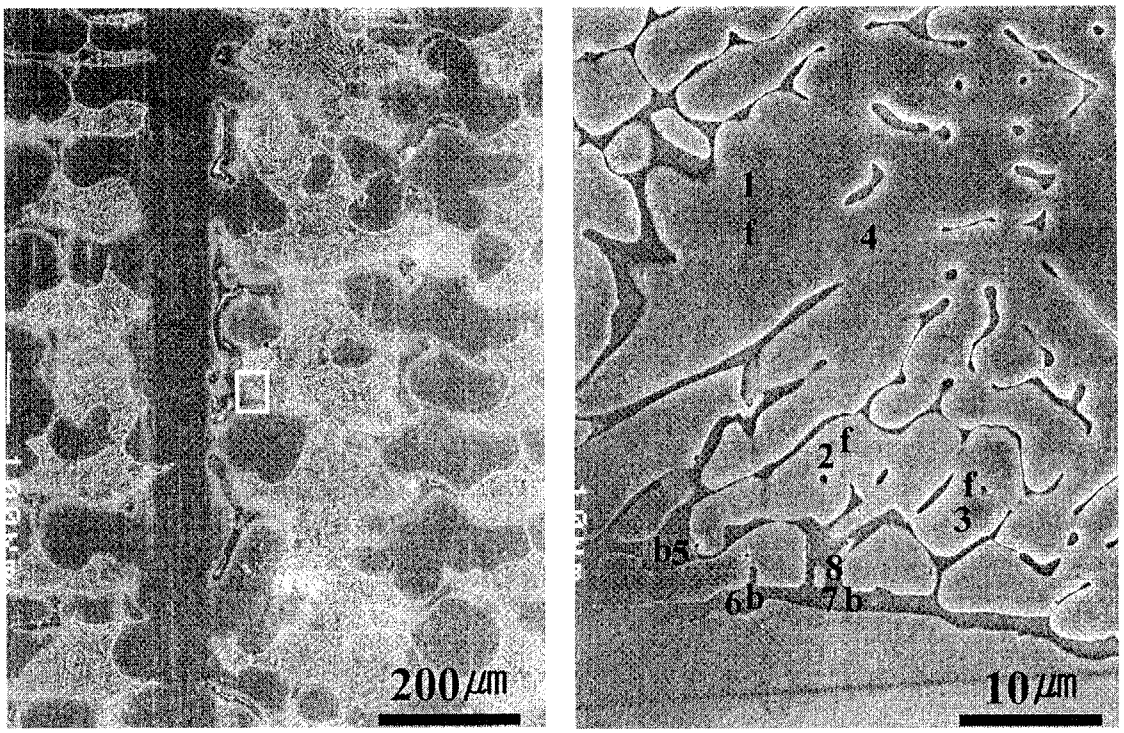
Fig. 3 Comparison of (a) optical micrograph and (b) autoradiograph of directionally solidified type 316L stainless steel (solidification direction : ↑)

boron atoms). Microstructural change was investigated by S.E.M and E.B.S.D investigated in detail.

Figure 4 illustrates higher magnification S.E.M micrograph of a dendrite arm which looks abundant in boron atoms and has been considered as boron containing ferrite phase. On the micrograph 'f' designates f.c.c (face centered cubic) and 'b' designates b.c.c (body centered cubic) crystal structure. E.B.S.D analyses reveal that finer dendrite-like phase forms within the dendrite arm, composing with f.c.c structured and dendrite-like gamma austenite in the matrix of b.c.c structured delta ferrite. Therefore in autoradiograph (Figure 3 (b)) dark dendrite arms are, in reality, composed of boron-bearing ferrite phase as matrix of the dendrite arm and boron-free austenite as growing phase within the arm. Therefore tracks on the autoradiograph is believed to come from the matrix ferrite phase, not from the growing austenite and this is attributed to the lack of spatial resolution of the current autoradiography technique. Resolution of neutron induced autoradiography is reported as about 2㎛ [5], but in this study it appears as larger than 5㎛. To be more useful in identifying fine structures, e.g. precipitates, inclusion, etc., spatial resolution of the autoradiography must be enhanced by adjusting neutron fluence and detector processing, or by better microscopy operation.

S.E.M/E.D.S analyses results (Table II) also confirm that the chemical composition of growing phase, corresponding with points 1, 2, 3,and 4 in Figure 4 (b), matches well with that

of typical austenite phase. And the composition of the remained matrix phase of the dendrite arm, which correspond with points 5, 6, 7, and 8 in Figure 4 (b), and appear to contain more



(a) (b)

Fig. 4 Identification of ferrite and austenite phases in directionally solidified type 316 L stainless steel (a) S.E.M micrograph (b) local points analyzed by E.B.S.D (f: f.c.c; b: b.c.c) and E.D.S (1, 2, 3, etc.)

Table II Chemical composition of local points by S.E.M/E.D.S analysis [wt %]

	Fe	Cr	Ni	Mo	Mn	Si
1	60.97	17.48	10.77	1.66	0.81	0.77
2	57.40	19.04	11.85	2.37	0.79	0.76
3	65.83	18.76	11.44	2.29	0.87	0.81
4	66.32	18.98	10.85	2.22	0.92	0.70
5	61.46	22.46	9.38	4.53	1.09	1.07
6	61.48	24.31	7.18	5.20	0.88	0.96
7	62.20	24.49	7.05	4.47	0.87	0.92
8	63.13	22.43	8.88	3.98	0.66	0.92

Cr (20.67～22.35 %) and Mo (3.29～4.14 %) and less Ni (6.40～8.58) than austenite also fits well with typical composition of ferrite phase.

Therefore b.c.c structured ferrite dendrite phase which preferentially contains boron atoms grows at the beginning stage of solidification and then f.c.c structured austenite phase which is lack of boron atom grows into the ferrite more or less in a dendritic manner, expelling boron atom. However, at distant location from liquid/solid interface (at lower temperature range) the preferential distribution of boron atoms was switched between. It would be attributed to the preferential atomic site of boron atom, i.e. between octahedral and tetrahedral site, or between interstitial and substitutional site.

4. Conclusion

1. Nine reference type 316 L stainless steel samples were successfully prepared with a different boron content (< 2, 2, 3, 5, 10, 20, 30 and 51 ppm).
2. Calibration curves for quantitative boron analyses of solution annealed (1100℃/1 hr) type 316 L stainless steel were obtained by neutron induced autoradiography. Thermal neutron fluences were 1.782×10^{13} and 1.16×10^{14} /cm^2 and linear relationship between track density vs. boron concentration was confirmed in the range of 10 to 51 ppm with correlation factor of 0.97 and 0.96 respectively.
3. Quantitative boron analyses along segregated grain boundary have been attempted through autoradiography. In the case of the sample with bulk concentration of 10 ppm and heat treated at 650℃ for 1 hr, segregated boron concentration in the boundary segment was estimated as 25 ppm.
4. Qualitative analyses for boron distribution by autoradiography revealed that boron atoms preferentially partitioned into primary ferrite dendrite phase, and then ferrite phase becomes consumed by growing austenite phase which also proceeds dendritically but contains much less boron.

References

[1] M. Tamura, Superalloys, Supercomposites and Superceramics, ed. J.K. Tien and T. Caulfield, 215 (Academic Press, Inc., USA 1989)

[2] A. Brownrigg, Boron in Steel - A Literature Review, The J. of the Australian Institute of Metals, **18,** 124 (1973)

[3] D.J. Naylor and W. T. Cook, *Constitution and Properties of Steels* ed. F.B. Pickering in Materials Science and Technology **7**, 433 (VCH Publishers Inc., U.S.A 1992)

[4] T.B. Cameron and J.E. Morral, *Boron in Steel*, ed. S.K. Banerji and J.E. Morral, 61 (A.I.M.E, U.S.A 1980)

[5] I.V. Radin, G.G. Ryabova and V.V. Perfilov, Nucl. Tracks Radiat. Meas. **20**, 297, Int. J. Radiat. Instrum., Part D (1992)

[6] J.D. Elen and A. Glas, J. Nucl. Mater., **34**, 182 (1970)

[7] S. Kawasaki, A. Hishinuma and R. Nagasaki, J. Nucl. Mater., **39**, 166 (1971)

JP0350248

1.3.5 Corrosion Mechanism on Heat Transfer Surface of Pressure Boundary Materials used in Nuclear Environments

K.Kiuchi*, H.Ogawa*, I.Ioka*, Y.Kuroda** and T.Anegawa***
*Japan Atomic Energy Research Institute, Department of Nuclear Energy System
2-4 Shirakata Shirane, Tokai-mura, Ibaraki-ken, 319-1195 Japan
Tel:+81-29-282-5395, Fax:+81-29-282-5864, Email:kkiuchi@popsvr.tokai.jaeri.go.jp
**The Japan Atomic Power Company, Research and Development Department
***Tokyo Electric Power Company, Nuclear Power Engineering Department

Abstract- *The ultra-high burnnp more than 100GWd/t and fast neutron spectrum tailoring are considered to be the most promising technologies applied to the advanced MOX LWRs for minimizing the electrical cost and waste management. The development of new cladding materials with the excellent irradiation properties has been conducted to realize these needs. Comparing with UO_2, to increase the internal pressure by FP gas release is accelerated with the co-production of Xe and He in MOX fuels. New stainless steels with the excellent irradiation properties, creep strength and compatibilities to high temperature water were selected to attain the reliability. The irradiation assisted stress corrosion cracking through the past experience in LWR plants is possible to inhibit by new steel making process. The problems of tritium release and PCMI is possible to inhibit by ductile niobium alloy lining.*

I. INTRODUCTION

The advanced light water reactors designed in ultra-high burnup more than 100GWd/t and/or fast neutron spectrum tailoring are considered to be the effective means on the economical and ecological standing points for using MOX fuels on the current fuel cycle up to realize LMFBRs. [1-3].Cladding materials with the excellent long performance under heavy neutron irradiation would be required to these developments. The major effort for the burnup extension has been carried out to modify claddings made of zirconium alloys used in the present LWRs fuels. However, limitations on the technologies have been gradually clarified with respect to the oxide growth and hydrogen uptake due to the accelerated corrosion on heat transfer surfaces under heavy neutron irradiation. Zirconium alloys were mainly selected for cladding alloys instead of stainless steels with respect to the neutron economy, by considering the low nuclear reaction cross-section by thermal neutrons. However, it is not the predominant factor on the materials selection for fuel claddings applied to the advanced LWRs using MOX fuels. Although the enrichment of ^{235}U in UO_2 fuels is limited within 5%, it of fissile Pu in MOX fuels is possible to enhance up to 20% as well as it of LMFBR. Therefore, the major critical issues underlying the selection of new cladding materials are considered to be the reliability under heavy neutron irradiation and the safety allowance to RIA and LOCA. The collaboration research project for developing the advanced fuel cladding between JAERI and electric companies had started from 1998. The difference in irradiation properties, the compatibility to high temperature water, pellet-clad interactions and the waste management were basically evaluated for selecting candidate alloys from major structural materials described in the previous reports[1-4]. From the primary screening results, we selected Fe-Cr-Ni austenitic alloys and niobium alloys as the candidate materials.

On the present study, the difference in representative properties required to cladding tubes for the advanced BWR was evaluated with computer simulation methods and experimental studies. New steel making technologies developed in basic study was attempted for minimizing the susceptibility to IASCC of stainless steels that is the most important problems on the practical use. The applicability was examined in the practical cladding tube making process as same as that of Zircaloys. On the other hand, the usefulness of niobium alloy with high melting point and the low reactivity with actinide elements was evaluated as liner materials for inhibiting PCMI and tritium permeation of claddings made of Fe-Cr-Ni austenitic alloys.

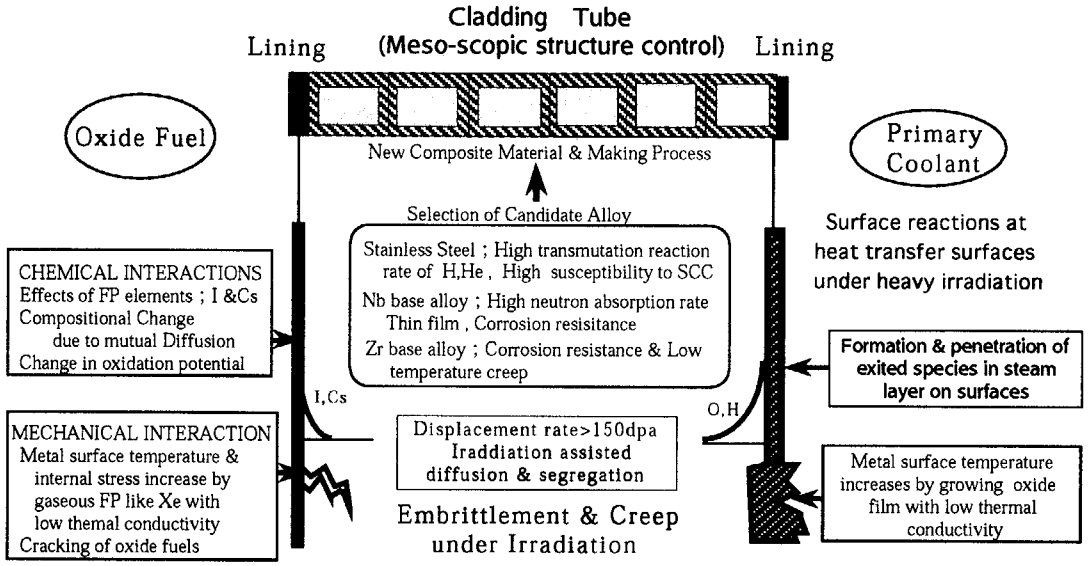


Fig.1 Irradiation effects expected in the ultra-high burnup MOX fuels

II. EVALUATION OF MAJOR REQUIREMENT FOR ADVANCED FUEL CLADDING

II.A Characteristics of MOX fuels

The difference in nuclear characteristics required to the full MOX fuel reactor core were examined in detail for clarifying the specifications required to the ultra-high burnup cladding with computer simulation method based on reactor design data of ABWR. Fig.1 shows the major parameters in relation to the reliability of MOX fuel claddings, by considering the coolant side corrosion, degradation of cladding by irradiation and pellet–clad interactions. The difference in technological problems among each candidate was also cited.

Fig. 2 shows the difference in the enrichment factor of fissile plutonium as a function of burnup among stainless steels, zirconium alloys and niobium alloys calculated using several codes[6-9]. It is compared with the limit for satisfying infinite multiplication factor higher than 1 on the cladding thickness with the same mechanical strength. The difference among three candidates would be within nearly 10%. On stainless steel claddings, the infinite multiplication factor on fast neutron spectrum reactors with the high conversion ratio is easy to maintain more than 1 by breeding fissile Pu. However, niobium alloys is difficult to apply for such claddings due to the strong resonance absorption in the fast neutron energy region.

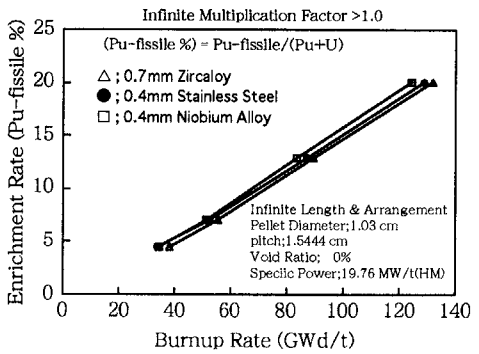


Fig. 2 A relation ship between Pu enrichment factor and burnup rate that is to attain the infinit multiprication factor higher than 1

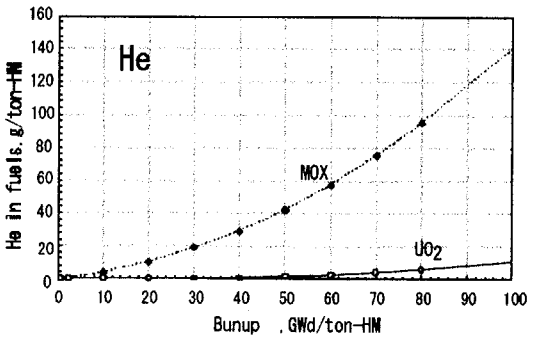


Fig. 3 Difference in helium contents as FP in each fuel plotted to burnup

The most important difference between MOX fuels and UO2 fuels on nuclear reactions is the chemical composition of rare gases in fission products. The gas release in gaps in MOX fuel claddings is accelerated with the releasing rate of He with the high permeation rate as shown in Fig.3 and 4. Comparing with UO_2 fuels, the high release rate in MOX fuels was already observed as operation data on LWRs. To inhibit the rare gas release is an important factor on BWRs operated at low pressure. To expand the plenum length is also an effective means to the countermeasure as seen in Fig.5. Accordingly, the optimization of alternative cladding materials aiming at ultra-high burnup should be evaluated by considering the balance among the reliability, waste management and manufacturing.

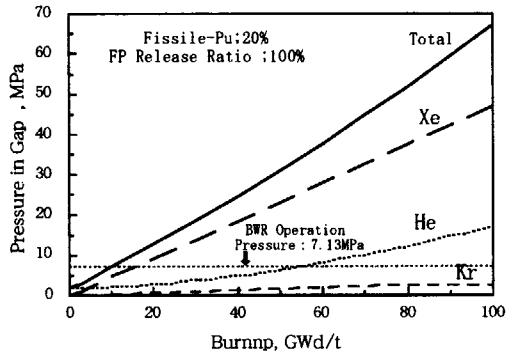


Fig. 4 The pressure of each rare gas formed in MOX as a function of burnup

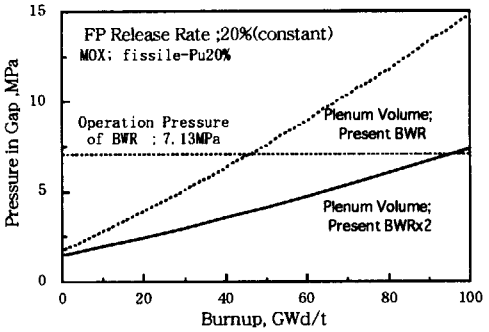


Fig. 5 Effect of the plenum length on the gap pressure due to release of FP gases

II.B Corrosion problems characterized in fuel cladding on commercial use of Zircaloys

The waterside corrosion is the most important technological problem on zirconium base alloys. Zircaloy-2 claddings in BWRs were suffered from nodular corrosion. It was inhibited by adjusting alloying elements and controlling metallographic

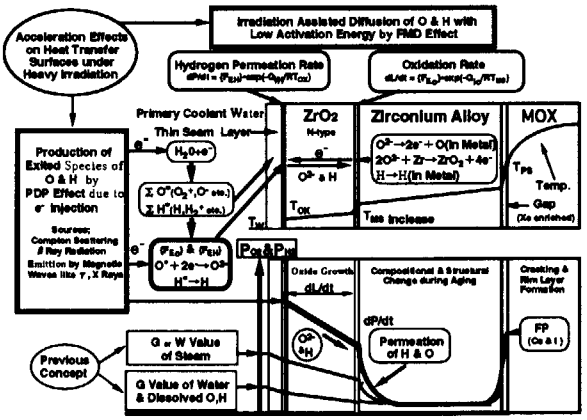


Fig. 6 A model for the accelerated corrosion of cladding tubes made of zirconium alloys

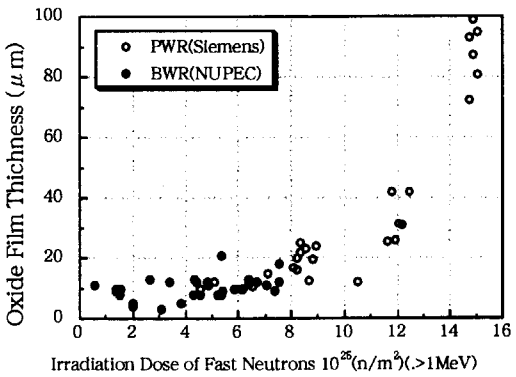


Fig. 7 The growth of oxide film on Zircaloys with dependent on the dose of fast neutron

structures for improving the distribution of intermetallic compounds. On the other hand, the improvement effect on uniform corrosion is not clear in both BWR and PWR claddings. We had proposed the corrosion model as shown in Fig 6, by considering the effect of low energy electrons formed under heavy neutron irradiation. The oxide growth rate is strongly dependent on the fast neutron flux as shown in Fig 7. The oxide growth rate on PWR Zircaloy cladding at high burnup region shows the Arrhenius relationship with dependent on the metal surface temperature as seen in Fig8. We had proposed the corrosion model as shown in Fig 6, by considering the

effect of low energy electrons formed under heavy neutron irradiation. The model suggests that it is difficult to inhibit the corrosion rate of zirconium alloys with mono-oxide layer of N-type semiconductor like ZrO_2. It is clear in the inhibition effect by niobium alloying. To increase addition contents of Nb is possible to form inner layer of Nb_2O_5. The alloying effect of Nb and Ta is also

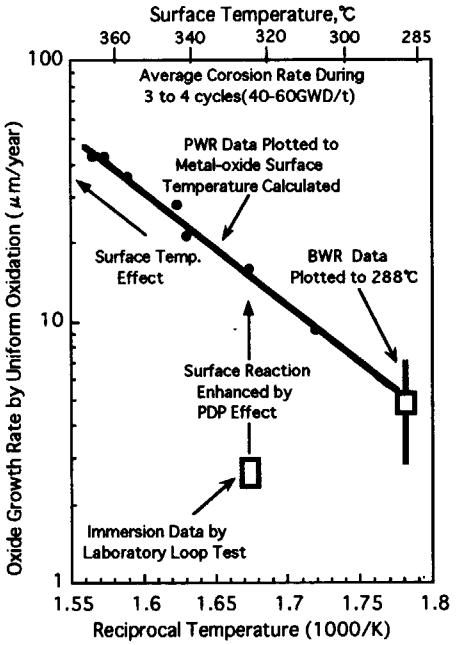


Fig. 8 Arrhenius plot of the growth rate of oxide film on Zircaloy-4 cladding tubes

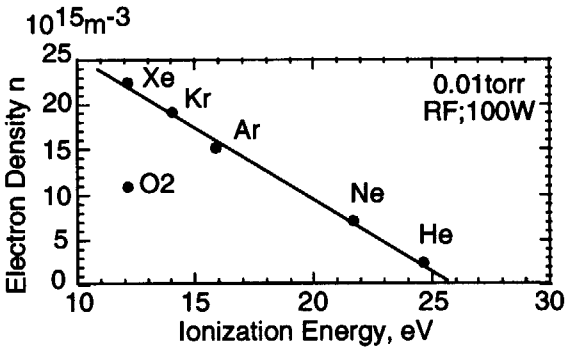


Fig. 9 Difference in the excitation yield of each rare gas as electron densities in low energy plasma excited by RF-source

known in the inhibition of titanium alloy with the same N-type semiconductor oxide film TiO_2. However, the alloying effect is limited in crystallographic characteristics due to the close packed hexagonal structure, because of Spinodal type decomposition at low temperature. The oxide growth of stainless steel claddings had been not experienced, because of the formation of thin passive film composed of binary layer with p-type M_3O_4 and N-type Cr_3O_3 that is led to parabolic rate low.

The growth of ZrO_2 with the low thermal conductivity acts to enhance the pellet surface temperature and to release heavy rare gases such as Xe with the low thermal conductivity as shown in Fig.10. The accumulation of Xe into a gap at medium burnup would be acting to enhance the fuel temperature. Fig.10 is temperature profiles by considering an extremely case of Xe ratio on the same gap spacing. The gas release behavior is strongly relation to the chemical reactivity of each rare gase. From experimental results concerning the excitation behavior of rare gases in low energy plasma, it was clarified that the excitation yield of ions and electrons depends on the binding energy of each gas. The formation of XeO was also detected. It is suggested to form the chemical compounds of heavy rare gases in the condensed phases under high pressure

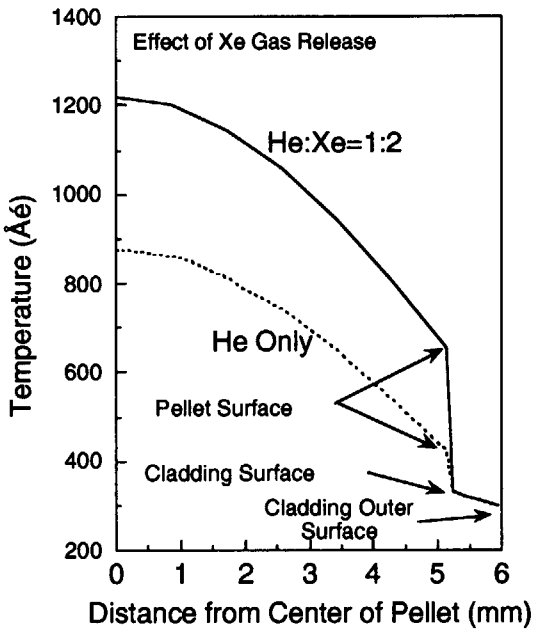


Fig. 10 Effect of Xe gas release on the temperature profile in pellets

II.C Optimization of stainless steels

The development of stainless steels applied for cladding materials would be required to maintain the sufficient phase stability of austenite to inhibit IASCC and ductility loss. It is dependent on the chemical composition of $Ni_{eff.}+Cr_{eff}$ that is the index in relation to austenite phase stability at irradiation temperatures lower than 773K as shown in Fig.11. From pre-examination study pursued in JAERI, following modification techniques were clarified to be effective means for this purpose[20-24]. Super-saturated solutes at irradiation temperatures affect to the sensitization and void swelling[25].

· Adjustment of chemical composition Cr and Ni contents would be optimized in 18-25wt%, 25-35wt% respectively for obtaining the sufficient phase stability of austenite and corrosion resistance. The selection of appropriate scavenger elements is required for the SAR process shown in later.

· Purification of alloy matrix ; To make the purified ingot through the combined melting techniques by VAR , EB-CHR and ESR process. Total interstitial impurity is possible to minimize less than 100appm.

· Modification of metallographic structure; To form the fine grain structure with uniformly dispersed precipitates through thermo-mechanical treatment so-called the SAR process consists of strain-aging and recrystallization at intermediate temperature as shown in Fig.12.

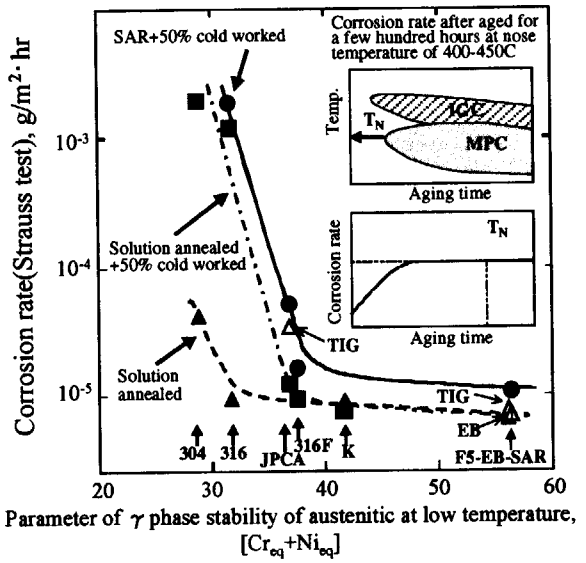


Fig. 11 Effect of major alloying element on the degradation .at low temp.

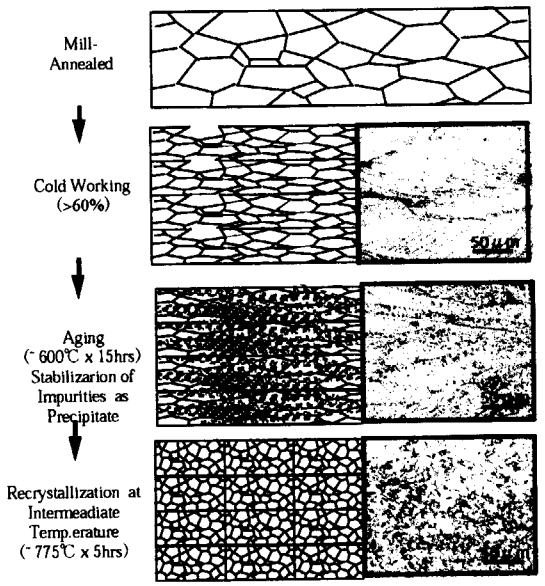


Fig. 12 A schematic view of micro-structural change during the SAR process

III. CHARACTERISTICS OF CHANDIDATES

The difference in corrosion behavior of candidate alloy in steam at 1200℃ was examined for evaluating the safety allowance to LOCA as shown in Fig.13. The corrosion resistance of stainless steels is superior to it of Zircaloys. Nb is possible to improve the corrosion resistance by alloying of Mo. The corrosion resistance of stainless steels is possible to improve by increasing Cr contents as well as waterside corrosion at the normal operation. The low mechanical strength of the purified steel is improved by changing very fine grain structure higher than ASTM No.10 due to the Hall-Petch strengthening effect[21]. As seen in Fig.14, the candidate steel has the sufficient thermal creep strength compared with it of Zircaloy-2. It is an advantage to maintain the mechanical strength on PCMI due to FP gases release and cracking of pellets accompanied with the burnup extension. On the other hand, one of engineering problems of stable austenite stainless steels is to decrease cracking resistance to welding. However, there is no problems on TIG welding of new steels , because harmful elements are removed by the purification process[32]

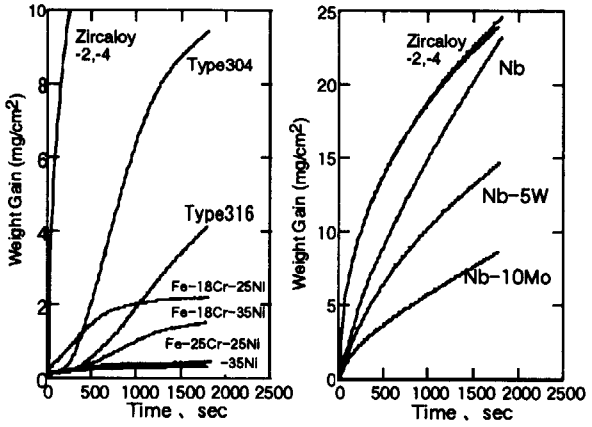


Fig. 13 Difference in oxidation rates as a function of test time in steam at 1200℃

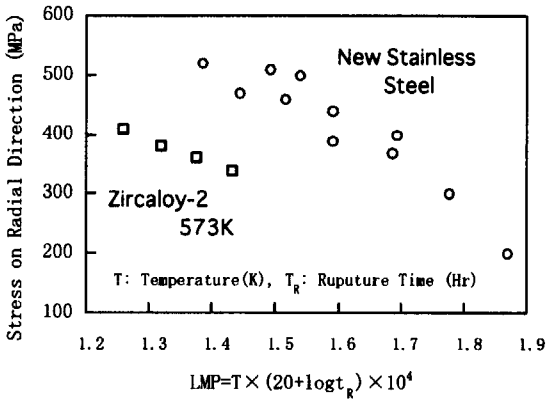


Fig. 14 Difference in creep strength between candidate alloy and Zircaloy-2

The difference in tritium release between cladding tubes is shown in Fig.15 based on LWRs practical data. The permeation rate of tritium of cladding tubes made of stainless steels is higher than it of Zircaloys. To inhibit the tritium release would be required with respect to minimize the environmental pollution. From basic study on compatibilities to stainless steels and fuels, Nb base alloy was selected to the appropriate lining for inhibiting both tritium release and PCI. Nb has the high melting point and excellent compatibility to fuels. Moreover, as shown in Fig.14, the safety allowance to water leak is superior to it of Zircaloys. The thickness of Nb liner for getting the sufficient inhibition effect to tritium permeation was examined by calculation analyses and experiments. Fig. 16 shows the change in tritium profile in stainless steel cladding with Nb liner with 0.01mm in thickness. The inhibition effect of niobium on tritium permeation is clearly seen. The advantage of Nb is the high solubility at low temperature without the formation of hydrides. Although Zr showed the brittle fracture, the ductility of Nb was maintained during the permeation tests of hydrogen.

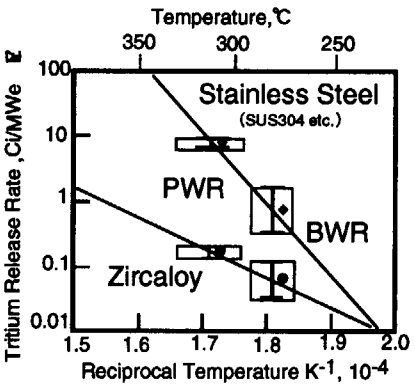


Fig. 15 Difference in tritium release rate on cladding tubes between Zircaloys and stainless steels used in LWRs

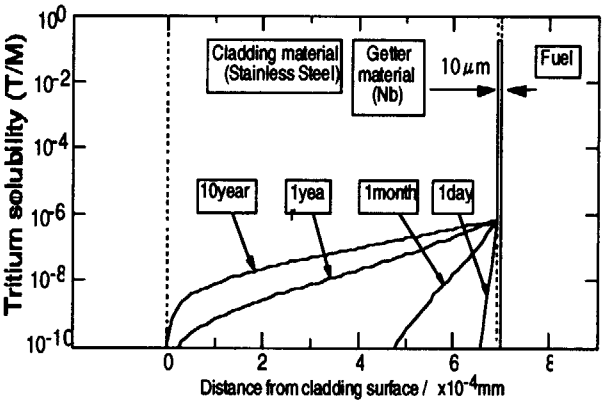


Fig. 16 Effect of Nb lining on the release of tritium in stainless steel cladding

The susceptibility to IGC and IGSCC of EB-SAR treated new steels was completely inhibited in un-irradiation tests. However, the most important problem under heavy irradiation is considered to be the high production rates of H and He by (n,p) and (n, a) transmutation reactions as stated in previous report. Irradiation tests using ion accelerators have been carried out to examine the basic irradiation properties. Test conditions were stated in another report in detail[25]. As shown in Fig.17, the ductility loss and the susceptibility to IASCC are relation to austenite phase stability. The initiation and growth of secondary irradiation defects would be

accelerated in type 316 steel with the low austenite stability. The difference in the growth of Frank loop is clearly seen in TEM photographs of two types of alloys. The growth of secondary irradiation defects of Fe 17Cr-14Ni is easier than it of Fe-24Cr-23Ni. Fig.18 shows the irradiation problems of stainless steel claddings underlying ultra-high burnup.. The major reason on environmental cracking of stainless steels experienced in the past LWRs is the sensitization due to the precipitation of chromium carbides. On new stainless steels, the sensitization and segregation of impurities were completely inhibited by the purification of austenite matrix by electron beam melting and the SAR thermomechanical treatment. The important problem at high dose near 50dpa is considered to be the channel fracture due to the difference in the internal stress among grains. On the new modification method is possible to improve the problem by minimizing the crystal grain size.

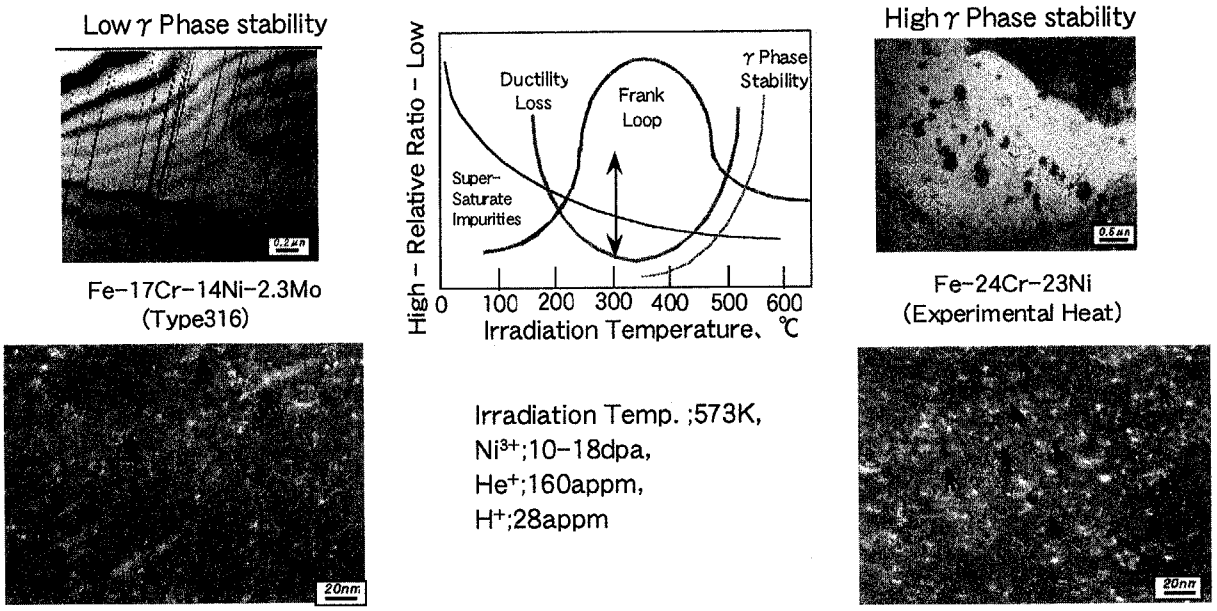


Fig. 17 A schematic view of irradiation effect in relation to the microstructural evolution and the difference in the micro-structural evolution of specimens irradiated by triple ion beam at the practical temperature

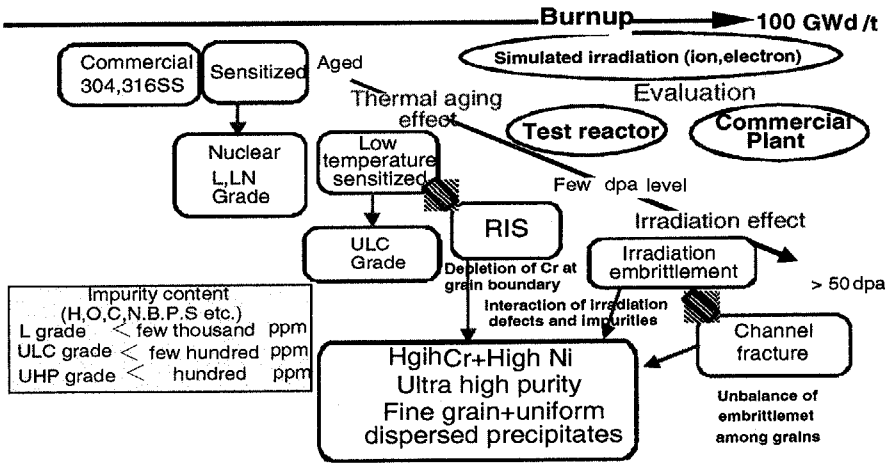


Fig. 18 The role of each countermeasure applied to improve irradiation properties depended on the irradiation dose of stainless steels

IV. CONCLUSIONS

Comparing with zirconium alloys, the important issues and technological problems were examined for optimizing stainless steels with niobium alloys liner selected as candidates applied to MOX fuel cladding tubes aiming at the ultra-high burnup ABWR as follows.

- The neutron adsorption cross section on the cladding tubes is nearly same among Zircaloys, stainless steels and niobium alloys with the same tensile strength.
- Comparing with UO_2, the gas release rate from MOX is accelerated with not only heavy rare gases such as Xe, but also He of which has the high yield in fission products and high permeation rate.
- The irradiation assisted corrosion is controlled with the direct surface reaction of oxygen and hydrogen excited by the low energy electrons with high current density under heavy irradiation. The corrosion rate is effectively suppressed in stainless steels with mixed layer oxide film than zirconium alloys with N-type semiconductor film.
- Technological problems underlying the practical use of stainless steels cladding on the past experiences on LWRs were the high susceptibility to IASCC and the environmental pollution by tritium.
- The IASCC is possible to minimize by so-called EB-SAR technique developed by JAERI. It is immunity to IGC and IGSCC, even if it is taken thermal histories at irradiation temperature.
- The tritium release and PCI are possible to inhibit by thin film coating of niobium alloy of which has the wide solubility range of hydrogen and the excellent compatibility with fuels.
-

ACKNOWLEDGEMENTS

The authors would like to thank Mr. N.Maruyama, M.Tanabe, and Y.Inohara of JAERI and for the experiment, and also thank to Dr. M.Fujiwara of KOBELCO Co. And Drs. M.Takizawa and Sato of MRI Co. for the computer simulation methods.

REFERENCES

1. T.J.PASHOS, APED-4260(1963).
2. R.DUCAN, "Stainless Steel Failure Investigation Program,"GEAP-5530(1968).
3. I.MILTER, "European Operating Experience," Joint Topical Meeting on Commercial Nuclear Fuel Technology Today," 75-CAN/ANS-100(1975).
4. V.PASUPATHI and P.LINGENSMITH, EPRI NP-2119(1981).
5. D.R.HARRIES, *Journal of Nuclear Materials*, **82**, 2(1979).
6. M.L.GROSSBECK, K.EHRLICH and C.WASSILEW, *Journal of Nuclear Materials*, **174**, 264(1990).
7. J.P.ROBERTSON, I.IOKA, A.F.ROWCLIFFE, M.L.GROSSBECK and S.JITSUKAWA, *ASTM STP 1325*, 671 (1999).
8. K.KIUCHI, I.IOKA, H.OGAWA, S.MIYAMOTO and Y.KURODA, "Development of New Cladding Materials Applied for Advanced LWR Aiming at Ultra-high Burn-up and Fast Neutron Spectrum," in this .
9. K.KIUCHI, M.KIKUCHI and K.KONDO, *Journal of Nuclear Materials*, **179-181**, 481(1991).
10. TIARA GROUPE, "JAERI TIARA Annual Report Vol.1(1992); April 1991-March 1992,"JAERI-M-93-047(1993).
11. J.F.ZIEGLER, "The Stopping and Range of Ion in Solids", Vol.1, Pergamon Press, New York(1985).
12. W.C.OLIVER and G.M.PHARR, *Journal of Material Research*, **7**, 1564(1992).
13. E.H.Lee, G.R.Rao, J.D.Hunn, P.M.Rice, M.B.Lewis, S.W.Cook, K. Farrel and L.K.Mansur, "Triple Ion-beam Studies of Radiation Damage Effects on EC316LN Austenitic Alloy for a High Power Spallation Neutron Source, *Proceeding of the Symp. On Materials for Spallation Neutron Source*, 1997 TMS Annual Meeting, Orlando, Florida, Feb. 9-13(1997).

This is a blank page.

1.4 New Characterization Technology

Chair: T. Staab

(University of Bonn, Germany)

M. Kitajima

(National Institute of Materials Science, Japan)

This is a blank page.

JP0350249

1____.4.1 DEFECTS IN FINE-GRAINED AND POROUS MATERIALS CHARACTERIZED BY POSITRON ANNIHILATION

T.E.M. Staab[1]*, R. Krause-Rehberg[2], and B. Kieback[3]

[1] *University Bonn, ISKP, Nußallee 14-16, D-53115 Bonn, Germany*
[2] *Martin-Luther University Halle-Wittenberg, Department of Physics, D-06099 Halle/Saale, Germany*
[3] *Technical University Dresden, Department for Materials Science, Momsenstraße 13, D-01062 Dresden, Germany*

Abstract

We investigate the annihilation parameters (lifetimes and intensities) for positrons becoming trapped at grain boundaries and at inner surfaces (pores), examining fine-grained nickel powder compacts (effective powder particle size $1 - 10\,\mu$m with grains in or even below the micron size). Furthermore, we can monitor grain growth and sintering (volume shrinkage) during successive heat treatment of powder compacts. To reach this aim, we correlate the annihilation parameters with results of a Monte-Carlo simulation and analytical solutions of the positron diffusion. We find that it is possible to determine an effective average powder particle size as well as grain sizes by positron lifetime spectroscopy.

Keywords: Positron Annihilation Parameters, Fine-Grained, Porous, Positron Thermalization and Diffusion, Grain-Boundaries, Pores.

1 Introduction

Fine-grained materials have become increasingly important in industrial applications during the last decade. This means that lattice defects are not evenly distributed inside these materials on a length scale about or below $1\,\mu$m, which is the usual range of the positron diffusion length. But the even distribution of defects is one of the key assumptions usually imposed when analyzing results of positron annihilation spectroscopy. Hence, it will be important in the future to thoroughly understand positron annihilation signals in inhomogeneous, *e.g.* fine-grained, materials.

Positron annihilation spectroscopy (PAS) has been established in the past 20 years as a powerful tool for the detection of lattice defects in metals and semiconductors. Typical defects detected by positrons in metals are usually related to vacancies (monovacancies, dislocations, small vacancy clusters). But also precipitates, interfaces, and inner surfaces (pores) can act as positron traps [1]. Usually, the defects are assumed to be evenly distributed in the sample (application of the standard trapping model [2, 3]). More recently there have been attempts to include inhomogeneous distributions of defects into the trapping model — called *diffusion trapping model* [4, 5]. Here, we will extend the

*Tel.: +49-228-73 2634, Fax: +49-228-73 2505, e-mail: staab@iskp.uni-bonn.de

detection of defects to fine-grained (100 nm ... 15 μm) and porous samples, discussing the sintering process as an example, by considering the effect of positron diffusion via a Monte Carlo simulation.

Sintering (here: *pressureless* sintering) means compactation and subsequent heat treatment of ceramic or metal powders [6, 7]. Sintering usually goes along with neck growth between neighboring powder particles and shrinkage, *i.e.* vanishing of pore space. In this article we will discuss the influence of changes in the microstructure on the sintering process.

Concerning PAS, we have to know, which fraction of the positrons will reach — dependent on powder particle sizes and shapes — the surface of powder particles, and additionally, will positrons be trapped there, and which positron lifetime is associated to that (see path 3 and 4 Fig. 1). On the other hand, we should not neglect defects (*e.g.* dislocations) inside the powder particles (path 2).

The motivation for positron studies on powder metallurgical materials was the idea of *defect induced diffusion* (*cf. e.g.* [8]) which should dominate over bulk diffusion (Nabarro-Herring creep). Earlier studies on the sintering process by PAS found, independent of green density or heating rate, a coincidence between decreasing average lifetime $\bar{\tau}$ and intensive shrinkage stage [9, 10]. While these works revealed an unusual high average lifetime in the as-pressed state, additionally, an increase of the average lifetime at about $0.4\,T_{\mathrm{M}}$ was noticed. This seems to be contrary to more recent results [11, 12]. But it has been shown how this contradiction can be resolved: In rare cases it is possible that the average positron lifetime increases while the density of *certain* defects decreases [13].

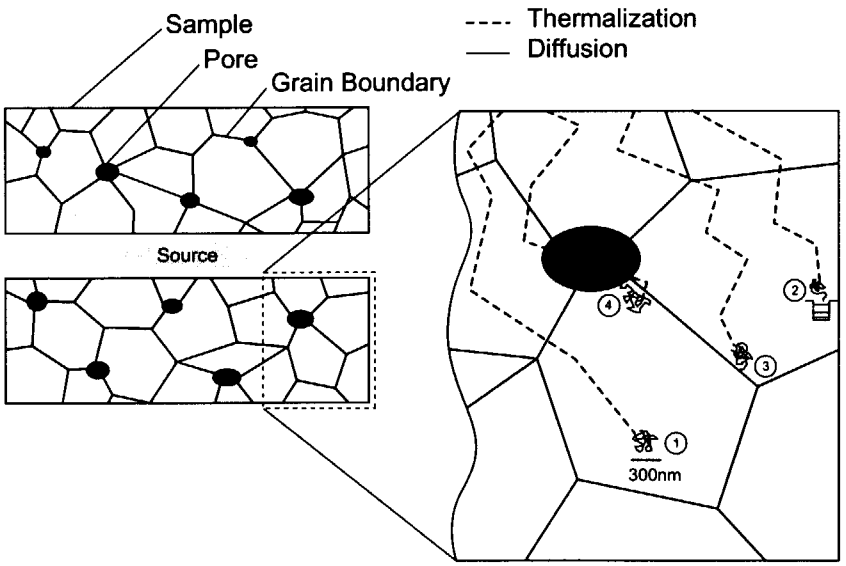


Figure 1: Two porous samples arranged in a source-sample sandwich: Pores (black regions) and grain boundaries (straight black lines) are shown. The detailed enlargement to the right shows thermalization (assumed to stop in the bulk) and diffusion paths of positrons entering the sample (diffusion paths are magnified). Different paths: 1: Diffusion stops in the bulk, 2: Trapping into a defect, 3: Diffusion to a grain boundary and trapping, 4: Diffusion to an inner surface and trapping to a surface state.

2 Positron Diffusion — Random Walk Simulation

In a porous or fine-grained sample one has to take into account, where the positrons are most likely to thermalize, and how the annihilation characteristic is influenced by the microstructure. Hence, we have to consider the limited positron diffusion length $L_+ = \sqrt{2d\,D_+\,\tau_{\text{eff}}}$ [14], where D_+ is the positron diffusion constant, τ_{eff} the effective lifetime, and d the dimension of the diffusive motion, *e.g.* $d = 2$ for surface diffusion. Assuming defect-free grains ($\tau_{\text{eff}} = 103\,\text{ps}$), one obtains for Copper or Nickel ($D_+ = 1.6\ \text{cm}^2/\text{s}$) $L_+ \approx 330\,\text{nm}$ [15].

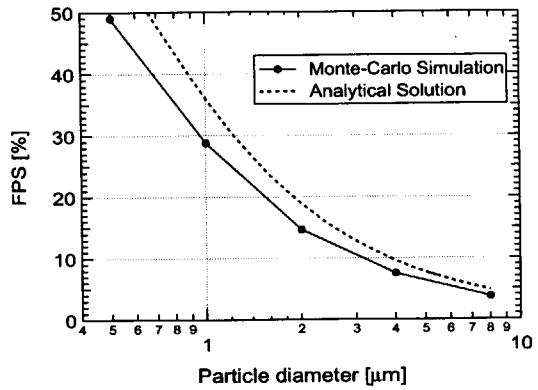


Figure 2: Monte Carlo simulation of the positron diffusion: Fraction of positrons reaching the particles surfaces (FPS) as a function of particle diameter for spherical particles. The analytical solution [16, 17] is dashed. Defect-free interior of particles is assumed.

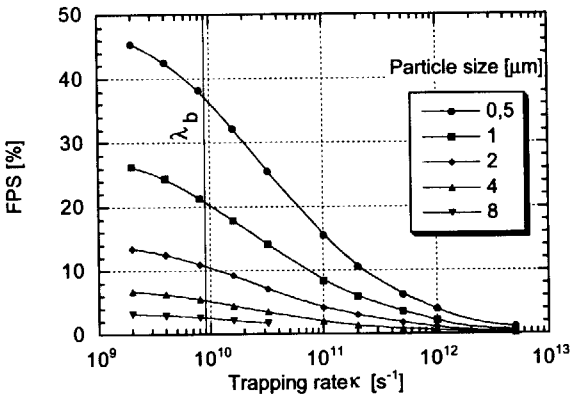


Figure 3: Fraction of positrons reaching the particles surface (FPS) in the presence of defects as a function of the capture rate κ. The particle diameter is valid for spherical particles. $\lambda_{\text{b}} = 1/\tau_{\text{b}}$ the annihilation rate in the bulk.

One can use analytical solutions of the diffusion equation [16, 17] or a Monte-Carlo simulation [15] (*cf.* figure 2 and 3) and compare to the fraction of positrons annihilating with parameters typical for grain boundaries or surfaces [11, 13, 15]. The main assumptions are that large angle grain boundaries possess so high defect densities that positrons passing them during their random walk motion will be trapped there (τ_{GB}). The same is valid for surfaces (τ_{surf}) (*cf.* the discussion in [11, 13]. Furthermore, traps inside powder particles or grains will be considered by their corresponding trapping rate κ (*cf.* Fig. 3).

3 Positron Results and Sintering Mechanisms

For all investigated powders the individual powder particles itself contain defects such as dislocations and grain boundaries in the as-produced state [11, 12], while pressing is increasing the dislocation density further [12].

Generically, annealing scales in most metals with the homologous temperature T/T_{M}, where T_{M} is the melting point: vacancy migration at $T \approx 0.16\,T_{\text{M}}$, vacancy cluster annealing at $T \approx 0.27\,T_{\text{M}}$, recrystallization at $T \approx 0.40\,T_{\text{M}}$, and grain growth at $T > 0.5\,T_{\text{M}}$ [13]. A combined study using metallography, line-profile analysis of x-ray broadening, Transmission and Scanning Electron Microscopy revealed large-angle grain boundaries

as the only detectable types of defects at temperatures relevant for sintering (shrinkage occurs at $T > 0.5\,T_{\mathrm{M}}$) [11, 12, 18].

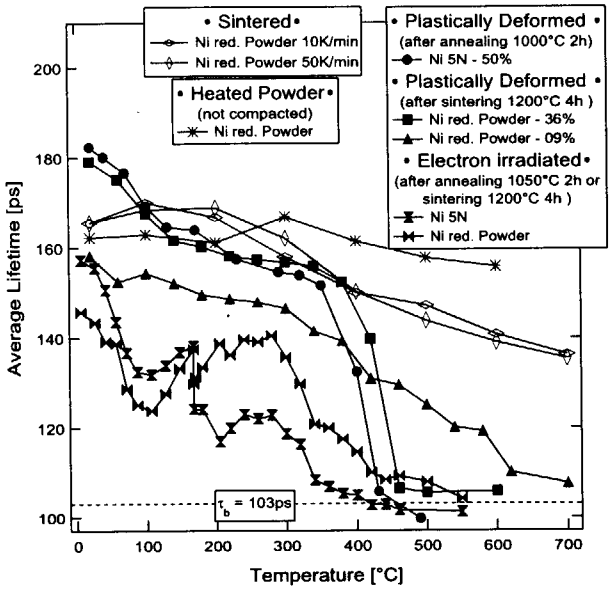


Figure 4: Annealing behavior up to 700°C for differently damaged Nickel samples. Note the similarity in the annealing behavior between uncompacted and compacted nickel powder. On the other hand defects induced by electron irradiation and plastic deformation have annealed out at 600°C.

While Nickel powder compacts show a very complicated defect structure below 600°C, the dislocation density drops between 300 and 500°C below the detection limit of $1 \times 10^8\,\mathrm{cm}^{-2}$ when recrystallization happens (*cf.* figure 5 and 6). The lifetime analysis reveals

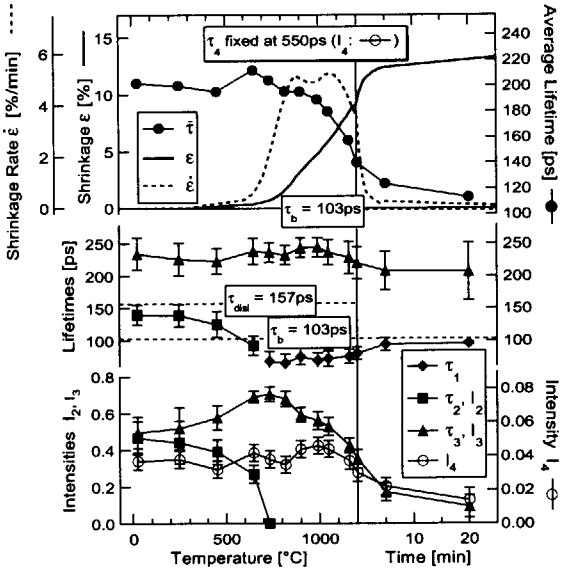


Figure 5: Nickel Reduction Powder: $\bar{L}_{\mathrm{P}} = 10\,\mu\mathrm{m}$, green density $\rho_{\mathrm{g}} = 0.65\,\rho_0$, and heating rate of $v_{\mathrm{A}} = 200\,\mathrm{K/min}$. Upper part: shrinkage ε and shrinkage rate $\dot{\varepsilon}$ together with the average lifetime $\bar{\tau}$. Lower part: decomposition of lifetime spectra.

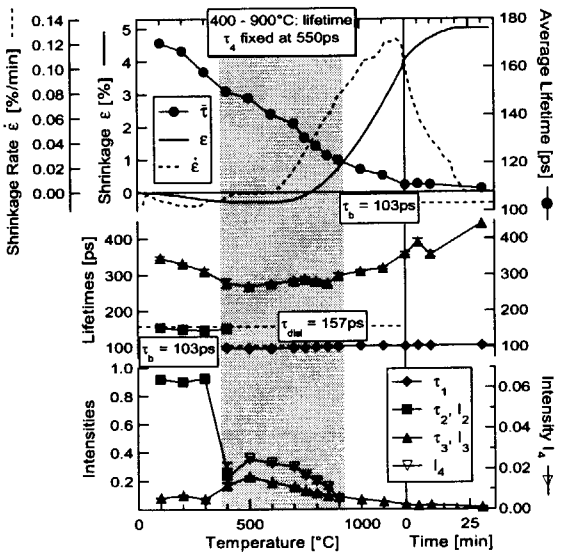


Figure 6: Compacts of nickel reduction powder ($\bar{L}_{\mathrm{P}} = 24\,\mu\mathrm{m}$, $\rho_{\mathrm{g}} = 0.78\,\rho_0$) sintered with a heating rate of $10\,\mathrm{K/min}$. Upper part: shrinkage, shrinkage rate, and average lifetime; lower part: decomposition of the spectra.

for $T > 0.5\,T_{\mathrm{M}}$ always $\tau_1 = \tau_{\mathrm{b}}$ (annihilation in undisturbed interior of grains), $\tau_3 = \tau_{\mathrm{GB}}$

(trapping at grain boundaries), and eventually $\tau_4 = \tau_{\mathrm{surf}}$ (trapping at powder particle surfaces). This indicates a powder particle size of less than 15 μm [12, 13]. While the decreasing intensity corresponding to $\tau_{\mathrm{surf}} \approx 550\,\mathrm{ps}$ means vanishing of pore space, the same for $\tau_{\mathrm{GB}} \approx 300\,\mathrm{ps}$ indicates grain growth inside each powder-particle. Approaching sintering temperature, the contact boundaries start moving, meaning that the grain sizes become larger than the original powder particle size.

Considering intermediate stage sintering, the driving force σ for sintering is given by the *Laplace pressure* (*cf.* [7] chapter 2.2) $\sigma = A_0\,(2\gamma_{\mathrm{S}} - \gamma_{\mathrm{GB}})/(\bar{L}_{\mathrm{P}})\,\Theta$ acting as capillary tension, where γ_{S} and γ_{GB} are surface and grain boundary energy, respectively, $\bar{L}_{\mathrm{P}}$ is the average powder-particle size, Θ the porosity and A_0 is a number ($1 \ldots 4$ according to the particles geometry). For *Nabarro-Herring* and *Coble* creep the estimated shrinkage rates are given by [7]

$$\dot{\varepsilon}_{\mathrm{NH}} = A_1\,\frac{D_{\mathrm{vol}}\Omega\,\sigma}{\mathrm{k_B}T}\,\frac{1}{\bar{L}_{\mathrm{G}}^2} \qquad \text{and} \qquad \dot{\varepsilon}_{\mathrm{C}} = A_2\,\frac{\delta_{\mathrm{GB}}D_{\mathrm{GB}}\Omega\,\sigma}{\mathrm{k_B}T}\,\frac{1}{\bar{L}_{\mathrm{G}}^3}\ , \tag{1}$$

respectively ($\bar{L}_{\mathrm{G}}$ is the average grain size, A_1, A_2 are empirical constants, Ω is the atomic volume, D_{vol} and D_{GB} are the coefficients for volume and grain boundary diffusion, respectively, while δ_{GB} is the effective grain boundary width).

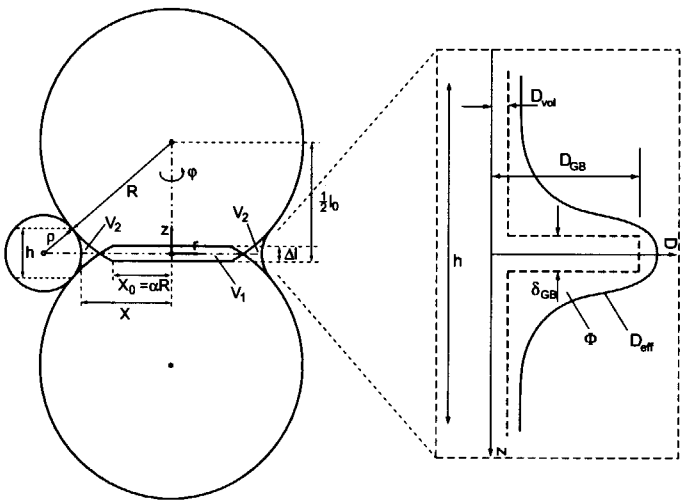


Figure 7: Modified two-particle-model: R is the original powder particle radius. Pressing causes flattening of the two-particle-contact, where $\alpha = X_0/R$ is the *initial flattening*. X_0 and l_0 are neck radius and particle distance after pressing. r, φ, z are cylindrical coordinates used for the calculations. Enlarged part: course of the diffusion coefficient along the neck radius. The other symbols are explained in the text.

Alternatively, one can use a two-particle model modified to include flattening of powder particles by pressing [19, 20, 21] (*cf.* Fig. 7). It estimates the shrinkage rate from the experimentally measured shrinkage. Material transport causes the volume V_1 to migrate to the neck region where it is deposited (V_2). Hence, the outer neck radius ρ, the inner neck radius X, and the neck heights h are enlarged. Simultaneously, the distance of the particle centers decreases by Δl. The structural activity Φ is the area below the curve of the effective diffusion coefficient D_{eff}. The profile for defect-free powder particles and relaxed grain boundaries is the dashed line, *i.e.* $T > T_{\mathrm{R}} = 0.4\,T_{\mathrm{M}}$. Taking into account Fick's law and appropriate boundary conditions one is lead to an equation for the shrinkage rate (see [12, 21, 22] for more details). Taking $l_0 = 2R\sqrt{1-\alpha^2}$ as starting length, one obtains for the shrinkage rate

$$\frac{\mathrm{d}}{\mathrm{d}t}\left(\frac{\Delta l}{l_0}\right) = 4\,\frac{\Omega\gamma_{\mathrm{S}}}{\mathrm{k_B}T}\,\frac{1}{\rho}\,\frac{1}{X^2R\sqrt{1-\alpha^2}}\int_{-h/2}^{h/2} D_{\mathrm{eff}}(t,z)\mathrm{d}z\ , \tag{2}$$

using the usual approximations $\Omega\gamma_S \ll k_B T$ and $\rho \ll X$ (For an exact derivation see [21]). In the case of relaxed boundaries one obtains for the integral part (structural activity) of equation (2) $\Phi = D_{vol}(h - \delta_{GB}) + \delta_{GB} D_{GB}$ used here.

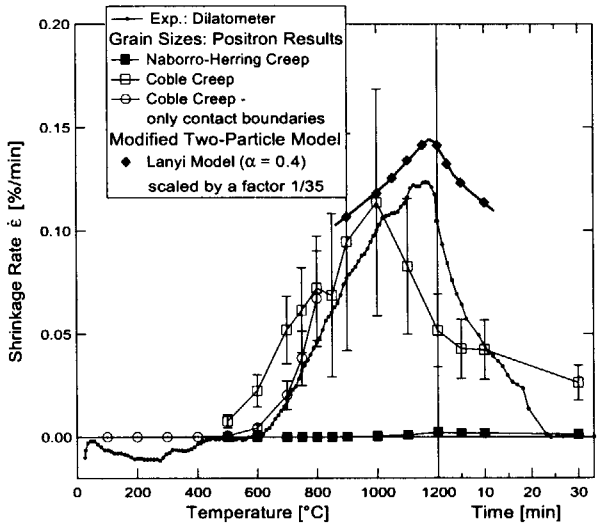


Figure 8: Calculated shrinkage rates: The decrease of the calculated rate is due to grain growth, where the grain size becomes larger than the powder particle size (Coble Creep). The assumption of the two-particle model are no longer valid when the grain size becomes larger than the original powder particle size.

In Figure 8 the shrinkage rates are estimated for diffusional creep according to the lifetime data, giving $\bar{L}_P$ and $\bar{L}_G$, while the two-particle model uses the experimentally determined shrinkage and $\bar{L}_P = R$ [11, 12]. Using the results for the effective powder-particle size $\bar{L}_P = 4.1\,\mu$m [12], Nabarro-Herring creep gives shrinkage rates, which are one order of magnitude too small, while Coble creep gives approximately the right rates (*cf.* Fig. 8). Dislocation creep is not considered, since at sintering temperature the density of dislocation is globally too small to act as vacancy sources and sinks. For the modified two-particle model, the estimated shrinkage rates are by a factor of 35 too high (scaled in Figure 8), while the qualitative tendency is right. The too high rates may be due to an underestimation of the influence of surface diffusion, or a deviation of powder particles from the assumed spherical shape [12].

4 Conclusions

Using positron annihilation spectroscopy it is indeed possible to obtain meaningful results when investigating powders or fine-grained materials. The main trapping sites are — dependent on powder particle and grain sizes — pores or particle surfaces ($\tau_{surf} \approx 550$ ps) and grain boundaries inside individual powder particles ($\tau_{GB} \approx 300$ ps). In all cases recrystallization at $0.4\,T_M$ is noticed by dislocation annealing. The further decrease of the average lifetime $\bar{\tau}$ during the intensive shrinkage stage has a generic reason: elimination of pore surfaces and grain growth.

It is possible to follow the sintering process, *i.e.* changes in microstructure and densification, by PAS, *i.e.* determining averages for powder particle and grain sizes. When densification has started at $T > 0.5\,T_M$ the surface signal vanishes and the only detectable defect lifetime is τ_{GB}, since all other defect have annealed out. Hence, we attribute this lifetime to positron trapping at grain boundaries. By use of a Monte-Carlo simulation of the positron diffusion we where able to show that grain sizes determined that way are consistent with other investigations.

One obtains reasonable shrinkage rates, consistent with grain-boundary diffusion (Coble creep) dominating over Nabarro-Herring creep as mechanism for material transport, while dislocation creep plays no role here.

References

[1] R. Krause-Rehberg and H. Leipner, *Positron Annihilation in Semiconductors*, 1st ed. (Springer Verlag, Berlin, Heidelberg, 1999).

[2] W. Frank and A. Seeger, Appl.Phys. **3**, 61 (1974).

[3] A. Seeger, Appl.Phys. **4**, 183 (1974).

[4] A. Dupasquier, R. Romero, and A. Somoza, Phys. Rev. **B48**, 9235 (1993).

[5] A. Dupasquier and A. Somoza, Mater. Sci. Forum **175-178**, 35 (1995).

[6] R. M. German, *Powder Metallurgy Science*, 1st ed. (Priceton, New Jersey, 1984).

[7] W. Schatt, *Sintervorgänge*, 1st ed. (VDI Verlag, Düsseldorf, 1992).

[8] W. Schatt, F. Friedrich, and K.-P. Wieters, Rev. Powder Metall. **3**, 1 (1986).

[9] W. Schatt and M. Hinz, Powder metall.internat. **20**, 17 (1988).

[10] R. Krause, W. Schatt, B. Vetter, and A. Polity, Cryst.Res.Technol. **25**, 819 (1990).

[11] T. Staab, R. Krause-Rehberg, B. Vetter, and B. Kieback, J.Phys:Condens.Matter **11**, 1757 (1999).

[12] T. Staab, R. Krause-Rehberg, B. Vetter, and B. Kieback, J.Phys:Condens.Matter **11**, 1807 (1999).

[13] T. Staab, R. Krause-Rehberg, and B. Kieback, J. Mater. Sci. **34**, 3833 (1999).

[14] R. Nieminen, in *Proceedings of the International School of Physics "Enrico Fermi" – Positron Solid State Physics*, edited by W. Brandt and A. Dupasquier (North Holland, Amsterdam, 1983), pp. 359–407.

[15] C. Hübner, T. Staab, and R. Krause-Rehberg, Appl.Phys. **A61**, 203 (1995).

[16] W. Brandt and R. Paulin, Phys. Rev. Lett. **21**, 193 (1968).

[17] A. Gainotti and C. Ghezzi, Phys. Rev. Lett. **24**, 349 (1970).

[18] C. Hübner, T. Staab, and H. Leipner, phys.stat.sol. (a) **150**, 653 (1995).

[19] P. Wellner, G. Gessinger, and H.-E. Exner, Z.Metallkde. **65**, 602 (1974).

[20] P. Lányi, Ph.D. thesis, Zentralins. Festkörperphysik und Werkstofforschung, Dresden, Germany, 1979.

[21] T. Staab, Ph.D. thesis, Martin-Luther Universität Halle-Wittenberg, Germany, 1996.

[22] D. Johnson and T. Clarke, Acta Metall. **12**, 1173 (1964).

JAERI－Conf 2003－001

JP0350250

1.4.2 MODELING OF POSITRON STATES AND ANNIHILATION IN SOLIDS

M. J. Puska
Laboratory of Physics, Helsinki University of Technology
P.O. Box 1100, 02015 HUT, Finland

Abstract

Theoretical models and computational aspects to describe positron states and to predict positron annihilation characteristics in solids are discussed. The comparison of the calculated positron lifetimes, core annihilation lineshapes, and two-dimensional angular correlation maps with experimental results are used in identifying the structure (including the chemical composition) of vacancy-type defects and their development e.g. during thermal annealing. The basis of the modeling is the two-component density-functional theory. The ensuing approximations and the state-of-the-art electronic-structure computation methods enable practical schemes with a quantitative predicting power.

Keywords: Positron annihilation, density-functional theory, defects in solids

1 Introduction

Positron annihilation can be used as a versatile tool to investigate materials properties[1, 2, 3, 4, 5]. The applications extend from the advanced problems of solid state physics, such as the determination of the Fermi surfaces of metals or high-temperature superconductors, to the industrial materials testing during processes like damage development under irradiation or wear conditions. In between there are important materials physics studies like those for the electronic and ionic structures of vacancy-type defects in metals and in semiconductors. The last types of applications are in the focus of the present review. Especially, we will describe theoretical models and computational tools to calculate positron states and annihilation in solids. Theoretical predictions support in an essential way positron experiments for identifying defects in solids and for determining even their chemical structure.

The use of positron annihilation in defect studies is based on the trapping of positrons from a delocalized bulk state to a localized state at the defect. The trapping is due to the reduced nuclear repulsion at the open-volume defects. Because the electronic structure seen by the positron at the defect differs from that in the perfect bulk crystal the annihilation characteristics change. The positron lifetime increases because the average electron density decreases. For the same reason the momentum distribution of annihilating electron-positron pairs becomes more peaked at low momenta. However, the positron density may sample the different atomic species of a compound materials with different relative probabilities in the bulk and at a defect. The defect may be surrounded by impurity atoms. In these cases the high-momentum region of the distribution, which is mainly due to annihilations with core electrons, reflects the chemical structure of the defect. The changes in the bond structure between the atoms neighboring the defect may also affect the low-momentum part of the distribution. In order to understand these changes and fully benefit from them in defect identification, theoretical calculations with high predictive power are indispensable.

The purpose of this paper is to review the theory and computational methods used for describing positron states and annihilation in solids. The ideas are discussed by the help of selected applications. The rest of the paper is organized as follows. In Sec. 2, we first review the two-component density–functional theory on which the calculations for positrons in solids are based on. Thereafter, we introduce the so-called conventional scheme, which simplifies considerably the treatment of localized positron states. Finally, in Sec. 2 a fast method to predict positron states and annihilation, the atomic superposition method, is described. In Sec. 3 we discuss how the theory is tested by comparing the predictions with experiments and as an example of defect identification a study for As-vacancy complexes in silicon is reviewed. Finally, in Sec. 4 we provide conclusions and speculations on the future directions.

2 Theory and calculation methods

2.1 Electron and positron densities: The two–component density–functional theory

In the density–functional theory (DFT) [6] the total energy of an electron system is given as a functional of the electron density n_-. The ground–state electron density is calculated by minimizing this functional and thereafter, in principle, all the ground–state properties can be determined. In the two–component density–functional theory (TC-DFT) [7] for electron-positron systems in an external electrostatic potential $V_{ext}(\mathbf{r})$ the total energy is written as a functional of the electron and positron densities n_- and n_+ (in atomic units)

$$E[n_-, n_+] = \tag{1}$$
$$F[n_-] + F[n_+] - \int d\mathbf{r} V_{ext}(\mathbf{r})[n_-(\mathbf{r}) - n_+(\mathbf{r})] - \int d\mathbf{r} \int d\mathbf{r}' \frac{n_-(\mathbf{r})n_+(\mathbf{r}')}{|\mathbf{r} - \mathbf{r}'|} + E_c^{e-p}[n_-, n_+].$$

Above, $E_c^{e-p}[n_-, n_+]$ is the electron–positron correlation energy functional and the functional $F[n]$ reads as

$$F[n] = T[n] + \frac{1}{2} \int d\mathbf{r} \int d\mathbf{r}' \frac{n(\mathbf{r})n(\mathbf{r}')}{|\mathbf{r} - \mathbf{r}'|} + E_{xc}[n], \tag{2}$$

where $T[n]$ is the kinetic energy of noninteracting electrons or positrons. $E_{xc}[n]$ is the exchange–correlation energy between indistinguishable particles and $E_c^{e-p}[n_-, n_+]$ is the electron–positron correlation energy functional. The most commonly used approximation for $E_{xc}[n]$ is the local density approximation (LDA) where the exchange–correlation energy is approximated as

$$E_{xc}[n] = \int n(\mathbf{r}) \epsilon_{xc}(n(\mathbf{r})) d\mathbf{r}. \tag{3}$$

Above, $\epsilon_{xc}(n(\mathbf{r}))$ is the exchange–correlation energy per particle in a *homogenous* one-component electron gas. $\epsilon_{xc}(n(\mathbf{r}))$ can be determined accurately by the Quantum Monte-Carlo (QMC) method [8] and practical parametrizations exists for it [9]. In contrast, the electron–positron correlation energy has not yet been determined accurately by the QMC method due to statistics requirements to decribe the pile-up of the electron (positron) density at the positron (electron) [10]. For the electron–positron correlation energy at the limit of vanishing positron density Arponen and Pajanne [11] have provided results

on the basis of many-body perturbation expansions. At finite positron densities, the correlation energy functional was first calculated by Lantto [12] using the hypernetted chain approximation. Parametrizations are presented *e.g.* in Ref. [13]. The electron–positron correlation is usually also treated within the LDA.

From the above total energy functional, one derives the two-component Kohn-Sham equations for the electrons and positrons, *i.e.*

$$-\frac{1}{2}\nabla_i^2\psi_i(\mathbf{r}) + \left[\frac{\delta E_{xc}[n_-]}{\delta n_-(\mathbf{r})} - \phi(\mathbf{r}) + \frac{\delta E_c^{e-p}[n_-, n_+]}{\delta n_-(\mathbf{r})}\right]\psi_i(\mathbf{r}) = \epsilon_i\psi_i(\mathbf{r}), \tag{4}$$

$$-\frac{1}{2}\nabla_i^2\psi_i^+(\mathbf{r}) + \left[\frac{\delta E_{xc}[n_+]}{\delta n_+(\mathbf{r})} + \phi(\mathbf{r}) + \frac{\delta E_c^{e-p}[n_-, n_+]}{\delta n_+(\mathbf{r})}\right]\psi_i^+(\mathbf{r}) = \epsilon_i^+\psi_i^+(\mathbf{r}), \tag{5}$$

where

$$\phi(\mathbf{r}) = \int d\mathbf{r}' \frac{-n_-(\mathbf{r}') + n_+(\mathbf{r}') + n_0(\mathbf{r}')}{|\mathbf{r} - \mathbf{r}'|} \tag{6}$$

is the total Coulomb potential. Here, $n_0(\mathbf{r})$ denotes the positive ionic or nuclear charge density providing the external potential $V_{ext}(\mathbf{r})$. Because in the positron spectroscopy measurements there is only one positron in the solid sample at the time, one makes a self-interaction correction when calculating positron states [7, 13] by dropping out the self-Coulomb and self-exchange terms from Eq. (5).

The electron and positron densities are obtained by

$$n_-(\mathbf{r}) = \sum_{\epsilon_i \le \epsilon_F} |\psi_i(\mathbf{r})|^2; \qquad n_+(\mathbf{r}) = |\psi^+(\mathbf{r})|^2, \tag{7}$$

where ϵ_F is the electron Fermi energy. $\psi_i(\mathbf{r})$ and $\psi^+(\mathbf{r})$ are the Kohn–Sham single particle eigenstates for electrons and the positron, respectively.

Using the TC-DFT one can compute the Hellman–Feynman forces, caused by the electrons and positrons, acting on the *ions* and move the ions accordingly. It has been shown [14, 13, 15] that the positron induced relaxations around, say, vacancies in semiconductors can be considerably large and affect also the annihilation characteristics.

Solving Eqs. (4)-(7) self-consistently yields the electron and positron densities and allows one to calculate the positron annihilation characteristics, which can be directly compared with experiment. The positron annihilation rate is calculated within the LDA as

$$\lambda = \pi r_0^2 c \int d\mathbf{r} n_+(\mathbf{r}) n_-(\mathbf{r}) g(0; n_+(\mathbf{r}), n_-(\mathbf{r})), \tag{8}$$

where $g(0; n_+, n_-)$ is the electron–positron pair correlation function or the enhancement factor evaluated at the positron in a homogenous two–component plasma with positron density n_+ and electron density n_-. r_0 is the classical electron radius and c is the speed of light. The inverse of the annihilation rate is the positron lifetime.

The momentum distribution of the annihilating electron–positron pairs can be written as

$$\rho(\mathbf{p}) = \pi r_0^2 c \sum_i \left| \int d\mathbf{r} e^{-i\mathbf{p}\cdot\mathbf{r}} \psi_i^{ep}(\mathbf{r}, \mathbf{r}) \right|^2, \tag{9}$$

where $\mathbf{p}$ is the total momentum of the annihilating pair, $\psi_i^{ep}(\mathbf{r}, \mathbf{r})$ is the two–particle wave function when the positron and electron reside at the same point. The two–particle wave function is in principle difficult to calculate and therefore it is usually written in terms

of the positron and electron single-particle wave functions $\psi_+(\mathbf{r})$ and $\psi_i(\mathbf{r})$, respectively. Within the LDA one obtains

$$\psi_i^{\mathrm{ep}}(\mathbf{r},\mathbf{r}) = \psi_+(\mathbf{r})\psi_i(\mathbf{r})\sqrt{g(0;n_+(\mathbf{r}),n_-(\mathbf{r}))}, \tag{10}$$

where all the many-body effects have been buried into the enhancement factor $g(0;n_+,n_-)$.

2.2 Delocalized positron states and the conventional scheme

For a positron delocalized in a bulk solid, the density n_+ vanishes at every point and the above TC-DFT equations can be simplified considerably. Namely, the positron cannot affect the electronic structure which can be solved self-consistently by setting the correlation potential $\frac{\delta E_c^{e-p}[n_-,0]}{\delta n_-(\mathbf{r})}$ and the positron density to zero. Using the calculated electron density, one can then solve for the positron state from the Schrödinger equation with the potential

$$V_+(\mathbf{r}) = \phi(\mathbf{r}) + V_{corr}(n_-(\mathbf{r})), \tag{11}$$

where $\phi(\mathbf{r})$ is the Coulomb potential, obtained from the electronic structure calculation and V_{corr} is the zero-positron-density limit of the correlation potential $\frac{\delta E_c^{e-p}[n,n_+]}{\delta n_+(\mathbf{r})}$. Within the LDA, a commonly used form for this potential is the parametrization by Boroński and Nieminen [7] who used the data by Arponen and Pajanne [11]. It is possible to go beyond the LDA using the the generalized gradient approximation (GGA) [16] or the weighted density approximation (WDA) [17, 18] which take the inhomogenous caharacter of the electron density explicitly into account.

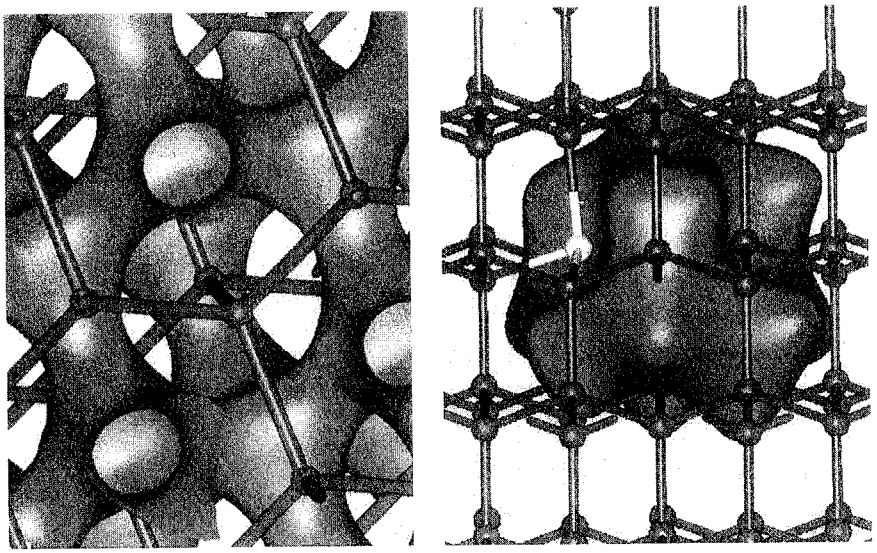
The calculation of the positron annihilation rate in Eq. (8) becomes also simpler for the delocalized positrons because the enhancement factor $g(0;0,n_-)$ depends only on the electron density. Instead of the LDA one can use for the enhancement factor the GGA [16] or the WDA [17, 18].

When calculating momentum distributions of annihilating electron-positron pairs Alatalo *et al.* [19] noticed that the LDA form of Eq. (10) may yield spurious effects at the high momentum region. They ended up using state-dependent enhancement factors and two-particle wavefunctions of the form

$$\psi_i^{\mathrm{ep}}(\mathbf{r},\mathbf{r}) = \psi_+(\mathbf{r})\psi_i(\mathbf{r})\sqrt{\lambda_j/\lambda_j^{\mathrm{IPM}}}, \tag{12}$$

where $\lambda_j^{\mathrm{IPM}} = \pi r_e^2 c \int d\mathbf{r}\psi_+^2(\mathbf{r})\psi_j^2(\mathbf{r})$ is the annihilation rate of the electron state ψ_j calculated using the independent-particle model (IPM) and λ_j is the annihilation rate obtained by a calculation utilizing the LDA or the GGA.

For a positron localized at a defect, the (average) density n_+ does not vanish and the above approximation is in principle invalid. Nevertheless, it has been widely applied since the calculations performed using the full two-component formalism tend to be time consuming and because the electron-positron correlation in the two-component plasma is inaccurately known. The ensuing scheme is called as the 'conventional' scheme. In the conventional scheme the electron density is first solved without the effect of the positron and then the positron state is calculated without any self-consistency iterations. The use of the conventional scheme can be justified by noticing that the positron and the electron screening cloud around it form a neutral quasiparticle which does not affect the average electron density of the system. Moreover, the results of the conventional scheme have been shown to be in agreement with those obtained by the two-component density-functional calculations [7, 13, 20].



(a) (b)

Figure 1: (a) An isosurface of the positron wave function in a perfect Si lattice. The positions of the Si atoms are denoted by blue spheres, and the electronic interatomic bonds as blue sticks. The positron lifetime in this state is according to experiments and theory about 220 ps. (b) An isosurface of the positron wave function at a vacancy surrounded by one Sb impurity. The Sb atom is denoted by a yellow sphere. The positron lifetime in this state is according to theory about 230 ps [From Ref. [24]].

2.3 Numerical methods for positron calculations

Schemes and programs for the pure electron-structure calculations can be used also in the positron calculations. The potential felt by the positron can be constructed from the calculated electron density. The positron wavefunction can be presented using expansions similar to those for the electron states, and the momentum distributions can be calculated accordingly.

However, within the conventional scheme the practical calculations can be further simplified by using instead of a self-consistent electron density the superposition of (neutral) free atoms. The scheme obtained, called as the atomic superposition method[21], is fast and thereby especially beneficial for extended low-symmetry systems such as grain boundaries in solids or reconstructed surfaces (with adsorbates). Due to a compensation effect, *i.e.* the positron density follows the relaxation of the electron density keeping electron-positron overlap approximately unchanged, the positron lifetime is well estimated although the electron density is non-self-consistent. Of course, the momentum distribution of annihilating electron-positron pairs at low momenta is strongly affected by the bonding structure of valence electrons and it cannot be realiably calculated from atomic orbitals. But the high-momentum region is mainly due to the inert core electrons, and there the free atom wavefunctions can be used in the momentum calculation [19].

In the atomic superposition method the full three-dimensional positron potential is constructed in a three-dimensional point grid. The positron wavefunction can then be calculated in the same grid using a real-space Schrödinger equation solver. An especially efficient method is the Raleigh quotient multigrid (RQMG) method [22]. Because in the

multigrid scheme errors on all different lenghs scales are efficiently reduced, the method suits well for large systems. Indeed, with the RQMG method the solution of the positron wavefunction in a system of thousands of atoms is a matter of a few cpu-minutes on a normal workstation [23]. As an example of the use of the atomic superposition method, Fig. 1 shows the density of a positron delocalized in a perfect Si-lattice as well as that for a positron trapped by a vacancy defect in Si.

3 Examples of positron calculations

The theoretical models and computational schemes for positron states and annihilation characteristics can be first tested by comparing the predictions with well-characterized experimental results, usually with those for perfect bulk crystals. Thereafter the methods can be used in applications with experimental data, for example, in the defect identification. We follow this idea in the discussion of the present section.

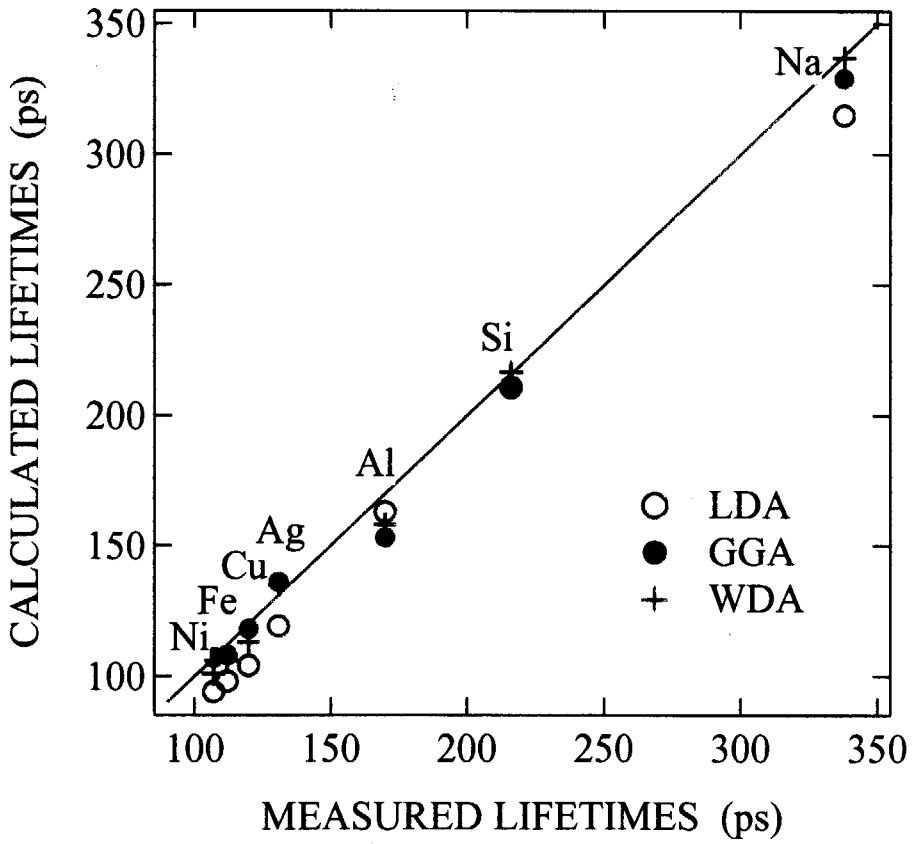


Figure 2: Calculated positron lifetimes in perfect bulk lattices as a function of the measured ones (The experimental values are quoted in Ref. [16]]). The open and solid circles give the LDA and the GGA results, respectively [16] whereas the crosses are obtained by the WDA [18].

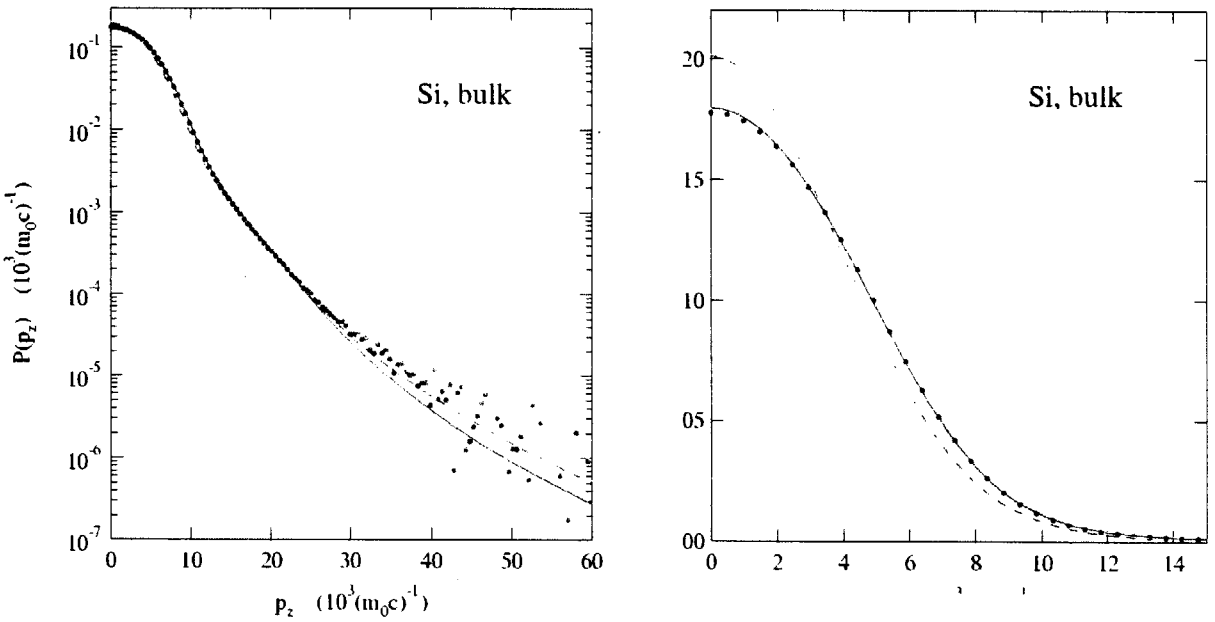


Figure 3: Positron annihilation probability density $P(p_z)$ for bulk Si. The experimental data (circles) [[36]] are shown together with two different theoretical calculations: (*i*) Self-consistent pseudo-valence-electron-density and free atom core (solid line) [[27]] (*ii*) Free atom valence and core electrons (dashed line). The theoretical curves are convoluted with a Gaussian in order to mimick the finite experimental resolution.

3.1 Comparisons between theoretical and experimental results

Positron lifetimes obtained by three different models for a selected set of bulk materials are compared in Fig. 2 with experimental data. The LDA calculation [4] uses the parametrization by Boroński and Nieminen [7] for the enhancement factor. In the GGA calculation [16] the enhancement factor is parametrized on the basis of the data by Arponen and Pajanne [11], whereas in the WDA calculation [18] the parametrization by Rubaszek and Stachowiak [25] is used in a state-dependent form. The LDA and WDA calculations do not use any adjustable parameters whereas there is one parameter in the GGA fitted to give an overall good agreement with experiment for a large number of bulk materials. All the works use in the numerical calculations of the self-consistent electronic structure and the positron state the linear-muffin-tin-orbital (LMTO) method. The overall agreement in comparison with experiment is good, especially in the case of the GGA and WDA. The GGA and the WDA have a tendency to decrease the positron annihilation with core electrons and thereby improve the agreement. The use of the non-self-consistent electronic structure and the atomic superposition method hardly affects the results on the LDA level and the changes are usually small within the GGA, too [16]. In conclusions, for the positron lifetimes the choice of the scheme is not very important in practice. More

important is that in defect identification one compares the differences between the bulk and defect lifetimes, so that possible systematic errors cancel.

The calculated momentum distributions of the annihilating electron-positron pairs can be compared with spectra of the two-dimensional angular correlation of annihilation radiation (2D-ACAR) and the coincidence Doppler-broadening (CDB) methods [1]. The 2D-ACAR gives detailed information about the valence electron momentum distribution integrated over one spatial direction. It is also possible to construct three-dimensional momentum distributions from the 2D-ACAR data [26]. The CDB technique gives momentum distributions integrated over two perpendicular directions. The CDB technique has been recently reviewed by Alatalo and Puska [5].

Fig. 3 compares CDB spectra (or the positron annihilation probability densities) for bulk Si simulated by two theoretical schemes with the measured one. One of the calculations uses the self-consistent valence electron density obtained with the pseudo-potential-plane-wave method and free atom core densities [27]. The fully three-dimensional positron wavefunction is used with valence electrons whereas a spherically symmetric positron wavefunction is assumed when calculating the core electron contribution to the momentum density. In the other calculation [5] the fast scheme by Alatalo *et al.* [19] is employed. In this scheme the free atom orbitals are used for all electrons. Furheron, the annihilation rates λ_j are calculated by using the fully three-dimensional positron wavefunction but the integral in Eq. (9) is performed by assuming spherically symmetric functions. Both of the calculations use the GGA for the annihilation rates and the state-dependent enhancement scheme of Eq. (12). In order to describe the low-momentum region the self-consistent valence electron density is necessary. But for the high-momentum part the non-self-consistent electron density is sufficient.

The case of bulk Si in Fig. 3 is perhaps easy to model with the present theories. The most accurate all-electron calculations [28] have resulted in a good agreement with experiment also in the case of bulk Al and graphite. They show that the spherical approximation for the positron state is good for Al. But for graphite, having a layer structure, the full three-dimensional positron wavefunction should be used. In the case of materials having 3d valence or semicore orbitals the above mentioned state-dependent enhancement gives usually too high intensities at high momenta in comparison with experiment [19]. Momentum (or energy) -dependent enhancement schemes may improve the situation [29, 30]. However, the struggle toward improvements may be hindered by the fact that the results seem to be sensitive to the details of the electronic structure calculation [31].

3.2 Applications in defect identification

The comparison of computed and measured positron annihilation characteristics has been intensively used in defect identification for several decades. One of the first works was the size-determination of small voids or vacancy agglomerates in neutron-irradiated metals by comparing the measured and calculated positron lifetimes [32]. Thereafter, theoretical predictions have been benefitted especially in the identification of structures of vacancy-defects and vacancy-impurity complexes in elemental and compound semiconductors [3]. In semiconductors, there are many possible defects trapping positrons. Therefore the combination of several experimental methods, such as the positron lifetime and coincidence Doppler broadening spectroscopies, with the theoretical work is necessary. In this review, we will consider the identification of vacancy-impurity complexes in As-doped Si as an example.

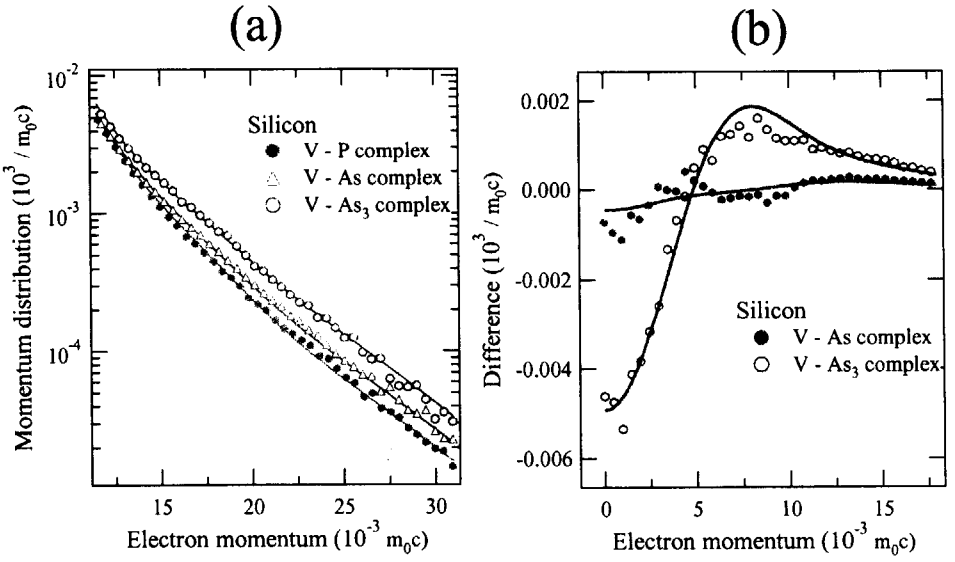


Figure 4: (a) High-momentum parts of the positron-electron momentum distributions. Measured results for positrons trapped in electron-irradiated P-doped (filled circles), electron-irradiated As-doped (triangles), and as-grown As-doped Si (open circles) samples as well as calculated distributions (solid lines) for vacancy-P, vacancy-As, and vacancy-As_3 complexes are shown. (b) Momentum differences of vacancy-As and vacancy-As_3 complexes with respect to the momentum distribution at the vacancy-P complex. The measured and calculated results are given by markers and solid lines, respectively [From Ref. [33]].

In a recent work, Saarinen *et al.* [33] used positron lifetime and CDB measurements in identifying structures of vacancy-impurity complexes in highly As-doped Si and discussed the As diffusion processes. The work shed thereby new light on the problem of the nature of compensating defects causing the saturation of the free electron densities at high doping levels. The measurements were complemented by calculations of the positron parameters. Valence electron structures were solved in the supercell approximation using the pseudopotential-plane-wave method. Free-atom core charge densities were superimposed in the pseudo-valence-electron density when calculating positron states and annihilation.

Measurements were performed for as-grown As-doped ([As] = 10^{20} cm−3) Si as well as for electron-irradiated P-doped ([P] = 10^{20} cm−3) and As-doped ([As] = 10^{20} cm−3) Si samples. According to the measurements, positrons are trapped in irradiated samples in irradiation-induced vacancy-type defects and annihilate with the lifetime of ∼250 ps which is clearly longer than that in perfect bulk, 220 ps. In the as-grown sample part of the positrons are trapped by vacancy-type defects and have also a lifetime of ∼250 ps. According to the theoretical calculations this lifetime corresponds to a single vacancy in Si and the lifetime is quite insensitive if neighboring Si atoms are substituted by impurities. There are, however, large differences in the positron-electron momentum distributions (Doppler spectra) for the trapped positrons as shown in Fig. 4. The measured distributions for electron-irradiated P-doped, electron-irradiated As-doped, and as-grown As-doped Si samples agree with the calculated distributions for positrons trapped at a single vacancy decorated with one P, one As, and three As atoms, respectively. The annihilation with As 3d-electrons raises the intensity at high momenta (Fig. 4a) rather

linearly as a function of the number of As atoms neighboring the vacancy. As shown in Fig. 4b, using the differences in momentum distributions, the agreement between theory and measurements is very good also at low momenta where the valence electron contributions dominate. Calculations assuming positron trapping at vacancies decorated with two or four neighboring As atoms do not result in agreement.

The main result of the work by Saarinen *et al.* is that complexes of a vacancy and three As atoms are formed in as-grown highly As-doped Si. These complexes are electronically inactive and account therefore for the observed saturation of the free electron density. The formation of the $V - As_3$ complexes is in agreement with the theoretical model for defect formation and diffusion by Ramamoorthy and Pantelides [34]. According to this model the formation energies for $V - As_n$, n > 2, are negative so that their formation is limited only by the diffusion of their constituent defects. At high temperatures the As diffusion starts by formation of $V - As$ -pairs. If As concentration is high enough there may be a second As-impurity as a fifth or closer neighbor of the first one and the migration of the As-V pair leads to the formation of the $V - As_2$ complex [35]. Ramamoorthy and Pantelides introduced a model according to which the diffusion of $V - As_2$ is very fast. The complex migrates through the lattice until it is captured by an other defect. With the highest probability this defect is a substitutional As impurity and a $V - As_3$ complex is formed. The scheme explains the abundance of the $V - As_3$ complexes and the missing of the $V - As_2$ complexes in samples of high As concentration. Recently, Ranki *et al.* [37] complemented the study by measuring the migration energies of the $V - As$ and $V - As_2$ pairs. They used electron irradiated As doped samples and performed thermal annealing.

4 Conclusion

Theoretical models and computational methods for positron states and annihilation characteristics in solids have reached the level of quantitative predicting power and an important status in the analysis of experimental data. Simple methods, such as the atomic superposition can give the first insight to the physical situation in question. The atomic superposition results are often even of high quantitative accuracy. This is especially true when predicting positron lifetimes and momentum densities of annihilating electron-positron pairs at high momenta. However, care has to taken in order to realize the limits of the method used. For example, the use of the self-consistent valence electron structure is necessary for the quantitative prediction of the momentum densities at low momenta. The self-consistent solution, including the determination of ion positions, may be necessary also when calculating positron states and lifetimes for defects in semiconductors. Finally, one should not forget the development of the theory of positron-electron interaction especially for a localized positron in an inhomogenous electron gas. Quantum Monte Carlo calculations would be indispensable for this purpose.

References

[1] R. Krause-Rehberg and H. S. Leipner, *Positron Annihilation in Semiconductors*, (Springer, Heidelberg, 1999).

[2] A. Dupasquier and A. P. Mills Jr. (Eds.) *Positron Spectroscopy of Solids*, (IOS Press, Amsterdam, 1995).

[3] K. Saarinen, P. Hautojärvi, and C. Corbel, in *Identification of Defects in Semiconductors*, edited by M. Stavola (Academic, New York, 1998).

[4] M. J. Puska and R. M. Nieminen, Rev. Mod. Phys, **66**, 841 (1994).

[5] M. Alatalo and M. J. Puska, Advances in Quantum Chemistry, in print.

[6] R. O. Jones and O. Gunnarsson, Rev. Mod. Phys. **61**, 689 (1989).

[7] E. Boroński and R. M. Nieminen, Phys. Rev. B **34**, 3280 (1986); R. M. Nieminen, E. Boroński, and L. J. Lantto, Phys. Rev. B **32**, 1377 (1985).

[8] D. M. Ceperley and B. J. Alder, Phys. Rev. Lett. **45**, 566 (1980).

[9] J. Perdew and A. Zunger, Phys. Rev. B **23**, 5048 (1981).

[10] L. Gilgien, *Modeling positron-electron correlations in condensed matter systems*, Thesis, University of Geneve, 1997.

[11] J. Arponen and E. Pajanne, Ann. Phys. (N.Y.) **121**, 343 (1979).

[12] L. J. Lantto, Phys. Rev. B **36**, 5160 (1987).

[13] M. J. Puska, A. P. Seitsonen, and R. M. Nieminen, Phys. Rev. B **52**, 10 947 (1995).

[14] L. Gilgien, G. Galli, F. Gygi, and R. Car, Phys. Rev. Lett. **72**, 3214 (1994).

[15] M. Saitoand A. Oshiyama, Phys. Rev. B **53**, 7810 (1996).

[16] B. Barbiellini, M.J. Puska, T. Torsti and R.M. Nieminen, Phys. Rev. B **51**, 7341 (1995); B. Barbiellini, M.J. Puska, T. Korhonen, A. Harju, T. Torsti and R.M. Nieminen, Phys. Rev. B **53**, 16 201 (1996).

[17] K. Jensen and A. B. Walker, J. Phys. F **18**, L277 (1988).

[18] A. Rubaszek, Z. Szotek, and W. Temmerman, Phys. Rev. B **58**, 11 285 (1998).

[19] M. Alatalo, B. Barbiellini, M. Hakala, H. Kauppinen, T. Korhonen, M. J. Puska, K. Saarinen, P. Hautojärvi, and R. M. Nieminen, Phys. Rev. B **54**, 2397 (1996).

[20] T. Korhonen, M. J. Puska, and R. M. Nieminen, *First-principles calculation of positron annihilation characteristics at metal vacancies*, Phys. Rev. B **54**, 15 016 (1996).

[21] M. J. Puska, and R. M. Nieminen, J. Phys. F **13**, 2695 (1983).

[22] J. Mandel and S. McCormick, J. Comput. Phys. **80**, 442 (1989); M. Heiskanen, T. Torsti, M.J. Puska, and R.M. Nieminen, Phys. Rev. B **63**, 245106 (2001).

[23] T. Torsti *et al.* unpublished.

[24] M. Hakala and M. J. Puska, unpublished.

[25] A. Rubaszek and H. Stachowiak, Phys. Status Solidi B **124**, 159 (1984).

[26] M. Saito, A. Oshiyama, and S. Tanigawa, Phys. Rev. B **44**, 10 601 (1991).

[27] M. Hakala, M. J. Puska, and R. M. Nieminen, Phys. Rev. B **57**, 7621 (1998).

[28] Z. Tang, M. Hasegawa, Y. Nagai, M. Saito, and Y. Kawazoe, Phys. Rev. B **65**, 045 108 (2002).

[29] A. Rubaszek, Z. Szotek, and W. M. Temmerman, Phys. Rev. B **61**, 10100 (2000).

[30] H. Sormann, G. Kontrym–Sznajd, and R. N. West, Mater. Sci. Forum **363–365**, 609 (2001).

[31] H. Sormann and M. Šob, Phys. Rev. B **64**, 045 102 (2001).

[32] P. Hautojärvi, J. Heiniö, M. Manninen, and R. M. Nieminen, Phil. Mag. **35**, 973 (1977).

[33] K. Saarinen, J. Nissilä H. Kauppinen, M. Hakala, M. J. Puska, P. Hautojärvi, and C. Corbel, Phys. Rev. Lett. **82**, 1883 (1999).

[34] M. Ramamoorthy and S. T. Pantelides, Phys. Rev. Lett. **76**, 4753 (1996).

[35] D. Mathiot and J. C. Pfister, Appl. Phys. Lett. 42 (1983) 1043.

[36] K. Saarinen and V. Ranki, unpublished.

[37] V. Ranki, J. Nissilä, and K. Saarinen, Phys. Rev. Lett. **88**, 105506 (2002).

JAERI－Conf 2003－001

JP0350251

1.4.3 STUDY OF RADIATION DEFECTS IN SEMICONDUCTORS BY MEANS OF POSITRON ANNIHILATION

R. Krause-Rehberg[1*], V. Bondarenko[1], F. Redmann[1], F. Börner[1], H. Feick[2†], E. Weber[2], C. Da Via[3], W. Egger[4], G. Kögel[4], P. Sperr[4], W. Triftshäuser[4]

[1]University Halle, Dept. of Physics, 06099 Halle, Germany
[2]University of California, Berkeley, California 94720, USA
[3]Brunel University, Uxbridge, United Kingdom
[4]Univ. der Bundeswehr, Werner-Heisenberg-Weg 39, 85579 Neubiberg, Germany

Abstract

In a nuclear environment, a strong degradation of important properties is observed for many materials which are otherwise very reliable. This is especially valid for silicon, the most important semiconductor. In the presented paper, two examples for the study of lattice defects in silicon by means of positron annihilation will be given. Firstly, the degradation of silicon detectors used for the particle detection in high-luminosity collider experiments starts to limit the lifetime of the whole experiment. An annealing experiment on n-irradiated Si will be presented. Beside the destructive effect of high-radiation conditions, such radiation-induced defects can have a beneficial result. This will be demonstrated for the creation of new gettering zones by high-energy self-implantation of silicon.

Keywords: Semiconductors, Radiation Defects, Neutron Irradiation, Getter Zones, Silicon, Rp/2 effect

1. Introduction

Semiconductor devices are sometimes exposed to a high radiation surrounding, e.g. in a nuclear environment or during space applications. Complex electronic systems rely in the function of each component. Thus, the study of the degradation of certain components under radiation conditions is crucial for the design of systems which can be operated in such an environment.

High-energy particles and γ-rays create Frenkel pairs or even larger showers of point defects. The interstitials are often movable already below irradiation temperature, so open-volume defects and defect complexes remain as a result of irradiation. Means of positron annihilation are especially sensitive in the characterization of such vacancy-type defects [1]. The defect-related positron lifetime is a measure of the open volume, and the intensity of the lifetime component allows the determination of the defect density. Moreover, the Doppler-broadening spectroscopy, especially the Doppler-coincidence spectroscopy provides information about the chemical environment of the detected defect. Thus, positron annihilation represent a unique tool for irradiation-induced defects.

In this paper we will present two recent examples of the application of this technique. In Chapter 2 we will show as an destructive example of radiation defects an annealing study of defects created during n-irradiation of Si. Damage by high-energy hadrons is typical for Si

*Corresponding author. Tel: +49-345-5525567 Fax: +49-345-5527160 E-Mail address: mail@PositronAnnihilation.net
† on leave from Center of Advanced European Studies and Research (CAESAR), Bonn, Germany

particle detectors in high-luminosity collider experiments, such as ATLAS [2]. Especially in the planned very high-luminosity collider experiments, like TESLA [3], the degradation of the detector might limit the lifetime of the experiment. Thus, there is strong demand for radiation-resistive detector materials.

In Chapter 3 we will present an example for the beneficial use of radiation defects (defect engineering). Si shows after high-energy self-implantation and subsequent annealing the appearance of two additional getter zones at R_p and $R_p/2$ (R_p ... projected range of implanted ion). Here, diffusing impurities such as Fe or Cu are captured, and the area for devices at the surface is protected.

2. Annealing study on n-irradiated Si

FZ silicon with original resistivity of 3 kΩcm and a carbon and oxygen content of about 10^{15} cm^{-3} was irradiated with 1 MeV neutrons to a dose of 5×10^{16} cm^{-2}. The sample was kept cold until the isochronal annealing experiment was performed. The sample was annealed in steps of 50 K for 15 min.

After irradiation and before the first annealing step, the average lifetime increased distinctly to about 278 ps at 20 K. (The reference level of defect-free Si is 218 ps). There is a distinct temperature dependence on the positron trapping (for details see Ref. [4]). At the two different measurement temperatures positron trapping is differently sensitive for different defects (Fig. 1). This becomes obvious in the course of the annealing experiment. While at low temperature almost nothing happens until 750 K annealing, at room temperature a distinct recovery step is already observed after the first annealing at 625 K. From the decomposition of the lifetime spectra (τ_2 = 290 ps at room temperature, and τ_2 = 320 ps at low temperatures) it can be concluded that at room temperature positron trapping to divacancies dominate, and at lower temperature a thermally more stable defect with a larger open volume is detected. Divacancy annealing is known to happen around 500 K [5] in agreement with our observation.

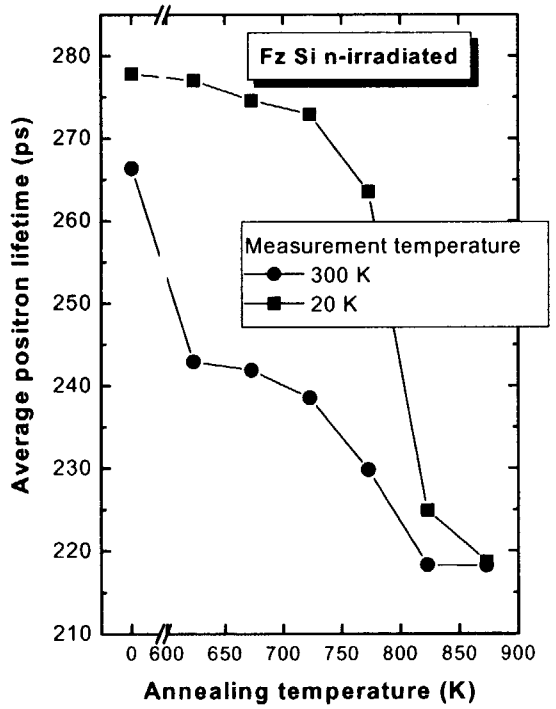


Fig. 1: Annealing experiment of n-irradiated Si (1 MeV, 5×10^{16} cm^{-2}). After annealing for 15min, the positron lifetime measurement was carried out 20 K and 300 K, respectively.

From a theoretical consideration of different small vacancy clusters in Si by Staab at al. [6] we can conclude that vacancy aggregates containing 3 or 4 vacancies are observed. They anneal around 800 K. A similar annealing stage was found in a correlated PL study using a part of the same sample. The I3/X line at about 1.03 eV also disappears in this temperature range, indicating that it might be linked to a multi-vacancy defect [4].

In an ongoing study we are now testing by combined positron and electrical measurements, whether the observed vacancy-type defects are responsible for the degradation of the electrical properties of Si particle detectors under high luminosity conditions. For this purpose isothermal annealings will be performed in order to compare the kinetics of the defect annealing observed in both techniques.

3. Study of getter zones in Si induced by high-energy self-implantation

In another experiment the so-called $R_p/2$ effect was studied. After high-energy self-implantation of Si (3.5 MeV, 10^{15} cm^{-2}) and subsequent annealing (30 s at 900°C) two gettering zones appear at R_p and at about $R_p/2$ which capture diffusing metallic impurities. These gettering zones can be seen after intentional Cu contamination of the sample in a SIMS measurement at a depths of 1.7 and 2.8 μm. The defects were identified to be interstitial-type dislocation loops at R_p and small vacancy clusters at $R_p/2$ ([7, 8, 9] and references therein). The latter result was confirmed in a slow-positron beam experiment for depth-resolution-improved defect profiling. A scan using a positron microbeam along a low-angle wedge through the defect layers of the implanted and annealed sample was applied (Fig. 2). Such an experiment was performed using the Munich Scanning Positron Microscope (positron energy 8 keV) on a beveled sample [9]. 45 positron lifetime measurements each separated by 11 μm were performed on a wedge of 0.81° angle. This gives a depth separation of 155 nm between two measurements. The accuracy of the depth profile is obvious (Fig. 3). From the defect-related lifetime τ_2 it was concluded that small vacancy clusters ($n \geq 10$) are found in the $R_p/2$ region, while defects with a smaller open volume, of the order of a divacancy, are found in the R_p zone [8].

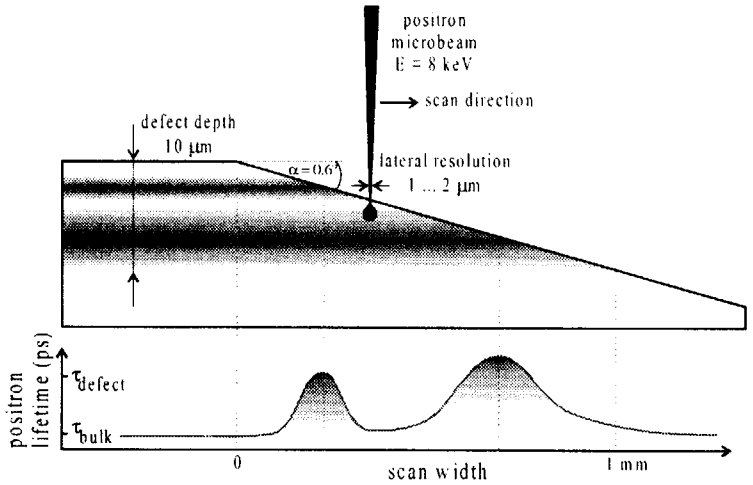


Fig. 2: Scheme of the depth profile measurement performed with the Munich Scanning Positron Microscope using a wedge-shaped sample. The defect depth profile can be obtained from the positron lifetime spectra measured when the beam scans along the wedge. At a wedge angle of 0.6°, a 10 μm deep profile corresponds to a distance of 1mm.

Although the wedge was produced by mechanical polishing, the layer of grinding defects does not affect the defect identification at a depth of about 400 nm (mean positron implantation depth). This was checked by comparing a Si sample which was polished completely (no wedge) with an untreated Si reference. The surface annihilation parameters were altered, but the positron diffusion length was found to be $L_+ = (220 \pm 15)$ nm for both samples. The same result was found for a sputtered sample after a surface removal of 250 nm. Only the surface S parameter was changed, while L_+ was similar to a reference sample [10].

4. Summary

Positron annihilation spectroscopy is a useful method for the identification and quantification of defects in materials exposed to high radiation in a nuclear environment. The method is especially sensitive for small open-volume defects such as vacancies and small vacancy clusters. Very detailed defect depth profiles can be obtained using a slow positron beam when the sample surface is removed stepwise to ensure optimum depth resolution. The removal can be done by ion sputtering or chemical etching. Another possibility is to prepare a beveled sample with a low-angle wedge through the defect-rich layer and measure a scan with a positron microbeam along the wedge. This method has the advantage that very deep defect

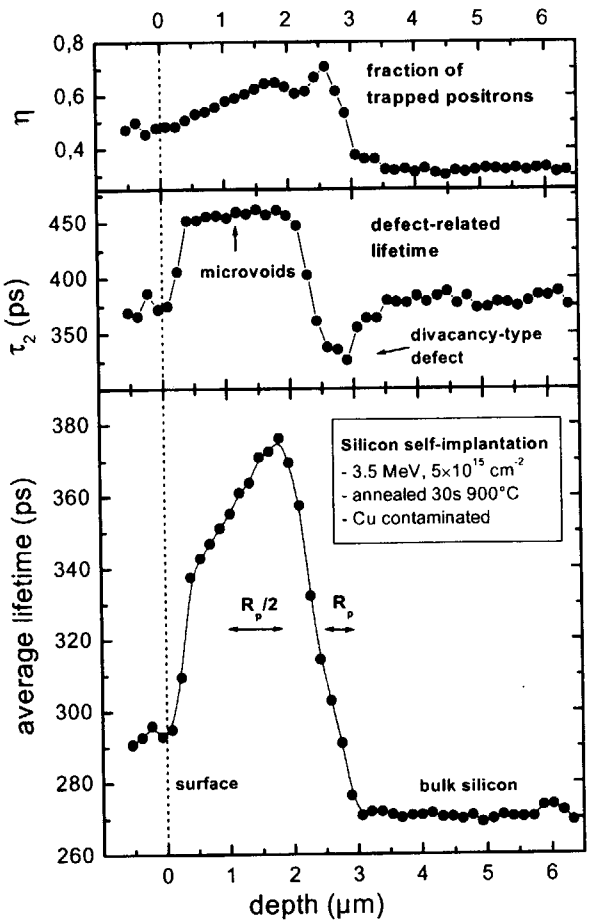


Fig. 3: Defect depth profile of a self-implanted Si sample (3.5 MeV, 5×10^{15} cm^{-2}, annealed 30s at 900°C, Cu contaminated) obtained using the Munich Scanning Positron Microscope. The sample surface was wedge-shaped polished. The profile was then taken as a line scan along the wedge with constant positron energy of 8 keV. Each positron lifetime measurement is separated by 11 μm corresponding to a depth difference of 155 nm. The depth scale was calculated with the wedge angle of 0.81°, and the mean positron implantation depth of 400 nm was added.

profiles can easily be studied with a constant depth resolution. It was shown for both methods for the case of silicon that the surface defect layer created during sputtering and during wedge polishing is small enough not to affect the detection of the defects under investigation.

Acknowledgement

Use of facilities at Lawrence Berkeley National Laboratory's Materials Science Division are gratefully acknowledged. Work at Berkeley is supported by the Department of Defense MURI program through AFOSR under contract F49620-99-1-0289 (G. Witt, program manager).

5. References

[1] R. Krause-Rehberg and H. S. Leipner, *Positron annihilation in semiconductors* (Springer-Verlag, Berlin, 1999).
[2] http://press.web.cern.ch/Atlas/Welcome.html
[3] http://tesla.desy.de
[4] V. Bondarenko, R. Krause-Rehberg, H. Feick, et al., to be published, (2002).
[5] A. Kawasuso, M. Hasegawa, M. Suezawa, et al., Appl. Surf. Sci. **85**, 280 (1995).
[6] T. E. M. Staab, M. Haugk, A. Sieck, et al., Physica B, 501 (1999).
[7] R. Krause-Rehberg, F. Börner, and F. Redmann, Appl. Phys. Lett. **77**, 3932 (2000).
[8] R. Krause-Rehberg, F. Börner, F. Redmann, et al., Physica B, to be published (2001).
[9] R. Krause-Rehberg, F. Börner, F. Redmann, et al., Appl. Surf Sci., accepted for publication.
[10] R. Krause-Rehberg and F. Börner, Talk given at PSSD-99 in Hamilton, Canada, 20.-23. August 1999 http://www.ep3.uni-halle.de/positrons/talks/PSSD99.pdf

JP0350252

4.4 CHARACTERIZATION OF NANOPARTICLE AND POROUS ULTRA LOW-K USING POSITRON BEAM

Jun Xu[a1], J. Moxom[1], R. Suzuki[2], T. Ohdaira[2], and A. P. Mills, Jr.[3]

[1]Oak Ridge National Laboratory, P. O. Box 2008, Oak Ridge, TN 37831
[2] Natl. Inst. of Advanced Industrial Science and Technology, Tsukuba, Ibaraki 305-8568, Japan
[3]Department of Physics, University of California, Riverside, CA 92521

Abstract

Nanoparticle materials are important because they exhibit unique properties due to size effects, quantum tunneling, and quantum confinement. As particle sizes are reduced to the nanometer scale, presence of vacancy clusters is expected to affect properties of nanomaterials. A combination of positron lifetime spectroscopy, which tells size of vacancy clusters, and coincidence Doppler broadening of annihilation radiation, which tell where vacancy clusters are located was used to study defect structures on nanomaterials of Au nanoparticles embedded in MgO. Vacancy clusters were found on the surfaces of Au nanoparticles.

When the packing density between multilevel interconnects in microelectronic devices increases, a low dielectric constant material is needed to minimize RC delay. Porous oxide films are some of these new low-k materials that have been actively studied by the microelectronics industry. An ideal porous material would consist of a network of closed, small pores with narrow size distribution. However, large and interconnected pores, so called "killer pores", result in high current leakage and poor mechanical strength. Clearly, characterization and understanding of pore size and interconnectivity are important to optimize the design of porous materials. Using positron beam, we have found that pore percolation in porous methyl-silsesquioxane (MSQ) films strongly depends on the molecular mass of pore generators.

Keywords: Nanoparticles, Vacancy, Positron lifetime spectroscopy, Coincidence Doppler broadening, Ultra low-k, pore interconnectivity, Porous methyl-silsesquioxane (MSQ) films.

1. Nanoparticle Materials

As sizes of embedded particles are reduced to the nanometer scale, the surface-to-bulk ratio increases significantly. Therefore, surface effects can dominate bulk properties and an understanding of nanosurfaces becomes important. In this chapter, we discuss characterization of vacancy clusters that reside on surfaces of embedded nanoparticles. Gold nanoparticles embedded in MgO are of importance because of their unique optical and electronic properties [1-3]. A long-standing goal is to produce a size-tight network of metallic nanoparticles in an oxide matrix with minimized imperfections. Ion implantation and sequential annealing are being used as a means to achieve this goal [4]. Noticeably, creation of vacancy clusters and their various combinations are often associated with the nanoparticle formation processes. Also unavoidably, these vacancy clusters are expected to interact with embedded nanoparticles and alter the properties of nano systems.

The new spectroscopic method for characterization of surface vacancy clusters is a combination of positron lifetime spectroscopy, which tells size of vacancy clusters, and coincidence Doppler broadening of annihilation radiation, which tell where vacancy clusters are located. If these clusters are located on the surface of gold nanoparticles, namely the interface

[a] Corresponding author. Email: xuj2@ornl.gov

between the particle and host matrix, the surroundings of the clusters should include both particle atoms and the matrix atoms. Doppler broadening of annihilation radiation (DBAR) with two-detector coincidence should be able to reveal these atomic constituents, and therefore elucidate the location of vacancy clusters.

1.1 Vacancy clusters

Experimental description can be found in [5, 6]. A brief description of generation of nanoparticles is as following two steps: (1) MgO (100) single crystals were implanted with 1.1 MeV gold ions at a dose of $6x10^{16}$ Au ions/cm^2. The depth profiles of the gold concentration were measured by Rutherford back-scattering spectroscopy (RBS), using 2.3 MeV α particles. This shows that the Au implants are primarily located in the range of 0.16-0.4 μm, while MgO remains crystalline after implantation. (2) The implanted MgO crystals were annealed at 1200°C in an $Ar+O_2$ (5%) or $Ar+H_2$ (5%) atmosphere for 10 hours. Cross-section tunneling electron microscopy (XTEM) of these samples shows that rectangular Au metal nanoparticles are distributed in a size range of 0.5-7 nanometer with a peak population at 1.2 nm, as shown in Fig. 1.

Figure 2 shows the positron lifetime spectra for MgO (open circles), Au-implanted MgO (crosses) and Au nanoparticles embedded in MgO (solid circles). These spectra were deconvoluted using Laplace inversion [CONTIN, 7] into the probability density functions (pdf) as a function of positron lifetime. The insert of Fig. 2 shows the pdf spectra for the MgO samples accordingly. The positron lifetime components obtained for the MgO layer are (0.22±0.04) ns with (89±3%) contribution and (0.59 ±0.07) ns with (11±3%) contribution, For Au-implanted sample without annealing, the major lifetime component increases to 0.32 ns. For Au nanoparticle-embedded MgO, lifetime components are (0.41±0.08) ns at (90%) and (1.8 ±0.3) ns at (7%).

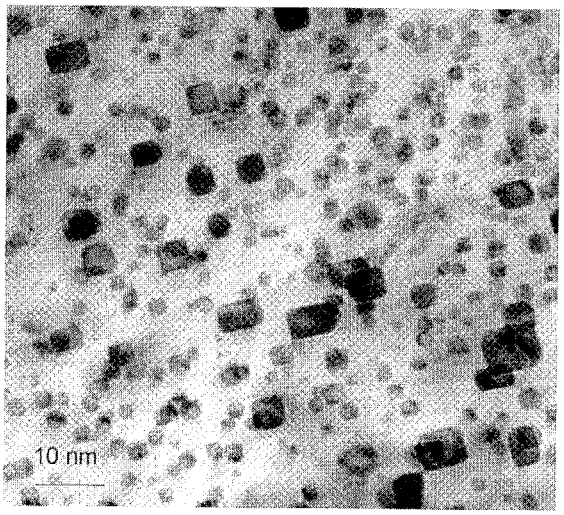


Figure 1. Cross section TEM image of Au nanoparticles embedded in MgO.

The positron lifetimes for different defects in MgO are calculated using Puska and co-workers' insulator model. In this model, the annihilation rates are determined by the positron density overlapping with the enhanced electron density that is proportional to the atomic polarizability of MgO [8, 9]. Based on comparison between experimental value and calculated value, the positron lifetime of the embedded Au nanoparticle layer, 0.41 ns, suggests that positrons is predominantly trapped in clusters consisting two Mg vacancies and two O vacancies. These specific four vacancy clusters are referred as "v_4". It is believed that the disturbance of the possible Au atoms near vacancy clusters on the electron density of the clusters is small and therefore was not considered in this calculation. The main component of the MgO layer, 0.22 ns, is due to positrons trapped at single vacancies of MgO (v_1). The vacancy cluster sizes for the longer

positron lifetimes are not calculated. They are estimated to be micro void in sub-nanometer dimension.

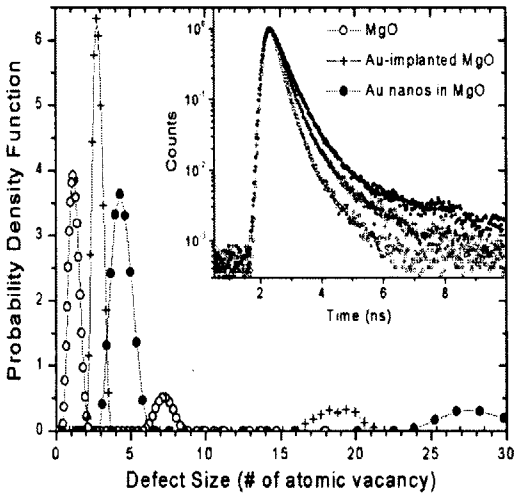


Fig. 2. Probability density functions (pdf) as a function of positron lifetime, resulting from Laplace inversion (CONTIN) of lifetime spectra (Insert) for MgO (open circles), Au-implanted MgO (crosses) and Au nanoparticles embedded in MgO (solid circles).

1.2 Coincidence Doppler Broadening

After detecting v_4 sites in the implanted MgO, the next task is to determine whether they lie in the matrix or at the nanoparticle surfaces. If these clusters are located on the surface of gold nanoparticles, namely the interface between the particle and host matrix, the surroundings of the clusters should include both particle atoms and the matrix atoms. Doppler broadening of annihilation radiation (DBAR) with two-detector coincidence should be able to reveal these atomic constituents, and therefore elucidate the location of vacancy clusters. 2D- DBAR has been measured using a system similar to that developed by Asoka-Kumar and Lynn [10]. Figure 3 (left) shows the two dimensional data, while Fig. 3 (right) shows the normalized ratio as a function of photon energy for Au nanoparticle (solid circles) and MgO layers (open circles). In the high-energy range (> 513 keV), the spectrum for Au nanoparticle layer shows two enhanced bands at 514.3 keV and 518.5 keV. These bands are dramatically different from that of the MgO layers, where normalized intensity is flat above the silicon. The difference is largely attributed to the surrounding Au atoms of the defects since the Au nanoparticle is different for the two environments. To confirm that the difference is due to the Au atoms, we measure the Doppler broadening spectrum for a pure Au film, shown as the solid line in Fig. 4(right). The Si-normalized spectrum for Au film also shows two main enhanced bands: 514.3 keV and 518.5 keV. This is consistent with the features of Au films observed in Myler and co-workers' work [11], in which Au annihilation line was also normalized by that of perfect Si. There are a high degree of similarity between the Au films structures and the Au nanoparticle layer. This supports the interpretation that the positrons, trapped at the v_4 sites (as we know it from lifetime spectra), annihilate with the electrons associated with Au nanoparticles. Of course, the defects' environment includes the MgO matrix, which also contributes to the energy deviation spectrum. It is concluded that vacancy sites where positrons are trapped are located in the Au nano surfaces.

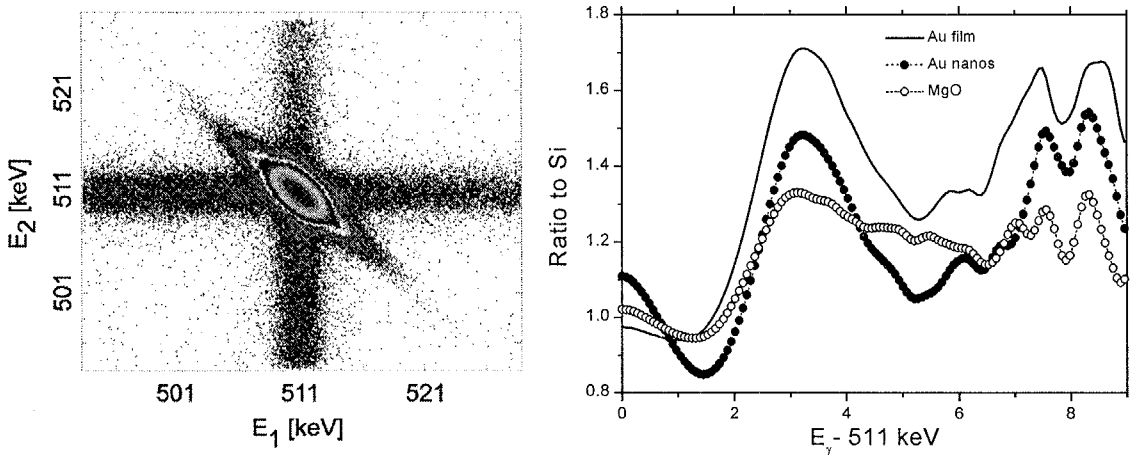


Figure 3 (left) Two-dimensional spectrum of annihilation radiation of positrons injected into a p-Si (100), with 8 Ω-cm. The diagonal feature indicates the condition of $E_1+E_2=1.022$ MeV; (right) Normalized annihilation lines as a function of photon energy for Au nanoparticle layer (solid circles), MgO layer (open circles), and Au film (solid line)

1.3 Quantum dot-anti dot coupling

Based on both positron lifetime spectroscopy, which shows v_4 clusters as positron traps, and coincidence Doppler broadening spectroscopy, which shows an Au environment of the trapped positrons, we propose the model that Au nanoparticles are partially surrounded by v_4 defects as they are embedded in the MgO. Positrons remain trapped in the clusters of four atomic vacancies which yield the v_4 lifetime. However, when the trapped positrons annihilate with surrounding Au electrons, annihilation momentum structure reflects the Au atoms, as well as the surrounding MgO.

Sub-nanometer vacancy clusters are a special group of quantum anti-dots that have a localized electronic structure. A great deal of literature has been accumulated on "anti-dot" or quantum void systems in semi-conductor or metal-oxide thin films [12]. When anti-dots are attached to the nanoparticles, as suggested by the positron analysis, electrons in the particles are transferred to a localized state of the vacancy clusters, reducing the electron density, n. The surface plasmon resonant frequency, ω_{sp}, is determined in the first order by electron density. Therefore the frequency decreases according with the decrease of the electron density in the nanoparticles.

Electronic transfer from Au nanoparticles to vacancy clusters depends on the relative positions of the highest occupied orbital (HOMO) of the metallic nanoparticles and the localized states of the vacancy clusters. Figure 4 schematically shows the density of states diagram for the interface between a metallic nanoparticle and MgO matrix in the presence of vacancy clusters. The bottom of the MgO conduction band is 1.3 eV below the vacuum level with a 7.8-eV gap to the top of valance band [13]. The partially occupied *6sp* orbital of Au metal is 4.6 eV below the vacuum level and the fully occupied band of *5d* electrons is 6.3 eV below the vacuum level [14]. If Au is present as nanoparticles, these energy levels are found by photon emission spectroscopy to depend on the size of the particle [15, 16]. For 1.2 nm Au cubic particles, the 6sp electron energy is shifted by 0.9 eV toward the vacuum level and 5d electrons shift 0.4 eV similarly, as shown in the figure. For electron transfer from the Au particles to the v_4 clusters, our data suggest that the v_4 localized-state should be 2.6 eV higher than that of an F center, an oxygen vacancy

occupied by two electrons. This suggestion is qualitatively consistent with an early finding that F_n centers produce an energy level higher than that of F centers [17]. It is clear that more measurements and theoretical calculation are needed to evaluate localized states of the vacancy clusters and Au nanoparticle energy levels as a function of particle size.

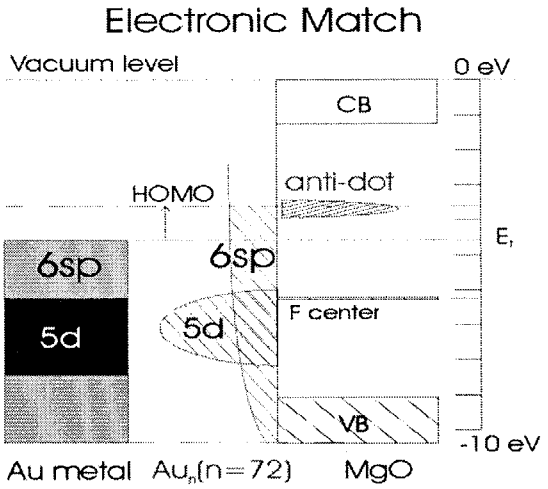


Figure 4. Schematic diagram of the energy band structure for the interface between Au nanoparticles and MgO with various defects. For comparison, energy diagram for Au metal is also shown.

2. Nanopore Materials-Ultra Low k

A typical advanced nanopore material is porous oxides or polymers that have ultra low dielectric constant ($k < 2$). Ultra low-k is significant in producing high speed electronic devices such as the interconnect structure shown in Figure 8. SiO_2, which has a dielectric constant of about 4, is currently used as dielectric material between interconnects in most microelectronic devices. When the packing density between multilevel interconnects increases, a low dielectric constant material is needed to minimize RC delay. By taking advantage of the low dielectric constant of the air (~1) and introducing pores into a dielectric material, the dielectric constant can be effectively reduced to less than 2.0. This approach has initiated a major effort in semiconductor interconnect research and development [18, 19]. Porous methyl-silsesquioxane (MSQ) films are some of these new low-k materials that have been actively studied by the microelectronics industry. For example, it has been shown that porous MSQ films can have a dielectric constant as low as k=1.5 with 50% polymer loadings and still have high breakdown voltages [20].

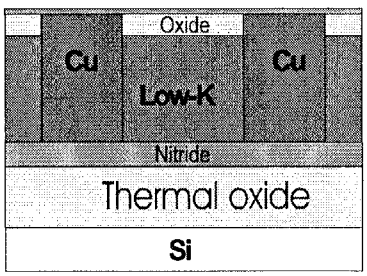


Figure 5. Schematics of a typical interconnect used in advanced electronic devices. Note that low-k material is between Cu electrodes.

An ideal porous material would consist of a network of closed, small pores with narrow size distribution. However, when the loading of pore generator is high, large and interconnected pores, so called "killer pores" may be generated, resulting in high current leakage and poor mechanical strength. Clearly, characterization and understanding of pore size and interconnectivity are important to optimize the design of porous materials. Positron annihilation spectroscopy has unique advantages for characterizing pores because ortho-positronium (o-Ps), a positron-electron pair with spin state of 1, is preferentially formed and trapped in the pores. Its subsequent

annihilation photons carry characteristics that are associated with pore structures. Recently, positron annihilation spectroscopy has been used to characterize pore structures of low-k films [21-26]. In this chapter, we discuss studies of porosity and interconnectivity of pores in porous MSQ films by measuring o-Ps 3γ emission and o-Ps lifetimes. The results clearly show that pore percolation in the films strongly depends on the characteristics of the polymers and provide a direction in developing the ideal low-k films.

Porosity in the films is introduced by mixing methyl-silsesquioxane (MSQ) with a triblock copolymer (porogen), followed by spin coating on a Si(100) substrate and subsequent thermal curing and decomposition of the porogen. Various poly(ethylene oxide-*b*-propylene oxide-*b*-ethylene oxide) (PEO-*b*-PPO-*b*-PEO) triblock copolymers were used as porogen and obtained from BASF (Pluronic® P103, P105, F38, and F88) [27]. The polymers are in the form of either paste or solid with various relative molecular masses, and ethylene oxide mass fractions, as described in Table I. The loading of the porogen was 30% by weight. The thickness of the samples was approximately 0.6 μm. The mixture was cured by heating at 120°C after spin coating. The porogen was decomposed during subsequent annealing at temperature of 500 °C, leaving pores in MSQ matrix. The dielectric constants of these films were around 2.0.

2.1 Ps Out diffusion- Interconnectivity of pores

When monoenergetic positrons inject into a porous MSQ film, they are quickly thermallyzed and distributed around a depth that is determined by the positron incident energy. Both thermal and non-thermal positrons diffuse in films, some of which form positronium being trapped in pores. If pores in the MSQ films are interconnected, an open-channel results. If the open channel ends at the surface, o-Ps can diffuse from the film into vacuum through the channel. Based on Ps diffusion in pores, the deeper the Ps is formed, the longer is its diffusion path, the greater the chance it annihilates into 2γ via collision with the wall of the channel, and the yield of 3γ annihilation events is lower. Such a decrease of 3γ yield as a function of depth constitutes a mean to measure the diffusion length and therefore to elucidate the pore interconnectivity.

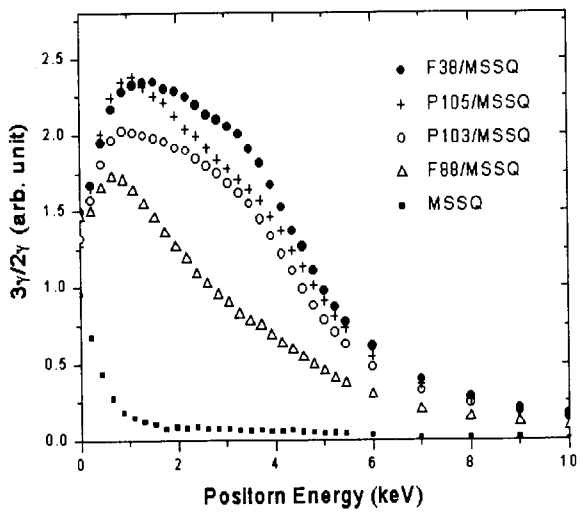


Figure 6. The profiles of relative 3γ o-Ps fraction as a function of positron beam energy, representing a mean depth from the surface, for porous MSQ films.[26]

Figure 6 shows relative 3γ o-Ps fraction as a function of positron energy, or depth from the surface. At the surface, the 3γ o-Ps fraction was approximately 1.5 for all films, which is attributed to o-Ps formation at the MSQ surface. In the porous layers, represented by positron energy below

~4.5 keV, large fractions profiles were found dependent on molecular weight of porogen generally. At higher incident energies, the o-Ps emission yield was also zero because the positrons were implanted deeper into the Si substrate, where there were no pores. Two main features are displayed in all profiles: the first is the increase of o-Ps fraction as the depth increases in the near surface region. This feature is believed due to the profile of o-Ps formed initially. Originally, the near surface positrons may re-emit into the vacuum and so their resulting o-Ps is low there. The second feature is the decrease of o-Ps fraction as a function of depth. This fits into the Ps out diffusion model. The depth-profiles of these 3γ o-Ps fractions depend on the type of porogens initially used for pore generation.

These 3γ o-Ps fraction profiles were analyzed in similar to the models used for Ps diffusion in ice [28], and for Ps diffusion in low-k films [24]. In the previous models, the intial positron deposion profile is an exponential function with respect to the depth. Athough an analog expression of the out diffusion probability can be given by the exponential, the deposition profile is hardly believed to be exponential. In the analysis, a Makhovian distribution was used to represent the intial positron deposition profile.

The diffusion lengths of o-Ps, listed in Table I, depend on molecular weights of porogens. For F88/MSQ film, the diffusion length is 330 nm, the shortest among the group, suggesting a low degree of interconnectivity of pores. For other films, diffusion lengths are long, (750-1330 nm), longer than the film thicknesses, suggesting a high interconnectivity of pores for these films. It is noted that the parameters obtained by the fitting may vary with the models used. However, their relative variation with respect to molecular weight of porogens is still valid.

2.2 Positronium lifetime spectroscopy

o-Ps trapped in pores can annihilate mainly versus collisions with pore wall and then o-Ps lifetime reveals the collision frequency and elucidate pore size. If o-Ps escape into the vacuum via interconnected open pores, the lifetime is the characteristic o-Ps vacuum lifetime, 142 ns. Therefore the intensity of the 142-ns component povides the degree of interconnectivity.

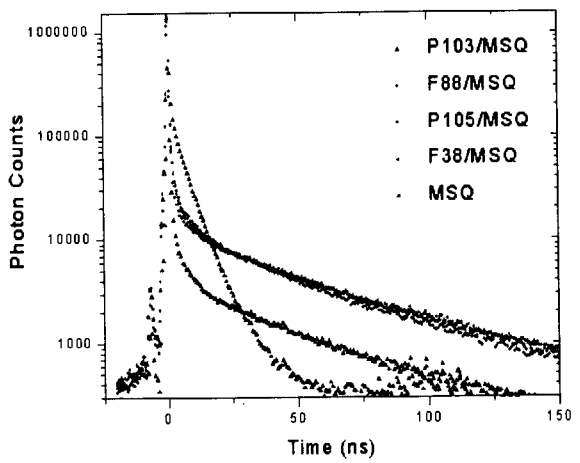


Figure 7. Positron annihilation lifetime spectra for porous MSQ films generated by mixing MSQ film with different triblock copolymers: P103, F88, P105, and F38. A spectrum for non-porous MSQ is listed for comparison.[26]

The porous MSQ films were evaluated using positronium lifetime spectroscopy. Figure 7 shows positron lifetime spectra for the porous MSQ films with positron energy of 3.3 keV. This energy corresponds to a mean depth of approximately 340 nm, which is roughly the center of the films. Fitting of the lifetime spectra shows that the pore component of the lifetime spectra varies with type of porogen, as shown in Table I. In addition, a long-lived component with lifetime nearly equal to the vacuum o-Ps lifetime, 142 ns, was observed for porogen F88 with a fraction about 4%.

The true fraction of this component is believed to be larger than the measured value because the gamma-ray collimator may block the photons emitted from the vacuum o-Ps. For comparison, Figure 3 also shows a positron lifetime spectrum of MSQ film without pores generated. The main positron component is 4.7 ns, attributed to native free volumes of the non-porous MSQ film.

For subnanometer free volumes, the Tao model [29] is conventionally used to relate positron lifetimes to free volume sizes. For nanometer pores as studied here, Gidley's model [21, 22] was used to relate the positron lifetimes to pore sizes. The 47 ns lifetime for the F88 copolymer-generated porous film yields a pore size of 3.7 nm in diameter, if the pores are assumed to be a closed sphere, while the 54 ns lifetime for the P103 copolymer-generated film corresponds to size of 4.3 nm diameter pores. It is pointed out that more future work is needed to relate positronium lifetimes and pore sizes, especially for uncapped films since positronium lifetimes of those samples include both contributions from closed pores and open pores.

porogen	molecular mass	PEO mass fraction	L_{Ps}(nm)	τ (ns) Uncapped	
F88	11400	80%	330	47	
P105	6500	50%	750	54	
P103	4950	30%	1200	54	
F38	4700	80%	1330	53	

Table I. Molecular mass, PEO mass fraction, o-Ps diffusion length (L_{Ps}), pore lifetime (uncapped), and pore lifetime (capped) for porous MSQ films templated with various porogens.

1.3 Dependence on molecular weight of porogen

For the porous MSQ film templated by F88 triblock copolymer porogen, which has the largest molecular mass in the samples studied, the positronium diffusion length was found to be the shortest and the pore size is the smallest. This result suggests that the pores in porous MSQ films generated with this larger molecular-mass polymer are smaller and more closed. For P103 porogen, which has a low ethylene oxide fraction and light molecular mass, positron diffusion length was long and o-Ps lifetime was long. This indicates that pores are large and interconnected.

Since it is difficult to avoid pore interconnection at a high loading of pore generators, understanding of the relationship between polymers and pore structures are important to control the pore generation. PEO-*b*-PPO-*b*-PEO triblock copolymers are random coils in the solution of MSQ precursors and form a closed core-shell structure during curing at 120°C. [20] The PPO block resides next to the hydrophobic MSQ surface as a shell to minimize interfacial energy, while the hydrophilic PEO block is buried inside as a core. After subsequent heating at 500°C, the polymers are decomposed, leaving pores behind in the matrix. The rapid formation of core-shell structure depends on the chain mobility of PPO and PEO blocks, which in turn determines the pore size and its percolation. Shorter polymer chains, such as F38, are more mobile and therefore likely to form larger core-shell domains and to be percolated. The larger pore size and longer o-Ps diffusion length for the F38/MSQ film compared to those of the F88/MSQ film are consistent to the assumption. Solid state NMR shows that PEO blocks is predominantly crystallized in the bulk block copolymers and less mobile than the PPO block [20, 30]. Polymers with higher PEO wt% are more restricted to form a larger core-shell domains, thus each domain is more isolated, similar to the effect of higher molecular weight. The larger interconnectivity in the P103/MSQ films seems to be related to both the smaller molecular weight and the smaller PEO wt%.

Acknowledgement Authors thank A. Ueda and D. Henderson of Fisk University for their contributions of the MgO samples. This research was sponsored by the Division of Chemical Sciences, Geosciences, and Biosciences, Office of Basic Energy Sciences, U.S. Department of Energy, under Contract DE-AC05-00OR22725 with Oak Ridge National Laboratory, managed and operated by UT-Battelle, LLC.

References

1. Budai, J. D., White, C. W., Withrow, S. P., Chisholm, M. F., Zhu, J., and Zuhr, R. A., *Nature, **390**, 384 (1997).*
2. Chan, W. C. W. and Nie, S., *Science, **281**, 2016 (1998).*
3. Chen, S., Ingram, R. S., Hostetler, M. J., Pietron, J. J., Murray, R. W., Schaff, T. G., Khoury, J. T., Avarez, M. M., Whetten, R. L., *Science, **280**, 2098 (1998).*
4. White, C. W. et al., *Mat. Science Reports, **4**, 43 (1989).*
5. Xu, J, Mills, A. P., Jr., Ueda, A., Henderson, D., Suzuki, R., and Ishibashi, S., *Phys. Rev. Lett., **83**, 4586(1999)*
6. Xu, J, Moxom, J., Somieski, B., White, C. W., Mills, A. P., Jr, Suzuki, R., Ishibashi, S., *Phys. Rev. B, Vol 64, 113404 (2001).*
7. Gregory, R. B., *Nucl. Instru, Meth., **A302**, 496 (1991).*
8. Puska, M. J., Makinen, S, Manninen, M., and Nieminen, R. M., *Phys. Rev. B **39**, 7666 (1989).*
9. Puska, M. J, in *Positron annihilation*, edited by Dorikens-Vanpraet, L., Dorikens, M., and Degers, D. (World Scientific, New Jersey, 1988), P101.
10. Asoka-Kumar, P., Alatalo, M., Ghosh, V. J., Kruseman, A. C., Nielsen, B., and Lynn, K. G., *Phys. Rev. Lett. 77, 2097 (1996).*
11. Myler, U., Goldberg, R. D., Knights, A. P., lawther, D. W., and Simpson, P. J., *Appl. Phys. Lett. **69**, 333(1996).*
12. Maasilta, I. J. & Goldman, V. J., *Phys. Rev. Lett. **84**, 1776, (2000)*; and references thereafter.
13. Fukumi, K., Chayahara, A., Kadono, K., Sakaguchi, T., and Hirono, Y., *J. Appl. Phys. 75, 3075 (1994).*
14. Tjeng, L. H., Vos, A. R., Sawatzky, G. A., *Surf. Sci. **235**, 269 (1990).*
15. DeHeer, W., *Rev. Mod. Phys. **65**, 611 (1993).*
16. Taylor, Cheshnovsky, Smalley, *J. Chem. Phys. 96, 3319 (1992).*
17. Evans, B. D., Comas, J., and Malmberg, P. R., *Phys. Rev. B, **6**, 2453 (1972).*
18. *Semiconductor Res. Corp., International Technology Roadmap for Semiconductors 1999*
19. Miller, R. D., *Science 286, (1999) 421.*
20. Yang, S., Mirau, P. A., Pai, Chien-Shing, Nalamasu, O., Reichmanis, E., Lin, E. K., Lee, Hae-Jeong, Gidley, David W., § and Sun, J., *Chem. Mater. **13**, (2001) in press.*
21. Gidley, D.W., Frieze, W.E., Dull, T.L., Yee, A.F., Ryan, E.T., Ho, H.-M., *Phys. Rev. B **60,** (1999) R5157.*
22. Gidley, D.W., Frieze, W.E., Dull, T.L., Sun, J., Yee, A.F, Nguyen, C.V., Yoon, D.Y., *Appl. Phys. Lett. **76,** (2000) 1282.*
23. Petkov, M.P., Weber, M.H., Lynn, K.G., Rodbell, K.P., submitted to *Appl. Phys. Lett. (2000).*
24. Rodbell, K.P., Petkov, M.P., Weber, M.H., Lynn, K.G., Volksen, W., and Miller, R. D., *Materials Science Forum Vols. 363-365, (2001) 15.*
25. Suzuki, R., Ohdaira, T., Shioya, Y., Ishimaru, T., *Jpn. J. Appl. Phys., Vol. 40, (2001) L414.*
26. Xu, Jun and Moxom, Jeremy, Yang, Shu, Suzuki, R., and Ohdaira, T., *Applied Surf. Sci., In press, (2002).*
27. *http://www.basf.com/static/OpenMarket/Xcelerate/Preview_cid-982931200019_pubid-974236729499_c-Article.html.*
28. Eldrup, M., Vehanen, A., Shultz, P.J., Lynn, K.G., *Phys. Rev. B **32,** (1985) 7048.*
29, Tao, S. J., *J. Chem. Phys. 56, (1972) 5499-5510.*
30. Mirau, P. A., Yang, S., *Chem. Mater. 14, in press, (2002).*

JP0350253

1.4.5 TIME-DOMAIN VIBRATIONAL STUDY ON DEFECTS IN ION-IRRADIATED CRYSTAL

M. Kitajima

Materials Engineering Laboratory, National Institute for Materials Science (NIMS),
1-2-1 Sengen, Tsukuba 305-0047, Japan

Abstract

We have studied the effects of point defects on coherent phonons in ion-implanted bismuth and graphite. Ultrafast dynamics of coherent phonons and photo-generated carriers in the femtosecond time-domain have been investigated by means of pump-probe reflectivity measurements. Point defects are introduced by irradiating graphite with 5 keV He^+ ions. For Bi the dephasing rate of the A_{1g} phonon increases linearly with increasing ion dose, which is explained by the additional dephasing process of the coherent phonon originated from scattering of phonons by the defects. For graphite, introduction of the defects enhances the carrier relaxation by opening a decay channel via vacancy-states, which competes efficiently with carrier-phonon scattering. The coherent acoustic phonon relaxation is also accelerated due to an additional scattering by defects. The linear fluence-dependence of the decay rate is understood as scattering of propagating acoustic phonon by single vacancies.

Keywords: femtosecond, coherent phonon, defect, semimetal, reflectivity

1. Introduction

Ion implantation into the crystal is of great interest because it is a key process of manipulating material properties. Until now, lattice disorder in solids induced by ion implantation has been extensively studied by using Raman spectroscopy.[1,2] The phonon correlation length of GaAs (100) during 5 keV He^+ irradiation was estimated from Raman line shape of the longitudinal optical phonon.[2] Such *in situ* measurements allow us to observe phonon localization in the presence of point defects at the initial stage of low energy ion irradiation.

Recent advances of ultrashort light pulses enable us to generate and observe coherent lattice vibrations in the time domain. There have been presented several observations of coherent phonons in bismuth and other semimetals.[3-6] In these experiments the coherent A_{1g} mode has been observed in the femtosecond time scale, and the displacive excitation of

*corresponding author. Tel: +81-298-59-2836 Fax: +81-298-59-2801.
E-mail address:kitajima.masahiro@nims.go.jp

coherent phonons (DECP mechanism) has been proposed for the generation of the coherent phonon.[3,7] In this mechanism, photo-excited carriers create a nonequilibrium electron distribution, and as a result, crystal lattice begins to oscillate around the new equilibrium position. The phonon dephasing rate can be generally described as a sum of the anharmonic decay rate and the pure dephasing rate.[8] The main channel of the relaxation of the coherent A_{1g} phonon in bismuth is the dephasing process originating from the phonon-phonon interaction caused by anharmonicity of the lattice potential.[6]

Lattice defects in semiconductors have been investigated in low temperature grown GaAs. Dekorsy *et al.* compared the dynamics of electric field, transport, and coherent phonons in as-grown and annealed low-temperature (LT) GaAs by an electro-optic technique, and suggested that the differences in the decay time of the coherent LO phonon and the photo-excited carrier were related to the different microscopic forms of excess arsenic and point defect density.[9] Scholz et al. have reported results of femtosecond pump-probe optical absorption experiments for coherent phonons on *F* centers in KBr .[10] These reports indicate that the femtosecond pump-probe technique is useful to study the effect of defects on ultrafast dynamics of phonons. There are a few reports on coherent A_{1g} phonons in the polycrystalline Bi film[11] and in the ion-implanted Bi polycrystalline film.[12] However the origin of the dephasing for the coherent phonon due to defects is not yet clear, and systematic measurements on coherent phonon dynamics in ion-implanted materials are required to understand the dephasing process.

Graphite is a model two-dimensional system in solid-state physics and has many industrial applications. Carrier dynamics of graphite was studied by pump-probe reflectivity measurements in 1990, in which the photoexcited carriers were observed to be equilibrated with the lattice and recombine within 1 ps.[13] The same technique has been widely applied to investigate the lattice dynamics of semiconductors and semimetals.[14] The lattice vibration of graphite, however, was not observed directly in the time domain until the recent work by Mishina and co-workers,[15] because it requires detection of a reflectivity change as small as $\Delta R/R_0 \sim 10^{-7}$. Although they revealed the generation and detection mechanism of the coherent acoustic phonon of graphite, they have left the relaxation dynamics of the coherent phonon undiscussed.

In this paper, the effect of ion implantation on dephasing of the coherent phonon is examined for bismuth and graphite by using a femtosecond pump-probe technique. The relaxation time of the coherent optical phonon in Bi films and graphite is precisely measured for various ion doses. The obtained decay rate for the coherent A_{1g} mode increases linearly with the dose. Our experimental results directly show that the phonon-defect scattering process plays an important role on the dephasing of the coherent phonon in addition to the anharmonic decay process in ion-implanted bismuth.

2. Experimental

The bismuth films studied in this work were prepared by vapor deposition on polished Si(001) substrates at room temperature. They were about 5000 Å thick, and x-ray-diffraction measurements showed that they were polycrystalline. The graphite used as samples were highly oriented pylolytic graphite (HOPG). In order to examine the effect of point defects, 500 keV Bi^+ ions were implanted into the polycrystalline films, and 5 keV He^+ ions into HOPG at various doses, respectively. The damage depth for bismuth deduced from the Monte Carlo calculation (TRIM) was about 2000 Å,[16] and the damage profile was almost a Gaussian function with a peak at 710 Å from the surface. The maximum value of DPA (displacement per atom) calculated using TRIM was 0.03 for the dose of $2x10^{15}Bi^+/cm^2$. The femtosecond pump-probe measurements were performed at room temperature. The light source used was a mode-locked Ti:sapphire laser with a central wavelength of 800 nm and pulse width of 70 fs. A standard reflection-type pump-probe configuration was employed.[11] Pump and probe beams were polarized orthogonal to each other to avoid scattered pump beam, and were focused to a diameter of about 100 μm on the samples. The penetration depth of the laser beams was about 1300 Å, and covered well the irradiation damage area in which point defects exist. The reflectivity change $\Delta R/R$ was measured as a function of the delay time by scanning the optical path length of the probe beam.

3. Results and Discussion

Figure 1 shows the transient reflectivity change obtained for bismuth films implanted with doses from $1x10^{14}Bi^+/cm^2$ to $2x10^{15}Bi^+/cm^2$. Coherent oscillations of the fully symmetric A_{1g} mode (the frequency is 97.3 cm^{-1} = 2.92 THz at 295 K[12]) are observed on the non-oscillatory background component that corresponds to the reflectivity change due to electronic excitation and relaxation. The time-domain wave form of the background component is obtained by subtracting a oscillatory component from the transient reflectivity change and is indicated with the dashed lines in Fig.1. The rise time of the background component decreases from 200 fs to 60 fs and the decay time also decreases from 3.7 ps to 2.2 ps with increasing ion dose. The effect of ion implantation on photo-excited carriers is caused by carrier-defect (vacancy) scattering that would originate from deformation potential perturbation by local strain around the defects.[17] In Fig.1 the initial amplitude of the coherent phonon oscillation at a dose of $2x10^{15}Bi^+/cm^2$ is smaller than those at smaller doses by a factor of 0.8. This decrease in the amplitude is simply explained by using a vibrational time correlation function in which the amplitude of the coherent oscillation depends on the inverse of the decay rate, i.e., the decay time, of the coherent phonon.[18]

In order to estimate the dephasing time τ of the coherent A_{1g} mode for various doses, the time derivatives of the reflectivity change are derived from time domain data in Fig.1. The dephasing time τ and the frequency of the A_{1g} mode are obtained by fitting the time-domain

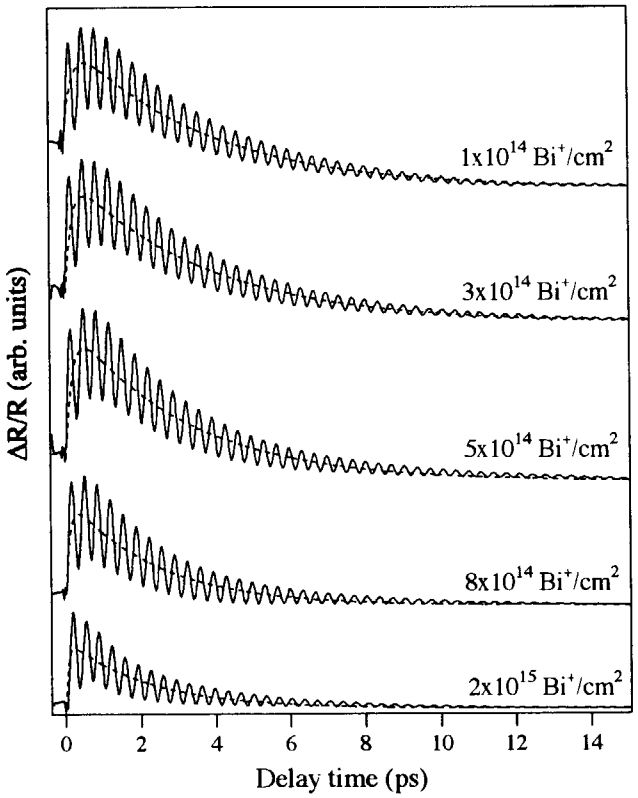


Fig. 1. Time-resolved isotropic reflectivity change for the bismuth films at various ion doses.

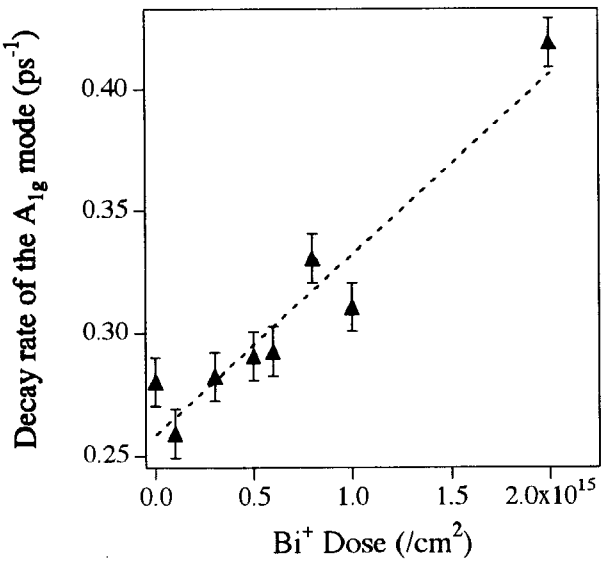


Fig. 2. The decay rate of the coherent A_{1g} phonon as a function of Bi ion dose. The dashed line is a fitting to the data using Eq. (1) with τ_o = 3.86 ps.

data to a damped harmonic oscillation with a single exponential decay. The dephasing time decreases from 3.86 ps to 2.39 ps as the dose increases, being clearly seen with the guide envelopes of a single exponential decay. The decrease in the dephasing time can be qualitatively explained by the scattering of phonons by defects in ion-implanted bismuth. The frequency of the A_{1g} mode is 97.4 cm^{-1} (the time period is 342 fs) at a dose of $1x10^{14}Bi^{+}/cm^{2}$. A small frequency shift toward the high frequency side by 0.4 cm^{-1} was observed with increasing dose from $1x10^{14}Bi^{+}/cm^{2}$ to $2x10^{15}Bi^{+}/cm^{2}$. A possible explanation for the frequency shift is compressive strain due to the formation of defects.[17] Figure 2 shows the decay rate of the coherent A_{1g} mode obtained from the inverse of the dephasing time τ. The decay rate increases linearly with increasing ion doses from $1x10^{14}Bi^{+}/cm^{2}$ to $2x10^{15}Bi^{+}/cm^{2}$. The dephasing process of the coherent optical phonons in solids have been considered to be anharmonic decay due to phonon-phonon interaction in the *k*-space.[19] This decay process depends mainly on the lattice temperature. In the present study the dose-dependence of the decay rate (Fig.2) suggests clearly the existence of additional dephasing process, i.e. phonon-defect scattering. This scattering process is thought to be a pure dephasing process due to an elastic scattering of coherent phonons introduced by perturbing potential by defects.[17] In this case the combined scattering rate $1/\tau$ can be expressed as,

$$\frac{1}{\tau_{total}} = \frac{1}{\tau_0} + \frac{1}{\tau_{defect}}, \qquad (1)$$

where τ_0 is the anharmonic decay time, τ_{defect} is the phonon-defect scattering time constant that depends on the density of point defects introduced by the ion implantation. The second term in Eq. (1) is directly related to the linear dependence of the decay rate with ion dose in Fig.3 and is expressed as a function of ion dose through the number density of point defects, N;

$$\frac{1}{\tau_{defect}} = N\gamma(\omega_{A1g}), \qquad (2)$$

where γ is the frequency-dependent phonon-defect scattering rate. A similar expression for the defect-induced phonon scattering has been proposed in the investigation on the thermal conductivity of diamond.[20] Based on the assumption that the anharmonic decay process is not affected by the existence of defects, the experimental data in Fig.3 can be fitted with Eq.(1) and we obtained τ_0 = 3.86 ps as a constant. This value agrees roughly with that obtained for the as-grown Bi films (3.57 ps) in our measurements. Our experimental results indicate that the coherent phonon is scattered by point defects to lose its coherence.

Figure 3(a) shows the normalized anisotropic reflectivity change $(\Delta R_x-\Delta R_y)/R_0$ for unirradiated HOPG. The oscillation of the reflectivity has a frequency of 1.31 THz (42 cm^{-1}), as shown in the Fourier transform in the inset of Fig. 3(a), and corresponds to the coherent interlayer shearing (E_{2g1}) mode of graphite.[21] The decay time of the coherent E_{2g1} phonon was T_{E2g1}=11.6±0.9 ps for unirradiated graphite, which is in an agreement with the previous work. Upon ion irradiation, the amplitude of the coherent E_{2g1} phonon was decreased as shown in Fig. 3(b). The frequency of the coherent phonon was almost constant, except it showed a slight red-shift for very low fluences. The decay time, together with the decay rate $\Gamma_{E2g1}=1/T_{E2g1}$, was plotted as a function of ion fluence in Fig. 4. The decay time was decreased as the ion fluence increased above 4x10^{13} He^+/cm^2, while it was independent of ion fluence below 4x10^{13} He^+/cm^2. It is noted that the formation of vacancies was confirmed by means of

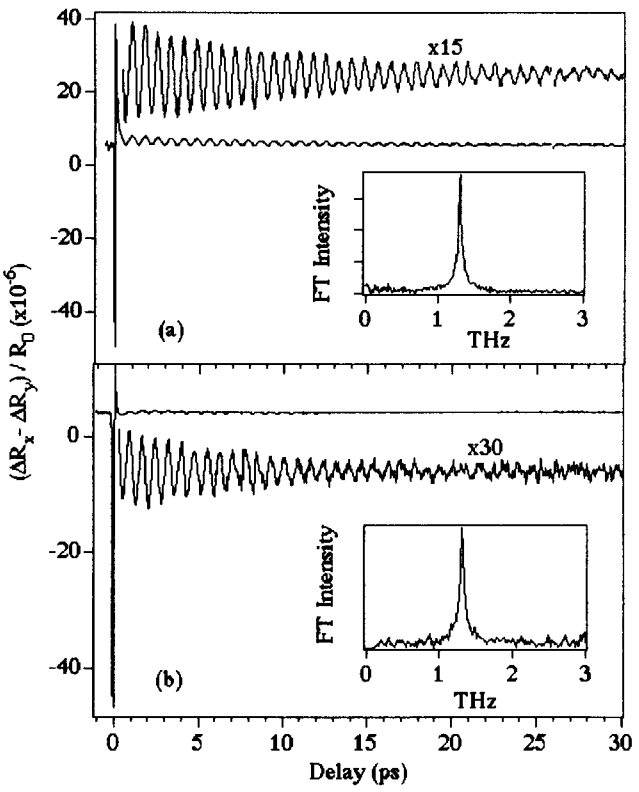


Fig. 3 Time-resolved anisotropic reflectivity change for unirradiated graphite (a) and graphite irradiated with 8x10^{13} He^+/cm^2 (b).

Raman scattering spectroscopy even below $4x10^{13}$ He^+/cm^2.

The relaxation of coherent phonons is generally determined by scattering by incoherent phonons (thermal lattice vibration), impurities, and defects. The contribution of phonon-phonon scattering is expected to be small for the coherent E_{2g1} phonon in graphite, since the decay time was not significantly dependent on temperature.[15] Ion irradiation gives rise to additional damping due to phonon-vacancy scattering, Γ_v, that depends on ion fluence ϕ

$$\Gamma_{E2g1} = \Gamma_0 + \Gamma_v(\phi). \qquad (3)$$

The fluence dependence of graphite is explained by a simple model of scattering of propagating acoustic phonon by a single vacancy in analogy to capture of carriers by defects in low-temperature grown GaAs.[22] According to the model, the scattering rate of phonons by vacancies is given by

$$\Gamma_v(\phi) = N_v(\phi)\sigma_v v_{TA}, \qquad (4)$$

where σ_v is the cross section of a single vacancy given by $\sigma_v = \pi (a/2)^2$ with the interatomic distance a, and v_{TA} the group velocity of the E_{2g1} phonon in the long wavelength limit.[23] Raman measurements on the ion-irradiated HOPG samples confirmed that the number density of vacancies per unit volume N_V is given by

$$N_v(\phi) = N\sigma_d \nu_d \phi, \qquad (5)$$

with N the number density of C atoms in graphite, σ_d the displacement cross section, and ν_d the damage function.[24] This simple model reproduced the observed fluence dependence very well except for the low fluences below $4x10^{13}$ He^+/cm^2, as shown in Fig. 4. The deviation may be related to the slight redshift of the phonon frequency ω_{E2g1} observed for the same fluence range. Indeed, resonant (frequency-dependent) phonon scattering was observed for many single crystals containing defects and impurities.[20] However, the resonant scattering by defects leads only to an *increase* of the scattering rate at a resonant frequency, which is not the case in the present study. We interpret the deviation of Γ_{E2g1} from the linear fluence dependence in the low fluence range as follows. In ion-irradiated graphite, the relaxation of hot carriers via vacancy-states competes with carrier-phonon scattering. This would reduce the generation of incoherent (optical and acoustic) phonons and therefore scattering of the coherent E_{2g1} phonon by incoherent acoustic phonons. A similar, but much more remarkable initial decrease, followed by an increase, was observed also in the

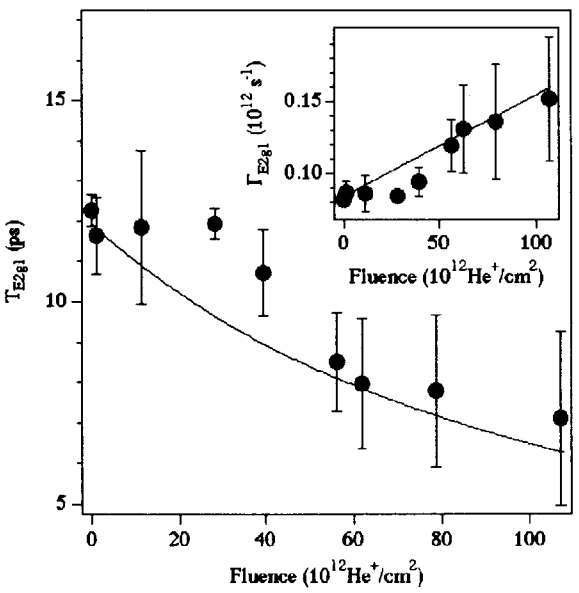


Fig. 4. The decay time T_{E2g1} and the decay rate Γ_{E2g1} of the coherent E_{2g1} phonon as a function of He ion fluence. The solid line and curve represent a model calculation after Eqs. (3)– (5).

decay rate for coherent optical phonon of ion-irradiated GaAs.[25]

Raman studies on ion-implanted crystals generally allow us to observe the asymmetric broadening of Raman peaks of phonons due to the relaxation of the wave-vector selection rule.[26] In our time-domain experiment, the band width of the Fourier transformed (FT) spectra for the A_{1g} mode is slightly broader even for the highly ion-implanted Bi film than that for the as-grown film. Moreover, the intensity of Raman peak of the A_{1g} phonon mode for the ion-implanted Bi films are very weak, and difference in the band widths in the frequency domain is not clear. Coherent phonon measurement in time-domain is thus of great advantage to study directly the dephasing of phonons.

4. Conclusion

The effect of point defects on the lattice vibration dynamics in ion-implanted bismuth was studied by using a femtosecond pump-probe reflectivity technique. The coherent oscillation of the A_{1g} phonon was observed in bismuth polycrystalline films implanted with Bi^+ ions at various doses. The decay rate of the A_{1g} phonon increased linearly with increasing dose, showing the existence of the additional dephasing process of the coherent phonon originated from scattering of phonons by the defects in ion-implanted Bi. We have also demonstrated that the dynamics of carriers and coherent acoustic phonon in graphite are very sensitive to vacancies created by ion irradiation. The obtained understanding should open a door to the control of ultrafast device properties by utilizing defects. For disordered materials such as ion-implanted solids, the time-domain measurement of the coherent phonon is a powerful tool to determine the dephasing rate of phonons precisely.

Acknowledgments

The author is grateful to K. Ishioka, S. Hishita, and M. Hase of NIMS, and K. Ushida of RIKEN for experiments and many discussions. This work was supported by the Nuclear Cross-over Research of MEXT, Japan.

References

[1] K. Ishioka, K. G. Nakamura, and M. Kitajima, Phys. Rev. B **52**, 2539 (1995).

[2] K. Ishioka, K. G. Nakamura, and M. Kitajima, Surface Science **357-358**, 495 (1996).

[3] H. J. Zeiger, J. Vidal, T. K. Cheng, E. P. Ippen, G. Dresselhaus, and M. S. Dresselhaus, Phys. Rev. B **45**, 768 (1992).

[4] Y. Liu, A. Frenkel, G. A. Garrett, J. F. Whitaker, S. Fahy, C. Uher, and R. Merlin, Phys. Rev. Lett. **75**, 334 (1995).

[5] M. Hase, K. Mizoguchi, H. Harima, S. Nakashima, M. Tani, K. Sakai, and M. Hangyo, Appl. Phys. Lett. **69**, 2474 (1996).

[6] M. Hase, K. Mizoguchi, H. Harima, S. Nakashima, and K. Sakai, Phys. Rev. B **58**, 5448

(1998).
[7] T. K. Cheng, J. Vidal, H. J. Zeiger, G. Dresselhaus, M. S. Dresselhaus, and E. P. Ippen, Appl. Phys. Lett. **59**, 1923 (1991).
[8] A. Laubereau and W. Kaiser, Rev. Mod. Phys. **50**, 607 (1978).
[9] T. Dekorsy, H. Kurz, X. Q. Zhou, and K. Ploog, Appl. Phys. Lett. **63**, 2899 (1993).
[10] R. Scholz, M. Schreiber, F. Bassani, M. Nisoli, S. D. Silvestri, and O. Svelto, Phys. Rev. B **56**, 1179 (1997).
[11] T. K. Cheng, S. D. Bronson, A. S. Kazeroonian, J. S. Moodera, G. Dresselhaus, M. S. Dresselhaus, and E. P. Ippen, Appl. Phys. Lett. **57**, 1004 (1990).
[12] K. Ishioka, K. Ushida, K. G. Nakamura, S. Hishita, and M. Kitajima, Jpn. J. Appl. Phys. **38**, L446 (1999).
[13] K. Seibert, G.C. Cho, W. Kütt, H. Kurz, D.H. Reitze, J.I. Dadap, H. Ahn, M.C. Downer, and A. M. Malvezzi, Phys. Rev. B **42**, 2842 (1990).
[14] T. Dekorsy, G.C. Cho, and H. Kurz, in *Light Scattering in Solids VIII*, edited by M. Cardona and G. Güntherodt (Springer, Berlin, 2000), p. 169.
[15] T. Mishina, K. Nitta, and Y. Masumoto, Phys. Rev. B **62**, 2908 (2000).
[16] J. F. Ziegler, J. P. Biersack, and U. Littmark, in The Stopping and Range of Ions in Solids (Pergamon, New York, 1985).
[17] W. A. Harrison, in Solid State Theory, International Series in Pure and Applied Physics, edited by L. I. Schiff (McGraw-Hill, 1970).
[18] M. Hase, K. Ishioka, M. Kitajima, and K. Ushida, Appl. Phys. Lett. **76**, 1258 (2000).
[19] F. Vallee, Phys. Rev. B **49**, 2460 (1994).
[20] D.T. Morelli, T.M. Hartnett, and C.J. Robinson, Appl. Phys. Lett. **59**, 2112 (1991).
[21] K. Ishioka, M. Hase, M. Kitajima, and K. Ushida, Appl. Phys. Lett. **78**, 3965 (2001).
[22] S. Gupta, J.F. Whitaker, and G.A. Mourou, IEEE J. Quantum Electronics **28**, 2464 (1992).
[23] M.J. Matthews, M.A. Pimenta, G. Dresselhaus, M.S. Dresselhaus, and M. Endo, Phys. Rev. B **59**, R6585 (1999).
[24] K. Nakamura and M. Kitajima, Phys. Rev. B **45**, 78 (1992).
[25] M. Hase, K. Ishioka, K. Ushida, and M. Kitajima, Proc. of the 25th Int. Conf. Phys. Semicond., Springer Proceedings in Physics **87**, 186 (2000).
[26] M. Kitajima, in Critical Reviews in Solid state and Material Sciences **22**, 275 (1997).

1.5 Fabrication and New Materials

Chair: V. Balek

(Nuclear Research Institute,

Czech Republic)

T. Mitsuhashi

(National Institute for Materials

Science, Japan)

This is a blank page.

JP0350254

1.5.1 SURFACE MODIFICATION OF CERAMIC MATERIALS INDUCED BY IRRADIATION OF HIGH POWER PULSED ICP

Takamasa Ishigaki*, Nobuhiro Okada, Naoki Ohashi and Hajime Haneda
National Institute for Materials Science
Advanced Materials Laboratory
Namiki 1-1, Tsukuba, Ibaraki 305-0044, Japan

Abstract

Newly developed pulse-modulated high-power inductively coupled plasma [ICP] is expected to offer the unique physico-chemical condition, such as the increased concentration of chemically reactive species, as well as the appropriate heat flux for materials processing. Two kinds of oxide materials, titanium and zinc oxide, were placed at the downstream of Ar-H_2 ICP and irradiated in the plasma of continuous [CN] and pulse-modulated [PM] modes. The CN-ICP irradiation at the position close to the plasma tail gave rise to the thermal reduction of oxides. In the PM-ICP irradiation, the degree of thermal reduction depended on the lower power level during pulse-off time, as well as the total electric power. Irradiation in PM-ICP led to the increased formation of oxygen vacancies in titanium dioxide. In the case of zinc oxide, the UV emission efficiency was improved by PM-ICP irradiation, while the green emission became predominant by CN-ICP irradiation at the appropriate position. Induced effects in the two oxides by PM-ICP would be related to the high concentration of hydrogen radicals in the plasma.

Keywords: thermal plasma, inductively coupled plasma, pulse modulation, non-equilibrium condition, surface modification, titanium dioxide, zinc oxide, green luminescence, UV luminescence.

1. Non-Equilibrium condition in pulse-modulated high power ICP

Pulse-modulated RF inductively coupled plasma[PM-ICP], in which non-equilibrium situation is expected to be induced at the instance of pulse-on and off, is an appropriate tool for advanced materials processing. Ishigaki et al. succeeded in PM-ICP generation, for the first time, at an adequate frequency, 1 MHz, to sustain a plasma with considerably large volume, and at a sufficiently high electric power of 17 kW, for materials processing[1]. An important feature was that the total energy of plasma can be decreased, while the maximum temperature, around 12,000K, remained unchanged in the pulse-on time, which was almost the same as that of continuous generation[2]. Also, it has been suggested by optical emission spectroscopy that PM-ICP could produce intentionally a non equilibrium state of particle temperatures and flux density of radical species[3,4]. Such conditions in PM-ICP plasma are expected to offer an unique physico-chemical condition for materials processing. Also, it was predicted that the pulse modulation gives the higher cooling rate at the plasma tail[5].

Figure 1 shows the optical emission from Ar(751 nm) and H_α lines detected at the middle and 10 mm below the bottom of RF coil of the induction plasma torch used. After the time instance of pulse-on, the emission at the middle of RF coil shows the overshoot with a

Corresponding author. Tel: +81-298-51-4005 Fax: +81-298-51-4005
E-mail address: ISHIGAKI.Takamasa@nims.go.jp

maximum, and this became larger for the low shimmer level. The overshoot of emission comes from the non-equilibrated situation induced by the rapid heating of plasma. It should be noted that hydrogen emission shows the overshoot even at the downstream, while the emission from Ar atoms shows no overshoot. When the plasma flow leaves from the high-temperature coil region, the temperature drops very rapidly to deviate from the equilibrium concentration of chemical species. In the pulsed-plasma, the quenching effect is enhanced by the induced condition following switching-on and off. The overshoot of hydrogen emission at the downstream is higher than that at the middle of coil, which should be the evidence of overpopulated concentration of chemically reactive hydrogen radicals.

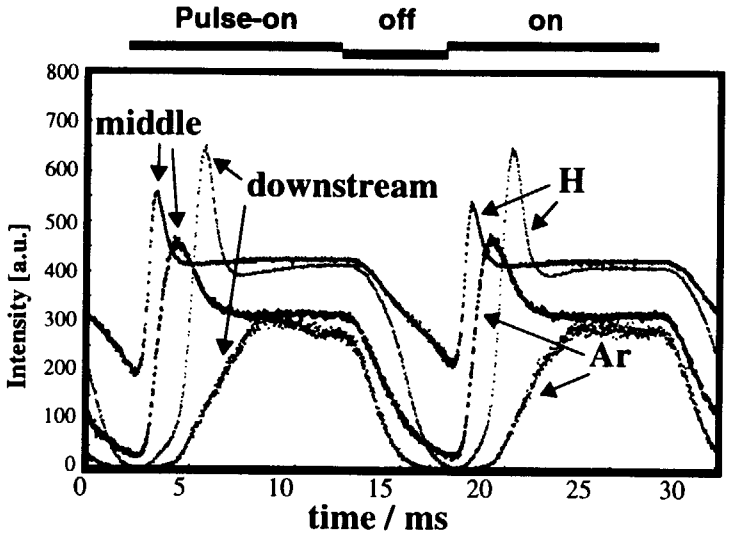


Fig. 1 Temporal change of emission of Ar(751 nm) and H_α at the middle and downstream of RF coil.

2. Irradiation of pulse-modulated ICP on ceramic materials

The interaction between plasma and materials was examined, as the information is essential to the advanced materials processing by PM-ICP. Disc compacts of titanium and zinc oxides placed at the downstream of plasma were treated in Ar-H_2 plasma of continuous[CN] and pulse-modulated[PM] generation modes.

Schematic of PM plasma generation has been shown elsewhere[1]. The inverter-type solid state power source supplies the electric power of 22 kW continuously with nominal frequency of 1 MHz. The RF power was modulated by imposing the external pulse signal from a pulse generator to switch a static induction transistor(SIT). As shown in Fig. 2, the mixture of Ar and H_2 was injected with swirl at the flow rate of 98 and 6 l/min, respectively. The torch design is the same as that used in our previous study for continuous

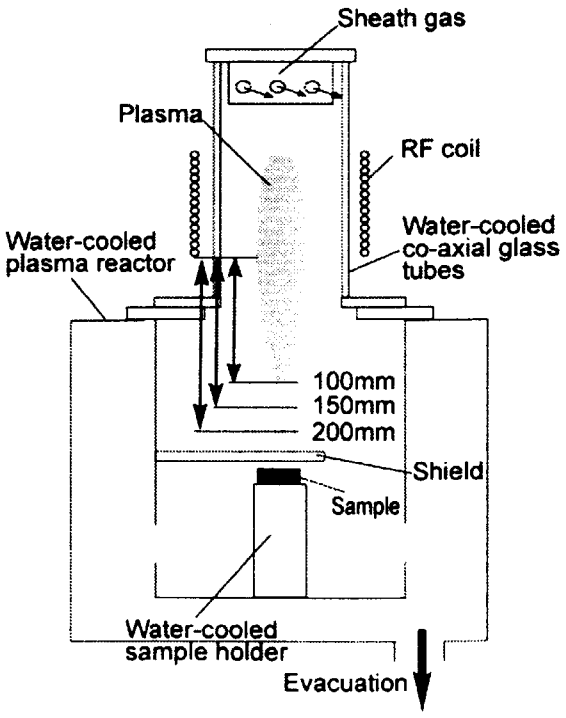


Fig. 2 Schematic of plasma torch and reactor.

steady operation[6]. Operation conditions are as follows. The plasma was firstly generated at the continuous power level of 13 kW and the reactor pressure was controlled at 26.6-99.8 kPa. Then, the external pulsing signal was imposed to switch to the pulse-modulated mode with pulse-on and -off times of 10 and 5 ms, respectively. The shimmer current level, which is the current ratio of the lower level of pulse-off time to the higher one of pulse-on time, is 0.53-0.58. Disk specimens, which were formed from TiO_2 and ZnO powders by isostatical pressing, were put on the water-cooled molybdenum holder and irradiated for 5 minutes in Ar-H_2 plasma of CN and PM generation modes.

Figure 3 shows the temporal change of RF current for pulse-modulated Ar-H_2 plasma generated at various pressures. Shimmer current ratio was set to be 58%, 56%, and 53%, for the reactor pressure of 99.8, 53.2, 26.6 kPa, respectively. The measured ratio of integrated RF power of pulse-modulated mode to that of continuous mode were 86%, 85%, 84% for 99.8, 53.2, 26.6 kPa, respectively.

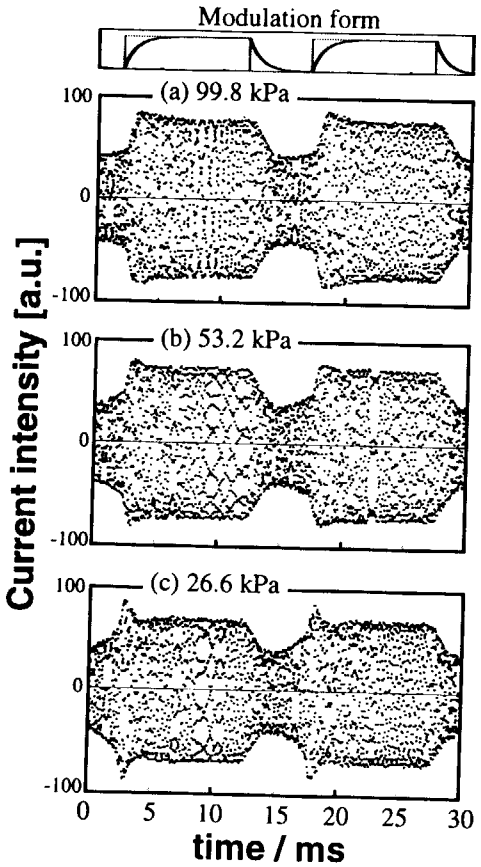


Fig. 3 Temporal change of RF current for Ar-H_2 plasma generated at various pressures: pulse-on time, 10 ms; pulse-off time, 5 ms.

The length of plasma flame changes depending on the plasma generating pressure, while the generation mode, continuous or pulse-modulated mode, did not give the difference of the apparent flame length. The decrease of reactor pressure gave the increase of flame length. The plasma flame generated at 26.6 kPa reached to the specimen placed at the position of 100 mm below RF coil, while the flame tail under the other conditions was above the specimens.

2.1 Surface Modification of Titanium Dioxide

Titanium dioxide is known to show photocatalytic activity, which is applicable to the air and water purification, the deodorizatipon, and the antibacterial and self-cleaning coating.

Recently, the visible-light-responsive photocatalyst has been reported by the plasma treatment of anatase-type titanium dioxide powder in an inductive-type RF hydrogen discharge at the pressure of 130 Pa, although the photocatalytic activity was limited in the ultraviolet region. The extension of photocatalytic activity region to the visible light was explained by a new energy state due to the formation of oxygen vacancies. It is also pointed out that oxygen vacancies may play a crucible role of the other distinguished property of titanium dioxide, the hydrophilic surface, which is antifogging and self-cleaning. To the contrary, the substitution of oxygen by hydroxyl group, i.e., the incorporation of hydrogen, leads to hydrofobic surface.

The plasma in the present work has induced the thermal reduction of titanium oxide. When the relatively heavy reduction occurs, the colour of specimen changed to black[7]. The coloration depended on the lower current level in PM mode as well as the sample position. As mentioned in the preceding paragraph, the useful surface should be the slightly reduced one, that is, the colour should be kept white or beige. Quite low concentration of induced oxygen vacancies was characterized by thermal desorption spectroscopy, in which the hydrogen desorption is able to be detected with high sensitivity. The increase of desorption in the temperature range from 200 to 500°C for as-irradiated specimens is shown in Fig. 4, which attributes to the hydroxyl groups chemisorbed on surface and/or diffused into the near surface. It is shown that the PM plasma irradiation gave rise to the formation of higher concentration of oxygen vacancies than the CN plasma irradiation. The difference would be related to the increased concentration of hydrogen radicals in the PM plasma, as the hydrogen radicals take out easily oxygen atoms to form oxygen vacancies.

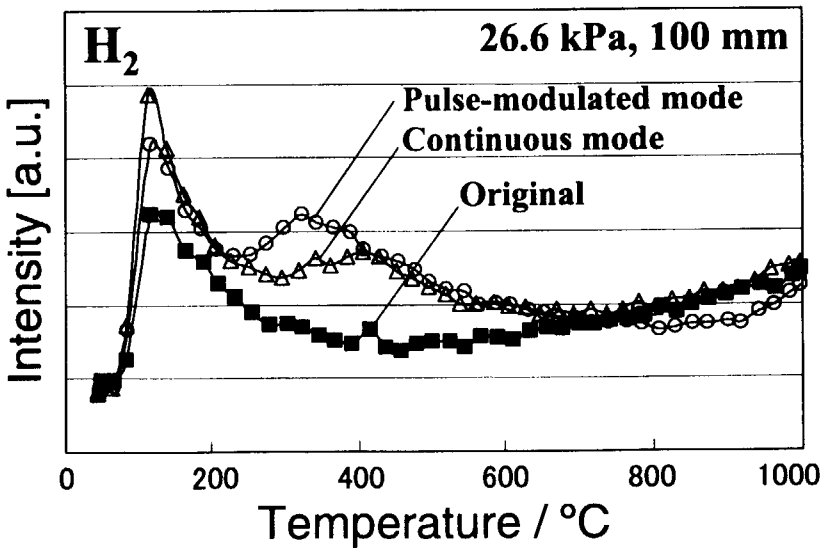


Fig. 4 Hydrogen desorption from original and plasma-treated titanium dioxide.

2.2 Improvement of UV and Green Emission of Zinc Oxide

Zinc oxide(ZnO) is known to be a high efficiency phosphor compound under low energy beam irradiation, which has been used for vacuum florescent devices and field emission displays. Recently, intensive efforts have been made to realize the UV emitting devices. It has been reported that the microwave hydrogen plasma irradiation enhances the UV emission, while the green emission is suppressed[8]. It was suggested that the dissolution of hydrogen should take a role of the improvement.

The influence of PM plasma irradiation was compared with the CN plasma irradiation on the cathodoluminescence(CL). As is the same in titanium oxide, the CN plasma irradiation

gave rise to the change of colour on the specimens placed at the highest position. The effects of CN and PM plasma irradiation were considerably different on the emission spectra[9]. As is clearly seen in Fig. 5, the ZnO powder giving green emission with high efficiency was obtained by the CN plasma treatment. On the other hand, efficiency of UV luminescence was significantly improved and the visible emission was suppressed by the PM plasma treatment. The difference of CL spectra is explained by the variation of heat flux in CN and PM plasma irradiation. It was reported that the green emission attributed to the donor state of oxygen vacancies[10]. The oxygen vacancies are compensated by the hydrogen incorporation to give the pure UV emission[11]. Oxygen vacancies are formed through the thermal treatment at the relatively high temperature, whereas the hydrogen incorporation can be attained through the moderate heating. Therefore, the difference in luminescence with the plasma generation mode again shows the advantage of pulse-modulated plasma for controlling heat flux and increasing chemically reactive radical species.

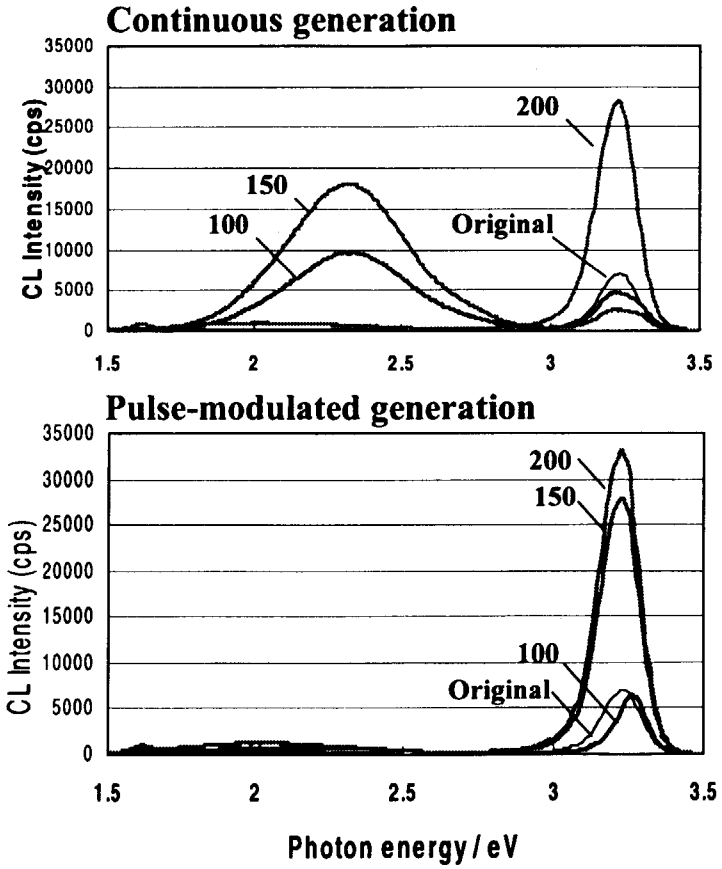


Fig. 5 Cathodoluminescence spectra of original and plasma-treated ZnO.

3. Summary

The effects of pulse modulation[PM] on the characteristic of ICP have been demonstrated in the plasma irradiation processing of two oxides, titanium and zinc oxides. The PM-ICP plasma, which distinctly showed non-equilibrium chemical aspect of thermal plasma, is expected to give further extension of thermal plasma materials processing.

References

[1] T. Ishigaki, X. Fan, T. Sakuta, T. Banjo and Y. Shibuya, Appl. Phys. Lett., **71**, 3787(1997).
[2] T. Sakuta, K.C. Paul, M. Katsuki and T. Ishigaki, J. Appl. Phys., **85**, 1372(1999).
[3] T. Sakuta and T. Ishigaki, Pure Appl. Chem., **71**, 1845(1999).
[4] T. Ishigaki and T. Sakuta, J. Intel. Mater. Syst. Str., **10**, 565(1999).
[5] M.M. Hossain, K.C. Paul, Y. Tanaka, T. Sakuta and T. Ishigaki, J. Phys. D, **22**, 1843 (2000).
[6] T. Ishigaki, Y. Moriyoshi, T. Watanabe and A. Kanzawa, J. Mater. Res.., **11**, 2811(1996).
[7] T. Ishigaki, N. Okada, H. Haneda and S. Ito, Thin Solid Films, **390**, 20(2001).
[8] T. Sekiguchi, N. Ohashi and Y. Terada, Jpn. J. Appl. Phys., **36**, L289(1997).
[9] T. Ishigaki, N. Okada, N. Ohashi, H. Haneda and T. Sakuta, Pure Appl. Chem., **74**, 435 (2002).
[10] K. Vanheusden, W.L. Warren, C.H. Seager, D.R. Tailant, J.A. Voigt and B.E. Grande, J. Appl. Phys., **79**, 7983(1996).
[11] N. Ohashi, T. Ishigaki, N. Okada, I. Sakaguchi, T. Sekiguchi and H. Haneda, Appl. Phys. Lett., **80**(4), (2002), in press.

JP0350255

1.5.2 EMANATION THERMAL ANALYSIS FOR CHARACTERIZATION OF SURFACE AND NEAR SURFACE LAYERS OF ADVANCED MATERIALS.

V. Balek[1*], T. Mitsuhashi[2], J.Šubrt[3]
[1]Nuclear Research Institute, CZ-250 68 Řež, Czech Republic
[2]National Institute for Materials Science, 1-1 Namiki, Tsukuba 305-0044, Ibaraki, Japan
[3]Institute of Inorganic Chemistry ASCR ,CZ- 250 68 Řež, Czech Republic

Abstract

A non traditional method, called emanation thermal analysis (ETA),was used the for characterization of surface and near surface layers of SiC based materials .This method consists in the measurement of the release of inert gas(radon) from the samples previously labeled to the depth of several tens of nanometers with the inert gas atoms. The ETA results brought about information about microstructure changes and transport properties of SiC/SiC_f composites on heating in the range 30-1300°C in argon and air, respectively. The annealing of structure irregularities which served as diffusion paths for radon was evaluated. The temperature range of the formation and crystallization of the silica layer resulting after oxidation of the SiC/SiC_f sample on heating in air was determined from the ETA results .

Keywords: emanation thermal analysis, radon, SiC/SiC_f , annealing,structure irregularities, near surface layers

1. Introduction

The behavior of advanced materials in nuclear environment has been investigated by various methods, including XRD, SEM, thermal conductivity measurements, etc. We have used to this aim the emanation thermal analysis (ETA)[1] based on the measurements of the release of inert gases (e.g. ^{220}Rn) from samples previously labeled with trace amounts of the inert gas . The ETA has been already advantageously used in the characterization of microstructure changes of the advanced materials under *in situ* conditions of their treatment in various environments. Various materials for nuclear technology, fusion technology, as well other advanced materials after ion beam treatments were investigated by means of ETA[1-3].In this study the ETA was used for the characterization of surface and near surface layers of SiC/SiC_f composite during heating in argon and air ,respectively .

2.Background of ETA applications

The ETA consists in the measurement of radon release rate from samples previously labelled by trace amounts of ^{228}Th and ^{224}Ra radionuclides [2,3]. Atoms of radon, ^{220}Rn, have been formed by the spontaneous α-decay of ^{228}Th and ^{224}Ra and incorporated into the near surface layers of the sample due to the recoil energy (85 keV $atom^{-1}$).

The mechanisms of radon release from labeled samples are (i) release due to the recoil energy of the radon atoms, (ii) diffusion in open pores, intergranular space or interface boundaries, respectively and (iii) radon diffusion in the matrix of the solids. The total measured radon release rate, E (also called emanating rate ,E), can be expressed as

*Corresponding author:bal@nri.cz

$$E(T) = E_R + E_D(T).S(T) \qquad (1)$$

where E_R is the radon release rate due to recoil , E_D is the radon release rate due to diffusion along structure irregularities, serving as radon diffusion paths, and S(T) is the function which describe the temperature dependence of changes in the number of radon diffusion paths.
It was supposed that the maximal penetration depths of ^{220}Rn recoiled atoms into SiC based samples was 83.6 nm (as determined by TRIM code[4]).Therefore, the high amount of ^{220}Rn situated next to the surface ensured the high sensitivity of ETA to changes of near surface microstructure. In the mathematical model used for the evaluation of ETA results it was supposed that the temperature dependence of the radon release rate, $E_D(T)$, due to diffusion involves parameters which determine the radon diffusion, taking into account the average diffusion length of radon $L_D=(D/\lambda)^{1/2}$,where D is the radon diffusion coefficient and λ is the radon decay constant. In the evaluation of the ETA results it was supposed that radon can migrate along several independent paths, such as micropores, intergranular space, as well as interface boundaries .Therefore, the mechanism of radon diffusion along two independent paths of the disordered heterogeneous solid was considered in the modeling.

In the case that the number of radon diffusion paths and/or surface area decreases on heating, the structural function S(T) has descending character, whereas if the number of radon diffusion paths increases during the sample heating, the structural function S(T) has increasing character. Several expressions for S(T) functions were recently proposed [5] for the description of changes of the structure defects amount in solids. The descending character of the S(T) function can be expressed by Eq.2

$$S(T) = 0.5\left[1 + \mathrm{erf}\frac{1-\frac{T_m}{T}}{\frac{\Delta T\sqrt{2}}{T}}\right] \qquad (2)$$

where erf is the sign for the integral Gauss function, T_m is the temperature of the maximal rate of the annealing of the defects which serve as radon diffusion paths, ΔT is the temperature interval of the respective solid state process. Eq.2 was used in this study to describe the temperature dependence of the annealing of near surface structure irregularities which have served as radon diffusion paths in SiC based materials.

3.Experimental

3.1.Materials

SiC_f/SiC composite was prepared by chemical vapor infiltration (CVI) from Nicalon CG fibers (Nippon Carbon Co.). Nicalon fibers were produced from polycarbosilane precursor and contained 11.8 wt % of oxygen and excess of C with respect to Si . The typical formula of the CG Nicalon is $SiC_{1.31}O_{0.36}$[6].It consists of relatively poor crystalline β-SiC and contains aggregates of uniformly dispersed nano-particles of SiC,SiO_2 and C[7] .This insured the densely bonded structure. The SiC/SiC_fcomposite manufactured by CVI has excellent resistance to heat and oxidation and maintains strength even up to 1200°C in air. Because of small thermal expansion coefficient the Nicalon based materials have excellent dimensional stability. It has been applied in the field of advanced technologies and space development .It is also a candidate material for fusion technology because of its radiation stability and low activation in the neutron flux.

3.2.Labeling of the samples for ETA measurements

Atoms of ^{220}Rn were incorporated by the recoil energy (85keV $atom^{-1}$) of spontaneous α–decay of the parent radionuclides ^{228}Th and ^{224}Ra ,respectively . The ^{228}Th radionuclide (half-life 1.9 years) absorbed on the sample from acetone solution represents a the quasi -permanent source of ^{220}Rn atoms (half-life 55 sec) . The specific activity of the sample was 10^5 Bq per gram.

3.3. ETA measurements

The labeled sample (size 3x3x2mm) was situated in a furnace (see Fig. 3 in Ref. [3]) and heated in the temperature range 30-1300 °C at the rate of 6 °C/min in the flow of argon or oxygen, respectively. The constant flow of the gas(flow rate 50ml/min) took the radon released from the sample into the measuring chamber of radon radioactivity. The resulting ETA curve is presented as a temperature dependence of the radon release rate E (in relative units); $E = A_\alpha / A_{total}$, where A_α is α-radioactivity of radon released in unit time from the labeled sample, and A_{total} is the total γ -radioactivity of the labeled sample. The A_{total} value is proportional to the rate of radon formation in the sample. Semiconductor and NaI(Tl) detectors were used for the α–and γ-radioactivity measurements, respectively .

4. Results

Thermal stability of Si-C-O Fibers (Nicalon CG) has been investigated by several authors [6-12]. Active and passive oxidation mechanisms were proposed for SiC fibres heat treated in oxidizing gas environments with different oxygen partial pressure. The active oxidation mechanism was proposed [8] for the formation of silica layer on the SiC surface heated in the gaseous environment with relatively high oxygen partial pressure (2.5×10^3-10^5 Pa).Silica is one of the few oxides which have extremely low oxygen permeability up to high temperatures. Consequently, the silica formed on the SiC surface serves as the barrier against further oxidation of the SiC core.

However, there has been a lack of information about the thermal behavior of the SiC based materials when heated in oxygen containing gas medium in the temperature range below 1200°C.Therefore, the ETA was used in this study to characterize microstructure changes of SiC_f/SiC composites during heating in the range 30-1300°C.Radon atoms,^{220}Rn, formed by spontaneous α-decay of ^{224}Ra,were used as the microstructure probe. Moreover, the microstructure of the SiC_f/SiC composite samples was characterized before and after the heat treatments by means of SEM

Fig. 1 depicts the experimental ETA results of SiC_f/SiC composite sample on heating in argon and air,respectively.We assumed that the radon release in the range 30-200°C was controlled by the "single jump" diffusion mechanism along near surface structure irregularities. The decrease of the radon release rate, E, observed in the range 250-700°C indicated the annealing near surface structure irregularities(Fig. 1).The ETA results were evaluated by using the mathematical model proposed recently[5]. Temperature dependencies of the S(T) functions, obtained by modeling ,which characterize the annealing of near surface structure irregularities, were used for the assessment of the thermal behavior of the samples in the temperature range 250–700°C. Fig.2 presents the respective S(T) temperature dependencies of the SiC_f/SiC sample corresponding to the heating in argon and air, respectively.

Moreover, differences in the thermal behavior of SiC_f/SiC composite in air and argon, respectively, were revealed by ETA on heating up to 1300°C. We assumed that the ETA effect in the range 700-1000°C, observed on sample heating in air (Fig.1,curve2) indicated the formation of amorphous silica and its subsequent crystallization to cristoballite. This assumption is in agreement with the statement of other authors [8,12] that amorphous silica is formed at the beginning of the SiC oxidation and at low temperatures, and tends to crystallize at longer times,

at higher temperatures. We supposed that the enhanced radon release rate observed on sample heating at elevated temperatures was controlled by bulk diffusion mechanism.
In order to examine in detail the effects observed in Fig.1,curve 2 at the elevated temperatures ,the model curves characterizing the S(T) function and the radon diffusion in bulk,respectively [5] were substracted from the experimental ETA curve. The curve resulting after this computer treatment is presented in Fig. 3 together with the experimental ETA curve. From Fig.3 we assumed that the formation of cristobalite from amorphous silica layer was achieved at the temperature of 750°C(1023 K).

5. Conclusions and recommendations

The ETA made it possible to obtain additional information about thermal behavior of SiC/SiC composite materials. Microstructure changes taking place in surface and near surface layers of the samples were characterized by means of ETA under *in situ* conditions of the heat treatment in argon and air, respectively. Effects of radiation, corrosion, as well as ion bombardment on the microstructure development of advanced materials can be advantageously characterized by means of ETA.

Acknowledgments

This work was sponsored in parts by the Ministry of Education, Culture, Sports, Science and Technology of Japan (Nuclear cross-over project), EFDA/ EURATOM Program (Research Task TTMA-001) and the Ministry of Education of the Czech Republic (Project LN00A028 for the financial support of SEM equipment).The authors highly appreciate the experimental assistance of Mgr. E. Klosová and Dr. I.M. Bountseva in ETA measurements and evaluation.

REFERENCES

[1] V. Balek, J.Toelgyessy, Emanation Thermal Analysis and other Radiometric Emanation Methods, in G.Svehla (Ed.) Wilson and Wilson's Comprehensive Analytical Chemistry, Part XII.C, Elsevier Sci. Publ. (1984) p.43-71
[2] V. Balek,J.Subrt, T.Mitsuhashi, I.N.Beckman, K.Gyoryova, J. Therm. Anal.Cal.**67**,15(2002)
[3] V. Balek, Thermochim. Acta **192**, 1 (1991)
[4] I.N.Beckman,V.Balek, J.Them. Anal. Cal. **67**,49(2002)
[5] J. F. Ziegler, J. P. Biersack, The stopping and range of ions in solids, Pergamon Press, New York, 1985
[6]T.Mah, N.L.Hecht,D.E.Mc Cullum, J.R.Hoenigman, H.M.Kim, A.P.Katz ,H.A.Lipsitt, J.Mat. Sci. **19**,1191(1984)
[7] Y.T.Zhu,S.T.Taylor,M.G.Stout, D.P.Butt andT.C.LoweJ.Am.Ceram.Soc. **81**, 655(1998)
[8] T.Shimoo,Y.Morisada,K.Okamura,J.Amer.Ceram.Soc. **83**,3049(2000)
[9] M.Takeda,A.Urano,J.Sakamoto and Y.Imai, J.Amer.Ceram.Soc. **83**,1171(2000)
[10] J.A.Costello and R.E.Tressler, J.Amer.Ceram.Soc. **69** ,674(1986)
[11] J.A.Heuer, L.U.Ogbuji and T.E.Mitchel,J.Amer.Ceram.Soc. **63**,354 (1980)
[12] K.L.Luthra, J.Amer.Ceram.Soc.**74** ,1095(1991)

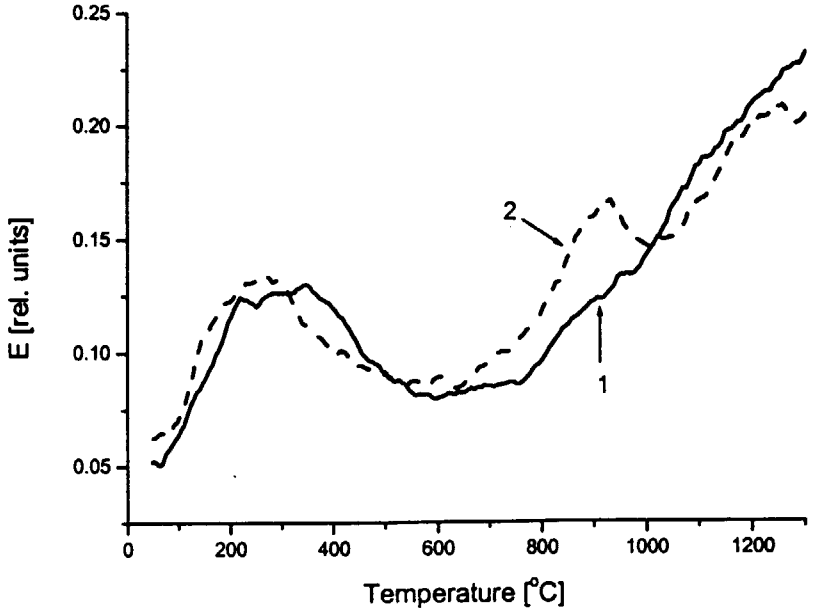


Fig. 1 Comparison of the thermal behavior of the Nicalon CG based SiC_f /SiC composite during heating in argon (curve 1) and air(curve 2), respectively.

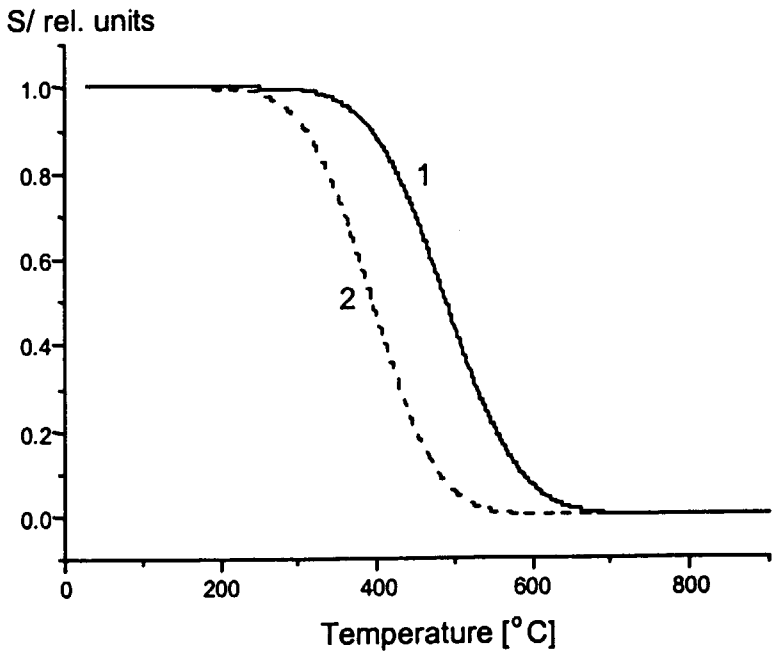


Fig. 2 Temperature dependencies of the function S(T), used for the characterization of the annealing of near surface structure irregularities in Nicalon CG based SiC_f /SiC composite during heating in argon (curve 1) and air(curve 2), respectively.

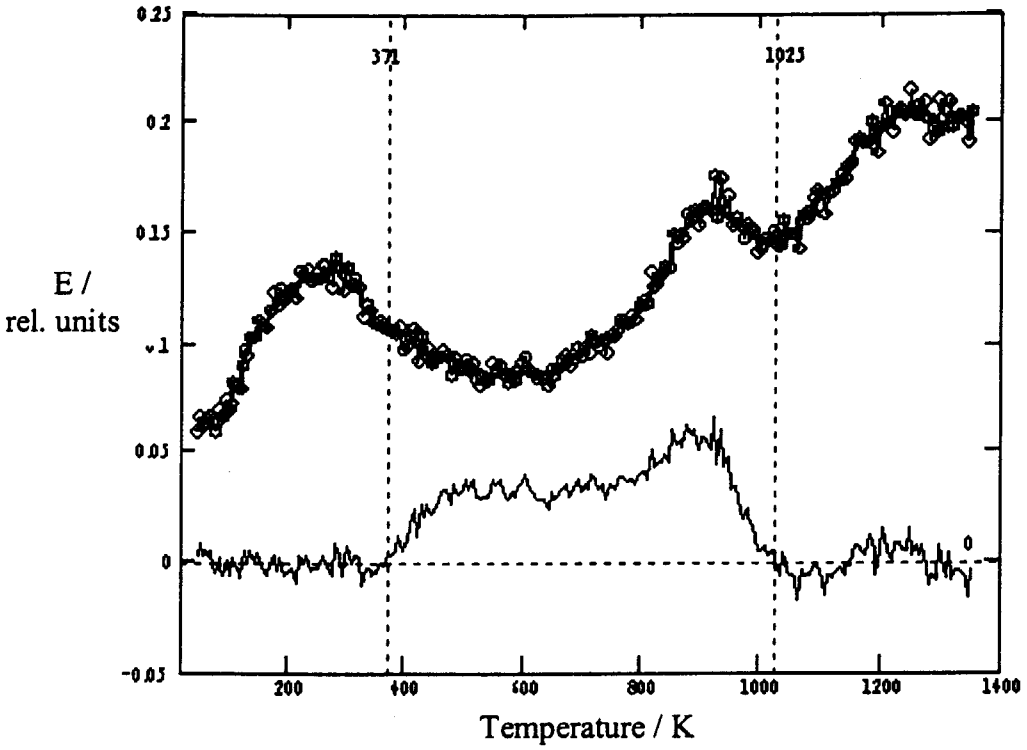


Fig. 3. Experimental ETA results of the SiC_f/SiC composite obtained on heating in air (dots) and the results of the computer treatment after subtraction of the model curves characterizing the annealing of structure irregularities and the radon diffusion in bulk of the sample, respectively.

JP0350256

1.5.3 KINETIC STUDY OF SOLID-STATE PROCESSES

Jiří Málek[1*], Takefumi Mitsuhashi[2]
[1]Joint Laboratory of Solid State Chemistry, Academy of Sciences of the Czech Republic & University of Pardubice, Studentská 84, CZ-532 10 Pardubice, Czech Republic
[2]National Institute for Materials Research, Advanced Materials Laboratory, 1-1 Namiki, Tsukuba, Ibaraki 305-044, Japan

Abstract

A simple method for kinetic analysis of solid-state processes has been developed and the criteria capable of classifying different processes are explored. They provide a useful tool for the determination of the most suitable kinetic model. The method has been applied to the analysis of calorimetric data corresponding to the crystallization processes in amorphous ZrO_2. It is found that the crystallization kinetics of amorphous powder sample exhibits a complex behavior under non-isothermal conditions. A two-parameter model provides a satisfactory description of the crystallization process for isothermal and non-isothermal conditions. This enables better control of crystallization extent in fine ZrO_2 powders that is important for preparation of zirconia ceramics with defined properties.

Keywords: kinetics, crystallization, nucleation, growth, calorimetry, zirconium oxide

1. Introduction

The kinetics of solid state processes is generally considered to be a rather controversial topic [1-3]. Most analyses of kinetic data are based on the assumption that the kinetic parameters are intrinsic constants that uniquely characterize a solid-state process under study. This approach may lead to erroneous conclusions as solid-state process usually exhibit rather complex kinetics [4].

There are two main reasons for studying solid-state kinetics despite above-mentioned limitation. One reason is the practical importance of the ability to predict kinetic behavior of a given system under defined conditions. Another reason is related to an understanding of underlying mechanism corresponding to the kinetic process. In the first case we can find a suitable mathematical description for most solid-state processes and, therefore, we may be able to optimize the kinetics. In the second case, however, things are more complicated and the exploration the mechanism of the solid-state process is an uneasy task where a careful study including several complementary experimental techniques and morphological observation is needed.

The rate of chemical reaction is usually expressed to be proportional to the concentration of reactants, raised to a power. In the case of solid-state processes, the concentration is replaced by the fractional conversion α ($0 \le \alpha \le 1$). The rate law than can be expressed by a simple differential equation:

$$(d\alpha/dt) = K(T) \cdot f(\alpha) \qquad (1)$$

where K(T) is a temperature dependent rate constant and $f(\alpha)$ is an algebraic expression of the kinetic model. There are several simple kinetic models that have been developed on the

* Corresponding author. Tel: +420-40-603-6553 Fax: +420-40-603-6361
E-mail address: jiri.malek@upce.cz(1st Author)

assumption of the simplified geometry of the diffusion processes [5-7], the reaction interface and its spatial movement [8], or the nucleation and growth processes [9-12].

Usually, it is not that difficult to find a suitable rate law from experimental data. However, its interpretation, in terms of underlying kinetic mechanism may be perplexing. For instance, the second-order kinetics of chemical reaction can also result from a complex reaction scheme. The situation is even more complicated in solids where the reactants are spatially constrained, they exhibit irregular shapes, polydispersity, preferred orientations, etc. [4] Under such circumstances, it is reasonable to expect some deviations from the kinetic models mentioned above. This idea led to formulation of empirical kinetic model containing the smallest possible number of kinetic exponents, so that there is yet some flexibility sufficient to describe real data as closely as possible [1,13]. Table I shows two empirical kinetic model (RO,AC) and the Johnson-Mehl-Avrami nucleation-growth model (JMA) that is frequently used for the description of the crystallization kinetics in amorphous solids.

Table I **The kinetic models and maxima (α_y^*, α_z^*) of the y(α) and z(α) functions**

Model	Symbol	f(α)	α_y^*	α_z^*
Reaction order [1]	RO(n)	$(1-\alpha)^n$	0	$1-n^{1/(1-n)}$
Autocatalytic [14,15]	AC(M,N)	$\alpha^M(1-\alpha)^N$	M/(M+N)	$>\alpha_y^*$
Nucleation-growth [9-12]	JMA(m)	$m(1-\alpha)[-\ln(1-\alpha)]^{1-1/m}$	$1-\exp(m^{-1}-1)$	0.632

In the following sections we will focus on the analysis of isothermal and non-isothermal calorimetric data corresponding to solid-state processes. A simple method of kinetic analysis will be described. This method than will be applied to the crystallization of amorphous zirconia under non-isothermal conditions and the role of nucleation and growth processes will be discussed. Finally, the conclusion about applicability of the JMA model in non-isothermal conditions will be drawn.

2. The method of kinetic data analysis

The shape and symmetry of the kinetic curve defined by Eq.(1) strongly depends on experimental conditions. The function f(α) should be invariant in this respect. It can easily be separated from K(T) function as shown below using the y(α) function obtained by transformation of Eq.(1). In isothermal conditions this function can be written as:

$$y(\alpha) \propto (d\alpha/dt) = k \cdot f(\alpha) \qquad (2)$$

If the Arrhenius type rate constant is assumed then the y(α) function can be written in non-isothermal conditions as follows:

$$y(\alpha) \propto (d\alpha/dt)\cdot \exp(E_a/RT) = A \cdot f(\alpha) \qquad (3)$$

The E_a is an apparent activation energy that should be determined independently from several experiments conducted at different heating rates [16]. As the parameters k and A in Eqs.(2) and (3) are constants the y(α) function is proportional to the kinetic model. Though the y(α) function is useful, its shape and maximum α_y^* (see Table I) does not provide an unambiguous information about the most suitable kinetic model [17].

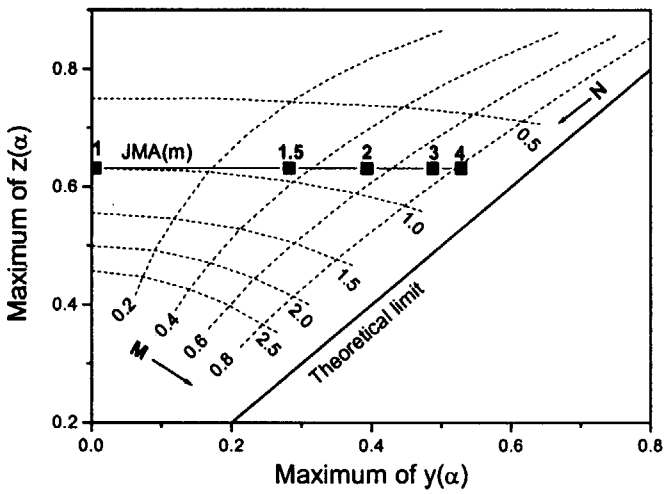
This is why we need an additional function called z(α) that can be also obtained by a simple transformation of experimental data [17,18]. In isothermal conditions such function can be written as:

$$z(\alpha) \propto (d\alpha/dt)\cdot t = f(\alpha)\cdot g(\alpha) \qquad (4)$$

and the z(α) function can be written in non-isothermal conditions (for Arrhenius rate constant) as follows [18,19]:

$$z(\alpha) \propto (d\alpha/dt)\cdot T^2 = C\cdot f(\alpha)\cdot g(\alpha) \qquad (5)$$

where $g(\alpha) = \int_0^\alpha [f(\alpha)]^{-1} d\alpha$ and the parameter C in Eq.(5) is a constant.



The maxima of the y(α) and z(α) function (see Table I) are characteristic parameters that can easily be used for the kinetic model discrimination. This is shown in Fig.1. It has been shown recently [19] that $\alpha_z^* > \alpha_y^*$ which can be considered as a theoretical limit of any kinetic model (thick solid line in Fig.1).

Fig.1 The kinetic diagram showing the differences between the kinetic models. The broken lines correspond to the different values of kinetic exponents of the AC(M,N) model. The JMA(m) model is represented by points connected by the solid line.

The method of kinetic analysis outlined above has a general validity and it can be used for any type of kinetic data and for most of the f(α) functions. The kinetic diagram is especially effective in the case of a systems that exhibit a complex behavior. Such behavior is observed for example in the case of the crystallization kinetics in amorphous solids [19,20]. In the following section we will show the applicability of this method to the crystallization of amorphous and partially crystalline zirconia.

3. Experimental

An amorphous zirconia was prepared by precipitating a 0.1M stirred aqueous solution of $ZrOCl_2.8H_2O$ with a 1M solution of ammonia added slowly at room temperature. The precipitated hydrated zirconia was washed, filtered and vacuum dried at R.T.

Table II Partially crystallized zirconia samples prepared by annealing at T_{iso} for 1h

Sample	T_{iso} (°C)	Fraction crystallized
A	-	-
B	340	8 %
C	360	19 %
D	365	22 %
E	367	25 %
F	370	42 %
G	375	66 %

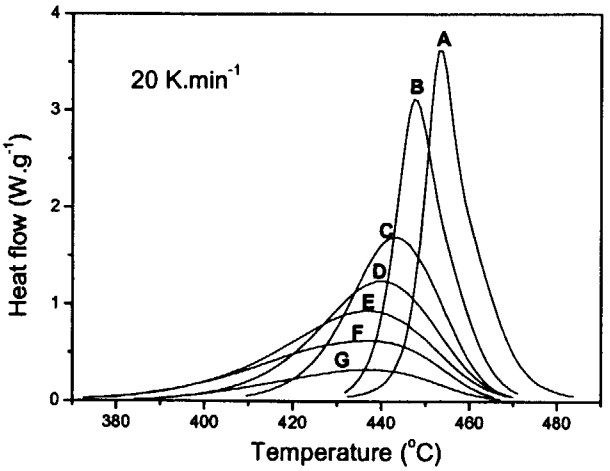


Fig.2 DSC curves of ZrO_2 samples shown in Table II

This partially dried amorphous powder (residual water content 13.7 %) was used to crystallization kinetics measurements by means of Diffrential Scannig Calorimetry (DSC) in a dry nitrogen flow. Partially crystallized samples were prepared by annealing of this powder at different temperatures for 1 hour (see Table II). Crystalline phase identification was performed by using X-ray diffraction (XRD). The morphology of amorphous and partially crystallized samples was examined by SEM and HRTEM.

4. Results and discussion

Fig.2 shows the DSC curves for amorphous sample (A) and partially crystallize samples (B-G) obtained under non-isothermal conditions (heating rate: 20 $K.min^{-1}$). The maximum of the crystallization peak is shifted to lower temperatures with increasing crystallinity of the sample, probaly due to the fact that the nucleation process is supressed in partially crystalline samples and zirconia crystals grow from preexisting nuclei [21]. Another feature of these data is that the

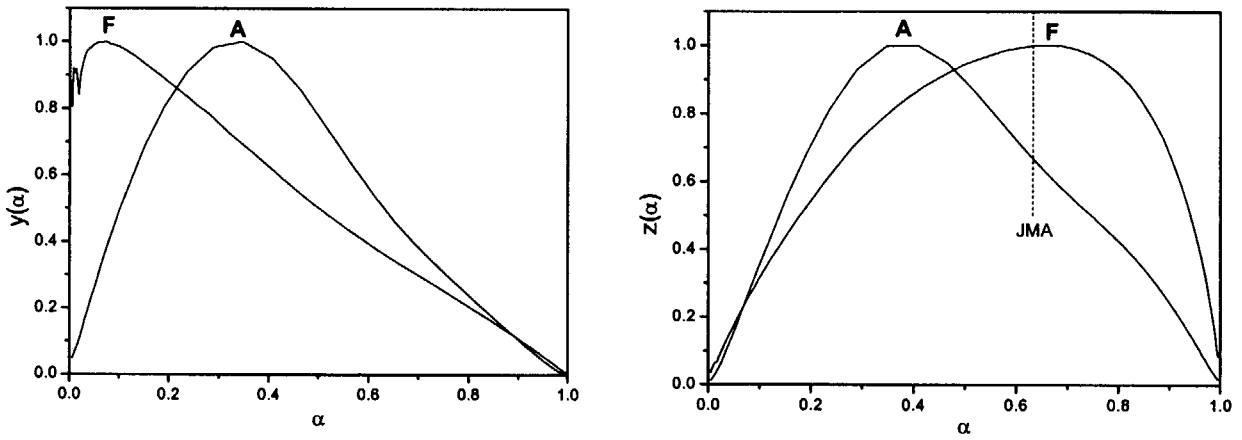


Fig.3 The y(α) and z(α) plots corresponding to amorphous zirconia (A) and partially crystallized (42%) sample (F) calculated by Eqs.(3) and (5) for data shown in Fig.2.

symmetry of the crystallization peak changes as a function of the fraction crystallized. This affects considerably both the y(α) and z(α) function as shown in Fig.3. The apparent activation energy needed to calculate the y(α) function was determined to be 264±11 $kJ \cdot mol^{-1}$ for sample A, and 234±4 $kJ \cdot mol^{-1}$ for sample F [21].

It is evident that the maximum of the z(α) function for sample A is considerably lower than predicted for the JMA(m) model. Nevertheless, there is a shoulder that appears close to 0.632 (see Table I). This rather complicated shape of the z(α) function could be explained assuming that there is non-negligible nucleation during the crystal growth for $\alpha < 0.5$. At higher conversion, however, zirconia crystals are growing from a practically constant number of nuclei. In contrast, the behavior of partially crystallized sample is quite different. The maximum of the z(α) function well corresponds to the prediction for the JMA(m) model. Almost linearly shaped y(α) function suggests that the kinetic exponent should be close to $m = 1$.

A complex crystallization behavior of amorphous (A) and all partially crystallized zirconia samples (B-G) can be visualised in the kinetic diagram shown in Fig.4. The basic part of the diagram is redrawn from Fig.1. The areas confined by by solid lines corresponds to the RO(n) and JMA(m) models. It is assumed that the typical experimental inaccuracy in maxima of the y(α) and z(α) function is ± 0.02.

The total area of the diagram corresponds to the AC(M,N) model.Therefore, the autocatalytic model is a plausible mathematical description of all kinetic models discussed. It is evident that the amorphous sample A exhibits fast self-accelerated crystallization and, therefore, the corresponding point in the kinetic diagram is located near the theoretical limit.

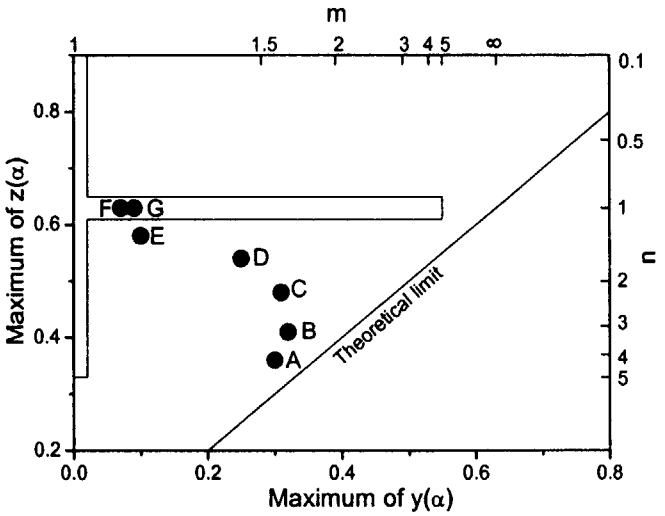


Fig.4 The kinetic diagram for the crystallization of amorphous and partially crystalline zirconia (see Table II). The areas confined by solid lines correspond to the RO(n) and JMA(m) models.

This self-acceleration process gradually slows down in partially crystalline samples (≤ 25 %) as the system approaches the region where the JMA(m) model can be applied (≥ 42 %). The kinetic exponent m is close to 1, which well corresponds to nearly linear dependence of the y(α) function. This value of m is expected in the case of the growth of very small particles dispersed in amorphous matrix. The HRTEM observations revealed that a great number of randomly distributed tetragonal zirconia nanocrystals (approx. 13 nm in size) are formed after heat treatment of as prepared powder [21]. Similar crystal size was estimated from the corrected halfwidth of (011) XRD peak (15±5 nm). The Rietveld analysis of XRD data confirmed [22] that the structure of crystalline phase is very similar to high temperature of t-ZrO_2 [23].

It is obvious that the crystallization process in amorphous amorphous zirconia and partially crystalline samples (< 42%) reveals a complex behavior that cannot be interpreted in terms of the JMA(m) kinetic model. This is easy to understand, because the JMA(m) model is, strictly speaking, only valid under isothermal conditions. Its validity can be extended to non-isothermal conditions [24,25] when the nucleation process takes places during the early stages of transformation, and it becomes negligible during the grystal growth. This seems to be consistent with the fact that the crystallization process in partially crystallized sample F well corresponds to the JMA(m) model. In this case one can expect that the nucleation process is over and the crystals are growing from a practically constant number of nuclei as has been anticipated above. The difference of 37 $kJ \cdot mol^{-1}$ between the value of E_a for amorphous and partially crystalline sample is probably associated with the fact that the nucleation process is no longer operative for a partially crystallized sample.

As we have pointed above, the complex crystallization process in amorphous zirconia can be described by the AC(M,N) model. This is shown in Fig. 5a where the non-isothermal DSC data for amorphous sample are compared with theoretical curves calculated by using Eq.(1), kinetic exponents M = 0.58 ± 0.08, N = 1.35 ± 0.05 and Arrhenius temperature dependence of the rate constant. It is assumed that measured heat flow can be written as $\phi = \Delta H \cdot (d\alpha/dt)$, where $\Delta H = 157 \pm 3$ $J.g^{-1}$ is the crystallization enthalpy of amorphous sample. This model can also be used to predict the crystallization extent under isothermal conditions. This is shown in Fig.5b where the experimental data and calculated α-T plots are compared. The isothermal data were obtained by annealing of amorphous sample in DSC instrument at various

temperatures for 1 hour. These samples were subsequently quenched to R.T. and measured at 10 $K.min^{-1}$. The conversion during isothermal annealing was estimated from $\alpha = (\Delta H - \Delta H_i)/\Delta H$, where ΔH_i is the crystallization enthalpy measured after annealing. The curve was calculated by using following equation that can be obtained by integration of Eq.(1):

$$\int_0^{\alpha} \frac{d\alpha}{\alpha^M (1-\alpha)^N} = A \cdot \exp\left(-\frac{E_a}{RT}\right) \cdot t \qquad (6)$$

It is clearly seen that the AC(M,N) model provides a reasonably good prediction for $\alpha \geq 0.2$, but apparently fails for lower conversions. This seems to be consistent with a complex character of crystallization process in amorphous zirconia.

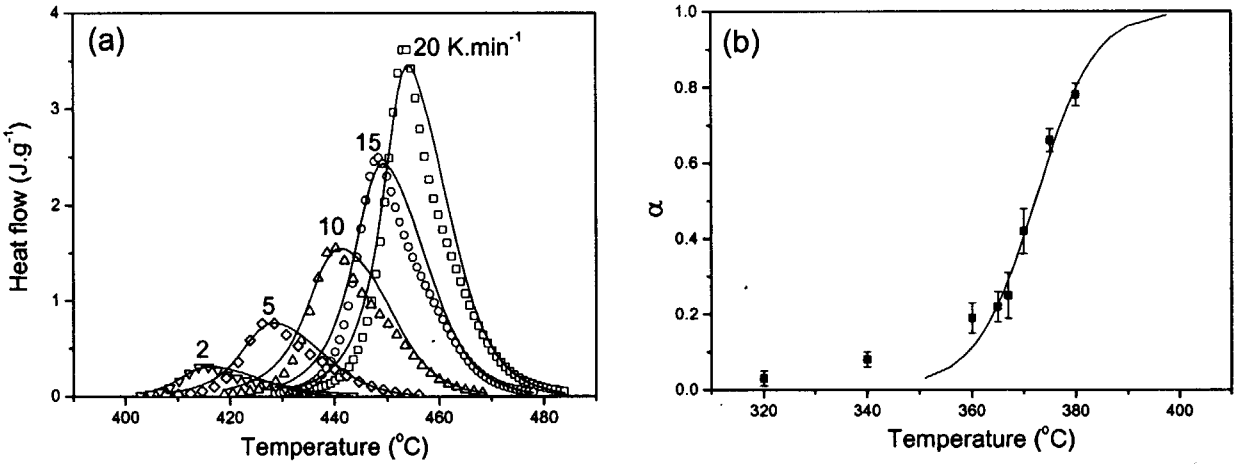


Fig.5 (a) Experimental DSC data for amorphous zirconia sample (points) and curves calculated for AC(M,N) model (solid lines). (b) Crystallization extent for zirconia annealed isothermally for 1 hour at different temperatures (points) compared with the prediction of this model.

5. Conclusions

The results shown above for crystallization of amorphous zirconia clearly indicate that the proposed method based on the kinetic diagram is very useful for the kinetic analysis of solid-state processes. The kinetic diagram helps to visualize the complexity of this kinetic process and provides a useful tool for the determination of the most suitable kinetic model.

It seems that the nucleation and crystal growth processes are overlapped at the beginning of crystallization of amorphous zirconia. As a consequence, the JMA(m) nucleation-growth model cannot be used under non-isothermal conditions, and the two parameter AC(M,N) model should be used instead. This model provides a reasonably good prediction both in non-isothermal and isothermal conditions.

Acknowledgment

This work was supported by the Cross-over Research Project of Nuclear Energy; promoted by The Ministry of Education, Culture, Sports, Science and Technology of Japan.

References

[1] M. E. Brown, D. Dollimore, A.K. Galwey, *Comprehensive Chemical Kinetics* (Elsevier, Amsterdam 1980).

[2] J. Šesták, J. Therm. Anal. **16,** 503 (1979).

[3] M. Maciejewski, J. Therm. Anal. **38,** 51 (1992).
[4] J. Šesták, J. Therm. Anal. **36,** 1997 (1990).
[5] J.B. Holt, J.B. Cutler, M.E. Wadsworth, J. Am. Ceram. Soc. **45,** 133 (1962).
[6] W. Jander, Z.Anorg. Allg. Chem. **163,** 1 (1927).
[7] A.M. Ginstling, B.I. Broushtein, Zh. Prikl. Khim. **23,** 1327 (1950).
[8] D.A. Young, *Decomposition of Solids* (Pergamon, Oxford 1966).
[9] W. A. Johnson, R.F. Mehl, Trans. Am. Inst. Miner. Eng. **135,** 419 (1939).
[10] M. Avrami, J. Phys. Chem. **8,** 212 (1940).
[11] A.N. Kolmogorov, Izvestia Akad. Nauk USSR, Ser Math. **1,** 355 (1937).
[12] B.V. Erofeev, Dokl. Acad. Sci. USSR **52,** 511 (1946).
[13] J. Šesták, G. Berggren, Thermochim. Acta **3,** 1 (1971).
[14] M.E. Brown, Thermochim. Acta **300,** 93 (1977).
[15] W.L. Ng, Aust. J. Chem. **28,** 1169 (1975).
[16] H.L. Friedman, J. Polym. Sci. **C6,** 183 (1964).
[17] J. Málek, Thermochim. Acta **138,** 337 (1989).
[18] J. Málek, Thermochim. Acta **200,** 257 (1992).
[19] J. Málek, Thermochim. Acta **355,** 239 (2000).
[20] J. Málek, T. Mitsuhashi, J.M. Criado, J.Mater. Res. **16,** 1862 (2001).
[21] J. Málek, T. Mitsuhashi, J. Ramírez-Castellanos, Y. Matsui, J. Mater. Res. **14,** 1834 (1999).
[22] J.Málek, L. Beneš, T. Mitsuhashi, Powder Diff. **12,** 96 (1997).
[23] G. Teufer, Acta Crystallogr. **15,** 1187 (1962).
[24] D. W. Henderson, J. Non-Cryst. Solids **30,** 301 (1979).
[25] T. Ozawa, Bull. Chem. Soc. Jpn. **57,** 639 (1984).

JP0350257

JAERI－Conf 2003－001

1.5.4 Microstructure of SiC Ceramics Fabricated by Pyrolysis of Electron Beam Irradiated Polycarbomethylsilane Containing Precursors

Yunshu XU [1*], Shigeru TANAKA[2]

[1] Institute of Nuclear Physics and Chemistry, CAEP. Mianyang, China 621900

[2] Takasaki Radiation Chemistry Research Establishment, JAERI. Takasaki, Japan 370-1292

Abstract

A modified gel-casting method was developed to form the ceramics precursor matrix by using polycarbomethylsilane (PCMS) and SiC powder. The polymer precursor was mixed with SiC powder in toluene, and then the slurry samples were cast into designed shapes. The pre-ceramic samples were then irradiated by 2.0MeV electron beam generated by a Cockcroft-Walton type accelerator in He gas flow to about 15MGy. The cured samples were pyrolyzed and sintered into SiC ceramics at 1300°C in Ar gas. The modified gel-casting method leaves almost no internal stress in the pre-ceramic samples, and the electron beam curing not only diminished the amount of pyrolysis gaseous products but also enhanced the interface binding of the polymer converted SiC and the grains of SiC powder. Optical microscope, AFM and SEM detected no visible internal or surface cracks in the final SiC ceramics matrix. A maximum value of 122 MPa of flexural strength of the final SiC ceramics was achieved.

Keywords: SiC ceramics, electron beam, ceramic precursor, polycarbomethylsilane,

1. Introduction

Silicon carbide (SiC) ceramics and SiC based ceramic composite possess various extraordinary properties [1] such as high temperature resistance (SiC dissociates at 2815°C), high hardness, high physical strength, low expansion factor and low neutron activation cross section, good resistance to corrosion by other materials. These outstanding properties make it possible to be widely used in extreme environment such as the first wall material of fusion reactor, turbine engine nozzles etc. Nevertheless, high quality SiC ceramics is very difficult to be fabricated through traditional ways.

Generally, conventional methods to fabricate SiC ceramics can be classified into 2 categories: 1) Using fine SiC powder and firing agent such as Al_2O_3 to form bonded ceramics at high temperature 1800~2200°C [2], traditional gel casting [3] technique belongs to this category; 2) Physically and/or chemically deposit SiC in molecular or atomic level to form

* Corresponding author. Stay at Takasaki Radiation Chemistry Research Establishment from Sept.2000 to Sept.2002, funded by JISTEC as an STA fellow. *E-mail*: xuy@taka.jaeri.go.jp.

bulk ceramics, such as chemical vapor deposition (CVD) method [4]. The first way is easy to produce in large scale, but the products properties are very limited, and high temperature firing facilities is needed. Furthermore, this method cannot be used to fabricate SiC_f/SiC composite as the SiC fiber decomposed at temperature higher than 1600°C [5]. The second way can produce high strength SiC ceramics, but takes long time to form even a small SiC bulk sample; Furthermore, expensive facilities have to be adopted.

In present paper, we used a modified gel-casting method to form the ceramics precursor matrix by using polycarbomethylsilane (PCMS) and SiC powder, followed by electron beam (EB) curing, to fabricate high quality SiC ceramics at lower sintering temperature (1300°C). The present modified gel-casting method leave almost no internal stresses in the precursor samples. Internal stress and volume shrinking are the two major reasons, which cause the formation of cracks in the final SiC ceramics matrix.

2. Experimental

2.1 Materials

Polycarbomethylsilane (PCMS), $[-Si(CH_3)HCH_2-]_n$, electronic grade, average Mw. is 800, m.p. 79~84°C, was purchased from Aldrich Chemical Company. Silicon carbide powder was purchased from Showa Denko Company; the grain size is about 4×10^2nm. Toluene and other chemical reagents used in experiments are all analytical pure grade.

2.2 Sample preparation and analysis

PCMS, SiC powder and toluene were mixed into slurry and degassed in a hybrid mixer. Then the slurry was casted into selected shapes, slowly dried in vacuum to remove residual toluene. After that the samples were irradiated in He gas flow to about 15MGy by 2.0MeV EB generated by a Cockcroft-Walton type accelerator. After quenching at 500°C, the cured samples were pyrolyzed and sintered into SiC ceramics at 1300°C in Ar gas.

The physical strength was measured by using an Instron 4302 type comprehensive mechanical property analyzer. The microstructure of the SiC ceramics was observed by using Keyence VH-6300 type CCD optical microscope, SPA400 type Atomic Force Microscope (AFM) and JSM-5600 type Scanning Electron Beam Microscope (SEM). Gel content was measured through solvent extraction [7] by using toluene.

3. Results and Discussion

3.1 Function of electron beam curing

Polymer precursor pyrolysis has been very successful in fabricating SiC ceramics fibers [6, 7], as well as infiltration of sintered porous ceramics to further density [8]. However, in recent years, reports [9] on polymer converted bulk SiC ceramics showed that it's very difficult to avoid the formation of surface and internal cracks mainly caused by the volume shrinkage, which occurred in the conversion process of polymer to ceramics.

Through high-energy radiation especially EB curing, SiC fibers have been successfully

fabricated by using polymer precursors [6~7]. The polycarbosilane (PCS) precursor used for synthesis of SiC fiber, after cured by electron beam to 12~15 MGy, will not form detectable cracks or bubbles. TGA and GC-FTIR analysis results [7] confirmed that CH_4, H_2 and other low molecular weight gaseous compound evolved out in both processes of EB irradiation and pyrolysis. The EB curing effectively diminished the pyrolysis gaseous production; moreover, 3-dimensional crosslinked infusible and insoluble gel was generated by EB irradiation, and the precursor's fibrous shape was reserved in the conversion process of polymer to ceramics.

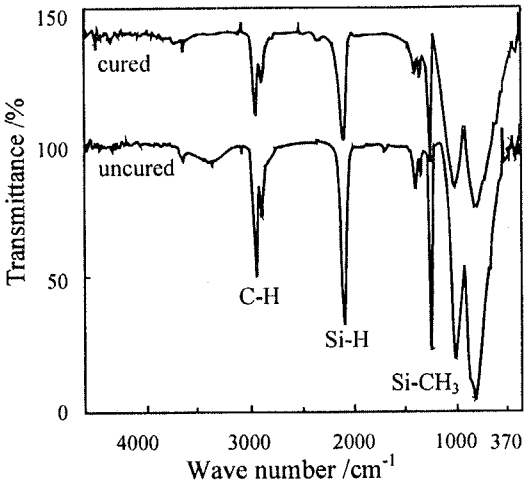


Fig.1 FTIR spectrogram of uncured PCMS and the 15MGy electron beam cured one.

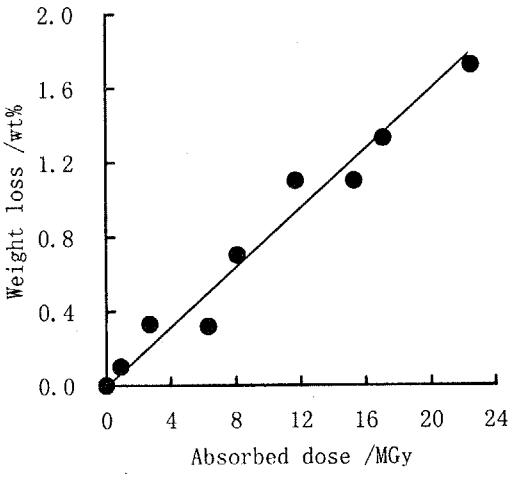


Fig. 2 Percent weight loss of PCMS after irradiated to various absorbed dose

However, PCS was not selected as precursor of SiC in this paper, because of its high brittleness at ambient temperature; it was very difficult to form bulk precursor samples of this polymer with enough mechanical strength.

The newly selected SiC ceramics precursor, PCMS, can also be effectively cured by EB. As shown in **Fig.1**, the strong and sharp FTIR peaks at 2105cm^{-1} caused by Si-H stretching, decreased after the sample was cured by 15MGy (gel content was about 75wt%); synchronously, the absorbance in 760～670cm^{-1} (Si-CH_2) increased, which indicates that -Si-CH_2-Si- type crosslinking bond was formed, mainly by the reaction of Si-H group, similar to the radiation curing mechanism of PCS [7].

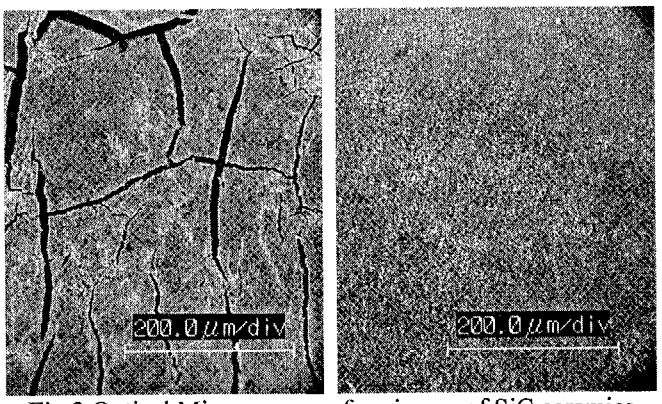


Fig.3 Optical Microscope surface image of SiC ceramics sintered from a) un-cured and b) EB cured precursors

The weight loss of PCMS, caused by the release of gaseous products, increased almost linearly within the experimental range of absorbed dose (**Fig.2**). Uncured precursors, either PCS or PCMS, generated large amount of gaseous products, and many bubbles as well as

cracks were detected in the bulk samples (**Fig.3a**). The cured PCMS bulk samples, after pyrolyzed and sintered, no cracks were observed as shown in **Fig.3b**.

3.2 Microstructure of the SiC ceramics

Only inorganic materials including SiC powder and binders such as alumina were used in traditional fabricating method [1] to minimize shrinkage during firing of the pre-ceramic part. Typically, the gel casting process [3] for forming ceramics, which was very successful in making complex-shaped automotive parts such as turbines, also sinters only inorganic powders at a high temperature of about 1800°C. These reported methods use inorganic binders or firing agent, which melt at high temperature forming glass phase, to "bind" SiC powder. As the traditional firing agent has poorer high temperature resistant properties than SiC, the application of these SiC ceramics is limited.

The PCMS converted SiC was used as binder to join the SiC powder together in this paper. EB curing possesses the well known advantage that crosslinking could be achieved without extra curing agent or any other chemicals; makes it possible to fabricate SiC ceramics with high purity and excellent high temperature resistant properties.

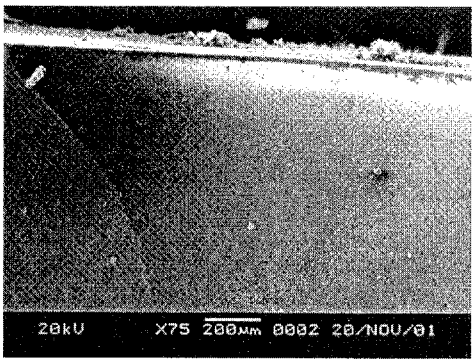


Fig.4 Cross-section SEM image of the SiC ceramics sintered from EB cured sample

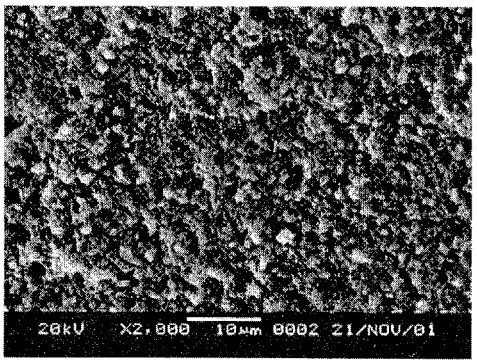


Fig.5 Highly amplified cross-section SEM image of the SiC ceramics sintered from EB cured samples

SiC ceramics sintered from 15MGy-cured PCMS containing precursor samples shows very good surface and internal structure integrity (**Fig.3~5**). The solid grains of SiC powders were well jointed by the PCS converted SiC as shown in **Fig.6**.

However, in the non-cured precursor samples, after pyrolyzed and sintered in Ar gas, some cracks were observed by optical microscope (**Fig.3**). As the density of SiC (**Tab.1**) is at least 2 times that of the polymer precursor, volume shrinking is unavoidable after PCMS is converted to SiC ceramics. The EB curing generated infusible gels, as well as diminished the gas evolution, "fixed" the solid structure of the polymer containing precursor samples. After pyrolyzed and sintered, PCMS was converted into

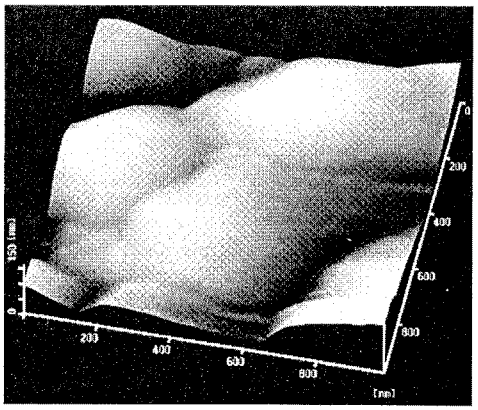


Fig.6 Atomic force microscope image of the SiC ceramics cross-section

SiC, and leaves "micro-porous" ceramics.

The PCMS converted SiC joined very well with the inorganic SiC powder as demonstrated by the AFM image shown in **Fig.6**. Whereas, some lacuna still existed in the samples, which might be caused by the non-uniform distribution of the polymers in the pre-ceramic samples. The micro-pores in the PCMS converted SiC area should be very small, as they were formed mainly by release of H_2 and CH_4 from the infusible EB cured precursor samples, and are not visible to presently used means.

3.3 Physical properties of the SiC ceramics

The modulus of SiC ceramics sintered from EB cured samples (7.1×10^4 MPa) is slightly higher than that of the non-cured (6.4×10^4 MPa). On the flexural strength of SiC ceramics, EB curing almost doubles the 3-point bending strength, as shown in **Fig.7**.

Compared to traditionally bonded SiC ceramics, the EB cured one possesses satisfactory physical strength, as shown in **Tab.1**. Similar value of 3-point bending strength to the composite bonded SiC ceramics was achieved at present.

Composite bonded SiC ceramics is a relatively new grade of product formed by slip casting. It uses high purity fine grain SiC powder, blended with elemental silicon and a binder system. It is formed into shapes via slip casting and is sintered in a controlled nitrogen atmosphere at temperatures exceeding 1400°C. Composite bonded silicon carbide has relatively high strength among conventional SiC ceramics products.

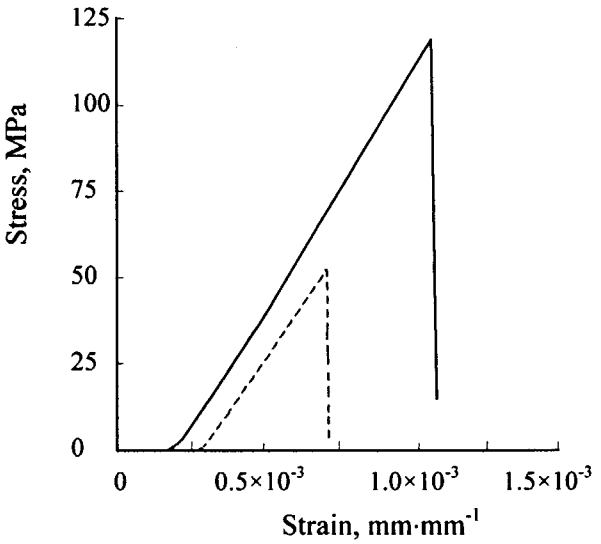


Fig.7 Effect of EB curing on the stress-strain properties of SiC ceramics (— EB cured, ····· direct fired)

Table 1. Physical properties of several SiC ceramics fabricated by bonding methods*

Product	Bulk Density ($g\cdot cm^{-3}$)	Porosity (%)	3-point bending strength (MPa)
Clay Bonded SiC	2.2-2.5	13-28	23
Nitride Bonded SiC	2.4-2.7	16	45-65.5
Oxy/Nitride Bonded SiC	2.2-2.4	18	41
Composite Bonded SiC	2.5-2.6	16	130
Present paper's SiC	2.3	~24	122

* Properties of other bonded SiC ceramics were selected from ref. [10].

Nitride bonded silicon carbide is commonly produced using a mixture of silicon carbide powder and finely divided elemental silicon, and sintered in a nitrogen atmosphere at high

temperature. Beginning at approximately 1100°C, the nitrogen gas and silicon metal react forming silicon nitride, or Si_3N_4, to bond the SiC powder together. If it is sintered in a controlled nitrogen and oxygen atmosphere, then oxy/nitride-bonded silicon carbide could be produced, which has slightly higher porosity, lower density and performance in wear applications. Clay bonded silicon carbide is normally formed via static pressing of a mixture of silicon carbide powder and clay, and the bond is formed during sintering where the clay softens and forms a glassy phase.

4. Conclusion

High quality SiC ceramics could be fabricated by using PCMS ceramics precursor and EB curing. The major effect of curing is: 1) To decrease the amount of gaseous pyrolysis products, and minimize volume shrinking in the process of polymer to ceramics; 2) To enhance the interface binding between polymer converted SiC and the SiC powder. The properties of SiC ceramic in present paper could be further improved by optimizing the distribution of PCMS in the precursor samples, the ratio of PCMS and SiC powder, and by using nano-sized SiC powder. As low firing temperature (1300°C) was adopted, the present result will be the basis for high quality SiC_f/SiC ceramics matrix composite (CMC) fabrication.

The presently achieved physical properties as shown in **Tab.1** are high enough to produce high-quality and complex-shaped fine ceramic parts such as gears used in high temperature wear application area. The point is that, using PCMS converted SiC as the binder, the resulted SiC engineering ceramics does not contain any high Z elements such as Al (formed from Al_2O_3 binder); this can decrease the neutron activation cross-section. The high temperature resistant property and the resistance to corrosion by other materials will also be better than conventional products,

References

[1] D. Zhao and W. Zhou, J. Xi'an Eng. Univ. 20(2), 23(1998)
[2] W. Böcker, H. Landfermann and H. Hausner, Powder Metallurgy Int. 11, 83(1979)
[3] K. Carolyn, ORNL Review, 28(4), 103(1995)
[4] A. J. Caputo and W. J. Lackey, Ceram. Eng. Soc. Proc. 5(7), 654(1984)
[5] T. Shimoo, H. Takeuchi and K. Okamura, J. Am. Ceram. Soc. 84(3), 566 (2001)
[6] S. Yajima and K. Okamura. *Nature,* 261, 683 (1976)
[7] Y. Xu, Y Song, R Huang and Y Fu, J Radiation Research and Radiation Processing (Chinese), 1998, 16(1), 1 (1998)
[8] R. H. Plovnick, D. J. Pysher, Mater. Res. Bull. 35, 1453 (2000)
[9] J. Wan, M. J. Gasch and A. K. Mukherjee, J. Mater. Res. 16(11), 3274 (2001)
[10] M. R. Metzger and M. L. Witmer, Technical Data of Silicon Carbide Products, Inc. USA. (2001)

This is a blank page.

1.6 Composite Materials

Chair: M. Hasegawa

(Tohoku University, Japan)

D. Fink

(Hahn-Meitner-Institut

Berlin, Germany)

This is a blank page.

JP0350258

1.6.1 PHOTOCONTROLLED SELECTIVE ISOLATION OF URANYL CATION FROM AQUEOUS SOLUTION ONTO A PHOTO-RESPONSIVE LANGMUIR-BLODGETT FILM

Yoshinobu IZUMI[1*], Takeshi YAMAMOTO[1], Tsuyoshi YAITA[2],
Kiminori USHIDA[3], Shoichi TACHIMORI[2] and Shigehiro NISHIJIMA[1]
[1]Department of Nuclear Engineering, Osaka University,
2-1 Yamada-oka, Suita, Osaka, 565-0871, Japan
[2]Japan Atomic Energy Research Institute,
Tokai-mura, Naka-gun, Ibaraki, 319-1195, Japan
[3]The Institute of Physical and Chemical Research,
2-1 Hirosawa, Wako, Saitama, 351-0198 Japan

Abstract

We applied a photo-responsive Langmuir-Blodgett (LB) film to selective isolation of uranyl cation from aqueous solutions. Uranyl cation was isolated onto a quartz plate covered with 5-octadecyloxy-2-(2-pyridylazo)phenol (PARC18) LB film which possesses the potential to form a complex with transition metal cations. The isolation process could be switched on by photoillumination. On the other hand, lanthanides (La, Ce, Nd, Gd, Er and Yb) were hardly isolated onto this film. Therefore, it was suggested that uranyl can selectively be collected from mixed solutions containing uranyl and lanthanides and that this process can be controlled by photoillumination. Detection limit of uranyl concentration in this system was also determined to be about 1.5 ppb.

Keywords: Langmuir-Blodgett film, photoillumination, uranyl, lanthanide, separation.

1. Introduction

Extraction of uranyl cation from aqueous solution is one of the most important processes in nuclear engineering[1]. This process can be applied to the re-collection of uranium from nuclear fuel waste, the collection of uranium from seawater, and other treatments that are valuable for optimum use of uranium resources on our planet.

The mechanism of partition across a liquid-liquid interface in solvent extraction, which is one of the most popular techniques in the collection of

*Corresponding author. Tel: +81-6-6879-7897 Fax: +81-6-6879-7889
E-mail address: izumi@nucl.eng.osaka-u.ac.jp (Y. IZUMI)

uranium, is essentially realized by the difference in its solubility into the two liquid phases. Thus the efficiency of the recovery depends on the equilibrium constant of the partition across the interface. Therefore, this method can be applied only to solutions containing uranium compounds with sufficiently high concentrations. On the other hand, in the case of low concentration of uranium, other types of extraction such as liquid-solid partitioning seem to be more effective, and these techniques have been reported and applied for practical use[2-4]. These methods are based on the use of an adsorbent containing some chemicals that can form complexes with uranium compounds.

Recent progress in the field of Langmuir-Blodgett (LB) film provided opportunities to develop various kinds of new functional materials[5]. M. -H. Liu *et al.* presented a novel example of an LB film, in which various metal cations in aqueous solutions can be combined by photoillumination[6]. Recently, we prepared the LB film of 5-octadecyloxy-2-(2-pyridylazo)phenol (PARC18), and found that it was applicable to separation of uranyl cation at a solid-liquid interface[7] The structural study of uranyl-PARC18 complex was performed by EXAFS[8].

In the present paper, we describe the selective isolation of uranyl from the mixed aqueous solution containing uranyl and some lanthanide cations. Detection limit of initial concentration of uranyl in this system was also estimated.

2. Experimental

The detailed descriptions of the synthesis of PARC18 were reported in a previous paper[7]. A 20-layer Y-type LB film was fabricated by successive deposition on a quartz plate at 30 mN/m at 293 K with nearly a unity transfer ratio (downstroke, 4 $mm \cdot min^{-1}$; upstroke, 2 $mm \cdot min^{-1}$), and was used in the present experiments. The total amount of PARC18 molecules was about 3×10^{-8} moles on each quartz plate. Uranyl(VI) nitrate, cerium(III) nitrate hexahydrate, lanthanum(III) nitrate hexahydrate, neodymium(III) nitrate hexahydrate, gadolinium(III) nitrate hexahydrate, erbium(III) nitrate hexahydrate and ytterbium(III) nitrate tetrahydrate was dissolved in a nitric acid solution. The LB plate was put into a 1-cm quartz cell containing aqueous solution of metal ions, and complex formation progressed with photoillumination using an ultrahigh-pressure mercury lamp (USHIO UI-501C, 500W) with a 330-nm band-pass filter (HOYA U330) at 299 K. The cell was located about 10 cm in front of the output of the collimating lamp house for some period, then was analyzed using a Shimadzu UV-2100 spectrophotometer to monitor the change in the optical absorption spectrum. For comparison, the dark reaction was also measured by using absorption spectroscopy. After 40 minutes of photo-accelerated reaction, the LB film which partly combined to metal cations

was dissolved in chloroform, back extracted by 0.1 N nitric acid solution, then the amount of collected metal cations was also measured by using ICP-mass spectrometer (VGPQΩ Fisions Instrument).

3. Results and Discussion

Before the experiments concerning LB film, we confirmed the complex formation in the condition of solution. **Figure 1** shows the optical absorption spectra of metal (U(VI), Ce(III), Gd(III) and Yb(III))-PARC18, and PARC18 dissolved in ethanol. PARC18 had a strong absorption (ε = 21600 $lmol^{-1}cm^{-1}$) at 380 nm. This absorption was attributed to diazo group[9]. In the cases of metal-PARC18 mixed solutions, this absorption decreased and another absorption at around 515 nm appeared. We consider that these absorptions were due to the metal-PARC18 complexes. Er(III), La(III), Nd(III)-PARC18 systems, that are not shown in this figure, also indicated almost the same tendency as other lanthanides. Therefore, PARC18 possesses the potential to form a complex with uranyl and lanthanide cations.

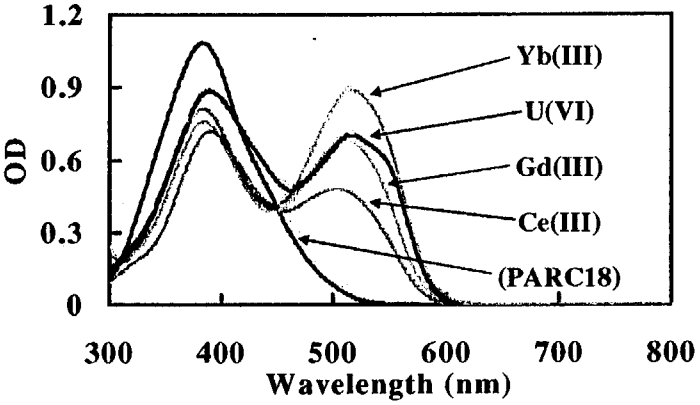


Fig. 1 The optical absorption spectra of metal-PARC18 and PARC18 dissolved in ethanol.

From this figure, we calculated the amount of PARC18 molecules combined to cations from a decrease of absorption at 380 nm, and estimated the molar absorption coefficients of metal-PARC18 complexes as 34400, 38700, 45500 and 52800 $lmol^{-1}cm^{-1}$ for U(VI), Ce(III), Gd(III) and Yb(III)-PARC18 complexes, respectively. The molar absorption coefficients of metal-PARC18 complexes were also estimated as 47400, 54600 and 49200 $lmol^{-1}cm^{-1}$ for La(III), Nd(III) and Er(III)-PARC18 complexes, respectively.

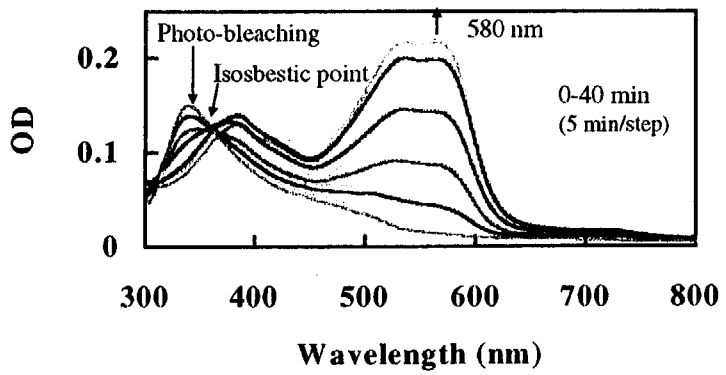


Fig. 2 Change in the absorption spectrum of PARC18 LB film during the photo-accelerated extraction process of uranyl from a solution of 0.5 mM U(VI) in 0.015 N nitric acid.

Figure 2 shows a series of absorption spectra which indicate the progression of the extraction process of uranyl from its solution of 5 x 10^{-4} M $UO_2(NO_3)_2$ in 0.015 N HNO_3. The initial absorption spectrum is attributed to *trans*-PARC18. Upon photoillumination, the spectrum gradually changed and a new absorption band appeared at around 580 nm. The isosbestic point was unclear but seemed to be located at around 360 nm. Therefore this reaction must undergo *via* photo-induced *cis-trans* transformation. And the resultant spectrum should be attributed to the uranyl-*cis*-PARC18 complex. The mechanism of uranyl adsorption and the structure of U(VI)- PARC18 LB film was reported in our previous paper[8]. **Figure 3** shows the amount of collected uranyl cations, which was measured by using ICP-mass, by PARC18 LB film under photoillumination and the dark. In the case of dark reaction, no significant yield of adsorption of uranyl cation was observed. On the other hand, the increase in the yield of uranyl cation was saturated after 20 minutes of photoillumination. Since the total amount of PARC18 molecules was about 3 x 10^{-8} moles in LB film, about 50% of PARC18 can be responsible for adsorption.

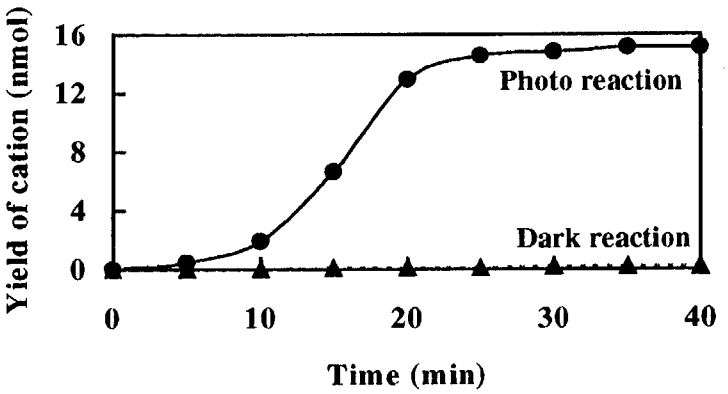


Fig. 3 The amount of collected uranyl cation by PARC18 LB film.

Figure 4 shows the yield of uranyl collection by 40-min photoillumination *versus* initial concentration (varied from 5 nM to 5 mM) of uranyl in aqueous solutions. The yield of uranyl collection was decreased with decrease in the initial concentration. Change in absorbance at 580 nm, in the case of aqueous solution of 5 nM uranyl, was negligible, however we could detect the uranyl collection by using ICP-mass. Therefore this system including PARC18 LB film and photoillumination is applicable to detection of low-concentration (5 nM =

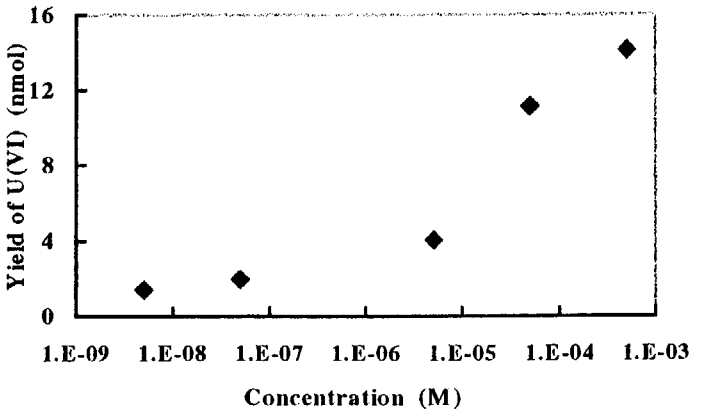


Fig. 4 The yield of uranyl collection by 40-min photoillumination vs. initial concentration of uranyl in aqueous solutions.

about 1.5 ppb) of uranyl.

Figure 5 shows the change in absorption spectra of PARC18 LB film during the photo-induced extraction process of Er(III). Initial concentration of Er(III) was 0.5 mM. Compared to the case of uranyl solution shown in **Fig. 2**, spectra were scarcely changed. In the cases of other lanthanide cations, spectra also changed scarcely. Moreover, almost no reactions were seen after a few hours in the dark. These results indicate that PARC18 LB film has very low reactivity with lanthanide cations, in spite of complex formation in the ethanol solution. Although the reason why lanthanide(III) cation hardly reacts with PARC18 LB film is not clarified at present, this LB system has applicability to selective separation of uranyl from the mixed aqueous solutions containing uranyl and lanthanides.

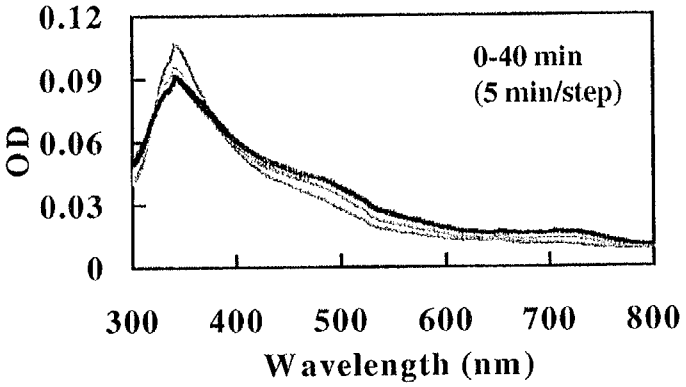


Fig. 5 The change in absorption spectra of PARC18 LB film during the photo-induced extraction of Er(III); concentration of Er(III) was 0.5 mM.

Figure 6 shows the amount of uranyl and lanthanides by 40-min photoillumination to PARC18 LB film, which was measured by using ICP-mass. In the case of separate solution system, which is containing only uranyl or one of lanthanide, the yield of uranyl collection was 12-190 times more than that of lanthanides. The yields of U(VI), La(III), Ce(III), Nd(III), Gd(III), Er(III) and Yb(III) were 1.51×10^{-8}, 8.11×10^{-11}, 9.55×10^{-11}, 4.85×10^{-10}, 1.04×10^{-9}, 1.24×10^{-9} and 5.48×10^{-10} moles, respectively. In the case of mixed solution system containing all of these cations, the yield of uranyl collection was 1.19×10^{-8} moles, which was lower (about 80 %) than the yield obtained from the separate solution. Since the yields of lanthanides collection was less than 4.0×10^{-10} moles, the yield of uranyl was 30 times larger than that of lanthanides. Therefore,

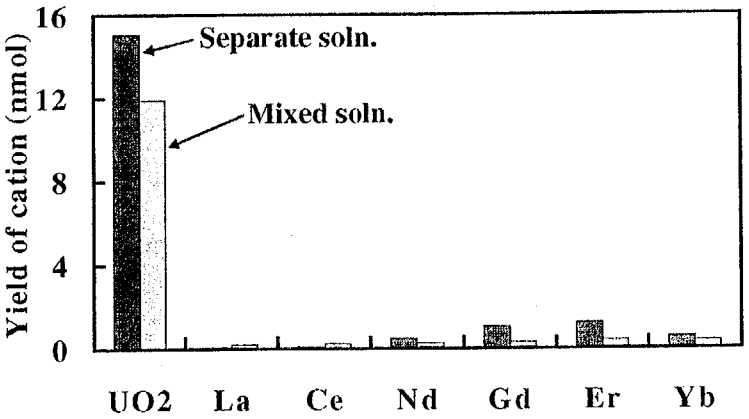


Fig. 6 The amount of uranyl and lanthanides collected by 40-min photoillumination of PARC18 LB film; concentration of each solute ions was 0.5 mM.

This LB film system, which is combined to photoillumination, is applicable to selective isolation of uranyl ion from the mixed aqueous solutions containing uranyl and lanthanide cations.

4. Conclusions

We succeeded in the selective isolation of uranyl from the mixed solutions containing uranyl and lanthanide cations by using PARC18 LB film and photo-accelerated adsorption reaction. This system including PARC18 LB film and photoillumination is applicable to detection of low-concentration (5 nM = about 1.5 ppb) of uranyl.

References

[1] M. Benedict, T. H. Pigford and H. W. Levi (Eds.), *Nuclear Chemical Engineering*, 2nd ed., McGraw-Hill, New York 1981.

[2] Y. Ozawa and T. Murata, *J. Nucl. Sci. Technol.*, **17**, 204 (1980).

[3] H. Omichi, A. Katakai, T. Sugo and J. Okamoto, *Sep. Sci. Technol.*, **20**, 163 (1985).

[4] C. Bernido, H. Omichi, A. Katakai and J. Okamoto, *ibid.*, **23**, 35 (1988).

[5] A. Ulman, *Ultrathin Organic Films*, Academic Press, New York, 1991.

[6] M. –H. Liu, K. Ushida, A. Kira and H. Nakahara, *J. Phys. Chem., B*, **101**, 1101 (1997).

[7] K. Ushida, M. –H. Liu and Y. Izumi, *Sep. Sci. Technol.*, **34**, 359 (1999); Y. Izumi, *The Production and Technique*, **52**, 56 (2000) (*in Japanese*).

[8] T. Yamamoto, Y. Izumi, M. Aoki, T. Yaita, S. Suzuki, H. Narita, S. Tachimori and K. Ushida, *J. Nucl. Sci. Technol.*, Submitted.

[9] Azobenzene dissolved in methanol indicates the absorption (ε = 17,400) at 314 nm.

JP0350259

1.6.2 CREATION OF NANOSCALE OBJECTS BY SWIFT HEAVY ION TRACK MANIPULATIONS

D. Fink[1]*, A. Petrov[1], N. Stolterfoht[1], M. Wilhelm[1], V. Hoffmann[1], A. Richter[2], M. Behar[3], L. Farenzena[3], R. Papaleo[4], K.Hirata[5], L. T. Chadderton[6], A. Schulz[7], W. R. Fahrner[8]

[1]Hahn-Meitner-Institut, Glienicker Str. 100, D-14109 Berlin, Germany
[2]Technische Fachhochschule Wildau, Germany
[3]Instituto de Física, UFRGS Porto Alegre, Brazil
[4]Instituto de Física, PUC Porto Alegre, Brazil
[5]National Institute of Chemical Research, Tsukuba, Japan
[6]ANU, GPO Box 4, Canberra, ACT 2601, Australia
[7]SDK GmbH, Am Gröpern, Quedlinburg, Germany
[8]Institut für Elektrotechnik, Fernuniversität Hagen, Germany

Abstract

In this work we give an overview of the possibilities to create new objects with nanoscale dimensions with ion tracks, for future applications. This can be realized in two ways: by manipulation of latent swift heavy ion (SHI) tracks, or by embedding specific structures within etched SHI tracks. In the first case one can make use of irradiation effects such as phase transitions and chemical or structural changes along the tracks. In the latter case, one can fill etched SHI tracks with metals, semiconductors, insulating and conducting polymers, fullerite, or colloides. Wires and tubules with outer diameters between about 50 nm and 5 μm and lengths of up to about 100 μm can be obtained. The most important production techniques are galvanic and chemical depositions. Ion Transmission Spectrometry has turned out to be an especially useful tool for the characterisation of the produced objects. Present studies aim at the construction of condensors, magnets, diodes, and sensors in etched tracks.

An obstacle for the practical realization of smallest-size polymeric ion track devices is the statistical distribution of the ion tracks on the target areas, which yields some pixels without any track, and other pixels even with overlapping tracks on a given sample. In a first test experiment we demonstrate that one can, in principle, overcome that problem by taking self-ordered porous foils as masks for subsequent high-fluence SHI irradiation.

Keywords: Ions, high energy, latent tracks, etched tracks, galvanic deposition, chemical deposition, nanowires, nanotubules, ion transmission spectrometry.

1. Introduction

Up to recently, tracks of swift heavy ions (SHI) have been a subject of academic studies rather than for practical applications. Only few fields showed up where SHIs could be applied usefully, such as the production of large areas of microporous thin polymer foils for applications mainly in filtering. In the meantime, however, first attempts have been made to

[1] Corresponding author. Tel.: 0049-30-8063-3029, Fax: 0049-30-8063-2293
E-mail address: Fink@hmi.de

incorporate thermoresponsive gels [1], metals, semiconductors and other matter [2] in etched SHI tracks, to obtain objects for new applications.

In this work we summarize the possibilities that SHI tracks still might have for other applications, where the SHI irradiation will have to be combined with other steps of manipulation, in order to arrive at the desired goal. These steps may comprise etching, annealing, galvanic or electrodeless material's deposition, low energy ion irradiation, or evaporation processes.

In principle, two different approaches can be distinguished: the use of as-implanted („latent") SHI tracks, or of structurally modified „etched" tracks [3]. Essentially etched tracks appear to exhibit still a great application potential.

2. Perspectives of applications of latent ion tracks

Four strategies show up here: the use of phase transitions (essentially in diamond and fullerite), material's chemical conversion (e.g. from polysilanes to SiC_x), trapping of specific impurities at latent tracks, and the ion-induced excess free volume in organic polymers. Up to now, there has not yet been invested much work in all these fields so that scientific background knowledge is quite poor.

2.1 Phase transitions

In the first case, one makes use of the long-known effect of destruction of the carbonaceous sp_3 structure and its transference to sp_2 by energetic radiation. By SHI irradiation of carbonaceous allotropes such as fullerene or diamond it is possible to restrict the zone of modification to a cylinder of only a few 10 nm in width. These zones exhibit a conductivity in the order of $\sim 10^{-1}$ Ωcm, no matter whether fullerite or diamond was the precursor material (for comparison: graphite: 8.1×10^{-4} Ωcm, amorphous carbon: ~ 1 Ωcm, ion-irradiated amorphous carbon: 10^{-1} Ωcm). This can be recorded by means of atomic force microscopy (AFM) with a conducting tip, Fig.1. With increasing distance from the track center, the resistivity drops strongly. These AFM images reveal that the modified zones in both fullerite and diamond show up as hillocks on the surface, due to the lower density of the transformed sp_2 enriched material. The current-voltage characteristics show a non-symmetric and nonlinear behaviour. One can recognize some peaks in the I/U characteristics, which indicates the occurrence of quantum effects in the carbonaceous nanowires.

As the conductivity along these carbonaceous nanowires is higher than that of their environment by many orders of magnitude, and as they protrude somewhat from their neighborhood, it has been proposed to use them as tips for field emission displays. In fact, field emission from irradiated diamond could already be verified [4]. Apart from this, the nonlinear track characteristics suggest possible future applications in electronics.

2.2 Material's chemical conversion

It was shown that polysilanes, irradiated by SHIs, are transformed to a silicon carbide-like matter, roughly characterized by SiC_x, with $x \approx 1$ [5]. This residue is insoluble in conventional solvents so that it can be easily separated from the original host matrix by dissolving the latter. It turns out that this residue has a soft spagghetti-like apearance, consisting of many nanowires with some fine structure, Fig.2a. Upon annealing of the irradiated target for a prolonged time at a temperature around the polysilane's melting temperature, the SiC_x apparently crystallizes and gains mechanical stability, Fig.2b. Therefore it has been proposed to use such crystalline nanorods as construction material in future micromechanics and microanalytics, e.g. as AFM tips.

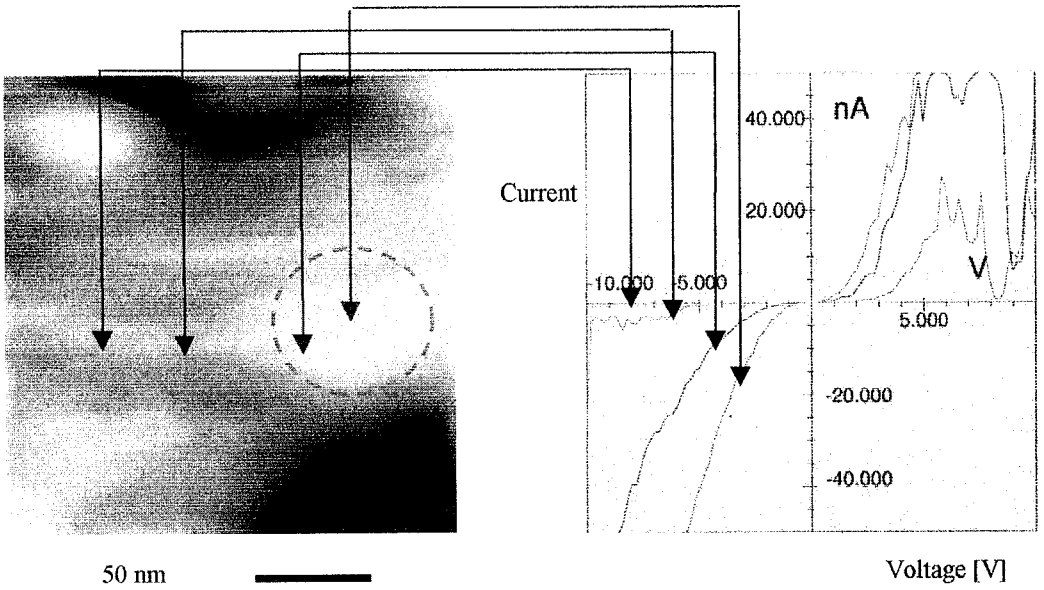


Fig.1. AFM image of a swift heavy ion track (~2.2 GeV Au) in fullerite. Left: height relief, right: current/voltage characteristics. The ion track, marked by a dashed circle, shows up as a hillock of a few nm height. Whereas the track center is conducting (a,b), the conductivity decreases rapidly with increasing distance from the track center (c,d).

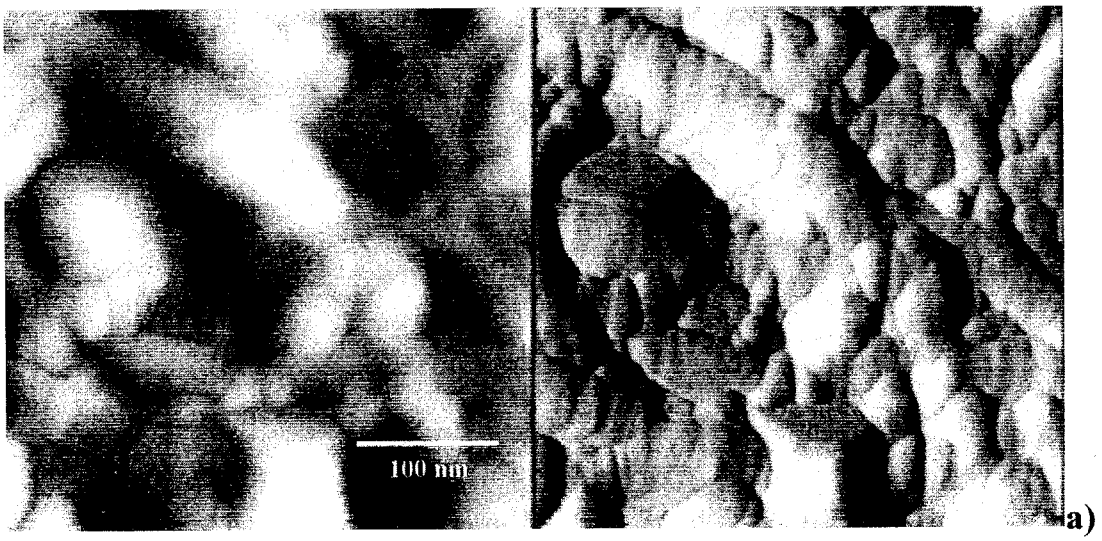


Fig.2. AFM images of SHI-irradiated (2.2 GeV Au) poly (metylphenyl silane), PMPySi. a) appearance of the insoluble residue SiC_x (x ~1) after leaching the soluble matrix (left: height, right: friction images), and b) image of a crystallized swift heavy ion track, after annealing the sample at 400°C for 6 hours in high vacuum.

2.3 Trapping of migrating impurities at tracks

In a recent work [6] it was shown that isolated Pd atoms, being produced *in situ* in PMMA by the decay of a suitable organometallic compound embedded in the polymer matrix,

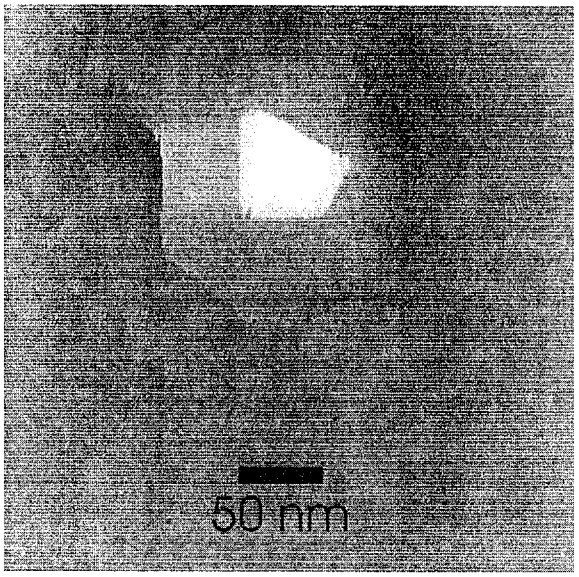


Fig. 2b)

migrate towards damage centers that had been created previously by low energy Ar^+ irradiation, to precipitate there and to form metallic clusters. In a similar way, it should be possible to use SHI tracks, which are long zones of linearly extended polymer damage, as nucleation centers for the precipitation of metals or metallic clusters embedded earlier in a polymer matrix. In this way, it should be possible to produce conducting nanowires within polymers. Such experiments are presently going on in our labs.

2.4 Liquid nanowires

High energy ion irradiation of polymers releases energy in the form of electronic excitation and ionization. This initiates radical formation, chain scissioning, and cross-linking. Though in general these effects occur simultaneously, in many common polymers (e.g. in PC, PET, CN, PSiO, etc.) chain scissioning dominates in the centers of non-overlapping ion tracks so that here small volatile reaction products are formed in abundance. Upon their degassing from the polymer matrix, narrow zones of excess free volume emerge that can, in principle, be filled up with liquids to form e.g. aqueous nanowires.

In fact, such wires have been studied to some extent [7], and relatively high current densities (typically 10 to 100 $\mu A/cm^2$, upon application of a few V) have been transmitted through them. One has found that even the moisture of ambient air absorbed within the tracks is already sufficient to initiate some ion track conductivity (though very low, typically 0.1 to 1 $\mu A/cm^2$, upon application of as much as about 20 V) [8].

Latent ion tracks in polymers are not just empty pores but contain a great amount of radiochemical debris („sponge model" [3]) and radicals. The first ones usually inhibits long-distance capillaric penetration of liquids, and the latter ones lead to strong sorption of the penetrant along the tracks. Consequently, the penetrant distribution is highly complex. In order to probe the latter, classical depth profiling techniques can be used, eventually also in combination with a modified tomographic approach that was especially developed for that purpose [9] (see, e.g. the study on the 3D distribution of LiCl solution in Ne irradiated PI [10]).

Latent ion tracks [11] or very narrow etched tracks [12] filled with aqueous solutions often exhibit switching properties due to the charging up of their inner surfaces and hence selective ionic transport,resulting in pulsed ion currents. As the same behavior is also found

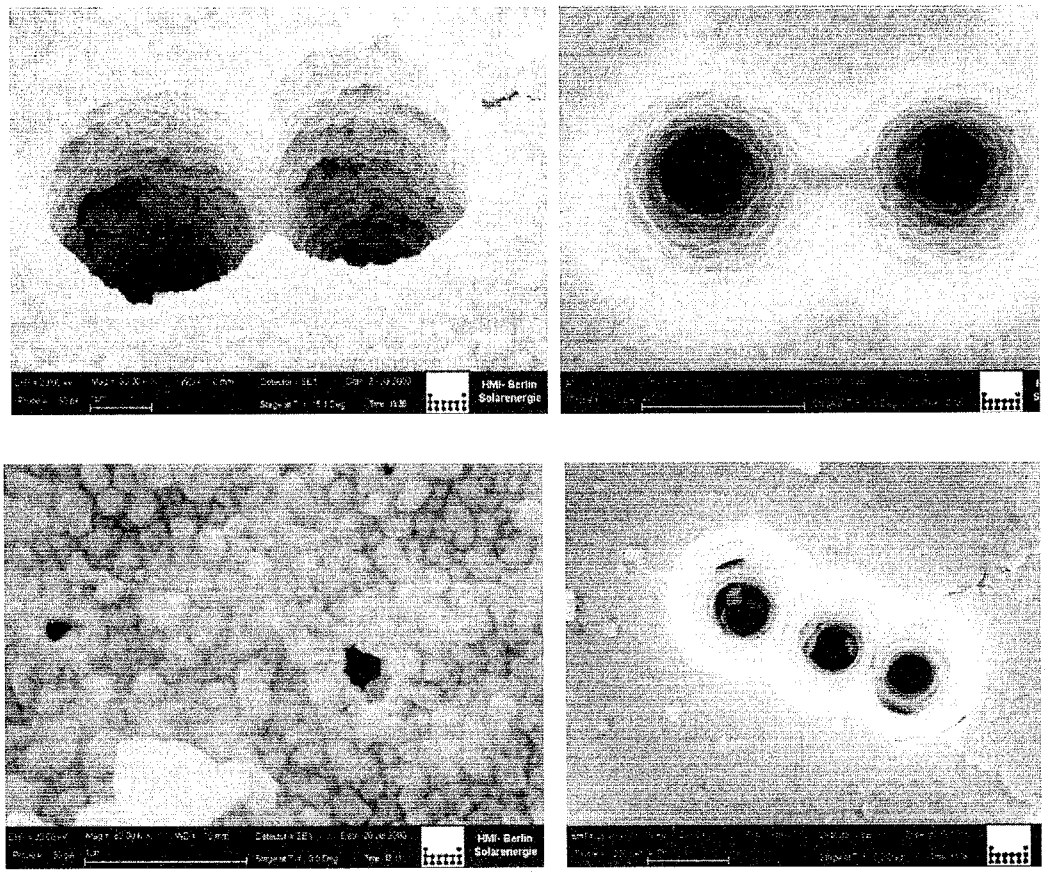


Fig. 3. Comparison of g layers deposited onto PI(top) and PET (bottom) after chemical activation (left) and ion-induced activation (right). In the first case, acidic $SnCl_2$ solution was used, in the second case the sample was ion-irradiated with 300 keV Ne^+ ions at a fluence of 10^{15} cm^{-2} , after the ion track etching and before the Ag deposition.

for natural current transport through membranes (e.g. in nerve cells), it has been suggested on the one hand to use ion tracks for modelling the still poorly understood biological current transport processes, and on the other hand to copy nature by production of an ion-track- and electrolyte-based nanoelectronics.

3. Perspectives of applications of etched ion tracks

Etching is the standard recipy to remove the radiochemical reaction products along polymeric ion tracks so that continuous straight pores emerge. Once this has been done the newly created free volume – called the etched track - can be filled, in principle, with any material to obtain any new nanostructure. Quite a number of these attempts have been already reported, see e.g. Refs. [2] and [3]. Massive or sponge-like rods and tubules with diameters between about 10 nm and 10 μm and lengths of up to about 100 μm can be obtained.

3.1 Galvanic deposition

Galvanic deposition inside the etched tracks leads to massive nanowires; the technique is, however, restricted to conducting matter. By galvanic deposition of alternating materials (e.g. Cu and Se) we had already produced first diode-like structures [13]. Attempts are going on to add a base contact to these or similar structures to produce ion-track-based field effect

transistors. P-n transitions can, of course, also be acomplished by connecting a track filled with a p-doped material (e.g. a conducting polymer) with a n-doped planar contact (e.g. a semiconductor).

Continuing the galvanic process after filling the etched track with e.g. Cu leads to mushroom-like structures that can serve as anti-wetting coatings [14].

By combination of galvanically produced conducting wires along tracks with metallic wires evaporated onto the polymer surface, we also try to produce micro-magnets, -transformers, and -oscillators [15]. Such structures should have less magnetic stray fields than corresponding evaporated planar structures due to better wdth/height ratios, and hence better quality factors.

3.2 Chemical Deposition

Chemical deposition has proven to be useful to create tubules of Cu, Ag, Au, and Ni [2,3]; in principle the same technique should also applicable to most II-IV and many III-V compounds. Multilayer deposition of tubules is possible. {Cu/Ni}, {Ni/Cu}, {Ag/TiO_2} [15], {TiO_2/PPy}, and {TiO_2/Au} [16] structures have already bee prepared. At present, the formation of first concentric {metal / insulator / metal} and {metal / semiconductor} structures is in preparation to pave the way for future concentric nano-condensors and –diodes.

The crucial point in chemical deposition is the preceding „activation" stage, which means the formation of nucleation centers (called illustratively: „molecular anchors" by Martin [2]) of high areal density on the inner etched track surfaces. This is necessary as the number of intrinsic surface defects that act as nucleation centers is too low to enable the formation of a continuous layer of the new material – in this case only few scattered nanocrystallites are deposited on the inner track surface. The activation is usually acomplished with acidic $SnCl_2$ or Pd complex salt solutions. One can also perform this activation by ion irradiation; in this way one can activate specific etch track regimes selectively, and one obtains much smoother layers of the deposit, Fig. 3. This should enable one to create even more complex structures.

Au tubules are used as electrodes in advanced miniaturized ion-track based sensors to determine e.g. the oxygen content in gases or liquids („Clarc cells"). In this way the volume of Clarc cells could be reduced by about two orders of magnitude, with a simultaneous gain in response time and pressure insensitivity, and at a much reduced price [14].

3.3. Adsorption of wetting liquids

Apart from the above mentioned techniques, tubules can be formed by adsorption of wetting liquids at the etch track walls. In this way, fullerene tubules have been created that exhibit temperature, pressure and humidity sensoring properties [17]. Also monomers of conducting polymers such as ethylene dithiophene (EDT) can be deposited on the inner track walls, to be polymerized *in situ* in a second step. Finally, that approach is feasible to deposit tubules of colloides such as $LiNbO_3$, SiO_2, or TiO_2. These materials are interesting due to their nonlinear optical properties, inertness, and photochemical activity, respectively.

3.4 Ion Transmission Spectrometry

Apart from scanning electron microscopy (SEM), Ion Transmission Spectrometry (ITS) [18] has turned out to be an especially useful tool for the quick characterisation of tubular structures. From the transmission of, e.g. energetic α particles from a radioactive source through micro-or nanoporous foils, one can deduce the track radius r_T via:

$$r_T = \frac{r_s L}{2d\left[1-\left(\frac{4T-1}{3}\right)^{0.87}\right]} \qquad \text{for } r_d \le 1 \quad (1a)$$

and

$$r_T = \frac{r_s L\sqrt{T}}{d} \qquad \text{for } r_d > 1 \quad (1b)$$

where T is the measured sample transmission, L the thickness of the microporous foil, r_s is the radius of the source, and d is the distance between source and sample. The quantity r_d is defined as $r_d = d \tan \varphi / r_T$, with φ being the beam divergence angle.

4. Non-statistical ion track distributions

The greatest obstacle for the future application of polymeric ion track devices is the statistical distribution of the ion tracks on the target areas, which leaves some sample areas without any, and others with overlapping tracks. Of course this can be overcome by writing sequentially ion by ion onto predetermined posistions, but the excessive time and cost of this operation renders that "single ion track approach" rather obsolete. Therefore one rather has to adopt the classical approach to irradiate ions through masks with a regular array of holes, at a fluence corresponding to multiple track overlapping. In this way, all sample pixels will contain at least some ion tracks. Conventional masks of good quality and narrow size are, however, extremely costly and hence prohibitive for the envisaged polymeric electronics which should establish a cheap alternative to the present silicon-based technology.

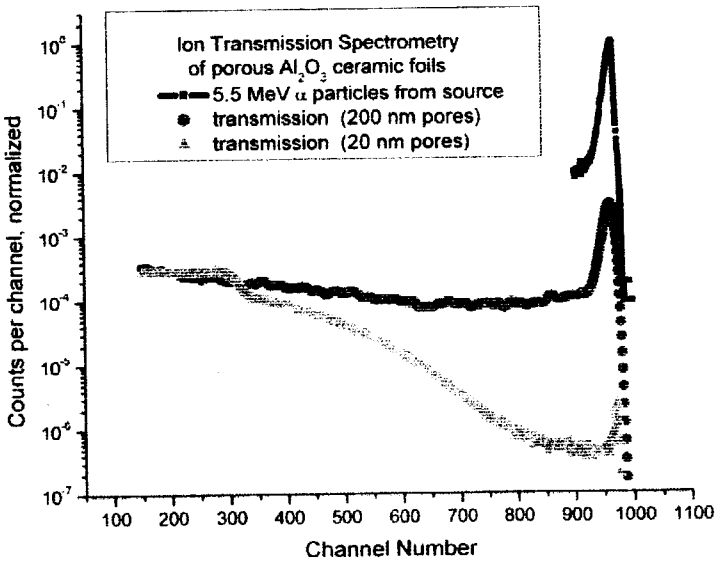


Fig. 4. ITS of 5.5 MeV α particles, transmitted through commercial Al_2O_3 foils of 20 and 200 nm pore size, respectively. The energy spectra show that ion transmission through the nanopores is, in principle possible, so that their application as masks for future SHI-track electronics appears feasible.

Therefore first test experiments have been undertaken to see whether it is also possible to use masks of cheap self-organizing materials such as commercially available Al_2O_3 ceramic foils for that purpose. Such foils have thicknesses of typically 100 μm and pore sizes of 20 to

200 nm. In fact, first ITS tests showed that ion transmission through such structures is indeed possible, Fig. 4. Based on this positive experience, tests with SHI transmission will follow.

5. Conclusions

The application of SHI tracks for advanced technologies is a field that has been neglected since long. Therefore this work summarizes the possibilities that emerged recently. Several strategies show up, such as the use of latent or etched tracks, massive wires or tubules, and chemical or ion-beam activation. It appears that the main drawback of ion tracks – their statistical distribution – can be overcome by the use of cheap self-organizing ceramic foils as masks. Therefore we feel that this approach will offer a future cheap alternative for some of the fields that are dominated nowadays still by the conventional Si-based microelectronics.

This work was enabled by the contribution of many colleagues. We are indebted especially to P.Yu.Apel, A.Berdinsky, P.Szimkowiak, A.Weidinger, A.Ulyashin, R.Klett, and to the accelerator and reactor teams in Berlin and Dubna for their generous support.

References

[1] M. Tamada, M. Yoshida, M. Asano, H. Omichi, R. Kakakai, R.Spohr, J. Vetter, Polymers **33**, 169 (1992).
[2] C. R. Martin, Science **266,** 1961(1994).
[3] D. Fink, *Ion Irradiation of Polymers: Fundamentals and Applications* (Springer, Heidelberg, to be published in 2003)
[4] M. Waiblinger, Ch. Sommerhalter, B. Pietzak, S. Klaumünzer, J. Krauser, B. Mertesacker, A. Weidinger, C. Roning, H. Hofsas, to be published.
[5] G. Herden, PhD. Thesis, Technical University, Berlin 2001 (in German)
[6] D.Fink, M.Müller, Y.Nakao, K.Hirata, Y.Kobayashi, M.Behar, J.R.Kaschny, J.Vacik, V.Hnatowicz, Nucl.Instr.Meth. **B166/167**, 610 (2000)
[7] R. Klett, PhD. Thesis, Humboldt-University, Berlin 1996 (in German)
[8] D. Fink, R. Klett, M. Müller, X. Hu, L. T. Chadderton, L. Wang, J. Hillenbrand, Radiat. Eff. Def. Solids **140**, 263 (1997)
[9] M. Müller, D. Fink, Nucl. Instr. Meth. **B34**, 162 (1988)
[10] D. Fink, M.Müller, A.Petrov, R.Klett, L. Palmetshofer, V. Hnatowicz, J. Vacik, J.Cervena, L.T.Chadderton, Nucl. Instr. Meth. .B (2002) in print
[11] D.Fink and R.Klett, Braz. J.Phys. **25,** 54 (1995)
[12] C. A. Pasternak, C. L. Bashford, Y. E. Korchev, T. K. Rostovtseva, and A. A. Lev, in: *Colloids and Sufaces, A: Physico-chemical and Engineering Aspects* **77**,119 (1993)
[13] A.. Biswas, D. K. Awasthi, B. K. Singh, S. Lotha, J. P. Singh, D. Fink, B. K.Yadav, B. Bhattacharya, and S. K. Bose, Nucl. Instr. Meth. B151, 84 (1999)
[14] Corresponding coatings, Clarc cells, and other ion-track based objects can be ordered by SDK-Technik GmbH, Quedlinburg, Germany
[15] A.Petrov, PhD.Thesis, Fernuniversität Hagen, Germany, in progress. To be published in 2005
[16] V. M. Cepak, Chem. Mater. **8**, 2109 (1996).
[17] A. S. Berdinsky D. Fink, A.V. Petrov, M. Müller, L. T. Chadderton, J. F. Chubaci, M. H. Tabacnics, Proc. MRS Fall Meeting, Boston 27.11.-1.12. 2001
[18] J. Vacik, J. Cervena, V. Hnatowicz, D. Fink, R.Klett, Radiation Eff. Def. Solids **140**, 307 (1997).

JAERI－Conf 2003－001

JP0350260

1.6.3 PLASMA-POLYMERIZED SiOx DEPOSITION ON POLYMER FILM SURFACES FOR PREPARATION OF OXYGEN GAS BARRIER POLYMERIC FILMS

N. Inagaki

Laboratory of Polymer Chemistry
Faculty of Engineering, Shizuoka University
3-5-1 Johoku, Hamamatsu, 432-8561 Japan

Abstract

SiOx films were deposited on surfaces of three polymeric films, PET, PP, and Nylon; and their oxygen gas barrier properties were evaluated. To mitigate discrepancies between the deposited SiOx and polymer film, surface modification of polymer films was done, and how the surface modification could contribute to was discussed from the viewpoint of apparent activation energy for the permeation process.

The SiOx deposition on the polymer film surfaces led to a large decrease in the oxygen permeation rate. Modification of polymer film surfaces by mans of the TMOS or Si-COOH coupling treatment in prior to the SiOx deposition was effective in decreasing the oxygen permeation rate. The cavity model is proposed as an oxygen permeation process through the SiOx-deposited Nylon film. From the proposed model, controlling the interface between the deposited SiOx film and the polymer film is emphasized to be a key factor to prepare SiOx-deposited polymer films with good oxygen gas barrier properties.

Keywords: SiOx film, Oxygen gas barrier, Plasma polymerization, Surface modification, Polyester, Polypropylene, Nylon

1. Introduction

Polyester (PET), polypropylene (PP), and Nylon films are good raw materials used for packaging of foods and drags, because of good performance in mechanical properties, thermal stability, and material design such as easy fabrication and easy care. However, they have a fatal defect as packaging materials. It is poor in oxygen barrier properties as well as water vapor barrier properties. Silicon oxide (SiOx) film is an interesting material from the viewpoint that the film possesses a high gas barrier property besides high thermal stability. If SiOx film can be deposited on surfaces of PET, PP, and Nylon films, the SiOx-deposited films will show high gas barrier properties, and will become a new packaging material. In deposition of SiOx on polymer film surfaces, there are essential problems related to discrepancies between deposited SiOx layer and polymer film. The deposited SiOx film is hard just like glass, and possesses high elastic modulus and small thermal expansion coefficient. On the other hand, the polymer film is flexible just like paper, and possesses low elastic modulus and large thermal expansion coefficient. Such discrepancies will lead to serious defects in the SiOx-deposited polymer films. Mechanical or thermal shocks will cause crevices in the deposited SiOx films, and barrier properties must be spoiled by the crevices.

Corresponding to N. Inagaki, Phone & Fax. 81-53-478-1161
E mail address: tcninag@ipc.shizuoka.ac.jp

In this study, SiOx films were deposited on surfaces of three polymeric films, PET, PP, and Nylon; and their oxygen gas barrier properties were evaluated. In addition to the evaluation, surface modification of the polymer films was applied for mitigation of discrepancies between the deposited SiOx and polymer film. How the surface modification could contribute to mitigation of the discrepancies was investigated.

2. Experimental.

2.1 Materials. Bi-axially oriented poly(ethylene terephthalate), PET, film (Trade name BOPET (Toyobo Co. Ltd.), 38 μm thickness), bi-axially oriented polypropylene, PP, film (Trade name U-10P#40 (Tosero Co. Ltd.), 40 μm thickness), and bi-axially oriented Nylon 6 film (Trade name Emblem (Unitika Ltd.), ON-25, 25 μm thickness) were used as base films for SiOx deposition. Tetraethoxysilane (TEOS), Triethoxysilane (TrEOS), tetramethoxysilane (TMOS), dimethyldimethoxylsilane (DMDMOS), tetramethylsilane (TMS), and N-(3trimethoxysilylpropyl) ethylenediamine triacetic acid, (Si-COOH), which were purchased from Gelest Inc. (Tullytown, PA), were used as chemicals for plasma polymerization and also as chemicals for the surface modification treatment.

2.2 Reactor used for Plasma Polymerization

A reactor used for plasma polymerization was one made by ourselves. The details of the plasma reactor is not described here because it has been represented elsewhere [1,2].

2.3 SiOx Deposition from Plasma Polymerization of TMOS/O2 Mixtures

The plasma polymerization of the TMOS/O_2 mixtures was performed at a system pressure of 39.9 Pa at rf powers of 60 W, and SiOx plasma polymers were deposited on the polymer film surface. The deposition rate of SiOx films was determined from a reading of the thickness monitor (Ulvac Co., Japan; model CRTM-1000).

2.4 Surface Treatment of Polymer Film Surfaces with TMOS or Si-COOH

In order to modify surface properties of the polymer films, modification reactions with TMOS and Si-COOH were done on the polymer film surfaces according to references 2 and 3.

2.5 XPS Spectra

XPS spectra were obtained on a Shimadzu ESCA K1 using a non-monochromatic MgKα photon source. The spectra were not smoothed and decomposed by fitting a Gaussian-Lorentzian mixture function to an experimental curve using a nonlinear, least-squares curve-fitting program, ESCAPAC, supplied by Shimadzu. The sensitivity factors (S) for the core levels were $S(C_{1s}) = 1.00$, $S(Si_{2p}) = 0.87$, and $S(O_{1s}) = 2.85$.

2.6 Oxygen Permeation Rate through SiOx-deposited Polymer film

The oxygen permeation rate through the SiOx-deposited polymer was measured in ranges of temperature from 10 to 35°C and of relative humidity from 0 to 90 RH% using a gas barrier tester (Mocon Inc., MN; model OX-TRAN 2/20). Three specimens were used for each measurement of the oxygen permeation rate. The oxygen permeation measurement for each specimen was done three times.

3. Results and Discussion

3.1 Choice of Silanes for SiOx Film Deposition and Chemistry of the Deposited SiOx Films.

Five silanes, TEOS, TrEOS, TMOS, DMDMOS, and TMS, which contained different C/Si atomic ratio of 8 to 4 and different bond structure (Si-O-C and Si-C bonds) between Si and C atoms, were used for the plasma polymerization. Table I compares the C/Si atomic ratio in the SiOx films deposited from the five silanes. The C/Si atom ratio in the deposited SiOx films, as shown in Table I, shows a dependence on the C/Si atomic ratio and the bond structure in the starting silanes: Silanes with a small C/Si atom ratio deposited SiOx films with a low carbon content, and silanes with Si-O-C bonds also deposited SiOx films with a low carbon content. From this viewpoint, TMOS is preferable to TEOS, TrEOS, DMDMOS, and TMS as a silane for SiOx deposition. However, TMOS is not yet a satisfactory material for the SiOx deposition because the deposited SiOx contained much carbonaceous components.

Table I Atom composition of SiOx films deposited from silanes

Silanes	Atom ratios			
	Starting compd		Deposited SiOx	
	C/Si	O/Si	C/Si	O/Si
$(C_2H_5O)_4Si$	8	4	3.2	1.9
$(C_2H_5O)_3SiH$	6	3	1.9	1.4
$(CH_3O)_4Si$	4	4	1.5	1.5
$(CH_3O)_2Si(CH_3)_2$	4	2	1.7	1.1
$Si(CH_4)_4$	4	0	2.5	

TMOS was mixed with oxygen and the mixture was plasma-polymerized for SiOx film deposition. Table II shows the C/Si and O/Si atom ratios in the deposited SiOx films as functions of the oxygen concentration in the $TMOS/O_2$ mixture. The mixing of oxygen gas, as shown in Table II, leads to large decreases in the C/Si atom ratio of the deposited SiOx films. From the table, we can conclude that the mixing of oxygen with TMOS contributes to the SiOx deposition with less carbonaceous component.

Table II Atom composition of SiOx films deposited from $TMOS/O_2$ mixtures

O_2 conc. in	Atomic ratio in SiOx	
$TMOS/O_2$ mix.	C/Si	O/Si
0	1.5	1.8
20	0.39	1.4
40	0.42	1.4
60	0.49	1.4

The chemical composition, especially the carbonaceous and silicone components, was investigated by XPS (C1s and Si2p) spectra. The C1s and Si2p spectra are not represented here for the sake of brief. The SiOx film deposited from TMOS showed an intensive and complex C1s spectrum on which a maximum peak appears at 286.9 eV due to C-O groups and a shoulder appears at 285 eV due to CH groups. The Si2p spectrum showed a maximum peak appears at 103.4 eV due to SiO_2 groups. On the other hand, for the SiOx films deposited from the $TMOS/O_2$ mixtures, the C1s spectra distributed from 283 to 286 eV and a maximum peak appears at 284.3 - 284.7 eV due to carbonized carbon. The Si2p spectra showed a peak at 103.4 eV due to SiO_2. Its FWHM value was 1.65 eV, which was smaller than that for the SiOx film deposited from TMOS (1.79 eV), indicating that the Si-O-Si networks in the SiOx films deposited from the $TMOS/O_2$ mixtures may grow more than those deposited from TMOS alone.

Oxygen Gas Barrier Properties of SiOx-deposited Polymer Films

SiOx films (100 nm thickness) were deposited on the surface of the PET and PP films, and the oxygen gas barrier properties for the SiOx-deposited films were evaluated. Table III shows typical results of the oxygen permeation rate through the SiOx-deposited films at 30°C at a relative humidity of 70%. The oxygen permeation rate was 44 cm^3/m^2-day-atm for the not SiOx-deposited PET film and more than 2000 cm^3/m^2-day-atm for the not SiOx-deposited PP film (2000 cm^3/m^2-day-atm is the maximum capacity of the permeation rate measurable with a Mocon equipment). The SiOx deposition, as shown in Table III, was effective in improving the oxygen gas barrier properties of the PET films. However, the SiOx deposition was ineffective for the PP films (Table III). This may be a result from differences based on intrinsic properties (glass transition temperature, elastic modulus, thermal expansion coefficient, etc.) of the two polymers. Poor adhesion between the deposited SiOx film and PP film may be a factor to fail in improvement of the oxygen gas barrier properties.

Table III Oxygen permeation rate through SiOx-deposited polymer films

Base polymer film	Oxygen permeation rate (cm^3/m^2-day-atm)		
	not SiOx-deposited	SiOx-deposited & SiOx-deposited	TMOS-modified
PET	44	0.1	
PP	> 2000	> 2000	37

In prior to the SiOx deposition, the PP film surface was modified with TMOS to have good affinity between the deposited SiOx film and the PP film. The modified and SiOx-deposited PP film, as shown in Table III, showed a large decrease in oxygen permeation rate from more than 2000 to 37 cm^3/m^2-day-atm. This indicates that modification of the interface between the deposited SiOx film and polymer film may be a key factor to improve oxygen gas barrier properties.

Nylon film is strongly influenced by extrinsic factors such as temperature and moisture conditions as well as intrinsic factors such as crystallinity, orientation, free volume, and cohesive energy of polymer chains, to change polymer structure. As a result, Nylon film shows drastic changes in the oxygen permeation rate. Especially humidity effects are distinguished in the oxygen permeation process. When water molecules contact to Nylon film surfaces, the molecules adsorb easily on the film surface, and diffuse into the inside of the film to interact strongly with Nylon molecules. As a result, there appear two effects of water molecules on the oxygen permeation process. One is that competitive absorption of water and oxygen molecules occurs in free volume of Nylon polymer matrix, and oxygen molecules are excluded from the free volume because of stronger interaction of water molecules with Nylon polymers than oxygen molecules. This exclusion of oxygen molecules leads to reduction of diffusive path available for oxygen molecules, and consequently, the oxygen permeation rate decrease. This phenomenon appears predominantly at low humidity less than 50 %RH. The other effect is that strong interaction of water molecules with Nylon polymer chains weakens inter- and intra-molecular hydrogen bonding among the Nylon polymer chains to enhance segmental motion of the polymer chains (plasticization of Nylon by water molecules). This plasticization contributes to diffusion of oxygen molecules, and conse-

quently, leads to increase in oxygen permeation rate though the Nylon film. This phenomenon appears predominantly at high humidity more than 50 %RH. This is the essential mechanism as to how water molecules influence oxygen permeation process through Nylon film.

The oxygen permeation rate for the Nylon film used this study showed similar changes with increasing the relative humidity to that reported by Hernandez [4]. For example, the oxygen permeation rate at 25°C was 36.6 and 19.8 cm^3/m^2-day-atm at relative humidity of 0 and 50 %RH, respectively. Over 50 %RH, the oxygen permeation rate increased gradually with increasing with the relative humidity, and reached 34.7 cm^3/m^2-day-atm at 80 %RH. These changes in oxygen permeation rate indicate difficulties in adhesion between the deposited SiOx film and the Nylon film, because of plasticization of Nylon film at 50 %RH. SiOx was deposited on the Nylon film surface, and the oxygen permeation rate through the SiOx-deposited Nylon film was measured as a function of the relative humidity. The SiOx-deposited Nylon film, as shown in Fig. 1, showed extremely lower oxygen permeation rate than the Nylon film. For example, the oxygen permeation rate of the SiOx-deposited Nylon film at 25°C and at 0 %RH was 1.6 cm^3/m^2-day-atm, which was 1/23 times lower than that for the Nylon film (36.6 cm^3/m^2-day-atm). The rates at 50 and CavitiesNylon filmCreviceOxygen moleculesSiOx film80 %RH were 2.7 and 6.1 cm^3/m^2-day-atm, respectively, which also were 1/7 – 1/5 times lower than those for the Nylon film (19.8 and 34.7 cm^3/m^2-day-atm). This comparison shows that the SiOx deposition contributes effectively to restraining the oxygen permeation through the Nylon film.

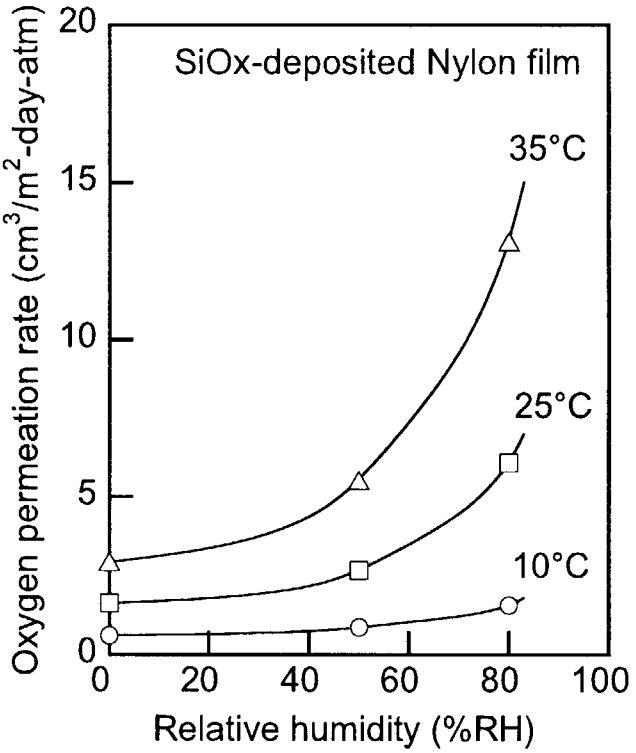


Fig. 1 Oxygen permeation rate through SiOx-deposited Nylon film as functions of relative humidity and temperature

How did the deposited SiOx films contribute to improvement of oxygen gas barrier propertied? The permeation process was analyzed to elucidate the contribution of the SiOx films. Apparent activation energy in the oxygen permeation process for the Nylon film and the SiOx-deposited Nylon film was estimated from the Arrhenius plot (Table IV). Apparent activation energy for the oxygen permeation process through the Nylon film was susceptible

Table IV Apparent activation energy for oxygen permeation process through SiOx-deposited Nylon film (25 μm thick)

Relative humidity (%RH)	Apparent activation energy (kJ/mol) Nylon	SiOx-deposited Nylon	TMOS-coupled & SiOx-deposited Nylon	Si-COOH-coupled & SiOx-deposited Nylon
0	34.8	44.9	38.9	34.4
50	56.5	54.0		
65	58.0			
70	59.7			
80	58.6	61.7	60.4	59.3
90	60.0			

to the relative humidity. The susceptibility was divided into two groups by humid condition: Under dry atmosphere (0 %RH), the apparent activation energy was small (34.8 kJ/mol); and under humid atmosphere, the activation energy was large (56.5 – 60.0kJ/mol). The SiOx-deposited Nylon film showed similar level of the activation energy to that for the Nylon film without 0 %RH. The SiOx-deposited Nylon film at 0 %RH showed slightly larger activation energy (44.9 kJ/mol) than the Nylon film (34.8 kJ/mol). The apparent activation energy for the SiOx-deposited Nylon film at 50 and 80 %RH was 54.0 and 61.7 kJ/mol, respectively, which were close in magnitude to those for the Nylon film (56.5 and 58.6 kJ/mol). This similarity indicates that there is essentially no difference in the mode of the oxygen permeation process between the SiOx-deposited Nylon film and Nylon film. In other words, the rate-determining process is not permeation through the SiOx film layer but that through the Nylon film layer. Why was the oxygen permeation rate for the SiOx-deposited Nylon film extremely lower (6.1 cm^3/m^2-day-atm) than that for the Nylon film (34.7 cm^3/m^2-day-atm), although there was no change in the permeation mode between the two Nylon films? The SiOx film deposited on the Nylon film surfaces must not be absolutely perfect without interstices but imperfect with many small interstices. Therefore, oxygen molecules will immerse easily into the SiOx layer from the interstices, travel along the crevices, and finally arrive on the Nylon film surfaces. Afterwards, the oxygen molecules will begin to permeate through the Nylon film layer. This is the story why the oxygen permeation rate for the SiOx-deposited Nylon film was extremely lower than the Nylon film. A SEM picture of the SiOx-deposited Nylon film showed parallel and eleven crevices (1 μm width and 160 μm long) on the SiOx film, indicating that the SiOx-deposited film was not absolutely perfect without interstices.

If the story that oxygen molecules permeate only through crevices in the deposited SiOx film is true, the sum of cross-section of the crevices can be estimated from the ratio of the oxygen permeation rates for the SiOx-deposited Nylon and Nylon films (eq. 1).

$$\text{Sum of cross – section of crevices (in cm}^2\text{)} = \frac{\text{Oxygen permeation rate through SiOx–deposited film}}{\text{Oxygen permeation rate through not SiOx–deposited film}} \times 47.1 \quad (1)$$

where 47.8 is the permeation area of the MOCON tester.
The estimation from eq. 1 is 8.6 and 6.7 cm^2 at 80 and 50 %RH, respectively, indicating that sum of the cross-section of crevices occupies 14 and 18% of the total area (47.8 cm^2) of the SiOx-deposited Nylon film, respectively. This is an incredible story because sum of cross-section of the crevices, which was estimated from the SEM picture, is about 6% of the total area. Other paths for permeation of oxygen molecules must exist in the SiOx-deposited Nylon films. A possible path may be cavities that were formed along walls of the crevices. This path is illustrated schematically as a cavity model in Fig. 2. The presence of these cavities has not yet been confirmed in a visual manner such as SEM, but we believe the presence of the cavities. This cavity model in Fig. 2 says an importance of the interface between the deposited-SiOx and Nylon films in the oxygen permeation process. The cavities might be formed in the neighborhood of the crevices, when the SiOx films were torn off from the Nylon film by the shock of the crevice formation. From this viewpoint, good adhesion between the SiOx and Nylon films may be a possible way for inhibition of cavity formation.

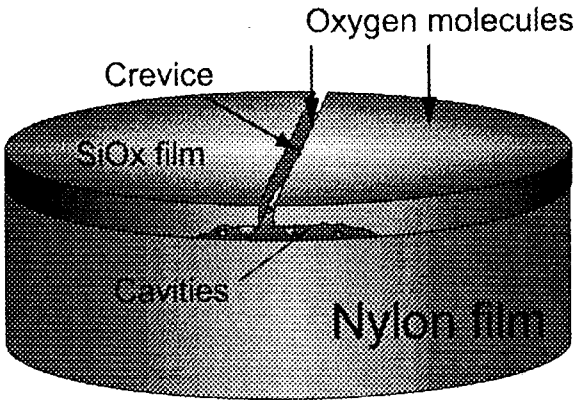


Fig. 2 Cavity model for oxygen permeation process through SiOx-deposited Nylon film

Effectiveness of Surface Modification of Nylon Film on Oxygen Barrier Properties

The Nylon film surface was modified in prior to the SiOx deposition in order to improve adhesion between the deposited SiOx and Nylon films. Silyl groups were introduced on the Nylon film surfaces by means of two different coupling reactions using TMOS or Si-COOH. We expected that the silyl groups introduced into the Nylon film surface could make strong affinity with the deposited SiOx films, and could contribute to inhibition of the cavity formation. On these modified Nylon film surface, SiOx films of 100 nm thick were deposited, and the oxygen permeation rate was measured as a function of the relative humidity and temperature. The two modified Nylon films showed lower permeation rates, especially at 80 %RH, than that for the not-modified Nylon film. The oxygen permeation rate at 25°C and 80 %RH for the TMOS- or Si-COOH modified and SiOx-deposited Nylon films was 4.7 and 4.9 cm^3/m^2-day-atom, respectively. On the other hand, the rate for the not-modified but SiOx-deposited Nylon film was 6.1 cm^3/m^2-day-atom. The oxygen permeation rate was decreased by 20 – 23 % by the surface modifications. From this viewpoint, the

surface modification with TMOS and Si-COOH was effective in improving oxygen gas barrier properties. How did these modifications improve oxygen gas barrier properties? Could the modification diminish the cavities?

The apparent activation energy for the oxygen permeation process for the TMOS-modified or the Si-COOH modified and SiOx-deposited Nylon films was estimated from the Arrhenius plot. The two modified and SiOx-deposited Nylon films, as shown in Table IV, showed similar activation energies of 60.4 and 59.3 kJ/mol at 80 %RH, and of 38.4 and 34.4 kJ/mol at 0 %RH, respectively. In addition to the similarity between the TMOS-modified or Si-COOH modified and SiOx-deposited Nylon films, these activation energies are comparable to those for the not-modified but SiOx-deposited Nylon film (61.7 and 44.9 kJ/mol at 80 and 0 %RH, respectively) and the Nylon film (58.6 and 34.8 kJ/mol, respectively). The coincidence of the activation energy among the four Nylon films indicates that the oxygen permeation operates in the same mode regardless of modified or SiOx-deposited surfaces. The permeation through the Nylon film is a rate-determining process. However, there is a large difference in the oxygen permeation rate among the four Nylon films. We believe that the oxygen permeation through the Nylon occurs in cavities that were formed along walls of the crevices, which is shown as a cavity model in Fig. 2. The cross-section of cavities formed in the TMOS-modified and Si-COOH modified Nylon films is estimated to be 14 % ((4.7 or 4.9)/34.7 = 0.14) of the total film area. On the other hand, the cross-section for the not-modified Nylon film is 18 % (6.1/34.7 = 0.18). This comparison shows that the surface modifications with TMOS and Si-COOH were efficacious in decreasing the oxygen permeation rate, but the contribution of the modified surface to inhibition of the cavity formation was not so powerful as we expected.

In conclusion, we summarize the oxygen permeation rate through SiOx-deposited polymer films.

(1) The SiOx deposition on PET and Nylon film surfaces led to a large decrease in the oxygen permeation rate.
(2) Modification of polymer film surfaces by mans of the TMOS or Si-COOH coupling treatment in prior to the SiOx deposition was effective in decreasing the oxygen permeation rate.
(3) The cavity model is proposed as an oxygen permeation process through the SiOx-deposited Nylon film. Oxygen molecules invade easily from the crevices of the SiOx films into the cavities, and arrive on the Nylon surface. A rate-determining process in the SiOx-deposited Nylon film system is the permeation step through the Nylon film.
(4) Controlling the interface between the deposited SiOx film and the polymer film is a key factor to prepare SiOx-deposited polymer films with good oxygen gas barrier properties.

References

[1] N. Inagaki, S. Tasaka, and H. Hiramatsu, *J. Appl. Polym. Sci.*, **71**, 2091 (1999).
[2] N. Inagaki, S. Tasaka, and T. Nakajima, *J. Appl. Polym. Sci.*, **78**, 2389 (2000).
[3] B. Pukansky and Z. Demjen, *Macromol. Symp.*, **139**, 93 (1999).
[4] R. J. Herrandez, *J. Food Eng.*, **22**, 495 (1994).

1.7 Surface Modification

Chair: T. Goto

(Tohoku University, Japan)

K. Kobayashi

(National Institute of Advanced

Industrial Science and

Technology, Japan)

This is a blank page.

JP0350261

1.7.1 CHARACTERIZATION OF SURFACES AND SUBSURFACES BY AN INTENSE POSITRON BEAM

Ryoichi Suzuki and Toshiyuki Ohdaira
National Institute of Advanced Industrial Science and Technology, AIST Central 2, Umezono, Tsukuba-shi, Ibaraki 305-8568, Japan

Abstract

Positron annihilation spectroscopy with an intense pulsed positron beam is a fruitful tool for the microstructure and impurity characterization of surfaces and sub-surfaces. In this paper, positron annihilation induced Auger electron spectroscopy, positron annihilation lifetime spectroscopy, and age-momentum correlation spectroscopy with an intense pulsed positron beam generated by an electron linac, are discussed. Several experimental results have shown the great potential of the pulsed positron beams for surface and near-surface studies.

Keywords: slow positron, electron linac, positron annihilation lifetime spectroscopy, age-momentum correlation spectroscopy, PAES

1. Introduction

At the electron linac facility of National Institute of Advanced Industrial Science and Technology (AIST), we have carried out researches on intense slow positron beams and their applications under the crossover research project. We have developed an intense pulsed slow positron beam for materials researches. The pulsed positron beam makes it possible to perform positron annihilation lifetime spectroscopy (PALS) and age-momentum correlation (AMOC) spectroscopy at various incident energies (i.e. various depths) as well as time-of-flight measurements of positron annihilation induced Auger electron spectroscopy (TOF-PAES) with high peak-to-background ratio, high count rate, and wide measurable time range. These measurement techniques are quite useful for impurity and microstructure characterization on surfaces and sub-surfaces.

In this paper, we discuss generation of an intense pulsed positron beam, positron annihilation-induced Auger electron spectroscopy, PALS, and AMOC measurements with the intense pulsed positron beam.

2. Generation of an Intense Pulsed Positron Beam

An intense positron beam of 10^8 e^+/s at the maximum intensity, which is generated with a high energy (~70 MeV) electron beam of the AIST linac, is used for the positron experiments [1,2]. The slow positrons generated at the converter/moderator section are magnetically transported to the positron measurement room via 22 m vacuum tube. The positron pulse corresponding the linac pulse (1 μs, 100 pps) is stretched to ~9 milliseconds as shown in Fig.1 to prevent saturation of the detectors.

The pulse-stretched positron beam is then short pulsed by a positron pulsing apparatus.

*Corresponding author. Tel: +81-298-61-5681, Fax: +81-298-61-5683
E-mail address: r-suzuki@aist.go.jp

The pulsing apparatus for positron lifetime measurements consists of a chopper, a sub-harmonic pre-buncher (SHPB) and a buncher. This apparatus can generate a short-pulsed positron beam of about 100 ps [3]. Furthermore, the incident energy of the pulsed positron beam can be varied by changing the sample voltage. Using this variable energy pulsed positron beam, we can measure positron lifetime spectra at desired depths from ~10 nm to several micrometers.

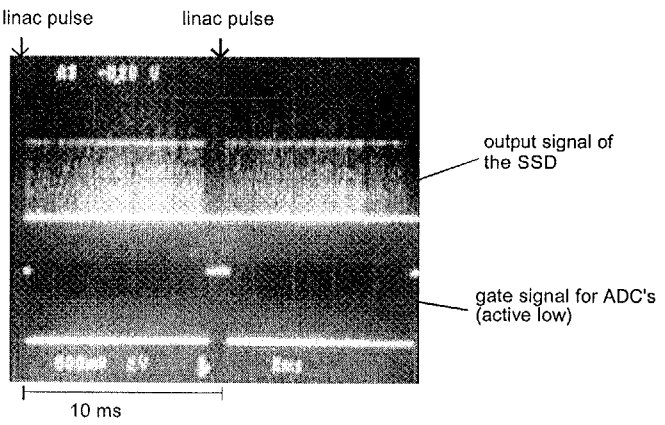


Fig. 1. Pulse stretched positron beam by the linear storage section.

The pulsing system for PAES consists of a chopper and a buncher to generate a few nano-second pulsed positron beam for time-of-flight measurements.

3. Positron annihilation-induced Auger electron spectroscopy

Positron annihilation-induced Auger electron spectroscopy (PAES) is known to have significant advantages over conventional Auger electron spectroscopy (AES) [4,5]. Since core electrons are removed by matter-antimatter annihilation in the case of PAES, the incident positron energy need not be larger than the core level ionization energy. Therefore, PAES permits the elimination of the large secondary electron background from the Auger spectra. Furthermore, the surface sensitivity of this technique is extremely high because the positrons are trapped at the surface state. In addition, the total energy dose of the positron beam is much lower than that of conventional AES because of low incident energy, relatively high efficiency of core electron excitation, and low background.

Several electron energy analyzing methods for PAES have been developed. One method uses a trochoidal energy analyzer or position sensitive detector with inhomogeneous magnetic field electron parallelizer and with ExB deflection plates [5]. The other method uses a cylindrical mirror analyzer similar to conventional electron AES [6]. We have developed

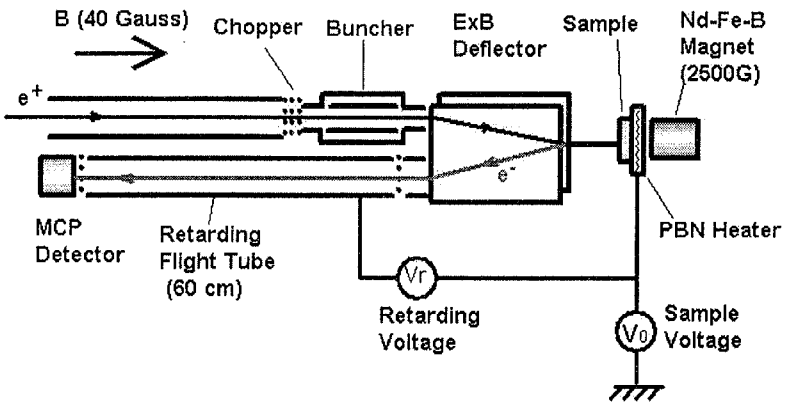


Fig.2 TOF-PAES apparatus.

other method, which use a time-of-flight technique with ExB deflection plates as shown in Fig.2 [7,8]. Using the TOF technique, we can measure PAES spectra with higher detection efficiency than that of the cylindrical mirror analyzer system.

Figure 3 shows an example of PAES spectra of oxygen adsorption on Si (111) surface. After the O_2 exposure of 1 L (1 L=10^{-6} Torr s), we found the decay of the O-KLL peak intensity. This result demonstrates that the TOF-PAES can be used for real-time observations of surface reactions. We applied this technique to the study of the initial stage of oxidation of Si surfaces, and found that PAES can detect a metastable adsorption state [9].

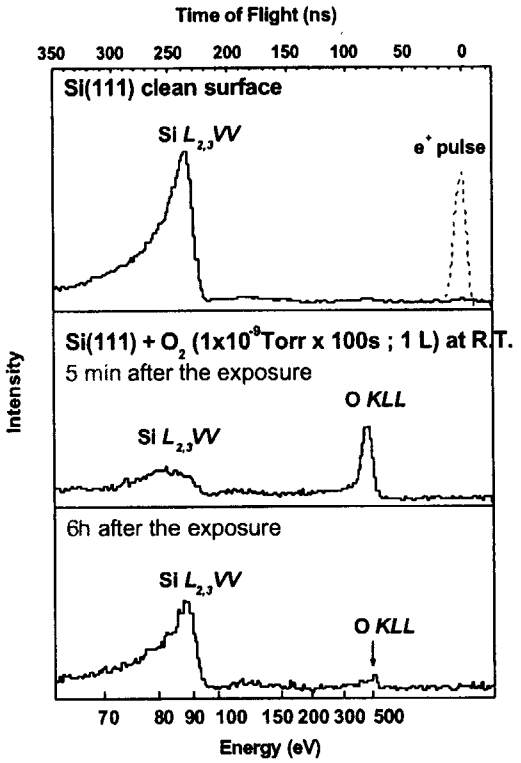


Fig. 3. TOF-PAES measurements for oxygen adsorption on Si(111).

4. Positron Lifetime Spectroscopy with a Variable Energy Positron Beam

Positron annihilation lifetime spectroscopy (PALS) is known to be sensitive to microstructural defects in solids because of the high sensitivity of positrons to the changes in local electron density. In many materials, a clear relationship between the positron lifetime and the size of the vacancy-type defect has been established [10]. Recent advances in generation and control of slow positrons enable us to generate variable-energy pulsed positron beams for positron annihilation lifetime measurements to study defects or free volumes in thin films, near surface regions, and surfaces [3,11]. By the use of an intense pulsed positron beam, we can measure PALS spectra with high count rate (5k-15k cps).

In Figure 4, an example of PALS experiments is shown. For future high-speed microelectronic devices, copper interconnection with low dielectric constant (low-k) interlayer films is required to decrease RC (R: interconnect resistance, C: interlayer dielectric capacitance) delay. Recently, porous SiO_2 and silica-based films are of great interest for low-k films. Since Ps formation occurs with high probability and the o-Ps annihilate via pick-off process in SiO_2-based materials, positron annihilation spectroscopy (especially PALS) gives useful information on the size of the pores. Figure 4 shows the PALS spectra for plasma enhanced chemical vapor deposition (PECVD) grown low-k films with a source gas of hexamethyldisiloxane (HMDSO, $(CH_3)_3SiOSi(CH_3)_3$) under different LF(380 kHz) powers, at an incident energy of 4 keV [12]. The lifetime of the long-lived o-Ps component strongly depends on the LF power. The average cavity volume calculated from the distribution of Fig.4 ranges from 0.33 nm^3 to 1.05 nm^3. There is apparent correlation between the k-value (2.66-4.13) and the pore size [12].

Figure 5 shows another example of PALS experiments. The sample is a dielectric coated multilayer mirror for ultra-violet (λ=350 nm) free electron laser (UV-FEL) experiments [13]. The mirror has alternating dielectric (Ta_2O_5/SiO_2) layers of λ/4 thickness with a λ/2-thick SiO_2 layer on top for surface protection. The initial loss of the new mirror was observed to be 250 ppm at the optimized wavelength of 350 nm. The sample was exposed to undulator radiation of 3.5 mAh at room temperature in an electron storage ring. Then, these mirrors were exposed to RF induced O_2 plasma to remove carbon at the surface. Finally, the samples were annealed for 180 min at 230°C. In the PALS spectra, a long-lived o-Ps component of ~1.5 ns was observed in low energy region corresponding to the first amorphous SiO_2 layer as well as in high energy region corresponding to the SiO_2 substrate. As shown in Fig. 5, the long-lived component intensity I_L strongly depends on the exposure of the undulator radiation and annealing.

After the irradiation of undulator radiation, the loss in the mirror increased from 250 ppm to 3849 ppm. After the O_2 plasma treatment, no significant change was observed in the long-lived component while the loss in the mirror was restored to 802 ppm. This restoration is due to carbon removal from the surface by O_2 plasma. After 230°C annealing, the intensity of the long-lived component was mostly restored to that of the initial sample, and the loss in the mirror was also restored to 297 ppm. These results revealed that bond-breaking type defects relating to the degradation of the mirror are created at weak bonds, e.g. Si-O-H, oxygen vacancies, and/or peroxy linkages, in the SiO_2 layer.

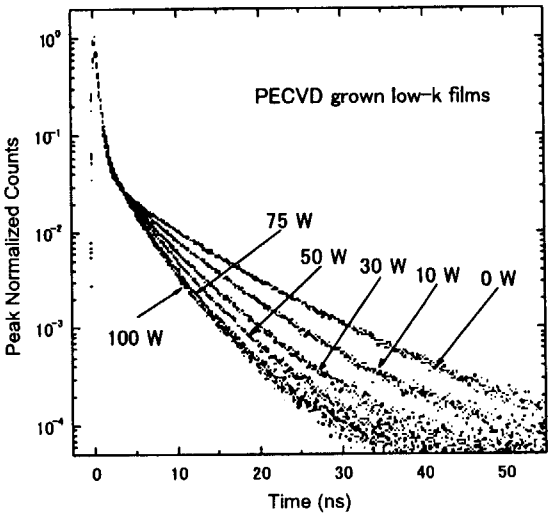


Fig 4. PALS spectra of double-frequency PECVD grown low-k films under different LF powers.

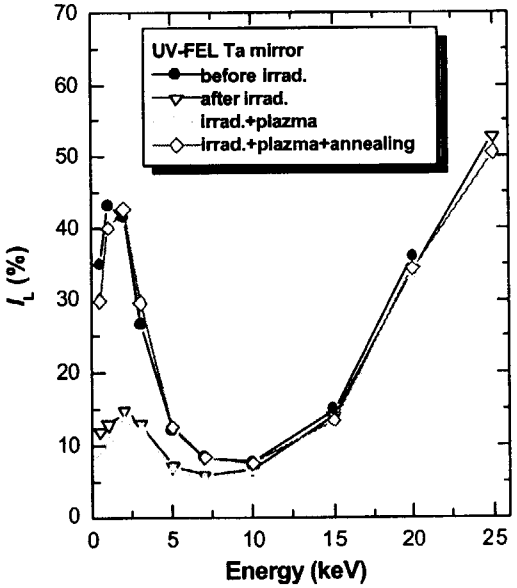


Fig. 5. The intensity of long-lived component for Ta_2O_5/SiO_2 dielectric mirror.

5. Age-Momentum Spectroscopy with a Variable Energy Positron Beam

Correlated measurements of the positron lifetime and of the Doppler shifts of annihilation radiation (age-momentum correlation, AMOC) are known to provide more detailed information than individual measurements. Recently, we have developed an AMOC apparatus for the intense pulsed slow positron beam [14].

Figure 6 shows an example of AMOC experiments. The sample is a thermally grown SiO_2 thin film on crystalline Si. The S parameter as a function of annihilation time at the positron incident energy of 2 keV is shown in Fig.6. The S parameter in the small age region (<0.5 ns) is significantly larger than that in the large age region. The result of the positron lifetime analysis shows that there exists a high intensity (60%) of long-lived component, which can be attributed to ortho positronium. The large S parameter in small ages indicates the self-annihilation of para-positronium, whereas the small S parameter at long ages is dominated by the pick-off annihilation of positrons in the ortho positronium. As can be seen in Fig.6, the S(t) curve of 2 keV is almost flat after ~0.5 ns, suggesting that the momentum distribution of o-Ps is almost the same as that of free positron annihilation. This suggests that both o-Ps atoms and free positrons annihilate with the same electrons, i.e. predominantly annihilate with electrons of oxygen in the Si-O network because oxygen is dominant at the first layer of the micro-void wall.

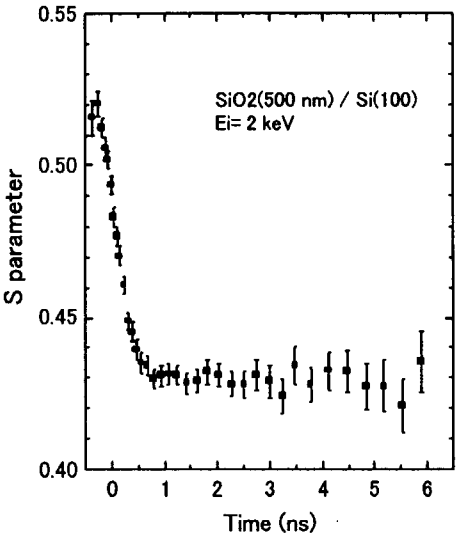


Fig. 6. S parameter as a function of annihilation time obtained by the AMOC apparatus.

6. Conclusion

We discussed positron-annihilation-induced Auger electron spectroscopy, positron annihilation lifetime spectroscopy, and age-momentum correlation spectroscopy with an intense pulsed positron beam. Several experimental results on surfaces and near surface regions demonstrate their extremely high sensitivity to surface impurities on surfaces and defects in near surface regions. These measurements will be quite useful for characterization of high performance functional materials.

References

[1] T. Akahane, T. Chiba, N. Shiotani, S. Tanigawa, T. Mikado, R. Suzuki, M. Chiwaki, T. Yamazaki and T. Tomimasu: Appl. Phys. A **51**, 146 (1990).

[2] R. Suzuki, T. Mikado, M. Chiwaki, H. Ohgaki, and T. Yamazaki: Appl. Surf. Sci. **85**, 87 (1995).

[3] R. Suzuki, Y. Kobayashi, T. Mikado, H. Ohgaki, M. Chiwaki, T. Yamasaki and T. Tomimasu: Jpn. J. Appl. Phys. **30**, L532 (1991).

[4] A. Weiss, R. Mayer, M. Jibaly, C. Lei, D. Mehl, and K.G. Lynn: Phys. Rev. Lett. **61**, 2245 (1988).

[5] C. Lei, D. Mehl, A.R. Koymen, F. Gotwald, M. Jibaly and A. Weiss: Rev. Sci. Instrum. **60**, 3656 (1989).
[6] H.Q. Zhou, S. Yang, E.S. Jung, and A.H. Weiss: Materials Science Forum **175-178**, 255 (1995).
[7] R. Suzuki, T. Ohdaira, T. Mikado, H. Ohgaki, M. Chiwaki, and T. Yamazaki: Appl. Surf. Sci. **100/101**, 297 (1996).
[8] T. Ohdaira, R. Suzuki, T. Mikado, T. Yamazaki: J. Electron Spectroscopy and Related Phenomena **88-91**, 677 (1998)
[9] T. Ohdaira, R. Suzuki, T. Mikado: Appl. Surf. Sci. **149**, 260 (1999).
[10] Dannefaer: Positron Annihilation, eds. L. Dorikens-Vanpraet, M. Dorikens and D. Segers (World Scientific, Singapore, 1989) p. 86.
[11] D. Schödlbauer, P. Sperr, G. Kögel and W. Triftshäuser: Nucl. Instrum. & Methods. B **34**, 258 (1988).
[12] R. Suzuki、T. Ohdaira、Y. Shioya, T. Ishimaru, Jpn. J. Appl. Phys. **40**, L414, (2001).
[13] R. Suzuki, T. Ohdaira, K. Yamada, T. Yamazaki, N. Sei, T. Mikado, T. Noguchi, H. Ohgaki, S. Sugiyama, M. Chiwaki, T. Shimizu, M. Kawai, M. Yokoyama, S. Hamada, K. Saeki, N. Nishimura, T. Tomimasu J. Radioanalytical & Nucl. Chem. **211**, 47 (1996).
[14] R. Suzuki, T. Ohdaira, T. Mikado, G. Venugopal Rao: Mater. Sci. Forum, **363-365**, 661 (2001).

JP0350262

1.7.2 ULTRA-HIGH TEMPERATURE OXIDATION BEHAVIOR OF CHEMICAL VAPOR DEPOSITED SILICON CARBIDE LAYERS

Takashi Goto
Institute for Materials Research, Tohoku University
2-1-1 Katahira, Aoba-ku, Sendai 980-8577, Japan

Abstract

The active oxidation, passive oxidation and bubble formation of CVD SiC were studied in O_2 and CO_2 at temperatures from 1650 to 2000K. The active oxidation rates in O_2 increased with increasing oxygen partial pressure (P_{O2}); however, those in CO_2 showed the maxima at specific P_{O2}. The passive oxidation kinetics in O_2 were either linear-parabolic or parabolic depending on temperature and P_{O2}, whereas that in CO_2 was always parabolic. The activation energies for the parabolic oxidation in O_2 and CO_2 were 210 and 150kJ/mol, respectively, suggesting different rate-determining process between these atmospheres. The bubble formation was controlled by temperature and P_{O2} being independent of oxidant gas species

Keywords: active oxidation, passive oxidation, bubble formation, parabolic, linear-parabolic, CO_2, O_2, CVD, SiC

1. Introduction

Silicon carbide (SiC) has been widely studied because of potential as high temperature structural materials, due to excellent high-temperature mechanical properties and oxidation resistance [1]. The oxidation behavior of SiC has been investigated using mainly sintered bodies. Since the oxidation of SiC is strongly affected by impurity or additives, highly pure and dense specimens such as CVD SiC should be used to understand the intrinsic oxidation behavior. On the other hand, CVD SiC is also used for coatings such as a nose cone of space vehicle and combustion chambers. Therefore, it is practically important to study the oxidation of CVD SiC in wide-ranged oxygen partial pressures at high temperatures.

The oxidation behavior of SiC can be classified into three features, i.e., active oxidation, passive oxidation and bubble formation. Many reports have been published on the passive oxidation of SiC mainly in O_2 [1]. A few papers report the oxidation of SiC in CO_2 [2-4]; however, the oxidation kinetics have not been investigated in detail. The bubble formation is an important issue to use SiC at extremely high temperatures. Although several papers have dealt with this phenomenon briefly [5,6], no research on the bubble formation has been conducted in CO_2 atmosphere.

In this paper, these three distinct oxidation behaviors have been studied by using CVD SiC in CO_2 and O_2 atmospheres at high temperatures from 1600 to 2000K.

*Corresponding author: Tel.: +81-22-215-2105
E-mail address: goto@imr.edu

2. Experimental

Yellow-colored translucent CVD SiC plates were used as specimens. The impurity level is ppb according to the analysis of manufactures, and (111) plane is strongly oriented to the surface. The specimens were cut to a disk with 10 mm in diameter, and were mirror-polished. An electric furnace with cubic zirconia heaters was used to increase the temperature up to 2473K. The mass changes were continuously monitored by an electro-balance. A zirconia wire with a hook was used to hold the specimen in the furnace. The specimens were heated in a flowing Ar gas. At a specific temperature, oxidant gases (i.e., O_2-Ar, CO-CO_2 and CO_2-Ar gases) were introduced in the furnace. Oxygen partial pressure was controlled by changing the gas mixing ratios. CO_2 gas dissociates into CO and O_2 at high temperatures. The oxygen partial pressure (P_{O2}) in CO_2 containing atmosphere was calculated from the thermodynamic data of CO_2-CO-O_2 system.

The structure of surface oxide layer was investigated by an X-ray diffractometer (XRD). The surface and cross-section of the specimen after the oxidation were observed by a scanning electron microscope (SEM) and an optical microscope.

3. Results and discussion

3.1 Active oxidation

The mass loss due to active oxidation became significant with increasing P_{O2}. The active oxidation rates in O_2-Ar (k_a) were independent of time. The values of k_a increased linearly with P_{O2}, and were proportional to nearly $V^{1/2}$ (V; gas velocity) [7]. These suggest that the inward diffusion of oxidant in a gas boundary layer may be rate-controlling for the active oxidation. An abrupt change from the mass loss (active oxidation) to a small mass gain (passive oxidation) appeared at P_{O2}= 160Pa at 1873K for example, which is called as active-passive transition oxygen partial pressure (P_{O2}^t).

Wagner [8] proposed a model to explains the transition behavior for Si. By applying this model, the theoretical P_{O2}^t value may be given as eq.(1).

$$P_{O2}^t = 1/2(D_{SiO}/D_{O2})^{1/2} P_{SiO}^{eq} \quad (1)$$

where P_{SiO}^{eq} is the equilibrium vapor pressure of SiO(g), D_x is a diffusion constant of x-species in the gas boundary layer. The D_{SiO}/D_{O2} ratio could be assumed as 0.8 [9]. There are several probable thermal equilibria to calculate the P_{SiO}^{eq}

Figure 1 summarizes the reported P_{O2}^t for single crystal, sintered and CVD SiC in O_2-Ar atmospheres [9-13]. The temperature dependence of experimental P_{O2}^t was in agreement with the calculated values from the Wagner model. The Wagner model could be fundamentally

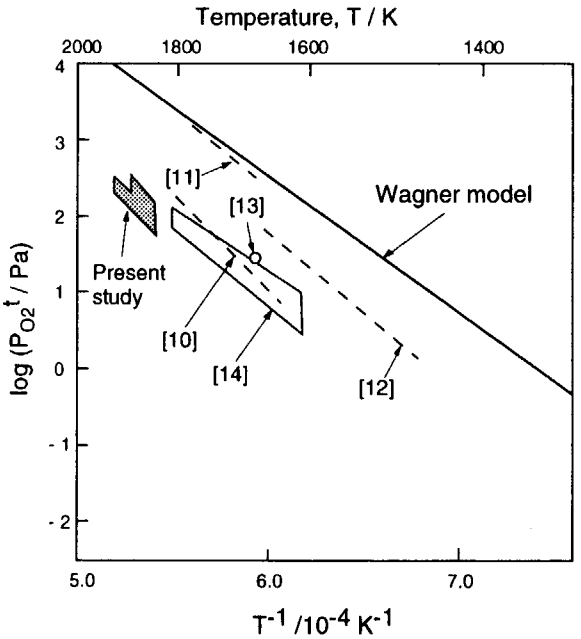


Fig. 1 Effect of temperature on active-passive transition oxygen partial pressure (P_{O2}^t) for sintered, single crystal and CVD SiC.

suitable to explain the transition behavior; however the experimental values were 1/10 to 1/100 times smaller than the calculated values. This model contains too simplified assumptions, and the constants used in the calculation may not be exactly precise at high temperatures

The active oxidation behavior of CVD SiC in CO-CO_2 atmosphere is depicted Fig. 2. The active oxidation rate in CO-CO_2 (k_{CO}) showed maxima at P_{CO2}/P_{CO}= 10^{-2} to 10^{-3} [14]. In the P_{CO2}/P_{CO} region lower than the maxima, free carbon layer was found on the SiC surface. In the P_{CO2}/P_{CO} region higher than the maxima, granular or porous layer of SiO_2 was observed on the SiC surface. The k_{CO} values in the P_{CO2}/P_{CO} region higher than the maxima decreased with increasing P_{CO2}/P_{CO}. This behavior is a contrast to that in O_2-Ar atmosphere. The k_{CO} values decreased with increasing P_{CO2}/P_{CO}, and there was almost no mass change at P_{CO2}/P_{CO}= 4 at 1873K, where the vaporization and formation of SiO_2 might have proceeded at almost the same rates. If the active-passive transition is defined as the condition for "a small mass gain", the transition P_{CO2}/P_{CO} value would be 4 at 1873K. On the other hand, if it is defined as the condition for "SiO_2 formation", the transition P_{CO2}/P_{CO} would be 10^{-2} to 10^{-1}.

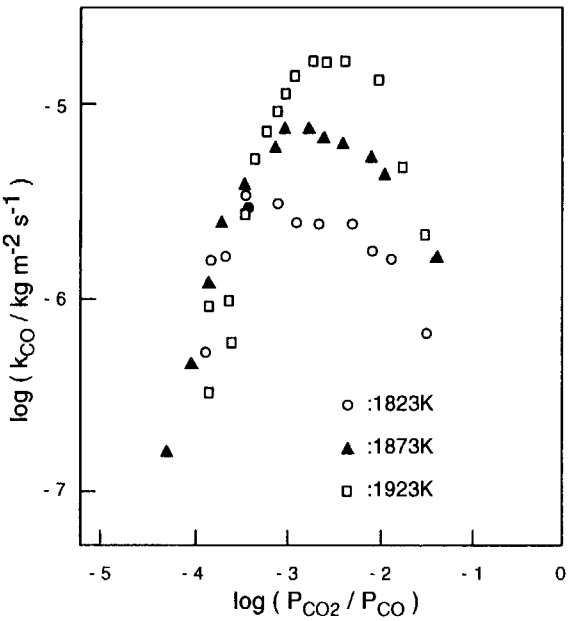


Fig. 2 Effect of P_{CO2}/P_{CO} on active oxidation rates for CVD SiC in CO-CO_2.

Heuer and Lou [15] have explained the active-passive transition of SiC and Si_3N_4 by using so-called volatility diagram. Figure 3 demonstrates the calculated volatility diagram for Si-C-O system at 1873K, in which the equilibrium vapor pressures of SiO(g) or SiO_2(g) and the stable solid phases are indicated as a function of P_{O2} and P_{CO2}/P_{CO} ratio. The transition should occur at P_{O2} more than "isomolar line, Im" (the line of P_{SiO}= $2P_{O2}$) in O_2-Ar. Since the O_2 gas comes from the ambient atmosphere, the P_{SiO} should be less than $2P_{O2}$. The experimental P_{O2}^{t} value (E_O) was more than the Im line and the calculated value from the Wagner model (W_O). On the other hand, in CO-CO_2, the transition P_{O2} should be more than "Isobaric (Ib) line" (the line of P_{SiO}= P_{CO}). The calculated P_{CO2}/P_{CO} from the Wagner model (W_{CO}) and experimental value (E_{CO}) are indicated in Fig. 3. At P_{CO2}/P_{CO}= 10^{-2} to 10^{-1} the decomposition and formation of SiO_2 would

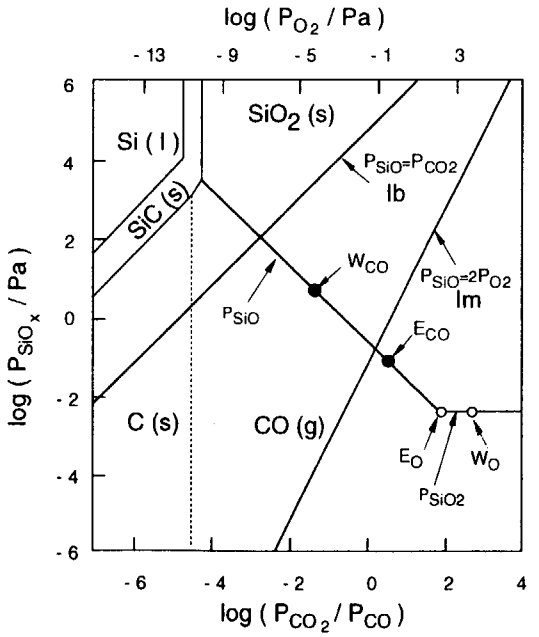


Fig. 3 Effect of P_{CO2}/P_{CO} on active oxidation rates for CVD SiC in CO-CO_2.

have proceeded simultaneously. The E_{CO} would mean the condition where the decomposition and the formation of SiO_2 occur at the same rate. The Wagner model does not take into account the decomposition of SiO_2. The model simply predicts the lowest P_{CO2}/P_{CO} condition for the SiO_2 formation. The experimental P_{CO2}/P_{CO} for the SiO_2 formation was almost in agreement with the W_{CO} value.

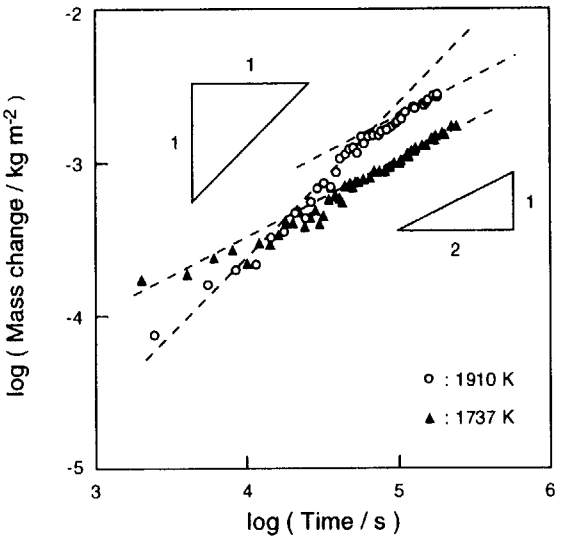


Fig. 4 Time dependence of mass gain in O_2 (P_{O2}=0.1MPa) at 1737 and 1910K for CVD SiC in logarithmic scales.

3.2 Passive oxidation

Opila and Nguyen [2] have studied the oxidation of CVD SiC in CO_2 at temperatures from 1473 to 1673K by thermogravimetry; however they have not detect significant mass change. Fitzer and Ebi [3] reported the parabolic mass gain in CO_2 at 1673K, but at 1773K the parabolic mass gain was observed initially, and sharp mass loss in later periods. Antill and Warburton [4] reported that the oxidation rates in CO_2 were 1/20 times slower than those in O_2 at temperatures from 1273 to 1573K; however the mass change curves were not presented.

We have measured the passive oxidation behavior of high purity CVD SiC in O_2 and CO_2. Figure 4 shows the relationship between time and mass gain in pure O_2 in both logarithmic scale. The gradient of the line was half at 1773K indicating parabolic kinetics. At 1910K, on the other hand, the gradient was one in the initial stage up to 60ks indicating linear kinetics, then the gradient changed to half indicating parabolic kinetics. This behavior is commonly called as "linear-parabolic" kinetics. In O_2, the oxidation kinetics was either parabolic or linear - parabolic depending on temperature and P_{O2}, whereas it was always parabolic in CO_2. Figure 5 summarizes the behavior of oxidation kinetics as functions of temperature and P_{O2}. The boundary between linear-parabolic and parabolic kinetics was independent of gas species, but depended on P_{O2} and temperature.

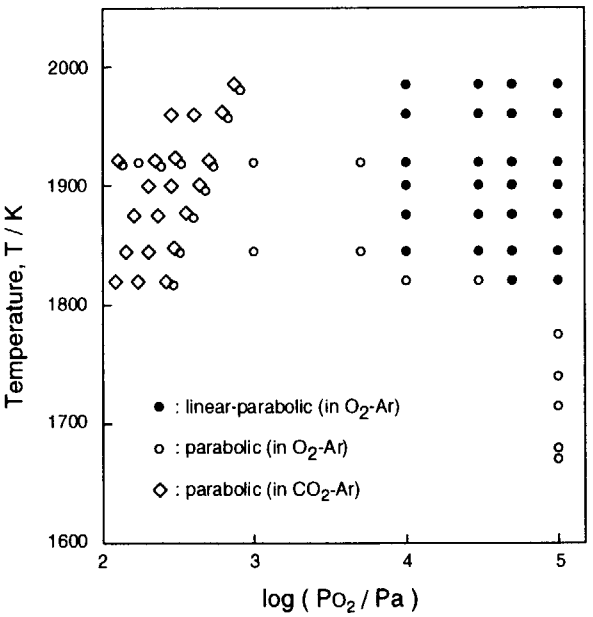


Fig. 5 Effects of temperature and P_{O2} on the oxidation behavior for CVD SiC in O_2-Ar and CO_2-Ar.

In both CO_2 and O_2 atmospheres, the relationship between k_p and P_{O2} was represented as $k_p \propto P_{O2}^{n}$, where n= 0.08 to 0.18 in O_2-Ar, and n= 0.37 to 0.53 in CO_2-Ar at temperatures from 1875 and 1985K. The weak P_{O2} dependence in O_2-Ar

suggests that the parabolic oxidation may be controlled by the outward diffusion of oxide vacancy or CO molecule. The strong P_{O2} dependence in CO_2-Ar, on the other hand, may be caused of inward diffusion of oxidant. Since the molecule size of CO_2 (0.3nm in dia.) is bigger than oxide ion, O^{2-} (0.14nm in dia.), the diffusion of interstitial O^{2-} may be rate-controlling in CO_2-Ar.

Figure 6 represents the Arhhenius plot of k_p obtained in CO_2 and O_2 atmospheres. The activation energy in pure CO_2 (290kJ/mol) was greater than that in pure O_2 (210kJ/mol). However, if the oxidant in CO_2 is not CO_2 molecule but dissociate oxygen, the k_p values should be compared under the same P_{O2}. The k_p values at P_{O2} 260Pa in O_2-Ar and CO_2-Ar are also plotted in Fig. 11. The activation energy at P_{O2} 260Pa in O_2-Ar is 210kJ/mol, which is in agreement with that in pure O_2. On the other hand, the activation energy at P_{O2}= 260Pa in CO_2-Ar is 150kJ/mol, which is much smaller than that in pure CO_2. The difference of activation energy between O_2 (210kJ/mol) and CO_2 (150kJ/mol) suggests the different rate-controlling step between these atmospheres. Figure 7 summarizes the k_p values for single crystal and CVD SiC in O_2 [16-20]. The activation energy values have ranged from 120 to 400kJ/mol in the literature. There is a general trend that the higher temperature the greater the activation energy. It is commonly accepted that the relatively low activation energy of 80 to 120kJ/mol may correspond the permeation of oxygen molecule in amorphous silica, and the high activation energy of 230 to 400kJ/mol may suggest the diffusion of oxide ion in amorphous silica or cristobarite [1]. The activation energy value obtained in the present work (210kJ/mol in O_2) is close to value for the vacancy diffusion of oxide ion.

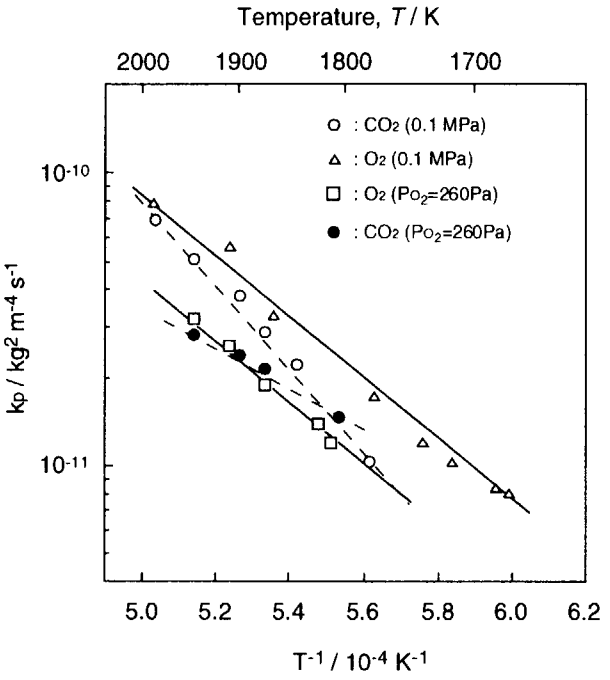


Fig. 6 Effect temperature on the parabolic rate constants (k_p) in O_2-Ar and CO_2-Ar.

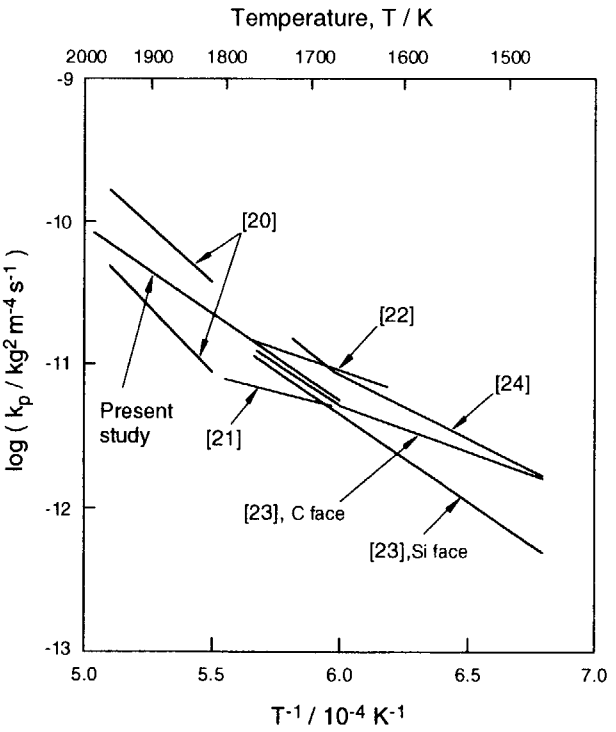


Fig. 7 Comparison of parabolic rate constants (k_p) for single crystalline and CVD SiC in literatures with those of present study

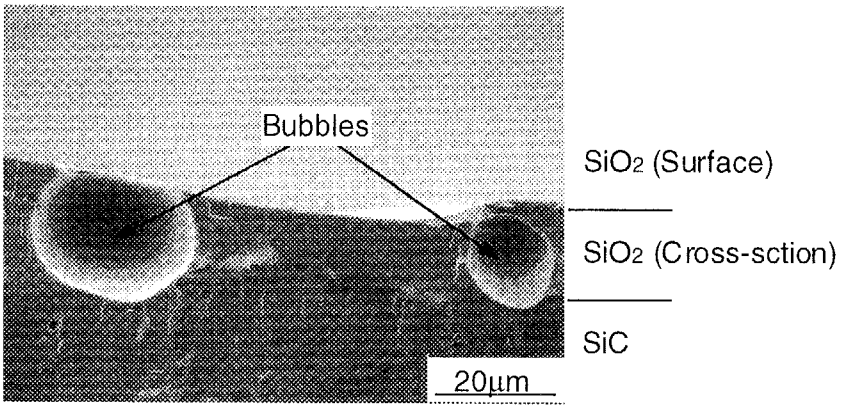


Fig. 8 Cross-section of silica layer with bubbles formed at 1990K in O_2-Ar (P_{O2}=100kPa).

3.3 Bubble formation

A few papers have reported the bubble formation at less than 1773K in hot-pressed (HP) SiC [5,6]. Since HP SiC bodies are added with metal oxides such as Al_2O_3, silicate phases are contained in the oxide layer. The melting point of pure silica is generally higher than that of silicates, thus the bubble formation temperature of CVD SiC must be higher than that of impure SiC sintered bodies. Schirocky et al.[5] and Jacobson [21] reported the bubble formation at 1973-2023K and at 2073K for CVD SiC, respectively. However, no paper reported the effect of gas species or P_{O2} on the bubble formation of CVD SiC.

Figure 8 depicts the cross-section of bubbles formed at 1990K in O_2-Ar (P_{O2}= 100kPa). The thermogravimetry is advantageous to detect the bubble formation because mass change curves indicate characteristic zigzag-shapes due to the sequence of bubble-formation and -rupture. Figure 9 demonstrates a transition condition from parabolic to bubble formation at 1965K and P_{O2}= 700Pa, where the significant zig-zag mass change curve was overlapped with the parabolic mass gain. Figure 10 depicts the effects of temperature and P_{O2} on the boundary between passive and bubble formation. The boundary changed depending on temperature and P_{O2}, but being independent of the gas species (i.e., O_2 or CO_2). At P_{O2}> 5kPa, the transition from linear-parabolic to bubble formation took place at around 1985K. At P_{O2}< 5kPa, the transition temperature was broader and decreased with decreasing P_{O2}. The bubbles should form when the total pressure (P_{tot}) inside the bubbles exceeds at least the ambient gas pressure (0.1MPa). Since CO gas accumulates at the SiC/SiO_2 interface, the carbon activity (a_c) may increase and finally reach to unity [22]. Figure 11 demonstrates the temperature dependence of P_{tot} in the bubble for the following two cases. The one is that carbon-saturated SiC (a_c=1) reacts with SiO_2, and the other is that the stoichiometric reaction of eq.

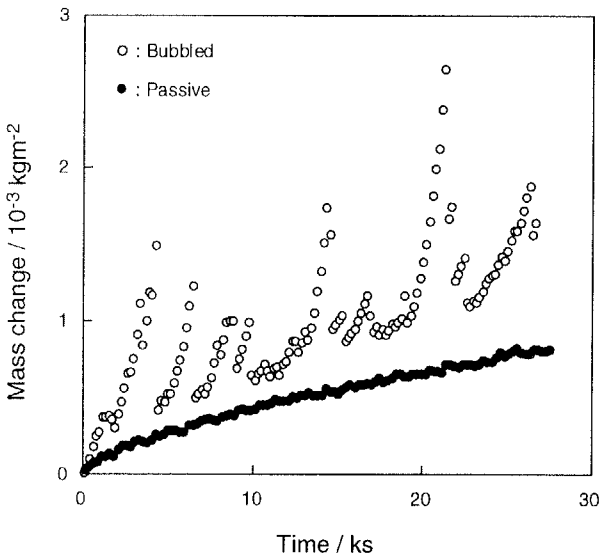


Fig. 9 Time dependence of mass change at 1965K and P_{O2}=700Pa.

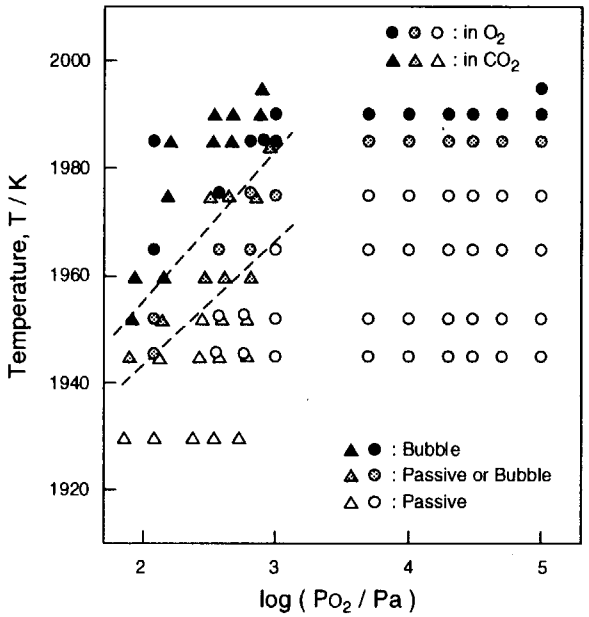


Fig.10 Effects of temperature and P_{O2} on the boundary between passive oxidation and bubble formation in O_2-Ar and CO_2-Ar atmosphere.

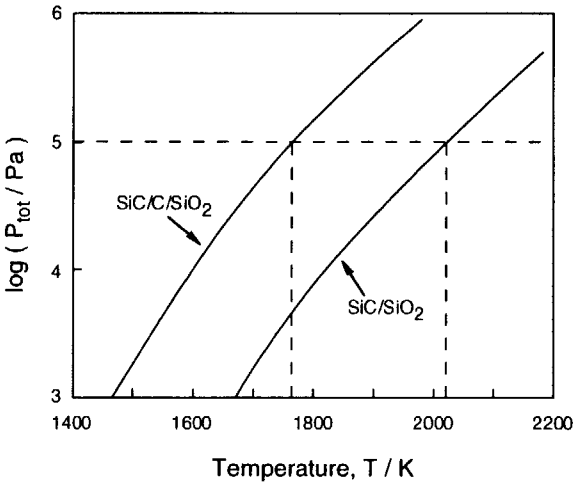


Fig.11 Temperature dependence of total pressure inside bubbles (P_{tot}) for the carbon saturated and the stoichiometric conditions.

(3) proceeds at the SiC/SiO_2 interface.

$$SiC(s) + 2SiO_2(s) = 3\,SiO(g) + CO(g) \quad (3)$$

The transition temperature at P_{O2}> 5kPa was about 1985K. This may suggest the slight increase of a_C at the SiC/SiO_2 interface. At P_{O2}< 5kPa, the transition temperature decreased with decreasing P_{O2}. The CO to CO_2 ratio calculated from the CO_2-CO-O_2 equilibrium should increase with decreasing P_{O2} in CO_2-Ar. The increase of CO partial pressure in the ambient atmosphere might increase the a_c significantly at the SiC/SiO_2 interface. This might have decreased the bubble formation temperature.

4. Summary

The transition from active to passive oxidation in O_2-Ar was clearly observed. The active oxidation rates in O_2-Ar increased with increasing P_{O2}. The active oxidation rates in CO-CO_2 (k_{CO}) showed the maxima at about $P_{CO2}/P_{CO} = 10^{-2}$. The k_{CO} values decreased with increasing P_{CO2}/P_{CO}, and the active oxidation gradually changed to the passive oxidation. The active-passive transition in both atmospheres could be explained by the Wagner model and the volatility diagram.

The passive oxidation was classified into linear-parabolic and parabolic behavior depending on temperature and P_{O2}. In O_2-Ar, the parabolic rate constant (k_p) values were almost independent of P_{O2}, and the activation energy for the parabolic oxidation was 210kJ/mol. In CO_2-Ar, the k_p values increased significantly with increasing P_{O2}, and the activation energy was 150kJ/mol. The oxidation kinetics could be different between these atmospheres.

In much higher temperature region, the bubble formation was observed in O_2-Ar and CO_2-Ar. The transition from passive oxidation to bubble formation depended on P_{O2} and temperature. The linear and parabolic oxidation rates were accelerated by the bubble formation.

References

[1] T. Narushima, T. Goto, T. Hirai and Y. Iguchi, Mater. Trans. JIM **38**, 821 (1997).

[2] E. Opila and Q. N. J. Nguyen, J. Am. Ceram. Soc. **81**, 1949 (1998).

[3] E. Fitzer and R. Ebi, *Silicon Carbide 1973* (University of South Carolina Press, USA 1974), 320.

[4] J. E. Antill and J. B. Warburton, AGARD CP-52, 10 (1970).

[5] G. H. Schroky, T. E. Mitchell and A. H. Heuer, Adv. Ceram. Mater. **2**, 137 (1987).

[6] D. M. Mieskowski, T. E. Mitchell. and A. H. Heuer, Comm. Am. Ceram. Soc., c-17 (1984).

[7] T. Narushima, T. Goto, Y. Iguchi and T. Hirai, J. Am. Ceram. Soc. **74**, 2583 (1991).

[8] C. Wagner, J. Appl. Phys. **29**, 1259 (1958).

[9] J. W. Hinze and H. C. Graham, J. Electrochem. Soc. **123**, 1066 (1976).

[10] M. Balat, G. Flamant, G. Male and G. Pichelin, J. Mater. Sci. **27**, 697 (1992).

[11] E. A. Gulbransen, K. F. Andrew and F. A. Brassart, J. Electrochem. Soc. **111**, 1311(1966).

[12] H. E. Kim and A. J. Moorhead, J. Am. Ceram. Soc. **73**, 1868 (1990).

[13] W. L. Vaughn and H. G. Maahs, J. Am. Ceram. Soc. **73**, 1540 (1990).

[14] T. Narushima, T. Goto, Y. Yokoyama, Y. Iguchi and T. Hirai, J. Am. Ceram. Soc. **76**, 2521 (1993).

[15] A. Heuer and V. L. K. Lou, J. Am. Ceram. Soc. **73**, 2785 (1990).

[16] T. Narushima, T. Goto and T. Hirai, J. Am. Ceram. Soc. **72**, 1386 (1989).

[17] G. H. Schiroky, R. J. Price and J. E. Sheehan, Rept. No. GA-A18696, GA Technologies (1986).

[18] L. U. J. T. Ogbuji and E. J. Opila, J. Electrochem. Soc. **142**, 925 (1995).

[19] Z. Zheng, R. E. Tressler and K. E. Spear, J. Electrochem. Soc. **137**, 854 (1990).

[20] J. A. Costello and R. E. Tressler, J. Am. Ceram. Soc. **69**, 674 (1986).

[21] N. S. Jacobson, J. Am. Ceram. Soc. **76**, 3 (1993).

[22] N. S. Jacobson, K. N. Lee and D. S. Fox, J. Am. Ceram. Soc. **75**, 1603 (1992).

JP0350263

1.7.3 STUDY OF NANOPOROUS STRCUTURE OF SPUTTER-DEPOSITED SILICON OXIDE THIN FILMS BY POSITRON ANNIHILAITION SPECTROSCOPY IN RELATION TO GAS BARRIER COATING

Y. Kobayashi*

National Institute of Advanced Industrial Science and Technology, Tsukuba, Ibaraki 305-8565, Japan

Abstract

Long-term radiation resistance of organic polymers in the presence of oxygen is strongly influenced by radiation-induced oxidation. We confirmed that the gas barrier coating of silicon oxide is able to effectively suppress radiation-induced oxidation of polypropylene and polyethylene. In the present work, nanoporosity of sputter-deposited silicon oxide films was studied by positron annihilation spectroscopy with a hope of gaining information pertinent to the development of high-performance gas barrier coating.

Keywords: gas barrier coating, pore characterization, positron annihilation.

1. Introduction

We have been concerned with gas barrier coatings of silicon oxide on polymers to improve long-term radiation-resistance of organic polymers in the presence of oxygen [1]. Degradation of polymers irradiated with γ-rays or UV light proceeds slowly through chemical reactions between free radicals produced by radiations and oxygen molecules permeated into the polymer. Formation of a gas barrier can reduce the oxygen permeation, thereby suppressing the oxidation and degradation of polymers subjected to radiations.

Experimental demonstration of the usefulness of silicon oxide coating in suppressing radiation-induced oxidation of polymers is given in Figs.1 and 2. On both top and bottom surfaces of 1 mm thick polyethylene and 3 mm thick polypropylene samples, silicon oxide films were deposited for a thickness of 180 nm by radio-frequency magnetron sputtering using SiO_2 as a target. The depth profiles of carbonyl groups measured by microscopic infrared absorption spectroscopy after prolonged γ-irradiation in air are shown in the figures. The γ-ray dose rate was 110 Gy/hr and accumulated total dose after approximately one-month irradiation was 100 kGy. The data for uncoated samples are shown with solid circles and those for the samples with silicon oxide coatings are shown with open circles. Larger amounts of carbonyl groups are observed in the center of uncoated polyethylene, indicating that the sample is highly oxidized after γ-irradiation in air. On the other hand, polyethylene with silicon oxide coating is oxidized only in the near-surface regions and the central part of the sample is little affected. In the case of polypropylene both the samples are less oxidized compared with polyethylene, but the effect of silicon oxide coating in suppressing radiation-induced oxidation is evident.

As we believe that proper control of open porosity is very important for developing high performance coatings, we characterized the nanoporous structure of silicon oxide films by

*Corresponding author. Tel/Fax: +81–298–61–4622.
E-mail address: y-kobayashi@aist.go.jp (Y. Kobayashi).

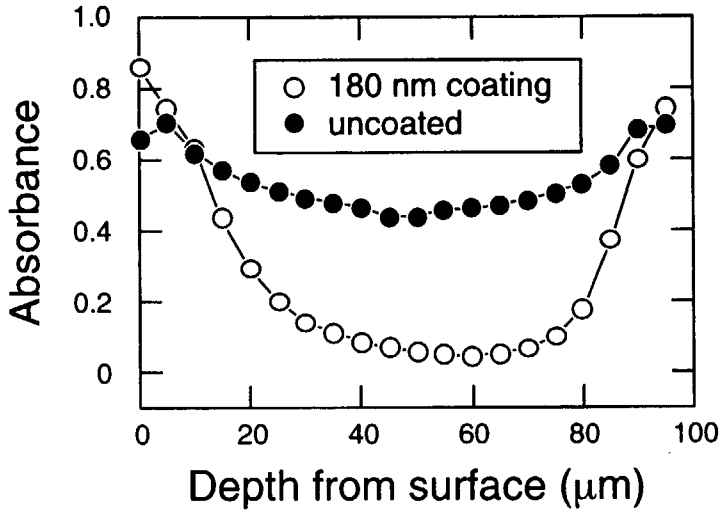


Figure 1. Depth profiles of carbonyl groups in γ-irradiated polyethylene.

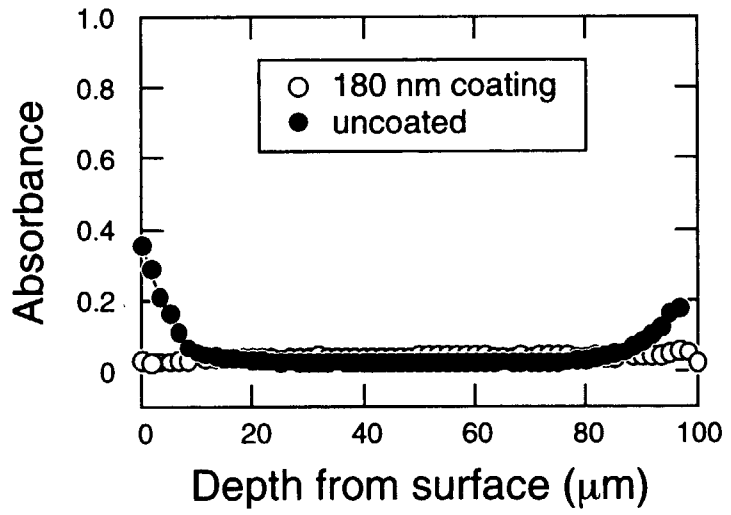


Figure 2. Depth profiles of carbonyl groups in γ-irradiated polypropylene.

Table I. Thickness and refractive index at 630 nm of uncapped silicon oxide films, sputter-deposited at different argon pressures.

Ar pressure (Pa)	Film thickness (nm)	Refractive index	$I_{3\gamma}$ (%) at 2–7 keV
0.1	807	1.47	0
0.25	1040	1.46	0.9
0.5	1092	1.43	5.4
1.0	962	1.39	14
1.5	782	1.38	16

positron annihilation spectroscopy. Two different techniques were used; positron annihilation γ-ray spectroscopy and positron annihilation lifetime spectroscopy. In free space, spin-parallel *ortho*-positronium (*o*-Ps) decays into 3γ-rays with a lifetime of 142 ns. When *o*-Ps is localized in a closed pore, 2γ pick-off annihilation, which occurs upon collision with the pore walls, acts as a competing decay process. This reduces the probability of decay by 3γ annihilation relative to that by 2γ annihilation, allowing the pore to be characterized by positron annihilation γ-ray spectroscopy. In addition, as the pore becomes smaller, the *o*-Ps lifetime decreases. Thus the pore dimensions can therefore be quantified by positron lifetime spectroscopy. There are several advantages of positron annihilation over other methods for nanopore characterization; it is nondestructive; it is sensitive to holes of 0.3–50 nm in size and it can detect isolated closed pores that are not accessible with molecular probes.

In the present study, pore connectivity and open porosity were evaluated from the fraction of *o*-Ps escaping from uncapped samples into vacuum, which was determined by positron annihilation γ-ray spectroscopy. Additional information on positronium (Ps) formation was obtained from Doppler broadening of 2γ annihilation photons. The characteristic pore size was estimated by measuring *o*-Ps lifetimes in capped films, with the help of an empirical correlation.

2. Experimental

Silicon oxide films were deposited on Si substrates at different argon pressures ranging from 0.1 to 1.5 Pa for 90 min, under stable argon plasma generated by a magnetron sputtering system (ANELVA L332S-HFS9) at a constant radio-frequency of 13.56 MHz and a discharge power of 450 W. The thickness and refractive index of the uncapped films, determined by spectroscopic ellipsometry, are listed in Table I. The presence of any voids, open or closed, reduces the refractive index, which then serves as a measure of total film porosity. The maximum total porosity in our films is estimated to be about 20 %. Positron annihilation γ-ray spectroscopy and positron annihilation lifetime spectroscopy were conducted with the systems described elsewhere [2,3].

3. Results and discussion

Figure 3 shows the absolute fraction of positron 3γ decay ($I_{3\gamma}$) of uncapped samples, determined from positron annihilation γ-ray spectra, as a function of incident positron energy

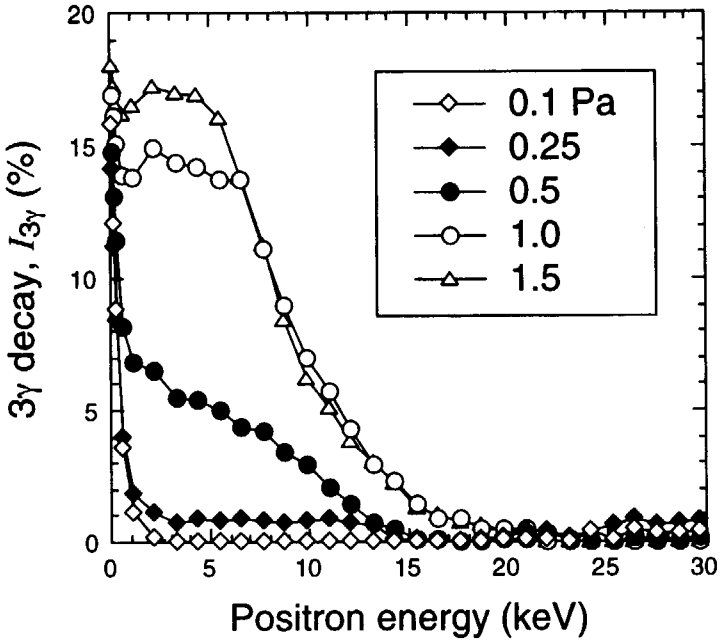


Figure 3. $I_{3\gamma}$ versus incident positron energy for uncapped samples.

(E) from 80 eV to 30 keV. In determining $I_{3\gamma}$, a sample of silica aerogel was used as a standard. Above 20 keV, no 3γ annihilation is observed for any of the samples studied, because the majority of the positrons annihilate in the Si substrate with no Ps formation. At lower positron energies, more positrons are implanted into the silicon oxide films and $I_{3\gamma}$ for the samples prepared at relatively high argon pressure, increases. $I_{3\gamma}$ in the film deposited at the lowest argon pressure of 0.1 Pa remains unchanged until E becomes as low as 1 keV. From Table I we see that $I_{3\gamma}$ at 2–7 keV is well correlated with the film refractive index, indicating a correlation between 3γ annihilation of o-Ps and total film porosity. As E is reduced from 1 keV, $I_{3\gamma}$ for all the samples increases rapidly and reaches about 15 % at 80 eV. The sharp increase of the 3γ annihilation fraction at $E < 1$ keV has been observed for nonporous silicon oxide and is due to the intrinsic decay of o-Ps, which is released from the near-surface region of the sample and annihilates in the sample chamber of the positron beam system.

Doppler broadening of 2γ annihilation photons was characterized by the S parameter, which is the fraction of γ-ray counts in the central part of the 0.511 MeV peak to the total counts contained in the whole peak. Figure 4 shows the incident positron energy dependence of the S parameter for samples prepared at different argon pressures. It is seen from the figure that the S parameters for the film prepared at 0.1 Pa are extremely low. Electron spin resonance (ESR) measurements showed that the film contains a larger amount of E' centers compared with films prepared at higher argon pressures (Fig.5). On the basis of this observation, we attribute the low values of the S parameter for the 0.1 Pa film to the inhibition of Ps formation by paramagnetic E' centers [4,5].

Positron lifetime spectroscopy for the uncapped films was conducted at a positron energy of 3.3 keV, so that the majority of positrons are implanted into the deposited film. The γ-ray energy window of a BaF_2 detector was set at 450–600 keV to monitor o-Ps pick-off anni-

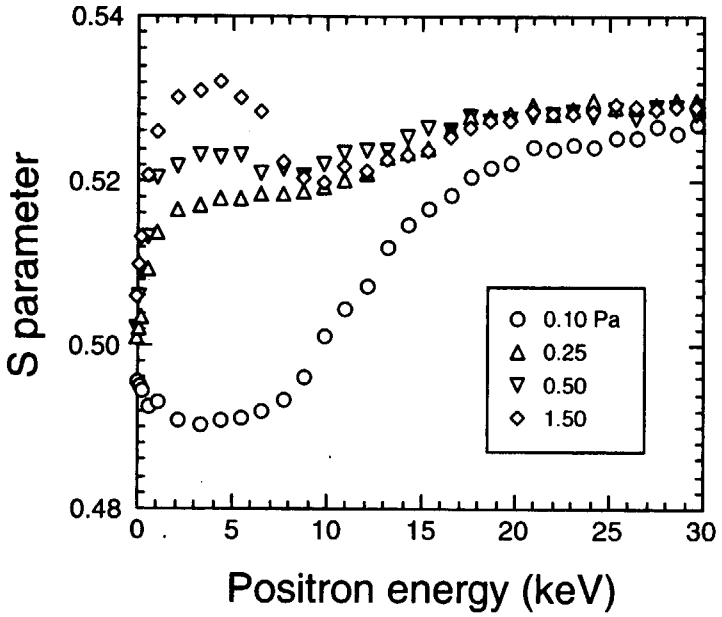


Figure 4. *S* versus incident positron energy for uncapped samples.

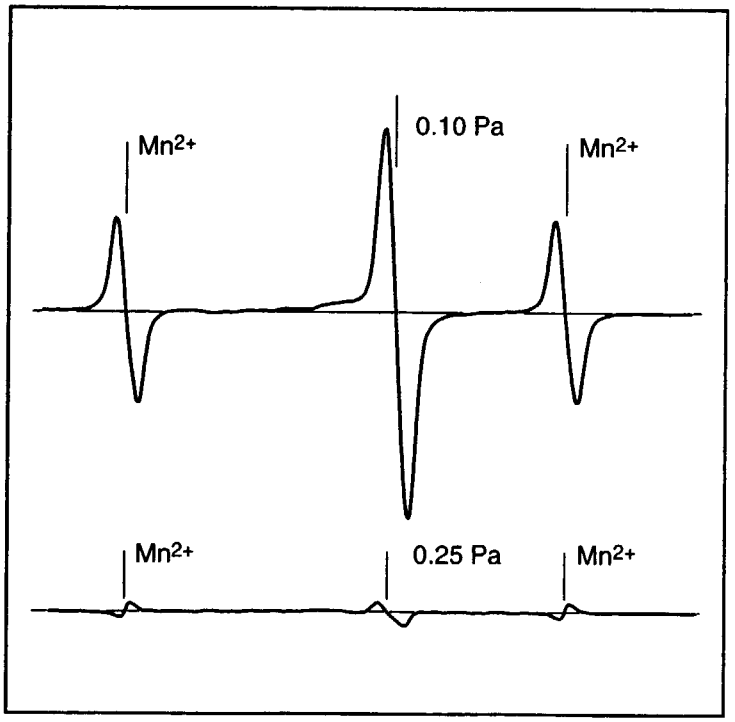


Figure 5. ESR spectra of sputter-deposited silicon oxide films prepared at argon pressures of 0.1 Pa and 0.25 Pa.

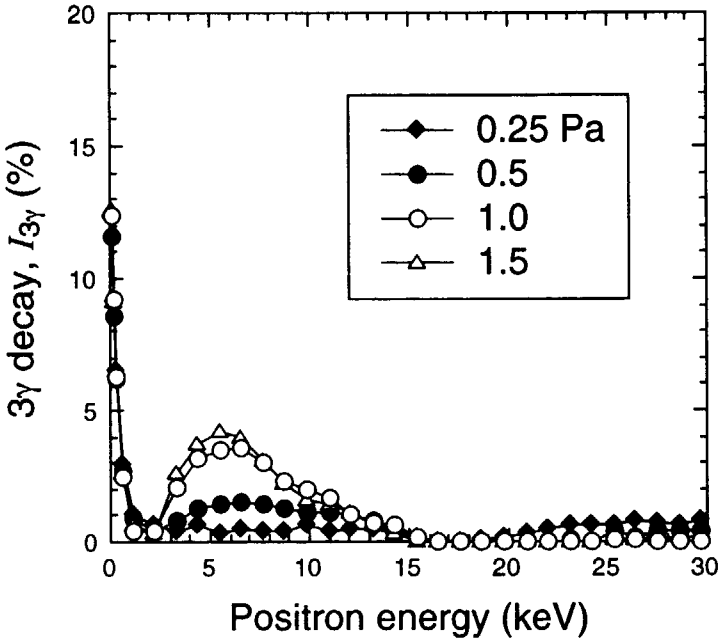


Figure 6. $I_{3\gamma}$ versus incident positron energy of capped samples.

hilation. The film prepared at the lowest argon pressure of 0.1 Pa showed two o-Ps components with lifetimes shorter than 5 ns. The contribution of such short-lived o-Ps to 3γ annihilation is negligible and the results are consistent with the low $I_{3\gamma}$ in Fig.3. For films prepared at higher argon pressures, longer-lived o-Ps with lifetimes up to 50 ns were observed. However, in light of the larger $I_{3\gamma}$ in Fig.3, the associated relative intensity was too small to conclude that all of the o-Ps atoms annihilated in the film.

$I_{3\gamma}$ of the capped samples is shown in Fig.6. The capping was done by sputter-deposition of 100 nm thick silicon oxide at an argon pressure of 0.1 Ps on top of films deposited at higher pressures for 90 min. The $I_{3\gamma}$ values of the capped films measured at E = 2–7 keV are much lower than those of the uncapped films. For example, $I_{3\gamma}$ of the capped 1.5 Pa film at 5.5 keV is only 4 %, whereas that of the uncapped films at 3.3 keV is as high as 17 %. These results show that films deposited at high argon pressures have open porosity, and a large fraction of o-Ps formed inside the film is able to diffuse back to the surface and escape there into vacuum, giving rise to high 3γ fraction.

Positron lifetime spectroscopy of the capped samples was conducted at 5.5 keV. Typical lifetime spectra are shown in Fig.7. The lifetime and intensity of long-lived o-Ps obtained by three-component analysis are listed in Table II. Both parameters substantially increase with increasing argon pressure from 0.25 to 1.0 Pa. Also included in Table II are characteristic pore sizes estimated from the o-Ps lifetime. To quantify the pore size over 1 nm in radius we used a simple empirical equation of Ito et al. [6], derived by extending the Tao-Eldrup relation for o-Ps trapped in a subnanometer-size hole. It is seen from Table II that the film deposited at 0.25 Pa has pores of 0.8 nm in radius. The pore size increases to 2.6 nm at 1.5 Pa. The variation of the pore size as a function of argon pressure is correlated with the variations of the refractive index and total film porosity (Table I).

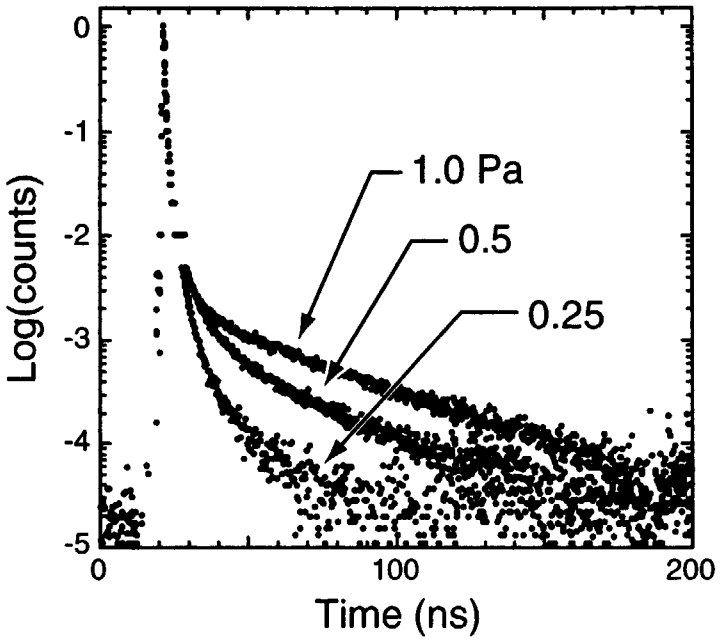


Figure 7. Background-subtracted positron lifetime spectra of capped films, prepared at argon pressures of 0.25, 0.5 and 1.0 Pa. Data were taken at a positron energy of 5.5 keV.

Table II. Lifetime parameters of long-lived *o*-Ps for capped silicon oxide films.

Ar pressure (Pa)	*o*-Ps lifetime (ns)	*o*-Ps intensity (%)	Pore radius (nm)
0.25	13.7	1.5	0.8
0.5	28.9	4.5	1.3
1.0	46.1	10.1	2.3
1.5	49.5	10.0	2.6

4. Conclusion

Thin silicon oxide films sputter-deposited at high argon pressures contain highly connected, open pores, whose average size is much larger than the molecular diameter of oxygen (0.375 nm). The film prepared at an argon pressure of 0.1 Pa contains a larger amount of paramagnetic E' centers compared with the films prepared at higher pressures. We hope that the results obtained in the present work are useful for the future development of high-performance gas barrier coatings.

Acknowledgment

The study was conducted in collaboration with W. Zheng, T. B. Chang, K. Hirata, K. Ito, R. Suzuki and T. Ohdaira at the National Institute of Advanced Industrial Science and Technology, Japan.

References

[1] W. Zheng, Y. Kobayashi, K. Hirata, T. Miura, T. Kobayashi, M. Iwaki, T. Oka and Y. Hama, J. Appl. Polym. Sci., **83**, 186 (2002).

[2] Y. Kobayashi, I. Kojima, S. Hishita, T. Suzuki, E. Asari and M. Kitajima, Phys. Rev., **B52**, 823 (1995).

[3] R. Suzuki, Y. Kobayashi, T. Mikado, H. Ohgaki, M. Chiwaki, T. Yamazaki and T. Tomimasu, Jpn. J. Appl. Phys., **30**, L532 (1991).

[4] K. Ito, Y. Kobayashi, et al., to be published.

[5] M. Hasegawa, M. Tabata, M. Fujinami, Y. Ito and H. Sunaga, Nucl. Instrum. Meth. Phys., Res. B, **116**, 347 (1996).

[6] K. Ito, H. Nakanishi and Y. Ujihira, J. Phys. Chem. B, **103**, 4555 (1999).

1.8 Computational Science

Chair: D. J. Bacon

(The University of Liverpool, UK)

H. Kaburaki

(Japan Atomic Energy Research Institute, Japan)

This is a blank page.

JP0350264

1.8.1 BEHAVIOR OF CU ATOMS IN α-FE UNDER IRRADIATION: A COMPUTER SIMULATION STUDY

Naoki Soneda [1,2*], Akiyuki Takahashi [2], Shiori Ishino [3] and Genki Yagawa [2]
[1]Central Research Institute of Electric Power Industry (CRIEPI)
2-11-1 Iwado-kita, Komae-shi, Tokyo 201-8511, Japan
[2]University of Tokyo, 7-3-1 Hongo, Bunkyoku, Tokyo 113-8656, Japan
[3]Tokai University, 1117 Kitakaname, Hiratsuka-shi, Kanagawa 259-1292, Japan

Abstract

Behavior of Cu atoms in α-Fe is of primary concern to understand the mechanism of neutron irradiation embrittlment of reactor pressure vessel materials. We present our recent atomic-scale computer simulation results on the diffusion mechanism of a Cu atom as well as interactions between Cu atoms and point defects by means of the molecular dynamics and the Monte Carlo computer simulation techniques.

Keywords: Fe-Cu, diffusion, vacancy mechanism, vacancy, SIA, cluster formation

1. Introduction

Neutron irradiation embrittlement of reactor pressure vessel materials is one of the concerns for the aged nuclear power plants. It is widely accepted that the embrittlement is related to the hardening of the materials, which is primarily caused by two reasons[1]: clustering of impurity Cu atoms and formation of matrix damage. Especially the role of Cu clustering is very important because a large portion of embrittlement is owing to the Cu clustering when the RPV materials are subjected to from low to medium amount of neutron irradiation. The details of the Cu clustering has recently been studied by such sophisticated experimental techniques as 3D atom probe[2] and coincidence Doppler broadening[3] techniques, and many aspects of the clustering have becoming clearer. However, the details of the mechanism of the clustering, especially the interactions between the Cu atoms and the lattice defects such as vacancies, self-interstitial atoms (SIAs), and their clusters produced during neutron irradiation, have not been well understood yet.

In this paper, we address above questions by means of atomistic-scale computer simulations. We describe the simulation results obtained on the diffusion mechanism of Cu atoms in α-Fe. Then we present how such diffusing Cu atoms can interact with lattice defects produced during neutron irradiation.

*Corresponding Author Tel: +81-3-3480-2111 Fax: +81-3-3430-2410
E-mail address: soneda@criepi.denken.or.jp

2. Diffusion mechanism of Cu atoms

A Cu atom is a slightly over-sized atom in α-Fe matrix, and in general such solute atoms are thought to diffuse by vacancy mechanism. However, the details of the mechanism are not well understood. Thermal ageing experiments show that in Fe-Cu alloys Cu atoms form precipitates at the pre-existing dislocations first, and then in the matrix[4]. Recent 3D atom probe observations of irradiated RPV materials also show that Cu clustering can take place at dislocations as well as in the matrix[5]. So our objective is to understand the detailed mechanism of the Cu diffusion to explain these experimental observations.

In order to perform the simulation of Cu diffusion by vacancy mechanism in α-Fe, we first calculate the migration energies of a vacancy at various positions around a Cu atom as shown in Fig. 1. Classical MD method with the Finnis–Sinclair type interatomic potential for Fe-Cu binary alloys developed by Ackland et al.[6] is used to calculate these energies. We then use these energies in the kinetic lattice Monte Carlo (KLMC) simulations. We put one Cu atom and one vacancy in the KLMC computation box, and let the vacancy jump in the crystal. When the vacancy meets the Cu atom, they switch positions. The probability for a vacancy to chose one jump site out of to the eight neighboring lattice sites is calculated from the Boltzmann's factors determined by the corresponding migration energies in these directions.

We analysed the KLMC results in two ways. First, we measured the lifetime of the Cu-vacancy pair. More precisely, we define that a Cu atom and a vacancy form a diffuse Cu-vacancy pair when they are located within the 5th nearest neighbor distance. Once such diffuse pair is formed, we then count the number of vacancy jumps before the dissociation of the pair. Fig. 2 shows the results of the mean lifetime of the diffuse pair as a function of crystal temperature. Results for the perfect isotropic jumps are also shown for comparison. The results show that as the temperature decreases, the lifetime of the diffuse Cu-vacancy pair

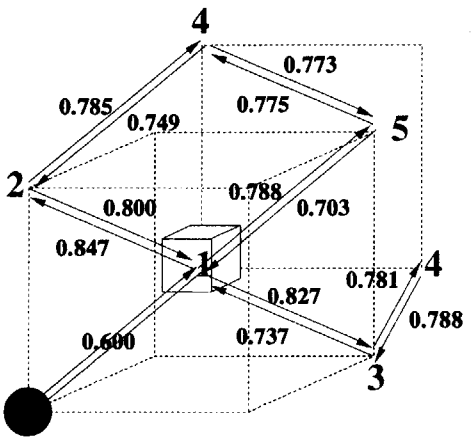


Fig. 1 Migration energies (eV) of a vacancy at various positions around a Cu atom.

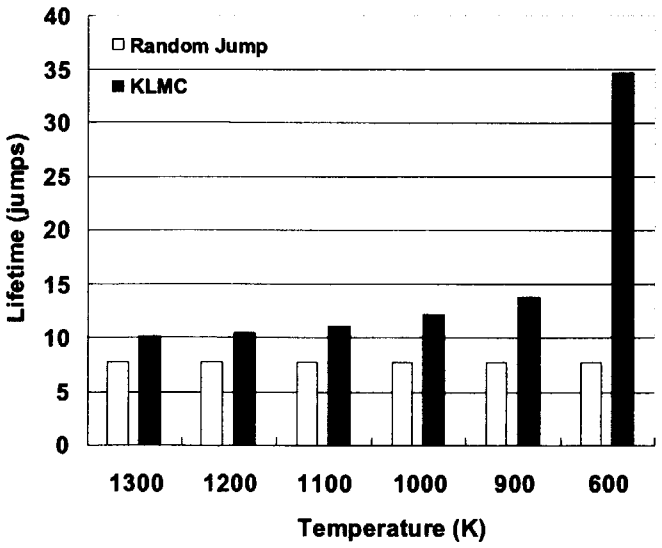


Fig. 2 Lifetime of a diffuse Cu-vacancy pair

becomes longer. This gives us such a picture that once a diffuse pair is formed, the vacancy jumps around the Cu atom for a while rather than goes away from the Cu atom with very short residence time.

Next, in order to examine the migration of the Cu atoms, we measured the net Cu displacement during the lifetime of the diffuse vacancy pair. Fig. 3 shows the fractions of the different displacement distances at three different temperatures. It can be seen that in almost 90% cases, a Cu atom does not move at all or just moves to the 1st nearest neighboring site. However, this does not mean that a Cu atom does not make jumps. We actually observed that once a diffuse pair is formed, a Cu atom does make several jumps in general by exchanging positions with the vacancy. If even number of switches happen, then the Cu position does not change. If odd number of switches happen, then the Cu atom makes one net jump to the 1st nearest neighbor distance position. Furthermore, more importantly, in the rest of the 10% cases, the Cu atom makes more than two net jumps. The largest displacement distance that we observed in the simulations is the 12th nearest neighbor distance. This tendency is enhanced at the lower temperatures.

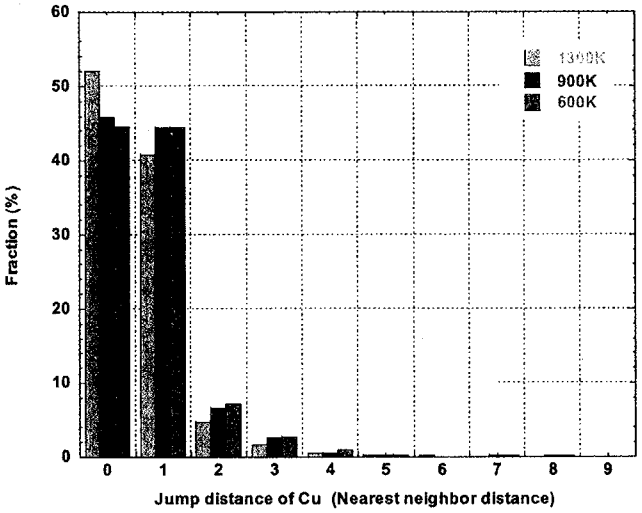


Fig. 3 Cu displacement distance during the lifetime of the diffuse Cu-vacancy pair.

The above results suggest the followings. First of all, the vacancy mechanism of the Cu migration is not a simple position exchange which results in opposite net flows of vacancies and Cu atoms. Rather, it is the migration of a diffuse Cu-vacancy pair, in which the vacancy and the Cu atom effectively migrate in the same direction. In this sense, the diffusion of a Cu atom in α-Fe occurs by a "dragging" mechanism by a vacancy. Secondly, though the 10% fraction for the cases of more than two net jumps is not large, we should say that it is still very effective, because once the diffuse Cu-vacancy pair dissociates, the Cu atom will have to wait for a fair amount of time in average before the next vacancy arrives at the Cu atom and forms a new Cu-vacancy pair to transform the Cu atom.

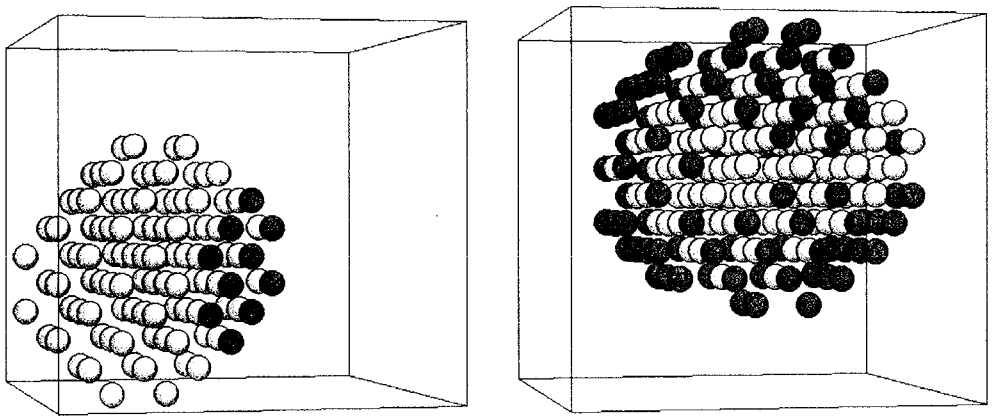
3. Cluster formation of Cu atoms and point defects

3.1 Cu-vacancy cluster

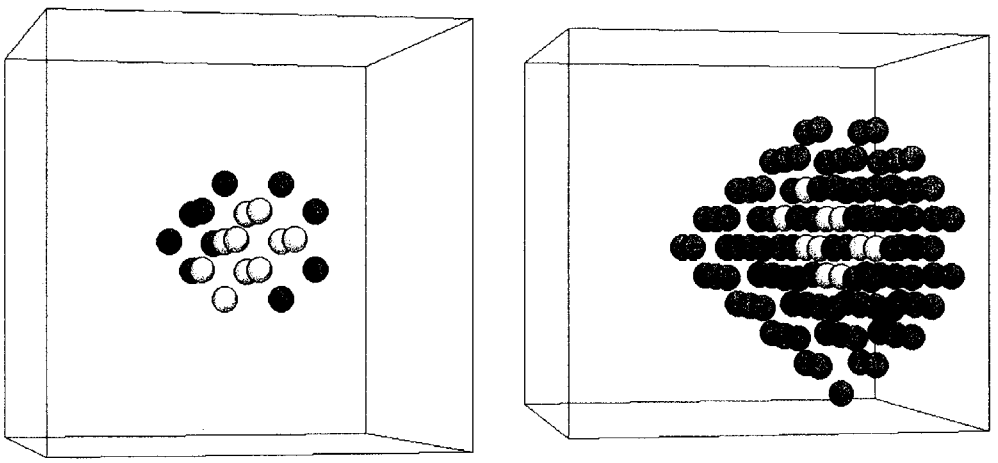
The idea of the dragging mechanism of Cu diffusion in α-Fe is very consistent with the experimental observations in which Cu atoms form precipitates at the sinks of vacancies such as dislocations and grain boundaries. If we accept this idea, then the next question on the

interaction between Cu atoms and point defect clusters naturally arises because the point defect clusters such as vacancy clusters and SIA loops can be sinks of migrating single vacancies. In this section, we study the structures of Cu-vacancy clusters.

A lattice Monte Carlo (LMC) computer simulation method following the Metropolis algorithm[7] is used to search for energy minimum atomic structures of vacancy-Cu clusters. Initially, a given number of vacancies and Cu atoms are randomly located at the lattice sites of a computation box with a size of $15\times15\times15a_0$ where a_0 is a lattice parameter. Then, any two out of the vacancies and Cu atoms are randomly picked up to calculate the crystal energy change due to the position exchange of the two. If the energy becomes lower by the position exchange, the new configuration is adopted. If not, the new configuration is adopted with the



(a) 100vacancies and 10 Cu atoms　　(b) 100 vacancies and 100 Cu atoms



(c) 10 vacancies and 10 Cu atoms　　(d) 10 vacancies and 100 Cu atoms

Fig. 4　Typical structures of vacancy-Cu clusters. Yellow and red circles are vacancies and Cu atoms, respectively.

probability of the Boltzmann's factor, $\exp(-\Delta E / kT)$, where ΔE is the crystal energy change, k the Boltzmann's constant and T the crystal temperature, respectively. This process, i.e. one LMC step, is repeated until the minimum crystal energy is reached. The crystal temperature is initially set to 600K, and then it is decreased by 5K at every 100 LMC steps (simulated annealing). After the LMC calculation is completed, the positions of Fe and Cu atoms, which are fixed at lattice sites of the computation box during the LMC calculation, are relaxed by MD using numerical quenching algorithm in order to calculate the final crystal energy. In both LMC and MD calculations, the interatomic potential developed by Achland et al. for Fe-Cu alloys is again used. Ideally, MD quenching calculation may need to be performed after each LMC step. We tested this, and confirmed that both approaches, MD quenching after every LMC step and one MD quenching after LMC minimization is completed, give the same results.

Figures 4(a) to (d) show typical structures of vacancy-Cu clusters. First of all, we confirmed that Cu atoms and vacancies form a stable mixed cluster rather than forming a separated Cu precipitate and a vacancy cluster. One can see that the vacancies form a cluster at the center of the vacancy-Cu cluster, (a *central vacancy cluster*), whose structure is independent of the number of Cu atoms, and is almost identical to that of the pure vacancy cluster. Secondly, Cu atoms tend to sit on the surface of the central vacancy clusters as can be seen in Figs. 4(a) to (d). In addition, when the number of Cu atoms is much smaller than that of the surface lattice sites, Cu atoms tend to agglomerate locally on the surface of the central vacancy cluster as shown in Fig. 4(a), rather than to occupy isolated surface lattice sites. In other words, the surface of the central vacancy cluster is locally coated by Cu atoms when the number of Cu atoms is smaller than the surface lattice sites. On the other hand, when the number of Cu atoms are much larger than that of the vacancies, the whole surface of the central vacancy cluster is coated by Cu atoms, and the central vacancy cluster is buried in a shell of Cu atoms as can be seen in Fig. 4(d).

The structure of a central vacancy cluster buried in a Cu shell is consistent with experimental observations. Hasegawa et al. [3] measured the lifetimes and the momentum spectra of the gamma rays emitted at the annihilation of positrons in neutron-irradiated Fe-1.3wt.%Cu model alloys using a conventional lifetime measurement technique and a sophisticated coincidence Doppler broadening technique of positron annihilation experiments. Their results show that vacancy type defects having long lifetimes are produced during the neutron irradiation, and furthermore the high momentum spectra of the annihilation gamma rays are almost identical to those for pure Cu crystals. This means that the atoms that sit on the surface of the vacancy clusters are all Cu atoms, and this is completely consistent with our simulation results.

3.2 Cu-SIA cluster

Using the same computational strategy, we next studied the interactions between Cu atoms and SIA clusters (loops). Fig. 5 shows typical atom arrangements of SIA-Cu clusters. When there is only one Cu atom, the Cu atom is located at a position of tension stress. This is reasonable as the Cu atom is a slightly over-sized atom in α-Fe matrix. When there are eight Cu atoms and four SIAs, however, the situation is very different, and four Cu atoms form a crowdion which replaces one SIA as shown in Fig. 5(b). When we increase the number of Cu atoms to 16, all the SIAs are replaced by the four-member Cu crowdions as shown in Fig. 5(c). More interestingly, however, when we further increase the numbers of SIAs and Cu atoms up to 20 SIAs and 20 Cu atoms as shown in Fig. 5(d), only three SIAs are replaced by four-member Cu crowdions, and the other eight Cu atoms are placed next to the Cu crowdions but outside of the SIA loop. In other words, a small Cu precipitate is formed at the edge of the

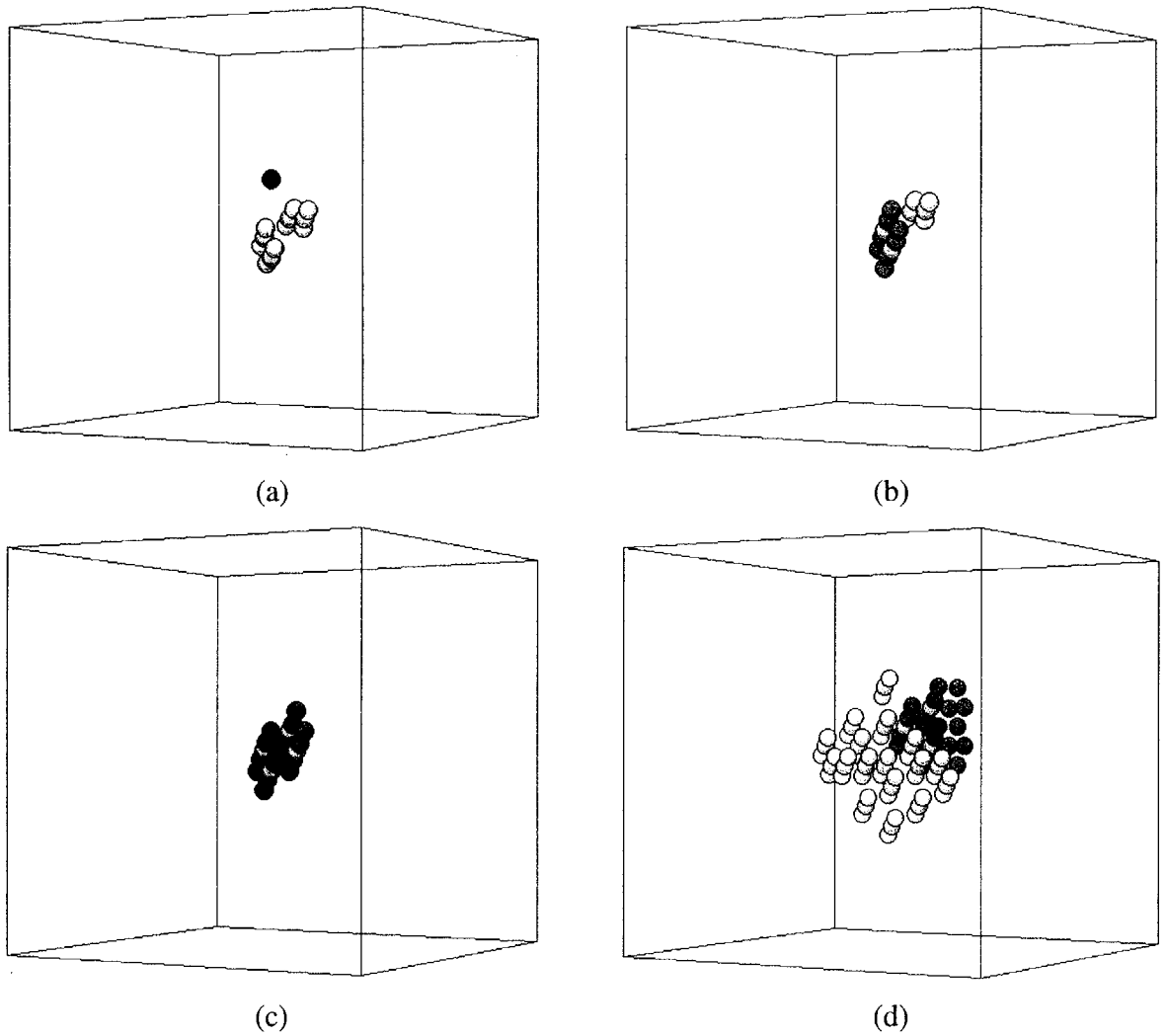


Fig 5 Stable structures of SIA-Cu clusters with (a) four SIAs and one Cu atom, (b) four SIAs and eight Cu atoms, (c) four SIAs and 16 Cu atoms, and (d) 20 SIAs and 20 Cu atoms, respectively. Yellow and red circles represent Fe atoms in SIAs and Cu atoms respectively, and the green circles show the lattice sites occupied by two atoms.

SIA loop.

The above results are the new findings obtained by the computer simulations, and there is no direct experimental evidence. In the thermal ageing experiments of Fe-Cu alloys, it was found that Cu precipitates are formed at dislocations first, and then in the matrix. The present results suggest that there is a possibility that not only line dislocations but also dislocation loops can be preferable sites for the Cu atoms to precipitate. However, the next question is how this kind of SIA-Cu clusters, especially such configuration as Fig. 5 (d), can be formed. As we see in chapter 2, Cu atoms diffuse by the vacancy mechanism, and it is clear that such diffusing Cu atoms can't replace the Fe atoms of SIA dumbbells. The SIA dumbbell should absorb the vacancy very easily to annihilate by pair recombination. Therefore, we investigated two further possibilities to answer this question.

The first possibility is an that a SIA loop performing 1D motion runs over a pre-formed bcc Cu precipitate. The point here is that the center axis of the SIA loop motion[8] do not coincide with the center the Cu precipitate (offset impact). We performed this MD simulation, and confirmed that the SIA loop is trapped by the Cu precipitate to form such a configuration as that shown in Fig. 5 (d). The binding energy between the SIA loop and the Cu precipitate is more than 2eV.

Another approach is to look for a different meta-stable configuration of SIA-Cu clusters. We investigate this by assuming a constraint condition to our MC calculation strategy, in which we do not allow Cu atoms to replace the Fe atoms of the SIA dumbbells so that resulting configuration can be formed by the Cu atom diffusion by the vacancy mechanism. The result shows that Cu atoms still prefer to precipitate out at the edge of the SIA loop. If such a Cu precipitate absorbs a couple of SIAs, then the configuration will be easily converted to that of Fig. 5(d).

4. Conclusion

In the operating RPV materials, we have vacancies and SIAs produced during the displacement cascades caused by neutron irradiation. We show in the present paper that the Cu impurity atoms diffuse in the α-Fe matrix by the vacancy dragging mechanism, and further more, such diffusing Cu atoms can form stable clusters with not only vacancies but also SIAs produced by cascaades. These are the results investigated in details for the first time by computer simulations, but some of the results are very consistent with experimental observations.

Our research group is now aiming at performing a multi-scale computer simulations where we simulate from the displacement cascades to the yield stress change using several different computational techniques. The results shown in this paper is a part of such our efforts. This approach works well so far for the RPV embrittlement problem, and we believe that we can apply this kind of techniques to the other similar radiation damage problems.

References

[1] G.R. Odette, G.E. Lucas, Radiat. Eff. Defects Solids 144 (1998) 189.

[2] R.G. Carter, N. Soneda, K. Dohi, J.M. Hyde, C.A. English, W.L. Server, J. Nucl. Mater., 298 (2001) 211.

[3] Y. Nagai, Z. Tang, M. Hasegawa, T. Kanai, and M. Saneyasu, Phys. Rev. B, 63 (2001) 134110.

[4] E. Hornbogen and H0P. Jung, Z. Metallk. 55 (1964) 691.

[5] N. Soneda, RG. Carter, K. Dohi, C.A. English, J.M. Hyde, W.L. Server, unpublished work.

[6] G. J. Ackland, D. J. Bacon, A. F. Calder and T. Harry, Phil. Mag. A, 75(1997) 713.

[7] M. Metropolis, A. W. Rosenbluth, A. H. Teller and E. Teller, J. Chem. Phys. 21(1953) 1087.

[8] N. Soneda, T. Diaz de la Rubia, Philosophical Magazine A, **81** (2001), 331.

2. Poster Session

This is a blank page.

JP0350265

2.1 EFFECT OF ION IRRADIATION ON STRUCTURAL AND ELECTRICAL PROPERTIES OF BSCC THIN FILMS

Shunichi Hishita[1*], Sang Sub Kim[2], and Jong Ha Moon[3]
[1]Advanced Materials Laboratory, National Institute for Materials Science
1-1, Nakimi, Tsukuba, Ibaraki 305-0044 Japan
[2]Department of Materials Science and Metallurgical Engineering,
Sunchon National University, Sunchon 540-742, Korea
[3]Department of Materials Science and Engineering,
Chonnam National University, Kwangju 500-757, Korea

Abstract

Effects of oxygen ion irradiation and subsequent thermal annealing of $Bi_2Sr_2Ca_1Cu_2O_x$ (Bi-2212) films deposited on $SrTiO_3(001)$ using pulsed laser deposition were studied. It was found that compared to the simply heated film the ion irradiated and thermally annealed one showed a leaf-like morphology and an improved conducting behavior of Bi-2212 phase. Our results suggest that amorphization by oxygen ion bombardment and recrystallization by thermal annealing might be a suitable process for the preparation of patterned c-axis oriented Bi-2212 films with appropriate superconducting properties.

Keywords: BSCC, Bi-2212, superconductor, thin film, recrystallization, ion irradiation, amorphization, thermal annealing, morphology, critical temperature

1. Introduction

$Bi_2Sr_2Ca_{n-1}Cu_nO_x$ (Bi-22(n-1)n) has been widely studied on since the discovery of the superconductivity [1]. This system is thought one of the most promising high T_c superconducting compounds for its use in applications ranging from power transmission cables to Josephson junction-based electronic devices [2-5]. It has been demonstrated that the Bi-2212 has high critical current density (J_c) above $5x10^9$ A/m^2 at 4.2 K and 10 T [2]. Its thin film form has been successfully prepared using various deposition methods [6-9]. However, to get a high quality Bi-2212 thin film applicable to electronic devices, it is required to optimize growth conditions very carefully.

The ion implantation technique has been recognized one of the most convenient method to modify and/or fabricate a wide variety of materials. It has been employed in high-T_c superconductivity research primarily in two ways, i.e. to fabricate thin film specimens by adding the extra elements, and to modify the superconducting properties. The attempts to fabricate the superconducting films by direct ion implantation, however, have been considerably less successful. With considerable efforts, Nastasi et al. have succeeded to fabricate the YBCO thin films by Y ion implantation with the same heat treatment as that required in preparing the bulk samples [10]. The attempts to modify the superconducting properties have been successfully reported. Koch et al. have firstly reported the fabrication of the dc SQUID from the YBCO thin film by ion implantation [11]. The ion implantation was used as a patterning tool by destroying the superconductivity of the film. The critical current improvement is one of the most successful application of ion implantation to the high-T_c superconductor. Civale et al. have produced large enhancements in flux pinning by

* Corresponding author. Tel: +81-298-58-5643 Fax: +81-298-52-7449.
* *E-mail address:* HISHITA.Shunichi@nims.go.jp

introducing the columnar defects in YBCO crystals [12]. In contrast with J_c, T_c is decreased by ion implantation [13]. The degradation of T_c is thought due to the introduction of electron scattering centers [14] and the formation of weak links[15].

The another capability of ion implantation for materials modification is the ion beam induced crystallization. Since the first report for the Si recrystallization by ion beam [16], this technique has been applied successfully to grow epitaxial films of a wide variety of materials at lower temperature [17-21]. The crystal growth of high-T_c materials at lower temperature with ion beam, however, has never been reported to the authors' knowledge. The authors have also tried to achieve the lower temperature growth of BSCC films with ion beam, and not succeeded yet. During these trials we have found an interesting phenomenon relating to the T_c improvement. In this paper we report the effect of the pre-amorphization by oxygen ion beam on the superconductivity of heat-treated Bi-2212 films on $SrTiO_3$ prepared by pulsed laser deposition (PLD).

2. Experimental

Fully c-axis oriented Bi-2212 films were initially prepared using PLD on $SrTiO_3(001)$ substrates. A pulsed KrF excimer laser (248 nm, 30 ns duration, 10 Hz) was line-focused onto a target rotating at 8 rpm. The laser beam energy was set at 100 mJ/pulse (about 1 J/cm^2). The substrates were positioned to face parallel to the target. The target-to-substrate distance was fixed to be approximately 5 cm. The target was prepared by a conventional ceramic powder processing. Commercial powders of $SrCO_3$, CuO, Bi_2O_3, and $CaCO_3$ were weighted to the composition of $Bi_2Sr_2Ca_1Cu_2O_x$, mechanically mixed, pressed to the disc, and sintered for 60 hr at 850 °C.

A substrate temperature of 600 °C and a pressure of 8×10^{-1} torr of oxygen were chosen to prepare the Bi-2212 films. $SrTiO_3(001)$ single crystal substrates were cleaned ultrasonically in acetone and methyl alcohol sequentially for 10 min, and loaded into the chamber,. Film thickness was measured by the cross-sectional scanning electron microscope (SEM) to be about 200 nm.

After the deposition, the samples were firstly irradiated in vacuum with 50 keV O^+ ions at a fluence of 5.0×10^{18} ions/m^2 at room temperature, then with 110 keV O^+ ions at the same fluence. This two-step ion irradiation was adopted to induce complete amorphization of the whole films without causing a serious compositional change. After the irradiation, to recrystallize the samples, they were annealed thermally at 800 °C for 1 hr in air.

SEM and x-ray diffraction were used to investigate the microstructures and phases of the films, respectively. Four-probe method was used to measure the temperature-resistivity characteristics of the sample.

3. Results and discussion

Figure 1(a) illustrates a typical x-ray powder diffraction (XRD) pattern of the as-deposited Bi-2212 films on $SrTiO_3(001)$. Only the Bragg reflections corresponding to the positions of the $Bi_2Sr_2Ca_1Cu_2O_x$ (00*l*) reflections appear with the reflections of $SrTiO_3$, indicating that a single $Bi_2Sr_2Ca_1Cu_2O_x$ phase formed on $SrTiO_3(001)$ with the (001) plane of the film parallel to the substrate (001) plane. This c-axis-oriented film was amorphized by the two-step ion irradiation. As shown in Fig. 1(b), the $Bi_2Sr_2Ca_1Cu_2O_x$ film reflections are completely disappeared, indicating that the whole film was amorphized. This amorphous film was thermally annealed for 1 hr at 800 °C in air to induce recrystallization. For a comparison, the as-deposited film was simply heated for 1 hr at 800 °C in air. Figure 1(c) shows the XRD pattern of the simply heated film. As shown in Fig. 1(d), the thermal annealing after the ion irradiation recovered a fully c-axis oriented film of the same phase and crystal orientation in

nature comparing to the simply heated one. The crystallinity of the irradiated–annealed film might be superior to that of the simply heated one. It is reasonable to think that this recrystallization in an aligned manner was occurred most likely following the mechanism of the solid-phase epitaxial regrowth.

In contrast to the similarity in the XRD patterns, the morphology of the film annealed after the ion irradiation shows a remarkable change. Figures 2(a) and 2(b) show typical surface morphologies of the simply heated and the irradiated-annealed films observed by SEM, respectively. The simply heated one shows small grains dispersed in a featureless matrix. In sharp contrast, the irradiated-annealed one shows a leaf-like morphology, which is known as one of characteristics of the Bi-2212 phase [22]. The leaf-like grains usually favor the formation of oriented films. As can be seen in Fig. 2(b), the grains are oriented in a small variety of directions, consistent with the (00*l*) orientation confirmed by the x-ray diffraction.

The ion irradiation and thermal annealing process influenced the resistivity curves as shown in Fig. 3. The resistivity curve for the as-deposited film shows the semiconducting behavior. By heating at 800 °C the film was evolved to the superconductor. The resistivity of the simply heated film descends at about 80 K, and drops to zero at 27 K. It is surprising that the Bi-2212 mono-phased c-axis oriented film shows the much lower critical temperature (T_c) than a typical Bi-2212 superconductor. The lower T_c might be originated from the poor crystallinity of the Bi-2212, the off-stoichiometric composition of the film, and/or the less carrier doping by insufficient annealing in oxygen. Interestingly, for the irradiated-annealed film, the resistivity descends at about 85 K, and drops to zero at 61 K, which is in agreement with a characteristic behavior of a Bi-2212 phase. According to the calculation results by Monte Calro simulation code [23], the implanted oxygen concentration performed in this study is at most 1 % for oxygen in stoichiometric Bi-2212, and the total vacancies generated at oxygen site is 20 times as many as the implanted oxygen. The effect of increased oxygen atoms in the film might be negligible for the

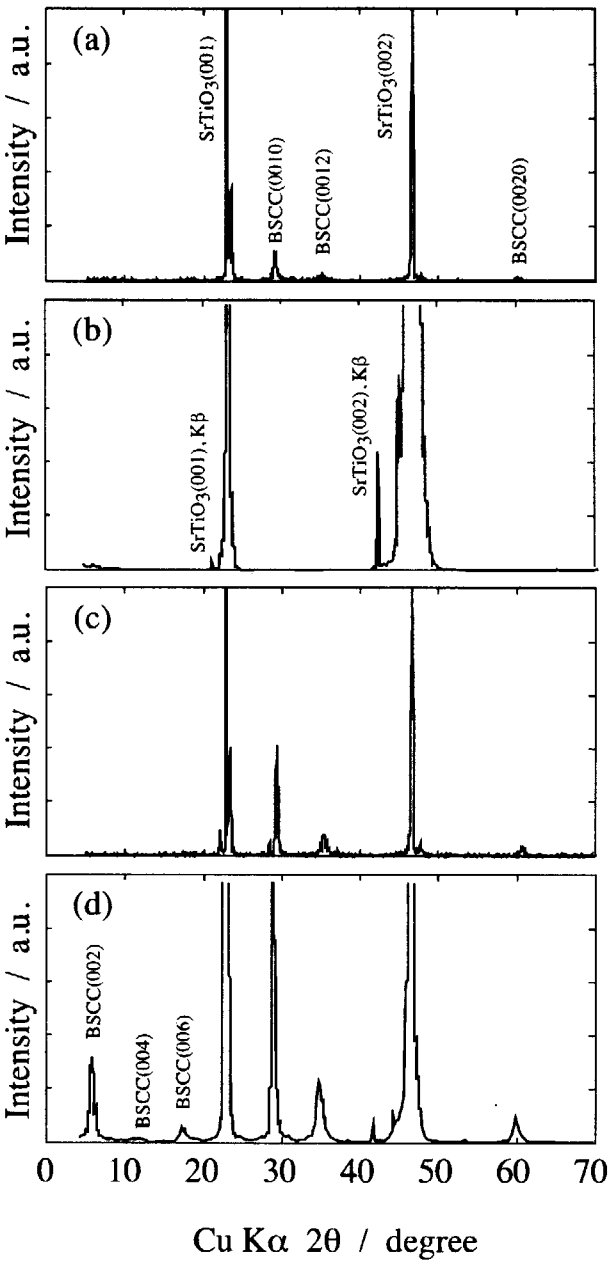


Fig. 1. XRD patterns of (a) the as-deposited film, (b) the amorphized film by the oxygen ion irradiation, (c) the film simply heated at 800 °C, and (d) the film annealed at 800 °C after ion irradiation. The films are on the $SrTiO_3$(001) substrate. BSCC indicates the Bi-2212 phase.

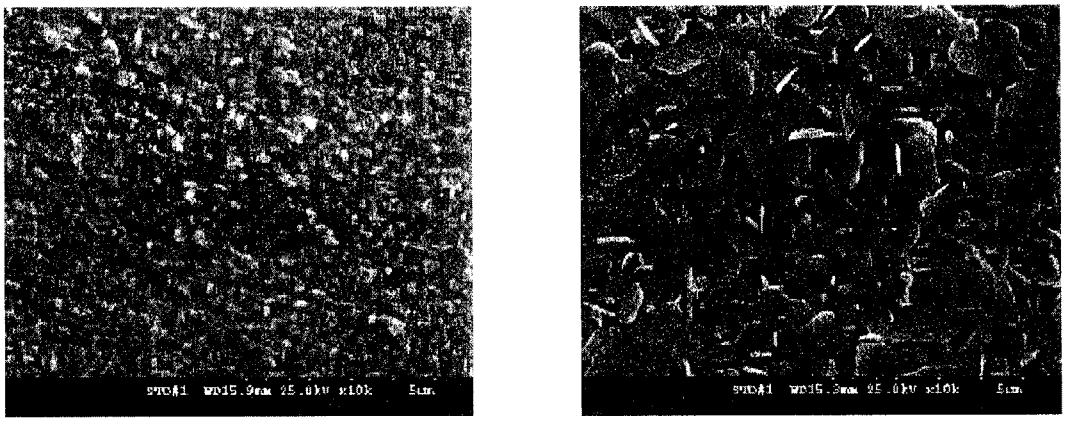


Fig. 2. SEM photographs of (a) the simply heated Bi-2212 film, and (b) the irradiated-annealed Bi-2212 film on a $SrTiO_3$(001) substrate.

annealing process. It is most likely that the bombardment by the accelerated oxygen ions generates crystal defects intensively in the as-deposited Bi-2212 film as many as yielding its amorphization. This process should increase the internal energy and the diffusivity of the atoms in the film considerably, and accelerate the crystallizing transformation during the annealing, thereby achieving a better crystallinity and superconductivity of the Bi-2212 phase. Further investigation is necessary to discuss in detail the mechanism of the ion irradiation influence on the characteristics of the Bi-2212 film.

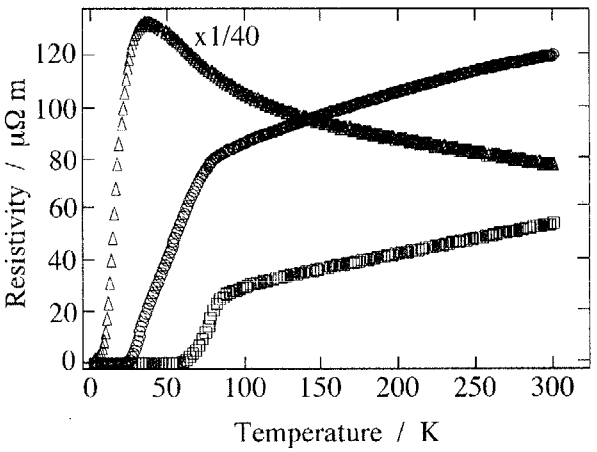


Fig. 3. Temperature-resistivity characteristics of the as-deposited film (Δ), the simply heated one (○), and the irradiated-annealed one (□).

4. Conclusions

A fully c-axis oriented Bi-2212 single phase Bi-2212 film was prepared on $SrTiO_3$(001) using pulsed laser deposition. The two-step oxygen ion irradiation induced complete amorphization of the oriented as-deposited film. The subsequent thermal annealing reproduced a fully crystallized, c-axis oriented film by most likely the mechanism of the solid-phase epitaxial regrowth. The recrystallized film showed a leaf-like grain morphology and a significant improvement of T_c, implying that the process (amorphization by oxygen ion bombardment and recrystallization by thermal annealing) is an effective way to obtain a patterned c-axis oriented Bi-2212 film with better supercondting properties.

References

[1] H. Maeda, Y. Tanak, M. Fukutomi, and T. Asano, Jpn. J. Appl. Phys. **27**, L209 (1988).
[2] H. Miao, H. Kitaguchi, H. Kumakura, K. Togano, and T. Hasegawa, Physica C **301**, 116 (1998).
[3] R. Wördenweber, Supercond. Sci. Technol. **12**, 86 (1999).
[4] Y. Satoh, S. Arisawa, A. Fukuyo, Y. Takano, A. Ishii, T. Hatano, and K. Togano, Physica C **363**, 130 (2001).
[5] M. Nagao, M. Sato, and H. Maeda, Appl. Phys. Lett. **79**, 2612 (2001).
[6] N. Kubota, T. Sugimoto, Y. Shiohara, and S. Tanaka, J. Mater. Res. **8**, 978 (1993).

[7] P. Bove, D.J. Rogers, F.H. Teherani, J. Cryst. Growth **220**, 68 (2000).
[8] M. Nevriva, J. Stejskal, J. Leitner, D. Sedmidubský, P. Beran, and A. Strejc, Physica C **341-348**, 2383 (2000).
[9] S. Sakamoto, T. Okamoto, and Y. Saito, Jpn. J. Appl. Phys. **39**, 5099 (2000).
[10] M. Nastasi, J.R. Tesmer, M.G. Hollander, J.F. Smith, and C.J. Maggiore, Appl. Phys. Lett. **52**, 1729 (1988).
[11] R.H. Koch, C.P. Umbach, G.J. Clark, P. Chaudhari, and R.B. Laibowitz, Appl. Phys. Lett. **51**, 200 (1987).
[12] L. Civale, A.D. Marwick, T.K. Worthington, M.A. Kirk, J.R. Thompson, L. Krusin-Elbaum, Y. Sun, J.R. Clem, and F. Holtzberg, Phys. Rev. Lett. **67**, 648 (1991).
[13] G.P. Summers, E.A. Burke, D.B. Chrisey, M. Nastasi, and J.R. Tesmer, Appl. Phys. Lett. **55**, 1469 (1989).
[14]A.E. White, K.T. Short, R.C. Dynes, A.F.J. Levi, M. Anzlowar, K.W. Baldwin, P.A. Polakas, T.A. Fulton, and L.N. Dunkleberger, Appl. Phys. Lett. **53**, 1010 (1988).
[15] G.J. Clark, F.K. LeGoues, A.D. Marwick, R.B. Laibowitz, and R.H. Koch, Appl. Phys. Lett. **51**, 1462 (1987).
[16] M. Takahashi, J. Nakata, and K. Kajiyama, Jpn. J. Appl. Phys. **20**, 2205 (1981).
[17] S.T. Johnson, J.S. Williams, and E. Nygren, J. Appl. Phys. **64**, 6567 (1991).
[18] K. Oyoshi, S. Hishita, S. Suehara, T. Aizawa, and H. Haneda, Nucl. Instrum. Method Phys. Res. B **121**, 184 (1997).
[19] S. Hishita, K. Oyoshi, S. Suehara, and T. Aizawa, Nucl. Instrum. Method Phys. Res. B **121**, 157 (1997).
[20] S. Hishita, K. Oyoshi, S. Suehara, and T. Aizawa, Nucl. Instrum. Method Phys. Res. B **148**, 549 (1999).
[21] S. Hishita, T. Aizawa, S. Suehara, and H. Haneda, Appl. Surf. Sci. **169-170**, 296 (2001).
[22] A. Ishii and T. Hatano, Physica C **340**, 173 (2000).
[23] J.F. Ziegler and J.P. Biersack, SRIM ver. 2000.10 (1999).

JP0350266

2.2 FORMATION MECHANISM OF SIC IN C-SI SYSTEM BY ION IRRADIATION

Shunichi Hishita*, Takashi Aizawa, Shigeru Suehara, and Hajime Haneda
Advanced Materials Laboratory, National Institute for Materials Science
1-1, Nakimi, Tsukuba, Ibaraki 305-0044 Japan

Abstract

The irradiation effects of 2 MeV He^+, Ne^+, and Ar^+ ions on the film structure of the C-Si system were investigated with RHEED and XPS. The ion dose dependence of the SiC formation was kinetically analyzed. The SiC formation at moderate temperature was achieved by 2 MeV ion irradiation when the thickness of the initial carbon films was appropriate. The evolution process of the SiC film thickness consisted of the 3 stages. The first stage was the steep increase of the SiC, and was governed by the inelastic collision. The second was the gentle increase of the SiC, and was governed by the diffusion. The last was the decrease of the SiC, and was caused by the sputtering. The formation mechanism of the SiC was discussed.

Keywords: ion beam induced chemical reaction, ion beam induced epitaxial growth, silicon carbide thin film, electronic stopping power, nuclear stopping power

1. Introduction

Silicon carbide (SiC) is one of the major candidates for the next-generation semiconductor and for high-temperature electronic devices. It has the wide band-gap (2.2 eV), high electron mobility (1000 cm^2/Vs)[1], high saturated electron drift velocity (calculated as 2.7×10^7 cm/s at 2×10^5 V/cm)[2], and thermal stability (stable over 2000 K). The growth of epitaxial SiC films on silicon substrates has been reported with high substrate temperature more than 1000 K [3-10]. In 1999 the authors have firstly reported the room temperature growth of epitaxial SiC thin films on Si substrates by ion irradiation [11]. The dose dependences of the chemical states of C and Si [12], and of the fraction of formed SiC [13] have been already reported. In this paper, we compare the effect of irradiation ion species (He^+, Ne^+ and Ar^+) on the formation of SiC, and discuss the mechanism of the reaction.

2. Experimental

The detailed experimental setup is described elsewhere [13]. Irradiation of the samples with 2 MeV He^+, Ne^+ and Ar^+ was performed with ion current densities of 20, 10 and 10 mA/m^2, respectively. For eliminating the effect of beam heating, the sample temperature was maintained at 623 K using a resistive heater during ion irradiation. XPS measurements were conducted with Mg Kα excitation (VG Scientific, ESCALAB 200-X with ECLIPSE data-system). The binding energy of XPS spectra was calibrated by the Si 2p peak (99.3 eV [14]) from the "bulk" Si (100) sample. A single crystal SiC (Nippon Steel Corp., 6H) was also used as a reference material.

Non-doped Si single crystals of (100) orientation were used as substrates. In order to develop cleaned surfaces, all the crystals were heated at 1473 K under a vacuum ($< 5 \times 10^{-7}$ Pa) for 1 min after ordinary chemical treatment. The cleaned surface of Si (100) was confirmed 2x1 reconstruction with RHEED and LEED, and no trace contamination was observed by XPS.

The carbon films of thickness between 0.05 to 50 nm were evaporated onto the Si substrates

* Corresponding author. Tel: +81-298-58-5643 Fax: +81-298-52-7449.
* *E-mail address:* HISHITA.Shunichi@nims.go.jp

at 300 K. The thickness of the initial carbon films was determined from the XPS intensity ratio of C 1s and Si 2p peaks, and was calibrated with the RUMP simulation [15] of UHV-RBS spectra and with the absolute C 1s XPS intensity from the monolayer graphite on Ni (111) [16].

3. Results and discussion

The RHEED patterns and the XPS spectra indicated the formation of epitaxial SiC thin films by irradiation of 2 MeV He^+, Ne^+ and Ar^+ ions when the thickness of the initial carbon films was appropriate. The epitaxial growth of SiC by He^+ irradiation was observed in the samples whose thickness of the initial carbon film were less than 0.07 nm. When the thickness was more than 0.08 nm, the RHEED pattern of the samples showed no visible change by He^+ irradiation, indicating the amorphous structure. The critical thickness of the initial carbon film for growing the epitaxial SiC thin film was increased in the order, He^+, Ne^+, Ar^+. Figures 1 and 2 show the typical RHEED pattern and XPS spectrum of the irradiated sample which had the epitaxially grown SiC thin film. The C 1s XPS spectrum, as shown in Fig. 2, can be resolved into two components; one peak is centered at 284.3 eV, and the other is at 283.2 eV. The former can be assigned to amorphous carbon. The latter is identical to that of SiC. The energy positions of the resolved peaks were independent on the amount of ion dose or the carbon thickness, indicating the presence of two chemical states of the carbon: One is amorphous carbon, and the other is that reacted with Si, named SiC carbon. The carbon atoms in irradiated films are in either of these two states independent on the amount of ion dose or the film thickness. The amount of SiC, i.e. the thickness of SiC film, was calculated from the peak area ratio of SiC carbon to amorphous one in C 1s XPS spectrum assuming that the conversion factor of the carbon atomic density to the SiC thickness is the same as that of the carbon film.

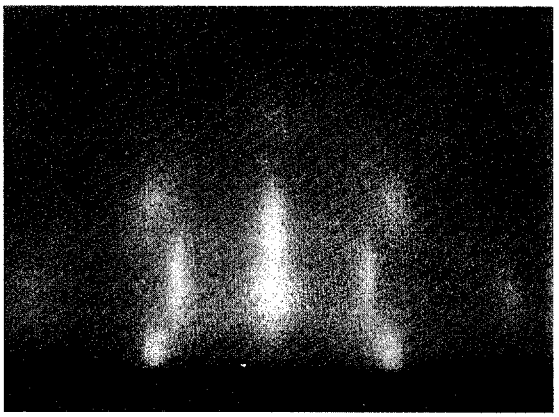


Fig. 1. RHEED pattern of the Ar^+ irradiated sample. The azimuth of the incident electron beam was [110] direction of the Si substrate. The initial carbon thickness was about 0.1 nm, and the ion dose was 2.8×10^{20} ions/m^2.

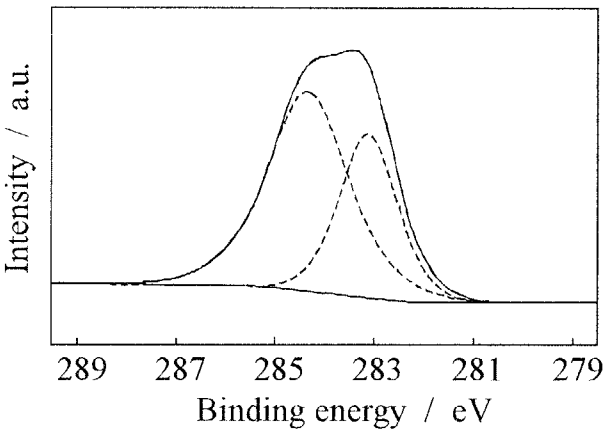


Fig. 2. C 1s XPS spectrum of the Ar^+ irradiated sample. The thickness of the initial carbon film was about 0.9 nm. The ion dose was 5.6×10^{19} ions/m^2. Solid line is the measured spectrum, and dashed are the resolved ones.

Figures 3-5 show the evolution of the thickness of SiC films with the amount of the ion dose. In the case of He^+ irradiation (Fig. 3), the evolution can be divided into two stages. The thickness of SiC films was steeply increased up to about 0.08 nm, followed by the saturation to about 0.13 nm, even if the initial carbon thickness was more than 0.13 nm. This indicates that the carbon atoms in the layer about 0.13 nm in thickness react with Si atoms to

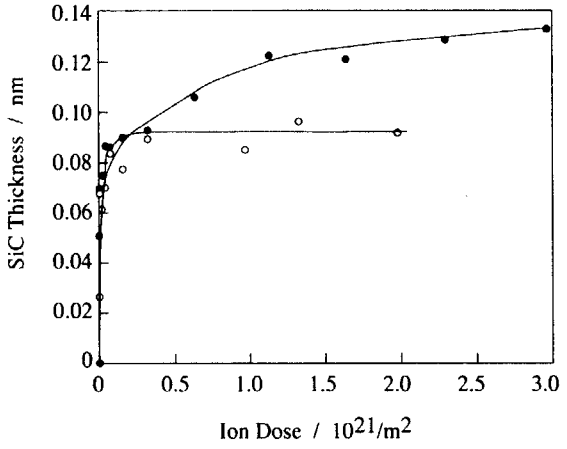


Fig. 3. He^+ ion dose dependence of SiC film thickness. The initial carbon thickness is 0.17 nm for solid circle, 0.08 nm for open circle, respectively.

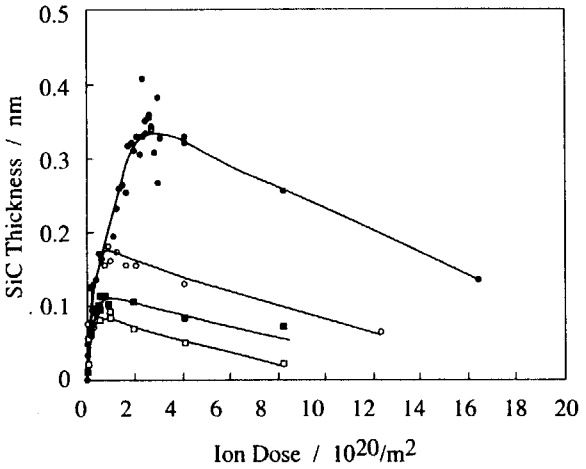


Fig. 4. Ne^+ ion dose dependence of SiC film thickness. The initial carbon thickness is 0.85 nm for solid circle, 0.25 nm for open circle, 0.15 nm for solid square, 0.1nm for open squaer, respectively.

form the SiC film by 2 MeV He^+ irradiation. The layer 0.13 nm in thickness is equivalent to the atomic density $1.8x10^{19}$ atoms/m^2 monolayer for Si (100) when assuming the density of the carbon film is identical to that of graphite. In the case of Ne^+ irradiation (Fig. 4), the evolution can be divided into 3 stages. The thickness of SiC films was steeply increased up to about 1 nm, followed by relatively slow increase, and decreased lineally. In the case of Ar^+ irradiation (Fig. 5), the evolution is divided into 2 stages. The thickness of SiC films was increased firstly, followed by decreasing. It was suggested by comparing the dose amount that in the case of Ar^+ irradiation the experimental setup and procedure had less capability for distinguish the two-stage increasing process of SiC thickness like shown in the He^+ and Ne^+ cases. Thus, the evolution process of SiC film thickness is thought to consist of three stages, steep increase (abbreviated as G1), gentle increase (G2), and linear decrease. In the decrease process, the amount of total carbon was also decreased. This indicates that the decrease process is caused by the sputtering.

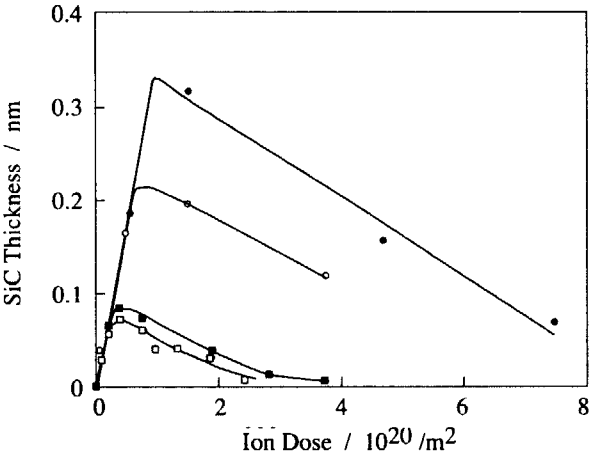


Fig. 5. Ar^+ ion dose dependence of SiC film thickness. The initial carbon thickness is 0.9 nm for solid circle, 0.6 nm for open circle, 0.13 nm for solid square, 0.1 nm for open square, respectively.

The energy for the SiC film formation should be supplied by the irradiated ions. The total energy transferred from the irradiated ion is a sum of the nuclear and electronic contributions. The nuclear contribution is related to the sputtering, and the electronic one is to the excitation of the Si-C bond formation. The energy transferred from the ions to the C-Si system was estimated by the Monte Calro simulation code TRIM [17] for a carbon film of 1 nm in thickness in thickness on a Si film of 10 μm and for a "bulk" SiC. The estimated values

Table 1. The energy value transferred from one 2 MeV-ion and the sputtering rate.

	Electronic energy to (eV/nm)		Nuclear energy to (eV/nm)		Sputtering rate for (N/nm)	
	C	Si	C	Si	C	SiC
He^+	313	243	0.262	0.241	0.0008	0.0002
Ne^+	1974	1765	21.6	20.0	0.1	0.02
Ar^+	2099	1963	101	99.5	0.3	0.08

are listed in Table 1. The sputtering rate was calculated from the vacancy generation process with the assumption that the displacement energies were 28 eV for C and 15 eV for Si, and the lattice binding energy was 3 eV. The sputtering rates shown in Table 1 are consistent with the results shown in Figs. 3-5, i.e. the SiC thickness was not decreased for He^+ irradiation, gently decreased for Ne^+ irradiation, and steeply decreased for Ar^+ irradiation. Figure 6 shows the correlation between the SiC film growth rate and the transferred energy. The growth rate was estimated from the slope of the G1 or G2 regions in Figs. 3-5. The slope of G1 for Ar^+ irradiation was assumed identical to that of G2. The He^+ irradiation could grow the epitaxial SiC when the initial carbon film was thin enough. This suggests that the electronically transferred energy is the dominant one for initiating the reaction between carbon and silicon and growing the epitaxial film. This is consistent with the G1 lines shown in Fig. 6. The G1 lines indicate the linear relationship between the SiC growth rate and the electronically transferred energy. The electronically transferred energy to C atoms might be more dominant for the G1 process because of the better linearity of its G1 line. For the G2 process, however, the nuclear energy transfer is indicated to have a dominant contribution.

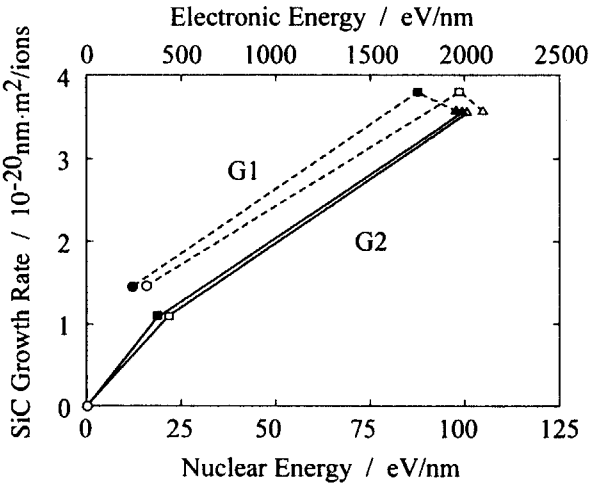


Fig. 6. Relationship between the SiC growth rate and the transferred energy. The solid line (G2) is the plot for the nuclear energy transfer. The broken line is one for the electronic energy transfer. The solid symbols are for Si, and the opens are for C. The circles are for He^+, the triangles are for Ne^+, and the squares are for Ar^+, respectively.

The formation mechanism of the SiC film can be considered as follows: The high energy ions irradiated to the carbon film on Si substrates transfer the energy to the C and Si atoms by the inelastic collision (the electronic contribution). The atoms become to the excitation state. If the excited C atom and Si atom are adjacent each other, the excitation state is relaxed by making the C-Si bond, i.e. the formation of SiC. This process is the G1 process. The formation of SiC is occurred only at the interface of the carbon film and the Si substrate. When the carbon thickness is rather large, the outer C atoms in the carbon film are not adjacent to the Si atoms in the substrate. The C atoms (or the Si atoms) are forced to diffuse to the partner atom. The diffusion energy is supplied by the elastic collision (the nuclear contribution). Thus, the diffusion process governs the formation of SiC. This is the G2

process. The growth of the turbostratic graphite reported in ref. [11] should be the other way for relaxation. The excited C atoms not to reach the partner Si atom encounter to the other C atom on the diffusion way, and make the C-C bond to become the graphite.

Further investigation is necessary to discuss in detail the mechanism of the epitaxial growth by ion irradiation.

4. Conclusions

The irradiation effects of 2 MeV He^+, Ne^+, and Ar^+ ions on the film structure of the C-Si system were investigated. The ion dose dependence of the SiC film formation was kinetically analyzed. The SiC formation at moderate temperature was achieved by 2 MeV ion irradiation when the thickness of the initial carbon films was appropriate. The evolution process of the SiC film thickness consisted of the 3 stages. The first stage was the steep increase of the SiC. The second was the gentle increase of the SiC. The last was the decrease of the SiC, and was caused by the sputtering. The electronically transferred energy was indicated to be the dominant one for the formation of SiC. The nuclear energy transfer process had, however, a significant contribution to the atomic diffusion which was the dominant process for the SiC formation when the carbon thickness was rather large.

References

[1] W.E. Nelson, F.A. Halden, and A. Rosengreen, J. Appl. Phys. **37**, 333 (1966).
[2] D.K. Ferry, Phys. Rev. **B12**, 2361 (1975).
[3] Koji Takahashi, Shigehiro Nishino, and Junji Saraie, J. Electrochem. Soc. **139**, 565 (1992).
[4] Wook Bahng and Hyeong Joon Kim, Thin Solid Films **289-291**, 181 (1996).
[5] K.-W. Lee, K.-S. Yu, J.-H. Boo, Y. Kim, T. Hatayama, T. Kimoto, and H. Matsunami, J. Electrochem. Soc. **144**, 1474 (1997).
[6] Y.H. Seo, K.S. Nahm, E.-K. Suh, H.J. Lee, and Y.G. Hwang, J. Vac. Sci. Technol. **A15**, 2226 (1997).
[7] Q. Wahab, R.C. Glass, I.P. Ivanov. J. Birch, J.-E. Sundgren, and M. Willander, J. Appl. Phys. **74**, 1663 (1993).
[8] A.V. Hamz, M. Balooch, and M. Moalem, Surf. Sci. **317**, L1129 (1994).
[9] S. Henke, B. Stritzker, and B. Rauschenbach, J. Appl. Phys. **78**, 2070 (1995).
[10] D. Chen, R. Workman, and D. Sarid, Surf. Sci. **344**, 23 (1995).
[11] Shunichi Hishita, Keiji Oyoshi, Shigeru Suehara, and Takashi Aizawa, Nucl. Instr. Meth. Phys. Res. **B148**, 549 (1999).
[12] S. Hishita, K. Oyoshi, S. Suehara, and T. Aizawa, Key Eng. Mater. **169-170**, 179 (1999).
[13] Shunichi Hishita, Takashi Aizawa, Shigeru Suehara, and Hajime Haneda, Appl. Surf. Sci. **169-170**, 296 (2001).
[14] J.F. Moulder, W.F. Stickle, P.E. Sobol, and K.D. Bomben, *Handbook of x-ray photoelectron spectroscopy* (Physical Electronics, Minnesota 1995)
[15] L.R. Doolittle, Nucl. Instr. Meth. Phys. Res. **B9**, 344 (1985).
[16] T. Aizawa, R. Souda, Y. Ishizawa, H. Hirano, T. Yamada, and C. Oshima, Surf. Sci. **237**, 194 (1990).
[17] J.F. Ziegler and J.P. Biersack, SRIM 2000.10 (1999).

JP0350267

2.3 PATTERN-DEPOSITION OF ZINC OXIDE PARTICLES USING SELF-ASSEMBLED MONOLAYER TEMPLATE

Noriko Saito,[1,*] Hajime Haneda[1] and Kunihito Koumoto[2]
[1] Advanced Materials Laboratory, National Institute for Materials Science,
1-1 Namiki, Tsukuba, Ibaraki 305-0044, JAPAN
[2] Department of Applied Chemistry, Graduate School of Engineering, Nagoya University,
Furo-cho, Chikusa-ku, Nagoya 464-8603, JAPAN

Abstract

We fabricated ZnO micropattern by low temperature aqueous solution process. Photo-patterned self-assembled monolayer (SAM) with phenyl/OH-surface functional groups was used as a template. Selective electroless deposition of ZnO was realized on Pd catalyst adhered only to the phenyl-surfaces. The as-deposited ZnO shows 500-800 nm visible light photoluminescence. Patterned monochromatic cathodoluminescence image was successfully demonstrated for 1 μm-width lines.

Keywords: ZnO, self-assembled monolayer, selective deposition, luminescence

1. Introduction

ZnO is one of the promising phosphor materials because of its ability to retain high efficiency even at low voltage excitation [1]. If its micropatterns can be produced by a simple process, the technique to arrange ZnO phosphor can enjoy widespread applications such as a high-resolution field emission display, which is a new small-sized flat panel display having higher resolution and better contrast compared with the liquid crystal version. ZnO patterns are also applicable to transparent electrodes or surface acoustic wave devices, and are greatly expected in the integration device technology.

In conventional patterning of ceramic thin films, it has been hard to find suitable etching conditions free of influence on the substrates at selective etching, or to obtain high-resolution pattern edges even after tearing the ceramic films during liftoff process. To solve these problems, selective growth techniques have recently been developed. For example, direct patterning is possible by photo-enhanced chemical vapor deposition methods [2]. Recently, Huang *et al.* have reported a novel synthesis of ZnO nanowires by a vapor transport and condensation process on Au-catalyzed surfaces selectively [3], and further succeeded in lasing ultraviolet light at room-temperature [4]. However, these growth processes require heat-treatments at high-temperatures, which can damage substances already present on the substrates. Thus, a new micropatterning technique at low temperatures is desired.

Biomimetic approach for selective deposition using SAM templates [5–10] is a versatile technique for such demands. By modifying the surface functional groups of the substrates, interaction with inorganic substances can be controlled and the deposition manner can be designed. The authors have recently reported patterning ZnO on SAMs through electroless deposition of ZnF(OH) [9, 10]. The precipitates, however, were not small enough for high-resolution patterning.

*Corresponding author. Fax: +81-298-55-1196, E-mail address: SAITO.Noriko@nims.go.jp

Izaki [11, 12] developed an electroless deposition method for polycrystalline particulate ZnO films through reduction of nitrate ions using dimethylamine-borane. By only immersing substrates in the aqueous solution maintained at ~60°C, crystalline ZnO particulate films were obtained on the Pd-catalyzed substrates. These conditions proposed for the film formation are thought to be suitable for the processing using SAM templates, because SAMs are not stable under severe conditions; at high temperatures or in high electric fields.

Calvert *et al.* [13, 14] have extensively investigated patterning of metals employing SAMs. They showed that Pd/Sn colloids adhered to the regions having specific surface properties, such as phenyl-terminated surfaces, but not to OH-terminated surfaces. Using patterned SAMs as templates, Cu or Ni lines ~0.4 μm in width were successfully electroless metallized along Pd catalyst attached on the phenyl-surfaces.

Recently, we have attempted micropatterning of ZnO by applying the above-mentioned techniques and succeeded in low-temperature (55°C) fabrication of ZnO micropatterns [15, 16]. In the present study, we investigated the luminescence properties.

2. Experimental

Figure 1 outlines our strategy for selective-deposition scheme employed to fabricate ZnO patterns. A SAM of phenyltrichlorosilane (PTCS) was prepared on a cleaned Si single crystal substrate (<100>, p-type, 15×15×0.5 mm). The substrate was immersed in an anhydrous toluene solution containing 1 vol% PTCS for 5 min under a N_2 atmosphere, followed by baking at 120°C for 5 min in air. The resultant SAM was exposed to UV through a photomask for 2 h in order to pattern the surface with OH- and phenyl-groups [14].

Prior to the deposition of ZnO, the phenyl-group regions of the substrate were selectively catalyzed. The substrate was immersed in a Pd/Sn colloid (Cataposit 44, SHIPLEY), and then accelerated with an acidic solution of HBF_4 (Accelerator 19, SHIPLEY). For electroless deposition of ZnO, the SAM substrate was soaked in an aqueous solution of $Zn(NO_3)_2$ (0.05 M) and dimethylamine-borane (DMAB) (0.01M) at 55°C for 30 min.

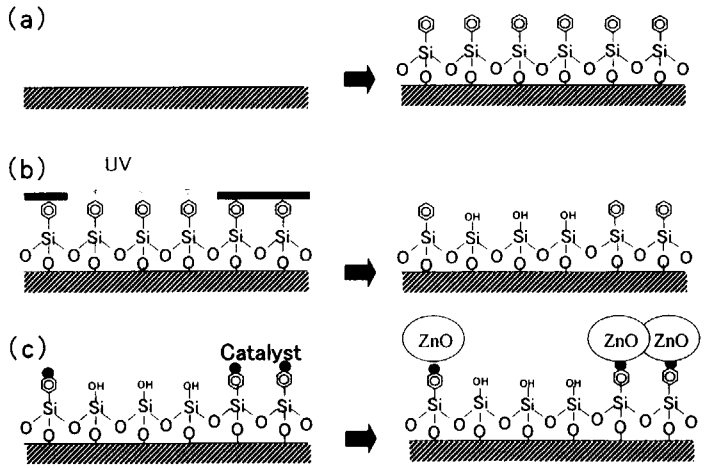


Figure 1: Schematic diagram of site-selective electroless deposition of ZnO on the phenyltrichlorosilane (PTCS) self-assembled monolayer (SAM) template. (a) Preparation of PTCS SAM. (b) Patterning of the SAM by exposing UV light through a photomask. (c) Site-selective catalyzation of the phenyl-surfaces and ZnO deposition on the catalyst.

Photoluminescence (PL) was measured at room temperature using 325 nm laser for the samples as-deposited and annealed at 800 °C for 2h. FT-IR transmittance was measured for the as-deposited and the annealed samples. Cathodoluminescence (CL) was measured at room temperature with an electron beam at the excitation voltage of 5 kV and current of 200 pA [17].

3. Results and discussion

The solution of zinc nitrate and DMAB was transparent during the reaction, and hence deposition occurred *via* heterogeneous nucleation on the Pd-catalyzed substrate. No deposition was observed on the non-catalyzed substrate. X-ray diffraction revealed that the deposits were randomly oriented polycrystalline ZnO.

Scanning electron microscope (SEM) photographs of the ZnO patterned on the SAM template are shown in Fig. 2. The white regions correspond to deposited ZnO, which indicate excellent selectivity of deposition occurring only on the phenyl-regions. The ZnO deposits consisted of particles about 0.2 μm in diameter. The finest line-pattern obtained by this method reached 1 μm in width (Fig. 2(b)). Ideally, drawing lines as fine as the particle size shall be possible by the present deposition method. The feature edge roughness was estimated as several times of the particle size.

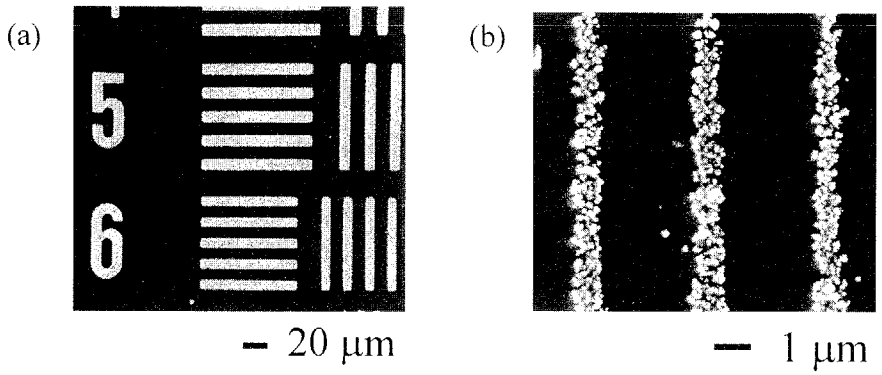


Figure 2: SEM photographs of the patterned ZnO: a) large feature size area and b) 1 μm-width lines. The white regions represent ZnO deposited on the phenyl-regions. Particles about 0.2 μm in diameter were deposited.

Broad visible-light (500–800 nm) PL and CL were observed for the as-deposited sample. For the annealed sample, the broad red color luminescence disappeared and usual green color luminescence of 530 nm appeared. Luminescence of the wavelength longer than that of usual green emission (red color) implies that the present sample contained some defects [18, 19]. The IR absorption due

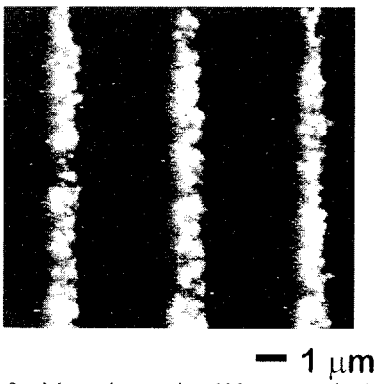


Figure 3: Monochromatic 600 nm cathodoluminescence image for the 1 μm-width line-pattern of ZnO.

to OH stretching observed only for the as-deposited samples implies that the red color luminescence is related to OH ions, which must have been introduced during the deposition carried out under the low-temperature, aqueous conditions. Figure 3 demonstrated monochromatic CL images of 600 nm observed from the same area as Fig. 2(b). The resolution was good enough to obtain virtually the same images as their SEM photos, except that the images looked blurred a little due to excitation by secondary electrons from neighbors.

4. Summary

We fabricated ZnO micropattern by employing photo-patterned PTCS SAM as a template. ZnO was electroless deposited selectively on the Pd catalyst attached to the phenyl-surfaces. The as-deposited ZnO shows 500-800 nm visible light PL and CL. Furthermore, patterned monochromatic CL image was successfully demonstrated for 1 μm-width lines. We hope the present patterning technique could be used as a low-temperature process to manufacture light-emitting devices for optoelectronic applications.

References

[1] K. Morimoto, Phosphor Handbook, (Ed: S. Shionoya and W. M. Yen), CRC Press, Boca Raton, 1998, Chap. 8.
[2] G. H. Lee, Y. Yamamoto, M. Kourogi, M. Ohtsu, Thin Solid Films, 386 (2001) 117.
[3] M. H. Huang, Y. Wu, H. Feick, N. Tran, E. Weber, P. Yang, Adv. Mater., 13 (2001) 113.
[4] M. H. Huang, S. Mao, H. Feick, H. Yan, Y. Wu, H. Kind, E. Weber, R. Russo, P. Yang, Science, 292 (2001) 1897.
[5] K. Koumoto, S. Seo, T. Sugiyama, W. J. Dressick, Chem. Mater., 11 (1999) 2305.
[6] Y. Masuda, W. S. Seo, K. Koumoto, Langmuir, 17 (2001) 4876.
[7] P. X. Zhu, Y. Masuda and K. Koumoto, J. Colloid Interface Sci., 243 (2001) 31.
[8] Y. Gao, Y. Masuda, T. Yonezawa and K. Koumoto, J. Ceram. Soc. Japan, 110 (2002) 379.
[9] N. Saito, H. Haneda, W. S. Seo, K. Koumoto, Langmuir 17 (2001) 1461.
[10] N. Saito, H. Haneda, W. S. Seo, K. Koumoto, K., Key Eng. Mater., 214-215 (2002) 203.
[11] M. Izaki, T. Omi, J. Electrochem. Soc., 144 (1997) L3.
[12] M. Izaki, J. Katayama, J. Electrochem. Soc., 147 (2000) 210.
[13] J. M. Calvert, M. S. Chen, C. S. Dulcey, J. H. Georger, M. C. Peckerar, J. M. Schnur, P. E. Schoen, J. Electrochem. Soc. 139 (1992) 1967.
[14] W. J. Dressick, J. M. Calvert, Jpn. J. Appl. Phys. 32 (1993) 5829.
[15] N. Saito, H. Haneda, T. Sekiguchi, N. Ohashi, I. Sakaguchi and K. Koumoto, Adv. Mater., 14 (2002) 418.
[16] N. Saito, H. Haneda, D. Li and K. Koumoto, J. Ceram. Soc. Japan, 110 (2002) 386.
[17] T. Sekiguchi, Mat. Res. Soc. Symp. Proc. 588 (2000) 75.
[18] N. Ohashi, T. Nakata, T. Sekiguchi, H. Hosono, M. Mizuguchi, T. Tsurumi, J. Tanaka, H. Haneda, Jpn. J. Appl. Phys., 38 (1999) L113.
[19] V. V. Osiko, Optic. Spectr., 7 (1959) 454.

JP0350268

2.4 Development of Nano-composite 9Cr-ODS Martensitic Steels by means of α to γ Phase Transformation

Takeji KAITO [1*], Shigeharu UKAI [1], Koichi HATAKEYAMA [1],
Masayuki FUJIWARA [2], Takanari OKUDA [3] and Toshimi KOBAYASHI [4]

1 Japan Nuclear Cycle Development Institute, O-arai Engineering Center; 4002, Narita-cho, O-arai-machi, Higashi-Ibaraki-gun, Ibaraki, 311-1393, JAPAN

2 Kobelco Research Institute Inc.; 1-5-5, Takatsukadai, Nishi-ku, Kobe, Hyogo, 651-2271, JAPAN

3 Kobe Special Tube Co. Ltd.; 1-5-5, Takatsukadai, Nishi-ku, Kobe, Hyogo, 651-2271, JAPAN

4 Sumitomo Metal Technology Ltd.; 1, Nishino-cho, Higashi-Mukojima, Amagasaki, Hyogo, 660-0856, JAPAN

Abstract

Leading technology development of the oxide dispersion strengthened (ODS) steels has being conducted in JNC particularly emphasizing fuel cladding application for the fast reactors, since they have a potential to realize the high burnup fuel and higher outlet coolant temperature operation. The improvement in formability and ductility, which are indispensable in the cold-rolling method for manufacturing cladding tube, were achieved by controlling the microstructure using technique α to γ phase transformation. The cold-rolling of hardened 9Cr-ODS steels was successfully made to manufacture cladding tubes by using cold-rolling pilger mill. The 9Cr-ODS martensitic cladding tubes manufactured using the technique showed that ring tensile and internal creep rupture strengths exhibit excellent performance far beyond that of conventional ferritic-martensitic steel (PNC-FMS). Adequate ductility in hoop direction was also maintained. These improvement in high temperature mechanical properties have been accomplished through a uniform distribution of nano-scale Y_2O_3-TiO_2 oxide particles of less than 5 nm size by mechanical milling process.

Keywords : Oxide dispersion strengthend steel, Martensitic steel, α to γ phase transformation, Y_2O_3, TiO_2, Cold-rolling, Cladding, Tensile strength, Creep rupture strength, Fast reactor

1. Introduction

The ferritic steels are well known to have excellent radiation resistant, but have inferior high temperature strength compared with the austenitic steels. This disadvantage can be overcome by introducing thermally stable dispersoids in the ferritic matrix. The ODS ferritic steels are the prospective cladding material for the advanced Liquid Metal Fast Reactors[1-5] as well as being applicable as a low activated fusion reactor material[6].

In the ODS ferritic steels with a basic composition of Fe-Cr-W-Ti-Y_2O_3, grain morphology control by recrystallization has been shown to be indispensable not only in softening the material hardened in the process of cold-rolling but also for suppressing the

*Corresponding author. Tel : +81-29-267-4141 Fax : +81-29-266-2904
E-mail address : takeji@oec.jnc.go.jp (F. authors)

strength degradation by grain boundary sliding[7-10]. As another approach, α to γ phase transformation was demonstrated to be capable method for controlling the grain morphology by using the ODS martensitic steels[11].

In this study, by applying α to γ phase transformation in the 9Cr-ODS martensitic steels, cladding manufacturing test is executed using the cold-rolling process at room temperature. The high temperature mechanical properties of the manufactured claddings are investigated, focusing on varying Y_2O_3 and Ti contents, which could significantly affect the mechanical properties of the 9Cr-ODS martensitic steels.

2. Experimental Procedure

2.1 Manufacturing Process

The manufacturing process of the 9Cr-ODS martensitic claddings is represented in Fig.1. The Ar gas atomized powders of martensitic steel (less than 150 μ m ϕ) were mechanically alloyed with Y_2O_3 powders (average diameter 20nm ϕ) and Ti powders in order to adjust the target composition as a function of Y_2O_3 and Ti contents. 10kg powder batches were agitated for 48hr in an Ar gas atmosphere at a rotational speed of 220rpm. The mechanically alloyed powders were then canned in 67mm diameter cans, and degassed at 673K in a 0.1Pa vacuum for 2hr. By using the hot-extrusion method 25mm diameter bars were made at an elevated temperature of 1423K.

M91, M92 and M93 claddings are manufactured by 2 times cold-rolling of about 50% reduction ratio at each rolling using pilger mill, in order to evaluate effects of Y_2O_3 and Ti contents on the mechanical properties. M11 claddings are manufactured through 4 times cold-rolling and intermediate heat-treatment to investigate possibility for demonstrating the fast reactor claddings.

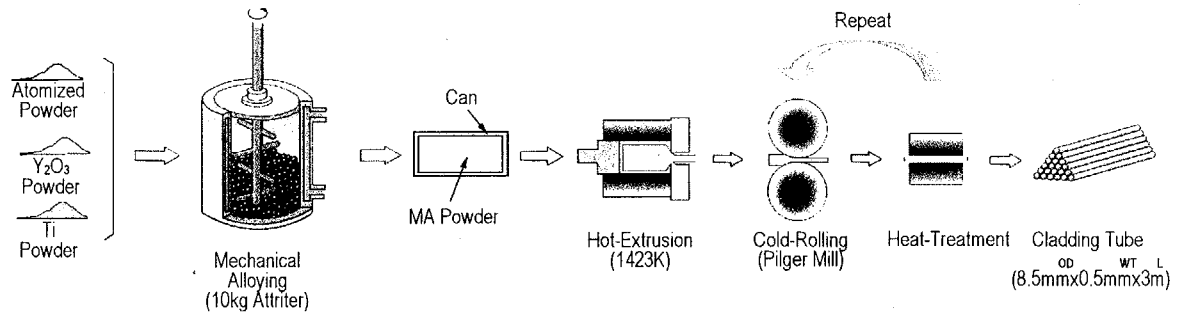


Fig.1 Manufacturing process of the 9Cr-ODS martensitic cladding

2.2 Evaluation Tests

The phase transformation temperature of 9Cr-ODS martensitic steels is determined by dilatometric measurement method. The disc type of specimens are used in 8mm diameter and 12mm thickness that are cut from the extruded bar of M11. The phase transformation is identified from vickers hardness and optical micrographs. The cladding manufacturing test is conducted using 2 rolled type of cold-pilger mill. For manufactured cladding, high temperature mechanical properties are evaluated by means of ring tensile and pressurized internal creep rupture tests, since the circumferential hoop is a dominant stress-loading direction in the fuel pin. In order to investigate the high temperature strength of 9Cr-ODS martensitic steels, oxide dispersion parameters are determined by the transmission electron microscopy observation of the thin foils. The partition of Ti into oxide particles and TiC

carbide precipitate is determined from quantitative analysis of the extracted residue that is separated from electrolytes by the filter with 200nm size mesh.

3. Phase Transformation

3.1 Phase Transformation Temperature

The thermal expansion data of M11 were measured using dilatometric measurement method. A characteristic Ac_1 and Ac_3 points, which are temperature for starting and finishing transformation of ferrite-martensite (α) into austenite (γ) during heating, were 1157K and 1233K, respectively. The phase transformation temperatures of the 9Cr-ODS martensitic steel are slightly higher than conventional ones[12]. Based on above measurement, standard temperature for normalizing and tempering of 9Cr-ODS martensitic steels was selected as 1323 K for 1hr and 1073K for 1hr.

3.2 Continuous Cooling Transformation (CCT) Diagram

At varying cooling rate from 1323K to room temperature after normalizing at 1323K, vickers hardness measurement and optical microstructure observation were executed for M11 cladding. The cooling rate was varied in the range of 50K/hr to 18,000K/hr. The hardness reaches more than 500Hv at the cooling rate of 18,000K/hr, and adequately decreases with decreasing cooling rate; the hardness is reduced to only 330Hv at cooling rate of less than 100K/hr. These drastic hardness responses in relation to the cooling rate are considered to be closely associated with morphology change caused by the martensite transformation from the austenite phase.

Based on above results, continuous cooling transformation (CCT) diagram was originally constructed for 9Cr-ODS martensitic steels, which is shown in Fig.2. In this diagram, martensite and ferrite phase fields are distinguished by characteristic lines: martensite start (Ms) and finish (Mf) lines and ferrite start (Fs) and finish (Ff) lines. At the highest cooling rate curve of 18,000K/hr that intersects with Ms and Mf lines, microstructure consists of martensite and small amount of δ -ferrite with higher hardness of 502Hv as shown in optical micrograph. On the other hand, slow cooling rate curve corresponding to 100K/hr and 50K/hr cut across Fs and Ff lines alone. Thus, their microstructure is formed only ferrite of 7 μ m grain size and carbides that induced lower hardness of 330Hv. The intermediate cooling rate of 1000K/hr contains both ferrite and martensite structures.

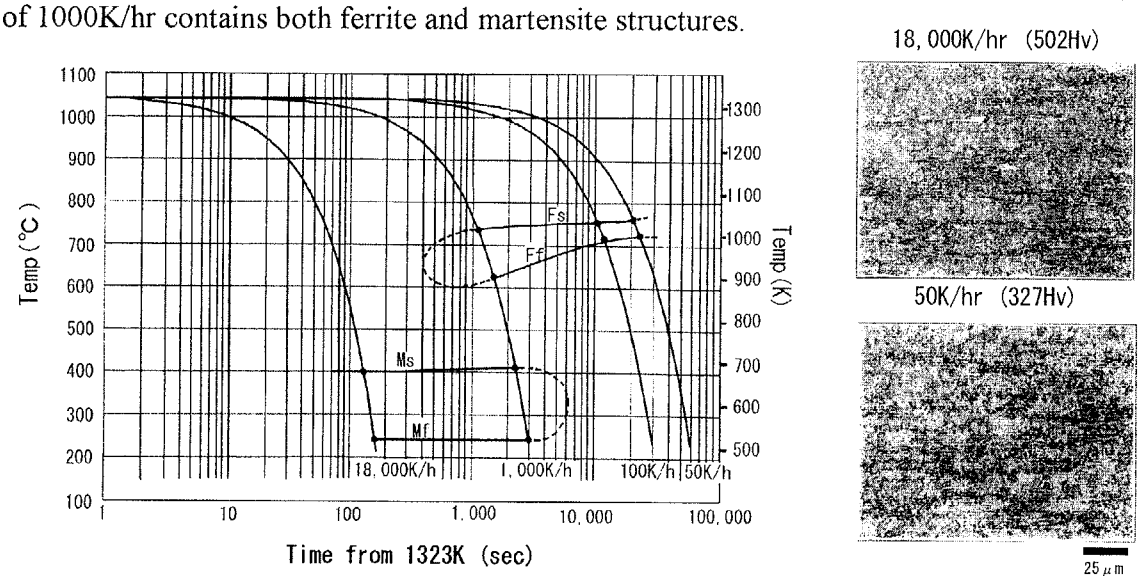


Fig.2 CCT diagram and corresponding optical macrograph of M11 cladding

With regard to the martensite phase transformation, its starting temperature Ms is around 673K, and is located within the range of published data band of conventional ferritic-martensitic steels[12]. This Ms point is reasonably interpreted with a content of the interstitial carbon in the steel, and effect of oxide particles could be minor. In contrast, the minimal cooling rate to obtain martensite phase is ranged in a few hundred K/hr for 9Cr-ODS martensitic steel, whereas conventional ferritic-martensitic steels take around 20K/hr, depending on the prior austenite grain size; finer grains display higher critical cooling rate[12]. Significant higher critical cooling rate in 9Cr-ODS martensitic steels, that is measured in this experiment, could be attributed to the very fine grain size of prior austenite, since grain growth is retarded through pinning by oxide particles during normalizing at 1323K for 1hr.

4. Cladding Manufacturing Test

In order to study a feasibility of manufacturing claddings from the mother tubes in the dimension of 18mm outer diameter and 3mm thickness, cladding manufacturing test was executed by means of pilger-mill rolling by 4 times into the final dimension of 8.5mm outer diameter, 0.5mm thickness and about 3m length. Based on the CCT diagram, cold-rolling of 9Cr-ODS martensitic steel claddings was carried out under the softened ferritic structure for mother tubes that is induced by slow cooling rate at 100K/h after normalizing at 1423K. Fig.3 represents the results of hardness change in the course of cladding manufacturing process. The cold-rolling was repeated 4 times with a reduction rate of near 45%; hardening occurs due to accumulation of cold-rolled deformation. The intermediate heat-treatment, that consists of slow cooling rate at 150K/hr from the austenitic phase, can successfully induce softening the hardened claddings. At the final step of cladding manufacturing, normalizing at 1323K for 1hr and then tempering at 1073K for 1hr were undertaken, in order to destroy the substantially elongated grain structure formed by cold-rolling.

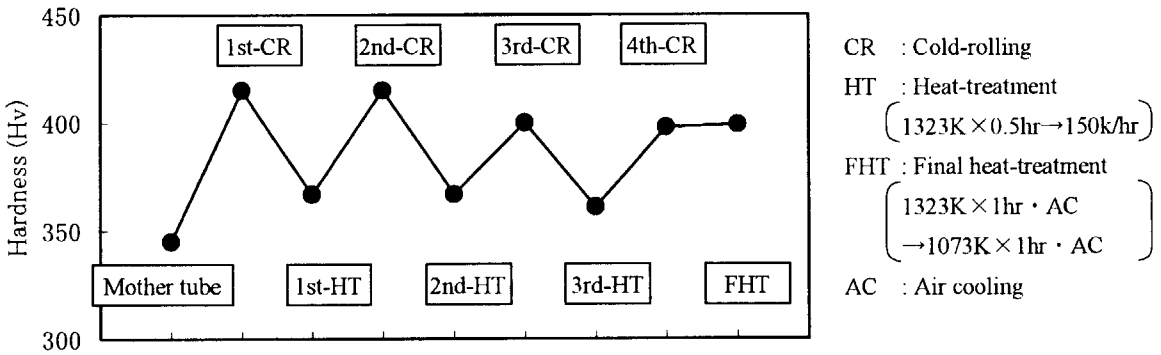


Fig.3 Hardness change in the course of M11 cladding manufacturing

The results of analyses of chemical composition in the manufactured claddings are listed in Table 1. The M93 and M11 have a nominal composition of 0.2mass% Ti and 0.35mass% Y_2O_3. M91 was prepared for evaluating the effect of lower Ti content of 0.12mass%, and M92 was for lower Y_2O_3 of 0.30mass%. Excessive oxygen (Ex.O) is defined as the oxygen content by subtracting oxygen coupled with Y_2O_3 from the total amount of oxygen in the material, which was analyzed by the inert gas melt method. The Y content was also analyzed by the inductively coupled plasma method, from which the Ex.O and Y_2O_3 contents were estimated. The Ex.O, N and Ar gases appear to be contained during mechanical alloying process. The 1.94mass% W was introduced as a solution hardening element.

Table 1 Chemical composition of manufactured claddings

Specimen No.	Chemical composition (mass%)								
	C	Cr	W	Ni	Ti	Y_2O_3(*1)	Ex.O(*2)	N	Ar
M91	0.11	9.26	1.94	0.022	0.12	0.34	0.05	0.010	0.0033
M92	0.13	9.00	1.94	0.022	0.20	0.30	0.04	0.010	0.0034
M93	0.12	8.99	1.94	0.022	0.20	0.35	0.06	0.010	0.0033
M11	0.13	9.00	1.95	0.021	0.20	0.37	0.06	0.013	0.0025

(*1) Y content×1.27, (*2) Total oxygen content－Y content×0.27

5. Mechanical properties

5.1 Tensile Properties

Fig.4 represents the ultimate tensile strength in the hoop direction at room temperature to 1073K, and that of the conventional ferritic-martensitic stainless steel (PNC-FMS) is also plotted[13]. All manufactured claddings show the improved tensile strength in the hoop direction over the entire temperature region. By increasing the Ti content from 0.12 (M91) to 0.20mass% (M93), the ultimate tensile strength is step-wise increase. The improvement in the ultimate tensile strength due to more addition of Y_2O_3 from 0.30 (M92) to 0.35mass% (M93) with the same content of 0.20mass%Ti is less significant. M11 claddings, that were manufactured by 4 times cold-rolling, have almost same composition as that of M93. From a comparison of results of tensile tests in M93 and M11 claddings, different manufacturing process has less effect on tensile properties. All of claddings show higher strength level than PNC-FMS, and strength ratio increases with increasing temperature particularly above 900K; strength improvement by Y_2O_3 dispersion was confirmed to be superior at the higher temperature.

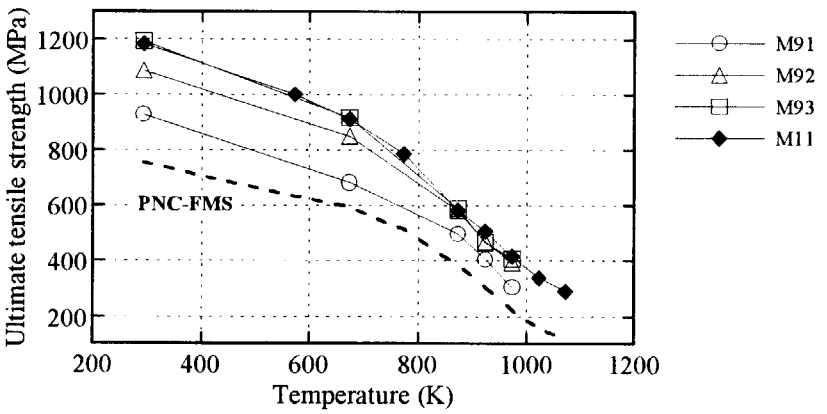


Fig.4 Ultimate tensile strength in the hoop direction of M91, M92, M93 andM11 claddings

The uniform elongation of PNC-FMS tends to decrease with increasing temperature, whereas in M11 claddings the uniform elongation is adequately maintained and increases over about 800K. This performance coincides with trend of ultimate tensile strength. The improved uniform elongation in M11 cladding could arise from the retardation of recovery and continuing work-hardening due to pining the dislocation by Y_2O_3 particles.

5.2 Creep rupture properties

The internal creep rupture strengths of M91, M92, M93 and M11 claddings and PNC-FMS[13] at 973K are shown for comparison in Fig.5. The slope of internal creep rupture lines among the 9Cr-ODS martensitic claddings is identical, and the only difference is the

strength level at the shorter times to rupture. This different strength level could be caused by the size of Y_2O_3 particles and inter-particles spacing among these claddings. The creep rupture strength also tends to significantly increase with increasing Ti contents from 0.12 to 0.20mass% in M92, M93 and M11 claddings. The addition of Y_2O_3 from 0.30 to 0.35weight% results in slightly improved strength. The longitudinal creep rupture data of M93 cladding are also represented. There is no difference in longitudinal and internal creep rupture strength: disappearance of strength anisotropy in both directions. Thus, the equi-axed grains induced by α to γ phase transformation led to the isotropic strength in 9Cr-ODS martensitic steel claddings.

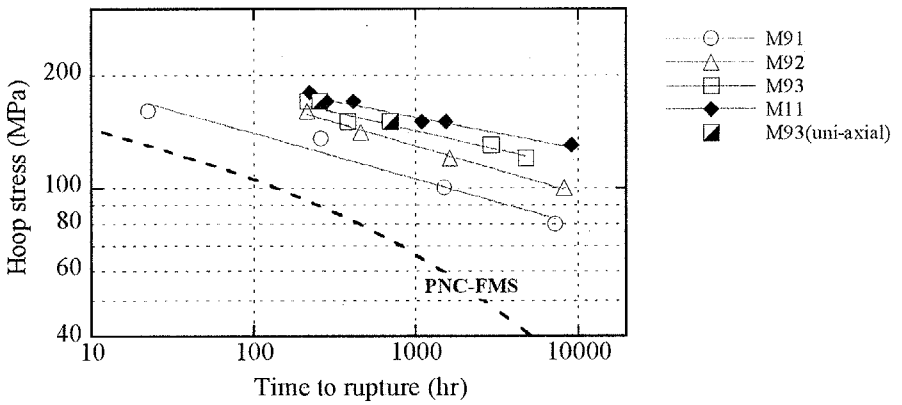
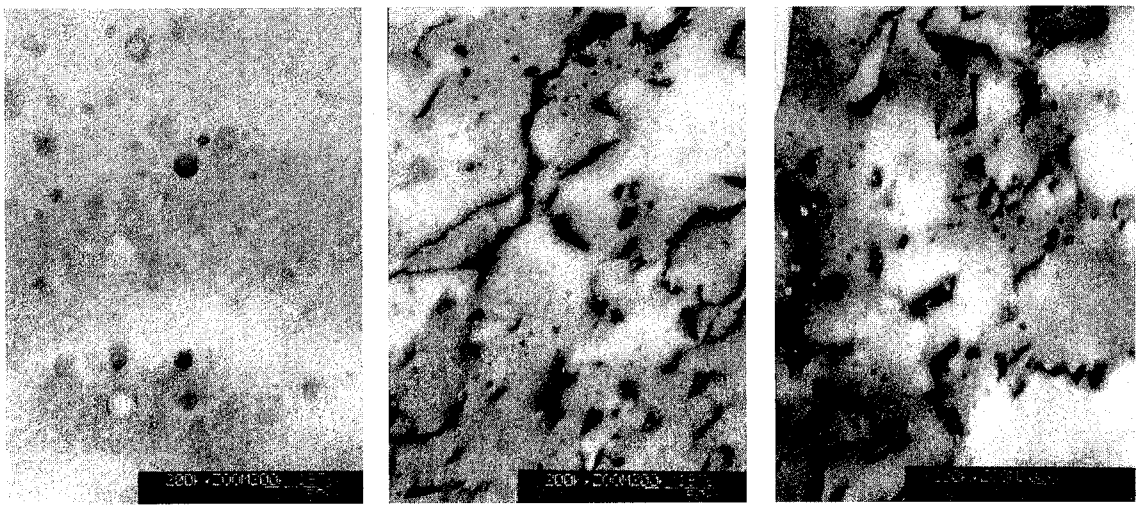


Fig.5 Internal creep rupture strength in the hoop direction at 973K

6. High Temperature Strength Evaluation

6.1 Oxide Particle Distribution

Since the high temperature strength of 9Cr-ODS martensitic steels is dominated by an existence of oxide particles in the martensitic steel matrix, a dispersion parameter of the oxide particles was measured based on the high magnification transmission electron micrographs. The high magnification of Y_2O_3 particles by transmission electron micrograph of thin film is represented in Fig.6. The shape of Y_2O_3 particles is nearly spherical. The oxide particle size is obviously reduced, and inter-particles spacing is shortened in M92 and M93 as



M91 M92 M93

Fig.6 Transmission electron micrograph of Y_2O_3 particles

compared with M91. The original size of oxide particles is about 20nm, and thus M92 and M93 containing 0.20mass% Ti have a significantly reduced size at a center of 3nm diameter with regular size distribution. In contrast, broad distribution ranging from 5 to 10nm in diameter is dominated in M91 with Ti content of only 0.12mass%. These observations provide evidence that Ti content significantly affects the particle size redistribution. It is considered that the results of significant reduction of Y_2O_3 particle size and shortened inter-particle spacing in the M92 and M93 by addition of 0.2mass% Ti is owing to the step-wise increase of tensile and creep rupture strength, as compared with M91 of 0.12mass% Ti.

6.2 Complex Oxide Composition

The noticeable improvement in tensile and creep rupture strength of M93 and M11 is attributed to remarkable refinement of the oxide particles. The major difference in the chemical composition among the manufactured claddings is only content of Y_2O_3 and Ti. Thus, Ti partition between oxide particles and other precipitates was investigated to clarify phenomena of the oxide particle refinement. From the electron diffraction measurement, TiC was confirmed to be main precipitate with a few hundred nm size that could be formed during the tempering at 1023K. Therefore, the electrolytes of M91 to M93 were taken, and then separated by the filter with 200nm size mesh. The quantitative analyses of each element in the extracted residue was executed. The Ti in the electrolytes passed through the filter with 200nm size mesh is assumed to be included in the very fine Y_2O_3 particles. Table 2 shows the results of analyses, where the soluble content of each element was calculated by subtracting concentration in precipitate from the total. The large parts of Ti exists as TiC precipitate, and most of W are solved in the matrix. Table 3 represents amount of TiO_2 estimated from the soluble Ti and Ex.O contents. The TiO_2 formation is restricted to an amount of soluble Ti in these cases, thus consequently mol% of TiO_2 is less than equivalent to Y_2O_3. These results suggest that $0.27Y_2O_3$-$0.73\ \alpha\ Y_2TiO_5$ are co-existed in the oxide particles of M91 and $0.06Y_2O_3$-$0.94\ \alpha\ Y_2TiO_5$ in M92 and $0.19Y_2O_3$-$0.81\ \alpha\ Y_2TiO_5$ in M93. The co-authors discovered that complex oxide formation of $\alpha\ Y_2TiO_5$ by combining Y_2O_3 and TiO_2 significantly reduces the oxide particle size. Thus, the extent of refinement would be dependent on degree of stoichiometry. The reason why M92 shows the extremely reduced size of oxide particles could be attributed to the nearly stoichiometric composition of α Y_2TiO_5.

Table 2 Results of quantitative analyses of elements in the extracted residue from electrolytes

No.	Cr (mass%)			Ti (mass%)			W (mass%)			C (mass%)		
	Total	Precipitate	Soluble	Total	Precipitate	Soluble	Total	Precipitate	Soluble	Total	Precipitate	Soluble
M91	9.08	1.22	7.86	0.13	0.077	0.053	1.93	0.32	1.61	0.12	0.12	0.00
M92	8.72	1.13	7.59	0.20	0.140	0.060	1.91	0.34	1.57	0.13	0.12	0.01
M93	8.72	1.15	7.57	0.21	0.150	0.060	1.92	0.35	1.57	0.13	0.12	0.01

*Elemant concentration in soluble was estimated by subtracting concentration in precipitates from the total

Table 3 Results of estimation of chemical form in complex oxide particles from soluble Ti, Y_2O_3 and Ex.O

No.	Soluble Ti (mass%)	Y_2O_3 (mass%)	Ex.O (mass%)	Estimated TiO_2 (mass%)		Chemical form (mol%)	
				from Ex.O	from soluble Ti	Y_2O_3	TiO_2
M91	0.053	0.34	0.05	0.125	0.088	1	0.73
M92	0.060	0.30	0.04	0.100	0.100	1	0.94
M93	0.060	0.35	0.06	0.150	0.100	1	0.81

7. Conclusion

The following results were obtained in this study:

(1) The CCT diagram of 9Cr-ODS martensitic steels was constructed, and higher minimum cooling rate is necessary for inducing the martensitic phase transformation due to their finer prior austenite grains in compared with conventional ferritc-martensitic steels.

(2) It was originally shown on the basis of the CCT diagram that claddings are able to be manufactured by cold-rolling under the softened ferrite phase induced by slow cooling at 150K/hr from austenite phase. Substantially elongated grains produced by cold-rolling were destroyed and successfully changed to the equi-axed homogeneous grains by using α to γ phase transformation at the final stage of the cladding manufacturing process.

(3) The homogeneous grains induced isotropic creep strength as we expected, although as-rolled claddings with elongated grains along rolling direction exhibited strong strength anisotropy. The manufactured claddings showed noticeable improvement in tensile and creep rupture strength that are considerably superior to PNC-FMS and even austenitic PNC316 at higher temperature and longer time to rupture. Adequate ductility is also maintained.

(4) The oxide particle distribution significantly affects the strength. From experiment with varying Ti and Y_2O_3 contents, Ti addition is the most effective for improving both tensile and creep rupture strength by reduction of Y_2O_3 particle size and shortening inter–particles spacing. The behavior of oxide particle size reduction is associated with a stoichiometry between Y_2O_3 and TiO_2.

References

[1] Huet,J.J., Nucl.Technol. 70,215(1985)

[2] Alamo,A., Regle,H., Pons,G. and Bechade,J.L., Mater.Sci. Forum, 88-90, 183-190(1992)

[3] Dubuisson,P., Schill,R., Hugon,M-P., Grislin,I. and Seran,J-L Effects of Radiation on Materials: 18th International Symposium, ASTM STP 1325, R.K.Nanstad, M.L.Hamilton, F.A.Garner and A.S.Kumar, Eds., American Society for Testing and Materials, West Conshohocken, 1999, pp.882-898

[4] Ukai,S., Harada,M., Okada,H., Inoue,M., Nomura,S., Shikakura,S., Asabe,K., Nishida,T. and Fujiwara,M., J.Nucl.Mater.204(1993)65

[5] Ukai,S., Harada,M., Okada,H., Inoue,M., Nimura,S., Shikakura,S., Nishida,T., Fujiwara,M. and Asabe,K., J.Nucl.Mater.204(1993)74

[6] Mukhopadhyay,D.K., Froes,F.H. and Gelles,D.S., J.Nucl.Mater. 258-263(1998)1209

[7] Ukai,S., Nishida,T., Okada,H., Okuda,T., Fujiwara,M. and Asabe,K., J.Nucl. Scie. and Technol. Vol.34, No.3, (1997) 256

[8] Ukai,S., Nishida,T., Okuda,T. and Yoshitake,T., J.Nucl.Mater. 258-263(1998)1745

[9] Ukai,S., Yoshitake,T., Mizuta,S., Matsudaira,Y., Hagi,S. and Kobayashi,T., J.Nucl. Scie. and Technol. Vol.36, No.8, (1999) 710

[10] Ukai,S., Okuda,T., Fujiwara,M., Kobayashi,T., Mizuta,S. and Nakashima,H.,to be published in J.Nucl. Scie. and Technol.

[11] Ukai,S., Nishida,T., Okuda,T. and Yoshitake,T., J.Nucl.Scie. and Technol.,Vol.35,No.4,(1998) 294,

[12] Alamo,A., Brachet,J., Castaing,A., Lepoittevin,C. and Barcelo,F., J.Nucl.Mater. 258-263(1998)1228

[13] Uehira,A., Ukai,S., Mizuno,T., Asaga,T. and Yoshida,E., J.Nucl.Scie. and Technol., Vol.37, No.9, (2000) 780,

JP0350269

2.5 MICROFABRICATION OF CROSSLINKED PTFE BY SYNCHROTRON RADIATION

Yasunori Sato[1*], Daichi Yamaguchi[1], Akihiro Oshima[1], Takanori Katoh[2], Shigetoshi Ikeda[3], Yasushi Aoki[2], Shigeru Tanaka[4], Yoneho Tabata[5] and Masakazu Washio[1]

[1] Advanced Research Institute for Science and Engineering, Waseda University, 3-4-1, Okubo, Shinjuku-ku, Tokyo, 169-8555 Japan

[2] Sumitomo Heavy Industries, Ltd., 2-1-1, Yato-cho, Nishitokyo, Tokyo, 188-8585 Japan

[3] Raytech Corporation, #402 Sousyu Bldg., 4-40-13, Takadanobaba, Shinjuku-ku, Tokyo, 169-0075 Japan

[4] Japan Atomic Energy Research Institute, Takasaki Radiation Chemistry Research Establishment, 1233 Watanuki-cho, Takasaki, Gunma, 370-1292 Japan

[5] Professor Emeritus, The University of Tokyo, 7-3-1, Hongo, Bunkyo-ku, Tokyo, 113-8656 Japan

Abstract

Microfabrication of crosslinked polytetrafluoroethylene (PTFE) using synchrotron radiation (SR) has been demonstrated for production of micro-components applicable to radiation fields. The method of microfabrication was readily capable of obtaining a microstructure with aspect-ratio of 25 made of crosslinked PTFE. The etching rate of crosslinked PTFE was higher than that of non-crosslinked PTFE. The results show that the etching rate of crosslinked PTFE depends only on the degree of crosslinking. The effect of molecular motion on etching process was discussed from temperature dependence on etching rate. Moreover, in order to examine whether any change of chemical structures and crystallinity would be induced by SR-irradiation on PTFE, SR-irradiated PTFE was measured by NMR spectroscopy and DSC analysis. The results showed that the crosslinking reaction of PTFE would be induced by SR-irradiation in the solid state.

Keywords: crosslinked PTFE, synchrotron radiation, microfabrication, modification, etching

1. Introduction

Polytetrafluoroethylene (PTFE) is a very unique polymeric material because of the various characteristic properties such as high electrical resistivity, chemical and thermal stability, potential biocompatibility and so on.[1] These advantageous features enable PTFE to apply in a variety of fields including electronics and medical application. However, PTFE is used less in nuclear facilities or aerospace environment, because PTFE is degraded by ionizing radiation with a small dose. Recently, crosslinked PTFE has been obtained by irradiation in its molten state under oxygen-free atmosphere.[2-6] The radiation crosslinking reaction induces the various changes of characteristic properties. The radiation durability and mechanical properties are much improved.[5,7,8] Therefore, crosslinked PTFE has the potential to be applied as a micro-component in radiation fields.

So far, several reports concerning microfabrication of non-crosslinked PTFE have been published. Pulsed laser ablation technique using vacuum ultraviolet laser[11] or ultra-short pulsed laser[12] have been attempted to produce microstructures of PTFE. However, the aspect-ratio was up to 1. So, laser ablation technique may not be appropriate to produce high

* Corresponding author. Tel: +81-3-5286-3893 Fax: +81-3-3205-0723.
E-mail address: 60110320@mn.waseda.ac.jp (Y. Sato)

aspect-ratio microstructures of PTFE. It has been reported that PTFE was efficiently decomposed by SR-irradiation. This method requires no chemicals to produce microstructures.[9,10] This fabrication method is simple and can be performed in shorter time in any other fabrication methods.

In this paper, we describe recent studies on micromachining of crosslinked PTFE and SR etching mechanism for PTFE and crosslinked PTFE.

2. Experimental

2.1 Materials

Non-crosslinked PTFE (Original) sheets with a thickness of 500 μ m were obtained from Asahi Glass Fluoropolymers Co. Ltd.. Two other types of non-crosslinked PTFE samples, low crystallinity sample (LC) and low molecular weight sample (LM), were also prepared. Crosslinked PTFE samples (RX) were prepared by electron beam (EB) irradiation in its molten state at 613 K in argon atmosphere (0.5kGy/s).[5]

2.2 SR Irradiation

The SR experiments were performed using beam-line (BL-4) of the compact normal conducting electron storage ring, AURORA-2S (manufactured by Sumitomo Heavy Industries, Ltd.).[13] The samples were placed in the vacuum chamber and were irradiated by the SR beam through a beryllium filter with a thickness of 10 μ m in order to cut off longer wavelengths deforming the transferred pattern due to local heating of samples. The temperature of the samples was controlled from room temperature to 473 K. The photon flux of the SR beam through the Be-filter was 3.2×10^{11} photons/s/mA/mm^2.

2.3 Measurements

The microstructures produced by SR direct photo-etching were observed by SEM and the etching depth was measured by optical microscope. The polymers irradiated by SR were analyzed by atomic force microscope (AFM; Seiko Instruments Inc. SPI3800-N), solid state nuclear magnetic resonance spectroscopy (NMR; JOEL CMX-400) and differential scanning calorimeter (DSC; Perkin Elmer DSC-7) for the investigation of the SR etching mechanism.

3. Results and discussion

3.1 Etching Rate Measurements

Microfabrication of Original by SR direct photo-etching was carried out successfully. Fig. 1 shows the SEM photograph of microstructure of RX-1600, where 1600 indicates the dose for crosslinking. It was produced by the irradiation at 413 K with a proximity X-ray mask. The quality of micromachining of crosslinked PTFE is as good as that of Original; the edges of micro-structures made of crosslinked PTFE were very sharp.[14]

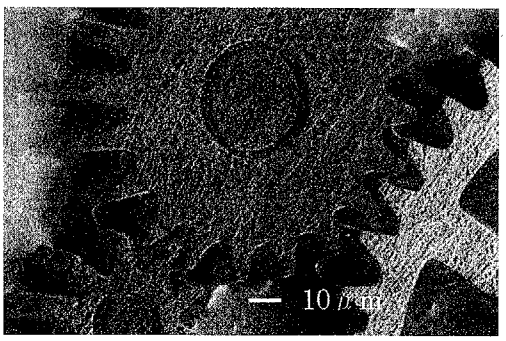


Fig.1 Micro-gear made of crosslinked PTFE (RX-1600) by SR direct photo-etching method

Fig. 2 shows the etching depth for Original and RX-1600 as a function of SR photon fluence in the case of the SR irradiation at 413 K. Here, etching depth is defined as a distance between the non-irradiated face and the top of the residual sample after etching. The etching rate of crosslinked PTFE is higher than that of Original.

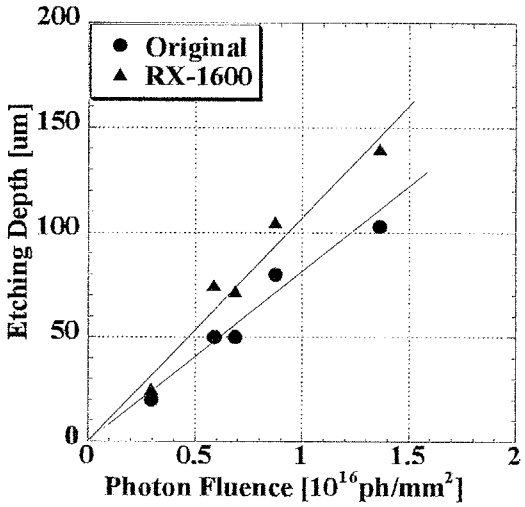


Fig.2 Relation between etching depth and SR photon fluence in case of SR-irradiated at 413 K

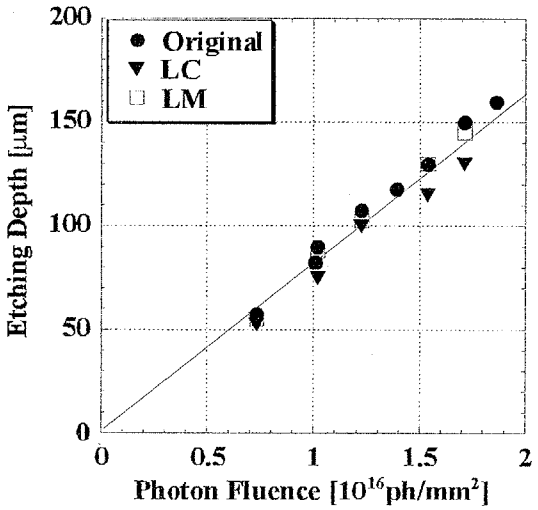


Fig.3 Relation between etching depth and SR photon fluence in case of SR-irradiated at 413 K

Although there is large difference about crystallinity or molecular weight between Original and crosslinked PTFE, it has been already proved that the etching rate would be hardly related to crystallinity and molecular weight (see Fig. 3).

The temperature dependence on the etching rate for Original and RX-1600 is shown in Fig. 4. As irradiation temperature is elevated, the etching rates become higher and the ratio of the etching rates of [RX-1600]/[Original] is smaller. Besides, although crosslinked PTFE could be etched at room temperature, Original could hardly be etched. The results shown in Fig. 4 indicate that molecular motion of crosslinked PTFE would play an important role in SR etching process. When the network is formed in PTFE, the changes in molecular

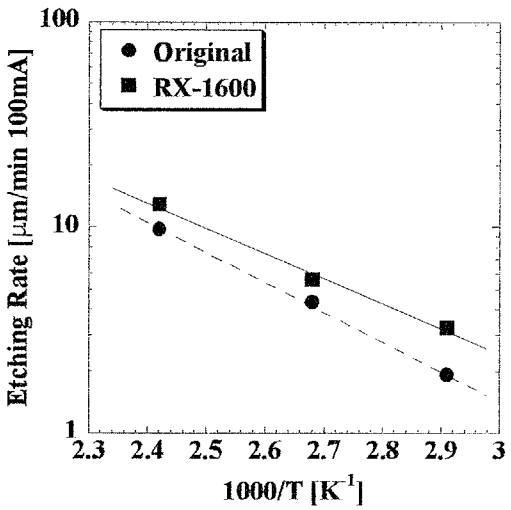


Fig.4 Temperature dependence of etching rate for Original and RX-1600

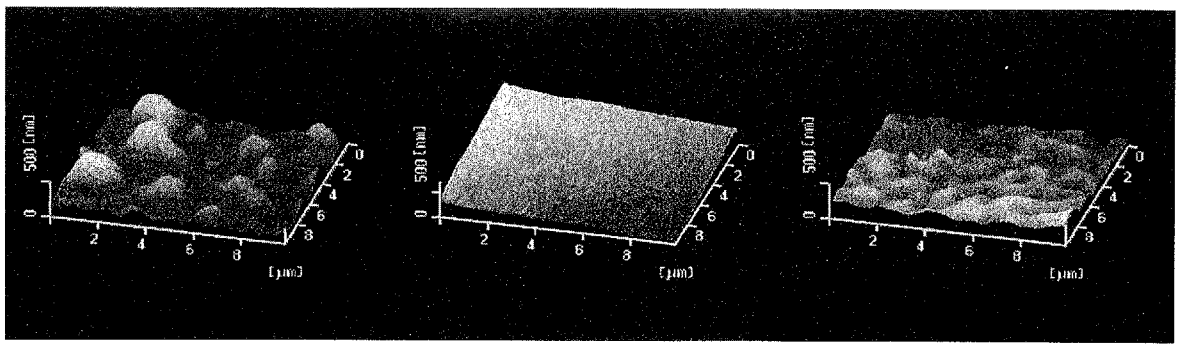


Fig.5 AFM images of surface morphology after SR etching (left; Original SR-irradiated at 413 K, center; RX-1600 SR-irradiated at 413 K, right; RX-1600 SR-irradiated at 343

conformation and mode of molecular motion should take place. As the results mentioned above, it may be reasonable to conclude that the enhanced molecular motion of crosslinked PTFE accelerates desorption of fragments produced by SR-irradiation.

In order to investigate SR etching mechanism, surface condition of the samples after SR etching at 343 K and 413 K was measured with AFM. Fig. 5 shows that the surface become smoother as the temperature during irradiation is higher and that the surface of RX-1600 is smoother than that of the Original in case of the same irradiation temperature. These results show that emitted fragments of RX-1600 reattaches the surface less than that of Original. The higher etching rate of crosslinked PTFE could be explained by such an accelerated desorption of crosslinked PTFE.

3.2 Surface Modification For Original

For examining whether any change of chemical structures would be induced by SR-irradiation on PTFE, Original irradiated by SR was measured by solid state ^{19}F NMR spectroscopy to find out change of the chemical structure. The magic angle spinning ratio of 16 kHz were used to overcome overlaps of the CF_3 and CF signals with the spinning side bands (*) of internal CF_2. The measurement was carried out at 423 K to make the resolution higher. Original with a thickness of 500 μ m was etched by SR-irradiation at 413 K, and the remained sample (SR-irradiated PTFE) with that of 100 μ m was measured by NMR spectroscopy. Fig. 6 shows that several new signals corresponding to CF_3, CF_2 and CF groups are observed for SR-irradiated PTFE. The appearance of the signal of CF means that crosslinking reaction could be induced in solid state PTFE by SR-irradiation at much below its melting temperature; 600 K.[17]

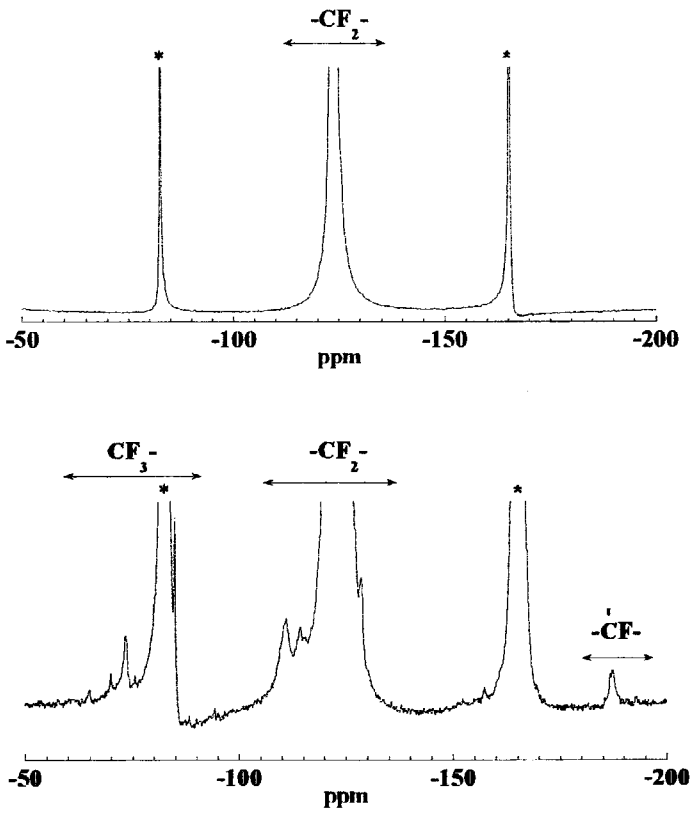


Fig.6 solid state ^{19}F NMR spectra of Original (upper) and SR-irradiated PTFE (lower); measured at 16kHz, 423K

Also our DSC results of the modified regions strongly suggest that the network structures are formed by SR-irradiation at 413 K, because the shift of the exothermic peak (*i.e. crystallization temperature)* toward lower temperature means that only smaller size crystallites can be formed in crosslinked PTFE (see Fig. 7). In general, the network formation hinders the polymer from crystallizing, so that the crystallization temperature becomes lower and the heat of crystallization decreases with increasing crosslinking density.[18]

It has been considered that the radicals formed in non-crosslinked PTFE below the melting

temperature are restricted to recombination with neighboring radicals due to satiric hindrance of the molecular chain and that crosslinking reaction cannot be induced by irradiation in solid state PTFE. Our results show that crosslinking structure could be formed in the solid state by SR-irradiation. The SR-irradiation with high dose rate should lead to generation of considerable amounts of radicals and much shorter distance among the radicals. Furthermore, it is known that the molecular motion in amorphous phase should be allowed over γ -relaxation temperature of 176 K. Therefore, radicals formed by SR-irradiation in amorphous phase would exceed structural restriction to react with other radicals and crosslinking network would be formed even in the solid state.

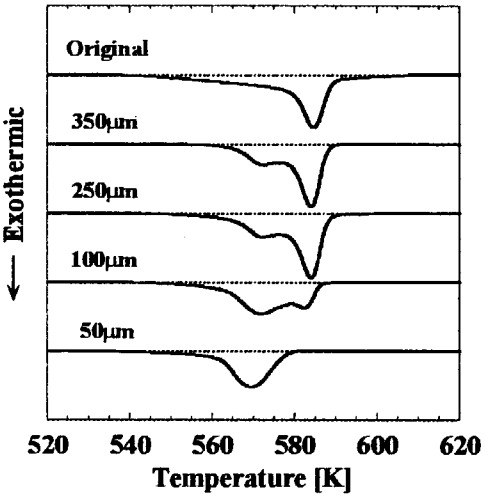


Fig. 7 DSC thermograms of crystallization for PTFE SR-irradiated at 413 K

4. Conclusion

Micromachining of crosslinked PTFE has been demonstrated successfully by SR direct photo-etching method. The etching rate of crosslinked PTFE is higher than that of non-crosslinked PTFE and the ratio of the etching rate of crosslinked PTFE to that non-crosslinked PTFE is higher at lower irradiation temperature. The etching rate depends on crosslinking density, which is related to chain mobility and mode of molecular motion. SR modifies inner region, in which crosslinking reaction is induced much below the melting temperature due to SR high dose rate. These findings might be very important for the development of microcomponents and other applications taking advantages of crosslinked PTFE, which is available not only in electronics or medical fields, but also in radiation field.

5. Acknowledgements

The authors would like to acknowledge the staff of the Irradiation Service Division in JAERI for EB irradiation. The authors also would like to acknowledge Prof. Y. Hama and Research Associate T. Oka of Advanced Research Institute for Science and Engineering, Waseda University for AFM measurements and Material Characterization Central Laboratory in Waseda University for NMR measurements.

5. References

[1] H. Mark, N. Bikales, C. Overberger, G. Menges, in: *"Encyclopedia of Polymer Science and Engineering"*, 2nd ed., J. Wiley & Sons, New York, Vol. 16, 577 (1964).
[2] M. Dole, in: *"The Radiation Chemistry of Macromolecules"*, Academic Press, New York, Vol. II, Chap. 9 (1973).
[3] Y. Tabata, *Proc. of Taniguchi Conf. "Solid state reaction in radiation chemistry."*, Sapporo, Japan, 118(**1992**).
[4] J. Sun, Y. Zhang, X. Zhong, X. Zhu, *Radiat. Phys. Chem.* ***44***, 655 (1994).
[5] A. Oshima, Y. Tabata, H. Kudoh, T. Seguchi, *Radiat. Phys. Chem.* ***45***, 269 (1995).
[6] Y. Tabata, A. Oshima, K. Takashika, T. Seguchi, *Radiat. Phys. Chem.* ***48***, 563 (1996).
[7] Y. Tabata, A. Oshima, *Macromol. Symp.* ***143***, 337 (1999).
[8] A. Oshima, S. Ikeda, T. Seguchi, Y. Tabata, *Radiat. Phys. Chem.* ***49***, 279 (1997).
[9] Y. Zhang, T. Katoh, M. Washio, M. Yamada, S. Hamada, *Appl. Phys. Lett.* ***67***, 872

(1995).
[10] T. Katoh, N. Nishi, M. Fukagawa, H. Ueno, S. Sugiyama, *Sensor and Actuators, **A89***, 10 (2001).
[11] S. Wada, H. Tashiro, K. Toyota, H. Niino, A. Yabe, *Appl. Phys. Lett. **63***, 211 (1993).
[12] H. Kumagai, K. Midorikawa, K. Toyoda, S. Nakamura, T. Okamoto, M. Obara, *Appl. Phys. Lett.*, ***65***, 1850 (1994).
[13] Y. Zhang, T. Hori, *Synchrotron Radiat. News*, ***13***, 32 (2000).
[14] D. Yamaguchi, T. Katoh, S. Ikeda, M. Hirose, Y. Aoki, M. Iida, Y. Tabata, M. Washio, *Proc. of RadTech Japan 2000 Symp.* Yokohama, Japan, 170 (2000).
[15] A. Oshima, S. Ikeda, E. Katoh, Y. Tabata, *Radiat. Phys. Chem. **62***, 39 (2001).
[16] U. Lappan, U. Geißler, K. Lunkwitz, *Radiat. Phys. Chem. **56***, 317 (2000).
[17] E. Katoh, H. Sugisawa, A. Oshima, Y. Tabata, T. Seguchi, T. Yamazaki, *Radiat. Phys. Chem. **54***, 165 (1999).
[18] T. Katoh, D. Yamaguchi, Y. Sato, S. Ikeda, Y. Aoki, M. Washio, Y. Tabata, *Appl. Surf. Sci.* **186**, 24 (2002).

JP0350270

2.6 ANATASE THIN FILM WITH DIVERSE EPITAXIAL RELATIONSHIP GROWN ON YITTRUM STABILIZED ZIRCONIA SUBSTRATE BY CHEMICAL VAPOR DEPOSITION

Takahira Miyagi*[1,2], Tomoyuki Ogawa[1,3], Masayuki Kamei[1], Yoshiki Wada[1], Takefumi Mitsuhashi[1] and Atsushi Yamazaki[1,2]

1. Advanced Materials Laboratory (AML), National Institute for Materials Science (NIMS), 1-1 Namiki, Tsukuba, Ibaraki 305-0044, Japan
2. Department of Resource and Environmental Engineering, School of Science and Engineering, Waseda University, 3-4-1 Okubo, Sinjuku-ku, Tokyo 169-8555, Japan
3. Department of Applied Physics and Physico-Informatics, Faculty of Science and Technology, Keio-Gijuku University, 3-14-1 Hiyoshi, Kohoku-ku, Yokohama, Kanagawa 223-8522, Japan

ABSTRACT

An anatase epitaxial thin film with diverse epitaxial relationship, YSZ (001) // anatase (001), YSZ (010) // anatase (110), was grown on a single crystalline yttrium stabilized zirconia (YSZ) (001) substrate by metal organic chemical vapor deposition (MOCVD). The full width at half maximum (FWHM) of the (004) reflection of this anatase epitaxial film was 0.4 °, and the photoluminescence of this anatase epitaxial film showed visible emission with broad spectral width and large Stokes shift at room temperature. These results indicate that this anatase epitaxial film possessed almost equal crystalline quality compared with that grown under identical growth conditions on single crystalline $SrTiO_3$ substrate.

Keywords: anatase, epitaxial growth, yittrium stabilized zirconia, photoluminescence,

1. Introduction

Anatase, the one of the polymorphs of TiO_2, has attracted much attention as a photocatalyst, and has been put to practical use as anti-bacterium tile etc. On the other hand, the understanding of anatase as a semiconductor material is not satisfactory because of the difficulty in fabricating high quality single crystalline anatase samples. Though the

*Corresponding author. TEL: +81 298 58 5646 FAX:+81 298 54 9062
E-mail address: miyagi.takahira@nims.go.jp (T.Miyagi)

of the single crystalline anatase using a chemical transport reaction method was reported[1], it is quite difficult to fabricate single crystals without contamination using this method.

Recently, the technique of growing high quality single crystalline anatase films was established by making good use of the heteroepitaxial technology and made it possible to get large area single crystalline anatase samples. $SrTiO_3$(001) has been widely used as a substrate material for epitaxial growth of anatase[2-4]. Because of the small lattice mismatch between $SrTiO_3$(001) and anatase(001) (3%), anatase were grown on $SrTiO_3$ substrate with the epitaxial relationship of $SrTiO_3$(001)//anatase(001), $SrTiO_3$(100)//anatase(100). On the other hand there have been reports on anatase epitaxial film grown on yttrium stabilized zirconia (YSZ) substrate to the best of our knowledge. It is important to confirm the epitaxial relationship of anatase film grown on YSZ substrate since the lattice mismatch between anatase and YSZ is much larger than that between anatase and $SrTiO_3$ and a polycrystalline film growth can also be expected. Therefore, in this study, we synthesized TiO_2 films on both substrates under the same conditions and evaluated the films using x-ray diffraction (XRD) and photoluminescence.

2. Experiments

The TiO_2 films were synthesized on the optically polished (001) plane of yttrium stabilized zirconia (YSZ) and strontium titanate ($SrTiO_3$) single-crystalline substrates using a metal organic chemical vapor deposition (MOCVD) apparatus. The substrates were ultrasonically cleaned with alkaline lotion (SEMICO-CLEAN) and then with deionized-water for 10 minutes, and finally annealed at 1000 °C in an oxygen atmosphere for two hours in order to get atomically flat surface. The metal-organic source used in this study was $Ti(i\text{-}OPr)_2(DPM)_2$, where $(DPM)=(C_{11}H_{19}O_2)$. This metal-organic source was contained in an evaporating dish placed in a vessel and kept at 110°C during the deposition. The source gas was carried into the reaction chamber using a carrier gas (Ar: 10 sccm). The temperature of the induction pipe was kept at 260 °C. The total pressure in the reaction chamber was kept at 1 Torr. The growth rates of these films were about 3 nm / min. The synthetic temperature was 750 °C. The oxygen flow rate was 150sccm.

The crystal structures of deposited TiO_2 films were identified by standard $\theta/2\theta$ scan XRD. The ω-rocking curves for (004) diffraction peak of anatase films were measured for the purpose of the evaluation of the crystalline quality. Pole figure XRD was carried out in order to investigate the epitaxial relationships between anatase thin films and their substrates. The (105) diffraction of anatase films, the (440) diffraction of YSZ substrate and the (204) diffraction of $SrTiO_3$ substrate were investigated. The thicknesses of both anatase films were measured by Fourier analysis of interference structure in x-ray specular reflection from film[5] and were unified to 250nm. These XRD measurements were carried

out using Materials Research Diffractomater system (MRD: Philips Co. Ltd.) and the incident x-ray beam was monochromized by a channel cut analyzer composed of two Ge single crystals in order to get the single profile of Cu $K\alpha_1$ radiation.

Photoluminescence of anatase films at room temperature was measured by using a photoluminescence measurement system (RPM2000: ACCENT OPTICAL Co. Ltd.). A 325 nm line of He-Cd laser (3.815eV) was employed as an excitation light source and luminescence spectra were measured by monochromator with CCD detector.

3. Results and Discussion

Fig.1 shows the standard $\theta/2\theta$ scan XRD of TiO_2 films grown on YSZ (001) (a) and $SrTiO_3$ (001) (b) substrates. In addition to the peaks due to the substrates, only the diffraction peaks assigned to the anatase (00*l*) could be observed, indicating that these films possessed *c*-axis orientation normal to the substrates surface. The insets of the fig.1 (a) and (b) show the ω-rocking curves of the (004) reflection of these anatase films; the both FWHM are 0.4 °. These narrow ω-rocking curves suggest that the *c*-axes of these anatase films are well oriented normal to the substrates. Furthermore, it is confirmed that these anatase epitaxial films possess almost equal crystalline quality.

Fig.2 shows the results of pole figure XRD of anatase films and their substrates. The (105) diffraction of anatase films, the (440) diffraction of YSZ substrate and the (204) diffraction of $SrTiO_3$ substrate were investigated. The spots of (105) diffraction of both anatase films show a clear fourfold rotation symmetry, suggesting that these anatase films possess an excellent in-plane orientation. In the anatase film synthesized on $SrTiO_3$ substrate, the (105) spots of the anatase film appear in the same rotation angle as the (204) spots of the $SrTiO_3$ substrate, which indicate that the epitaxail relationship between anatase film and $SrTiO_3$ (001) substrate is

Anatase (001)//$SrTiO_3$ (001) and Anatase (100)//$SrTiO_3$ (100).

On the other hand, the (105) spots of the anatase film grown on the YSZ substrate are observed at the position rotated from the (404) spots of the YSZ substrate by 45 . This result indicates that the anatase film grown on YSZ substrate possesses the diverse epitaxial relationship and this relationship between anatase film and YSZ substrates is

Anatase (001)//YSZ (001) and Anatase (100)//YSZ (110).

This epitaxial relationship can be easily understood based on the lattice orientation relationship illustrated in Fig. 3. The diagonal of anatase *a*-axis (0.5353nm) is in good agreement with lattice constant of YSZ substrate (0.5139nm) and the lattice mismatch is 4%.

Fig.4 shows the photoluminescence results of anatase epitaxial films grown on YSZ (001) and $SrTiO_3$ (001) substrates. These photoluminescence are similar in being broad and

showing large Stokes shift. The origin of this photoluminescence has been attribute to be the self-trapped excitons[6].

These XRD and photoluminescence results indicate that the anatase epitaxial film grown on YSZ substrate possesses almost equal crystalline quality compared with that grown on the $SrTiO_3$ substrate.

4.Conclusion

A high-quality crystalline anatase thin film was heteroepitaxaily grown by metal organic chemical vapor deposition on single crystalline YSZ (001) substrate. This anatase epitaxial film possessed the diverse epitaxial relationship; YSZ (001) // anatase (001), YSZ (010) // anatase (110), and the almost equal crystalline quality compared with that synthesized under the equal condition on single crystalline $SrTiO_3$ substrate.

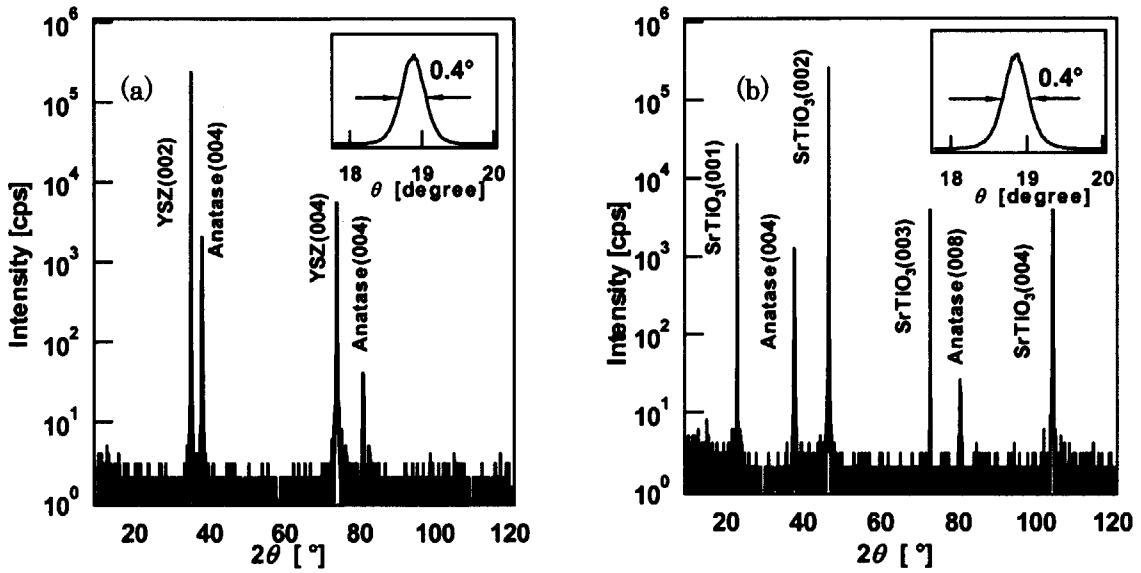
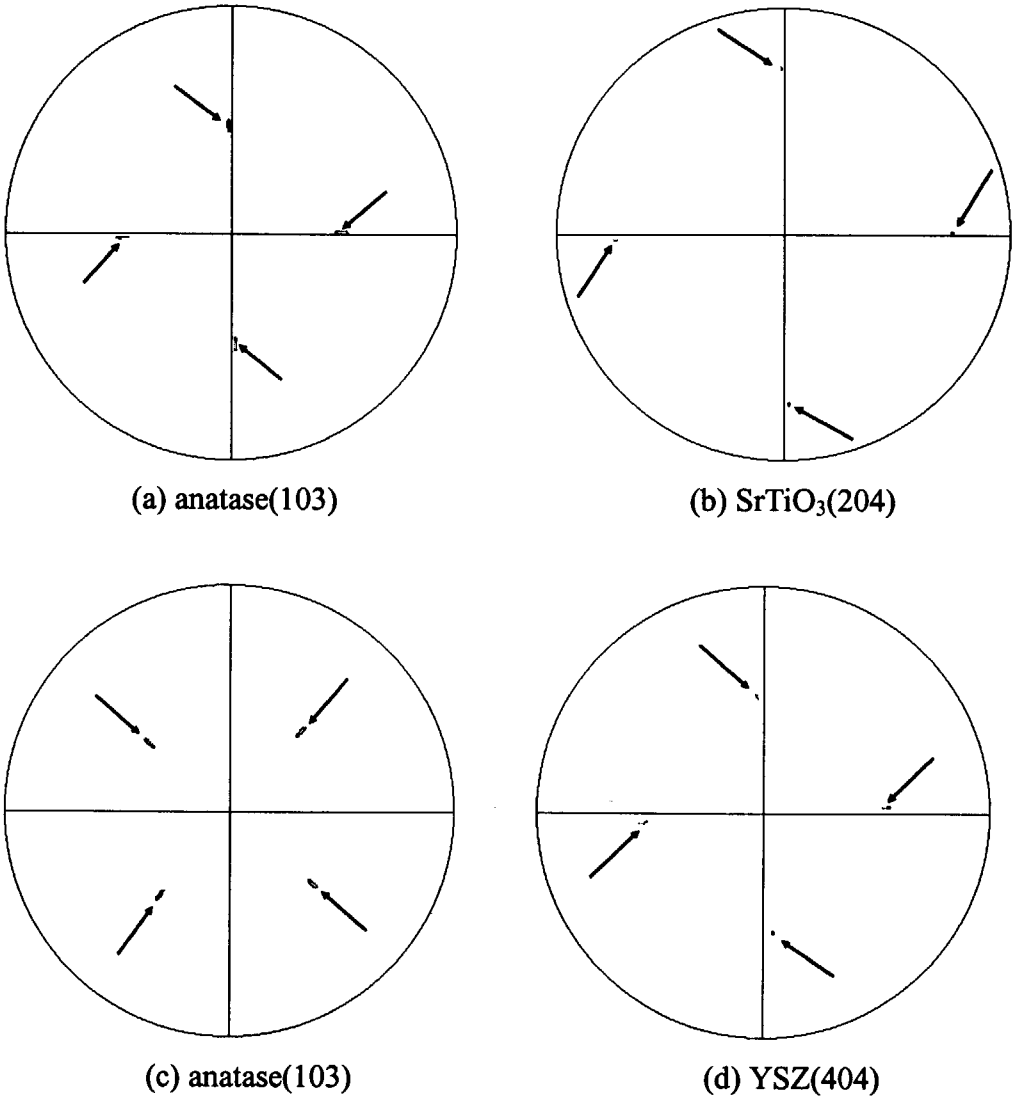


Fig.1 XRD patterns of anatase epitaxial films grown on YSZ (001) (a) and $SrTiO_3$ (001) (b) substrates. The insets show the results of ω-rocking curve measurements for anatase (004), and their FWHM are 0.4 .



(a) anatase(103)　(b) $SrTiO_3$(204)

(c) anatase(103)　(d) YSZ(404)

Fig.2 Pole figure for (103) diffraction of anatase films synthesized on $SrTiO_3$ (a) and YSZ substrate (c) and $SrTiO_3$(204) (b) and YSZ (404) (c).

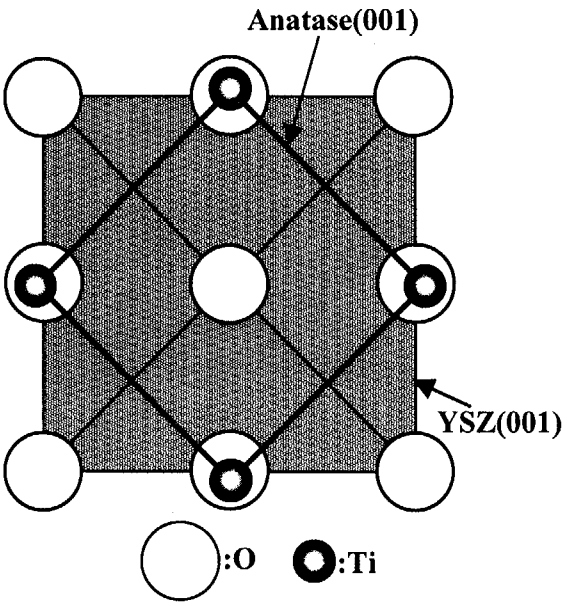


Fig.3 Schematic drawing of the epitaxial growth pattern of anatase(001) on YSZ(001).

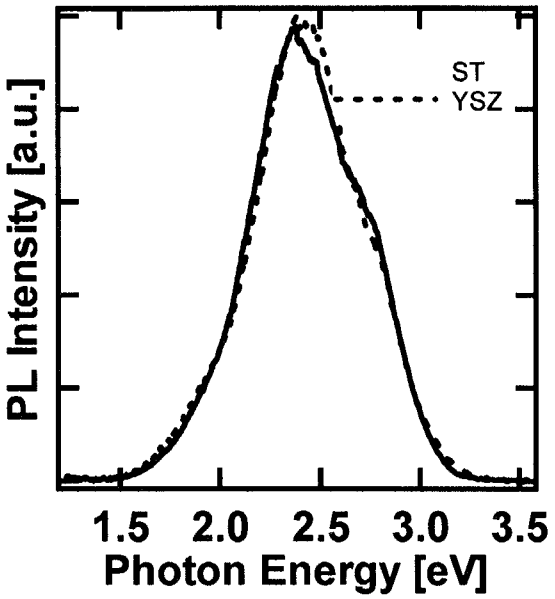


Fig. 4 Photoluminescence spectra of anatase films synthesized on single crystalline YSZ (001) and $SrTiO_3$ (001) substrates.

5.Reference

[1] H. Berger, H. Tang and F.Lévy, J. Cryst. Growth **130**, 108 (1993).

[2] W. Sugimura, A. Yamazaki, H. Shigetani, J. Tanaka, T. Mitsuhashi, Jpn. J. Appl. Phys. **36,** 7358 (1997).

[3] H. Saitoh, H. Sunayama, N. Tanaka and S. Ohshio, J. Ceram. Soc. Jpn. **106,** 1051 (1998).

[4] S. Chen, M. G. Mason, H. J. Gysling, G. R. Paz-Pujalt, T. N. Blanton, T. Castro, K. M. Chen, C. P. Fictie, W. L. Gladfelter, A. Fransiosi, P. I. Cohen and J. F. Evans, J. Vac. Sci. Tecnol. **A11** 2419 (1993).

[5] K. Sakurai and A. Iida, Jpn. J. Appl. Phys. **Vol.31** L113 (1992).

[6] H. Tang, H. Berger, P. Schmid, F. Lévy, and G. Burri, Solid State Commun. **87,** 847 (1993).

JP0350271

2.7 PHOTOLUMINESCENCE MEASUREMENTS OF ZnO HETEROSTRUCTURES

Yutaka Adachi[1*], Haruki Ryoken[2], Isao Sakaguchi[1],
Naoki Ohashi[1], Hajime Haneda[1] and Tadashi Takenaka[2]
[*1]Advanced Materials Laboratory, National Institute for Materials Science,
1-1 Namiki, Tsukuba, Ibaraki 305-0044, Japan
[2]Department of Electrical Engineering, Faculty of Science and Technology,
Science University of Tokyo, 2641 Yamazaki, Noda, Chiba 278-8510, Japan

Abstract

ZnO thin films were grown on $TbAlO_3$ single crystal substrates by pulsed laser deposition. In photoluminescence (PL) measurements, strong emissions from $TbAlO_3$ were observed with the emission from ZnO when the film thickness was less than 100nm. The relationship between the ZnO film thickness and the emission intensity from $TbAlO_3$ was investigated in order to determine the penetration depth of excitation light. Information on the heterostructures ranging from the surface to a depth of 300nm was obtained by PL measurements in this study, and the absorption coefficient for a wavelength of 325nm was estimated to be $1.31 \times 10^5\ cm^{-1}$.

Keywords: ZnO, $TbAlO_3$, heterostructure, ceramics integration, photoluminescence, absorption coefficient

1. Introduction

Zinc oxide (ZnO) is a II-VI semiconductor compound with a large band gap (≈ 3.4eV). It is an attractive material for many applications in optics and optoelectronics. For example, since room-temperature lasing has been observed in ZnO thin films, the epitaxial ZnO is a promising material for ultraviolet lasers[1], [2]. Because ZnO exhibits acoustooptical properties, it is used as a basic material for integrated acoustooptical devices and surface acoustic wave devices[3]. Doped ZnO layers can be used as transparent conducting windows for optoelectronic semiconductor devices.

A heterojunction is a key structure for constructing electronic and optical devices. For instance, ZnO/(Mg,Zn)O multiquantum wells[4] and the p-n junction composed of p-$SrCu_2O_2$/n-ZnO[5] have been fabricated for optical applications. In view of these applications, there is a need for more data on optical properties of ZnO films grown on various materials. The optical properties of ZnO thin films are determined from transmittance,

* Corresponding author. Tel: +81-298-51-3354 ext.503 Fax:+81-298-52-7449.
E-mail address: adachi.yutaka@nims.go.jp

reflectance and photoluminescence (PL) measurements. In a recent study, ellipsometry was used to analyze the optical properties of ZnO films[6]. PL measurements are often used to investigate the crystal quality of ZnO. In this study, the optical properties of ZnO films grown on $TbAlO_3$ single crystals were investigated using PL measurements. $TbAlO_3$ is perovskite-type rare-earth aluminate and is expected to be an efficient phosphor material or visible laser material. Strong Tb^{3+} ion emission (yellow-green) at room temperature has been reported for $TbAlO_3$ single crystals[7]. In the case of PL measurements of ZnO/$TbAlO_3$ heterostructures, the emissions from $TbAlO_3$ are observed when the ZnO layer grown on $TbAlO_3$ is very thin. In order to obtain accurate optical data on ZnO films, it is important to estimate the penetration depth of excitation light. In this study, the ZnO films with various thicknesses were grown on $TbAlO_3$ single crystal substrates, and the emission intensity of $TbAlO_3$ was investigated using PL measurement in order to determine the penetration depth of excitation light.

2. Experimental

The ZnO films used in this study were deposited by pulsed laser deposition (PLD) on $TbAlO_3$ (001) single crystal substrates. $TbAlO_3$ is orthorhombic, with lattice constants of a=0.5231nm, b=0.5305nm and c=0.7415nm[8]. The vacuum system was evacuated to $\sim 5.0 \times 10^{-7}$ Pa. A pulsed Nd:YAG fourth harmonic laser (λ =255nm, t_s=5ns) beam was focused on the sintered ZnO target (99.999%) with the energy density in the range of 1-2J/cm^2 and a pulse repetition rate of 10Hz. The films were deposited in an oxygen (99.9999%) partial pressure of 1.3 Pa and the substrate temperature of 400℃ was maintained during deposition. Film thickness was determined by counting laser pulses. The growth rate was 0.01-0.02nm per pulse. After deposition, the films were cooled at ~80℃ per minute at an oxygen pressure of 1.3 Pa.

The films were characterized by X-ray diffraction (XRD) and tapping-mode atomic force microscopy (AFM). Photoluminescence spectroscopy was performed using a He-Cd laser with an excitation wavelength of 325nm as a light source. The laser power was approximately 8mW.

3. Results and discussion

All the films obtained in this study were colorless. Figure 1 shows the XRD pattern of the ZnO film with a thickness of 400nm. This film showed (0002) and ($11\bar{2}0$) reflections of ZnO along with (002) and (004) reflections of $TbAlO_3$. This indicates that a polycrystalline ZnO film is grown on a $TbAlO_3$ (001) substrate. C-axis oriented film was not obtained. From the AFM observation of this film, the surface roughness and grain size were estimated to be about 25nm and 100nm, respectively.

The PL spectra obtained from samples with various thicknesses are shown in Fig.2. All the samples show a luminescence behavior with UV emissions associated with ZnO and green-yellow band emissions associated with $TbAlO_3$. The PL intensity associated with

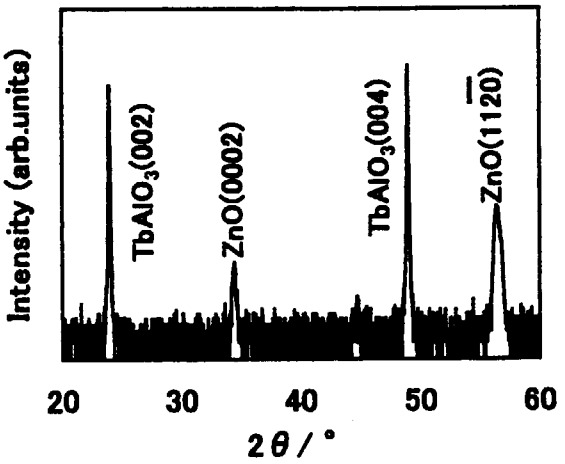


Fig. 1. XRD pattern of ZnO film grown on $TbAlO_3$ (001) substrate.

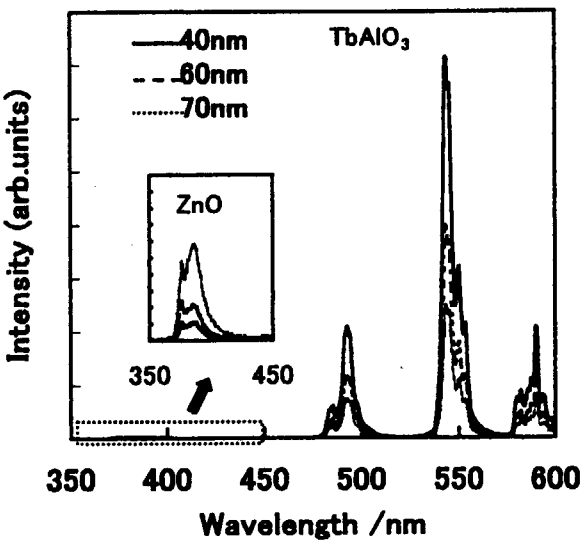


Fig. 2. PL spectra of ZnO films with 40, 60 and 70nm thicknesses grown on $TbAlO_3$ substrates. The UV emissions are from ZnO and the yellow-green band emissions are associated with $TbAlO_3$.

$TbAlO_3$ is strongly dependent on the ZnO layer thickness. The intensity of the green-yellow emissions decreases with increasing ZnO layer thickness. This suggests that the ZnO layer absorbs light energy and thus the intensity of the He-Cd laser beam that reaches the $TbAlO_3$ substrate decreases.

Figure 3 shows the relationship between the PL intensity of the peak at 543.6nm from the substrates and the ZnO film thickness. The peak intensity was normalized using the peak intensity of the area where the ZnO layer was not deposited. When the film thickness was 300nm, the peak at 543.6nm was very slight. This indicates that the optical properties of the film in the range of about 300nm from the surface can be determined from the PL measurements.

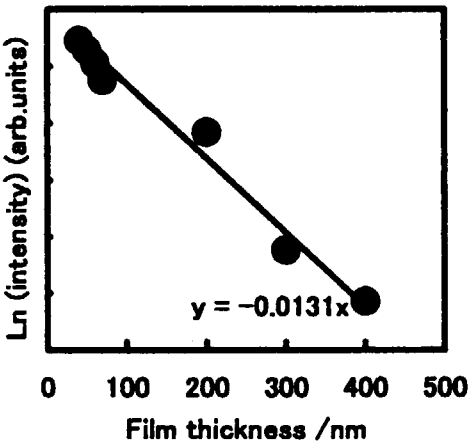


Fig.3. ZnO film thickness dependence of PL intensity of the peak at 543.6nm from $TbAlO_3$.

The absorption coefficient α is given by

$$I = I_0 \exp(-\alpha x), \tag{1}$$

where I_0 is the intensity of a beam of light incident on an absorbing medium and I is the intensity transmitted through a thickness x. The absorption coefficient of the ZnO film for light with a wavelength of 325nm is determined from this equation by assuming the following: (1) the emission intensity of $TbAlO_3$ is proportional to the intensity of the He-Cd laser beam that reaches the substrate; (2) the reflections at the interface are negligible; (3) the absorption in the visible region by ZnO is negligible; (4) the UV emissions from the ZnO film do not excite the emissions from the substrate. The calculated absorption coefficient was 1.31×10^5 cm^{-1}. The absorption coefficient obtained from the transmission and reflection measurement was reported to be 1.6×10^5 cm^{-1}[9]. The finding that the absorption coefficient is smaller than the reported value may be due to the influence of the excitation by the UV emissions from the ZnO film. This approach is not appropriate for an accurate evaluation of an absorption coefficient because many assumptions are required. It is considered that this approach is effective for a rough estimate of the penetration depth of excitation light in PL measurement.

4. Summary

ZnO thin films were grown on $TbAlO_3$ single crystal substrates by pulsed laser deposition. In PL measurements, strong emissions of $TbAlO_3$ were observed with the emission from ZnO film when the film thickness was less than 100nm. The relationship between the ZnO film thickness and the emission intensity from the substrate was investigated in order to determine the penetration depth of excitation light. Information on the heterostructures ranging from the surface to a depth of 300nm was obtained by PL measurements in this study, and the absorption coefficient for a wavelength of 325nm was

estimated to be 1.31×10^5 cm^{-1}.

References

[1] D. M. Bagnall, Y. F. Chen, Z. Zhu, T. Yao, S. Koyama, M. Y. Shen, and T. Goto, *Appl. Phys. Lett.*, **70**, 2230 (1997).

[2] P. Yu, Z. K. Tang, G. K. L. Wong, M. Kawasaki, A. Ohtomo, H. Koinuma and Y. Segawa, *J. Cryst. Growth*, **184/185**, 601 (1998).

[3] C. R. Gorla, N. W. Emanetoglu, S. Liang, W. E. Mayo, Y. Lu, M. Wraback and H. Shen, *J. Appl. Phys.*, **85**, 2595 (1999).

[4] H. D. Sun, T. Makino, Y. Segawa, M. Kawasaki, A. Ohtomo, K. Tamura and H. Koinuma, *Appl. Phys. Lett.*, **78**, 3385 (2001).

[5] H. Ohta, K. Kawamura, M. Orita, M. Hirano, N. Sarukura and H. Hosono, *Appl. Phys. Lett.*, **77**, 475 (2000).

[6] K. Postava, H. Sueki, M. Aoyama, T. Yamaguchi, Ch. Ino, Y. Igasaki and M. Horie, *Appl. Phys. Lett.*, **87**, 7820 (2000).

[7] M. Sekita, Y. Miyazawa, S. Morita, H. Sekiwa and Y. Sato, *Appl. Phys. Lett.*,**65**, 2380 (1994).

[8] S. Morita, T. Watanabe, M. Funayama, Y. Miyazawa and M. Sekita, *J. Cryst. Growth*, **166**, 370 (1996)

[9] J. F. Muth, R. M. Kolbas, A. K. Sharma, S. Oktyabrsky and J. Narayan, *J. Appl. Phys.*, **85**, 7884 (1999).

JP0350272

2.8 Characterization of SCC Crack Tip in Alloy 600 in Simulated Primary Water of PWR

Katsuhiko Fujii*, Koji Fukuya, and Nobuo Nakajima
Institute of Nuclear Safety System, Incorporated, Fukui 919-1205, Japan

Abstract

High-resolution observations on microstructure of SCC crack tips were carried out on alloy 600 exposed to a simulated PWR primary water environment. A focused-ion beam (FIB) micro-processing has been applied to prepare electron transparent foils for cross-sectional observations of the crack tips. Cr rich oxides ($(Cr,Fe)_3O_4$ and Cr_2O_3) and a metallic Ni phase were identified at the crack tip and along the grain boundary ahead of the crack tip. Oxide layers on the crack walls were identified as a double layer structure. The inner layer consisted of Cr rich oxides and the outer layer consisted of NiO. Similar microstructure was observed in cross sections of surface oxide layers that were prepared by using the same FIB technique. The inner layer consisted of Cr rich oxides and a metallic Ni phase and was covered by the outer layer of $NiFe_2O_4$ and NiO. In addition, Cr rich oxides were observed along uncracked grain boundaries intercepted by the surface. It is suggested that selective oxidation of chromium occurs at the crack tips, grain boundaries and inner layers. The observations of oxygen penetration along the grain boundaries support a larger diffusivity of oxygen in the stressed grain boundary than that in the unstressed one.

Keywords: Crack tip, PWSCC, Surface oxide layer, TEM, FIB, Alloy 600, PWR

1. Introduction

Stress corrosion cracking (SCC) of alloy 600 is one of the important material degradation issues in primary water of pressurized water reactors (PWRs). A number of studies have been performed on the nucleation and propagation of SCC, and several mechanisms based on observed phenomena were proposed. Although the mechanistic models such as the slip dissolution, hydrogen embrittlement and internal oxidation [1-4] have been proposed, none of them has been fully established to explain primary water SCC (PWSCC). Additionally it is well accepted that characteristics of surface oxide layers play an important role in PWSCC of alloy 600 from a number of studies [5-9] that have been performed on the structure, composition and thickness of the oxide layers by means of surface analysis techniques such as auger electron spectroscopy (AES), X-ray photoelectron spectroscopy (XPS), secondary ion mass spectroscopy (SIMS), glow discharge spectroscopy (GDS) and other methods. However there is no general agreement on the mutual relation between the oxide layer characteristics and the origin of the SCC. The oxide layer structure are proposed based on surface analysis data but actual microstructures of the oxide layers have not been observed directly and grain boundary corrosion can not measure by the means of the surface analysis techniques.

In order to make clear the SCC mechanism, it is necessary to be understood electrochemical reaction, behavior of reaction products and that of solved hydrogen in the material at SCC crack tip regions and surface oxide layers. Essential to research into the

*Corresponding author. Tel: +81-770-37-9114, Fax: +81-770-37-2009.
E-mail address: fujiik@inss.co.jp (F. Author).

mechanism are not only macroscopic approaches such as SCC susceptibility evaluation changing material compositions and environmental factors and the former surface analysis but also microscopic approaches such as direct characterization of the crack tips and surface oxide layers.

Ion beam milling techniques have been developed to prepare cross-sectional samples with electron transparent portions at crack tips [10, 11], and studying the direct characterizations of the crack tips was started. Thomas and Bruemmer [12] have used this method and high-resolution analytical transmission electron microscopy to characterize the microstructure and microchemistry of crack tips in alloy 600 exposed at 330 °C in simulated PWR primary water (30-50 cc/kg H_2). They have reported that the microstructure consisted of Cr-rich oxides and a spongy Ni phase. Since the published data on the crack tip microstructure are quite limited, more high-resolution analyses are required to establish the microstructural feature of SCC crack tips.

In this study, a new technique has been used to prepare electron transparent foils including crack tips and surfaces by using the FIB micro-processing that has the major advantage for thinning a selected area to less than 50 nm comparing other preparation methods such as the ion beam milling techniques [13]. We carried out direct characterizations of SCC crack tip and surface oxide layer microstructures in alloy 600 exposed at 360 °C in simulated PWR primary water (30 $cc H_2/kg H_2O$) by using a field emission gun transmission electron microscope (FEG-TEM) and an energy dispersive X-ray spectroscope (EDS).

2. Experimental

The material used in this study was alloy 600 mill-annealed at 980 °C for 45 minutes. The chemical composition is shown in Table 1. SCC cracks were introduced by conducting constant load SCC tests in the simulated PWR primary water (500 ppm B + 2 ppm Li, 30 cc/kg H_2) at 360°C under the load of 350 MPa for 5000 hours. The shape of the uniform gauge test pieces is shown in Fig. 1.

The plates, parallel to the load direction and perpendicular to the sample surface, were cut out from the cracked parallel portion of the tested piece as shown in Fig. 2(a) by using a microsaw taking care not to give damages to the crack tip microstructure. The plate specimen has 2 mm in length to the load direction, 1 mm in width, and 0.3 mm in thickness. The specimens were then mechanically polished to a thickness less than 30 μm as shown in Fig. 2(b) and mounted on a V-shaped grid. FIB processing using Ga ion beams with an accelerating voltage of 30 kV was used to process a crack tip region into an electron transparent foil for high-resolution TEM observation and analysis. Figure 3 shows the FIB processing procedure in this study. In the first step, a block shown as area 1 shown in Fig. 3(b) was removed using FIB draft-milling in order to put the crack tip region in the FIB thinning portion. In the second step, area 2 shown in Fig. 3(c) was milled by FIB micro-processing until the foil thickness is less than 50 nm. The obtained electron transparent portion is 10 μm in width and 5 μm in depth. By shifting the direction of the Ga ion beam from that of crack propagation, the electron transparent foil was obtained without damaging the crack structure.

For the cross sectional observations of the surface oxide layers and the uncracked grain boundaries intercepted by the surface, plate-shaped specimens were cut out of the stressed parallel part shown in Fig. 2. The same FIB methods were then applied to the specimens. However gold and tungsten were deposited on the exposed surface before the FIB milling in order to protect the surface from the Ga ion beams and show the original outer point of the surface.

A high-resolution FEG-TEM with an accelerating voltage of 300 kV was used for the

observation of the crack tip microstructure. The compositions were analyzed by EDS with an electron beam focused to the diameter of 1 nm. The crystallography of the microstructure was characterized by electron micro-diffraction using the electron probe diameter of 20 nm.

3. Results and discussions

3.1 Microstructure of crack tip region

Figure 4 shows a low magnification TEM image of the crack tip region of about 10 μm depth. The length of the intergranular crack was less than one grain. The black arrows show the beam direction of the FIB micro-processing. The white arrow shows the tip of the opened crack. The grain boundaries and triple point were observed ahead of the crack tip. Figure 5 shows the characteristic X-ray images from Cr, Fe, Ni and O together with a TEM image of the same area. The crack tip region was locally divided into Cr-concentrated and Ni-concentrated portions. A high concentration of oxygen was detected in the Cr-concentrated portion. Microcrystalline oxides of 50 nm diameter or less were observed at the crack tip and ahead of the crack tip. From the results of EDS point analyses and electron micro-diffraction analyses as shown in Fig. 6, Cr rich oxides with the rhombohedral Cr_2O_3 and spinel structures were formed. Figure 7 shows the EDS spectrum and micro-diffraction pattern from the Ni-concentrated portion. Metallic Ni phases of 50 nm diameter or more with the fcc structure were detected.

Granulated NiO were observed on the crack walls covered with a thin Cr rich oxide layer. According to a thermodynamic evaluation of the stability boundary condition for Ni/NiO in the PWR primary water [14], the SCC test in this study was carried out on NiO stable condition. Therefore, the NiO is considered to be an oxide formed by a precipitation process. From this fact, the region where the NiO was observed is in 'opened crack', and the region where the metal Ni phase was observed is not exposed to water directly.

Thomas and Bruemmer [12] have characterized the crack tip microstructure in alloy 600 cracked at 330 °C in simulated PWR primary water (30-50 ccH_2/kgH_2O). This condition is the Ni stable one on the Ni/NiO stability. Polycrystalline oxide with cubic NiO structure was observed along the crack walls to a short distance ahead of the open crack tip. Predominant Ni-Cr-Fe oxide with the NiO structure and local phases containing Cr rich oxides with a Cr_2O_3 structure and Ni enriched metal were found in the intergranular penetration zones along high angle grain boundaries intercepted by the main crack. These are quite similar to the microstructure observed in this study. This fact suggests that the oxidation along a grain boundary ahead of stress corrosion cracks in alloy 600 occurs independently of the water environment such as dissolution hydrogen content.

High-resolution TEM observation and fine-probe compositional analysis were not possible due to sample thickness limitations. Qualitative point-analyses showed that oxygen existed on the grain boundary that located at least 5 μm from the crack tip.

Oxygen needs to be diffused inward by some mechanism for the intergranular oxide to develop. The formation of a porous structure phase as a result of vacancy introduction during oxidation has been proposed as this mechanism [15]. In addition, it has been suggested that stress enhances the rate of oxygen penetration along grain boundaries from the observations of stressed and unstressed alloy 600 samples exposed in steam at 400°C [16]. In this study, microcrystalline oxidized particles were observed along the grain boundaries ahead of the cracks where was applied higher stress. It may be possible that these areas provide paths for fast diffusion of oxygen and that stress enhances the diffusion.

The diffusion of oxygen in grain boundaries was directly analyzed by measuring the depth of oxides formed at grain boundaries ahead of cracks. Based on the approximation for the one dimensional slab diffusion, a simple equation is proposed:

$$x = K\sqrt{Dt} \quad (1)$$

where x is the diffusion distance, K is the constant, D is the diffusion coefficient, and t is the exposure time.

The diffusion distance of 5 μm was obtained by measuring the maximum depth of the oxides in this investigation. From the exposure time of 5000 h, the ratio of the square of the depth to the time, which has the dimension of the diffusion coefficient, is calculated as $x^2/t = 1\times10^{-18}$ m^2/s. Woodford and co-workers [17,18] have measured the diffusion of oxygen in grain boundaries of Ni-270 at temperatures from 800 to 1300 °C based on measuring the depth of CO_2 cavities formed at grain boundaries in unstressed specimens exposed in air. The results of the measurements of this study and Woodford and co-workers are summarized in Fig. 8. The line was fitted to the aggregate data of Woodford and co-workers using least-squares fitting of Arrhenius' equation. The depth of the grain boundary penetration in this study was much larger than that estimated from the data at high temperatures, which was referred to the discussion about applicability of an internal oxidation mechanism for SCC in alloy 600 [19]. This fact gives limited evidence the applied stress enhances the rate of oxygen penetration in the process of SCC.

It is considered that the microstructures of the crack tips and grain boundaries are generated through the processes of oxygen penetration along the grain boundary and then Cr oxidation. Because the oxidation potential of Cr is lower than those of Ni and Fe, Cr oxides were formed first and Ni was ejected and clustered. Such selective internal oxidation of Cr along grain boundaries has been reported in Ni-Cr alloys oxidized in 1 atmosphere oxygen at temperatures below 1100 °C [20]. The selective Cr oxidation along grain boundaries has been reported in alloy 600 during 400 °C steam exposures [16]. Recently the selective Cr oxidation has been observed in Hastelloy C-276 cracked in supercritical water including sodium chloride [21]. From these facts, it is suggested that the selective internal oxidation of Cr along grain boundaries has an important role for corrosion of Ni based alloy.

3.2 Microstructure of surface oxide layer

Figure 9 shows X-ray images of the distribution of Cr, Fe, Ni and O in the external surface oxide film on the stressed part together with a cross section TEM image of the same area. It is clear that the oxide film has a double layer structure. The outer layer consisted of a $NiFe_2O_4$ spinel and a cubic NiO that covers up the granular $NiFe_2O_4$. The inner layer consisted of Cr rich oxides, such as Cr_2O_3 and $(Cr,Fe)_3O_4$, and a metal Ni phase. The microstructure of the inner layer was identical to that of the crack tip and the grain boundary ahead of the crack. The thickness of the inner oxide layer was directly evaluated as about 800 nm from the distribution of oxygen in Fig. 9. Several microstructures for oxide layers [22, 23] have been reported based on the surface analysis data using AES and other methods. However the microstructure of oxide layers is not fully understood. This is because the area to be analyzed by former surface analysis methods such as AES is more extensive than the size of microstructures and hence the resulting data are not enough to directly evaluate the microstructures. This study has made it possible for the first time to directly observe that the inner oxide layer consists Cr-rich oxides and a metallic Ni phase. However, much more data for the structure of oxide film, including the effects of environmental and material factors, is required in order to investigate the oxidization mechanism.

Figure 10 shows a TEM image of the cross section of the uncracked grain boundary intercepted by the surface and an O K_α X-ray image of the same area. The penetration of oxygen was detected at a depth up to about 3 μm along the grain boundary. It became clear that oxygen penetrated from the surface in crack-free grain boundaries. From Eq. (1) the diffusivity of oxygen, x^2/t, is calculated as 5×10^{-19} m^2/s. This value is smaller than that in the

grain boundary ahead of the crack. However the diffusivity of oxygen along the stressed grain boundary intercepted by the surface also was much larger than that estimated from the data at high temperatures as shown in Fig. 8.

4. Conclusions

Electron transparent foils including SCC crack tips and surface oxide layers have been prepared by using FIB micro-processing. Direct characterization of the crack tip and surface oxide layer microstructures in alloy 600 exposed to simulated primary water environment were carried out by using FEG-TEM and EDS. The conclusions are,

(1) Cr rich oxides (Cr_2O_3 and $(Cr,Fe)_3O_4$) and a metallic Ni phase are formed in the crack tip and the grain boundary ahead of the crack tip.
(2) The crack walls are covered with thin Cr rich oxides. Granulated NiO are existed on the crack walls directly exposed to water.
(3) Similar microstructure was observed in cross sections of surface oxide layers. The inner layer consisted of Cr rich oxides and a metallic Ni phase and was covered by the outer layer of $NiFe_2O_4$ and NiO. In addition, Cr rich oxides were observed along uncracked grain boundaries intercepted by the surface.
(4) From the oxidation depth along the grain boundary ahead of the crack tip and intercepted by the surface, the oxygen diffusion rate, x^2/t, in the stressed grain boundary is calculated as 1×10^{-18} m^2/s and 5×10^{-19} m^2/s, respectively. The rates are much larger than that estimated from the data in the unstressed grain boundaries at high temperatures.
(5) It is suggested that the oxygen fast diffusion in the stressed grain boundaries and the selective Cr oxidation at the grain boundaries are important for the corrosion of Ni based alloy in PWR primary water.

References

[1] F.P. Ford and P.L. Andresen, Proc. 3rd Int. Symp. on Environmental Degradation of Materials in Nuclear Power Systems –Water Reactors, AIME, 789 (1987).
[2] N. Totsuka and Z. Szklarska-Smialowska, Corrosion **43** 734 (1987).
[3] P.M. Scott and M.Le Calvar, Proc. 6th Int. Symp. on Environmental Degradation of Materials in Nuclear Power Systems –Water Reactors, TMS, 657 (1993).
[4] T. Yonezawa, Proc. 9th Int. Symp. on Environmental Degradation of Materials in Nuclear Power Systems –Water Reactors, TMS, 15 (1999).
[5] Z. Szklarska-Smialowska, W-K. Lai and Z. Xia, *Corrosion*, **46**, 853 (1990).
[6] C. Soustelle, M. Foucault, P. Combrade, K. Wolski and T. Magnin, *Proc. 9th Int. Symp. on Environmental Degradation of Materials in Nuclear Power Systems –Water Reactors*, 105 (1999).
[7] N.S. Mcintyre, D.G. Zetaruk and D. Owen, *J. Electrochem. Soc.*, **126**, 750 (1979)
[8] N. Hakiki et al., *Fontevraud 3*, 327 (1994)
[9] T. Nakagawa, N. Totsuka, N. Nakajima, *Proc. JSCE Materials and Environments 2001*, B-201 (2001)
[10] N. Lewis, D.J. Perry and M.L. Bunch, Proc. Microscopy and Microanalysis, 550 (1995).
[11] J.S. Fish, N. Lewis, W.J.S. Yang, D.J. Perry and C.D. Thompson, Proc. 8th Int. Symp. on Environmental Degradation of Materials in Nuclear Power Systems –Water Reactors, 266 (ANS, 1997).
[12] L.E. Thomas and S.M. Bruemmer, Proc. 9th Int. Symp. on Environmental Degradation of Materials in Nuclear Power Systems –Water Reactors, 41 (1999).
[13] L.A. Giannuzzi and F.A. Stevie, Micron, **30**, 197 (1999).

[14] J.W. Cobble, R.C. Murray Jr., P.J. Turner and K. Chen, EPRI Report NP-2400 (1982)
[15] A.V. Katsman, H.J. Grabke, L. Levin and T. Werber, Mat. Sci. Forum, **207-209**, 737 (1996).
[16] R.C. Newman, T.S. Gendron and P.M. Scott, Proc. 9th Int. Symp. on Environmental Degradation of Materials in Nuclear Power Systems –Water Reactors, 79 (1999).
[17] R.H. Bricknell and D.A. Woodford, Acta Metallurgica, **30**, 257 (1982).
[18] R.G. Iacocca and D.A. Woodford, Metal. Trans. A, **19A**, 2305 (1988).
[19] R.W. Staehle and Z. Fang, Proc. 9th Int. Symp. on Environmental Degradation of Materials in Nuclear Power Systems –Water Reactors, TMS, 69 (1999).
[20] Y. Shida, G.C. Wood, F.H. Scott, D.P. Whittle and B.D. Bastow, Corr. Sci., **21**, 581 (1981).
[21] Y. Sato, Y. Watanabe, Y. Kurata and H. Kim, Proc. JSCE Materials and Environments 2000, C-305 (2000).
[22] J. Robertson, Corrosion Science, **32**, 443 (1991).
[23] B. Stellwag, Corrosion Science, **40**, 337 (1998).

Table 1 Chemical composition (wt.%)

C	Si	Mn	P	S	Ni	Cr	Fe
0.030	0.35	0.36	0.009	0.001	74.85	16.16	8.64

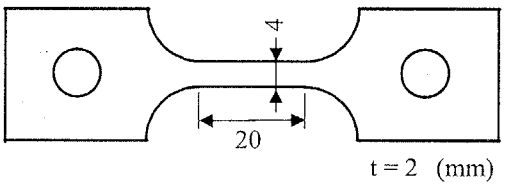


Fig. 1 Shape of the SCC test piece.

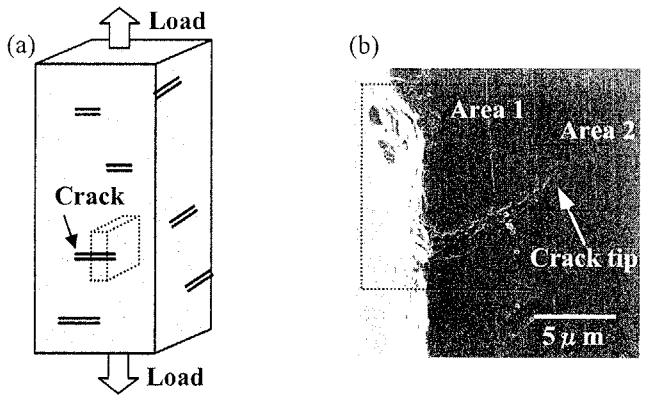
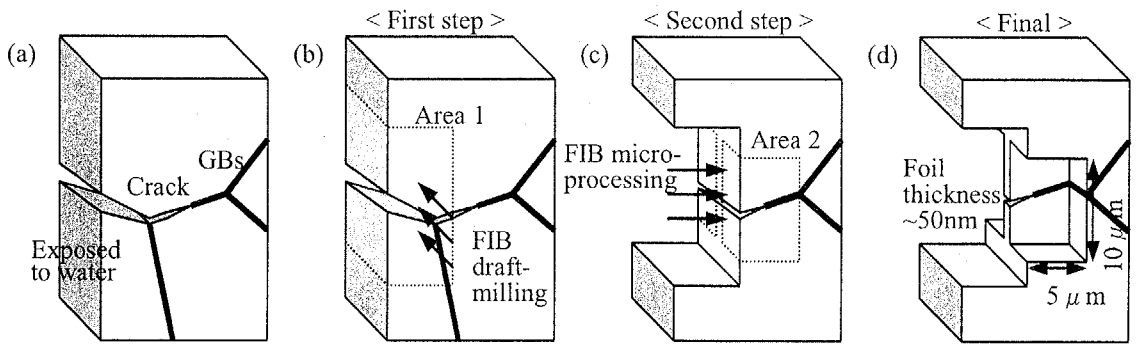


Fig. 2. (a) A schematic diagram of cutting out a specimen from the SCC test piece, and (b) SEM image of a typical SCC crack.



(FIB: Ga ion beams accelerated 30 kV)

Fig. 3. Schematic diagrams of FIB preparation.

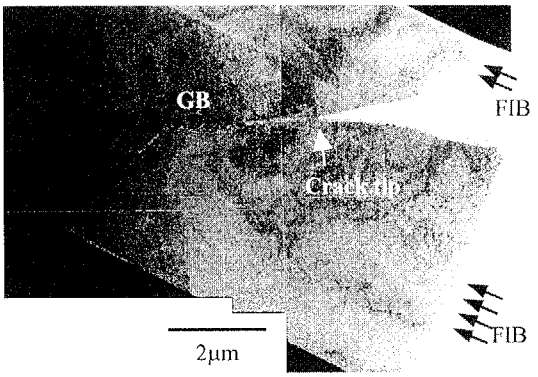


Fig. 4. Low magnification TEM image after FIB micro-processing.

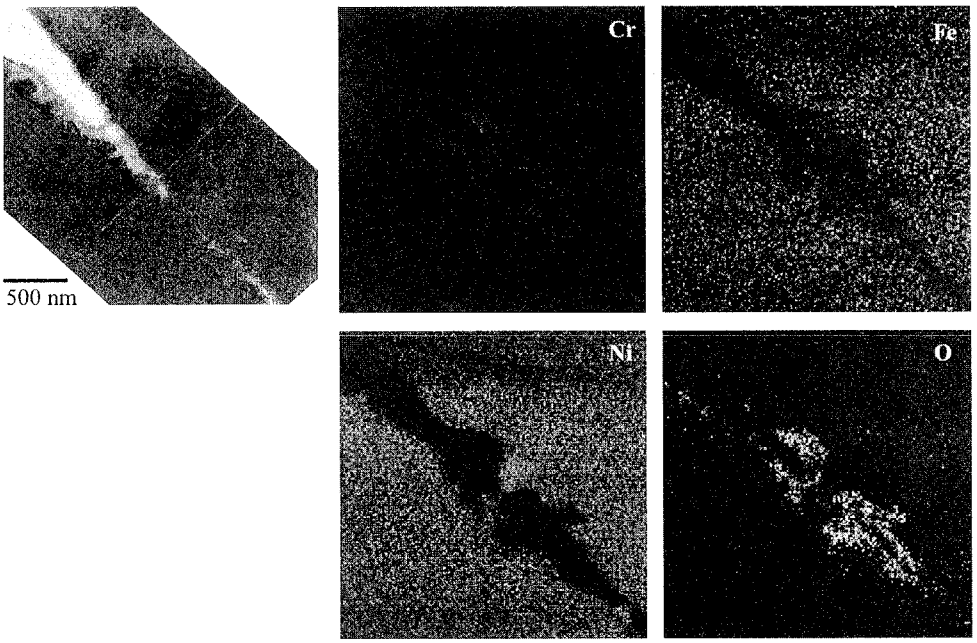


Fig. 5. TEM image of the crack tip region and elemental maps of the same area.

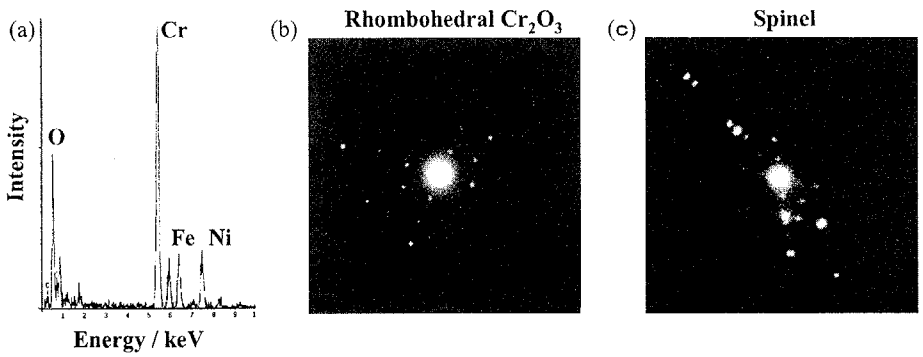


Fig. 6. EDS spectrum and micro-diffraction patterns from Cr rich oxides.

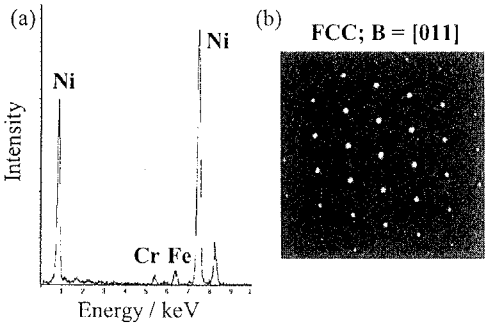


Fig. 7. EDS spectrum and micro-diffraction pattern identified metallic Ni.

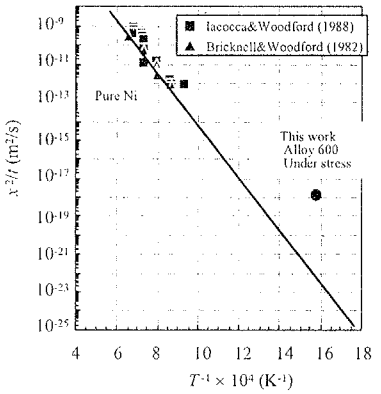


Fig. 8. Depth of grain boundary penetration of oxygen versus 1/T.

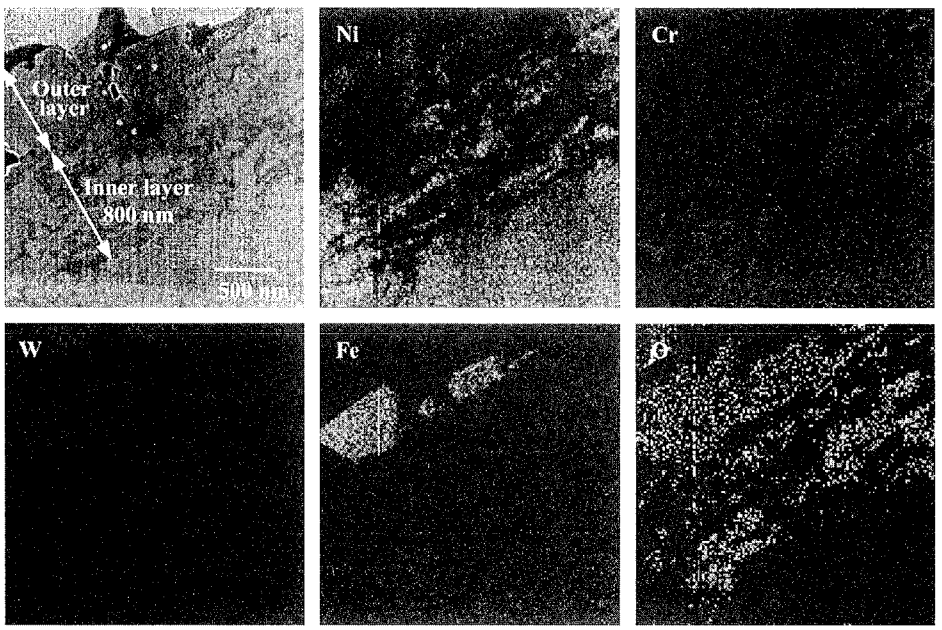


Fig. 9 TEM image of the surface oxide film and elemental maps of the same area.

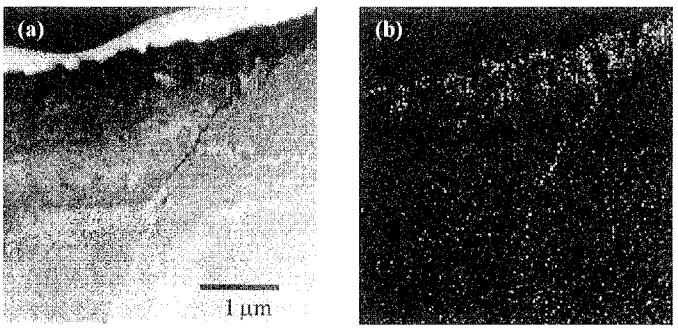


Fig. 10 (a) TEM image of uncracked grain boundary intersected by the surface and (b) oxygen map of the same area.

JP0350273

2.9 VACANCY FORMATION ENERGY OF METALS DETERMINED BY USING POSITRON AGE-MOMENTUM CORRELATION TECHNIQUE

Naoki Suzuki,[1*] Kazuyoshi Manabe,[2] Yoshiko Itoh,[1] Akira Goto,[1] and Toshio Hyodo[2]
[1]The Institute of Physical and Chemical Research (RIKEN),
2-1 Hirosawa, Wako-shi, Saitama 351-0198, Japan
[2]Institute of Physics, Graduate School of Arts and Sciences, University of Tokyo
3-8-1 Komaba, Meguro-ku, Tokyo 153-8902, Japan

Abstract

The vacancy formation energy E_v for Pb and Sn are determined by using the positron age-momentum correlation (AMOC) technique. The reported values of E_v for them are scattered over a considerable range because their S-parameter do not saturate even close to the melting points. S_v for the trapped positrons, however, are obtained by extrapolating the time dependent S-parameter S(t). We determined the E_v for Pb and Sn using the S_v thus obtained.

Keywords: AMOC, Pb, saturation trapping, Sn, time dependent S-parameter, vacancy formation energy.

1 Introduction

The positron annihilation technique is one of the most powerful technique to determine the vacancy formation energy E_v for various metals[1].

If the material contains only one type of vacancies, E_v is determined through the quantitative analysis of the change in the momentum distribution of the positron annihilation γ-rays by assuming the so-called two-state trapping model[2, 3]. In such analysis, the line shape parameter S of the momentum distribution spectrum $N(p)$, which is defined as

$$S = \frac{\int_{\pm\Delta p} N(p)dp}{\int N(p)dp}, \tag{1}$$

is used, where Δp is a properly fixed momentum width. The S-parameter satisfies the following equation,

$$\frac{S - S_f}{S_v - S} \propto \exp(-\frac{E_v}{k_B T}), \tag{2}$$

where S_f and S_v are the specific S-values corresponding to the positrons in the bulk and in the vacancies.

In this analysis, it is necessary to heat the sample up to the temperatures where almost all the positrons are trapped into vacancies before annihilation (saturation trapping); the S-parameter around these temperatures represents S_v. When the saturation trapping of the positrons does not occur even near the melting temperature, it is rather difficult to

*Corresponding author. Tel: 81484679464, FAX: 81484615301.
E-mail address: nsuzu@postman.riken.go.jp (First Author).

determine E_v with high accuracy since the uncertainty of S_v disturbs the result of the fitting.

MacKenzie and Lichtenberger[5] proposed that the threshold temperature at which thremally generated vacancies produce measurable positron trapping is proportional to E_v. This analysis has an advantage in measuring the E_v where saturation trapping does not occur. However, there is no theoretical explanation that justifies the analysis. Actually, the E_v for In obtained by this method is 0.42eV[5], whereas that obtained by the positron age-momentum correlation (AMOC) technique (see below) is 0.48±0.02eV[6].

Recently, a method to determine S_v for the trapped positron directly by using the AMOC technique was developed by the present authors. This method characterizes the AMOC spectrum $N(p,t)$ (number of counts vs. the momentum of the annihilating electron-positron pairs and the positron lifetime) in terms of the time-dependent line-shape parameter $S(t)$, which is defined as

$$S(t) = \frac{\int_{\pm\Delta p} N(p,t)dp}{\int N(p,t)dp}. \tag{3}$$

Since the lifetime of the trapped positrons is appreciably longer than that in the bulk, S_v can be determined by the extrapolation,

$$S_v = \lim_{t\to\infty} S(t). \tag{4}$$

Analyzing the S-parameter with S_v thus obtained, the E_v for indium was successfully determined[6].

In the present study, we measured E_v for Pb and Sn by using this method.

2 Experiment

The block diagram of the used AMOC system is shown in Fig. 1. A pair of fast scintillation counters measures the positron lifetime. One detects the 1.27MeV nuclear γ-ray, which makes the start signal. The other provides the stop signal by detecting one of the 511keV annihilation γ-rays. A high purity Ge detector detects the second annihilation γ-ray for the simultaneous measurement of the Doppler broadened annihilation γ-ray energy spectrum. A 2mm thick Pb plate was placed between the source and the Ge detector to reduce the tail on the high energy side of the spectrum resulting from simultaneous detection of low energy scattered γ-rays[7]. A personal computer controls two analogue-to-digital converters(ADC's) and accumulates both the positron lifetime and the energy of the annihilation γ-rays.

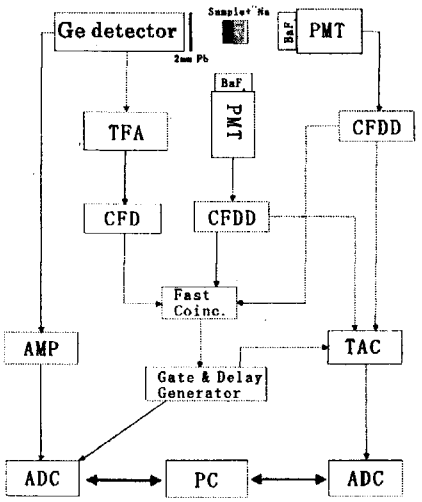


Figure 1: The block diagram of the AMOC system.

The energy resolution was 1.1keV (FWHM, measured at 512keV from ^{106}Ru), equivalent to the momentum resolution of 4.3×10^{-3}mc (~0.59a.u.). The time resolution was 220ps(FWHM).

A pair of polycrystalline 4-nine Pb and 5-nine Sn specimens were annealed and etched before the measurements. Five μCi carrier-free ^{22}NaCl was deposited directly on one of the specimens and covered with another. The temperature was controlled within $\pm$0.5K by a PID temperature regulator.

3 Results and Discussion

The AMOC spectrum of Pb at 540K is shown in Fig. 2.

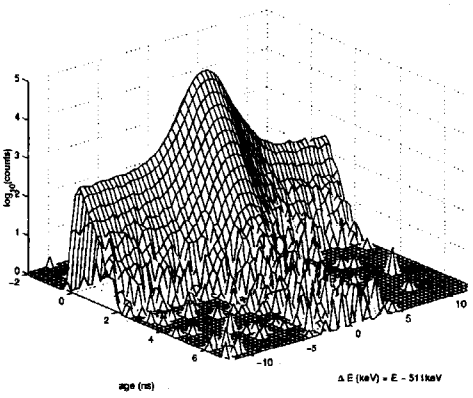


Figure 2: The AMOC spectrum for Pb at 540K.

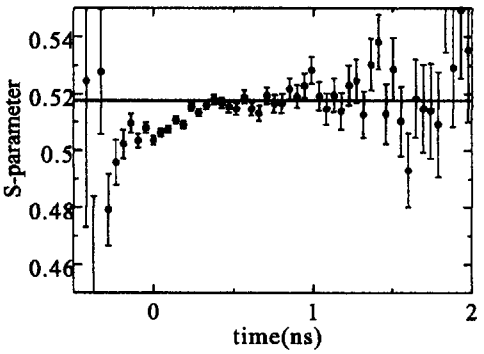


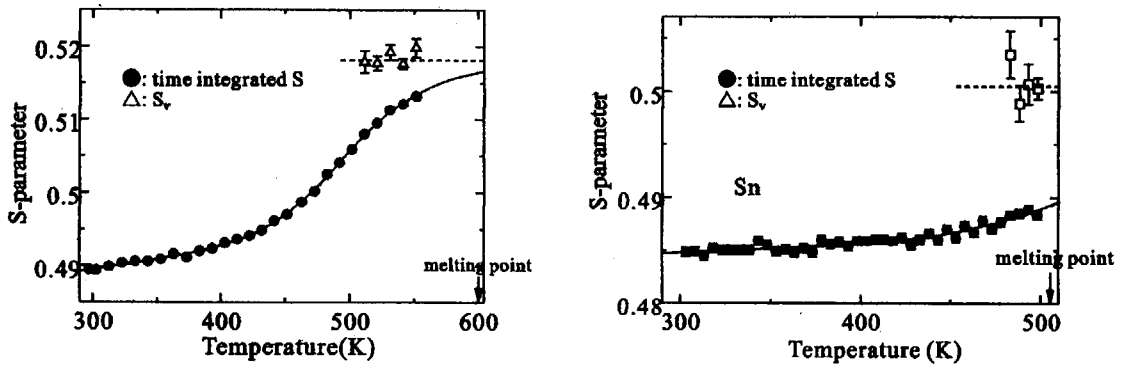
Figure 3: Time evolution of $S(t)$ for Pb at 540K.

Figure 3 shows the time-dependent S-parameter $S(t)$ for Pb at 540K. It is seen that $S(t)$ increases gradually with time, representing the increase in the fraction of the trapped positrons. The leveling off after 0.5ns indicates that almost all the annihilation γ-rays in this time range are from the trapped positrons, i.e. the $S(t)$ after 0.5ns corresponds to S_v. Although the considerable fraction of the positrons still annihilate before trapping at this temperature, we can determine the S_v in this way. The solid line in Fig. 3 represents S_v. In practice, S_v was determined by fitting the theoretical function[8] predicted by the two-state trapping model to $S(t)$.

The triangles in Fig. 4(a) show the S_v determined for the temperatures $T \geq 510K$. The closed circles in Fig. 4(a) show the S-parameter obtained by the conventional time-integrated Doppler broadening measurements. It is seen that the S-parameter is still increasing at the temperatures just blow the melting point (601K), as reported in previous works. The solid line and the dashed line represent Eq. 2 and a linear function simultaneously fitted to the data for S and S_v, respectively. The fits are good. The E_v for Pb thus determined is 0.67 ± 0.03 eV.

The result of the Sn are shown in Fig. 4(b). We see that only $\sim$15% positrons are trapped in vacancy at even close to the melting temperature. We analyze assuming that S_v is constant, because the number of measuring points are not so many and the errors are considerably large. The E_v for Sn thus determined is 0.57 ± 0.12 eV.

Table 1(a) and Table 1(b) summarizes the E_v values for Pb and Sn reported so far. All of them are obtained by the positron annihilation techniques except for the result of Kramer and Nölting[9], which was obtained by the specific heat measurement. Considerable differences are seen among these values. Our results are highly trustable because the



(a) S parameter for Pb

(b) S parameter for Sn

Figure 4: S parameter for Pb and Sn plotted against the temperature.

references	E_v (eV)	method
Kramer, *et al.*[9]	0.39±0.03	SH
McKee, *et al.*[10]	0.50±0.03	TM
Dryzek, *et al.*[11]	0.51±0.005	
Mackenzie, *et al.*[5]	0.52	TT
Dryzek, *et al.*[11]	0.54±0.01	TM
Triftshäuser[13]	0.54±0.02	TM
Rice-Evans, *et al.*[12]	0.56±0.03	TM
Sharma, *et al.*[14]	0.65±0.05	TM
The present work	0.67±0.03	AMOC

(a) Pb

references	E_v (eV)	method
Kramer, *et al.*[9]	0.46±0.02	SH
Dedoussis, *et al.*[15]	0.50±0.01	TM
Dedoussis, *et al.*[15]	0.50±0.05	TM
Shah, *et al.*[16]	0.51±0.01	TM
Segers, *et al.*[17]	0.51±0.02	TM
Segers, *et al.*[17]	0.54±0.03	TM
Mackenzie, *et al.*[5]	0.56	TT
Rice-Evans, *et al.*[18]	0.56±0.01	TM
Mackenzie, *et al.*[19]	0.57	TT
The present work	0.57±0.12	AMOC
Puff,*et al.*[20]	0.58	TT

(b) Sn

Table 1: E_v for Pb and Sn reported so far; TM: trapping model, TT: threshold temperature, SH: specific heat measurement.

present analysis is free from the uncertainty of Sv and does not depend on any empirical parameters.

The error of our result for Sn is large compared to others. It has to be noted, however, the fraction of the trapped positron is only ~15%.

On the other hand, the fraction deduced from the results of the analysis of the simple trapping model are ~30%[15], ~50%[15], ~30%[17], 60-70%[18], respectively. This means that the simple trapping model analysis is not trustable when no saturation trapping does not occur, even when the analysis fits the data well.

4 Conclusion

We have measured the E_v for Pb and Sn by using the newly developed AMOC technique. Highly reliable values for Pb and Sn have been yielded. The fraction of the trapped positron in Sn near the melting temperature was observed only ~15%, much smaller than the reported values.

5 Acknowledgement

We thank Dr. Y. Nagashima and Dr. H. Saito for their valuable discussion. The present work is supported by the RIKEN Special Postdoctoral Researchers Program and the REIMEI Research Resources of Japan Atomic Energy Research Institute.

References

[1] For example, R. N. West in *Positron in Solids*, ed. by P. Hautojärvi (Springer, 1979) 89.

[2] B. Bergersen and M. J. Stott, *Solid State Commun.* **7** (1969) 1203.

[3] D. C. Connors and R. N. West, *Phys. Lett.* **30A** (1969) 24.

[4] Masao Doyama in *Positron Annihilation*, edited by R. Hasiguti and K. Fujiwara (The Japan Institute of Metals, Sendai, 1979), p.13.

[5] I. K. MacKenzie and P. C. Lichtenberger, *Appl. Phys.* **9**, (1976) 331.

[6] N. Suzuki, Y. Nagai, Y. Itoh, A. Goto, Y. Yano, and T .Hyodo, *Phys. Rev.* **B** (2001) 180101(R).

[7] Chang Tianbao, Tang Hsiaowei and Li Yaoqing, in *Positron Annihilation*, ed. by P. C. Jain, R. M. Singru and K. P. Gopinathan (World Scientific, Singapore, 1985) 212.

[8] M. Koch, K. Majer, J. Major, A. Seeger, J. P. F. Sellschop, E. Sideras-Haddad, H. Stoll and S. H. Connell, *Mater. Sci. Forum* **105-110** (1992) 671.

[9] W. Kramer and J. Nölting, *Acta Metall.* **20** (1972) 1353 (in German).

[10] B. T. A. McKee, W. Triftshäuser and A. T. Stewart, *Phys. Rev. Lett.* **28** (1972) 358.

[11] J. Dryzek, *Phys. stat. sol. (b)* **209** (1998) 3.

[12] P. Rice-Evans, I. Chaglar, and F. A. R. El Khangi, *Phil. Mag. A* **5** (1976) 543.

[13] W. Triftshäuser, *Phys. Rev. B.* **107** (1975) 4634.

[14] S. C. Sharma, S. Berko, and W. K. Warburton, *Phys. Lett. A* **58** (1976) 405.

[15] Sp. Dedoussis, Stef. Charalambous, and M. Chardalas, *Phys. lett.* **62A** (1977) 359.

[16] Nareshchandra Shah, and A. L. Catz, *Phys. Rev. B* **30** (1984) 2498.

[17] D. Segers, L. Dorikens-Vanpraet, and M. Dorikens, *Phys. stat. sol. (a)* **59** (1980) 543.

[18] P. C. Rice-Evans, Moussavi-Madani, F. A. R. El Khangi, and K. U. Rao, *Phil. Mag. A* **52** (1985) 431.

[19] I. K. MacKenzie and J. Fabian, *Can. J. Phys.* **58** (1980) 1635.

[20] W. Puff, P. Mascher, P. Kindl, and H. Sormann, *Appl. Phys. A* **32** (1983) 183.

JP0350274

2.10 THERMAL DIFFUSIVITY AND HEAT CAPACITY MEASUREMENTS OF Li_2ZrO_3 AND Li_2TiO_3 WITH THE LASER-FLASH METHOD

Tsuyoshi Hoshino[1*], Yoichi Takahashi[2], Takayuki Terai[1], Michio Yamawaki[1]

[1] Department of Quantum Engineering and Systems Science, Graduate School of Engineering, Univ. of Tokyo, 7-3-1 Hongo, Bunkyo-ku, Tokyo, 113-8656, Japan

[2] Department of Applied Chemistry, Chuo University, 1-13-27, Kasuga, Bunkyo-ku, Tokyo, 112-8551, Japan

Abstract

Thermal diffusivity of $0.95Li_2ZrO_3 + 0.05ZrO_2(Li_2O/ZrO_2 = 0.95)$ was determined from 300 to 1200 K, and thermal diffusivity and heat capacity of $0.916Li_2TiO_3 + 0.017Li_4Ti_5O_{12}(Li_2O/TiO_2 = 0.95)$ were determined from 300 to 1100 K and 300 to 1000 K, respectively, by using the laser-flash method. Then, their thermal conductivities were calculated up to 1000 K using smoothed values of the thermal diffusivity and heat capacity.

Keywords: tritium breeding material, Li_2ZrO_3, Li_2TiO_3, thermal diffusivity, heat capacity, thermal conductivity, laser-flash method

1.Introduction

Tritium breeding materials for thermonuclear fusion reactors are required to have good thermal properties, especially high thermal conductivity, as well as satisfactory tritium breeding characteristics.

In this respect, Li_2O, $LiAlO_2$, Li_4SiO_4, Li_2ZrO_3 and Li_2TiO_3 have been considered as candidate ceramic materials for tritium breeding[1]. Li_2TiO_3 has been recently noticed as a prominent candidate because of its fairly good tritium release behavior[2] and its low activation characteristics. Several thermal property data of Li_2TiO_3 have been hitherto reported[3-6]. These data are, however, inconsistent with each other. Thermal property date are primarily important for the blanket design, as the thermal energy produced by the nuclear fusion has to be transferred to the coolant through the blanket material.

In this study, the values of thermal diffusivity of nearly stoichiometric Li_2ZrO_3 ($Li_2O/ZrO_2 = 0.95$, as designated $95Li_2ZrO_3$) are determined from 300 to 1200 K. The values of thermal diffusivity and heat capacity of $Li_2TiO_3(Li_2O/TiO_2 = 0.95$, as designated $95Li_2TiO_3$) are determined from 300 to 1100 K and 300 to 1000 K, respectively, by using the laser-flash method. The thermal conductivity values are then derived.

*Corresponding author. Tel: +81-3-5841-7420 Fax: +81-3-5841-7420
E-mail address: hoshino@starling.q.t.u-tokyo.ac.jp

2.Experimental

2.1.Sample

The sintered samples of Li_2ZrO_3 and Li_2TiO_3 were kindly provided by Dr. Roux, CEA, at Saclay, France.

Li_2ZrO_3

The sample in the shape of a disk pellet 9.17mm in diameter and 1.10mm thick was prepared in CEA by heating a mixture of Li_2CO_3 and ZrO_2 at 973 K for 3 hr and then 1073 K for 3 hr. The resulting product was isostatically pressed at 300MPa and was sintered for 3 hr at 1273 K.

The characteristics of the sample are as follows: porosity ; 0.186(81.4%T.D), and composition ; $0.95Li_2ZrO_3$ (monoclinic) + 0.05 ZrO_2 (monoclinic). In the case of this Li_2ZrO_3 sample, Li_2CO_3 and ZrO_2 powders are mixed in proportions corresponding to the molecular ratio Li_2O/ZrO_2 = 0.95. This sample is designated as $95Li_2ZrO_3$, in reference to $100Li_2ZrO_3$(Li_2O/ZrO_2 = 1.00). It has been pointed out that the $95Li_2ZrO_3$ is considerably more stable as compared to $100Li_2ZrO_3$[2].

Li_2TiO_3

The sample in the form of a disk pellet, 11.0mm in diameter and 2.0mm thick, was prepared by heating a mixture of Li_2CO_3 and TiO_2 at 973 K for 3 hr and then 1125 K for 3 hr. The resulting product was isostatically pressed at 150MPa and was sintered for 3 hr at 1323 K.

The characteristics of the sample are as follows: density ; $2.976\times10^{-3}kg\cdot m^{-3}$, porosity ; 0.137(86.3%T.D), and composition ; $0.916Li_2TiO_3$ (monoclinic) + $0.017Li_4Ti_5O_{12}$ (cubic). In the case of this Li_2TiO_3 sample, Li_2CO_3 and TiO_2 powders are mixed in proportions corresponding to the molecular ratio Li_2O/TiO_2 = 0.95. This sample is designated as $95Li_2TiO_3$, in reference to $100Li_2TiO_3$(Li_2O/TiO_2 = 1.00). It has been pointed out that the $95Li_2TiO_3$ is considerably more stable as compared to $100Li_2TiO_3$[2].

2.2.Measurements of thermal properties

The apparatus used was a laser-flash calorimeter Model LF/TCM-8510B of Rigaku Co.. The surface of the sample was coated with a thin layer of carbon film to provide sufficient energy absorption. Then, the sample was heat-treated at 1100 K.

Thermal diffusivity measurements were made from room temperature to 1100 K, by analyzing the rear-surface temperature history just after a flash of laser irradiation on the front surface of the sample by the use of logarithmic method[7]. Adjustments for pulse-width effect were made by gravity method[8].

Details of heat capacity measurements by laser-flash calorimetry were described in a previous paper[7]. A brief outline of the present measurements is as follows. First, the heat capacity of the $95Li_2TiO_3$ sample at room temperature was determined by comparison with a Ni reference sample. The same absorbing disk made of glassy carbon (mass 0.030 g) was used in these measurements. The temperature dependence of the heat capacity was then determined on the same $95Li_2TiO_3$ sample up to 1100 K.

3.Results on Li_2ZrO_3

The thermal diffusivities determined are shown in Fig.1. The scatter of the data is within ±3%. At 1200K, the thermal diffusivity shows a decrease, probably because of a phase transition. It should be noted that after several heating-cooling cycles up to 1200K, Li_2ZrO_3 sample was broken in pieces. This suggests that the anisotropic thermal expansion of Li_2ZrO_3 may cause the generation of microcracks on heating[9].

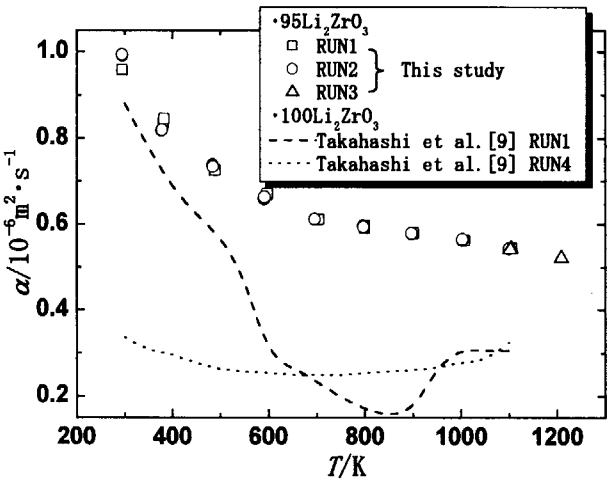


Fig.1. Temperature dependence of thermal diffusivity of Li_2ZrO_3

4.Results on Li_2TiO_3

4.1.Thermal diffusivity

The obtained thermal diffusivities of $95Li_2TiO_3$ are shown in Fig.2 in comparison with literature values. The scatter of the present data is within ±3% over the temperature range measured. The thermal diffusivity decreased with temperature from 0.012 $cm^2 \cdot s^{-1}$ at room temperature to 0.005 $cm^2 \cdot s^{-1}$ at 1100 K. Roux[5] reported the thermal diffusivity of the similar $95\%Li_2TiO_3$ up to 1000 K and her values agree well with the present results. The present values are slightly higher (at maximum by 8% at 800 K), probably reflecting the higher density of the sample than that of Roux. On the other hand, the reported data on $100Li_2TiO_3$ samples of the similar true density[3, 4] are considerably lower, especially at lower temperatures (by about 20% at 300 K), than those of the present study.

The present values are best fitted with eq.(1),

$$(\alpha/m^2 \cdot s^{-1})^{-1} = 14.2 + 0.256\,(T/K) - 7.95\times10^{-5}\,(T/K)^2 \qquad (300<T/K<1100) \qquad (1).$$

4.2.Heat capacity

Results of the heat capacity measurements are shown in Fig. 3. The scatter of the data is within ±3% up to 1000K, whereas above this temperature the data varied considerably as seen in Fig. 3. The high-temperature X-ray diffraction analysis performed on this sample indicated the occurrence of β-γ phase transition at around 1100 K (Fig.4), and thus we concluded that the observed large scatter was caused by detachment of the thermocouple from the rear surface of the sample. Therefore, we deleted the data for above 1000 K and the smoothed values up to 1000 K were obtained as tabulated in Table 1.

The present result agrees fairly well, below 500 K, with the data obtained by Roux[5] on the similar $95Li_2TiO_3$ sample. Above 500 K, the present data are lower than those of Roux. It is noted that the values of JANAF Thermochemical Tables for $100Li_2TiO_3$[6] lie just between the present ones and those of Roux. Several other sets of recent data on $100Li_2TiO_3$ are also shown in Fig. 3.

The present values are best fitted with eq.(2),

$$C_p/J \cdot K^{-1} \cdot g^{-1} = 1.33 - 1.20\times10^{-5}(T/K) - 2.84\times10^{4}(K/T)^2 \qquad (300< T/K <1000) \qquad (2).$$

4.3.Thermal conductivity

The values of thermal conductivity of the $95Li_2TiO_3$ sample were calculated from the smoothed values of thermal diffusivity and heat capacity of this study using eq.(3),

$$\lambda = \alpha \cdot C_p \cdot \rho \qquad (3),$$

where λ : thermal conductivity, α: thermal diffusivity, C_p: specific heat capacity, and ρ : density. For the density of the sample, the value at room temperature was used up to 1000 K. The resulting values of thermal conductivity are given in Table 1 for selected temperatures from 300 to 1000 K. They are also shown in Fig. 5, together with the literature values[3-5].

The present results agree very well with those of Roux[5]. It should be noted that both the results are on the similar $95Li_2TiO_3$ of the same origin. In contrast, the other reported values on $100Li_2TiO_3$[3,4] are considerably lower, particularly below 700 K.

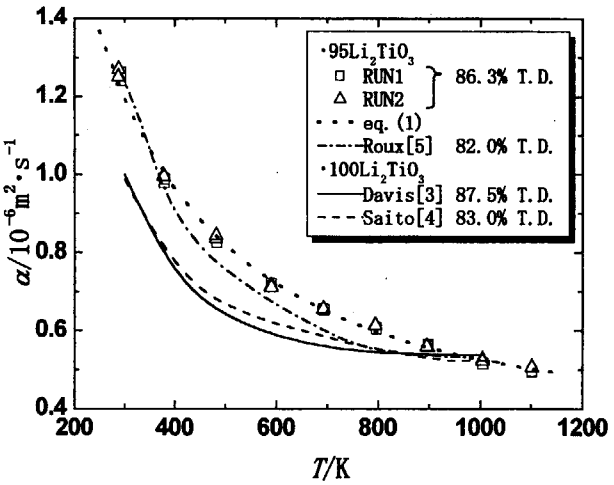


Fig.2. Temperature dependence of thermal diffusivity of Li_2TiO_3

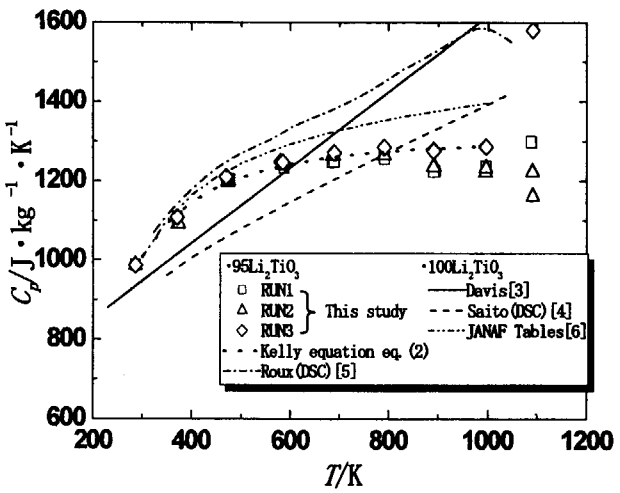


Fig.3. Temperature dependence of specific heat capacity of Li_2TiO_3

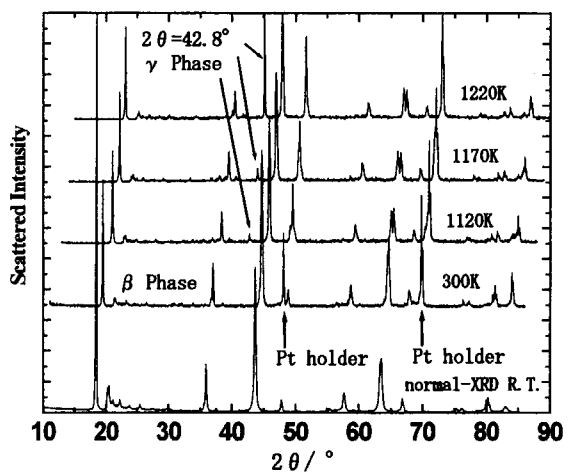


Fig.4. High-temperature X-ray diffraction patterns of Li_2TiO_3

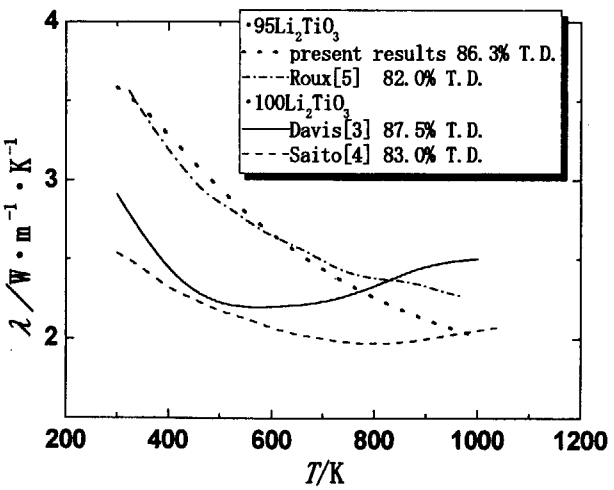


Fig.5. Temperature dependence of thermal conductivity of Li_2TiO_3

Table.1 Experimental values of thermal diffusivity and specific heat capacity, and calculated values of thermal conductivity of $95Li_2TiO_3$

T/K	$\alpha/10^{-6}\cdot m^{-2}\cdot s^{-1}$	$10^{-3}C_p/J\cdot kg^{-1}\cdot K^{-1}$	$\lambda/W\cdot m^{-1}\cdot K^{-1}$
300	1.19	1.01	3.59
400	0.964	1.15	3.29
500	0,819	1.21	2.95
600	0.720	1.24	2.66
700	0.649	1.26	2.44
800	0.596	1.27	2.26
900	0.556	1.28	2.12
1000	0.526	1.29	2.01

5.Discussion

The thermal conductivity of $95Li_2TiO_3$ ($0.916Li_2TiO_3 + 0.017Li_4Ti_5O_{12}$) is higher than the reported values of $100Li_2TiO_3$. This result appears to be contrary to the general theory. The authors speculated that the structure of $95Li_2TiO_3$ may be the cause for such an abnormal behavior. And hence, the following specimens were prepared and examined by using XRD technique : (ⅰ)100%Li_2TiO_3, (ⅱ)100%$Li_4Ti_5O_3$ and (ⅲ)mixture of (ⅰ)+ (ⅱ) ($0.916Li_2TiO_3 + 0.017Li_4Ti_5O_{12}$).

Results of XRD analysis are shown in Fig. 6. In case of (ⅲ) i.e. mixture sample ($0.916Li_2TiO_3 + 0.017Li_4Ti_5O_{12}$), $100Li_4Ti_5O_{12}$ (ⅱ) peaks (at 2θ = 57.4° , 63.0° ,and 66.3°) appeared. The XRD pattern of (ⅳ)$95Li_2TiO_3$ sample provided by Dr. Roux and used in this work was nearly the same as that of the (ⅰ)$100Li_2TiO_3$ sample and indicated no presence of $Li_4Ti_5O_{12}$. This means that the $95Li_2TiO_3$ sample used in this work was nonstoichiometric compound $Li_{2-x}TiO_{3-y}$.

Moreover, we compared XRD pattern of $100Li_2TiO_3$ with $95Li_2TiO_3$. A powder mixture of Li_2CO_3 and TiO_2 is calcined under air at 1223K for 15 hr, and the resulting product was isostatically pressed at 150MPa and was sintered at 1273 K for 15 hr and then 1323 K for 15 hr. In spite of the same heating condition, the peaks of $95Li_2TiO_3$ from 2θ = 20.0° to 30.0° are sharper than those of $100Li_2TiO_3$ (Fig.7). This result indicates that $95Li_2TiO_3$ sample is nearly a single phase with larger grains. This seems to be the reason why the thermal characteristics of the $95Li_2TiO_3$ sample was better than that of the $100Li_2TiO_3$.

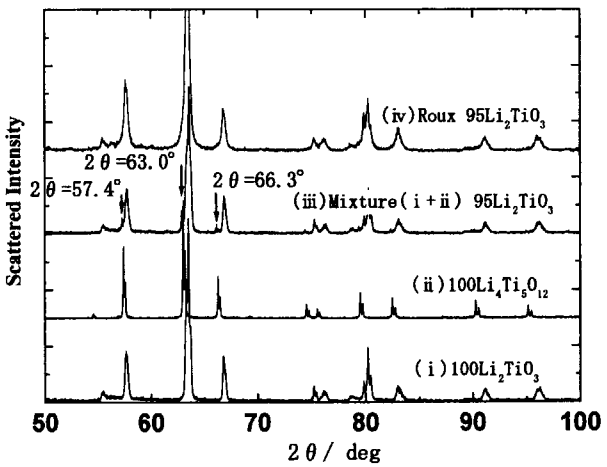


Fig.6. X-ray diffraction patterns of several compounds of Li and Ti

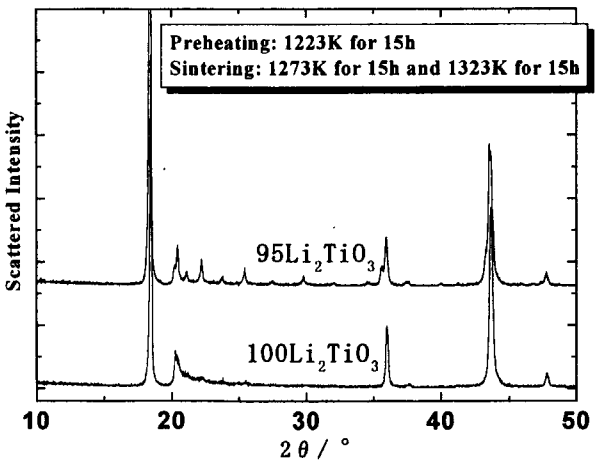


Fig.7. X-ray diffraction patterns of $100Li_2TiO_3$ and $95Li_2TiO_3$

6.Conclusion

Li_2ZrO_3

Thermal diffusivity of $95Li_2ZrO_3$ were determined from 300 to 1200 K. At 1200K, the thermal diffusivity shows a decrease, because of a phase transition. It should be noted that after heating-cooling cycles of about 10times up to 1200K, $95Li_2ZrO_3$ sample was broken in pieces.

Li_2TiO_3

Thermal diffusivity and heat capacity of $95Li_2TiO_3$ were determined from 300 to 1100 K and 300 to 1000 K, respectively, and thermal conductivity values were calculated using the experimental values. It was found that the thermal conductivity of $95Li_2TiO_3$ is higher than the reported value of $100Li_2TiO_3$, indicating possible advantage of the $95Li_2TiO_3$ as a tritium breeding material. The $95Li_2TiO_3$ sample was shown to have a nonstoichiometric composition and have the better thermal characteristics than $100Li_2TiO_3$.

Acknowledgment

The authors would like to thank Dr. Roux of CEA, Saclay, France for providing the Li_2ZrO_3 and Li_2TiO_3 samples of this study.

References

[1] K. Yamaguchi, A. Suzuki, M. Tonegawa, Y. Takahashi, M. Yasumoto and M. Yamawaki, J. Mass Spectron. Soc. Jpn. Vol.47 (1999) 10

[2] N. Roux, J. Avon, A. Floreancig, J. Mougin, B. Rasneur and S. Ravel, J. Nucl. Mater. 233-236 (1996) 1431

[3] J. W. Davis and A. A. Haasz, J. Nucl. Mater. 232 (1996) 65

[4] S. Saito, K. Tsuchiya ,H. Kawamura, T. Terai and S. Tanaka, J. Nucl. Mater. 253 (1998) 213

[5] N. Roux, Proc.Sixth International Workshop on Ceramic Breeder Blanket Interactions, October 22-24, 1997, Mito City, Japan (1998) 139

[6] M. W. Chase, Jr., NIST-JANAF Thermochemical Tables, 4th ed., J. Phys. Chem. Ref. Monograph 9, Am. Inst. of Phys., Woodbury, (1988) 1515

[7] Y.Takahashi, H. Yokokawa, H. Kadokura, Y. Sekine and T. Mukaibo, J. Chem. Thermodyn. 11 (1978) 379

[8] T. Azumi and Y. Takahashi, Rev. Sci. Inst. 52 (1981) 1411

[9] Y. Takahashi, T. Ohsato and T. Terai, Fusion Engineering and Design 17 (1991) 25

JP0350275

JAERI－Conf 2003－001

2.11 POSITRON ANNIHILATION STUDY ON DEFECTS IN ION-IMPLANTED Si

T. Akahane[1*], M. Fujinami[2] and T. Sawada[2]

[1]National Institute for Materials Science, Advanced Materials Laboratory,
1-1 Namiki, Tsukuba-shi, Ibaraki, 305-0044, Japan
[2]Department of Advanced Materials Science, The University of Tokyo
7-3-1 Hongo, Bunkyo-ku, Tokyo, 113-0033, Japan

Abstract

Two-detector coincidence measurements of the Doppler broadened annihilation spectra with a variable energy positron beam are carried out for the study of the annealing behavior of Si implanted with As, P, Cu and H ions. In P-implanted Si, growth of the defect complexes are observed in coincidence Doppler broadening spectra up to 400°C. In Cu-implanted Si, the formation of defect-Cu complexes is indicated. In H-implanted Si, the passivation effect of hydrogen on positron traps are observed in the low temperature region up to 400°C.

Keywords: Positron beam, Doppler broadening, Defects, Si, Ion implantation

1. Introduction

The doping of semiconductors by the process of ion implantation has been widely used in the fabrication of integrated circuits. Detailed knowledge on defects induced by ion implantation and their annealing behavior are of great technological importance. The variable energy positron beam has been proven to be unique tool for studying near surface defects in solids. Coincidence detection of annihilation photons with two Ge detectors can eliminate random background and yield good signal-to-noise ratio in Doppler broadening measurements, especially for high momentum region, where the core electron contribution is large.[1] Thus, coincidence Doppler broadening(CDB) measurements are expected to provide additional information about the atoms surrounding the annihilation site.[2] In the present study, we have applied this technique with a variable energy positron beam to study annealing process of defects induced in Si by implantation of As, P, Cu and H ions.

2. Experiments

The Doppler broadening of the annihilation radiation was measured with two Ge detectors. The energy resolutions of detectors are 2.0 keV and 2.4 keV(FWHM) for the 1.33 MeV gamma ray of ^{60}Co. Positrons from ^{22}Na source were moderated with W single crystal foil or W mesh and guided magnetically to the specimen. Coincidence count rate was about 300/s

*Corresponding author. Tel +81-298-51-3354 ext. 502: Fax +81-298-55-3848:
E-mail AKAHANE.Takashi@nims.go.jp

and more than 10^7 counts were accumulated for each spectrum. Ion implantation was carried out on p-type 10Ωcm Si(100) crystals grown with Czochralski (Cz) method. Implantation conditions for each ion are shown in Table 1. After implantation, the samples were annealed in N_2 atmosphere for 30 min at various temperature. In CDB measurements, positron energies were fixed with values shown in Table 1. Conventional Doppler broadening measurements with single detector were also carried out with varying the positron energy.

Table 1. Ion implantation condition and positron energy in CDB measurements.

Ion	Implantation energy	Dose	Positron energy
As	100 keV	2 x 10^{14}/cm^2	2.5 keV
P	100 keV	2 x 10^{14}/cm^2	3 keV
Cu	140 keV	2 x 10^{14}/cm^2	4 keV
H	60 keV	1 x 10^{16}/cm^2	6 keV

3. Results and discussion

The measured Doppler broadening spectrum under different condition are shown in Fig. 1. The diagonal cross-section of the two-dimensional CDB spectrum has two orders of magnitude better signal-to-noise ratio compared with conventional Doppler broadening spectrum obtained with single detector. The CDB spectra for Si implanted with As are shown in Fig. 2. They are depicted as the ratio to bulk Si as the momentum distribution extends over several orders of magnitude and small but significant difference may be obscured with a normal plot. S versus W plot of CDB spectra are shown in Fig. 3. Here, S stands for the low momentum component up to 2.5×10^{-3} m_0c. W is for high momentum component from 8×10^{-3} m_0c to 15×10^{-3} m_0c. Comparison between experimental data shown in Fig. 2 and calculation for divacancy[3] indicates that divacancy is the dominant defect in as-implanted Si, which is consistent with the result of earlier experiments[4]. Only

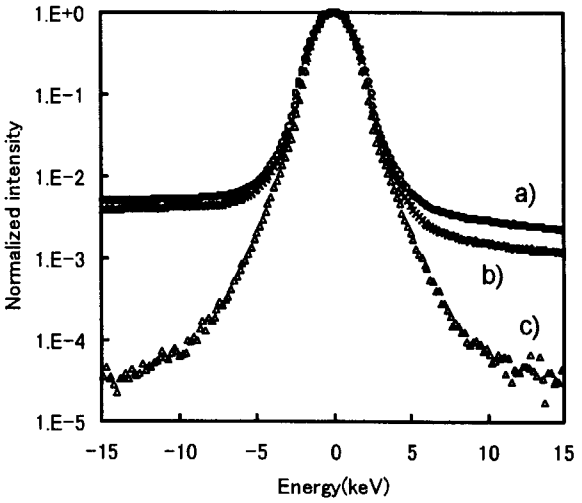


Fig. 1 The measured energy spectrum under different conditions. a):conventional Doppler broadening spectrum with one detector. b): one-detector spectrum with coincidence condition. c): diagonal cross section of CDB spectrum.

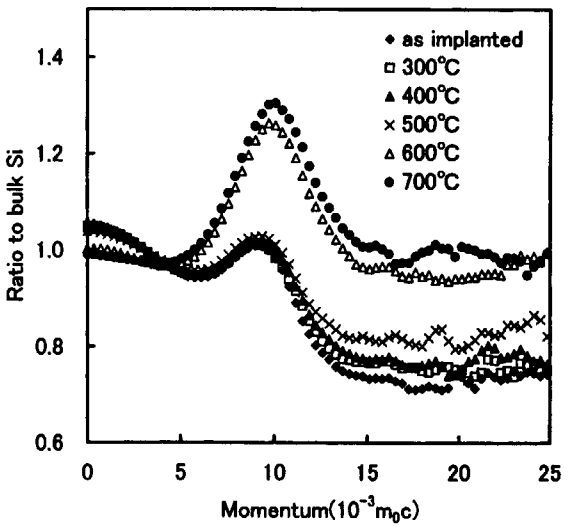


Fig. 2 CDB spectra for Si implanted with As

small changes of the CDB spectra are observed up to 400°C. Pronounced peak around $10x10^{-3}$ m_0c appears after 600°C annealing. The origin of this structure is not known at present. Peaks around this region come from difference between rapidly decreasing momentum distribution around Jones zone in crystalline Si and slowly varying momentum distribution of localized electrons.[3] Positrons trapped at V-O complexes are known to give a peak around $10x10^{-3}$ m_0c. Conventional S parameter measurements, though, show no peak for the sample annealed at 600°C. In the present experiments, V-O complexes may not be the origin of these peaks. The other possible candidate is the positrons annihilating on the sample surface. By annealing, diffusion length of positrons becomes larger. The provability for positrons injected with a fixed energy can reach surface is increased.

The CDB spectra for Si implanted with P are shown in Fig. 4. S-W plot of CDB spectra are shown in Fig. 3 with those for Si implanted with As. Close resemblance is seen between as-implanted samples for both ions. It supports that the dominant defect in as-implanted Si is divacancy. In the early stage of the annealing up to 400°C, though, annealing behavior is somewhat different. In case of P implantation, S becomes larger with annealing temperature, which indicates divacancies agglomerate to larger vacancy complexes. It is unlikely that oxygen atoms in Cz-Si are involved in these vacancy complexes because CDB spectra around $10x10^{-3}$ m_0c shows very small changes up to 500°C. Annealing at 600°C increases the peak around $10x10^{-3}$ m_0c with the still high S value, which may indicate the formation of V-O complexes.

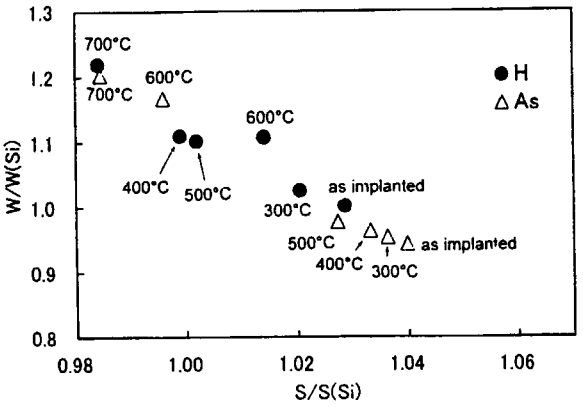


Fig. 3 S-W plot of CDB spectra for Si implanted with As and P. Data labels are annealing temperature.

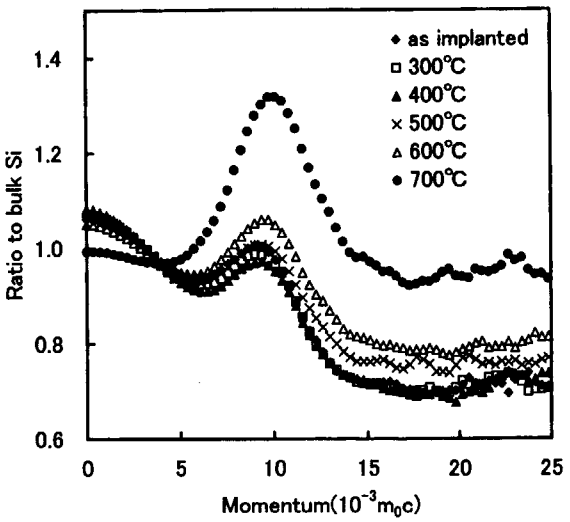


Fig. 4 CDB spectra for Si implanted with P.

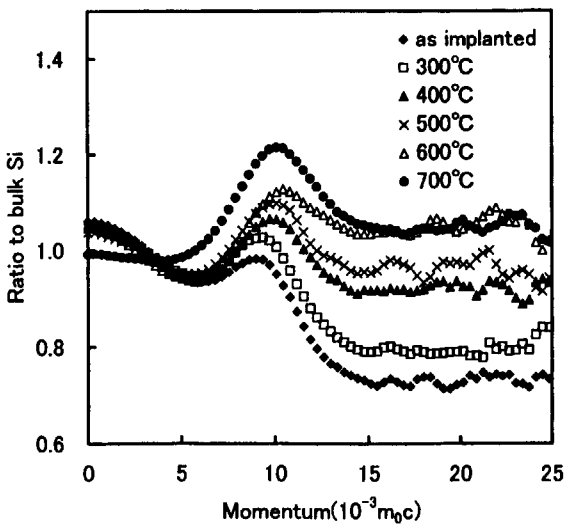


Fig. 5 CDB spectra for Si implanted with Cu.

The CDB spectra for Si implanted with Cu are shown in Fig. 5. Annealing behavior is quite different in case of Cu implantation compared with As and P. Shape of the CDB spectrum for as-implanted state is similar with the case of As and P. Again it indicates that large part of positrons are trapped at divacancy. Evolution of defects starts at lower temperature. High momentum component above $15x10^{-3}$ m_0c in CDB spectra become larger with low temperature annealing compared with the case of As and P. Also peak position and shape are different, which indicate that some part of trapped positrons annihilate with other element than Si. The CDB spectrum for annealed Cu is shown in Fig. 6 as the ratio to that for Si. The CDB spectrum for Cu has larger high momentum component over about $10x10^{-3}$ m_0c because Cu has larger core than Si. The CDB spectra for Cu-implanted Si annealed at 600°C and 700°C have larger high momentum components, which may come from annihilation with Cu core electrons. It is provable that Cu atoms exist in vacancy complexes.

The CDB spectra for H-implanted Si are shown in Fig. 7. The results of conventional Doppler broadening measurements are shown in Fig. 8. The CDB spectrum is different from those for As and P even as-implanted state. Annealing is considered to be performed with at least three steps. Peaks in the conventional S parameter measurements, which reflect the distribution of positron trap site, are seen in near surface region than expected from the range of H ion up to 300°C.[5] It indicates that the defects induced around the range of H ion are at least partly passivated with H ion

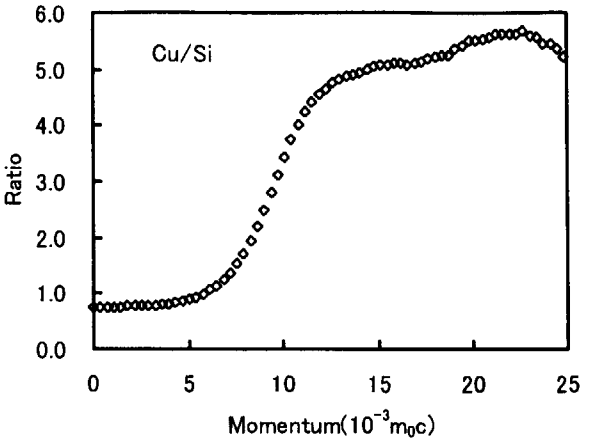


Fig. 6 CDB spectrum for pure Cu shown as the ratio to that for Si.

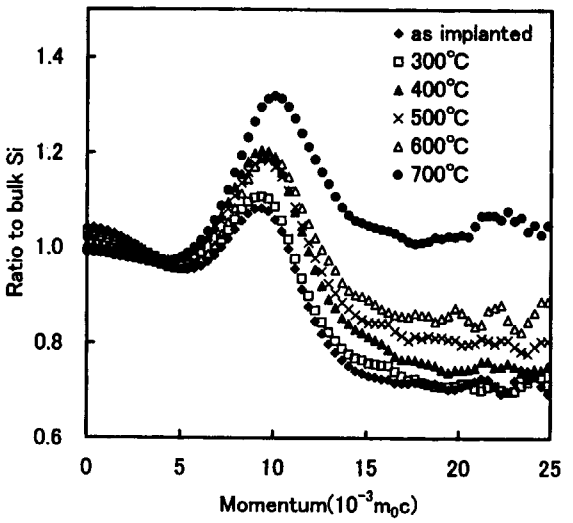


Fig. 7 CDB spectra for Si implanted with H.

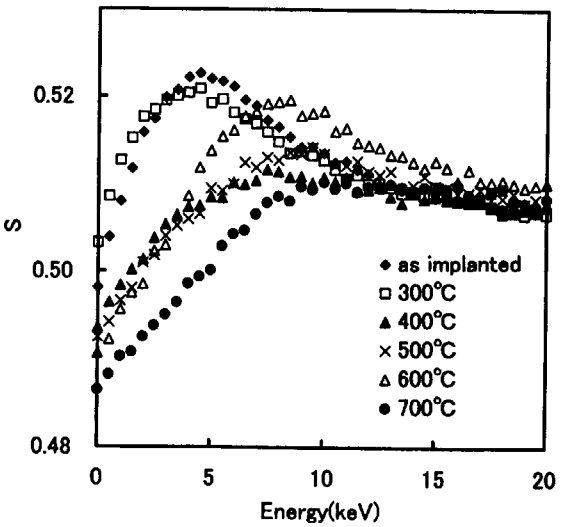


Fig. 8 S-parameter of conventional Doppler broadening spectra for Si implanted with H.

itself.[6] From 400°C to 600°C, these hydrogens are released, which results in increase of S parameter while the CDB spectra in high momentum region do not change much. These defect complexes are annealed out at higher temperature.

In conclusion, different annealing behavior of Si implanted with various kinds of ions is shown with CDB measurements. CDB measurement is a powerful tool for investigation of defects. Though, combination with other techniques such as lifetime, conventional Doppler broadening measurements, first principle calculation is necessary for full utilization of CDB measurements.

References

[1] K. G. Lynn, J. R. MacDonald, R. A. Boie, L. C. Feldman, J. D. Gabbe, M. F. Robbins, E. Bonderup and J. Golovchenko, Phys. Rev. Lett. **38**, 241 (1977)

[2] M. Alatalo, H. Kauppinen, K. Saarinen, M. J. Puska, J. Makinen, P. Hautojarvi and R. M. Nieminen. Phys. Rev. **31**, 4176 (1995).

[3] Z. Tang, T. Nonaka, Y. Nagai and M. Hasegawa, Mat. Sci. Forum **363-365**, 67 (2001).

[4] A. Uedono, S. Tanigawa, J. Sunaga and M. Ogasawara. Jpn. J. Appl. Phys. **29**, 1867 (1990).

[5] M. Fujinami, T. Akahane and T. Sawada, Mat Sci. Forum **363-365**, 52 (2001).

[6] R. S. Brusa, M. Duarte Naia, A. Zecca, C. Nobili, G. Ottaviani, R. tonini and A. Dupasquier, Phys. Rev B **49**, 7271 (1994).

JP0350276

2.12 MECHANICAL CHARACTERIZATION OF MAGNESIUM ALUMINATE MgO· nAl_2O_3 SPINEL SINGLE CRYSTALS IRRADIATED WITH Cu^- IONS

Takahito Ohmura[1], Chi-Gyu Lee[2], Naoki Kishimoto[2]
[1]Materials Engineering Laboratory and [2]Nanomaterials Laboratory
National Institute for Materials Science
1-2-1 Sengen, Tsukuba, Ibaraki, 305-0047 Japan

Abstract

Ion-irradiation response of spinel single crystals was investigated using a nanoindentation technique. Specimens of stoichiometric (n=1) and non-stoichiometric (n=2.4) single crystals of MgO n(Al_2O_3) spinel were irradiated with 60keV Cu^- ion at room temperature. Dose rate ranged from 1 to 100 $\mu A/cm^2$, and a total dose was kept constant at 3×10^{16} ions/cm^2. Both plastic hardness and elastic modulus of all the irradiated specimens were softened. Radiation-induced swelling simultaneously occurred. Rutherford back scattering spectroscopy detected disordering of spinel crystalline structure. Accordingly, the radiation-induced softening and swelling are ascribed to accumulation of point defects associated with the disordering. In comparison between the stoichiometric and the non-stoichiometric specimens, the radiatioin-induced softening is suppressed in the non-stoichiometric composition.

Keywords: MgO n(Al_2O_3) spinel, ion-irradiation, mechanical properties, nanoindentation, microstructure

1. Introduction

Magnesium aluminate spinel MgO nAl_2O_3 has great potential of application to fusion reactors as an insulating and dielectric material because it exhibits high resistance to radiation damage with high-energy particles [1-5]. Many studies have been performed on the microstructural characterization in order to reveal a response to neutron or ion irradiation and to understand the mechanism of the high resistance to radiation damage [6-17]. The mechanical property is one of important issues for using the materials safely in a fusion environment. However, only a few studies have been performed on mechanical characterization of neutron- or ion-irradiation layers for spinel [11, 19-21]. Particularly, in the case of the ion irradiation, a damaged layer exists within a sub-micron depth, and therefore conventional tests are not applicable.

Recent progresses in depth-sensing nanoindentation technique have made it possible to probe mechanical properties of materials in a nanometer scale [22-26], and the damaged layer of sub-micron thickness can be directly evaluated. Some studies were carried out on measurements for ion-irradiated spinel by nanoindentation technique to reveal relationship between microstuructural change and hardness shift. Devanathan *et al.* [11] reported that

*Corresponding author. Tel: +81-298-59-2253 Fax: +81-298-59-2201
E-mail address: OHMURA.Takahito@nims.go.jp (Takahito Ohmura)

both hardness and Young's modulus increased in the lower dose stage corresponding to metastable phase, subsequently decreased in the higher dose of amorphous phase irradiated with Xe^{2+} ion under cryogenic condition. Izumi *et al.* [21] showed that the stoichiometric and non-stoichiometric spinel exhibited a radiation hardening in the fluence range from 2.4×10^{18} to 2.0×10^{20} He^{+}/m^{2} at temperatures from 300 to 870 K. Further systematic studies are necessary to clarify the whole behavior of irradiation response in mechanical properties for spinel. In the present study, nanoindentation techniques are applied to ion-irradiated spinel in order to reveal the mechanical properties, and then we consider the effects of stoichometry and dose rate. Relationship between the mechanical properties and microstructures are discussed.

2. Experimental

Single crystal wafers of stoichiometric (n=1) and non-stoichiometric (n=2.4) MgO nAl_2O_3 spinel were employed. Samples were cut into 15 mm diameter and 1 mm thickness and one side of each was polished in mirror finishing to be prepared for ion irradiation. A part of sample surface was masked in order to prevent the samples from elevating temperature. Ion irradiations were conducted with 60 keV Cu^{-} ions at room temperature. Dose rates ranged from 1 to 100 $\mu A/cm^2$, and total dose were kept constant at 3×10^{16} ions/cm^2, which corresponds to peak damage of about 23 displacements per atom (dpa).

Nanoindentation tests were carried out on the irradiated surfaces using Hysitron Triboscope with a Berkovich type diamond indenter. Indenter tip truncation was calibrated by the area function method [26]. Elastic modulus and plastic hardness were calculated by initial unloading stiffness analysis [25,26]. The elastic modulus E_r is expressed as

$$E_r^{-1} = \frac{1-\nu_s^2}{E_s}, \tag{1}$$

which is based on the Hertz contact theory of

$$E^{*-1} = E_r^{-1} + \frac{1-\nu_i^2}{E_i}, \tag{2}$$

where E^* is a composite elastic modulus, E and ν are Young's modulus and Poisson's ratio, respectively. The subscripts s and i represent sample and indenter, respectively. Thermal drift rate in a tip displacement was measured prior to each test, and then penetration depth was corrected assuming the rate to be constant during testing period of about 10 seconds. Typical drift rate was less than 0.1 nm/s. Peak load ranged from 20 to 1000 μN, and 5 tests were conducted under the same condition at different positions on the specimen surface. Step height at the masked/exposed boundary was measured with atomic force microscopy to study a swelling behavior. Rutherford backscattering spectroscopy was carried out to characterize the lattice disordering.

3. Results and Discussion

3.1 Radiation response of plastic hardness and elastic modulus

Typical load-displacement curves for the stoichiometric specimens of three different irradiation conditions are shown in fig. 1. Two curves for each sample are simultaneously plotted. As shown in the figure, the two curves of the same sample coincide with each other and are deviated within less than 1 nm or so. Therefore, the difference in P-h curves among the different irradiation conditions is meaningful. The irradiated samples show the deeper maximum penetration depth than that of non-irradiated one, indicating a significant irradiation-induced softening. Additionally, the penetration depth is larger for a sample of 3 $\mu A/cm^2$ than for that of 100 $\mu A/cm^2$, showing the softening behavior depends on the dose rate.

One of the most important quantities in evaluation of mechanical properties by indentation technique is a ratio of the damaged layer thickness to penetration depth corresponding to the deformed zone beneath the indenter. The depth profile of damage calculated by TRIM code is shown in fig. 2. The profile of Cu atomic density, which is for implanted ions, is also shown as a reference. The depth of damage peak is about 10 nm, and the maximum depth can be estimated to be about 55 nm.

In order to reveal the depth dependence of hardness in the damaged layer, various peak load tests were made, and then calculated hardness was plotted as a function of penetrated contact depth of the indenter in fig. 3. The plotted data represent the depth dependence for a non-stoichiometric (n=2.4) sample irradiated at a dose rate of 10 $\mu A/cm^2$. The peak load ranges from 20 to 1000 μN and corresponding contact depth ranges from 5 to 40 nm. The hardness is almost constant in the depth range shallower than 10 nm. In the further deep range, the hardness increases with increasing contact depth and gradually approaches the value of the non-irradiated specimen. The depth dependence of the hardness is due to an influence by the non-damaged hard substrate, and the constant hardness in the depth range shallower than 10 nm shows the hardness of damaged layer only. In a case of

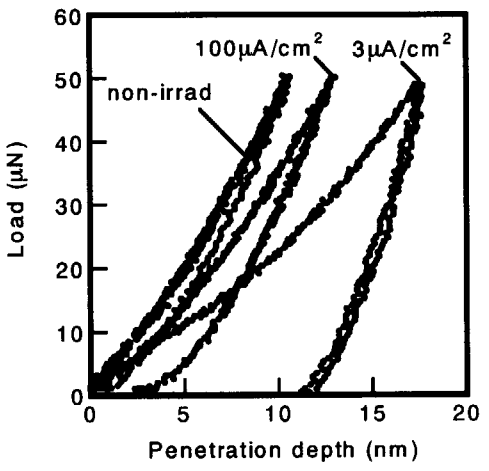


Fig. 1 Typical load-displacement curves for stoichiometric (n=1) magnesium aluminate spinel single crystals.

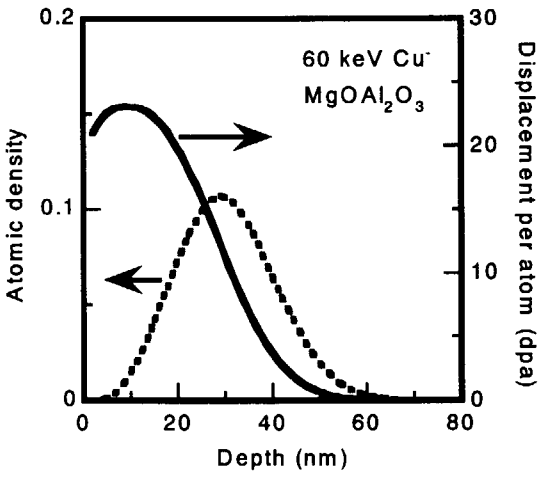


Fig. 2 Depth profile of damage calculated by TRIM code and Cu atomic density for stoichiometric sample.

layer-structured specimens, such as thin films or coatings, a critical penetration depth of existing of substrate constraint is 1/5 - 1/6 of film thickness [27]. The ratio of the critical depth of 10 nm and damaged depth of 55 nm coincides with the value in the literature. Therefore, the hardness in the penetration depth of about 10 nm is hereafter employed as hardness of damaged layer for all the samples. Hardness for the stoichiometric (n=1) and the non-stoichiometric (n=2.4) samples are plotted as a function of the dose rate in fig. 4. The data of a non-irradiated sample are also plotted. All the irradiated samples show lower hardness than those of non-irradiated ones, indicating significant irradiation-induced softening. Comparing the stoichiometric sample with the non-stoichiometric one, the former shows lower hardness in the entire dose-rate range except 1 μA/cm^2. The dose rate dependence of hardness for both the stoichiometric and non-stoichiometric samples shows a zigzag manner especially for stoichiometric one.

Elastic modulus is plotted as a function of maximum penetration depth in fig. 5. The elastic modulus increases with increaseing the maximum penetration depth in the whole depth range of 5-50 nm. Therefore, the data of even 20 μN peak load may be affected by hard substrate, and it is hard to determine the critical depth of influence of substrate. However, the data in the relatively shallow depth of 10 nm or so is considered to represent certain elastic properties of the damaged layer and qualitative is possible. Accordingly, the data of around 10 nm penetration depth, which is the same condition as in the case of the plastic hardness, is employed as an elastic modulus of the damaged layer.

Figure 6 shows elastic modulus represented as a function of the dose rate. These behaviors are similar to the plastic hardness as shown in fig. 4. Distinct irradiation-induced depression of elastic modulus occurs. The value is lower for stoichiometric samples than for those of non- stoichiometric ones. The dose rate dependence shows a zigzag behavior. In order to consider the softening mechanism, the hardness normalized by elastic modulus is shown in fig. 7. The H/E_r values are regarded as almost constant in the range of 1-10 μA/cm^2. Considering that the elastic moduli may be estimated to be larger than the true value because of the hard substrate (as previously mentioned in fig. 5), they might be closer to

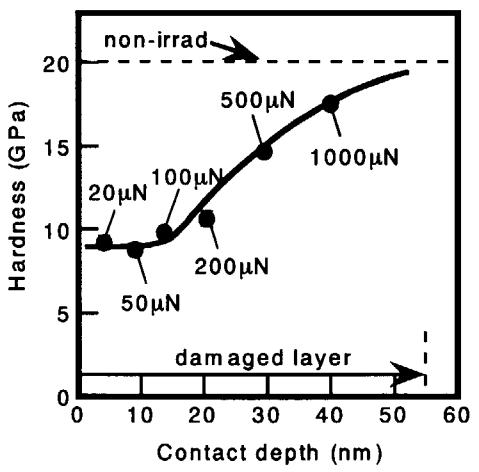


Fig. 3 Calculated hardness in various peak loads as a function of penetrated contact depth.

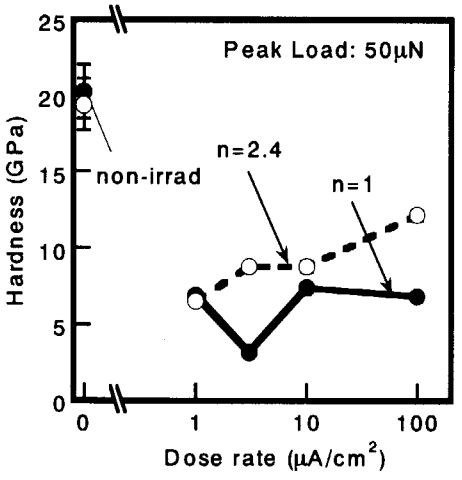


Fig. 4 Dose rate dependence of hardness of stoichiometric and non-stoichiometric sample.

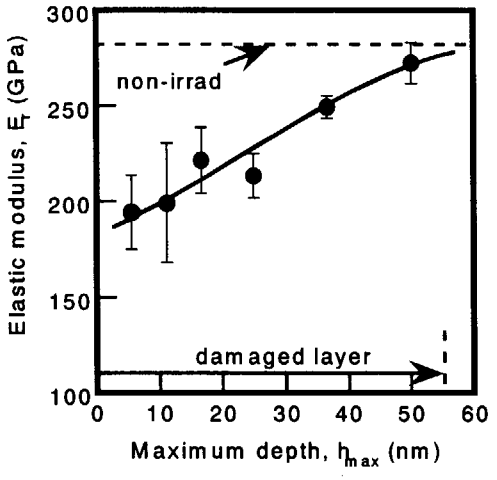


Fig. 5 Calculated elastic modulus in various peak load as a function of maximum penetration depth.

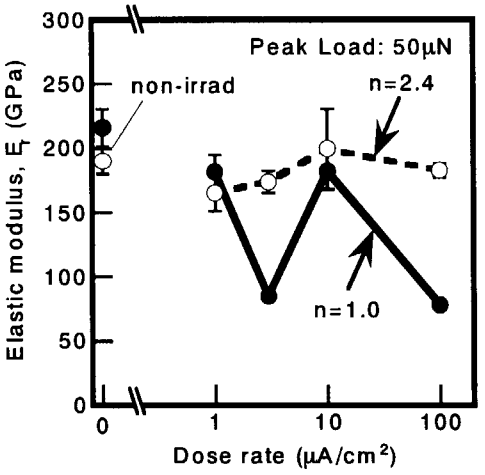


Fig. 6 Dose rate dependence of elastic modulus of stoichiometric and non-stoichiometric sample.

the non-irradiated one. The increase in 100 μA/cm^2, however, is open for question. Additionally, the difference between n=1 and 2.4 is smaller than those in cases of fig. 4 and 6. These results suggest that the irradiation-induced softening of plastic hardness is partly due to the depression of elastic modulus, because the resistance to plastic deformation in ceramics is generally dominated by intrinsic factor such as Peierls stress, which depends on a shear modulus.

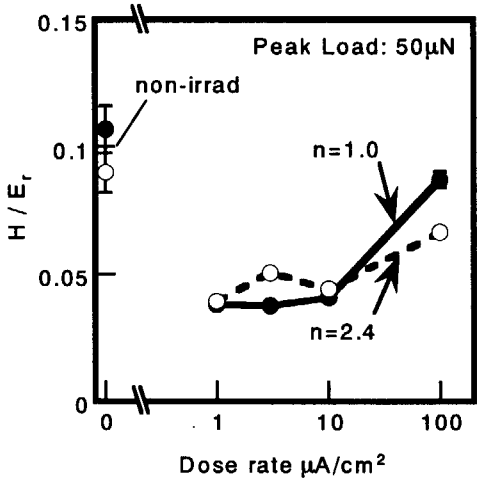


Fig. 7 Dose rate dependence of hardness normalized by elastic modulus of stoichiometric and non-stoichiometric sample.

3.2 Microstructural analysis

Irradiation-induced swelling behavior was revealed by measuring step-height at masked/exposed boundary. Fig. 8 shows the step-height versus dose rate for stoichiometric and non-stoichiometric samples. Large step-height means large volume expansion of swelling. As shown in this figure, the dose rate dependence is in a zigzag manner, which is similar to hardness and elastic modulus shown in fig. 4 and 6, respectively. The most important point is that the larger swelling at dose rate of 3 or 100 μA/cm^2 and the smaller swelling at 1 or 10 μA/cm^2 well correspond to the lower and the higher elastic modulus, respectively. In addition, the step-height is larger for stoichiometric samples than that of non-stoichiometric ones, and the zigzag amplitude of each of hardness, elastic modulus, and step-height is larger for stoichiometric samples than those of non-stoichiometric ones. These results suggest that the irradiation-induced depression of elastic modulus is due to swelling associated with accumulation of voids and vacancies, which causes a reduction of atomic density. The relatively high resistance to radiation damage of non-stoichiometric samples is

due to that point defect annihilation by interstitial-vacancy recombination occurs more significantly in the non-stoichiometric sample because the non-stoichiometric sample have a large amount of structural vacancies, as previously suggested in literature [18].

Fig. 9 represents RBS results for the stoichiometric and non-stoichiometric samples irradiated at 3 $\mu A/cm^2$. The spectrum of irradiated, aligned sample shows peaks of Al at 550 and O at 350 channel, indicating that the disordering of Al cation and O anion site in the spinel structure. The disordering behavior coincides with previous studies [18,19], especially under irradiation condition at room temperature [12]. Particularly, Al-cation disordering is more significant to be almost amorphized for stoichiometric samples, unlike non-stoichiometric ones. Accordingly, irradiation-induced reduction of elastic modulus associated with swelling is due to accumulation of point defects of Al cation and O anion disordering. Li *et al.* [20] have shown that the change in cation occupation sites have little influence on the elastic properties of neutron irradiated spinel. Therefore, the depression of elastic modulus detected in the present study is considered to be due to O anion disordering because a fraction of O anion sites is twice larger than that of Al cation sites in the magnesium aluminate spinel.

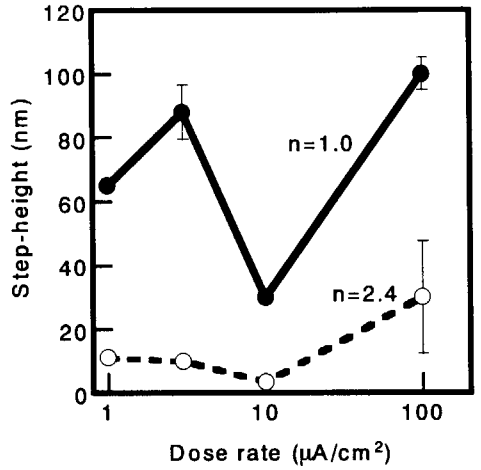


Fig. 8 Relationship between step-height at the masked/exposed boundary corresponding to swelling and dose rate of stoichiometric and non-stoichiometric samples.

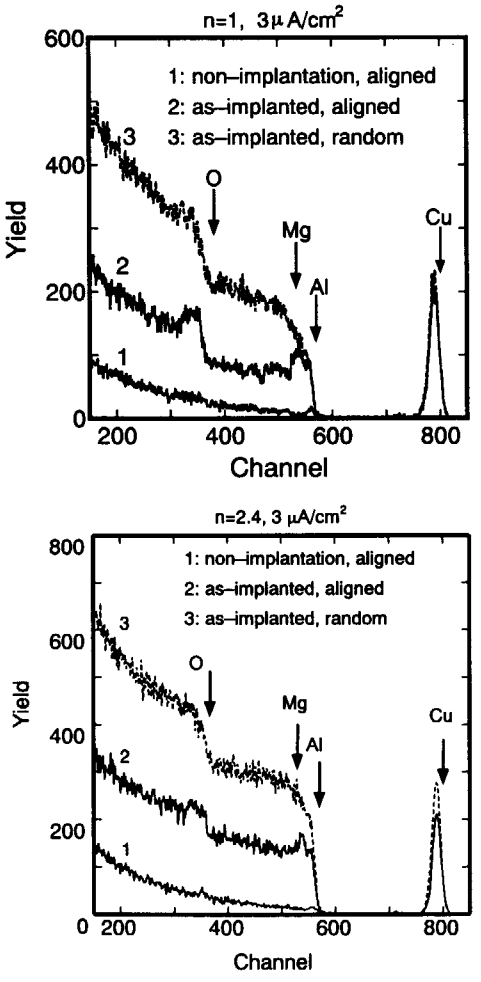


Fig. 9 Ion channeling spectra for (a) stoichiometric, n=1 and (b) non-stoichiometric, n=2.4 spinel single crystals. The irradiation dose rate is 3 $\mu A/cm^2$.

4. Conclusions

Mechanical properties of magnesium aluminate $MgO\ nAl_2O_3$ spinel single crystals irradiated with Cu ions were investigated by nanoindentation technique. Microstructural characterization of swelling and lattice disordering was also made. The relationship between mechanical properties and microstructure is considered. Following conclusions are obtained in the

present study:
(1) Irradiation-induced softening of plastic hardness and depression of elastic modulus occur for both stoichiometric and non-stoichiometric compositions even under the irradiation at room temperature.
(2) Since the dose rate dependence of swelling well corresponds to that of the elastic modulus, the irradiation-induced depression of elastic modulus is due to the swelling associated with accumulation of voids and vacancies, which causes reduction of atomic density.
(3) RBS analysis revealed site disordering of Al cations and O anions. Particularly, Al disordering in stoichiometric samples is significant and amorphization almost occur. Therefore, the swelling behavior is associated with accumulation of point defects of Al cation and O anion disordering.
(4) The hardness and elastic modulus of damaged layer are higher for non-stoichiometric samples than for stoichiometric ones in the dose rate higher than 3 $\mu A/cm^2$. This is be due to that point defect annihilation by interstitial-vacancy recombination is significant in non-stoichiometric sample.

References

[1] F. W. Clinard, Jr., and G. F. Hurley, J. Nucl. Mater. **108/109**, 655 (1982).
[2] F. W. Clinard, Jr., G. F. Hurley, R. A. Youngman, and L. W. Hobbs, J. Nucl. Mater. **133/134**, 701 (1985).
[3] S. N. Buckley, J. Nucl. Mater. **141-143**, 387 (1986).
[4] S. N. Buckley, and S. J. Shaibani, Phil. Mag. Lett. **55**, 15 (1987).
[5] L. W. Hobbs, F. W. Clinard, Jr., S. J. Zinkle, and R. C. Ewing, J. Nucl. Mater. **216**, 291 (1994).
[6] N. Yu, K. E. Sickafus, and M. Nastasi, Phil. Mag. Lett. **70**, 235 (1994).
[7] N. Bordes, L. M. Wang, and R. C. Ewing, J. Mater. Res. **10**, 981 (1995).
[8] R. Devanathan, K. E. Sickafus, N. Yu, and M. Nastasi, Phil. Mag. Lett. **72**, 155 (1995).
[9] K. E. Sickafus, N. Yu, R. Devanathan, and M. Nastasi, Nucl. Instrum. Meth. B **106**, 573 (1995).
[10] C. Kinoshita, K. Fukumoto, K. Fukuda, F. A. Garner, and G. W. Hollenberg, J. Nucl. Mater. **219**, 143 (1995).
[11] R. Devanathan, N. Yu, K. E. Sickafus, and M. Nastasi, J. Nucl. Mater. **232**, 59 (1996).
[12] S. Furuno, N. Sasajima, K. Hojou, K. Izumi, H. Ostu, T. Muromura, and T. Matsui, Nucl. Instrum. Meth. B **127/128**, 181 (1997).
[13] S. J. Zinkle, and C. Kinoshita, J. Nucl. Mater. **251**, 200 (1997).
[14] R. Devanathan, N. Yu, K. E. Sickafus, and M. Nastasi, Nucl. Instrum. Meth. B **127/128**, 608 (1997).
[15] S. J. Zinkle, and G. P. Pells, J. Nucl. Mater. **253**, 120 (1998).
[16] K. E. Sickafus, J. M. Wills, and N. W. Grimes, J. Am. Ceram. Soc. **82**, 3279 (1999).
[17] I. V. Afanasyev-Charkin, D. W. Cooke, V. T. Gritsyna, M. Ishimaru, and K. E. Sickafus, Vacuum **58**, 2 (2000).
[18] T. Soeda, S. Matsumura, C. Kinoshita, and N. J. Zaluzec, J. Nucl. Mater. **283-287**, 952 (2000).
[19] W. Dienst, J. Nucl. Mater. **211**, 186 (1994).
[20] Z. Li, S.-K. Chan, F. A. Garner, and R. C. Bradt, J. Nucl. Mater. **219**, 139 (1995).

[21] K. Izumi, K. Yasuda, C. Kinoshita, M. Kutsuwada, J. Nucl. Mater. **258-263**, 1856 (1998).
[22] M. Nishibori, K. Kinoshita, Thin Slid Films **48** (1978) 325.
[23] D. Newey, M. A. Wilkins, H. M. Pollock, J. Phys. E: Sci. Instrum. **15** (1982) 119.
[24] J. B. Pethica, in: V. Ashworth, W. Grant, R. Procter (Eds.), Ion Implantation into metals, Pergamon Press, Oxford, 1982, p.147.
[25] M. F. Doerner, W. D. Nix, J. Mater. Res. **1** (1984) 601.
[26] W. C. Oliver, G. M. Pharr, J. Mater. Res. **7** (1992) 1564.
[27] T. Ohmura a, S. Matsuoka, K. Tanaka and T. Yoshida, Thin Solid Films **385** (2001) 198.

JP0350277

2.13 FABRICATION OF Ni_3Al THIN FOILS BY COLD ROLLING AND THE MECHANICAL PROPERTIES

Toshiyuki Hirano[1], Masahiko Demura[1], Kyosuke Kishida[1] and Yozo Suga[2]
[1]National Research Institute for Metals, 1-2-1 Sengen, Tsukuba, Ibaraki 305-0047, Japan
[2]Nippon Cross Rolling Co., 697 Mobara, Mobara, Chiba 297-0026, Japan

Abstract

Thin foils of boron-free stoichiometric Ni_3Al below 100 μm in thickness were fabricated by cold rolling of the sheets which were sectioned from directionally solidified ingots. Two types of deformation microstructure associated with fine slip traces and coarse, wavy shear bands were observed in the foils, depending on the initial rolling direction. In the case of near <112> rolling direction, the microstructure was rather homogeneous associated with a single {110} texture. In the case of near <001> rolling direction, the microstructure consisted of repeated double bands with differently oriented slip traces, having two different {110} textures. Both type of the cold-rolled foils had very high fracture strength, 1.7~1.9 GPa, as a result of heavy cold reduction. They showed bending ductility but no tensile ductility. No significant difference in the mechanical properties was observed between the two deformation microstructures.

Keywords: Intermetallic compounds, Ni_3Al, cold rolling, foil, deformation microstructure, texture, mechanical properties

1. Introduction

Ni_3Al has attractive high-temperature mechanical properties and oxidation/corrosion resistance. Grain boundary brittleness, which used to be a major problem of this compound, has been overcome by small amounts of boron addition [1,2]. Since then extensive efforts have been made to develop Ni_3Al-based alloys into commercial use. Most of these efforts have been targeted for use in a bulk form, e.g. as-cast ingot, bar, tube, plate, sheet etc. [3]. In contrast, we are focusing on a plan to use Ni_3Al alloys in a foil form, e.g. honeycomb structure which has an advantage in lightweight and high-stiffness over solid materials. For this purpose ductile thin foils below 100 μm in thickness are required and furthermore, cold rolling is desirable for fabrication of the foils in terms of surface quality and fabrication cost. However, it has been very difficult to cold-roll Ni_3Al alloys to such thinner foils. Even with the beneficial effect of boron addition, the room-temperature ductility is not enough to reduce the thickness below 800 μm [4].

As an alternative to the boron-doping method, we found that directional solidification using a floating zone (FZ) method is very effective in improving the grain boundary brittleness of Ni_3Al [5-7]. By using the ductile directionally solidified ingots we recently have succeeded in fabricating thin foils of boron-free binary stoichiometric Ni_3Al below 100 μm in thickness by cold rolling as shown in Fig.1 [8]. Total reduction in thickness amounts to 95 %. The surface is crack-free and smooth, having a shiny metallic luster. As far as we know, such

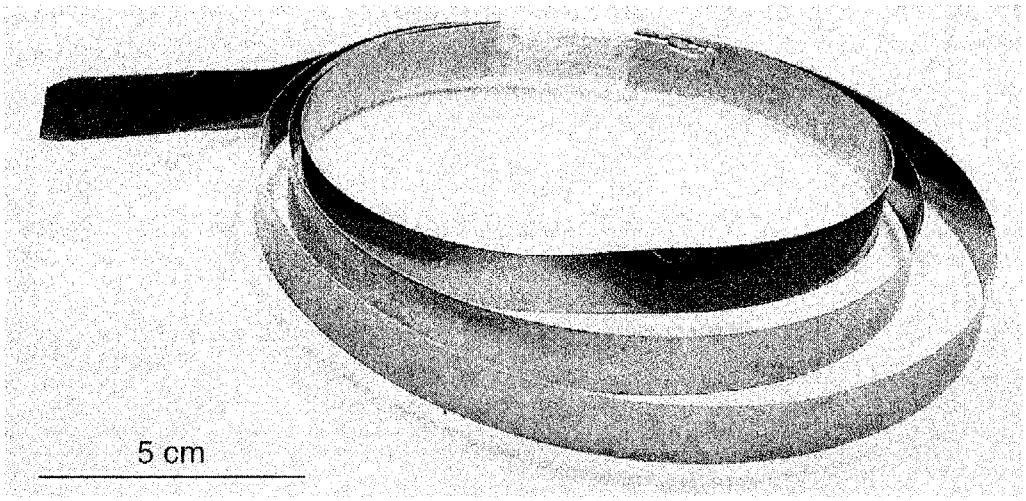


Figure 1: 91 μm-thick, 10 mm-wide and about 1-m long foil cold-rolled to 96% reduction.

thin foils of intermetallic compounds have never been fabricated by cold rolling so far. Fortunately the foils posses some tensile ductility, 3.0-14.6 %, at room temperature in air after recrystallization between 1273 and 1573 K. The results eliminate severe embrittlement for recrystallized foils, which proves a high potential for structural applications.

Here we present the fabrication of Ni_3Al thin foils by cold rolling and the mechanical properties at room temperature in air.

2. Experimental

Four rods, designated as Nos. 31-2, 41-1, 42-2, and 47-1 of boron-free binary stoichiometric Ni_3Al were grown by the FZ method in an image furnace with double halogen-lamps at a growth rate of 25 mm/h. The feed rod preparation and crystal growth procedure were previously described [5,8]. On average the grown rods were 12 mm in diameter and 150 mm in length. All the ingots were predominantly single crystal but contained columnar grains with low angle boundaries in places. Table I summarizes the Al contents of the four rods as determined by inductively coupled plasma spectroscopy. The Al contents are close to the stoichiometric composition (25 at.% Al).

The grown rods were sectioned into sheets along the growth direction by electric

Table I Al contents and initial orientation of the rolling sheets

Sample No.	Al content (at%)	Rolling plane	Rolling direction
31-2	24.4	{0.2 0.1 1.0}	<1.0 0.0 0.2>
47-1	24.6	{3.0 0.1 4.9}	<0.0 1.0 0.0>
41-1	24.7	{3.9 1.0 5.2}	<4.0 9.0 4.8>
42-2	24.8	{2.0 1.0 4.3}	<1.1 2.0 1.0>

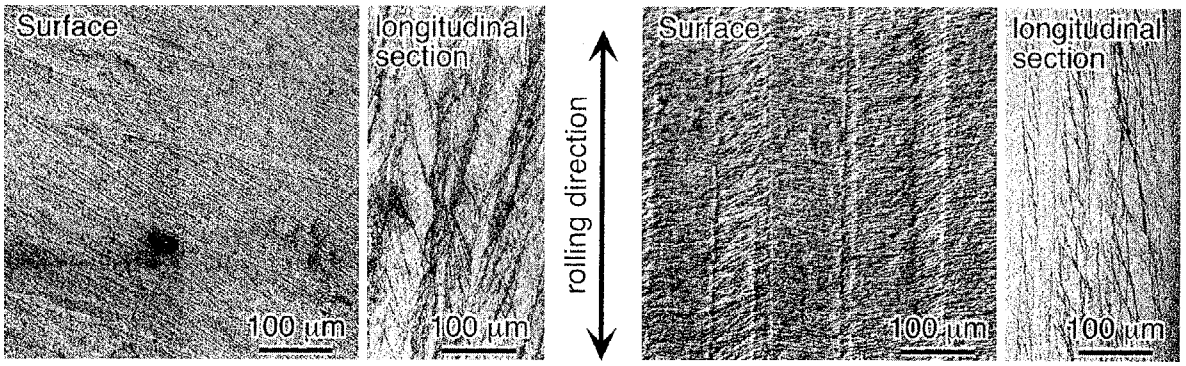
discharge machining (EDM). The initial rolling direction (RD) and normal direction (ND) of the rolling plane were determined by the Laue X-ray back reflection method as summarized in Table I. After mechanical polishing of the surface, the sheets were cold-rolled to about 300 μm in thickness by using four-high mills with a work roll diameter of 110 mm (10% reduction per pass). Then, they were rolled further using cemented carbide rolls having a roll diameter of 75 mm (2% reduction per pass). Both the cold-rolling operations were performed at room temperature in air without intermediate annealing or lubricant.

The rolling textures of the foils were measured by the X-ray Schultz back reflection method. The optical microstructures were examined on the surface and the longitudinal section by etching with strain sensitive etchant, Marble reagent (2.5 g $CuSO_4$, 30 cm^3 HCl, and 25 cm^3 H_2O). Also, the microstructures were examined by transmission electron microscopy. Basic mechanical properties of the cold-rolled foils were examined by using samples Nos. 42-2 and 47-1. Vickers hardness was measured along the thickness direction on the longitudinal section. Tensile specimens with gauge length of 10 mm and width of 5 mm were cut by EDM along the RD. Tensile tests were performed at room temperature in air at a strain-rate of $8x10^{-4}$ s^{-1}. The load data were collected at a frequency of 5 Hz with a computer. The fracture surface was examined using scanning electron microscope.

3. Results and Discussion

Microstructures

Figure 2 shows two typical types of deformation microstructure observed in the cold-rolled foils after chemical etching. The deformation microstructure depends on the initial RD. In the case of near <112> RD, samples Nos. 41-1 and 42-2, fine slip traces lie on the surface, being inclined about 60° to the RD (Fig. 2(a)). Also, coarse and wavy traces, which are regarded as shear bands, are observed on the longitudinal section similar to the case of boron-doped Ni_3Al [9-11]. Except for the shear bands, the deformation microstructure of these samples is rather homogeneous. In the case of near <001> RD, samples Nos. 31-2 and



(a) sample No. 42-2 (b) sample No. 47-1

Figure 2: Optical microstructures observed on the etched surface and longitudinal section of cold-rolled foils (83% reduction): (a) sample No. 42-2 and (b) No. 47-1.

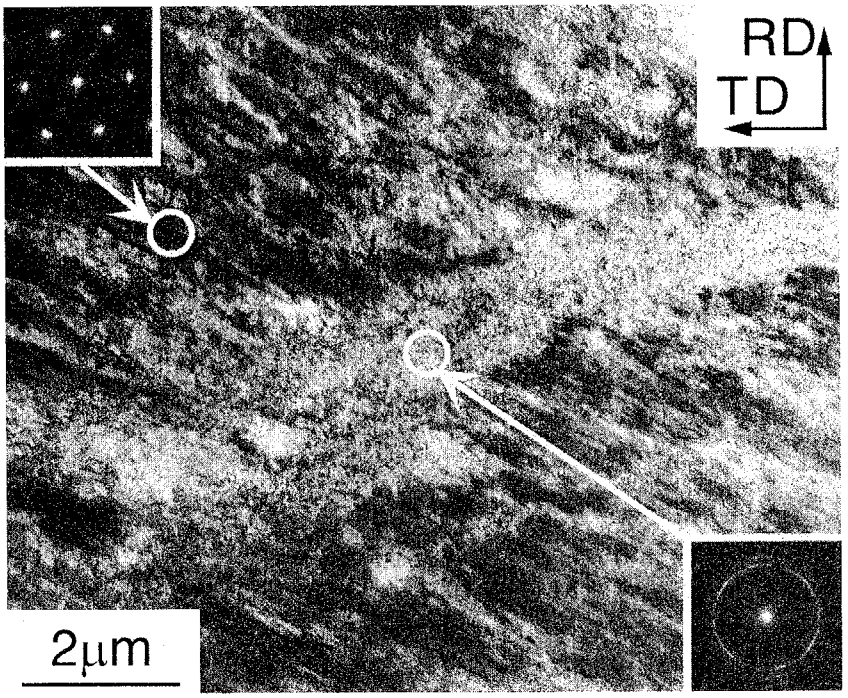


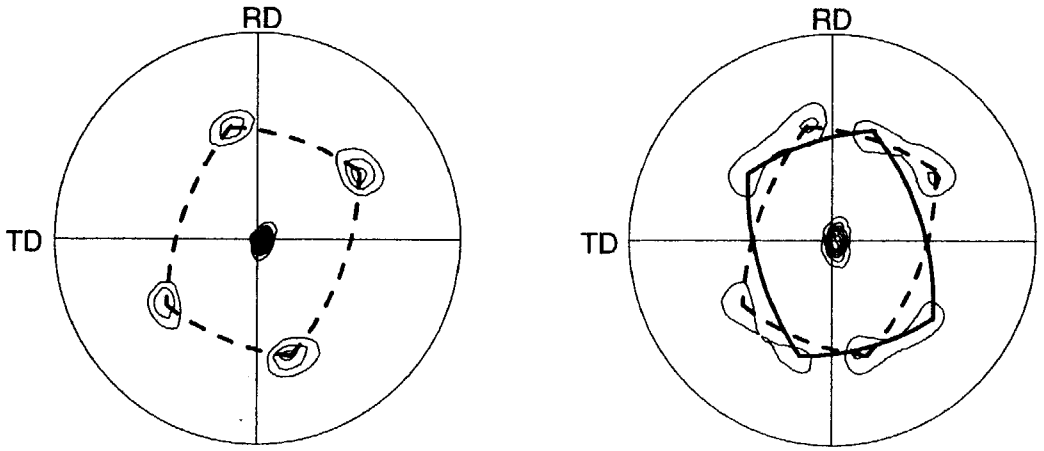
Figure 3: TEM micrograph of sample No. 47-1 cold-rolled to 92% reduction

47-1, the deformation microstructure is composed of repeated double bands with differently oriented surface slip traces (Fig. 2(b)). The width of the bands ranges from 20 to 100 μm parallel to the RD.

Figure 3 shows TEM micrograph of sample No. 47-1 cold-rolled by 92%. As a result of high reduction, many slip bands are observed with a high density of dislocations. In contrast to conventional fcc metals with high stacking fault energy such as Ni and Al, the dislocations are not arranged in cell structures or subgrains as Escher and Gottstein previously reported [12]. Instead they are rather uniformly accumulated. When the amount of reduction becomes larger than 90%, the shear bands consist of very fine grained-structure with less than 50nm in diameter as shown in the center of Fig 3, indicating an evidence of extremely severe plastic deformation. On a macroscopic level, two types of the deformation microstructure were observed, depending on the initial RD as described above. No clear difference, however, has been observed in the matrix between the two microstructures so far, except the bent slip bands.

Rolling Textures

Figure 4 shows the {220} pole figures of the cold-rolled foils, (a) sample No. 42-2 and (b) No. 47-1. In all the foils cold-rolled over 83% reduction, the {220} pole has a highest intensity peak at the ND associated with surrounding peaks about 60° away from the ND, which means that the foil surface was strongly oriented parallel to {110} plane during cold rolling. It is likely that the {110} rolling texture is a characteristic of the highly cold-rolled



(a) sample No. 42-2　　(b) sample No. 47-1

Figure 4: The {220} pole figures of the cold-rolled foils: (a) sample No. 42-2 (83% reduction) and (b) No. 47-1 (78% reduction). Open and solid squares represent {110}<$\bar{1}$13> and {110}<$\bar{1}$17> textures, respectively.

Table II　Summary of cold rolling

Sample No.	Thickness / μm		Reduction (%)	Rolling Texture	Structure
	Before rolling	After rolling			
31-2	959	315	67		
		73	92	{110}<$\bar{1}$13>+{110}<1$\bar{1}$7>	Banded
		57	94		
47-1	1789	384	78	{110}<$\bar{1}$14>+{110}<1$\bar{1}$4>	Banded
		96	95	{110}<$\bar{1}$12>+{110}<1$\bar{1}$2>	
41-1	2043	91	96	{110}<$\bar{1}$13>	
42-2	1907	319	83	{110}<$\bar{1}$14>	

Ni_3Al single crystals. Escher et al. found a similar single {110}<113> rolling texture in a 80% cold-rolled Ni-rich Ni_3Al single crystal [13]. Regarding the orientation of the RD, there is some difference between the samples, depending on the deformation microstructures in Fig. 2. Samples Nos. 41-1 and 42-2 which form homogenous deformation microstructures have a single {110} texture, while samples Nos. 31-2 and 47-1 which form the repeated double bands consist of two different {110} textures. The results are summarized in Table II.

Cold rolling is simply considered to be a combination of compression and tension toward the ND and the RD, respectively. The {110} texture can be understood in terms of compressive deformation normal to the rolling plane, as described elsewhere [8]. In compressive deformation, a crystal changes its orientation so that the normal direction to the

slip plane changes relative to the compressive direction, a process known as lattice rotation. Since the slip system in Ni_3Al is {111}<110> at room temperature and the samples used in this study are single crystals or preferred-oriented columnar crystals, the ND rotates toward the (011) pole by the activation of two sets {111}<110> slips, $(111)[01\bar{1}]$ and $(11\bar{1})[011]$, which lead to the formation of {110} texture. Regarding the RD, the difference between the samples is due to the initial RD. When the RD is oriented away from [001], the RD approaches toward $[\bar{1}12]$ by the activation of two sets {111}<110> slips, $(111)[\bar{1}01]$ and $(\bar{1}\bar{1}1)[011]$. This is the case for sample Nos. 41-1 and 42-2. However, when the RD is close to [001], samples Nos. 31-2 and 47-1, extra two sets of conjugate slips, $(111)[0\bar{1}1]$ and $(\bar{1}\bar{1}1)[101]$, must be activated, which lead the RD to rotate toward $[1\bar{1}2]$. As a result, the banded structures with two different {110} textures are formed.

Mechanical Properties

Mechanical properties were measured for the two cold-rolled foils by about 83% reduction, samples Nos. 42-2 and 47-1 which have different deformation microstructures as described above. Average Vickers hardness number was very high compared to that of the annealed Ni_3Al, 260: 604 for sample No. 42-2 and 649 for sample No. 47-1. In both the foils, there was no appreciable change in the Vickers hardness number along the thickness direction, indicating that the foils were homogeneously cold-rolled.

Figure 5 plots the engineering stress vs. engineering strain curves along the rolling direction. Both the foils fractured without appreciable plastic tensile elongation as a result of

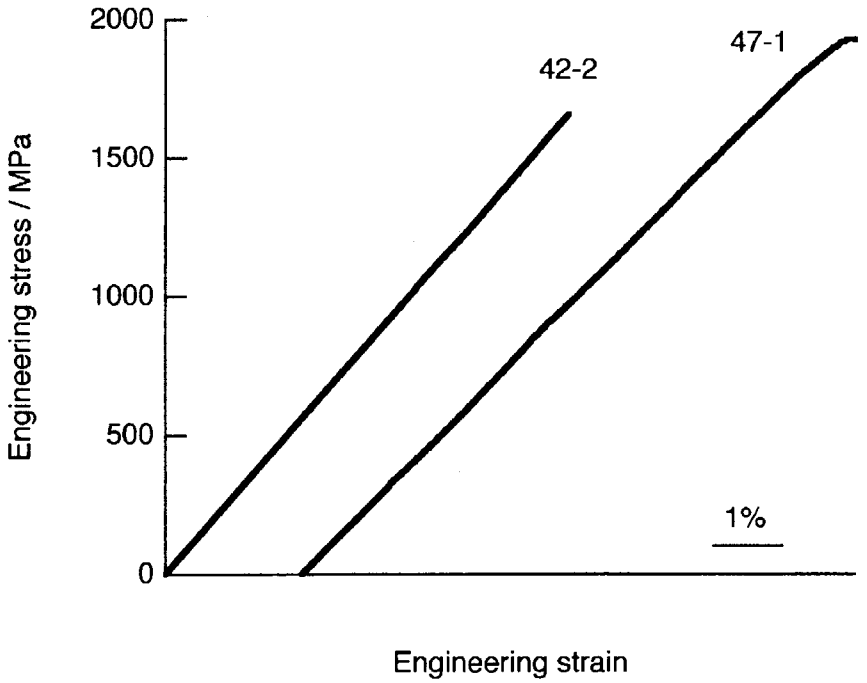
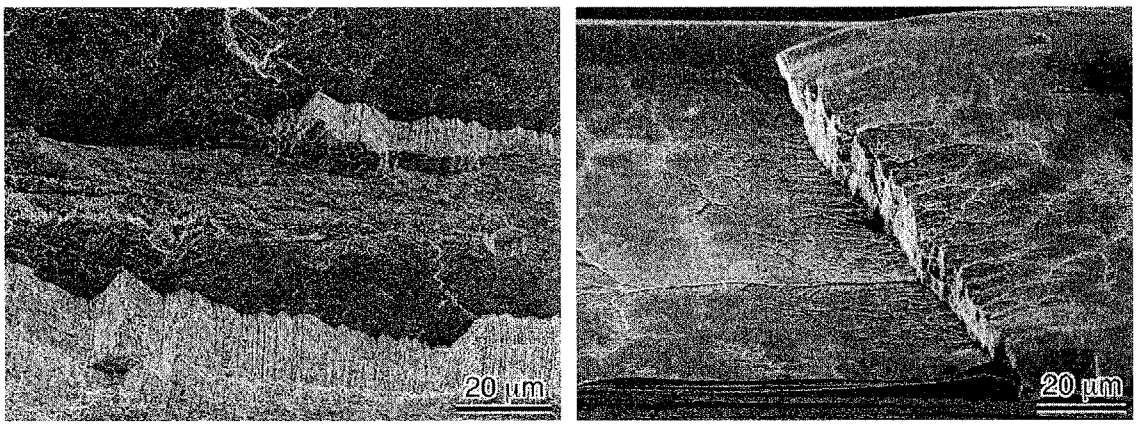


Figure 5: Engineering stress vs. engineering strain curves of the foils cold-rolled to 83% reduction of samples Nos. 42-2 and 47-1.

heavy cold-reduction. The fracture strength is very high, 1.7~1.9 GPa, which is more than three times as large as that of as-directionally-solidified Ni_3Al in simple tensile tests [6,7]. There is no large difference in the fracture strength between the two foils as well as the Vickers hardness number.

The fracture surface basically shows a brittle fracture mode, having cleavage-like facets partly as shown in Fig. 6. Though the foils fracture in such a brittle manner in tension, it is possible to plastically bend them, as shown in Fig.7. The reason of this bending capability is not clear but it is favorable for fabrication of honeycomb structure because the core sheet of the honeycomb structure is fabricated by bending.



(a) sample No. 42-2　　(b) smaple No. 47-1

Figure 6: Fracture surfaces of the tensile-tested foils in Figure 5: (a) sample No. 42-2 and (b) No. 47-1.

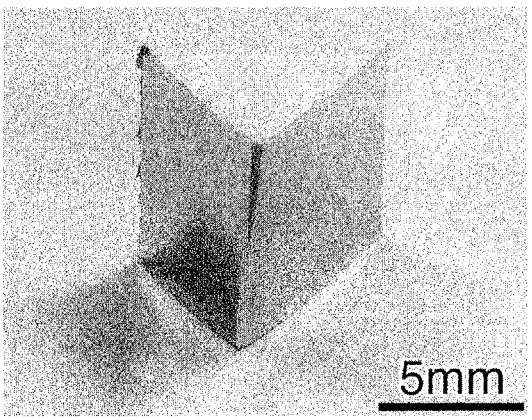


Figure 7: Photograph of 91 μm-thick foil cold-rolled to 96% reduction of sample No.41-1, showing bending capability.

4. Conclusion

Thin foils of boron-free stoichiometric Ni_3Al fabricated by cold rolling were examined in terms of microstructure, texture, mechanical properties and thermal stability. The followings are the results.

1. Two types of deformation microstructure were evolved during heavy cold rolling, depending on the initial RD. In the case of near <112> RD, the microstructure was rather homogenous associated with a single {110} texture. In the case of near <001> RD, the microstructure consisted of repeated double bands with differently oriented slip traces, having two {110} textures.

2. The cold-rolled foils had very high fracture strength, 1.7~1.9 GPa, as a result of heavy cold reduction. They showed no tensile but bending ductility. There was no significant difference on the mechanical properties between the two types of deformation microstructure.

Acknowledgments

This research was partly performed under the Originative Study Result Fostering Project funded by Japan Science and Technology Corporation. The assembly of the honeycomb structure was conducted by Drs. K. Minamida and M. Oikawa, Nippon Steel Techno-Research Corporation under this project. The authors would like to thank them for their contribution.

References

[1] K. Aoki and O. Izumi , Nippon Kinzoku Gakkai-shi, **43**,1190(1979).
[2] C. T. Liu, C. L. White and J. A. Horton, Acta metall., **33**,213(1985).
[3] V. K. Sikka, Mater. Res. Symp. Proc., **460**,15(1997).
[4] C. T. Liu and V. K. Sikka, J. Metals, **38**,19(1986).
[5] T. Hirano, Acta metall. mater., **38**,2667(1990).
[6] T. Hirano and T. Kainuma, ISIJ International, **31**,1134(1991).
[7] T. Hirano, Scripta metall. mater., **25**,1747(1991).
[8] M. Demura, Y. Suga, O. Umezawa, K. Kishida, E. P. George and T. Hirano, Intermetallics, **9**,157(2001).
[9] J. Ball and G. Gottstein, Mat. Res. Soc. Symp., **288**,897(1993).
[10] J. Ball and G. Gottstein, Intermetallics, **1**,171(1993).
[11] S. G. Chowdhury, A. K. Jena and R. K. Ray, Met. Mater. Trans. A, **29A**,2893(1998).
[12] C. Escher and G. Gottstein, Acta mater., **46**,525(1998).
[13] C. Escher, S. Neves and G. Gottstein, Acta mater., **46**,441(1998).

JP0350278

2.14 DYNAMICS OF COHERENT PHONONS IN ION-IRRADIATED BISMUTH STUDIED BY FEMTOSECOND PUMP-PROBE TECHNIQUE

M. Hase[1]*, K. Ishioka[1], M. Kitajima[1], S. Hishita[2], and K. Ushida[3]

[1]Materials Engineering Laboratory, National Institute for Materials Science (NIMS), 1-2-1 Sengen, Tsukuba 305-0047, Japan

[2] Advanced Materials Laboratory, National Institute for Materials Science (NIMS), 1-1 Namiki, Tsukuba 305-0044, Japan

[3]RIKEN (The Institute of Physical and Chemical Research), 2-1 Hirosawa, Wako 351-0198, Japan

Abstract

We have studied the effect of point defects on coherent optical phonons and photo-generated carriers in ion-implanted bismuth polycrystalline films and single crystals by means of pump-probe reflectivity technique. The dephasing time of the A_{1g} phonon decreases monotonically with increasing ion dose, which is explained by phonon-defect scattering. The relaxation time of photo-excited carriers decreases as the ion dose increases, being attributed to trapping of carriers by defect-induced deep levels. The behavior of the carrier and phonon dynamics for the polycrystalline film is compared with those for the single crystal.

Keywords : femtosecond, ion irradiation, coherent phonon, bismuth, defect

1. Introduction

Recent advances of ultrashort light pulses have made possible to generate and observe coherent lattice vibrations in the time domain. There have been several reports regarding dynamics of coherent phonons in bismuth and other semimetals.[1-5] In these experiments the coherent A_{1g} mode has been observed in the femtosecond (fs) time scale, and the displacive excitation of coherent phonons (DECP) mechanism has been proposed for the generation of the coherent phonon.[1,2] In this mechanism, photo-excited carriers create a non-equilibrium electron distribution, and as a result, crystal lattice begins to oscillate around the new equilibrium position. The phonon dephasing rate can be generally described as a sum of the anharmonic decay rate and the pure dephasing rate.[6] The main channel of the relaxation of

*corresponding author. Tel: +81-298-59-2837 Fax: +81-298-59-2801.
E-mail address:hase.muneaki@nims.go.jp

the coherent A_{1g} phonon in bismuth is the dephasing process originating from the phonon-phonon interaction caused by anharmonicity of the lattice potential.[5]

Lattice defects in semiconductors affect significantly phonon properties as well as electronic properties. Dekorsy *et al.* compared the dynamics of photo-excited carriers and coherent phonons in as-grown and annealed low-temperature (LT) grown GaAs by an electro-optic technique, and suggested that the differences in the decay time of the coherent LO phonon and the photo-excited carrier were related to the different microscopic forms of excess arsenic and point defect density.[7] Scholz *et al.* have reported results of fs pump-probe optical absorption experiments for coherent phonons on F centers in KBr.[8] These reports indicate that the fs pump-probe technique is useful to study the effect of defects on ultrafast dynamics of phonons. There are a few reports on dynamics of coherent A_{1g} phonons in the ion-irradiated Bismuth polycrystalline film.[9,10] However, the origin of the dephasing of the coherent phonon due to defects has not yet fully understood, and systematic measurements on coherent phonon dynamics in ion-irradiated crystals is also required to understand the dephasing process.

In this paper, we study the effect of ion irradiation on dephasing of coherent optical phonons in Bismuth polycrystalline films and in Bismuth single crystals. Ultrafast dynamics of coherent phonons and photo-generated carriers are precisely measured for various ion doses by using fs pump-probe technique. The dephasing time of the coherent A_{1g} mode decreases with ion dose in both polycrystalline films and single crystals. However, the behavior is significantly different between polycrystalline film and single crystal, which is discussed with carrier relaxation dynamics.

2. Experimental

The bismuth films studied in this work were prepared by vapor deposition on polished Si(001) substrates at room temperature. They were about 500 nm thick, and x-ray-diffraction measurements showed that they were polycrystalline. The bismuth single crystal was oriented along [001] and has a cleaved surface. In order to examine the effect of point defects, 500 keV Bi^+ ions were implanted into the polycrystalline films and single crystals at doses from $1x10^{14}$ to $1x10^{15} Bi^+/cm^2$. The damage depth deduced from the Monte Carlo calculation (TRIM) was about 200 nm,[11] and the damage profile was almost a Gaussian function with a peak at 71 nm from the surface. The fs pump-probe measurements were performed at room temperature. The light source used was a mode-locked Ti:sapphire laser with a central wavelength of 800 nm and pulse width of 60 fs. A standard reflection-type pump-probe configuration was employed.[1] Pump and probe beams were polarized orthogonal to each other to avoid scattered pump beam, and were focused to a diameter of about 100 μm on the samples. The penetration depth of the laser beams was about 130 nm, and covered well the irradiation damage area in which point defects exist. The reflectivity change $\Delta R/R$ was measured as a

function of the delay time by scanning the optical path length of the probe beam.

3. Results and Discussion

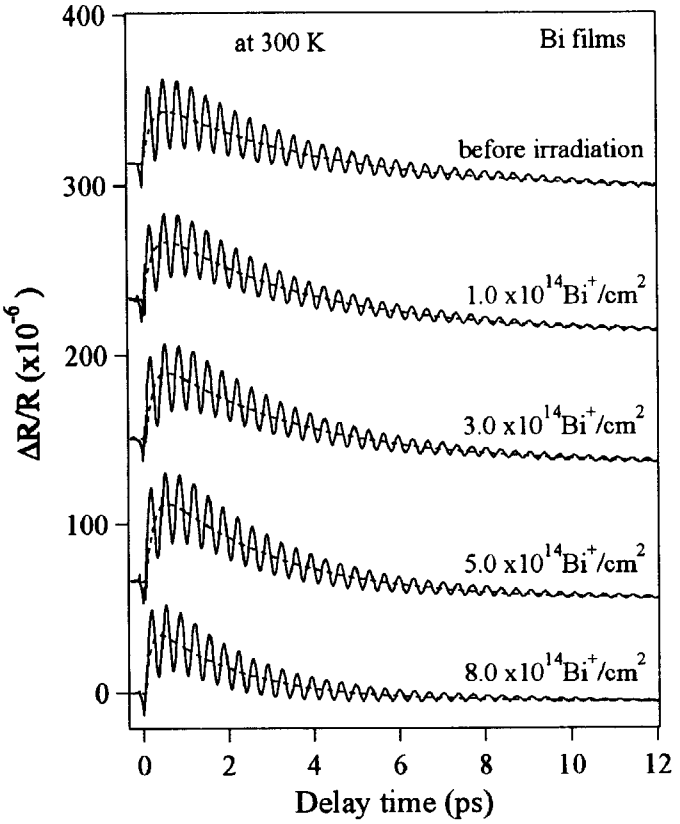


Fig. 1. Time-resolved reflectivity change for the bismuth films irradiated at various doses. The dashed lines represent electronic component.

Fig. 1 shows the transient reflectivity change obtained for bismuth polycrystalline films irradiated with doses from $1x10^{14}$ to $8x10^{14}Bi^{+}/cm^{2}$. Coherent oscillations of the fully symmetric A_{1g} mode, the frequency of which before irradiation is 97.3 cm^{-1} = 2.92 THz at 295 K [1,5], is observed on the non-oscillatory background component that corresponds to the excitation and relaxation of photo-generated carriers. The carrier background show initial rising, which would be due to carrier scattering between conduction valleys, e. g., $\Gamma \rightarrow$ L valley,[12] and its time constant decreases from ~ 200 fs to ~ 100 fs as the ion dose increases, suggesting a small modification of the electronic band structure. The dephasing time of the coherent A_{1g} mode is also affected by ion irradiation as discussed later.

Figure 2 shows the transient reflectivity change obtained for bismuth single crystals irradiated with doses from $1x10^{14}$ to $8x10^{14}Bi^{+}/cm^{2}$. Coherent oscillations of the fully symmetric A_{1g} mode are observed on the carrier background component. It is found that the carrier dynamics in Bismuth single crystals is apparently different from that in polycrystalline films. The rise time of the electronic component observed in single crystals, being ~ 50 fs for all the ion doses, is much faster than that in polycrystalline films. This difference in the carrier dynamics may suggest that electronic band structure for the polycrystalline Bismuth has semiconductor character rather than semimetal one[13]:the difference in the band structure near the Fermi level affects both optical transition from the valence bands to the conduction bands and carrier scattering between conduction valleys.

In order to obtain both the carrier relaxation time and the dephasing time of the coherent A_{1g} mode for various ion doses, the time evolution of the reflectivity changes in Fig. 1 and 2 are fitted by a damped harmonic oscillation with a single exponential decay [5];

$$\frac{\Delta R}{R} = A\exp\left(-\frac{t}{\tau}\right)\cos(\omega t+\phi)+B\left[\exp\left(-\frac{t}{\tau_1}\right)-\exp\left(-\frac{t}{\tau_2}\right)\right], \qquad (1)$$

where A is the amplitude, τ is the phonon dephasing time, ω is the frequency, and ϕ is the initial phase of the coherent phonon. The second term arises from the photo-excited carriers. B is the amplitude, and τ_1 and τ_2 are the relaxation time and the rise time of the electronic component, respectively.

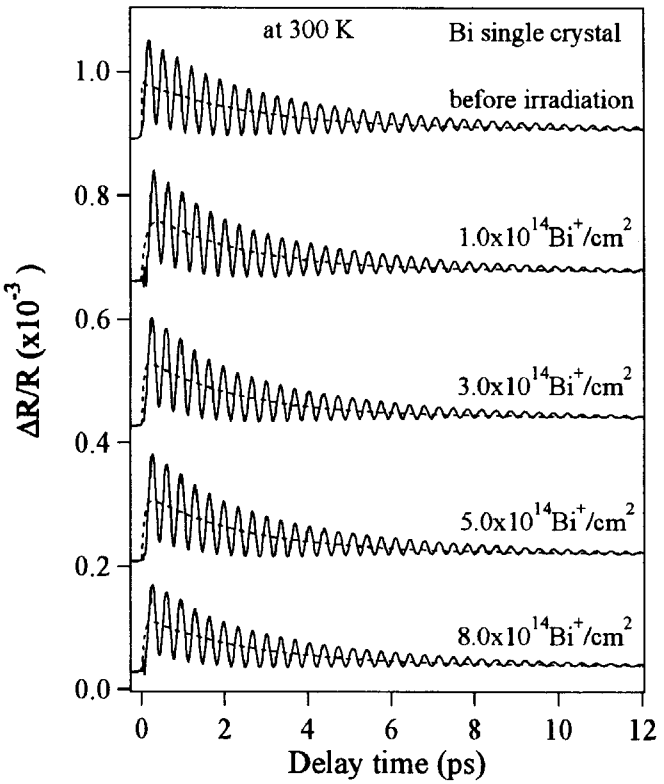


Fig. 2. Time-resolved reflectivity change for the bismuth single crystals irradiated at various doses. The dashed lines represent electronic component.

The carrier relaxation time obtained by the fitting are plotted in Fig. 3(a) as a function of ion dose. Before irradiation the carrier relaxation time for the polycrystalline film is longer than that for the single crystal, and it drastically decreases from 4.1 to 2.4 ps with increasing the ion dose. The long relaxation time for the polycrystalline film can be qualitatively explained by the fact that an existence of the band-gap increases the recombination time of electrons-hole pairs:the carrier relaxation time in semiconductors is much longer than that in metals.[14] On the other hand, the carrier relaxation time for the single crystal changes moderately, and it shows slight increase with ion dose. The decrease in the relaxation time of photo-excited carriers can be explained by trapping of carriers into defect-induced deep levels. The corresponding relaxation time τ_c is expressed by,[15]

$$\tau_c = 1/N_d \sigma v_d, \qquad (2)$$

where N_d is the concentration of vacancies, σ is the scattering cross section, v_d is the thermal velocity of the electrons. The dose dependence of the relaxation time for the polycrystal in Fig. 3(a) is well fitted by Eq. (2). However, the increase in the relaxation time for the single crystal cannot be explained by carrier-defect scattering. A plausible explanation is annealing of the crystal by ion irradiation, in which the higher-density ion irradiation will induce thermal annealing due to energy transfer from the ion particle to the lattice.

As shown in Fig. 3(b), the phonon dephasing time of the coherent A_{1g} mode for the polycrystalline film decreases from 4.1 to 3.4 ps with increasing the ion dose. The dephasing process of the coherent optical phonons in solids have been considered to be anharmonic decay

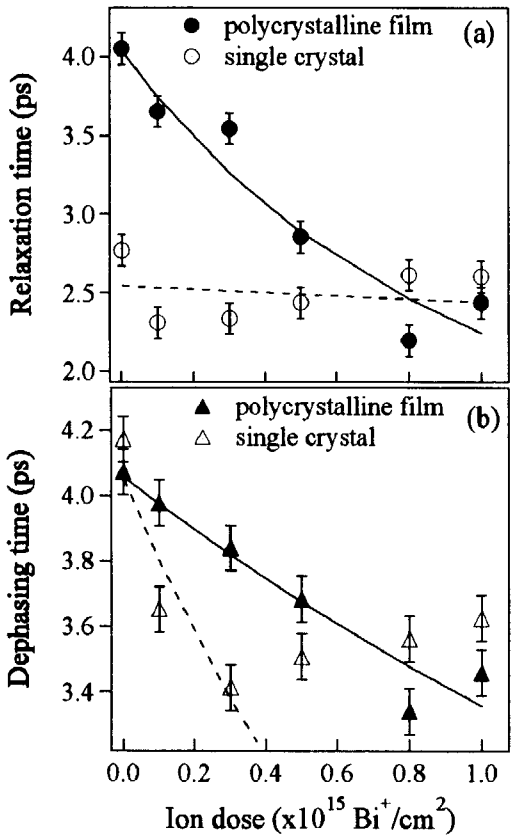


Fig. 3. Comparison of the carrier relaxation time (a) and the dephasing time of the A_{1g} mode (b) between single crystals and polycrystalline films. The solid and dashed curves in (a) represent fitting of the data with Eq. (2), and those in (b) represent fitting of the data with Eq. (3).

due to phonon-phonon interaction.[5] This decay process depends mainly on the lattice temperature. In the present study the dose-dependence of the dephasing time indicates clearly the existence of additional dephasing process, i.e. phonon-defect scattering. This scattering process is thought to be a pure dephasing process due to an elastic scattering of coherent phonons introduced by perturbing potential by defects.[10] The corresponding dose dependence of the dephasing time is given by,[10]

$$\tau_{defect} = 1/\gamma N_d , \qquad (3)$$

where γ is a phonon-defect scattering constant. The decrease in the dephasing time observed in polycrystals can be well fitted by using Eq. (3). On the other hand, the dephasing time for the single crystal decreases at low ion doses, and it increases at higher ion doses. The behavior of the dephasing time cannot be reproduced only by phonon-defect scattering as shown in Fig. 3(b). The increase in the dephasing time for the single crystal would originate from annealing of the crystal by ion irradiation. The dephasing time of the single crystal decreases with increasing ion dose from 0 to $0.3\text{x}10^{15}$ B^{+}/cm^{2}, although the carrier relaxation time increases slightly in this dose region. The difference in the dose dependence of the two time constants may be explained by the difference of annealing effect. Since the carrier relaxation is directly modified by the band structure, an elimination of defect-induced deep levels by annealing would firstly affect the carrier relaxation time and secondly affect the phonon dephasing time.

4. Conclusion

The effect of point defects on the dynamics of carrier and coherent phonon in ion-implanted bismuth was studied by using a fs pump-probe reflectivity technique. The dephasing time of the coherent A_{1g} phonon for the polycrystalline films monotonically decreased with increasing dose, showing the existence of the additional dephasing process of the coherent phonon originated from phonon-defect scattering. The decrease of the dephasing time and the increase in the dephasing time observed in the single crystal was attributed to phonon-defect scattering and annealing, respectively.

References

[1] H. J. Zeiger, J. Vidal, T. K. Cheng, E. P. Ippen, G. Dresselhaus, and M. S. Dresselhaus, Phys. Rev. B **45**, 768 (1992).

[2] T. K. Cheng, J. Vidal, H. J. Zeiger, G. Dresselhaus, M. S. Dresselhaus, and E. P. Ippen, Appl. Phys. Lett. **59**, 1923 (1991).

[3] G. A. Garrett, T. F. Albrecht, J. F. Whitaker, and R. Merlin, Phys. Rev. Lett. **77**, 3661 (1996).

[4] M. Hase, K. Mizoguchi, H. Harima, S. Nakashima, M. Tani, K. Sakai, and M. Hangyo, Appl. Phys. Lett. **69**, 2474 (1996).

[5] M. Hase, K. Mizoguchi, H. Harima, S. Nakashima, and K. Sakai, Phys. Rev. B **58**, 5448 (1998).

[6] A. Laubereau and W. Kaiser, Rev. Mod. Phys. **50**, 607 (1978).

[7] T. Dekorsy, H. Kurz, X. Q. Zhou, and K. Ploog, Appl. Phys. Lett. **63**, 2899 (1993).

[8] R. Scholz, M. Schreiber, F. Bassani, M. Nisoli, S. D. Silvestri, and O. Svelto, Phys. Rev. B **56**, 1179 (1997).

[9] K. Ishioka, K. Ushida, K. G. Nakamura, S. Hishita, and M. Kitajima, Jpn. J. Appl. Phys. **38**, L446 (1999).

[10] M. Hase, K. Ishioka, M. Kitajima, K. Ushida, and S. Hishita, Appl. Phys, Lett. **76**, 1258 (2000).

[11] J. F. Ziegler, J. P. Biersack, and U. Littmark, in: The Stopping and Range of Ions in Solids (Pergamon, New York, 1985).

[12] A. V. Kuznetsov and C. J. Stanton, Phys. Rev. B **51**, 7555 (1995).

[13] C. A. Hoffman, J. R. Mayer, F. J. Bartoli, A. Di Venere, X. J. Yi, C. L. Hou, H. C. Wang, J. B. Ketterson, and G. K. Wong, Phys. Rev. B **48**, 11431 (1993).

[14] J. Shah, in: Ultrafast Spectroscopy of Semiconductors and Semiconductor Nanostructures (Springer-Verlag, Berlin, 1999) Chap. 3, 4.

[15] S. Gupta, J. F. Whitaker, and G. A. Mourou, IEEE J. Quantum Electron. **28**, 2434 (1992).

JP0350279

2.15 DEVELOPMENT OF AN INTENSE PULSED ATOMIC HYDROGEN BEAM SOURCE

Atsushi Kubo[1,2*] and Masahiro Kitajima[1]

[1] Materials Engineering Laboratory, National Institute for Materials Science (NIMS)
1-2-1 Sengen, Tsukuba 305-0047, Japan

[2] Department of Physics, University of Tsukuba
1-1-1 Tennoudai, Tsukuba 305-8571, Japan

Abstract

A pulsed atomic hydrogen beam source has been developed especially for studies of surface reactions. Atomic hydrogen is generated using a microwave discharge in a quartz tube and is collimated to a beam by differentially pumped stages. A hydrogen dissociation fraction of ~70% and a beam flux of 4×10^{14} atoms $\cdot$ cm^{-2} s^{-1} with a spot size 7 mm in diameter are obtained. The beam is chopped with a mechanical disk chopper, and a pulse duration of 50 μs for a repetition rate of 100 pulses/s is obtained. The velocity distribution of the atomic hydrogen beam is fitted with a shifted Maxwell-Boltzmann distribution that gives a most probable velocity of 2820 m/s and a beam temperature of 150 K. The pulse beam generation of atomic oxygen is also briefly described.

Keywords: atomic hydrogen, radical source, microwave discharge, time-of-flight

1. Introduction

An experimental technique for the production of atomic hydrogen (H) is crucial in many research fields, such as gas/surface reactions, [1-3] gas phase reactions, [4] H-assisted molecular-beam epitaxy, [5] nuclear material, [6] and Bose-Einstein condensation of H. [7] In particular, chemical reactions of H with solid surfaces, such as the abstraction of chemisorbed species, [1-3] etching, and passivation with H, have been attracting much attention [8] not only due to fundamental interest but also due to practical applications in the semiconductor industry. In studies of surface reactions, the dissociation fraction of H_2 to produce H should be high, and the flux, the beam directivity, and the velocity distribution of the H should be controlled. Modulation of the beam is required for the determination of the velocity distributions of incident/reflected pulses and for the synchronization with pulsed lasers for

* Corresponding author. Tel: +81-298-592834 Fax: +81-298-592801.
E-mail address: kubo.atsushi@nims.go.jp (A. Kubo).

detection of reacted products. [1] There have been many reports on methods of generation of H, [9-13, 15] but only a few on pulsed H beam sources. The use of a microwave discharge is convenient for producing intense H beams. However, the degree of dissociation in the discharge is easily deteriorated by the recombination of H downstream. Thus, the design of H beam source requires techniques to prevent recombination. Adding water vapor to H_2 gas has been considered an effective method to maintain the intensity of H downstream, [11, 12] and Rettner has reported a pulsed H beam source using this technique. [1] However, this method is not suitable for experiments on surface reactions because water molecules, oxygen atoms and hydroxyl (OH) radicals are contained in the beam as plasma impurities. [11]

In this work, we developed a pulsed H beam source using a microwave discharge of high-purity H_2 gas (99.99999%) without addition of water. We obtained a dissociation fraction of more than 70% and an intense H beam with a flux about 4×10^{14} atoms$\cdot$ cm^{-2} s^{-1}. The velocity distribution of the pulsed H beam was determined using the time-of-flight (TOF) method. The beam source developed here should satisfy the requirements for the studies of surface reactions.

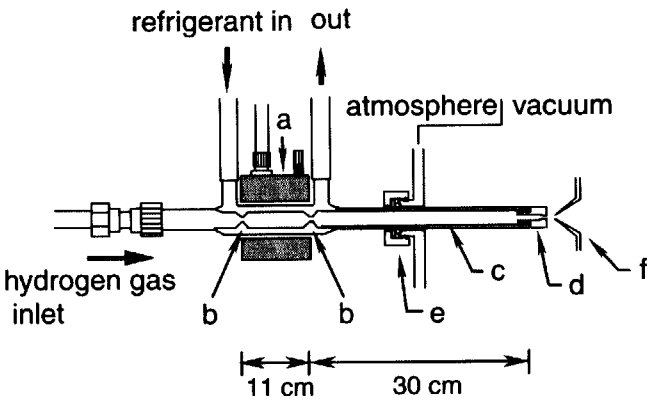


Fig.1. Schematic of the H source.
H atoms are generated and transported in a quartz tube (x): (a) microwave cavity, (b) constrictions, (c) Teflon tube, (d) Teflon nozzle, (e) o-ring vacuum seal, (f) skimmer. The lengths of the discharge region and of the transfer tube are 11 cm and 30 cm, respectively.

2. Experimental Apparatus

Figure 1 shows a schematic of the H source. A commercial 2450 MHz microwave cavity (a) was used for generating H plasma in the source (x) made of quartz tubes. To confine the plasma in the microwave cavity and to achieve a high dissociation fraction, both ends of the quartz tube of 6 mm inner diameter were narrowed to 1 mm in inner diameters (b). A similar method has been reported for a continuous-flow H source. [13] The discharge region of the quartz tube was surrounded by a cooling jacket using low-viscosity dimethyl polysiloxane as a refrigerant. The temperature of the quartz tube was maintained below 10 °C for both discharge on and off. The discharge region was followed by a 30-cm-long transport quartz tube, in which a Teflon tube of 4.7 mm inner diameter was inserted (c) to prevent recombination of H on the inner wall of the tube. [13, 14] A Teflon nozzle with an aperture of 1 mm diameter was attached to the end of the tube (d). The quartz tube, the Teflon tube and the Teflon nozzle were carefully degreased and passivated by soaking in phosphoric acid before use.

Figure 2 shows the whole apparatus for the generation of pulsed H beams, including

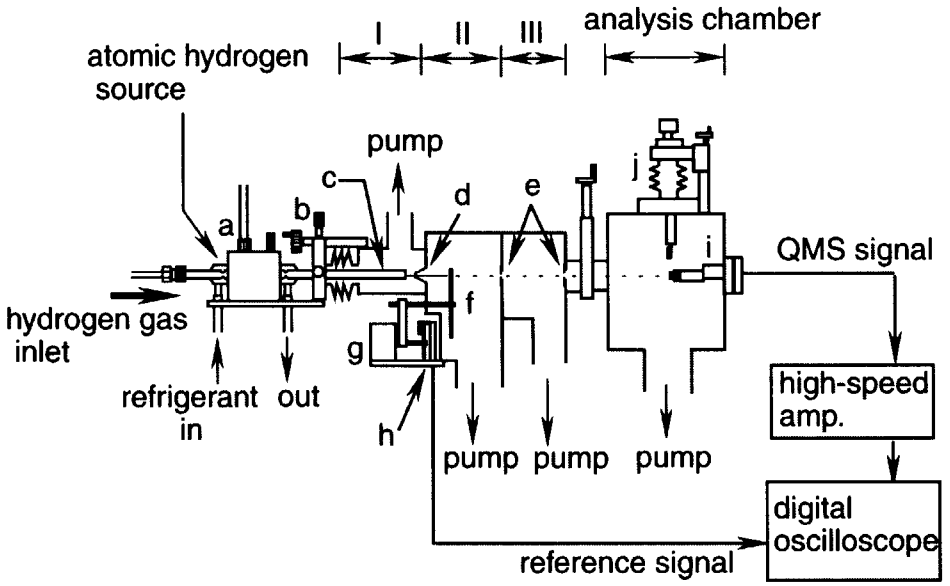


Fig.2. Schematic diagram of the whole apparatus for generating pulsed H beam.
The H atoms emitted from the source (Fig. 1) are skimmed, chopped, and collimated in the differential pumping stages (I, II, III), and then detected by a QMS(i) in the UHV analysis chamber. (a) cavity, (b) xyz stage, (c) quartz tube, (d) skimmer, (e) orifices, (f) chopper disk, (g) servomotor, (h) photodiode/photodetector unit, (i) QMS, (j) sample manipulator. The QMS signals are amplified with a high-speed amplifier and averaged using a digital oscilloscope. The photodiode/photodetector unit provides reference signals for the time-of-flight measurements.

the H source (Fig. 1). The H flow was collimated to a beam in a triply differentially pumped chamber (I , II and III). A skimmer (0.7 mm in diameter) (d) and two orifices (2.0 mm and 3.3 mm in diameter) (e) were placed between the differential pumping stages for beam collimation. The beam was chopped mechanically using a disk chopper with two diametric rectangular slits (f) driven by a servomotor (g) at 3000 rpm. The open time of the slit shutter was 50 μs for the maximum rotation speed. The beam was detected using a quadrupole mass spectrometer (QMS; ANELVA AQA-360) (i) in an ultrahigh vacuum (UHV) analysis chamber. The QMS signals were amplified using a high-speed amplifier (KEITHLEY Model 428) and then averaged by a digital oscilloscope (LeCroy 9350A, 500 MHz). The analysis chamber was pumped by a turbomolecular pump (SEIKO SEIKI, 550-l/s for H_2) to a pressure of 1×10^{-8} Pa. The pressure of the analysis chamber rose to $\sim3\times10^{-7}$ Pa when the chopper was opened. The velocity distribution of the H atoms was determined using the TOF method. The photodiode/photodetector unit (h) detected the chopper opening and provided the start triggers for TOF measurements. The distance between the nozzle and the chopper and that between the chopper and the QMS were 15 cm and 65 cm, respectively.

3. Results and Discussion

Figure 3 shows QMS spectra of the hydrogen beam with the microwave discharge on and off. The pressure of H_2 gas, P_{H_2}, at the gas inlet was 20 Pa, and the microwave power, W_m,

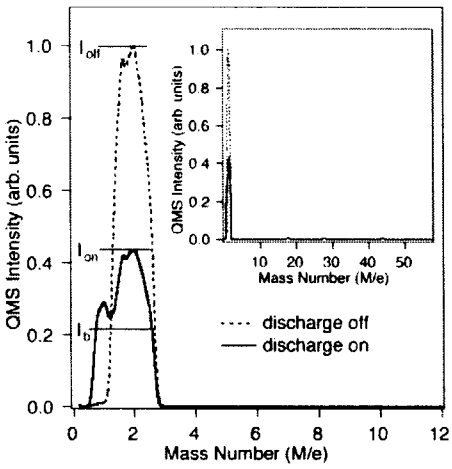


Fig.3. QMS spectra of the hydrogen beam with and without discharge. The intensities of H (M/e=1) increased with the discharge and that of H_2 (M/e=2) decreased. The intensities of heavier masses (M/e >2) in the wide range spectra did not change with the discharge (inset).

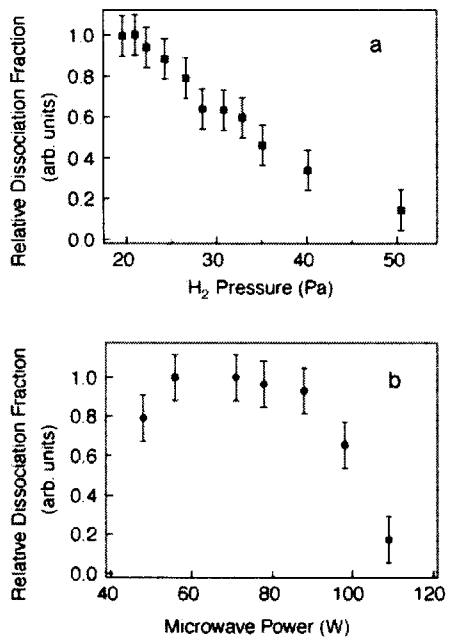


Fig. 4. (a) Dependence of the dissociation fraction on the pressure of hydrogen gas at W_m =58 W.
(b) Dependence of the dissociation fraction on the microwave power at P_{H2}= 22 Pa.

was 45 W. Upon igniting the plasma, the peak intensity of H_2 at M/e = 2 decreased, and the peak of H appeared at M/e = 1. No change in the intensity for other masses (i.e., impurities) was observed. The dissociation fraction in the beam, α, of H_2 was obtained from the following equation: [15]

$$\alpha = \frac{I_{off} - I_{on}}{I_{off} - I_b}, \quad (1)$$

where I_{off} and I_{on} were the peak heights of H_2 with the discharge off and on, respectively. The value I_b denoted the background height of H_2 when the beam shutter was closed. We obtained a dissociation fraction of 73% at P_{H_2} = 20 Pa and W_m = 45 W. Figure 4 shows the pressure dependence (a) and the microwave power dependence (b) of α. The value of α depended strongly on H_2 pressure. The H plasma was stable for H_2 gas pressures higher than 18 Pa. α had a maximum at P_{H_2} ~20 Pa, then decreased with increase of P_{H_2}. On the other hand, α was insensitive to the microwave power for W_m = 50–90 W.

During the discharge, we could observe H plasma, the color of which was the characteristic deep red, in the discharge region between the constrictions (Fig. 1, (b)) of the quartz tube. The brightness and the tone of the color correlated to the value of α. The color of the H plasma was thin red at the first stage of ignition, and then became brighter and deeper in about a minute, resulting in an increase in α. From the reports of other groups, [13, 15] it takes a much longer time (1 h to 6 h) to reach high α values. Under optimum conditions (P_{H_2} = 19–21 Pa, W_m = 45–70 W), the volume of the H plasma expanded to fill the discharge region and produced H at maximum α with good stability. When the quartz tube was not well cleaned or passivated, the H plasma became smaller in volume and weaker in brightness, resulting in lower α values. The cooling of the discharge region was essential for obtaining a high

dissociation fraction. Without cooling, the quartz tube became red-hot, which accelerated recombination reaction of H to H_2.

The diameter of the H beam spot (P_{H_2} = 20 Pa, W_m = 45 W) at the center of the analysis chamber was determined to be 7 mm using the color variation of a MoO_3 disk caused by a reduction reaction. [16] This agrees well with the size calculated from the diameters and geometrical locations of the skimmer and the orifices, showing a good directivity of the H beam. The beam flux of H was estimated as follows: The H atoms in the beam were assumed to be recombined to H_2 immediately, by wall scattering in the analysis chamber. We also assumed that the temperature of the H_2 in the analysis chamber was equal to room temperature (20 °C). Thus, the H beam flux, F (atoms· cm^{-2} s^{-1}), was

$$F = \frac{S \cdot \Delta P \cdot c_{H_2}}{k_B T} \cdot \frac{2\alpha}{A} \quad , \qquad (2)$$

where S was the H_2 pumping speed assumed for the analysis chamber, P the rise of pressure with the H beam source running, c_{H_2} the H_2 gas calibration factor of the pressure gauge, k_B the Boltzmann constant, T the room temperature, α the dissociation fraction, and A the area of the H beam. Using this equation, the flux of the H beam was calculated to be ~4×10^{14} atoms · cm^{-2} s^{-1}. This H-atom yield of the source corresponds to 0.6 ML/s for a Si(001) surface [1ML ~6.8×10^{14} cm^{-2} for Si(001)] and is sufficiently intense to detect surface reactions with measurable signal intensity.

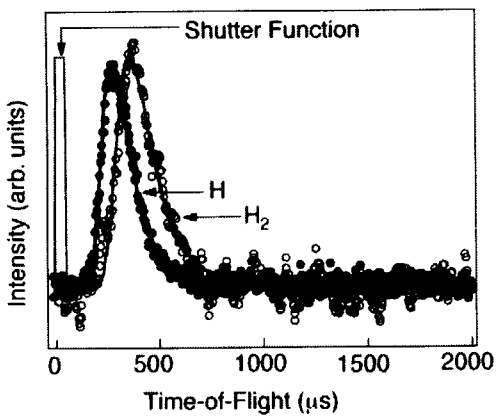


Fig.5. Time-of-flight spectra of pulsed H and H_2 beam. The H_2 gas pressures (P_{H_2}) and the microwave power (W_m) are 24 Pa and 57 W for the H-beam and 24 Pa and 0 W (discharge off) for the H_2-beam. The solid lines are the result of least-square fitting with the fitting function $g(t)$. The shutter function of the mechanical chopper $S(t)$ is also shown.

Figure 5 shows TOF spectra of pulsed H and H_2 beams. To our knowledge, the beam properties of H beams have not been characterized well. Here, we evaluated the beam temperature and the translational energy. The spectra were well fitted with a fitting function $g(t)$, which was defined as a convolution of a flux-weighted shifted Maxwell -Boltzmann distribution function $f(v)$ and a shutter function of the chopper $S(t)$:

$$g(t) = \int_0^t S(t-\tau) \cdot \frac{1}{\tau} f(L/\tau)\, d\tau \quad , \qquad (3)$$

where L was the distance between the chopper and the QMS. [17] The term $f(v)$ was written as

$$f(v)dv \propto v^3 \exp\left[-\frac{m(v-v_s)^2}{2k_B T_s}\right] dv \, , \qquad (4)$$

where v was the velocity of species, v_s the stream velocity, T_s the beam temperature, m the mass of

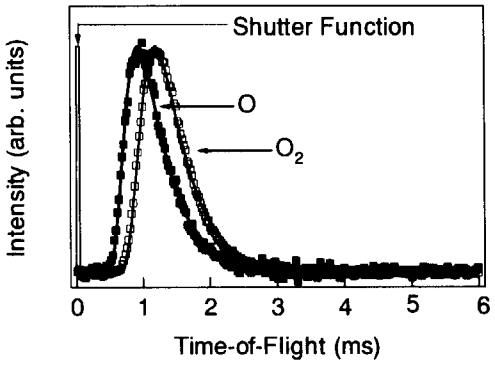


Fig.6. Time-of-flight spectra of pulsed O and O_2 beam. The O_2 gas pressures (P_{H2}) and the microwave power (W_m) are 35 Pa and 131 W for the O-beam and 35 Pa and 0 W (discharge off) for the O_2-beam.

species, and k_B the Boltzmann constant. [18] The term $S(t)$ was assumed to be a rectangular gating function,

$$S(t) = \begin{cases} 1 & \text{for } 0 < t < 50\mu s \\ 0 & t > 50\mu s . \end{cases} \quad (5)$$

The most provable velocity of the distribution v_{mp} ($df / dv = 0$) is

$$v_{mp} = \frac{1}{2}\left(v_s + \sqrt{v_s^2 + 12 k_B T_s / m}\right) . \quad (6)$$

Using these equations, v_s, T_s and v_{mp} were estimated for the H beam to be 1540 ±50 m/s, 150 ±10 K and 2820 ±60 m/s, respectively, whereas those for the H_2 beam were 1290 ±40 m/s, 120 ±10 K and 2010 ±60 m/s, respectively. The values of T_s of the H and H_2 beams showed a cooling from room temperature due to free jet expansion. The value of v_{mp} of the H beam corresponds to a translational energy of 0.042 eV.

We also applied the atomic beam source to generate pulsed atomic oxygen (O) beam. Contrary to the H beam, O beam required much higher microwave power to obtain good dissociation fraction. Figure 6 shows TOF spectra of pulsed O and O_2 beams measured at the O_2 gas pressure of 35 Pa and the microwave power of 131 W. The dissociation fraction was about 30%. The spectra were also well fitted by the fitting function $g(t)$ (Eq. (3)). The values of v_s, T_s and v_{mp} of the O beam were 350 ±10 m/s, 130 ±10 K and 660 ±20 m/s (0.036 eV), respectively, whereas those of the O_2 beam were 370 ±10 m/s, 100 ±10 K and 520 ±10 m/s (0.045 eV), respectively.

4. Conclusions

We developed an intense pulsed H beam source. High-purity H_2 gas was used without addition of water. The H plasma was generated by a microwave discharge and confined between two constrictions in a quartz tube cooled by a refrigerant. The H atoms generated were transported through a Teflon tube inserted in a quartz tube. This structure produced H stably with a high dissociation fraction. The stream of H was collimated and chopped mechanically into pulses in differential pumping stages. This pulsed H beam source satisfies the requirements for studies of surface reactions by having high-purity, a high dissociation fraction, good directivity, and a well-defined velocity distribution. This technique is also possible to obtain intense atom beams such as O.

References

[1] C. T. Rettner, J. Chem. Phys. **101**, 1529 (1994).

[2] J. Y. Kim and J. Lee, Phys. Rev. Lett. **82**, 1325 (1999).

[3] S. A. Buntin, J. Chem. Phys. **108**, 1601 (1998).

[4] T. Ibaraki, K. Kodera and I. Kusunoki, J. Phys. Chem. **79**, 95 (1975).

[5] T. Sugaya, M. Kaneko, Y. Okada and M. Kawabe, Jpn. J. Appl. Phys. **32** L,1834 (1993).

[6] E. Vietzke, M. Wada and M. Hennes, J. Nucl. Mater. **324**, 266 (1999).

[7] D. G. Fried, T. C. Killian, L. Willmann, D. Landhuis, S. C. Moss, D. Kleppner and T. J. Greytak, Phys. Rev. Lett. **81**, 3811 (1998).

[8] K. Oura, V. G. Lifshits, A. A. Saranin, A. V. Zotov and M. Katayama, Surf. Sci. Rep. **35**, 1 (1999).

[9] J. T. Yates, Jr., *Experimental Innovations in Surface Science*, Chap. 5, p. 682 (Springer -Verlag, New York, 1998).

[10] H. Pauly, *Atomic and Molecular Beam Methods,* ed. G. Scoles, Vol. 1, Chap. 4, p. 107 (Oxford University Press, Oxford, 1988).

[11] J. Kikuchi, S. Fujimura, M. Suzuki and H. Yano, Jpn. J. Appl. Phys. **32**, 3120 (1993).

[12] D. Spence and O. J. Steingraber, Rev. Sci. Instrum. **59**, 2464 (1988).

[13] B. P. Paolini and M. A. Khakoo, Rev. Sci. Instrum. **69**, 3132 (1998).

[14] R. Yamada, K. Nakamura and M. Saidoh, J. Nucl. Mater. **98**, 167 (1981).

[15] H. Nienhaus, B. Gergen, H. S. Bergh, A. Majumdar, W. H. Weinberg and E. W. McFarland, J. Vac. Sci. & Technol. A **17**, 670 (1999).

[16] I. Kusunoki, J. Vac. Soc. Jpn. **35**, 887 [in Japanese] (1992).

[17] D. J. Auerbach: *Atomic and Molecular Beam Methods,* ed. G. Scoles, Vol. 1, Chap. 14, p. 363 (Oxford University Press, Oxford, 1988).

[18] D. P. Woodruff and T. A. Delchar: *Modern Techniques of Surface Science*, Chap. 8, p. 391 (Cambridge University Press, Cambridge, 1986).

JP0350280

2.16 DESIGN OF A TRANSMISSION ELECTRON POSITRON MICROSCOPE

Masao Doyama[1*], M. Inoue[1], Y. Kogure[1],
Y. Hayashi[2], T. Yoshiie[2], T. Kurihara[3] and K. Tsuno[4]
[1]Teikyo University of Science and Technology, 2525 Yatsuzawa, Uenohara, Yamanashi 409-0193, Japan
[2]Reactor Institute, Kyoto University, Noda, Kumatori, Osaka 590-0494, Japan
[3]Institute of Materials Structure Science, KEK, Tsukuba 305-0801, Japan
[4]JEOL, Musashino, Akishima 196-0021, Japan

Key words: Positron microscopes, transmission positron microscopes, positron lenses, alteration of electron microscopes to positron microscopes.

Abstract

This paper reports the plans and design of positron-electron microscopes being built at KEK (High Energy Accelerator Research Organization), Tsukuba, Japan. A used electron microscope is altered. The kinetic energies of positrons produced by accelerators or by nuclear decays are not a unique value but show a spread over in a wide range. Positron beam is guided to a transmission electron microscope (JEM100SX). Positrons are moderated by a tungsten foil, are accelerated and are focused on a nickel sheet. The monochromatic focused beam is injected into an electron microscope. The focusing and aberration of positrons are the same as electrons in a magnetic system which are used in commercial electron microscopes. Imaging plates are used to record positron images for the transmission electron microscope.

1. Introduction

There are many crucial advantages in experiments using positrons compared with corresponding experiments using electrons. For example, in electron diffraction experiments, the diffracted electrons may not be the same that the incident electrons but some electrons ejected from a specimen are exchanged with incident electrons. The diffracted positrons are almost guaranteed to be the same that the incident positrons, because there are almost no positrons in the specimen.

To perform positron experiments, there are two important points. One is that the kinetic energies of positrons emitted from the nuclear decays or made by accelerators have not a unique value of kinetic energy but possess a spread over an energy range. The other point is that the intensities of positron beams are usually quite low.

Mono-energetic positron beam is required to focus positron beams. To create positron beams with enough intensity, an accelerator is commonly used. In this paper, a transmission electron-positron microscope being built at the KEK, Tsukuba, Japan is described. The expected intensity of the slow positron beam is 10^8 e^+/sec and soon the intensity is aimed at 10^9 e^+/sec in future [1].

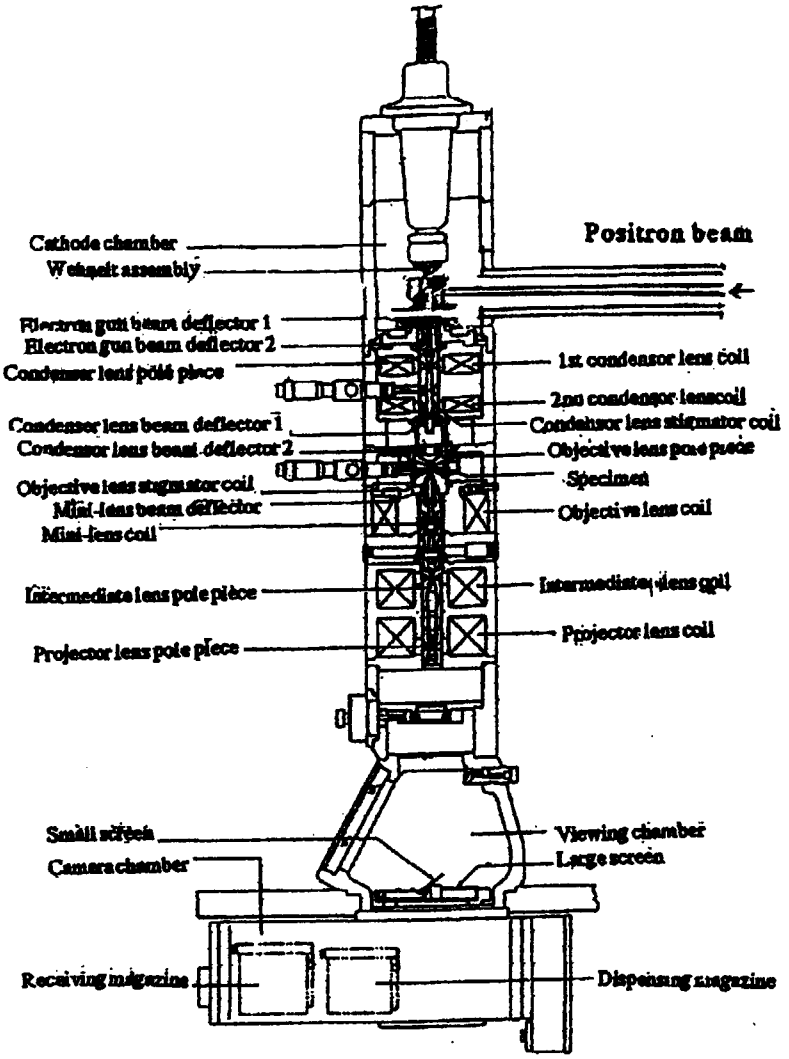


Fig. 1. Schematic diagram of electron-positron transmission microscope.

2. Transmission positron microscope

Although the scattering cross sections for positrons are similar to those for electrons at high energies, positrons penetrate deeper than electrons in materials, because they travel interstitial sites, far from nuclei. Channeling behavior of positrons is quite different from that of electrons.

The JEM100SX transmission electron microscope has been set at the end of the slow positron beam at KEK (Fig. 1). The positron beam coming from the positron transfer tube is focused on a tungsten foil (25 μ m in thickness). Positrons lose their energies, are thermalized in the foil and are ejected from the other surface. The ejected positrons are accelerated to 1 keV and focused by two sets of Einzel lens. Focused beam is introduced into the microscope (Fig. 2) and they are bent 90 degrees by an electric field deflector (Fig. 2). The Wehnelt assembly and the cathode chamber of the electron microscope are revised. This is an anode chamber for the positron microscope. The voltage of the lower plate of the deflector is kept at 40 kV, for example, against the ground. Simulation of positron beam

near the deflector is shown in Fig. 3. The other plate is kept at 41.5 kV. The positron lens system is also shown in Fig. 3. The scales are not proportional but schematic. The nickel foils can be annealed in the annealing chambers attached to the positron lenses. A specimen is mounted on the usual specimen stage on a screen mesh. The focusing and aberration of positrons are the same as those of electrons in a magnetic system, used in commercial electron microscopes. The characteristic feature of this plan is that commercially available electron microscopes can be used for positrons without changing the focusing system. Only the inversion of polarity of accelerating voltage is necessary. The advanced technology of electron microscopy can be used for positron microscopy. Imaging plates are used to record positron images. The column of the microscope is kept at the ground voltage. The final resolution should be better than positron re-emission microscopes (PRM).

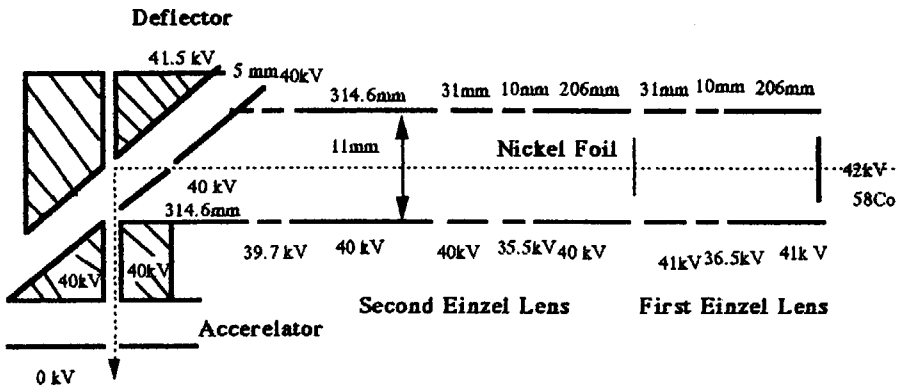


Fig. 2. Positron lens system, remoderator, deflector. Scales are not exact.

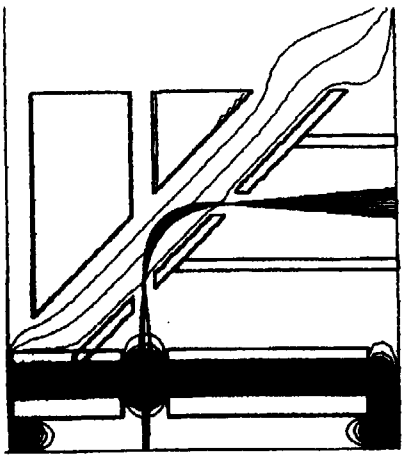


Fig. 3. Simulation of positron beam by deflector.

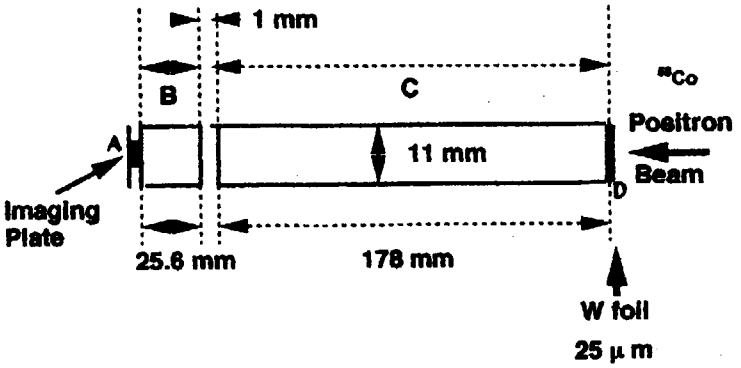


Fig. 4. Two lens system used in the present experiment

The positional resolution of PRM is limited by the diffusion length of positrons, when lattice defects are studied.

3. Positron lenses

Here we consider a set of two element lenses and a set of three element lenses (Einzel lens).

3.1 Two element lens

Two cylinders of inner diameter D = 11 mm are separated by g = 2 mm. The length of Cylinders 1 and 2 are 178 and 25.6 mm, respectively (Fig.4) and the corresponding voltages applied are +6 and +1 kV, respectively. ^{58}Co positron source and tungsten foil were kept at +7 kV. Figure 5 is an example of a profile of the positron intensity on an imaging plate which was grounded. When a series of two lens system is used higher voltages have to be applied to cylinders [3].

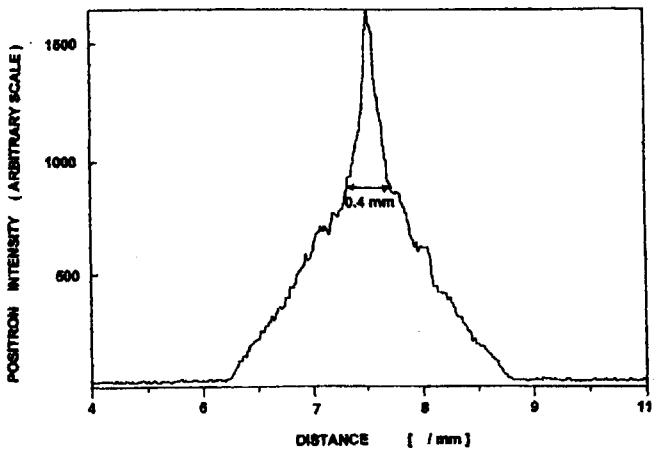


Fig. 5. Positron intensity profile of two cylinder lens, focused.

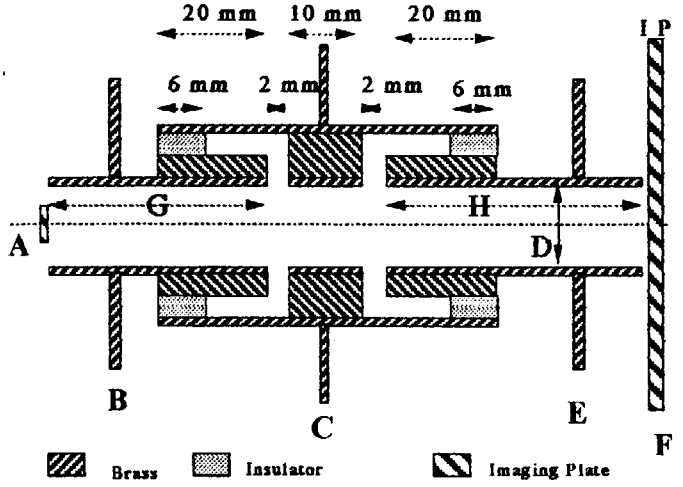


Fig. 6. Einzel lens. Examples of parameters are given in Table 1.

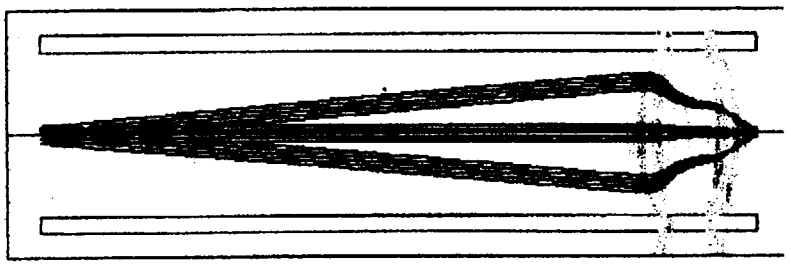


Fig. 7. Simulation of positron beam by Einzel lens shown in Fig. 6.

Table 1 Examples of Einzenl lens parameters corresponding Fig. 3.

Positron Source	A	+1 kV	+2 kV	+3 kV	+4 kV	+42 kV
Cylinders 1 & 3	B, E	0 kV	0 kV	+1 kV	+2 kV	+41 kV
Center Cylinder	C	-4.5 kV	-4 kV	-3 kV	-2 kV	+36.5 k
Imaging Plate	F	0 kV	0 kV	0 kV	0 kV	+41 kV
Length of Cylinder 1	G	206mm	206mm	206mm	206mm	206mm
Length of Cylinder 3	H	31mm	36mm	36mm	36mm	31mm
Magnification	M	1/9	1/8	1/8	1/8	1/9
Positron Energy Hitting Imaging Plate		1 kV	2 kV	2 kV	2 kV	1 kV

3.2 Three element lens (Einzel lens)

The Einzel lens geometry to be considered consists of three long coaxial cylinders of the same diameter D, separated by distance g. The voltage of the two and cylinders are kept at V_1, and the voltage of the center cylinder is kept at V_2. Positrons are accelerated while they travel from A to B [Fig. 6]. Fine adjustment can be made changing voltage V_2. Table 1 shows some of the examples in case of Einzel lens. To test the focusing, the positron energies hitting imaging plates were low so that imaging plates without coating were used. Detail calculations on a cylindrical electrostatic electron lens can be found in a paper by Read et al [2]. The advantage using Einzel lens is that the applying voltage can be kept almost constant. A simulation of focusing of positron beam is shown in Fig. 7.

4. Summary

A design of remodeling of a used commercial transmission electron microscope is presented. Transmission electron-positron microscopes are good to observe images of organic compounds and bio-materials, because of its deeper penetration depth, so that less damage is given to specimens. Theoretically the positional resolution of a transmission positron microscope is better than that of microscope using positron annihilation, because the diffusion length of positrons before captured by defects limits the positional resolution. Largest advantage is remodeling of commercially available transmission electron microscopes which have been highly developed. The positron beam source is equipped with electron source. The only positive accelerating voltage is supplied when positron image is taken. The focusing positrons is the same as elctrons.

Acknowledgement

This research is supported by the Grant-in-Aid by the Ministry of Education, Sports, Culture and Science and Technology. The authors express their thanks to Professor Karl F. Canter for his frequent kind discussions.

References

[1] H. Kobayashi et al. Proc. of the 1990 Linear Accelerator Conference, Albuquerque, New Mexico, U.S.A., 10-14 September, 1990. T. Shidera et al. Proc. of the 10th International Conference, Chicage, Illinois, U.S.A. 23-28 August, 1998.

[2] A.A.Adams and F. H. Read, J. Phys. E5 (1972) 150-155.

[3] M.Doyama, M.Inoue, Y.Kogure, T.Kurihara, A.Yagishita, T. Shidara, K.Nakahara, Y. Hayashi, T. Yoshiie, K. Tsuno, Materials Science Forum 363-365 (2001) 439-441.

JP0350281

2.17 DEVELOPMENT OF HIGH POWER CERAMIC LASERS AND POSSIBLE APPLICATION TO NUCLEAR FUSION

Takagimi Yanagitani[1*], Hideki Yagi[1], Ken-ichi Ueda[2], Jianren Lu[2], Alexander A. Kaminskii[3]

[1]Takuma Works, Konoshima Chemical Co., Ltd., 80 Kouda, Takuma, Mitoyo-gun, Kagawa 769-1103, Japan

[2]Institute of Laser Science, University of Electro-Communications, 1-5-1 Chofugaoka, Chofu, Tokyo 182-8585, Japan

[3]Institute of Crystallography of the Russian Academy of Sciences, Crystal Laser Physics Laboratory, Leninsky pr.59, Moscow 117333, Russia

Abstract

We have succeeded in fabricating high-transparent $Y_3Al_5O_{12}$ (YAG) and Y_2O_3 laser ceramic materials using vacuum sintering method. Compared with single crystal, ceramics have the following advantages, namely: (1) Ease of fabrication; (2) Less expensive; (3) Fabrication of large size and high concentration; (4) Multi-layer and multi-functional ceramic structure; (5) Mass production, etc.

On the base of Nd^{3+}:YAG ceramics, we performed high efficient and high power (up to 1.46kW) CW lasers with laser diode pumping. Optical properties of Nd:YAG ceramics, such as absorption, emission and fluorescence lifetime, were found to be similar to those of Nd:YAG single crystal. The thermal conductivity of Nd:YAG ceramics was measured, which is also found to be very similar to that of Nd:YAG single crystal.

The stimulated emission cross section of Nd^{3+}:Y_2O_3 happened to be in the range that is required for laser fusion driver. This makes Nd:Y_2O_3 a potential candidate for being used in laser fusion system. Some optical properties of Nd:Y_2O_3 ceramics were investigated and for the first time, CW room-temperature laser oscillation at two wavelength (1074.6 nm and 1078.6 nm) of ${}^4F_{3/2} \rightarrow {}^4I_{11/2}$ channel was obtained with a slope efficiency of 32%.

Keywords : Nd^{3+}:YAG, Nd^{3+}:Y_2O_3, ceramic laser, diode-pumped, solid-state laser, fusion driver

1. Introduction

Since Maiman discovered the ruby laser in 1960 [1,2], the solid-state lasers have been rapidly developed; especially resent years, solid-state lasers have been applied with remarkable success in various industrial capacities such as for taking physical measurements and for medical uses. Among all kinds of solid-state laser host material, YAG ($Y_3Al_5O_{12}$) single crystal is the best laser host material that has been grown since 1964 [3].

*E-mail address: yanagitani@konoshima.co.jp (T. Yanagitani)

However because of some disadvantages of crystal growth method, a time consuming, expensive and size-limited procedure, generally it is very difficult to grow high-quality large size of single crystals and the cost increases almost exponentially with the size of crystals. Such disadvantages make people try to find some other ways to produce laser materials. Besides single crystal materials, glass structure, glass-ceramic structure, and polycrystalline structure materials have been investigated in many years. For glass material, it is easy to get large size, but the thermal conductivity is about one order lower than that of single crystals, which make it seldom use in high power industrial lasers. Glass ceramic materials are substances of heterogeneous structure: crystal areas are embedded in a glass matrix [4], but laser efficiencies were not satisfying compared with single crystals.

Since 1960's, a number of people have speculated that a theoretically dense polycrystal of an isotropic, pure material would be optically indistinguishable from a single crystal of the same material. In 1966, E.Carnall reported polycrystalline ceramic laser material for the first time [5]. In his work, Dysprosium-doped CaF_2 lasers have been operated in both the hot-pressed polycrystal and single crystal forms at liquid-nitrogen temperature. Similar laser threshold was obtained to that of single crystal laser. After that, polycrystalline ceramic laser hosts had not received much attention for a long time primarily because their inferior optical quality to that of single crystal and glass materials.

In 1995, A.Ikesue fabricated transparent polycrystalline YAG by a solid-state reaction method using high-purity powders (>99.99wt% purity) [6]. An Oscillation experiment was performed on a CW laser by the diode laser excitation system using the fabricated ceramics. Laser output of 309mW were obtained with a slope efficiency of 28%. This is the first laser demonstration on Nd:YAG ceramics.

Since 1999, the authors began to fabricate polycrystalline YAG ceramics in a different way: Vacuum Sintering method, where the raw powder materials were prepared by nano-crystalline technology. Using these highly transparent Nd:YAG ceramics, slope efficiency of more than 60% was achieved under end-pumping scheme [7]. For high power, output powers of 31W→72W→84W were reported one after the other [8,9]. Recently, 1.46kW Nd:YAG ceramic laser was developed with an optical-to-optical efficiency of 42%[10].

Since the first half of 2001, we also pay more attention to Y_2O_3 ceramic material, a very promising material, which has potential application in laser fusion system or femto-second lasers.

Cubic Y_2O_3 crystal has been investigated for a long time as an active host material for lanthanide ions due to its favorable properties, such as its refractory nature, stability, ruggedness, and optical clarity over a broad spectral region, etc. In particular, thermal conductivity of Y_2O_3 is about two times larger than that of YAG, while the thermal expansion coefficients are very similar. However, it is extremely difficult to grow large-size high-quality Y_2O_3 single crystal by conventional growth methods because of its very high melting

temperature (2400℃) of Y_2O_3 and structural phase transition at 2280℃. What's more, the laser oscillation results of rare earth ions doped Y_2O_3 were not satisfying either. Quite recently, Nd:Y_2O_3 ceramics were developed as well by using the nanocrystalline technology and vacuum sintering method. Compared with single crystal growth method, it is easier to fabricate large size Y_2O_3 ceramics because of the lower sintering temperature - about 700℃ lower than melting temperature of Y_2O_3.

The possibilities of rare earth doped Y_2O_3 for being used in laser fusion system, and high power industrial lasers will be discussed.

2. YAG ceramic laser

2.1 Fabrication of highly transparent YAG ceramics

Fig. 1 shows the fabrication process of Nd:YAG ceramics. The aqueous solutions of Aluminum, Yttrium, and Neodymium chlorides were mixed together. This mixed aqueous solution was added dropwise and then mixed with an aqueous solution of ammonium hydrogen-carbonate. Then steps of filtration and washing with water were repeated several times, and then dried. The precursor thus obtained was calcinated at 1200℃ for several times, then the oxide raw powder is obtained. This powder is milled with solvent, binder and dispersion medium for 24 hours. The milled slurry is put in gypsum mold and dried, and then the desired form is obtained. After removing the organic component by calcining, such material is vacuum sintered at 1750℃, then highly transparent Nd:YAG ceramics can be obtained. The sintering time vary from 5 to 20 hours depending on the form of sample.

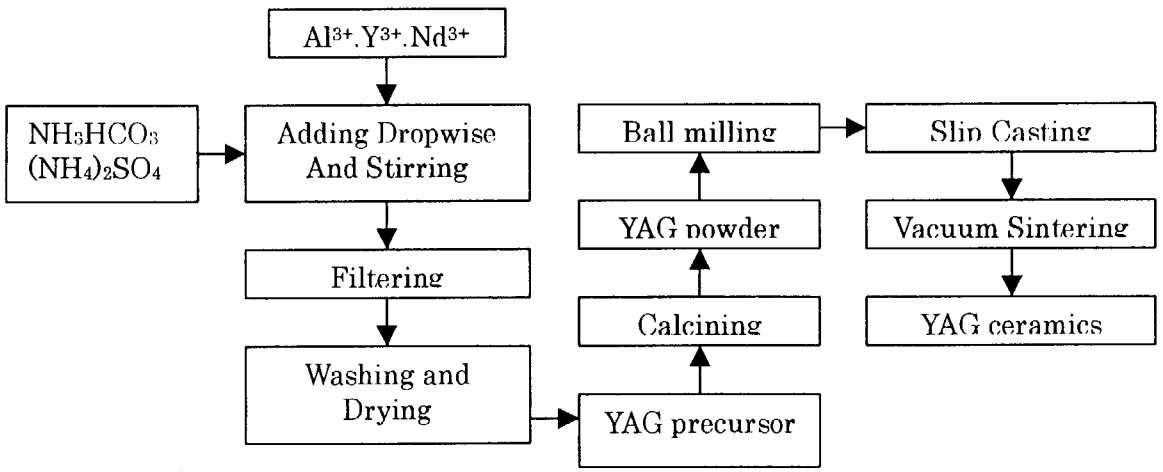


Fig.1: Fabrication process of transparent Nd:YAG ceramics.

Fig. 2 shows the picture of the polished slab and as-sintered rod of Nd:YAG ceramic samples. Fig.3(a) shows the reflection microscope image of YAG ceramic structure; Fig.3(b) shows the TEM image of YAG ceramic grain boundary. Reflection microscopy suggested that the pore volume concentration in our samples is about 1ppm and average grain size is about 10 μm in diameter. The width of grain boundary is only about 1nm. Such narrow grain

boundary and very low pore volume ensure very low scattering loss in the ceramic material.

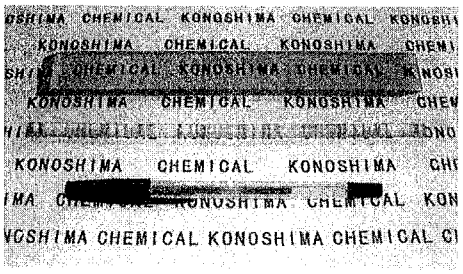


Fig.2: Picture of Nd:YAG ceramics

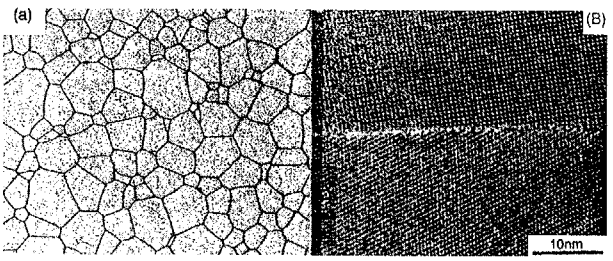


Fig.3: Optical reflection image (a) and TEM image of grain boundary (b).

2.2 Properties of YAG ceramic laser materials

The thermal conductivity is a very important factor for high power lasers. There are several ways to measure thermal conductivity, such as steady-heat-flow method (10), and flash method (11), etc. In our measurement, steady-heat-flow method was used and the following values were obtained.

$$k_{crystal} = 10.5 \pm 0.5(WT^{-1}m^{-1})$$

$$k_{ceramic} = 10.7 \pm 0.5(WT^{-1}m^{-1})$$

From these results, one can see that the thermal conductivity of YAG ceramic is very close to that of YAG single crystal. As we know, superior thermal property is one of the advantages that make YAG single crystal the most popular laser material. From the comparison of thermal conductivities between single crystal and ceramic, we can see that YAG ceramic should have very similar thermal properties to YAG single crystal.

Optical absorption and emission measurements were carried out using a ANDO AQ-6315A optical spectrum analyzer. ANDO AQ-4303B white light source was used for absorption measurement and a Mitsui MLD100 1W 807nm laser diode (LD) was used for fluorescence and laser experiments. A Φ3×2mm 0.9% Nd:YAG single crystal procured from Litton-Airtron Inc. was used for comparison.

The room temperature absorption spectra of 1% Nd:YAG ceramics and 0.9% Nd:YAG single crystal are shown in Fig.4. The Fresnel reflection has been subtracted from the absorption spectrum. If the absorption coefficient is assumed to be proportional to the neodymium concentration, the absorption coefficient of 0.9% single crystal should be 10% less than that of 1% ceramics. From the Fig.4, we see that the absorption coefficient of 0.9% Nd:YAG single crystal is about 15% less than that of 1% Nd:YAG ceramics. It means the actual neodymium concentration in single crystal may be a little less than 0.9% because it is hard to control the extra concentration in single crystals during the growing process. It is one of the advantages of Nd:YAG ceramics laser material that the rare earth ions concentration can be precisely controlled.

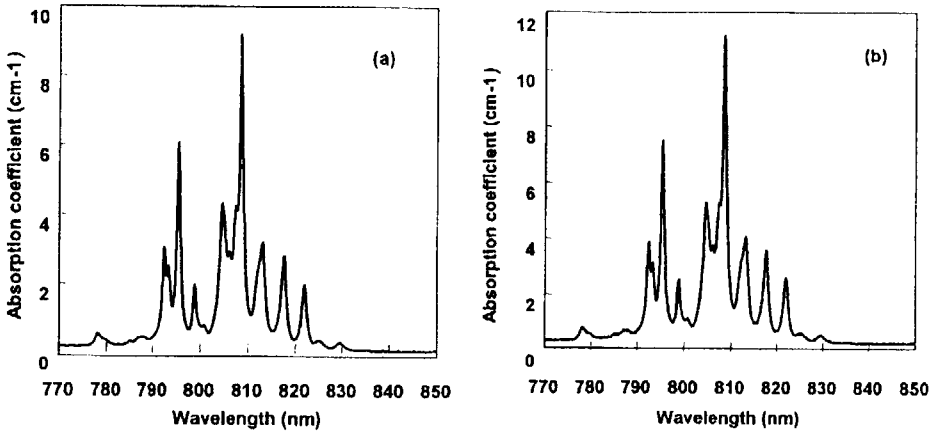


Fig.4: Room temperature absorption spectra of (a) 0.9% Nd:YAG single crystal and (b) 1% Nd:YAG ceramic.

Fig.5 shows the room temperature fluorescence spectrum for ${}^4F_{3/2}$ to ${}^4I_{11/2}$ transition of 1% Nd:YAG single crystal and ceramics, respectively. In order to have a clear comparison, the fluorescence spectrum for single crystal and ceramics were normalized and put together. From this figure, it can be seen that these two spectra are almost identical.

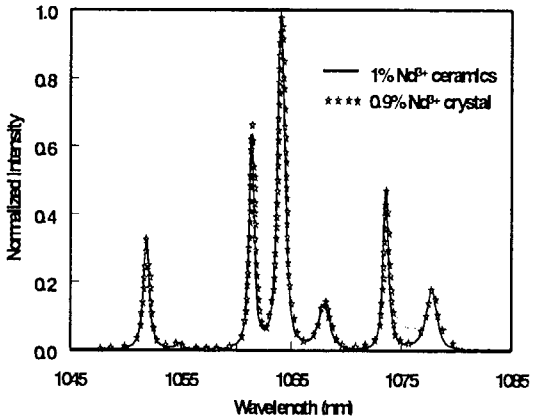


Fig.5: Fluorescence spectra of Nd:YAG single crystal and ceramic

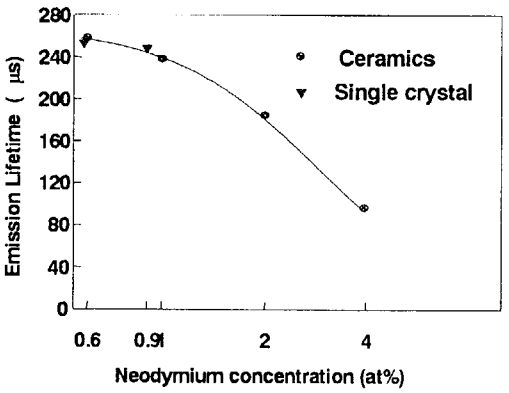


Fig.6: Fluorescence lifetime of Nd:YAG as a function of Nd^{3+} concentration

Using a quasi-CW LD produced by Hamamatsu Inc., the fluorescent lifetime for single crystal and ceramics have been obtained through curve fitting on fluorescence decay curve. The fluorescence lifetime for single crystal and ceramics are almost identical. Fig.6 shows the fluorescence lifetime of Nd:YAG ceramics versus neodymium concentration.

Using fluorescence spectrum and deduced Radiative lifetime, induced emission cross sections were calculated for Nd:YAG ceramic and single crystal, respectively. Around 1064nm, the main laser wavelength, stimulated emission cross section are 2.62×10^{-19} and 2.63×10^{-19} for YAG ceramic and single crystal, respectively. Such high emission cross-section results in low laser threshold and high laser efficiencies.

2.3 Laser experiment

End-pumped laser experiments were demonstrated on 1% and 2% neodymium doped YAG ceramics with thickness of 5mm and 2.5mm, respectively. An 807nm laser diode was used as a pump source whose maximum output power is 1W. A 5mm thick 0.9% Nd:YAG single crystal procured from Litton-Airtron Inc. was used for comparison with ceramics. Though the concentrations are different for single crystal (0.9%) and ceramics (1% and 2%), the absorbed pump powers are almost the same because of the adequate absorption length of the sample.

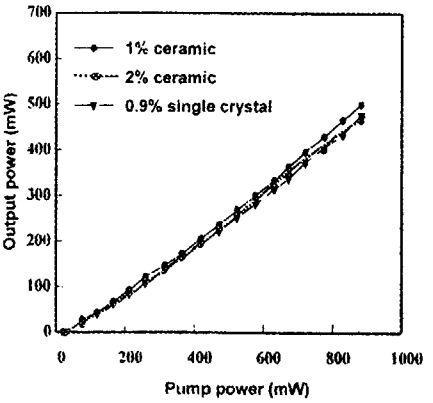


Fig. 7: CW laser output versus pump power

All samples were coated with HR1064nm/AR808nm films to act as a cavity mirror of the laser on one end, the other end was antireflection coated at 1064nm to reduce the intra-cavity loss. Output coupler is a concave mirror with 250mm radius and the reflectivity is 97% at 1064nm. The cavity length is about 20mm.

Fig.7 shows the laser output versus pump power for 1%, 2% Nd:YAG ceramics and 0.9% Nd:YAG single crystal at 1064nm. To have a reasonable comparison, absorbed pump power should be used to calculate the efficiencies. Table 1 lists all results calculated according to absorbed pump power for ceramic and single crystal, respectively. From the data listed in this table, one can see that whatever 1% and 2% Nd:YAG ceramic, both of them have very similar laser efficiencies to that of 0.9% Nd:YAG single crystal laser.

Table 1: Laser parameters calculated according to absorbed pump power

	Absorbed power	Output power	Threshold	Slope efficiency
1% Ceramic	840mW	499mW	20mW	60.9%
2% Ceramic	842mW	465mW	27mW	57.6%
0.9%crystal	795mW	474mW	20mW	61.2%

Quite recently, 1.46 kW Nd:YAG ceramic laser at 1064nm was demonstrated cooperating with Toshiba Corporation [9]. The laser rod diameter, length and Nd^{3+} doping ratio are 8mm, 200mm and 0.6%, respectively. The dependence of output power versus pump power was shown in Fig.8. The optical-to-optical conversion efficiency is 42%. The Nd:YAG ceramic laser material can almost be put to practical use.

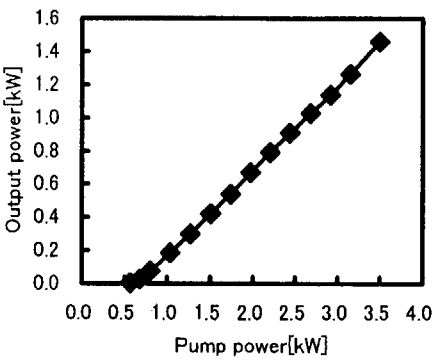


Fig.8: High power ceramic laser

3. Y_2O_3 ceramic laser

Using the same fabricating method of Nd:YAG ceramics, transparent neodymium doped Y_2O_3 ceramics were developed as well.

3.1 Optical properties of Nd:Y_2O_3 ceramics

The room-temperature absorption band areas of $^4I_{9/2} \rightarrow [^4F_{5/2}+^2H(2)_{9/2}]$ for 1.5at% Nd:Y_2O_3 ceramic sample is shown in Fig.9. From this figure, one can see that the maximum absorption coefficient (ca. 18cm^{-1}) is at around 820nm wavelength. It is quite different from that of Nd:YAG ceramic whose maximum absorption is around 808.6nm wavelength. Do to the spectrum restriction of our 1W LD, we have to tune the central emission of the LD to 808.6nm, the wavelength of the second absorption peak, where the absorption coefficient of this ceramic sample is about 13 cm^{-1}.

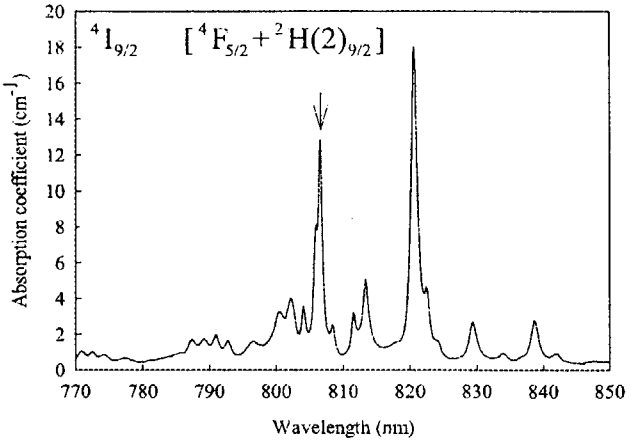


Fig.9: Room-temperature absorption spectrum of 1.5% Nd:Y_2O_3 ceramic

Using emission spectrum and radiative lifetime of Nd:Y_2O_3, stimulated emission cross section was derived which was shown in Fig.10. The maximum peak value of stimulated emission cross section is 5.2×10^{-20} cm^2 which is at wavelength of 1078.6nm. But the second peak value of stimulated emission cross section at 1074.6nm is 5.0×10^{-20} cm^2, which is very close to the maximum value.

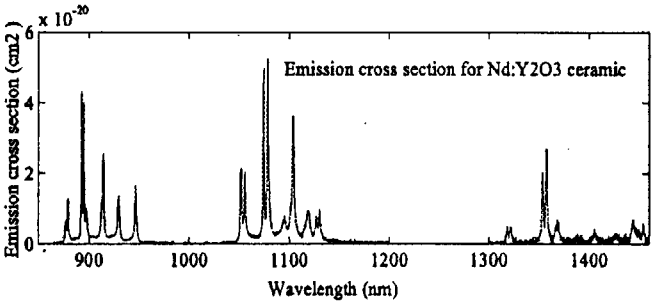


Fig.10: Emission cross section of Nd:Y_2O_3 ceramic

3.2 Laser performance of 1.5% Nd:Y_2O_3 ceramic

The setup was almost similar to what used to experiment on YAG. However, neither the anti-reflection coating nor the high reflection coating are given to Nd:Y_2O_3 ceramic. The resonator was composed of a high reflection mirror at 1064nm and a concave mirror with 250mm radius and the reflectivity is 97% at 1064nm wavelength although the laser lasing wavelength of Nd:Y_2O_3 is around 1074.6nm and 1078.6nm.

Fig.11 shoes the laser output versus pump

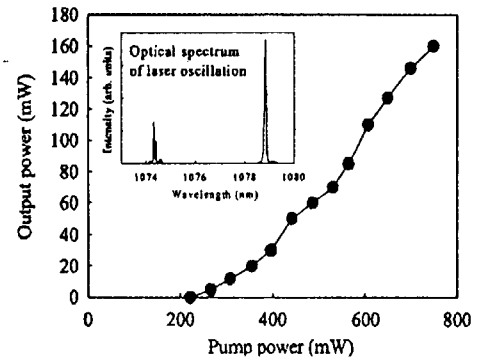


Fig.11: Input-output curve of 1.5% Nd:Y_2O_3 ceramic laser generated at two wavelength of $^4F_{3/2} \rightarrow {}^4I_{11/2}$

power for 1.5% uncoated Nd:YAG ceramic element. The threshold is 200mW, when pump power was increased to maximum of 742mW, laser output power of 160mW was obtained with a slope efficiency of 32%. The spectral composition of CW laser output was also shown in Fig.11. From this Figure, one can see that laser outputs were observed at both 1074.6nm and 1078.6nm wavelengths. The result of laser experiment shows that the quality of such kind of $Nd:Y_2O_3$ ceramics is good enough to be used as a highly efficient laser media. If this sample were coated with anti-reflection coatings, slope efficiency of more than 40% could be predicted.

Because of its many advantages, such as refractory nature, stability, ruggedness, optical clarity over a broad spectral region, broad emission band, especially high thermal conductivity, etc., $Nd:Y_2O_3$ ceramics is a very promising laser media that can be used in many fields, such as high power industrial lasers, laser fusion system, etc.

3.3 Possibilities for being used in laser fusion driver system

Ceramic laser material has great potential for being used in laser fusion driver system. As we know, laser materials, which can be used in laser fusion driver system, should have several features: Large aperture, proper emission cross-section and thermal shock parameters etc. Fig.12 shows the diagram of stimulated emission cross-sections and thermal shock parameters for various laser materials. The arrow pointed area indicates the suitable stimulated emission cross-section and thermal shock parameters for laser fusion drivers. Usually stimulated emission cross section less than 1×10^{-19} cm^2 and larger than 1×10^{-20} cm^2 is required. Because emission cross-section beyond this would cause parasitic oscillation while emission cross section below this cannot match the requirement for saturation flux limitation. Although several single crystals can match the requirement on emission cross-section and thermal shock parameters, but unfortunately, large-scale samples are extremely difficult to

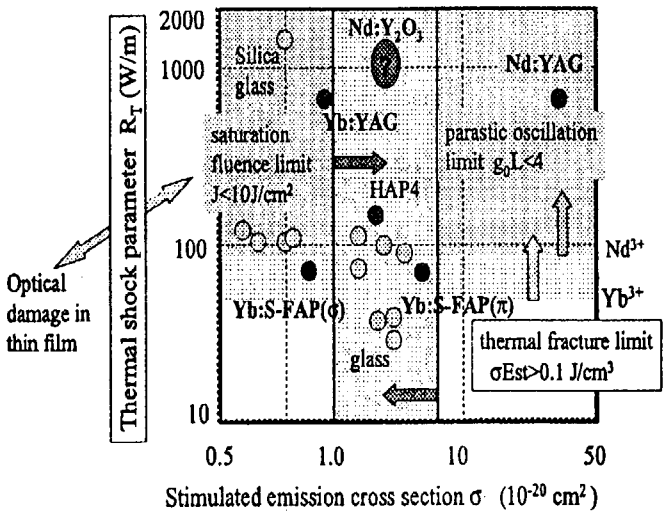


Fig.12: Solid state laser materials for fusion driver

be grown. As we know, to fabricate large size of transparent ceramic sample is not a problem, and also from calculated stimulated emission cross-section of Nd:Y_2O_3, we know that for two main laser lines of ${}^4F_{3/2} \rightarrow {}^4I_{11/2}$ channel, the stimulated emission cross section are 5×10^{-20} cm^2 and 5.2×10^{-20} cm^2, respectively, which are just in the range required for laser fusion driver system. Although the thermal shock parameter of Nd:Y_2O_3 hasn't been measured at present, as a high-melting temperature material, usually its thermal shock parameter should be much higher than that of glass which is now used in laser fusion drivers.

4. Conclusions

Nd:YAG and Nd:Y_2O_3 ceramics with excellent transmittance were fabricated successfully by vacuum sintering method in the present study. The optical properties of these specimens were investigated, and the significant results of this work can be summarized as follows:

(1) Highly efficient CW laser oscillation for Nd:Y_2O_3 was demonstrated under LD end pumping for the first time.

(2) Nd:YAG and Nd:Y_2O_3 ceramics have almost the same laser efficiency as that of single crystal.

(3) Nd:Y_2O_3 ceramic laser material has the possibilities for being used in laser fusion driver system.

5. References

[1] T. H. Maiman, *nature* 187, 493-494 (1960).

[2] T. H. Maiman, *Phys.Rev.Lett.* 4, 564-566 (1960).

[3] J. E. Geusic, H. M. Marcos and L. G. V. Uitert, *Appl. Phys. Lett.* 4, 182-184 (1964).

[4] G. Muller and N. Neuroth, *J. Appl. Phys.* 44, 2315-2319 (1973).

[5] E. Carnall, S. E. Hatch, and W. F. Parsons, *Materials Science Research*, 3, 165-173 (1966).

[6] A.Ikesue, T. Kinoshita, K. Kamata, and K. Yoshida, *J. Am. Ceram. Soc.* 78, 1033-1040 (1995).

[7] J.Lu, M. Prabhu, J. Song, C. Li, J. Xu, K. Ueda, H. Yagi, T. Yanagitani, and A. A. Kaminskii, *Jpn. J. Appl. Phys. Part 2 Lett.* 40, L552-L554 (2001).

[8] J.Lu, J. Song, M. Prabhu, J. Xu, K. Ueda, H. Yagi, T. Yanagitani, and A. Kudryasshov, *Jpn. J. Appl. Phys.* 39, L1048-L1050 (2000).

[9] J.Lu, T. Murai, K. Takaichi, T. Uematsu, K. Misawa, M. Prabhu, J. Xu, K. Ueda, H. Yagi, T. Yanagitani, and A. A. Kaminskii and A. Kudryasshov, *Appl. Phys. Lett.* 78, 3586-3588 (2001).

[10] J.Lu, M. Prabhu, K. Ueda, H. Yagi, T. Yanagitani, and A. Kudryasshov, *Laser Physics* 11, 1053-1057 (2001).

JP0350282

2.18 DESIGN OF A SPIN POLARIZED POSITRON BEAM AND A SPIN ROTATOR

F. Saito[1*], N. Suzuki[1], Y. Itoh[1], A. Goto[1], T. Kurihara[2], Y. Nagshima[3] and T. Hyodo[3]
[1]The institute of Physical and Chemical Research, Cyclotron Center
[2]Department of Basic Sciences, Graduate School of Arts and Science, University of Tokyo
[3]Institute of Materials Structure Science (IMMS), High Energy Accelerator Research Organization (KEK)

Abstract

A high intensity spin polarized slow positron beam is developing in RIKEN for the researches of surface and interface magnetism. A new design of the apparatus to improve beam transfer efficiency by making it compact and the simulation results are reported. Matching of electric field and magnetic field of a spin rotator is also discussed.

Keywords: positron beam, spin polarization, surface magnetism, spin rotator, polarimeter, ^{18}F source

1. Introduction

A high-intensity spin polarized slow positron beam is developing in RIKEN (The Institute of Physical and Chemical Research) for the researches of surface and interface magnetism. Using the spin polarized slow positron beam, the information of the electron at the first atom layer of the metal surface is selectively obtained by detecting annihilation γ rays of positronium (Ps), which is not formed in the bulk but formed only on the surface. The spin polarized slow positron beam is also expected as a powerful probe for the research of interface magnetism, for an example, giant magnetoresistance in metallic superlattice structures. A part of positrons implanted into the superlattice structures are trapped in the disorder region around the interface and annihilate with periphery electrons, so that annihilation γ rays give the information of the electrons around the interface.

A high intensity beam for surface research is obtained using electro-deposited ^{18}F source and an electro-polished tungsten moderator. ^{18}F (half-life 110 min.), the activity is more than several hundred mCi, is produced via $^{18}O(p,n)^{18}F$ reaction using AVF cyclotron in RIKEN. [1] The automatic source supply system to use such a short half-life ^{18}F source for long period of experiments was reported elsewhere. [2] High conversion efficiency of positron moderator is another important factor to realize an intensity beam. A stack of electro-polished tungsten mesh is expected to be a promising moderator. The conversion efficiency of a tungsten 12 stacked mesh moderator, the diameter of which electro-polished wire is about 10μm, is 7.5×10^{-4}. Although this value is lower than that of a solid rare gas moderator, the tungsten mesh moderator has the advantages that the handling is easier, stability of efficiency is higher and the cost is lower. [3]

The previous design [4] needs some improvements. In the present work, new design of the spin polarized slow positron beam apparatus and the simulation results of the beam transfer efficiency and matching of magnetic and electric field of a spin rotator are discussed.

* Corresponding author. Tel: +81-48-467-9464 Fax: +81-48-461-5301
E-mail address: fsaito@postman.riken.go.jp

2. Design and simulation

Fig. 1 shows the outline of the beam apparatus. A positron source, both an electro-deposited ^{18}F source and a sealed ^{22}Na source are utilized, is placed outside the vacuum chamber. The positrons emitted from the source pass into the chamber through a titanium window (20μm thick) and impinge on the tungsten stacked mesh moderator.

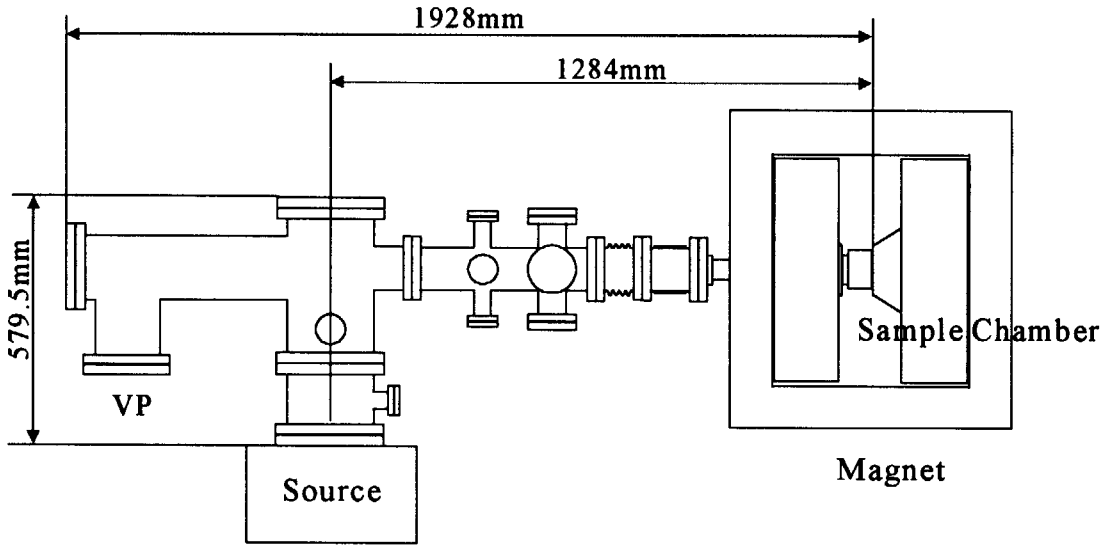


Fig. 1 Outline of beam apparatus

Fig. 2 shows electro-static lenses to transfer positrons. The positrons not only re-emitted forward from the moderator but also a part of positrons re-emitted backward are utilized for beam accelerated by a grid with the voltage of 400V. The positrons are transferred to a sample chamber by the electrostatic lenses of diameter from 10 to 24mm. The spin rotator placed before a parallel-plate deflector rotates the spin of the positrons.

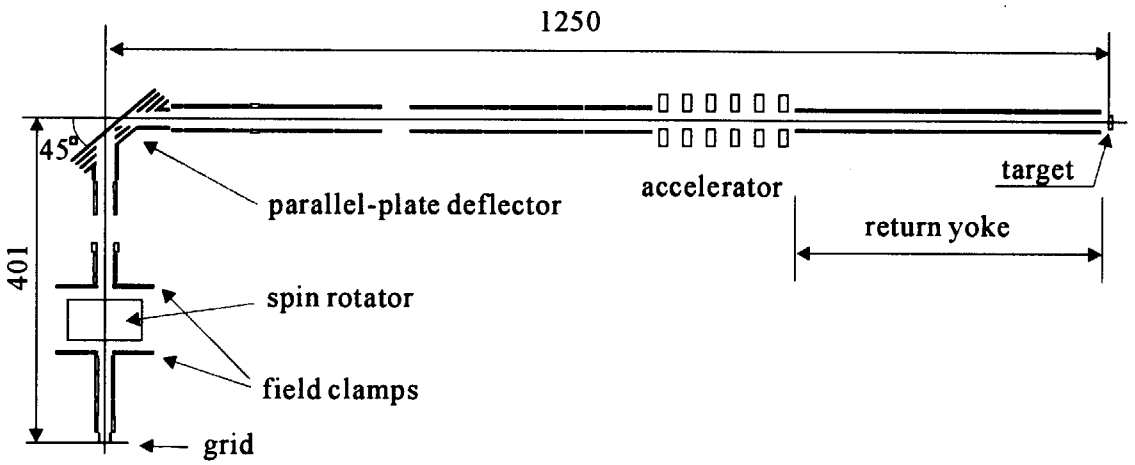


Fig. 2 Electrostatic lenses

The beam trajectory is bent in order to exclude non-thermalized positrons and annihilation γ rays from the source by the parallel-plate deflector. The positrons can be accelerated up to the energy of 30keV. The beam is transferred through a duct passes through the return-yoke and the pole piece of an electro-magnet to the sample chamber placed between the pole pieces. The electro-magnet is used as the polarimeter for the measurement of the spin polarization of the beam. The spin polarization will be obtained by the Doppler broadening measurement of γ rays from Ps annihilation in amorphous SiO_2 (a-SiO_2). [4]

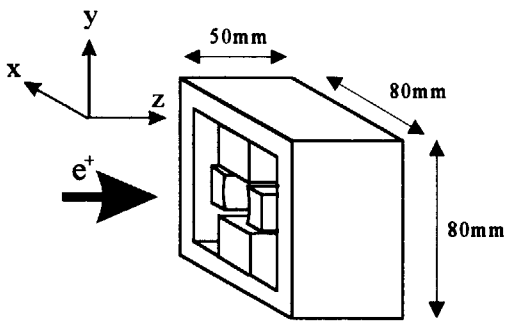


Fig. 3 Wien filter (used as a spin rotator) with curved surface electrodes

The simulation shows high efficiency of the beam transfer by this apparatus. In the simulation, we assumed that the positrons are emitted with the angle from 0 to 80 degree to the beam axis and with the initial energy from 1 to 3eV. The simulation shows all the positrons emitted from a circular area (diameter 6mm) can be transported to the target position with the energy 3, 13 and 30 keV. Although beam shape is deformed to be flat at the parallel-plate deflector, all the positrons are transferred within 10mm diameter at the target position. The beam transfer efficiency was simulated by means of Simion (Idaho N. E. Lab.).

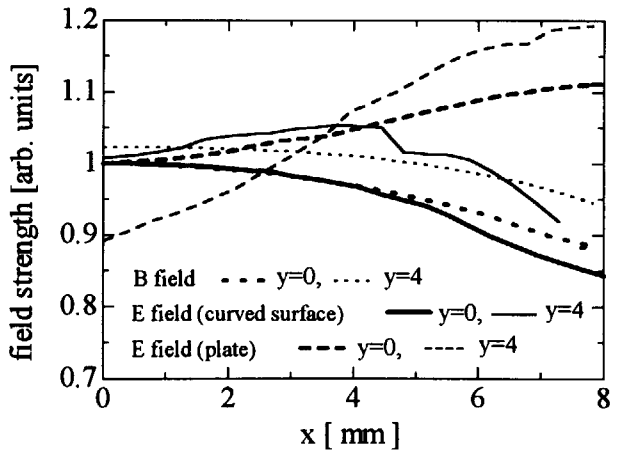


Fig. 4 Distribution of electric fields produced by curved surface electrodes and flat electrodes, and that of magnetic field normalized by the value at (x, y, z) = (0, 0, 0), respectively.

A Wien filter is used as the spin rotator, which has a electric field E and a magnetic field B perpendicular to the beam axis and to each other. When the beam passes through the magnetic field, the spin rotates around the magnetic field direction due to the Larmor precession with frequency $\omega = \left(eB/m\right)$, where e is a charge and m is the mass of a

positron. Then the rotation angle ϑ is represented as $\vartheta = l\omega/v = leB/mv$, where v is the velocity of the positron. The transverse motion of the positron by the magnetic field is cancelled by the electric field when the Wien condition $E + vB = 0$ is satisfied. Thus, the matching between the magnetic field and the electric field is crucial for the beam transfer. The schema of the spin rotator is shown in Fig. 3. The dimensions of the designed spin rotator are 50mm length along the beam axis, 20mm gap between the magnetic pole pieces and 16mm gap between the electrodes. The positrons (0.5keV) pass through the spin rotator with the beam diameter of 10mm or less. The magnetic and electric fields of the spin rotator were simulated by means of OPERA-3d/TOSCA (Vector Field, Ltd.). The electric field distributions of three types of electrodes, such as flat electrodes, flat electrodes with 4 pairs of auxiliary electrodes and curved surface electrodes are simulated. The strength of magnetic field and the electric field along the transversal direction (x-axis) to the beam axis (z-axis) at the center (z=0) of the spin rotator is shown in Fig. 4. The distribution of the electric field produced by the curved surface electrodes matches to that the magnetic field better than that produced by the flat electrodes at the position both y=0 and y=4. Although the flat electrodes with auxiliary electrodes require complicated fabrication, the effect of which is almost same as that of the curved surface.

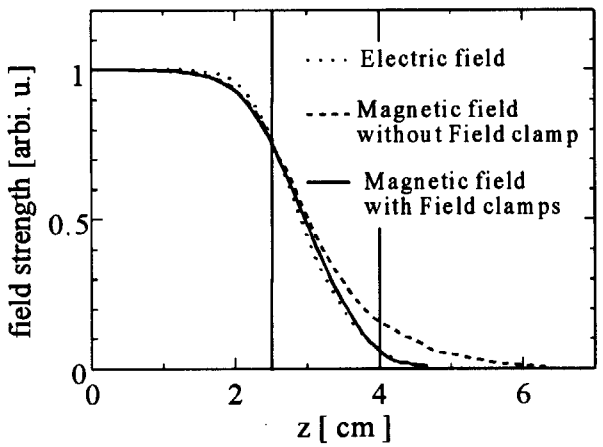


Fig. 5 Magnetic field and electric field at fringe, normalized by the value at the middle of the spin rotator (z = 0) The pole pieces and electrodes end at z = 2.5cm. A piece of field clamps is placed at z = 4cm.

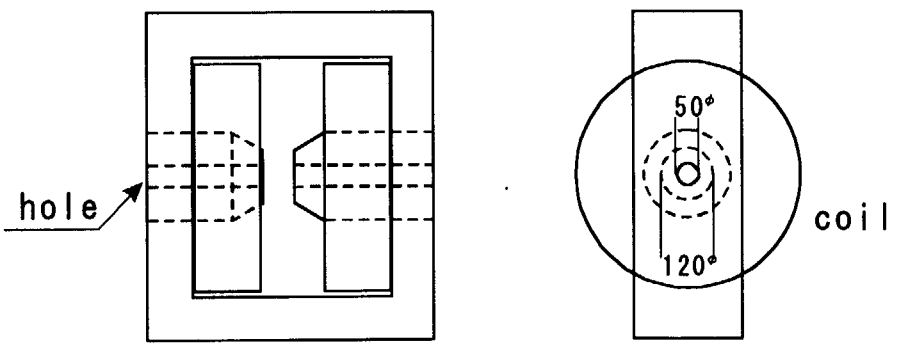


Fig. 6 Electro-magnet with a hole (diameter 50mm) to pass a beam duct

The matching of the magnetic and electric fields in the longitudinal direction to the beam axis is also simulated. The fringe magnetic field at the entrance and the exit of the spin rotator decreases more slowly than that of the electric field as shown in Fig. 5. A pair of field clamps reduces the tail of the magnetic field and matches it to that of the electric field (Fig. 5). The field clamps is consisted of two disks (3mm thick) made of Permalloy, which has an aperture (diameter 16mm).

The pole piece (diameter 120mm) of electro-magnet (Fig. 6) has a hole (diameter 50mm) to pass the duct. The uniformity of the magnetic field around the target position is also simulated. Fig. 7 shows the magnetic filed between the pole pieces along the transversal direction to the beam axis. The deviation is 0.5% or less at the target position within the area diameter 10mm.

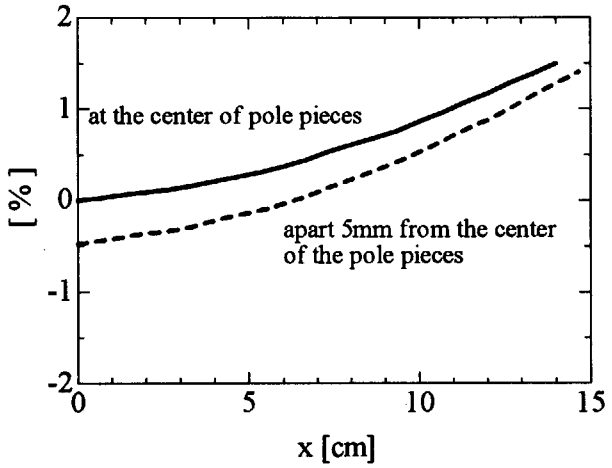


Fig. 7 Distribution of magnetic field of electro-magnet normalized by the value at (x, y, z) = (0, 0, 0) A solid line and a broken line show the values at (x, y, z) = (x, 0, 0) and (x, 0, 5), respectively.

In conclusion, we expect that this spin-polarized slow positron beam apparatus has high beam transfer efficiency and to be a powerful probe for the researches of surface and interface magnetism.

Acknowledgement
This work was supported by the Nuclear Cross-over Research Funds.

References

[1] F. Saito, Y. Nagashima, T. Kurihara, I. Fujiwara, R. Iwata, N. Suzuki, Y. Itoh, A. Goto and T. Hyodo, Nucl. Instr. And Meth. A **450,** 491 (2000)
[2] F. Saito, N. Suzuki, Y. Itoh, A. Goto, I. Fujiwara, T. Kurihara, R. Iwata, Y. Nagashima, T. Hyodo, Rad. Phys. and Chem., **52, 755 (2000)**
[3] F. Saito, Y. Nagashima, L. Wei, Y. Itoh, A. Goto and T. Hyodo, to be published in Appl. Surf. Sci.
[4] J. H. Kim et al., Rad. Phys. and Chem., **52,** 759 **(2000)**
[5] Y. Nagai, Y. Nagashima, J. H. Kim, Y. Itoh and T. Hyodo, Nucl. Instr. and Meth. in Phys. Res. B **171,** 199 (2000)

JP0350283

JAERI－Conf 2003－001

2.19 COMPUTATIONAL SIMULATION FOR CREEP FRACTURE PROPERTIES TAKING MICROSCOPIC MECHANISM INTO ACCOUNT

Masaaki Tabuchi*
National Institute for Materials Science, Sengen, Tsukuba, 305-0047, Japan

Abstract

Relationship between creep crack growth rate and microscopic fracture mechanism i.e., wedge-type intergranular, transgranular and cavity-type intergranular crack growth, has been investigated. The growth rate of wedge-type and transgranular creep crack could be characterized by creep ductility. Creep damages formed ahead of the cavity-type crack tip accelerated the crack growth rate. Based on the experimental results, FEM code that simulates creep crack growth has been developed by taking the fracture mechanism into account. The effect of creep ductility and void formation ahead of the crack tip on creep crack growth behavior could be simulated.

Keywords: Creep crack growth, Alloy 800H, 316 stainless steel, Creep fracture mechanism, C^* parameter, FEM analysis, Vacancy diffusion

1. Introduction

Understanding of creep crack growth behavior is important for the reliability evaluation of high temperature structural components. Creep crack growth properties are affected by microscopic fracture mechanism dependent on temperature and loading condition. For the long-term services, creep crack growth by grain boundary cavitation [1] is often observed. The creep life and ductility of irradiated damaged material for nuclear reactor also decreases because it is fractured in wedge-type or void-type intergranular fracture mode [2]. Type IV creep crack in heat affected zone of welded components grows accompanied by void formation ahead of the crack tip [3]. It would be necessary to evaluate the creep crack growth properties, taking microscopic features such as damage formation into account, for the accurate life prediction.

In the present work, creep crack growth tests were conducted using CT specimen of Alloy 800H and 316 stainless steel at various temperature and loading conditions. Creep crack growth behavior was characterized in terms of microscopic creep fracture mechanism. Based on the experimental results, the FEM analysis code, which simulates creep crack growth has been developed. In order to simulate formation and growth of voids by the vacancy diffusion, the vacancy concentration was calculated by solving diffusive equation under multi-axial stress condition. Creep crack growth properties of damaged materials were calculated by combining the critical strain criteria and vacancy concentration criteria. The calculated creep fracture properties were compared to experimental ones.

2. Experimental

Materials tested are Alloy 800H and 316 stainless steel plates. Creep crack growth tests were conducted using CT specimen of 50.8mm in width and 12.7mm in

*Corresponding author. Tel: +81-(0)298-59-2201 Fax: +81-(0)298-59-2201
E-mail address: tabuchi.masaaki@nims.go.jp (M. Tabuchi).

thickness. Fatigue pre-crack of 2.5mm was introduced at room temperature. After fatigue pre-cracking, side-grooves of 20% of thickness were machined.

The creep crack growth tests were conducted at temperature range from 873K to 1073K. Creep crack length was measured using D.C. electrical potential technique. Load line displacement was measured.

3. Results and discussions

3.1 Creep Fracture Mechanisms

Figure 1 shows microscopic features of creep cracks observed in CT specimens of Alloy 800H. Three types of creep crack growth, wedge-type intergranular, cavity-type intergranular and transgranular crack growth were observed depending on testing temperature and loading conditions. For higher stresses at lower temperatures, intergranular fracture due to the wedge-type cracking (W-type) was observed, because the fine γ' precipitates hardened the metal matrix. For lower stresses at higher temperatures, intergranular fracture due to the formation of cavities on grain boundaries (C-type) was observed. Large creep damaged zone ahead of the crack tip was observed for C-type crack growth. Transgranular fracture (T-type) was observed between the temperature and loading conditions of W-type and C-type.

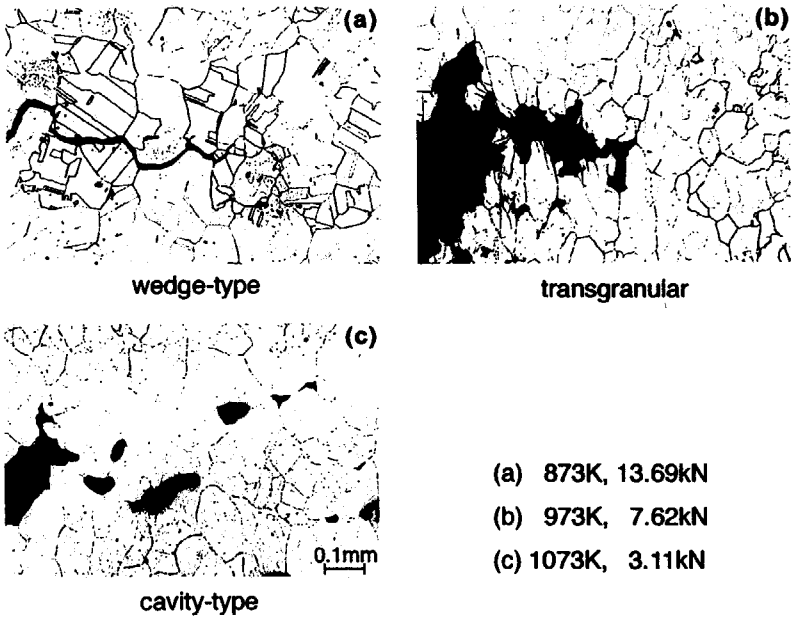


Fig.1 Microscopic features of creep cracks observed in CT specimens of Alloy 800H.

3.2 Characterization of Creep Crack Growth Rate in Terms of Fracture Mode

Creep crack growth rate was evaluated by C^* parameter calculated as follows [4];

$$C^* = \frac{n}{n+1} \frac{P\dot{\delta}}{B_N (W-a)} \left(\gamma - \frac{\beta}{n} \right) \qquad (1)$$

where, W is the specimen width, a is the crack length, P is the load, B_N is the net

thickness, $\dot{\delta}$ is the load line displacement rate, n is the creep exponent in Norton's rule and γ and β are the function of a and W. Materials constants of Norton's rule for Alloy 800H obtained from creep tests of smooth bar specimens are shown in Table I.

Table I Materials constants of Norton's rule for Alloy 800H.

Temperature	A ($MPa^{-n}h^{-1}$)	n
873K	$1.67x10^{-33}$	11.3
923K	$1.82x10^{-34}$	12.9
973K	$1.80x10^{-39}$	16.5
1073K	$4.94x10^{-28}$	13.5

The relationship between creep crack growth rate, *da/dt*, and C^* parameter for Alloy 800H is shown in Fig.2. The *da/dt vs.* C^* relations depend on the microscopic creep crack growth mechanism. The creep crack growth rate for W-type and C-type fracture mode was higher than that for T-type fracture mode. The creep crack growth rate for C-type mode exists between the upper bound for W-type and the lower bound for T-type mode.

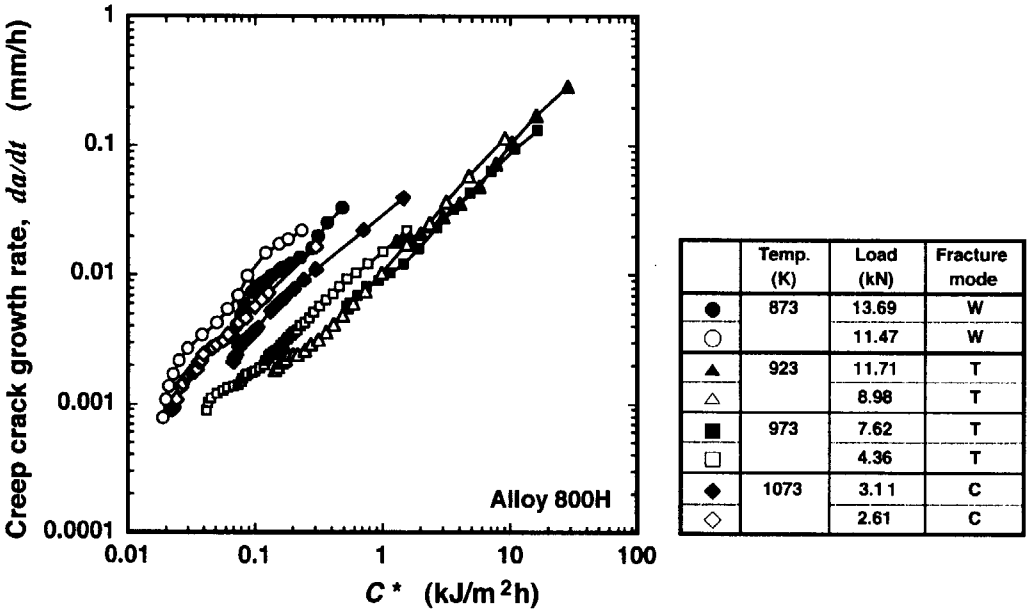


Fig.2 Relationship between creep crack growth rate, *da/dt*, *vs.* C^* parameter.

Creep ductility was dependent on creep fracture mechanism, and that was lower for W-type, higher for T-type, and medium for C-type fracture mode. It is considered that difference of creep ductility among fracture modes is one of the reasons why *da/dt* depends on creep fracture mode. Fig.3 shows the relationship between creep crack growth rate at C^*=1 kJ/m^2h *vs.* reduction of area for smooth bar creep specimens of Alloy 800H and 316 stainless steel. These relations were dependent on creep fracture mechanisms. For W-type and T-type fracture mode, the *da/dt* was inversely proportional to creep ductility as shown with the solid curve in Fig.3. Creep crack growth rate for W-type and T-type mode could be written as follows [5];

$$\frac{da}{dt} = \frac{6.26 \times 10^{-3}}{\varepsilon_f^*} C^{*0.92} \qquad (2)$$

where, ε_f^* is the creep ductility.

For C-type fracture mode, however, *da/dt* was faster than that predicted from Eq.2. The *da/dt* was accelerated as the testing temperature and time was increased for C-type fracture mode [6]. When creep voids are not formed ahead of the crack tip such as W-type and T-type fracture mode, the creep crack growth rate could be characterized by the creep ductility. When many voids and micro cracks are formed ahead of the crack tip, *da/dt* was accelerated than that predicted from creep ductility. In order to predict the creep crack growth rate under C-type fracture mode, it is necessary to consider not only creep ductility but also the effect of creep damages ahead of the crack tip. Vacancy diffusion and void formation accelerated under multi-axial stress condition at higher temperature should be taken into account.

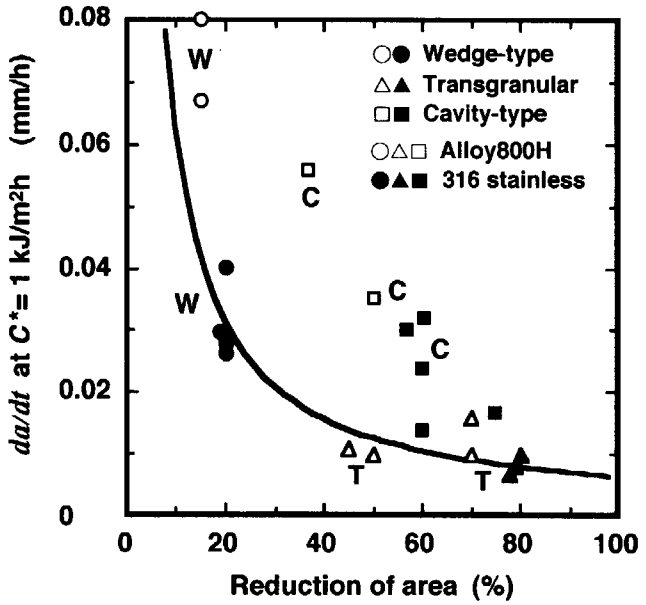


Fig.3 Relationship between *da/dt* at C^*=1 kJ/m^{2}h vs. creep ductility.

3.3 Computational Simulation for Creep Crack Growth

On the basis of these experimental results, we have conducted computational simulation for creep crack growth taking the fracture mechanism into account. The two-dimensional FEM analytical model of CT specimen is shown in Fig 4. For W-type and T-type fracture mode, the *da/dt* was inversely proportional to creep ductility; therefore the crack growth could be characterized by critical strain criteria. The creep strain distribution was calculated by FEM using Norton's creep constitutive equation shown in Table I. When the equivalent creep strain ahead of the crack tip reached to the critical value, which is the creep ductility of round bar specimen, the coordinate of the crack tip node was moved according to the method proposed by Hsu et al. [7]. The C^* line integral for the path shown in Fig.4 was calculated for every time step.

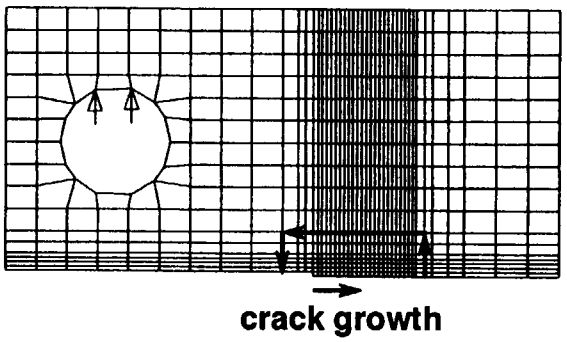


Fig.4 Analytical model for creep crack growth.

Comparison of computational and experimental relations of creep crack growth rate vs. C^* is shown in Fig.5. The symbols indicate experimental *da/dt* vs. experimental C^* calculated by Eq.1, and the line shows the computational *da/dt* vs. calculated C^* integral. In this case of T-type and W-type fracture mode, the crack growth rate could be predicted from Norton's creep rule and creep fracture strain. If we use half value of fracture strain for fracture criteria, the twice value of *da/dt* was obtained as shown with dashed line in Fig.5. These computational results coincide with the experimental ones that *da/dt* is inversely proportional to creep ductility.

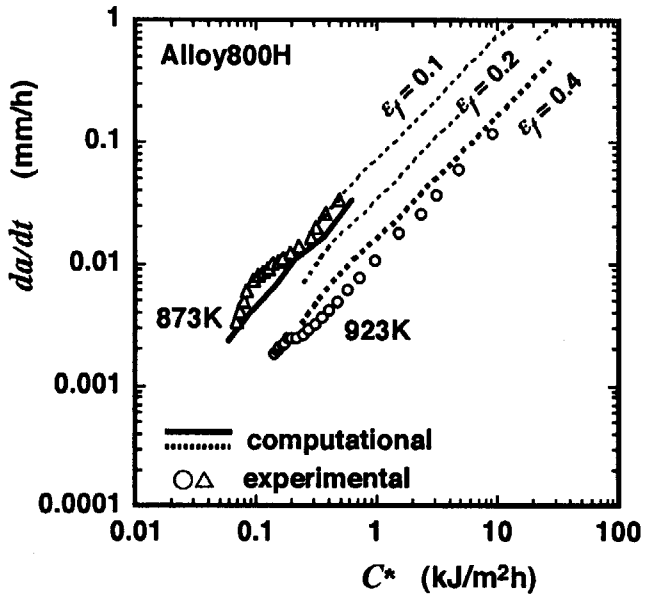


Fig.5 Comparison of experimental and computational relation between *da/dt vs.* C^* parameter.

Three-dimensional effect on creep crack growth properties is also important [1]. We have reported that creep crack growth rate increased as the specimen thickness increased because of the mechanical constraint effect [8]. Three-dimensional FE model and equivalent creep strain contour is shown in Fig.6. The creep crack growth of this model was calculated according to the method mentioned above. Fig.7 shows the computed crack growth curve. Three-dimensional effect that creep crack propagates faster in the center of specimen thickness than at the specimen surface can be

simulated. The calculated C^* value was larger in the center of thickness than in surface. For this computation, the same critical strain value was assumed for every crack path in the direction of specimen thickness. Further investigation would be necessary, because the critical strain for crack growth decreases under multi-axial stress condition such as in the center of thick specimen [5,8].

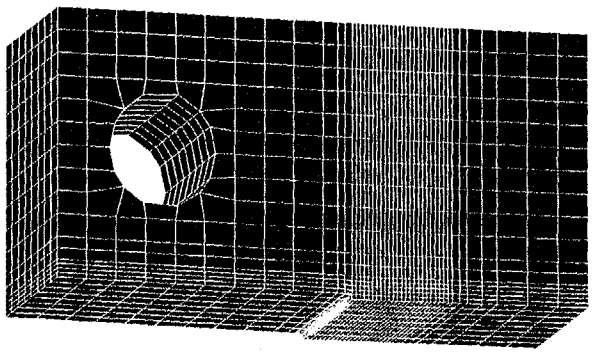


Fig.6 Equivalent creep strain contour of CT specimen.

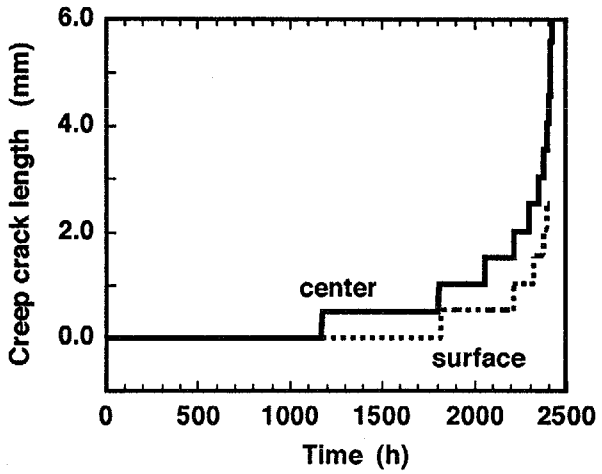


Fig.7 Three-dimensional calculation for creep crack growth.

3.4 Computational Simulation Taking Vacancy Diffusion into Account.

For C-type fracture mode, *da/dt* was faster than T-type due to the formation of voids ahead of the crack tip. In order to evaluate the effect of void formation for C-type mode, it would be necessary to analyze the crack growth taking vacancy diffusion into account under multi-axial stress condition. Vacancy diffusion, void initiation and crack propagation would be accelerated under multi-axial condition. Creep voids were observed in the center of CT specimen thickness, because the multi-axial effect is larger than in free surface. The vacancy diffusion equation under stress gradient is given as follows [9];

$$\frac{\partial C}{\partial t} = D\nabla\left(\nabla C + \frac{C}{RT}\nabla v\right) \qquad (3)$$

$$v = -\sigma_p \Delta V \qquad (4)$$

where, C is the vacancy concentration, D is the diffusion coefficient, R is the gas constant, T is the absolute temperature, σ_p is the hydrostatic stress and ΔV is the volume changes by vacancy diffusion. In order to simulate vacancy diffusion and concentration, Eq.5 in which weight function α_1 and α_2 are added is adopted [10,11].

$$\frac{\partial C}{\partial t} = \alpha_1 D \nabla^2 C + \alpha_2 \frac{D}{RT} \nabla C \nabla v \qquad (5)$$

The vacancy concentration around the crack tip is calculated by FEM according to Eq.5. The changes of vacancy concentration during creep ahead of the crack tip calculated by using α_2/α_1=300, ΔV=2.0e^{-6}(m^3/mol) and D=1.5x10^{-9}, 1.5x10^{-10}(m^2/s) are shown in Fig.8. The vacancy concentration increases higher in the center of specimen than in surface. This result is consistent with the experimental results that creep voids were observed in the center of CT specimen thickness.

In the present simulation, if the vacancy concentration reaches to the critical value, that means the void initiation, the stiffness matrix [K] around the crack tip is

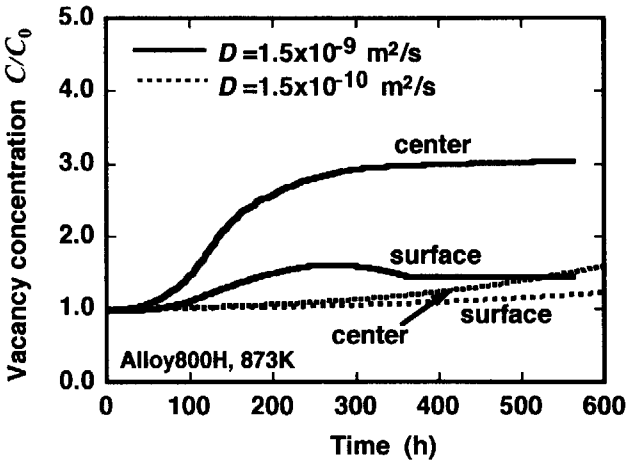


Fig.8 Changes of vacancy concentration ahead of the crack tip during creep.

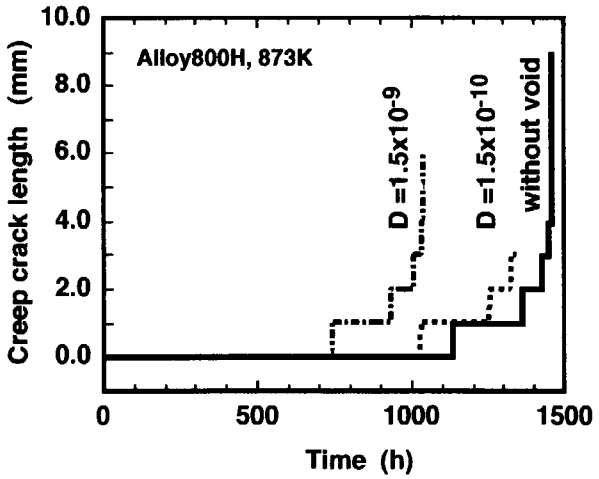


Fig.9. Example for simulation of creep crack growth taking the diffusion into account.

decreased as the vacancy concentration increased. The creep crack growth is simulated by combining the critical strain criteria and vacancy diffusion criteria. Fig.9 shows an example calculated by assuming that the critical vacancy concentration C/C_0 is 1.7. The qualitative results that crack initiation time and crack growth rate were accelerated were obtained while taking the void formation ahead of the crack tip into account. The quantitative evaluation for the effect of vacancy diffusion on crack initiation and growth under multi-axial condition should be the future work.

4. Conclusions

The relationship between creep fracture mechanism and creep crack growth behavior has been investigated on Alloy 800H and 316 stainless steel. Based on the experimental results, computational simulations for creep crack growth have been conducted. The results are summarized as follows;

(1) Three types of creep crack growth mechanisms, i.e., wedge-type intergranular, transgranular and cavity-type intergranular, were observed for Alloy 800H and 316 stainless steel depending on testing conditions.

(2) Creep crack growth rate was dependent on microscopic creep fracture mechanism. The growth rate of wedge-type and transgranular creep crack could be characterized by creep ductility. The creep damages formed ahead of the cavity-type creep crack were considered to accelerate the crack growth rate.

(3) The 3-D FEM code, which simulates creep crack growth, has been developed. The effect of creep ductility on *da/dt* vs. C^* relations could be simulated.

(4) The vacancy concentration was calculated by solving diffusive equation under multi-axial stress condition. The effect of void formation ahead of the crack tip on creep crack growth behavior could be evaluated.

References

[1] H. Riedel, *Fracture at High Temperatures* (Springer-Verlag, Berlin 1986).
[2] N. Yamamoto, H. Shiraishi, H. Kamitsubo, I. Kohno, T. Shikata and A. Hishimura, J. of Nuclear Materials **133&134**, 493 (1985)
[3] M. Tabuchi, T. Watanabe, K. Kubo, M. Matsui and F. Abe, Int. J. of Pressure Vessels & Piping **78**, 771 (2002).
[4] H.A. Ernst, *ASTM STP* 791, I-499 (1983).
[5] K.M. Nikbin, D.J. Smith and G.A. Webster, G.A., Trans. ASME, J. Eng. Mater. Tech. **108**, 189 (1986).
[6] M. Tabuchi, K. Kubo and K. Yagi, Proc. of 9th Int. Conf. on Fracture, Sydney, vol.1, 399 (1997).
[7] T.R. Hsu and Z.H. Zhai, Eng. Fract. Mech. **20**, 521 (1984).
[8] M. Tabuchi, K. Kubo and K. Yagi, Eng. Fract. Mech. **40**, 311 (1991).
[9] H.P. Leeuwen, Eng. Fract. Mech. **6**, 141 (1974).
[10] A.T. Yokobori, Jr., T. Nemoto, K. Sato and T. Yamada, Japan Soc. Mech. Eng. **59**, 104 (1993).
[11] K. Kikuchi and Y. Kaji, Proc. of 33rd Symposium on Strength of Materials at High Temperatures, Yokohama, Japan, 1 (1995).

JP0350284

2.20 A MOLECULAR-DYNAMICS SIMULATION OF DISPLACEMENT CASCADES IN α-IRON

Katsuyuki Kusunoki*
Computational Materials Science Center
National Institute for Materials Science

Abstract

A molecular-dynamics code has been developed for simulating the early process of radiation-induced defects generation and aggregation during displacement cascades in α-iron. This code reproduces the dynamics of various types of defects such as vacancies, interstitials, and their clusters in a crystal composed of a million atoms. Main procedures and results of the present simulation are as follows. Interactions among atoms were described by a many-body EAM potential. Every simulation was performed under 3D periodical boundary conditions. Cascades were introduced into crystals by giving a kinetic energy to a knock-on atom once at a time toward a crystallographic direction along low index axes i.e. <100>, <110> and <111> axes. The maximum number of Frenkel-type defects was generated for a case when the knock-on direction was along <110> axis. Interstitial atoms surrounding residual vacancies were observed to form several clusters shortly after pair annihilation of the Frenkel-type defects. Fast massive migration of the interstitial clusters was also observed.

Keywords: α-iron, displacement cascades, vacancy clusters, interstitial clusters, molecular-dynamics, EAM potential

1. Introduction

It will be of great interest for those engaged in the investigation of reactor materials to grasp vividly the atomistic process of irradiation damaging and defects production. Unfortunately the very early process of the irradiation damaging takes place within a very short time of an order of picosecond and the process itself can never be directly observed by experimental methods. A most promising method overcoming this difficulty is atomistic simulations using an interatomic potential. So far we have developed a molecular-dynamics code which we employed an embedded-atom-method (EAM) type interatomic potential repro-

* Tel: +81-298-59-2624 Fax: +81-298-59-2601

E-mail address: KUSUNOKI.Katsuyuki@nims.go.jp

ducing the crystal structure and properties such as vacancy formation energy, cohesive energy, and the elastic modulus of α-iron. It must be kept in mind that irradiation of a material by a knock-on particle with a kinetic energy inevitably bring into a large temperature gain in the material; a particle with 1eV will give an energy of about 10^4kT to the material. So the number of atoms in a system should be large enough to depress inadequate temperature gain at the very early process of irradiation in the simulations. This situation for an atomistic simulation of irradiation causes another difficulty in using computer resources under limited availability; if we want to sustain the average temperature of a target sample below 100K for a particle with 10keV, we must use a sample composed of more than a million atoms, resulting in a calculation costs such as a long CPU time and a large memory. We have found a solution to these problems in two ways and made a molecular-dynamics code, details of which will be described in the next section. As has been already reported experimentally, residual vacancies and interstitial atoms make their several aggregates shortly after pair annihilation of Frenkel pairs which are generated during initial displacement cascades. To analyze the dynamical process, massive movement and change in shape, of the aggregates, a cluster analysis code has been also developed.

2. Modeling and Method of the Present Simulation

2.1 Modeling of Samples

An α-iron crystal with a size of 78x80x82 in units of the lattice parameter was used as a sample. This sample was composed of about a million atoms, among which forces act by many-body interatomic potentials. The sample had not a cubic shape but a rectangular shape with 3D periodic boundary condition. The rectangularity of the sample shape was intended to avoid an occurrence of going and returning of a specific interstitial atom on a fixed axis in the sample with the periodical boundary.

2.2 Method of Molecular-Dynamics Simulation

A potential based on an embedded atom method (EAM), which was firstly proposed by Daw and Baskes [1], was applied for construction of α-Fe crystals used in the present MD simulations. The EAM potential is written as,

$$E_{tot} = \sum_i \phi_i(r_i), \tag{1}$$

$$\phi_i(r_i) = F_i(\rho_i) + \frac{1}{2}\sum_j \varphi_{ij}(r_{ij}), \tag{2}$$

$$\rho_i = \sum_j f_{ij}(r_{ij}), \tag{3}$$

where $F_i(\rho_i)$ is an embedding function of atom i in an electron density ρ_i, and $\varphi_{ij}(r_{ij})$ is a pair interaction term between atoms i and j. Detailed explanation for the above formulations is given in the Daw and Baskes' paper. Various types of functions have been proposed for actual form of the above embedding and pair interaction terms, and we used "potential 3" appearing in the paper of Haftel et al. [2]. This potential is well known to reproduce crystal structure, elastic properties, and surface reconstruction of real α-Fe. With use of this potential reasonable values for both the formation energies of <110> and <111> split interstitial as well as that of a vacancy in α-Fe have been also obtained by molecular static calculations [3].

We applied the Verlet formula [4] for integrating the equation of motion, where the initial size of the timestep was set to be $10^{-6}t_v$ (t_v is $0.974\text{x}10^{-13}$s) and the size was gradually set to be larger values of $10^{-3}t_v$ as the fast reactions among atoms subsided into lowering the atom velocities, of which the highest values were monitored at any time throughout the simulation.

In case for a system with a million atoms, more than 95% of the total CPU time is consumed for bookkeeping of atom positions. So we devised a pre-bookkeeping routine called 'blocking'. In this routine the system was divided into blocks and bookkeeping was made only between atoms in a specific block A and atoms belonging to blocks surrounding the block A. It took only about 0.01% of the total CPU time for this blocking routine and the CPU time required for the calculation of bookkeeping was reduced to 15% of the total CPU time. We also tried to save the CPU memory required for making bookkeeping for a system with 3D periodic boundaries. This was done by making no recording of atom positions in 26 imaginary boxes but only of the ones in a real box. In the present case, about 650MB of the CPU memory was saved.

During the period from knocking-on to the completion of pair annihilation of vacancies and interstitials reactions among atoms proceeded adiabatically due to very fast movement of atoms. Then we made no control of pressure and temperature during that period. If we made pressure control of the specimen at the very early stage of the knocking-on, the system might have exploded into fragments. Of course we must raise the temperature of a system when we want to accelerate the movements of defects, and in turn, we must lower both the temperature and the pressure of a system when we intend to make a precise determination of the formation energies and the activation energies of a defect. In the present simulations, both the temperature and pressure of the system were controlled after almost all the Frenkel pairs disappeared by pair annihilation of a vacancy and an interstitial atom. Temperature control was done using the momentum scaling method [5]. Pressure control was done with a slightly modified method of Abraham [6]. A brief explanation for the present

pressure control is as follows. According to the virial theorem, the pressure P is given as,

$$P = Nk_BT(1- < \Psi > /3Nk_BT)/V, \tag{4}$$

where V is the volume of the system and Ψ is given as,

$$\Psi = \sum_i r_i dE_{tot} / dr_i. \tag{5}$$

Now we assume that a very small change in the edge size of a simulation box with a length l_α for a direction α will alter the thermodynamics parameters as,

$$(V,P,T) \rightarrow (V(1+\Delta l_\alpha / l_\alpha), P', T'). \tag{6}$$

Then the change in the edge size is calculated from Eqs.4 and 5.

$$\Delta l_\alpha / l_\alpha = (3Nk_BT'P - 3P'V - \Psi)/\{3P'V + (\Psi_{1\alpha} + \Psi_{2\alpha})\}, \tag{7}$$

$$\Psi_{m,\alpha} = \sum_i \sum_j \frac{\alpha_{ij}^2}{r_{ij}^{2-m}} \frac{d^m E_{tot}}{dr_{ij}^m}. \tag{8}$$

Equating T' in Eq.7 to T at pressure control, we can avoid an abrupt adiabatic volume change which might have led to a sudden temperature raise or reduction of the system.

2.3 Method of Cluster Analysis

A cluster analysis was made for searching for the aggregates of interstitial atoms. We applied an algorithm devised by Sakamoto and Yonezawa [7]. In the present study we had a criterion for judging whether an atom belonged to an interstitial atom cluster or not; if a distance between the center of two atoms was less than a critical distance d_c, the atoms were decided to be of a cluster. The value of d_c was set to be $0.82a$, where a is the lattice parameter of α-iron. Investigating the size distribution of distances between the centers of any two atoms, we found that the value $0.82a$ was a minimum between two maxima, of which the first maximum was at about $0.82a$ and the second one was at about $0.86a$ i.e. the nearest neighbor distance between atoms in a perfect crystal of α-iron.

3. Results

3.1 Displacement Cascades

Cascades were introduced into crystals by giving a kinetic energy (from 4keV up to 20keV) to a knock-on atom once at a time toward a crystallographic direction along low index axes (<100>, <110>, and <111>), and the time evolution of the number of vacancies was monitored. The time giving the maximal number of Frenkel pairs changed from 0.3ps to 1.3ps as the knock-on energy increased from 4keV to 20keV. Knock-on-direction dependence of the

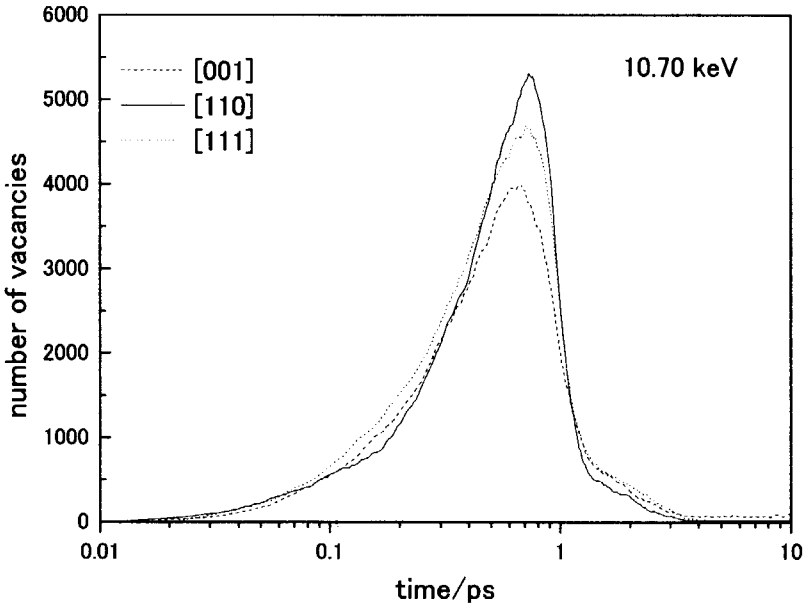


Fig.1 The time evolution of the number of vacancies generated after the knocking-on.

maximal number of the Frenkel pairs was also investigated. In case for low knock-on energies there was a tendency that the number of the Frenkel pairs were maximal when the knock-on direction was along <110> direction, whereas in case for high knock-on energies the knock-on-direction dependence of the maximal number of the Frenkel pairs wasn't noticeable. As an example Fig. 1 shows the time evolution of the number of vacancies when the knock-on energy was 10.7keV, where the number of Frenkel pairs reached to a peak at the time of 0.7ps.

3.2 Formation of Defect Clusters and Their Morphologies

Although almost all the Frenkel pairs disappeared within a few picoseconds, there remained interstitial atoms surrounding vacancies which aggregated on a (110) plane. Fig. 2 shows a morphological change in a displacement cascade when the knock-on direction was

along <110> axis and the knock-on energy was 6.4keV.

Figure 3 shows the formation process of interstitial clusters when the knock-on energy was 10.7keV and the knock-on direction was along <100> axis. It can be seen that interstitial atom aggregations gradually surround a region crowded with vacancies. In this case both the vacancy clusters and the interstitial atom clusters have a tendency to be a plate like shape parallel to a (110) plane. It was observed that residual single vacancies and vacancy clusters

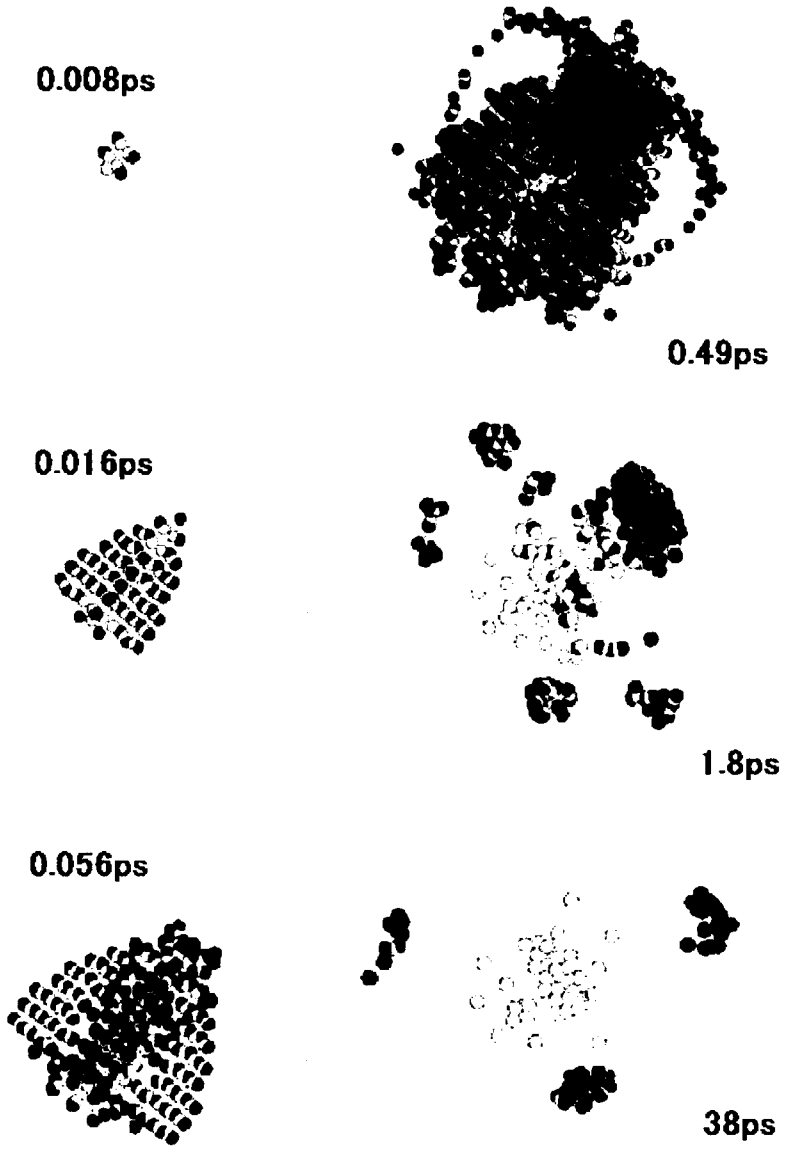


Fig.2 Time evolution of the morphology of a displacement cascade in case when the knock-on energy was 6.4keV and the knock-on direction was along <110> axis. Open circles indicate vacancies and filled circles indicate interstitial atoms.

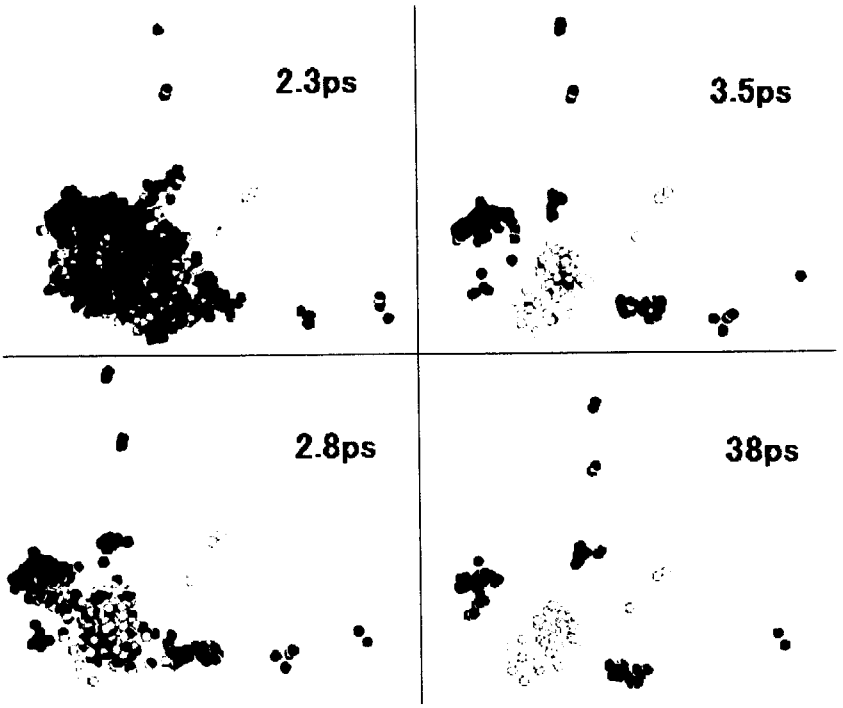


Fig. 3 Formation process of clusters of vacancies and interstitials. Open circles indicate vacancies and filled circles indicate interstitial atoms.

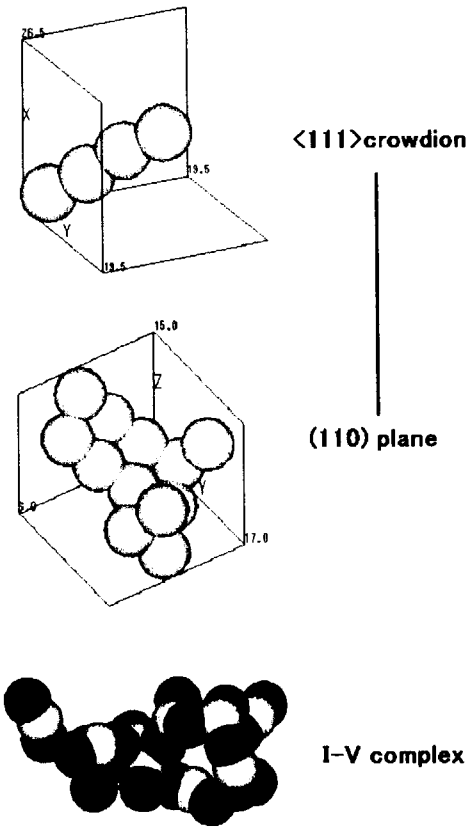


Fig. 4 Interstitial clusters and a complex of vacancies and interstitials. Open circles indicate interstitial atoms and filled circles indicate vacancies.

seldom move even at 900K. On the contrary interstitial atoms and their clusters were occasionally observed to move about very fast even at low temperatures below 100K. Detailed explanation for this surprising phenomenon will be a future subject.

Figure 4 shows various types of clusters observed in the present simulations. Cluster of interstitial atoms was initially generated from a <111> crowdion to a needle and then grown up to a plate like shape. Complexes of vacancies and interstitial atoms (or an aggregation of split interstitials) were also observed.

4. Conclusion

A molecular-dynamics code has been developed for simulating the early process of radiation-induced defects generation and aggregation. In order to save the CPU time and memories, a computation algorithm called 'blocking' was devised in addition to the bookkeeping of atom positions. Both the knock-on energy and the direction dependencies of the maximal number of the radiation-induced defects were investigated, and in case for low knock-on energies there was a tendency that the number of the Frenkel pairs were maximal when the knock-on direction was along <110> direction, but not a noticeable tendency among directions along <100>, <110> and <111> axes for high knock-on energies. Interstitial atoms surrounding residual vacancies were observed to form several clusters shortly after pair annihilation of the Frenkel pairs. Fast massive migration of the interstitial clusters was also observed.

References

[1] M. S. Daw and M. I. Baskes, Phys. Rev. **B29**, 6443 (1984).
[2] M. I. Haftel, T. D. Andreadis, J. V. Lill, and M. Eridon, Phys. Rev. **B42**, 11540 (1990).
[3] K. Kusunoki, submitted to J. Nucle. Mater.
[4] L. Verlet, Phys. Rev. **165**, 201 (1968).
[5] I. V. Woodcock, Chem. Phys. Lett. **10**, 257 (1971).
[6] F. F. Abraham, J. Vac. Sci. Technol. **2**, 534 (1984).
[7] S. Sakamoto and F. Yonezawa, Kotai-Butsuri **24**, 219 (1989).

JP0350285

2.21 MODELLING FOR NEAR-SURFACE INTERACTION OF LITHIUM CERAMICS AND SWEEP-GAS BY USE OF CELLULAR AUTOMATION

K.Shimura[1*], K.Yamaguchi[2], T.Terai[1] and M.Yamawaki[1]

[1] Department of Quantum Engineering and Systems Science, Graduate School of Engineering, The University of Tokyo, 7-3-1 Hongo, Bunkyo-ku, Tokyo 113-8656, Japan

[2] Japan Atomic Energy Research Institute, Shirakata 2-4, Tokai-mura, Naka-gun, Ibaraki-ken 319-1195, Japan

Abstract

Tritium release from the lithium ceramics as a fusion reactor breeder material is strongly affected by the composition of the sweep-gas as result of its influences with the material's surface. The typical surface processes which play important roles are adsorption, desorption and interaction between vacancy site and the constituents of the sweep-gas. Among a large number of studies and models, yet it seems to be difficult to model the overall behaviour of those processes due to its complex time-transient nature. In the present work the coarse grained atomic simulation based on the Cellular Automaton (CA) is used to model the dynamics of near-surface interaction between Li_2O surface and sweep-gas that is consisting of a noble gas, hydrogen gas and water vapour.

Keywords: Ceramic Breeder, Li_2O, Surface Interaction, Sweep-Gas, Cellular Automaton.

1. Introduction

Tritium release from the lithium ceramics as a fusion reactor breeder material is strongly affected by the composition of the sweep-gas as result of its influences with the material's surface. The typical surface processes which play important roles are adsorption, desorption and interaction between vacancy site and the constituents of the sweep-gas. It is also known that addition of H_2O into the sweep-gas increases the collection rate of the tritium from the ceramic breeder material. And so there is great importance to understand the interaction of water-contained sweep-gas with a ceramic breeder material. However among a large number of studies and models, yet it seems to be difficult to model the overall behaviour of those

*Corresponding author. Tel: +81-3-5841-7420 Fax: +81-3-5841-7420

E-mail address: shimura@tokai.t.u-tokyo.ac.jp

processes due to its complex time-transient nature. For the purpose of describing such acomplex systems, Cellular Automata (CA) are one of the very powerful tools [1][2] that has less restriction on conditioning the model compared with some methods based on differential equation such as Molecular Dynamics (MD). In general, CA are known as discrete mechanical system which is fully discrete in both independent and dependent variables. The system can be represented by some sets of so called transition rules that describe the microscopic interactions between cells. Then the states of each of those cells are updated according to the states and the corresponding rules in each time interval. Because of these characteristics, complex physical and chemical systems can be described by fairly simple manner. CA is also possible to imply highly non-linear boundary conditions in contrast to the model based on the differential equation. In the present work the coarse grained atomic simulation based on the Cellular Automaton (CA) is used to model the dynamics of near-surface interaction between Li_2O surface and sweep-gas that is considered to be consisting of a noble gas, hydrogen gas and water vapour. Moreover, in the model, adsorption and desorption of hydrogen and water at Li_2O surface is constructed and the validity and its applicability for further modelling of the tritium release are to be discussed.

2. Modelling

In this model, (110) surface of Li_2O which is known to be its most stable surface is considered. The ideal top three rows of the surface are sown in Fig.1,. O^{2-} ions are located on the O^{2-} lattice sites and empty sites E_0 are located on the interstitial sites in the O^{2-} sub-lattice, which are arranged regularly among Li^+ ions. The first step of the modelling is to discritise this surface as shown in Fig.2,. For convenience, O^{2-}, Li^+ and E_0 are rearranged in to the flat lattice consisting of square cells and each of those cells contain each of those ions. (110) surface of Li_2O shows an anisotropy that is the longitudinal and lateral length between the adjacent O^{2-} ions are different as illustrated in Fig.1,. Thus the size of each square cells of this model is taken as the averaged size. Secondly, a lattice that represents the gaseous phase is considered on top of the surface lattice. The lattice conditions such as cell's size, number of cells and etc. are the same as those for the surface lattice. This lattice reflects the condition of the sweep-gas and desorbed particles. However, the dynamics of adsorption and desorption are implemented as local interactions between those two layers in accordance to the thermally-activated processes.

At first the following adsorption and desorption mechanisms are considered in this model. For adsorption of H_2O vapour, H_2O is dissociatively adsorbed on pare of Vs and O^{2-} site. This process and its corresponding activation energy is then,

$$Vs_{(s)} + O^{2-}_{(s)} + H_2O_{(g)} \rightarrow 2OH^-_{(s)} \qquad ,E_{aH2O} = 25\text{kJ/mol [3]} \qquad (1)$$

Where Vs represents either E_0 (empty site) or V_0 (oxygen vacancy). Strictly speaking, E_0 and

V_0 are energetically different but it is known that there is no significant difference in the energetics between those two [3]. And hence E_0 and V_0 are treated in the same way. Contrary to this, desorption of H_2O is the reverse reaction and is described as recombination process of two OH^- site to produce a Vs and O^{2-} on the surface.

$$2OH^-_{(s)} \rightarrow Vs_{(s)} + O^{2-}_{(s)} + H_2O_{(g)} \qquad ,E_{dH2O} = 141kJ/mol\ [3] \qquad (2)$$

The sweep-gas is considered to be consisting of H_2O vapour and H_2 gas, so the next step is to make clear about H_2 desorption and adsorption mechanism. The adsorption mechanism of H_2 is dissociative and is as follows. One dissociative H atom is adsorbed on an O^{2-} to produce OH^- and another is adsorbed on the site existing between the two adjacent Li^+ [4]. *i.e.*

$$O^{2-}_{(s)} + E_{H_{(s)}} + H_{2(g)} \rightarrow OH^-_{(s)} + H_{(s)} \qquad ,E_{aH} = 25kJ/mol\ [3] \qquad (3)$$

Conversely desorption is then,

$$OH^-_{(s)} + H_{(s)} \rightarrow O^{2-}_{(s)} + E_{H_{(s)}} + H_{2(g)} \qquad ,E_{dH} = 157kJ/mol\ [3] \qquad (4)$$

The above processes are now implemented into the CA rules as illustrated in Fig.3,. It means that a particular positions with the defined local configurations at given time t are modified to the defined configurations at next given time of $t+1$ with the corresponding probability P_i {i | 1,2,3,4}. The probability P_i should reflect thermally-activated processes in order to make the CA model consisting with the chemical kinetics of Eq.1, Eq.2, Eq.3, and Eq.4,. Thus those can be expressed as follows.

$$P_1 = \frac{\max(E_{aH2O}, E_{s_1}) - E_{aH2O}}{E_s - E_{aH2O}} \qquad (5)$$

$$P_2 = \frac{\max(E_{dH2O}, E_{s2}) - E_{dH2O}}{E_s - E_{dH2O}} \qquad (6)$$

$$P_3 = \frac{\max(E_{aH}, E_{s3}) - E_{aH}}{E_s - E_{aH}} \qquad (7)$$

$$P_4 = \frac{\max(E_{dH}, E_{s4}) - E_{dH}}{E_s - E_{dH}} \qquad (8)$$

Where, $E_{s_i} = -RT \ln\left(\frac{a}{\tau\nu}\right)$, α is a random number with uniform distribution between 0 and 1.

Also, E_{aH2O} and E_{dH2O} are the activation energy for adsorption and desorption energy for H_2O respectively. Similarly to this E_{aH} and E_{dH} are the activation energy for adsorption and desorption energy for H_2. τ and ν represents time interval and the frequency factor respectively. *Esi* {i | 1,2,3,4} are the energy of the states that are corresponding to the thermal vibration.

Those expressions of transition probabilities illustrate the probability of potential barrier crossing for given processes. However the transition rules previously introduced above are the expression of spatial positions of each particle. As consequence, for the calculation of time dependence, the whole lattice are scanned through to find the local configurations which coincide with one of the transition rules in Fig.3, then the transition process occurs with respect to those probabilities for each time step. However this algorithm is sequentially carried out until steady state is observed.

3. Result and discussion

By using the above model, surface concentration of OH^-, O^{2-} and Vs are calculated for several conditions of different partial pressure of H_2 and H_2O as sown in Table 1. The result is illustrated in Fig.4, through Fig.6,. Moreover, Fig.4, illustrates the case of the partial pressures are taken as P_{H2O} = 1 Pa, P_{H2} = 100 Pa. It is seen that at transition stage, adsorption of H_2 is dominant since increase of OH^- and decrease of O_2^- occurs at similar rate and the increase of Vs shows the desorption of H_2O is simultaneously occurring. Also at steady state, Vs < O_2^- < OH^- has observed because of adsorption of hydrogen is the most dominant, then desorption of hydrogen is second dominant. Lastly the adsorption and desorption of H_2O comes the least dominant. This fact can obviously seen from the value of the partial pressure and the activation energy of each processes. Secondly, the partial pressures are taken as P_{H2O} = 1000 Pa, P_{H2} = 1000 Pa. It is seen from Fig.5, at transition stage, adsorption of H_2 and H_2O are dominant since rapid increase of OH^-. After some point, the effects of desorption of H_2O and H_2 appears as increase of Vs and decrease of O_2^- respectively. Then Vs < OH^- < O_2^- has been observed at steady state. The partial pressure of H_2 and H_2O is the same value in this case, and so the dominant processes is adsorption of H_2 and H_2O. Then desorption of H_2O comes next. The least dominant process is then desorption of H_2 due to its high activation energy. Thirdly the partial pressures are taken as P_{H2O} = 10000 Pa, P_{H2} = 1 Pa. Rapid increase of OH^- and decrease of O_2^- and Vs are seen from Fig.6,. Very fast decrease of O_2^- and Vs and increase of OH^- shows the adsorption of H_2O is the most dominant in this case. This is obvious since the partial pressure of H_2O is significantly large comparing to that of H_2. It is also seen that the processes are rapidly reaching to the steady state since the rate of adsorption is so fast that sites are immediately occupied after desorption of H_2O and H_2.

4. Conclusions

Cellular Automaton (CA) model for adsorption and desorption of H_2 and H_2O on Li_2O (110) surface is developed in this work. Preliminary calculation is made for the surface concentration of Vs, O_2^- and OH^- are carried out for various partial pressures of the sweep-gas. Those results show a consistency with the chemical model at steady state. However, it is foreseen that inclusion of tritium effect is rather simple in order to estimate the tritium release.

Strictly speaking, in order to clarify the validation of the model, it is necessary to compare the result with other model and/or some experimental result. From this point of view it can be said that this model is still under development. But one clear point that has to be stressed here is the present work provides many insights for the capability of CA to model more complex surface processes.

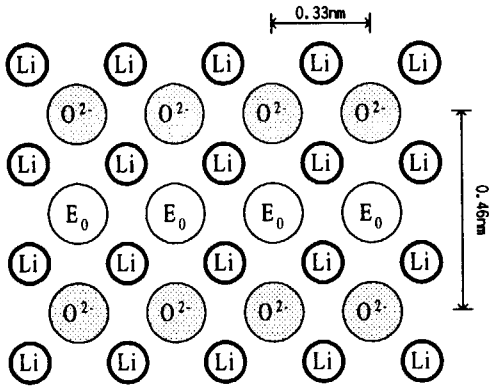


Fig.1, Li_2O (110) surface.

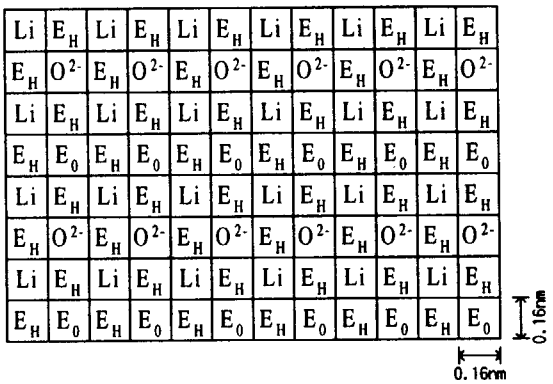


Fig.2, Discretised surface of Li_2O (110).

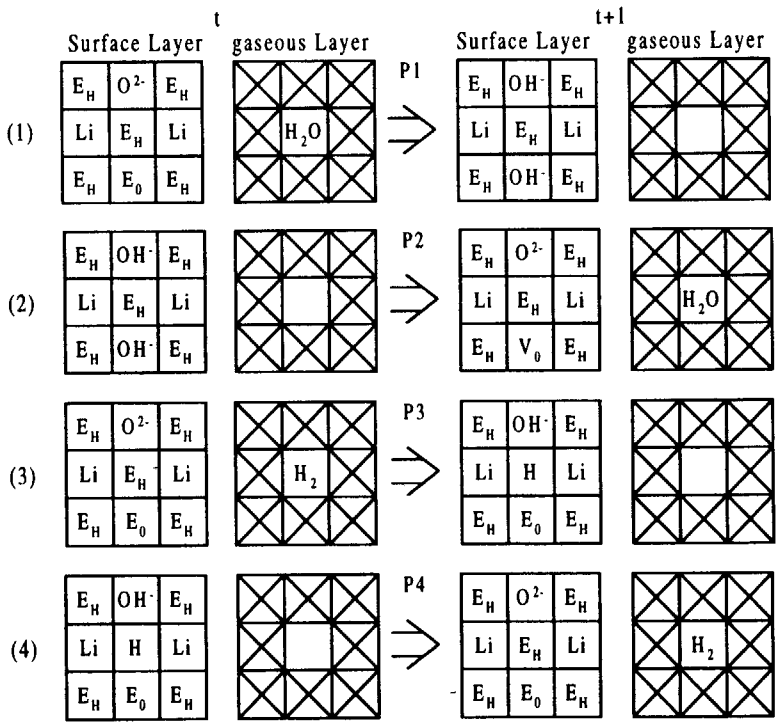


Fig.3, The transition rules of CA for each process. Where t represents the time before the transition, t+1 represents the time after the transition and also P_1 through P_4 represent the transition probabilities. See text for explanation of the symbols.

Table 1. The calculation conditions for this model.

H_2O partial pressure	H_2 partial pressure	Temperature
1 [Pa]	100 [Pa]	773K
1000 [Pa]	1000 [Pa]	773K
10000 [Pa]	1 [Pa]	773K

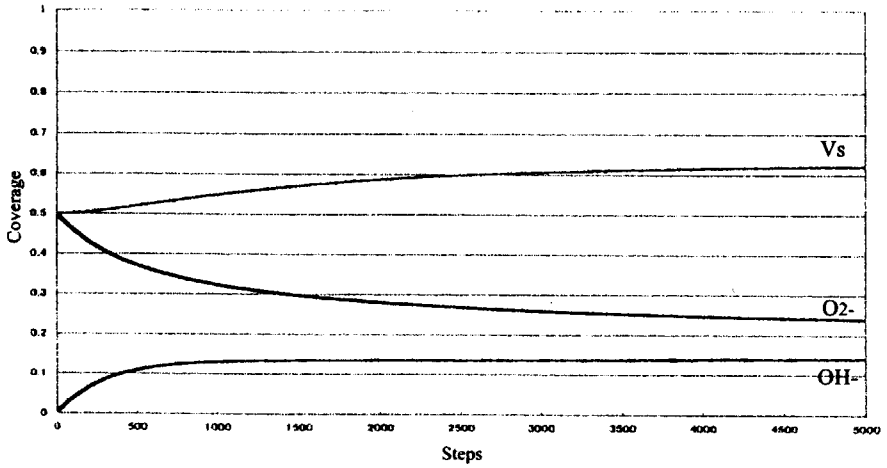


Fig.4, Result of CA calculation for P_{H2O} = 1 Pa, P_{H2} = 100 Pa.

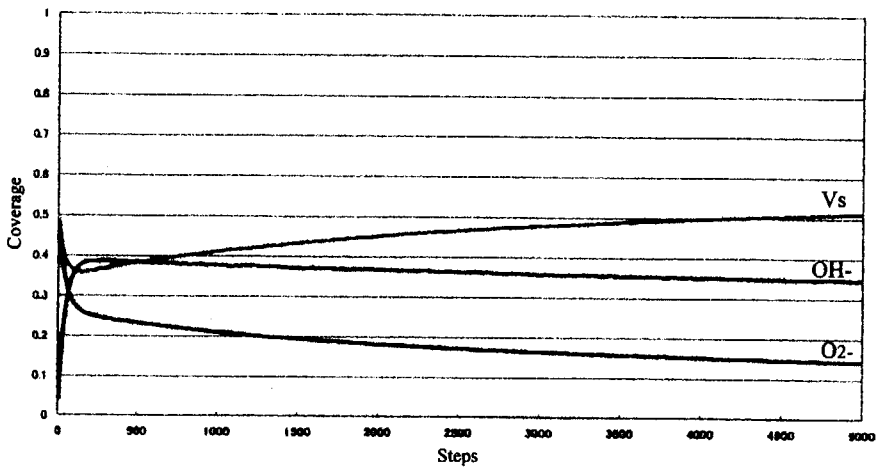


Fig.5, Result of CA calculation for P_{H2O} = 1000 Pa, P_{H2} = 1000 Pa.

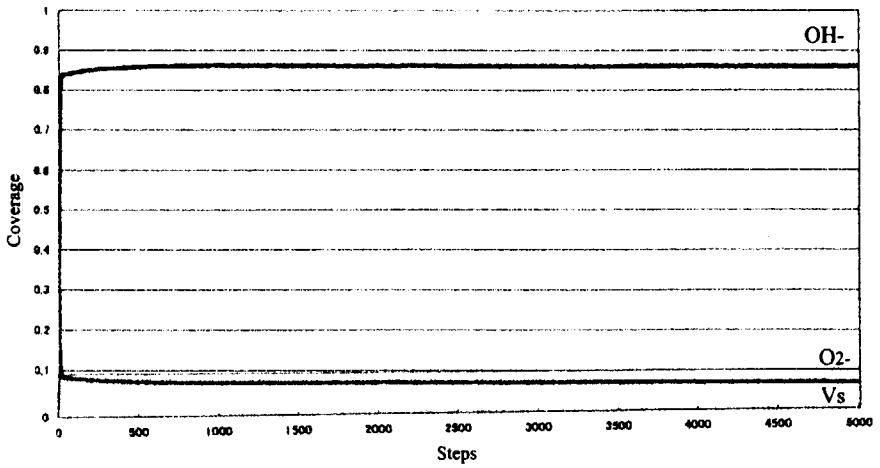


Fig.6, Result of CA calculation for P_{H2O} = 10000 Pa, P_{H2} = 1 Pa.

References

[1] N. Boccara, G.Y. Vichniac, and R. Bidaux, Springer Proceedings in Physics **46**, (1989)

[2] S. Wolfram, *Cellular Automata and Complexity*, (Addison-Wesley, 1994)

[3] D. Yamaki et al., Key Engineering Materials, **83**, 111-112 (1995)

[4] M.Taniguchi et al, Proc. of the 7th International Workshop on Ceramic Breeder Blanket Interaction (CBBI-7), Petten, Netherlands, Sep.14-16, 1998, 6(1999)

JP0350286

2.22 OBSERVATION OF INNER SURFACE OF FLAME-TOWER TYPE REACTOR FOR URANIUM CONVERSION

Ippei Amamoto[12*], Takayuki Terai[1], Hiroshi Umetsu[2]
[1]Dept.of Quantum Engineering and Systems Science, Graduate School of Engineering, University. of Tokyo,2-11-16 Yayoi, Bunkyo-ku, Tokyo (113-8656),Japan
[2]Ningyo-toge Environmental Engineering Center, Japan Nuclear Cycle Development Institute,1550 Kamisaibara-mura,Tomata-gun,Okayama (708-0698),Japan

Abstract

A fluorination reactor, which has been used to convert uranium tetrafluoride (UF_4) into uranium hexafluoride (UF_6), was completed after approximately 6000 hours operation at the uranium conversion facility in Japan. The observation of its inner surface was carried out to understand its corrosive condition and mechanism.

The main wall of the reactor is made of Monel Alloy and its operational temperature is approximately 450 ℃ at external surface under gaseous fluorine atmosphere.

A sampling was undertaken from the most corrosive part of the reactor wall, and its analysis was carried out to obtain the data for the condition of appearance, thickness, macro and micro structure, etc.

The results of observation are as follows:

(1) The thickness decreased evenly (average 3.9 mm/year);

(2)The chemical composition of corrosive products as coating was mainly nickel fluoride (NiF_2), which suggested that the corrosion mechanism could have been caused by the high temperature gas corrosion;

(3)The total amount of coating was lower than that of a loss in thickness. For some reason, some of coating would seem to become extinct on the surface of the wall. The deterioration of coating, which formed a protector on the wall due to excess heating of the wall, the sand erosion effect by UF_4, etc. have contributed to this state of condition.

Keywords: flame-tower type reactor, corrosion, coating, Monel Alloy, uranium conversion

I .Introduction

The uranium hexafluoride (UF_6) conversion test operation was carried out at the refining and conversion facility of Nuclear Cycle Development Institute (JNC, formerly known as the Power Reactor and Nuclear Fuel Development Corporation) from 1982 to 1999. The fluorination volatilization technique that was necessary to operate under the high temperature of fluorine atmosphere was applied to produce UF_6 in this facility. Therefore, Monel Alloy (nickel-30copper alloy) known as a highly corrosion resistance material against the fluorine atmosphere was selected as the reactor's main

Corresponding author, Tel.0868-44-2211
Fax.0868-44-2833
E-mail: amamoto@ningyo.jnc.go.jp

material.

The observation of the aging condition of the reactor material after long period operation offers an interesting study for some engineers who are concerned with the fluorination technology. Some mechanism of a loss in thickness of the reactor material after 6,000 hours fluorination operation was analysed in this paper.

Ⅱ.Outline of Fluorination Reactor

1.Historical Background of Fluorination Reactor

The fluorination reactor, which is the subject of this investigation, is the flame-tower type reactor used at Ningyo-toge Environmental Engineering Centre of JNC. It was built in 1988 and converted natural UF_4 and recycled UF_4 into UF_6 after 6000 hours operation which ended in July 1999.

2.Specification of Fluorination Reactor

The schematic diagram of the fluorination reactor is shown in **Table 1**, and **Fig.1** shows its main specification. This fluorination reactor is a kind of vertical flame-tower type reactor. The gaseous fluorine and UF_4 powder as raw materials were supplied from the top of the reactor. The reaction between fluorine and UF_4 occurred on the way, forming gaseous UF_6, to reach the bottom part of the reactor. As this reaction was a heat generation reaction, a coil-type cooling system was prepared around the reactor' wall. Further more, a jacket-type cooling system, which would be very effective, was set around the third zone of reactor.

Table 1 SPECIFICATION OF FLOURINATION REACTOR

OPERATING TIME	1900hours with the coil-type cooling system 4100hours with the jacket-type cooling system
DIAMETER	ϕ 140 (ID)
HIGHT	3500mm
MATERIAL	MONEL ALLOY400 (Ni-30Cu)
DESIGN THICKNESS	8mm (marsin:5mm)
DESIGN PRESSURE	0.3kgf/cm^{2}G
DESIGN TEMP.	440℃
OPERATING PRESSURE	approx.-600mmH_2O (0.942atm)
OPERATING TENP.	approx. 450℃ (WALL TEMP.)

3.Operational Condition

Fig.2 represents the F_2 fluorination material balance. Nitrogen as the sealing gas was supplied from

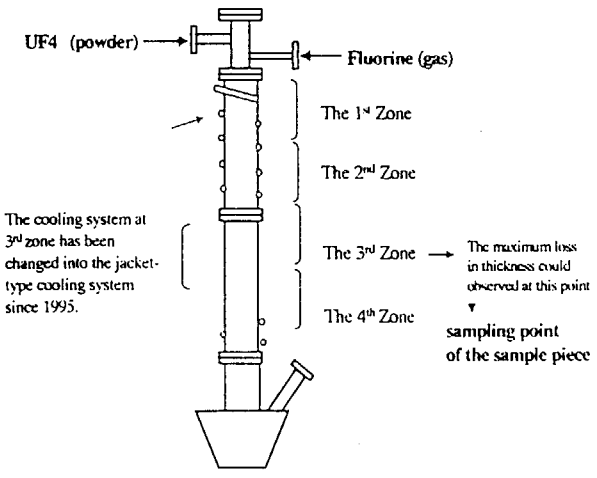


Fig.1 Schematic Design of Fluorination Reactor

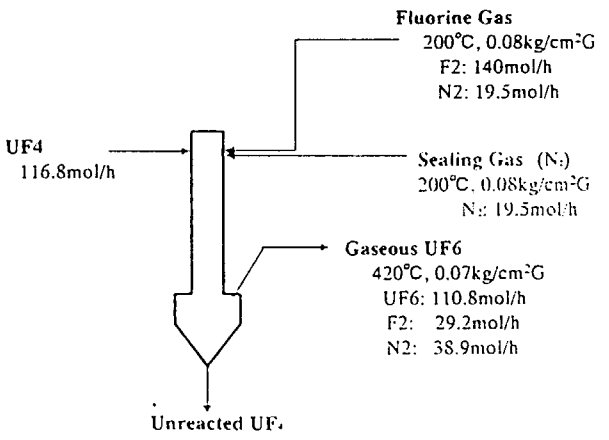


Fig.2 Material Balance of Fluorination Reactor

①, and F_2 and UF_4 were supplied from ② and ③, respectively. The gaseous UF6 as the product by this reaction was discharged through ④ as shown below.

UF4(s) + F2 (g) ⟶ UF6 (g)

Generated UF_6 was then recovered at the cold trap step, and transported to the uranium enrichment facility after filling into the specific cylinders. On the other hand, unreacted UF_4 was recovered from the bottom of reactor.

4. Wall Thickness Measurement

The wall thickness of the reactor, which was measured in 1997, is shown in **Fig.3**. Its corroding condition is considerably correlated with the position of reactor, i.e., the noticeable corrosion can be observed at the third zone of the vertical axis, and E-H of the horizontal axis. **Fig.4** shows the thickness change of the G-line at the third zone. From this figure, vigorous corrosion (approx.11.5mm/year) occurred before the 95-1 campaign. Meanwhile, as the cooling system was changed from the coil-type to the jacket-type because it was regarded as a higher efficiency cooling system after the 95-1 campaign, the G-line was corroded mildly almost the same as other parts of the reactor (approx.1.1mm/year). This phenomena means that the operating temperature would affect the corrosion rate.

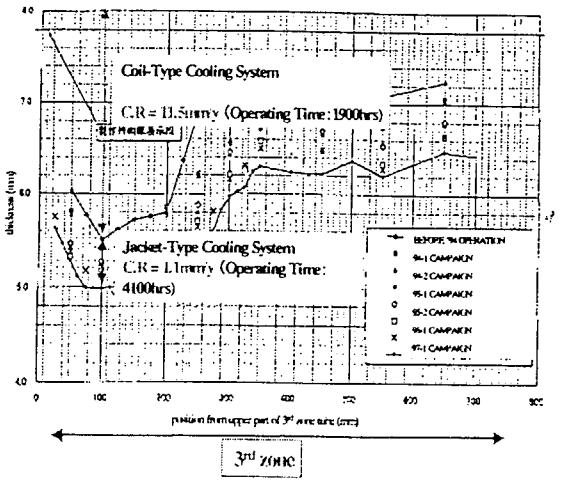


Fig.3 Thickness Measurement of 3rd Zone Tube

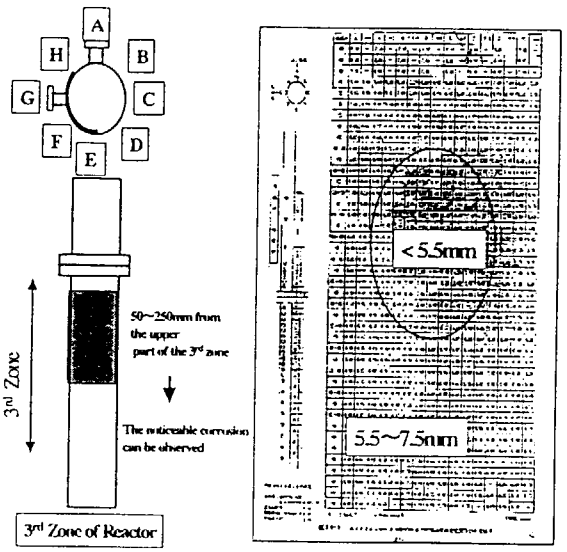


Fig.4 Thickness Change of G-line at 3rd Zone

Ⅲ.Result and Discussion

1.Observation of Sample Piece

The observation of the sample piece obtained from reactor was carried out to clarify the corrosion mechanism. Results of observation were discussed as below:

(1) Damage Condition by Corrosion

The inner surface of sample was covered with white observed. The sample was corroded almost equally and it presented unevenness of surface judging from its section structure. The local corrosion

such as intergranular corrosion or pitting corrosion could not be observed on this sample.

(2) Corrosion Rate

The corrosion rate of this sample is 3.9mm/year average, and 4.1mm/year maximum.

(3) Corrosion Coating Analysis

White coloured coating on the inner surface of sample was nickel fluoride (NiF_2) mainly, and other fluorides compounds from the X-ray diffraction analysis result. This coating could be a product formed as a result of the reaction between Monel Alloy and fluorine gas. The result of Focused Ion Beam (FIB) presents this NiF_2 coating as relatively dense, and the defect such as exfoliation or void could not be observed on the interface between the coating and the base metal (see Fig.5).

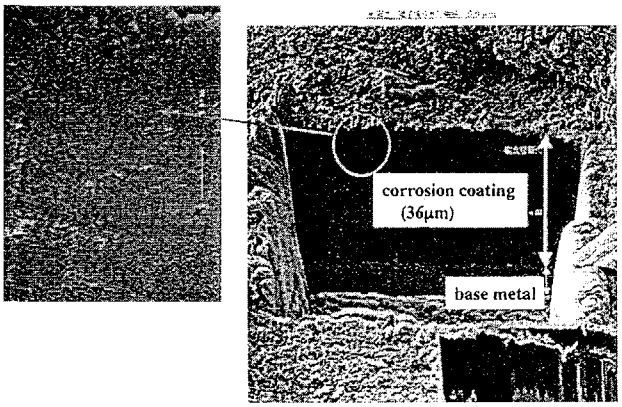


Fig.5 NiF2 Coating Observation with FIB

2. Discussion

From the result of the observation of sample piece, the halogen corrosion was proceeded by fluorine gas in the reactor. The halide surface coating, which is formed by the reaction between gaseous halogen and base metal, generally becomes the protector, which is one of the most important determining factors against corrosion.

The corrosion mechanism of the reactor, especially with regard to NiF_2 as coating is discussed in this paper.

(1) Halide Corrosion

In case of halide corrosion, the behaviour of weight change can be grouped into several patterns as shown in **Fig.6**. When the corrosion coating behaves as a stable protector, the corrosion is progressed by the material diffusion in the coating. As the corrosion rate is in inverse proportion to the thickness of the coating in this case, the weight change presents the curve ① in **Fig.6**, which reaches its equilibrium at some specific time.

Two curve-types, ② and ③, present the weight changes at higher atmospheric temperature. As the formation of coating and its volatilization occurs at the same time, both curves drop as time proceeds. Especially, voids could be formed on the interface between coating and the base metal where the partial pressure of the halogen gas is lower which means halide compounds are easier to volatilize. The curve

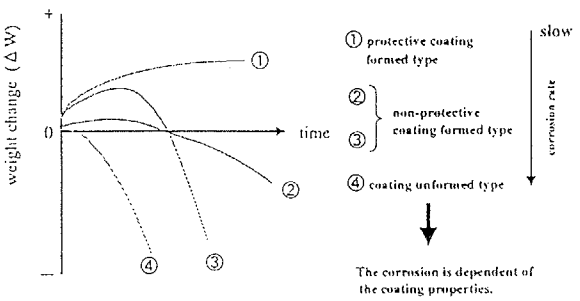


Fig. 6 Several Patterns of Weight Change by Corrosion

④ shows the weight change when the coating volatilizes vigorously.

In general, the behaviour of weight change is apt to shift from ① to ④ with rising temperature, and the higher temperature promotes the deterioration of the coating as a resist.

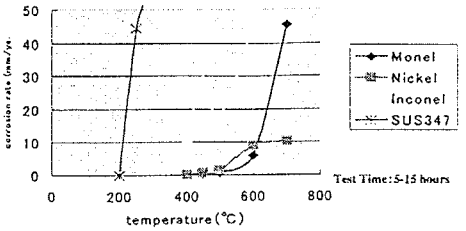
The curve-type ② or ③ of corrosion would occur on the reactor with most of the coating disappearing except for a little of the NiF_2 coating remaining on the inner surface of the sample.

(2) Corrosion Rates of Metals by Fluorine

Fig.7 shows the corrosion rates of various kinds of metals due to the effect of fluorine gas.

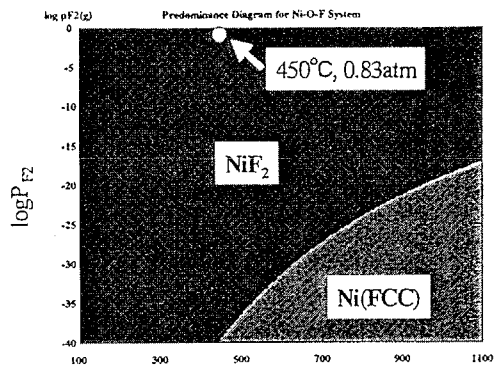
Fluorine gas reacts with many metals even at the room temperature and forms fluoride coatings. As the fluorides coatings are basically very stable in the range of low temperature, their corrosion rates are slow. However, the coating, as a protector, becomes worse in the range of high temperature, nickel or nickel-alloy, which is known to be a higher corrosion-resisting metal against fluorine, was used at 350℃, or more. Monel Alloy is the strongest material up to 600℃ in **Fig.7** Its corrosion rate is <0.5mm/year under 500℃, however, it increased to 6mm/year at 600℃ because of the deterioration of its coating as a resist.

Though Monel alloy as the reactor's main material was expected to have sufficient corrosion resistance, at an operation temperature of 450℃, its corrosion occurred vigorously and the corrosion rate was 3.9mm/year.



W.R.Meyer and W.B.Delong: Chem. Eng. Progr., 44, 359 (1948)

Fig.7 Corrosion Rates of Various Kinds of Metals due to Effect of F2



P_{F_2} (F_2 partial pressure) = operating pressure(atm) × mole fraction rate (F_2)
= 0.942 × 140/ 159.2 = 0.83 (atm)

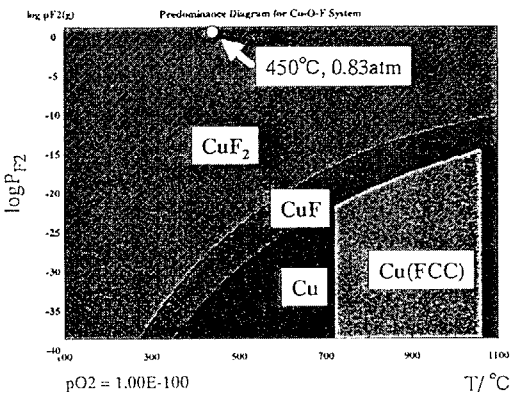


Fig.8 Relation between Stable Phase of Ni and Cu and Temperature at F_2 Atmosphere

(4)Thermodynamic Consideration of Fluoride Coatings

The thermodynamic analysis was carried out for some fluoride coatings as the corrosiveness of materials in fluorine gas atmosphere was closely connected with the stability of fluoride coatings.

(a)Consideration on Stable Phase of Coating in Fluorine Gas Atmosphere

The relation between the stable phase of nickel and copper and the temperature in fluorine

atmosphere is shown in **Fig.8** (pO_2=1.0×10^{-100}atm).

If oxygen partial pressure is very low, NiF2 or CuF2 can form a stable phase of fluoride at around 450℃. As the fluorine partial pressure in the reactor is P_{F2}=0.942(operational pressure)×140/159.5 (mole fraction) = 0.83 atm ($\log P_{F2}$=－0.08), the formation of coating such as NiF_2 or CuF_2 is estimated on the surface of Monel Alloy.

(b)Standard Gibbs Energy of Formation of Fluorides

The reaction formula of metal and gaseous halogen is generally presented as below:

$$M + (n/2)X_2 \longrightarrow MXn$$

If the value of ΔG^0/kJmol^{-1} (=RTlnP_{X2}) denoted the standard Gibbs energy of formation for above mentioned formula is smaller, the dissociation pressure of product becomes lower which means the product forms a rather stable phase.

Fig.9 shows the typical metals' standard Gibbs energy of formation of Fluorides. From this figure, those metals form the stable fluoride compounds in order Al>Cr>Fe>Ni>Cu at 450℃ which is the operational temperature. From this point, NiF_2 would seem to be a more stable fluoride than CuF_2.

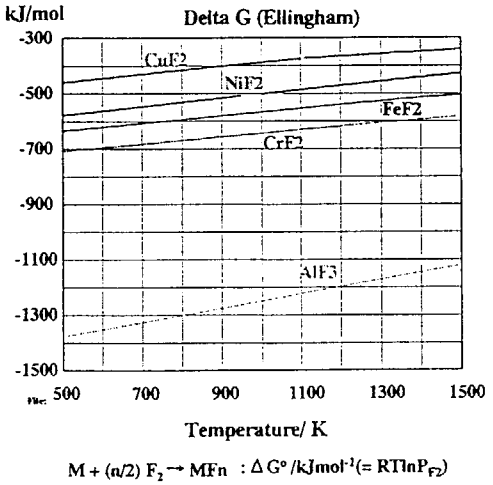


Fig.9 Standard Gibbs Energy of Formation of Fluorides

(c) Reaction Products in Reactor

The thermodynamic calculation result of the reaction products in the reactor is shown in **Fig.10**. The fluorine gas tended to react with nickel preferentially in a wide range of the temperature (from room temperature to over 800℃), and formed NiF_2. Although the whole fluorine was consumed by the reaction with nickel in this simulation, fluorine would react with UF_4 and produce UF_6 after forming the NiF_2 coating during the real operation. However, when the NiF_2 coating came off for some reason, Monel Alloy would be corroded by fluorine again.

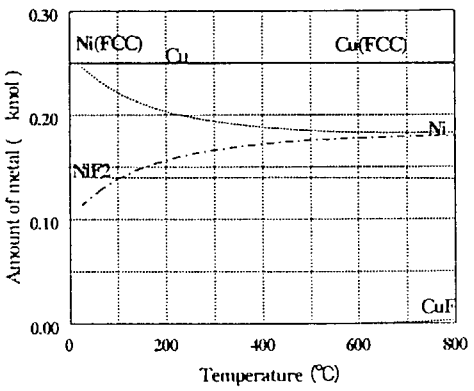


Fig.10 Thermodynamic Calculation of Reaction Products in Reactor

Ⅳ.Conclusion

This fluorination reactor was expected to maintain good corrosion resistance at the operating temperature of 450℃ after forming the NiF2 coating on the surface of Monel Alloy which is

the main material of the reactor. However, severer corrosion was observed which indicated that there may be other factors that promoted this corrosion.

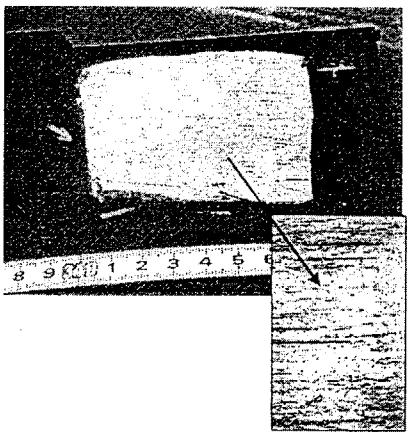
Two potential factors could be found from the results of observation:

(1) Rise in Wall Temperature

The corrosion rate proceeded obviously during the use of the coil-type cooling system. However, it slowed down after the jacket-type cooling system was used, which suggested the reactor wall temperature is one of the determining factors responsible for the corrosion rate. The corrosion rate of Monel Alloy rose rapidly at over 500℃ as shown in **Fig.7**. If the coil-type cooling system had not worked sufficiently well during fluorination, corrosion would have accelerated with the rise in the wall temperature.

(2) Erosion

The damage cases by sand-erosion can often be found on some equipments, which handled particles such as UF_4 in the gaseous atmosphere. The damage rate by sand erosion is apt to be higher than ordinary erosion, and this trend would be more obvious at higher temperature. Especially in the corrosive atmosphere such as the gaseous halogen, if the resisting coating on the surface of the material is damaged by erosion, corrosion would accelerate due to the erosion-corrosion.



* The white coating could be seen on the inner surface of sample piece.

* The scratch marks could be observed on the sample piece.

Fig.11 Observation Inner Surface of Sample Piece

As remarkable damage could be observed at the specific position of the reactor (the third zone), erosion would work partially by the drift. Furthermore, as the vertical lines on the NiF_2 coating of the sample are the scratch marks in the direction of the flow of UF_4, the coating would be eroded (see Fig.11).

With due consideration, some countermeasures should be taken to maintain the safe condition of a fluorination reactor such as a better wall cooling system i.e. jacket-type cooling system, etc., drift control by the inner fluid analysis, wall thickness measurement with a heat-resisting ultrasonic probe, and so on.

Acknowledgement

The authors wish to thank Mr. N.Okuyama (Toyo Engineering Corp., Chiba, Japan) and Mr.M. Nonura (JNC,Okayama,Japan) for their helpful advice on these analysis.

References

[1] E.L.Liening, "Material of Construction for the Halogens", Process Industries Corrosion,315
[2] T.F.Degnan, "Material of Construction for the Hydrofluoric Acid and Hydrogen fluoride", Process Industries Corrosion, 275
[3] D.M.Hise, " Corrosion from the Halogens", NACE Chemical Industries
[4]C.M.Schillmolller, "Select the Right Alloy for Hydrofluoric Acid Service",Chemical Engineering Progress,Vol.144,No.5,259
[5] Mars G.Fontana, "CORROSION ENGINEERING", McGraw Hill
[6] Mars G.Fontana, "CORROSION SCIENCE AND TECHNOLOGY" Vol.5.Chapter 2, McGraw Hill
[7]H.Umetsu, I. Amamoto, et al., "Observation of Internal Condition of UF_6 Conversion Reactor (1)", Proc.2001 Fall Meeting of the Atomic Energy Society of Japan, Sapporo, Japan, Sept.19-21, 2001,651
[8] O.Takanobu, I. Amamoto, et al., "Observation of Internal Condition of UF_6 Conversion Reactor (2)", Proc.2001 Fall Meeting of the Atomic Energy Society of Japan, Sapporo, Japan, Sept.19-21, 2001,652

JP0350287

2.23 STUDY ON SYNTHESIS TECHNIQUE AND THERMAL ANALYSIS OF Na-Fe COMPLEX OXIDES

Futaba Ono[1*], Masahisa Tonegawa[1], Takayuki Terai[1], Michio Yamawaki[1], Tomohiro Furukawa[2], Fumiyoshi Ueno[2], and Kazumi Aoto[2]

[1] Department of Quantum Engineering and System Science, Graduate School of Engineering, The University of Tokyo, 7-3-1 Hongo, Bunkyo-ku, Tokyo, 113-8656, JAPAN

[2] Advanced Material Research Gr., Advanced Technology Div., O-arai Engineering Center, Japan Nuclear Cycle Development Institute, 4002 Narita, O-arai, Ibaraki, 311-1393, JAPAN

Abstract

As a coolant of Fast Breeder Reactors, sodium reacts with oxygen and moisture in air at elevated temperature. And it is known that structural material is damaged by its by-products. Although the reliable thermodynamic data of Na-Fe complex oxides was needed in order to clarify the corrosion mechanism and to examine the technique of corrosion protection, each data is different by researchers. In this study, synthesis technique of high purity Na_4FeO_3 as one of Na-Fe complex oxides under low oxygen potential has been established in order to get reliable thermodynamic data. For synthesis, the following reaction was used; $2Na_2O + FeO = Na_4FeO_3$ (ΔH_{298K}=104.49kJ/mol) in a sealed up vessel at 873K for 100h. Na_2O reagent used was refined at 973K for about 1h in vacuum, where impurity (Na_2O_2) in the reagent was decomposed. In order to keep low oxygen potential in the vessel, mixture of Na_2O and FeO was filled up in the vessel by applying vibration. X-ray diffraction patterns were taken in nitrogen environment to identify the reaction product, and it was confirmed that pure Na_4FeO_3 crystal was obtained.

In addition, thermal analysis of the samples has been performed by using a differential scanning calorimeter to determine the melting point and to check a possibility of another phase transformation. The sealed up sample holder made of platinum was used for the analyses. From the analyses, the melting point of Na_4FeO_3 was determined to be 1,008±15K.

Keywords: Na-Fe complex oxides, Na-Fe-O system, FBR, Sodium, Sodium Oxides

1. Introduction

In the case of sodium leakage from secondary circuit of FBRs, sodium reacts with oxygen and moisture in air, and the structural material is damaged by its by-products.

* Corresponding author. Tel:+81-29-287-8456 Fax:+81-287-8458

E-mail address: ono@tokai.t.u-tokyo.ac.jp

It is reported that the corrosion mechanism of the material depends on oxygen potential and humidity in the environment, and that two corrosion mechanisms have been reported until now [1], [2]. In order to clarify the corrosion mechanism in detail and to examine the development of protection method against corrosion, it is needed to obtain reliable thermodynamic data of corrosion products, i.e. Na-Fe complex oxides. However, reported data of the compounds are different and scattered depending on the authors [3],[4],[5]. According to Dai et al [5], Na_4FeO_3, which is stable under low oxygen potential in Na-Fe-O system, decomposes at 904±8K. However, according to the authors' previous observation on the reaction between Na_2O and Fe [6], solidification of Na_4FeO_3 occurred at about 950K. Thus the melting point of Na_4FeO_3 seems to be higher than that of Dai et al [5].

In this study, in order to obtain reliable thermodynamic data of Na_4FeO_3, development of the synthesis technique as well as thermal analysis has been performed on this complex oxide.

2. Experiments

2.1 Synthesis of Na_4FeO_3

Na_2O and FeO were used as starting materials for the synthesis of Na_4FeO_3. The purity of the starting materials is shown in Table 1. In order to synthesize high purity complex oxide, Na_2O reagent was refined by annealing at 973K for 1h in vacuum. This is because the dominant impurity in Na_2O reagent was Na_2O_2;

$$Na_2O_2(s) \rightarrow Na_2O(s) + \frac{1}{2}O_2(g) \qquad (1)$$

Table 1 Purity of the reagents

Reagent	Purity (%)	Manufacturing Company
Na_2O	>86.57	Atomergic Chemetal Corp.
FeO	99.9	Kojundo Chemical Laboratry Co. Ltd.
FeO	99.5	Rare Metallic Co. Ltd.

The mixing of Na_2O and FeO was performed in an Ar glove box under O_2 concentration<1ppm and dew point<193K. In this study, the following reaction was used for the synthesis:

$$2Na_2O(s) + FeO(s) = Na_4FeO_3(s) \qquad \Delta H_{298K} = -104.49\,kJ/mol \qquad (2)$$

The mixture of Na_2O and FeO was inserted in a quartz tube, and then heated up in an electric furnace. An example of the apparatus is shown in Fig. 1. The reaction temperature

was fixed at 873K according to preliminary tests, and synthesis time was examined based upon the results of X-ray diffraction (XRD) tests of the samples after the tests. In order to decide the best condition for the synthesis, three methods, "Ar gas flow", "in vacuum" and "air-tight", were carried out. In Ar-gas-flow and in-vacuum methods, the samples were compressed using a hydraulic jack to keep the low oxygen potential inside the sample during runs. In air-tight method, the sample was filled up in the air-tight vessel by means of vibration. In these experiments, the volume of the sample is considered as a testing parameter. After the synthesis, XRD analysis was performed on the samples kept in nitrogen.

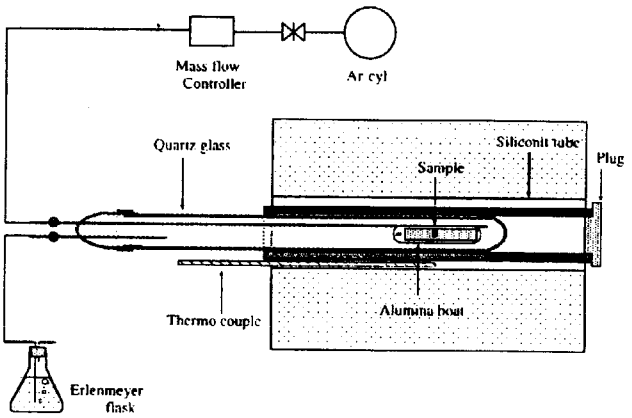
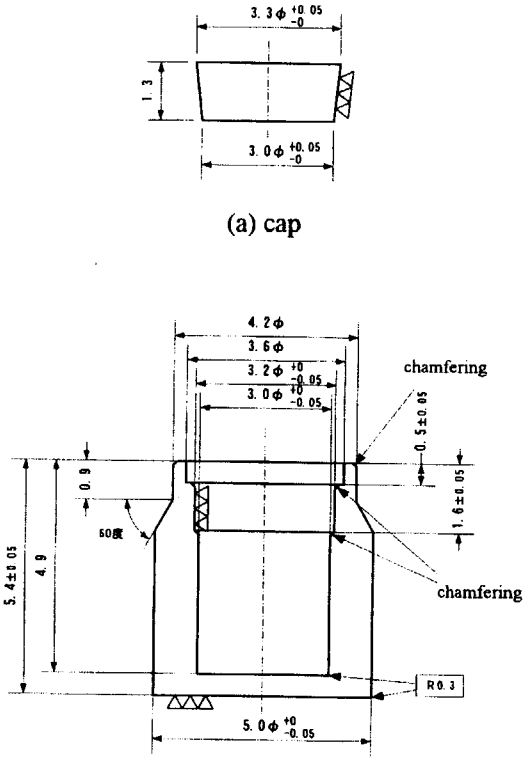


Fig. 1 Apparatus for synthesis of Na-Fe complex oxides



(a) cap

(b) body

Fig. 2 Sample holder

2.2 Thermal Analysis

Thermal analysis of the samples has been performed using a differential scanning calorimeter (DSC), Type Modified DSC8270, manufactured by Rigaku Corporation in order to obtain the melting point and examine phase transformation. The sample holder used was air-tight and made of platinum (Fig. 2), and filling the sample and sealing were performed in the glove box. In examining the effect of the oxygen potential in the sample holder, the volume of the sample was changed as a testing parameter. The heating rate was fixed to 2-10K/min.

3. Results and Discussions

3.1 Synthesis of Na_4FeO_3

The XRD results for the three methods are shown in Table 2. In the "Ar flow" and

"in vacuum" methods, Na_5FeO_4 and Na_3FeO_3 etc. with 3+ iron oxides were detected as the dominant components, while Na_4FeO_3 was not detected. From these results, it was considered that, although the samples were compressed in order to keep low the oxygen potential, the oxygen potential was not sufficient to form Na_4FeO_3, so that sodium was evaporated from the sample, in the case of the Ar flow and in-vacuum methods. On the other hand, Na_4FeO_3 was detected in both cases of the air-tight methods. While other complex oxides coexisted in case of the airtight- with -Ar method, only Na_4FeO_3 formed in case of the no-gas-airtight method. This seems to be because the Ar gas included a small amount of oxygen as impurity.

Table 2 Result of Na_4FeO_3 Synthesis tests

	Na_4FeO_3	Na_5FeO_4	Na_3FeO_3	$Na_{31}Fe_8O_{29}$
Ar Flow			++	+
In vacuum		++	+	++
		+		++
Airtight with Ar	+	+		++
Airtight (no gas)	+++			

* Intensity ; (+++) > (++) > (+)

3.2 Thermal Analyses

The XRD results after DSC analyses are shown in Fig. 3.

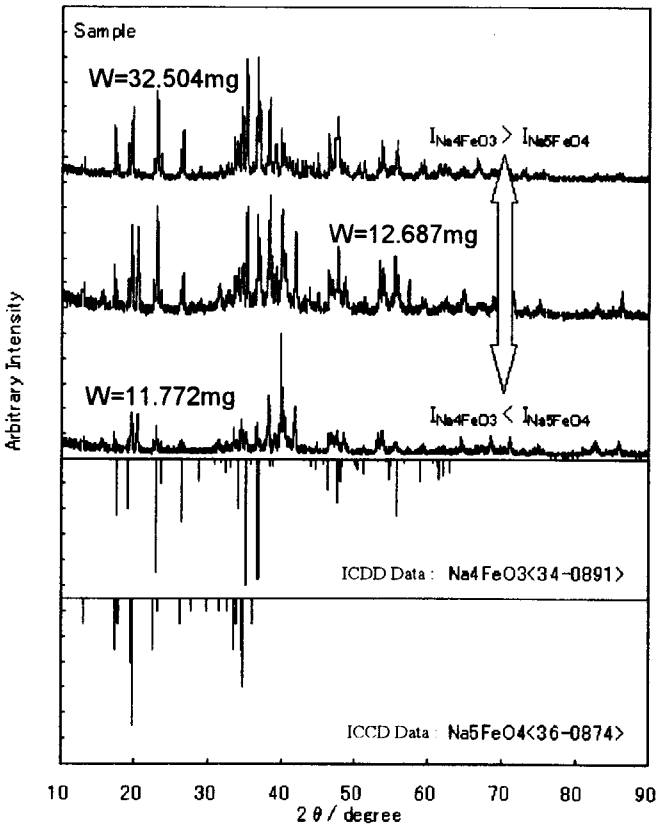


Fig. 3 XRD results after DSC analyses

The X-ray intensity ratio of Na_4FeO_3 to Na_5FeO_4 exhibited in Fig.3 can be attributed to the amount of sample filled in the sample holder, where, the larger the amount of sample, the more Na_4FeO_3 formed. The DSC curve for the case of the largest amount sample filling

is shown in Fig. 4. Even in this case, a small amount of Na_5FeO_4 coexisted as shown in Fig.3 which may suggest that it would be very difficult to get completely pure Na_4FeO_3 by this method. By comparing with the result of small sample amount case, it seems that a large peak at about 1,010K in the temperature rising curve shows the melting point of Na_4FeO_3, while another the peak at about 950K seems to be attributed to a transformation or solidification temperature of Na_5FeO_4.

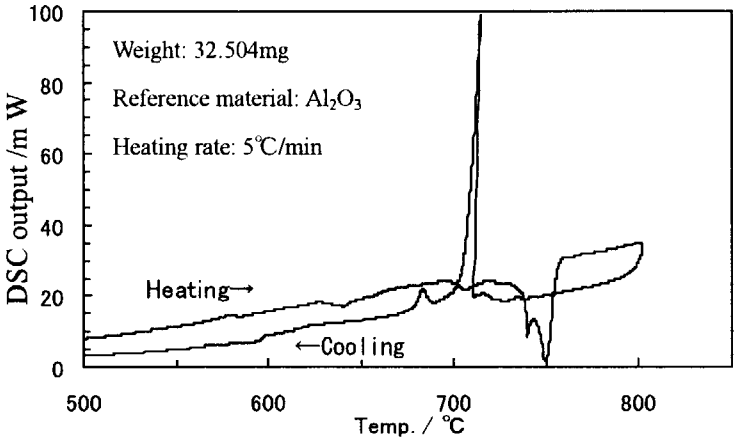


Fig. 4 DSC curve of Na_4FeO_3

In order to confirm whether the peak at about 1,010K is the melting point of Na_4FeO_3, a larger airtight container with less oxygen potential effect upon the melting point measurement was manufactured, and a melting point measurement test was performed by using this container. The observed temperature change of the container, the photograph of the sample and the XRD test result are shown in Figs. 5, 6 and 7, respectivery. The trace of melting was clearly observed in Fig.6, while XRD result showed that Na_4FeO_3 did not change to another compound during the test. Also, Fig.5 shows peaks corresponding to a phase change to occur at 1008K. Based on these results, the melting point of Na_4FeO_3 has been decided to be 1008 ± 15K.

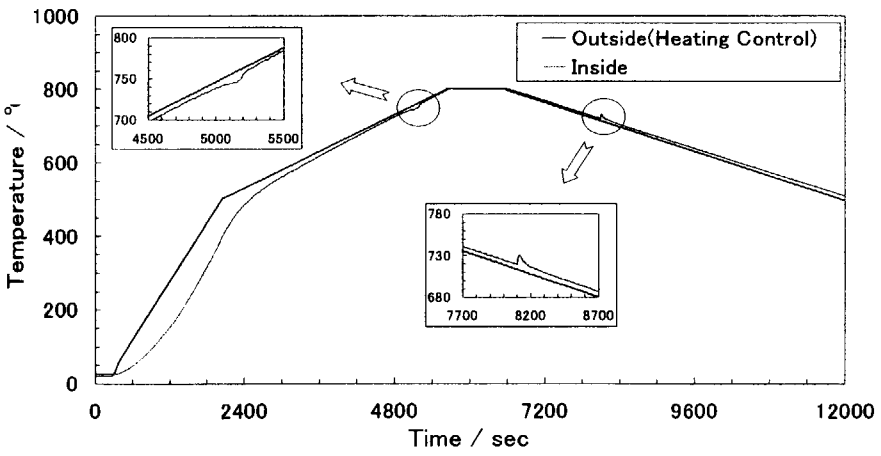
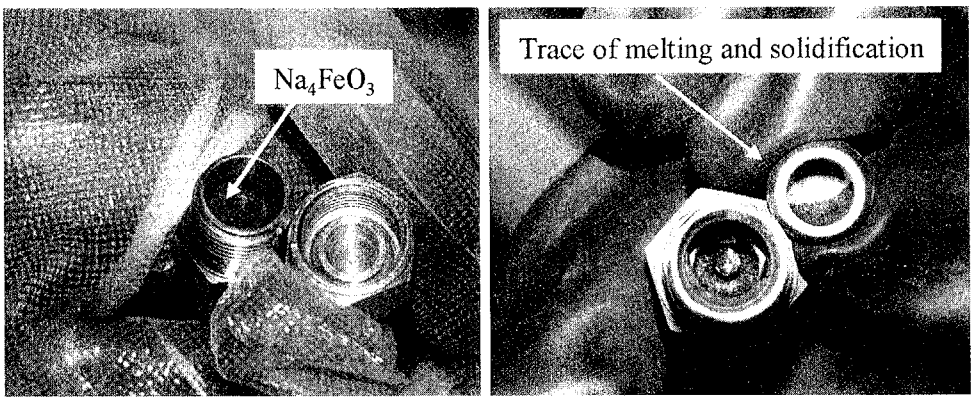


Fig. 5 Temperature change behavior of airtight container



(a) Before the test (b) After the test

Fig. 6 Photographs of the sample in the container

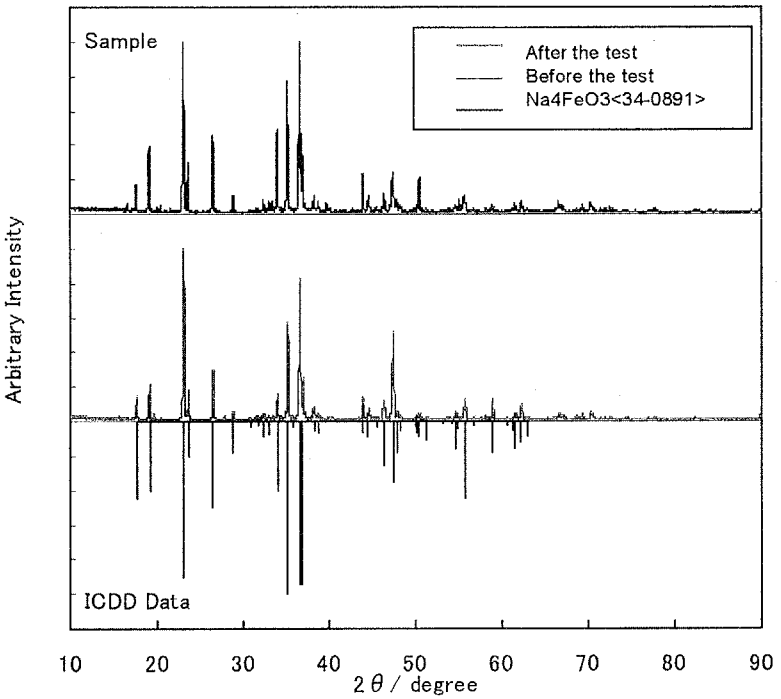


Fig. 7 XRD results of the sample

4. Conclusions

(1) Three methods were performed to synthesize high purity Na_4FeO_3. Nearly pure Na_4FeO_3 crystal can be synthesized with the method named "airtight without Ar". It can be said that it is vitally important to exclude oxygen-containing Ar gas for synthesis of pure Na-Fe-O complex oxide.

(2) In order to obtain reliable thermodynamic data, thermal analysis of Na_4FeO_3 was carried out using DSC. From the measurement, it is concluded that the melting point of Na_4FeO_3 is 1,008±15K.

References

[1] W.Ito et al., Journal of the Atomic Energy Society of Japan, vol.39, p.704-732 (1997) <in Japanese>

[2] K.Aoto, Proceedings of the Symposium on High Temperature Corrosion and Material Chemistry, 98-9, p.287-298 (1998)

[3] G.W.Horslay, Journal of the Iron and Steel Institute, p.43-48 January (1956)

[4] M.G.Barker and D.J.Wood, Journal of the Less-Common Metals 35, p.315-323 (1974)

[5] W.Dai et al., Metallurgical Transaction B Vol.15B, June (1984)

[6] T.Furukawa et al., Proceedings of the Symposium on High Temperature Corrosion and Material Chemistry, 98-9, p.312-323 (1998)

[7] K.Aoto et al., Proceedings of the Symposium on High Temperature Corrosion and Material Chemistry, 98-9, p.275-286 (1998)

JP0350288

2.24 DEVELOPMENT OF SSRT FACILITY WITH ABILITY OF IN-SITU OBSERVATION DURING SCC TEST IN HIGH TEMPERATURE WATER FOR IRRADIATED MATERIALS

J. Nakano[1]*, T. Tsukada[1], M. Kikuchi[1], Y. Kaji[1], H. Ugachi[1], Y. Miwa[1],
S. Terakado[2], T. Kohya[2], N. Mita[2], S. Endo[2]and H. Tsuji[1]
[1]Department of Nuclear Energy System and [2]Department of Hot Laboratories
Japan Atomic Energy Research Institute (JAERI),
Tokai-mura, Naka-gun, Ibaraki-ken, 319-1195, JAPAN

Abstract

Irradiation assisted stress corrosion cracking (IASCC) is one of the key issues for the life management of light water reactor (LWR) core components as well as one of the possible degradation phenomena of structural materials of international thermonuclear experimental reactor (ITER). For understanding IASCC phenomenon, development of slow stain rate test (SSRT) facility with ability of in-situ observation during SSRT in high temperature water for irradiated materials was initiated. The SSRT facility, which has already been installed in a hot cell, consists of a water make-up system, a pressurized high temperature water circulation system, a tensile testing system with an autoclave, a monitoring/purification system, a hydrogen peroxide injection system, and an observation/recording system. The autoclave has a sapphire window for in-situ observation of the specimen. Images through the window can be recorded using the CCD camera system. Since the SSRT facility is designed for irradiated materials under boiling water reactor (BWR) condition, the maximum operational parameters are as follows ; temperature : 573 K, pressure :10 MPa and flow rate : 30 ℓ /h. To simulate the normal water chemistry (NWC) and hydrogen water chemistry (HWC) under BWR environment, dissolved oxygen and hydrogen concentrations (DO and DH) can be controlled within the range of 10 ppb - 32 ppm and 10 ppb - 2.8 ppm, respectively. Hydrogen peroxide can be injected into the autoclave to simulate influence of

*Corresponding author . Tel : +81-29-282-5348 Fax : +81-29-282-5349
E-mail address : lantis@popsvr.tokai.jaeri.go.jp

hydrogen peroxide produced from radiolysis of water in the reactor core.

Keywords: in-situ observation, IASCC, SSRT, high temperature water, Post Irradiation Examinations, Hot Laboratory

1. Introduction

Irradiation assisted stress corrosion cracking (IASCC) is caused by synergistic effects of neutron irradiation, stress/strain and high temperature water on structural materials. IASCC is one of the key issues for the life management of light water reactor (LWR) core components and is concerned as one of the possible degradation phenomena of structural materials of international thermonuclear experimental reactor (ITER). In study of SCC, slow strain rate test (SSRT) in corrosive environment has often been applied, and in-situ observation technique during SSRT for non-irradiated materials have been reported[1-2]. The phenomenon during SSRT includes both the crack initiation and the crack growth stages. To isolate the crack initiation stage from the crack growth stage will be very useful for understanding the IASCC phenomenon thoroughly. Hence development of in-situ observation technique during SSRT for irradiated materials was initiated.

2. Specification of the SSRT facility

Fig. 1 shows schematic flow diagram of the SSRT facility which has already been installed in a hot cell. As seen Fig. 1, the SSRT facility consists of (A) a water make-up system, (B) a pressurized high temperature water circulation system, (C) a tensile testing system with an autoclave, (D) a monitoring/purification system, (E) a hydrogen peroxide injection system and (F) an observation/recording system. Location of the SSRT facility in the hot cell is shown in Fig. 2. Fig. 3 shows the autoclave with a sapphire window for in-situ observation of the specimen. Images through the window can be recorded using the CCD camera system. Since the SSRT facility is designed for irradiated materials under boiling water reactor (BWR) condition, the maximum operational parameters are as follows ; temperature : 573 K, pressure :10 MPa and flow rate : 30 ℓ/h. To simulate the normal water chemistry (NWC) and hydrogen water chemistry (HWC) under BWR environment, dissolved oxygen and hydrogen concentrations (DO and DH) can be controlled within the

range of 10 ppb – 32 ppm and 10 ppb - 2.8 ppm, respectively[3-4].

In the water make-up system, the levels of DO and DH are controlled by bubbling of oxygen/helium and hydrogen/helium mixture gas and pure helium gas into the treatment tank which has a volume of 100 ℓ. High purity water from the treatment tank is pressurized by high pressure pump and sent into equipments in the hot cell. The water is heated by preheater and heater at the autoclave. Since heat affects wall of the cell, the water is sent to outside of the cell after cooling. The autoclave has a volume of 1.77 ℓ and clutch sealing mechanism which can be opened and shut easily using manipulators. In tensile testing mechanism, maximum load is 20 kN and range of cross head speed is 1×10^{-7} to 10 mm/min.

The monitoring/purification system consists of filters, ion exchangers and water chemistry monitoring equipments. After depressurizing, the water from the hot cell is monitored the water chemistry i.e. conductivity, DO, DH and pH. By changing monitoring line, the water chemistry of inlet water also can be monitored. A crud filter traps solid particles in the water and ion exchanger fixes dissolved ions in itself to keep low conductivity (< 0.1 μS/cm). The purified water returns the treatment tank. Hydrogen peroxide can be injected into the autoclave to simulate influence of hydrogen peroxide produced by radiolysis of water in the reactor core. To suppress decomposition of hydrogen peroxide by contact with metal surface, a poly tetra-fluoro-ethylene (PTFE) inner liner was used[5-6].

Fig. 4 shows the observation/recording system. Since SSRT takes long test period, the images during SSRT can be taken by timer and recorded automatically. CCD camera, camera stand and light are equipped in the hot cell. Images taken by the CCD camera are reproduced on the monitor outside the hot cell and recorded. The equipments put in the hot cell are designed to be easy to be operated by manipulators.

3. Safety issues and countermeasures

Since installation in a hot cell and using of irradiated specimen, the facility has the safety mechanisms which work by detecting unusual conditions. Main safety issues and countermeasures are as the following.

· Overheating : In the case of overheating of heater at autoclave and preheater, electric power to them is cut, though electric power to cooling unit, which removes heat from water before

passing through the wall of the hot cell, is not cut to remove the heat promptly.

·Excess pressure : In the case of excess pressure, all heaters and pumps are stopped. If pressure in the system increase further by remaining heat, the pressure will be remove from safety valves.

·Hydrogen leakage : Since the facility has an ability of hydrogen addition, hydrogen leakage is concerned. Treatment tank and hydrogen gas cylinder are covered with explosion prevention cases, and hydrogen leakage sensors are installed inside the cases. When the sensor detected hydrogen during SSRT, supply of hydrogen will be stopped. Hydrogen after bubbling is exhausted through a vent on the treatment tank to ventilation system of the hot facility usually.

·Water leakage : To avoid water leakage, open/shut part of the autoclave has a structure of double O-ring. Water leakage sensors are equipped under the pressurized water line, and the whole system is stopped by sensing of water leakage.

·Oil leakage : A sensor for oil level of high pressure pump is equipped, and the whole system is stopped by sensing of oil leakage.

·Electricity failure : In the case of short electricity failure (< 3 s), whole system is recovered by electric power from a backup battery automatically and SSRT can be continue. In the case of long electricity failure ($\geqq$ 3 s), a load to the specimen is removed automatically and the whole system is stopped.

4. Future scope

At present, the facility is treated prefilming to lower the conductivity (< 0.1 μS/cm) of the water. After keeping the low conductivity, in-situ observation during tensile test for unirradiated material will be performed as a trial test. After the test, in-situ observation during SSRT for irradiated material will be performed. Based on images from in-situ observation, it is expected to isolate the crack initiation stage form the crack growth stage during IASCC test.

References

[1] T. Shibata and T. Haruna, Zairyo-to-Kankyo, Vol. 41, p. 809-815, (1992).

[2] J. Tani, H. Hirano and S. Kato, Komae Research Laboratory Rep. No. T97014, Central

Research Institute of Electric Power Industry, (1998).

[3] H. Hirano, Zairyo-to-Kankyo, Vol. 48, p. 747-752, (1999).

[4] S. Suzuki, Zairyo-to-Kankyo, Vol. 48, p. 753-762, (1999).

[5] C.C. Lin, F. R. Smith, N. Ichikawa, T. Baba and M. Itow, International Journal of Chemical Kinetics, Vol. 23, p. 971-987, (1991).

[6] S. Uchida, N. Shigenaka, M. Tachibana, Y. Wada, M. Sakai, K. Akamine and K. Ohsumi, Journal of Nuclear Science and Technology, Vol. 35, No.4, p. 301-308, (1998).

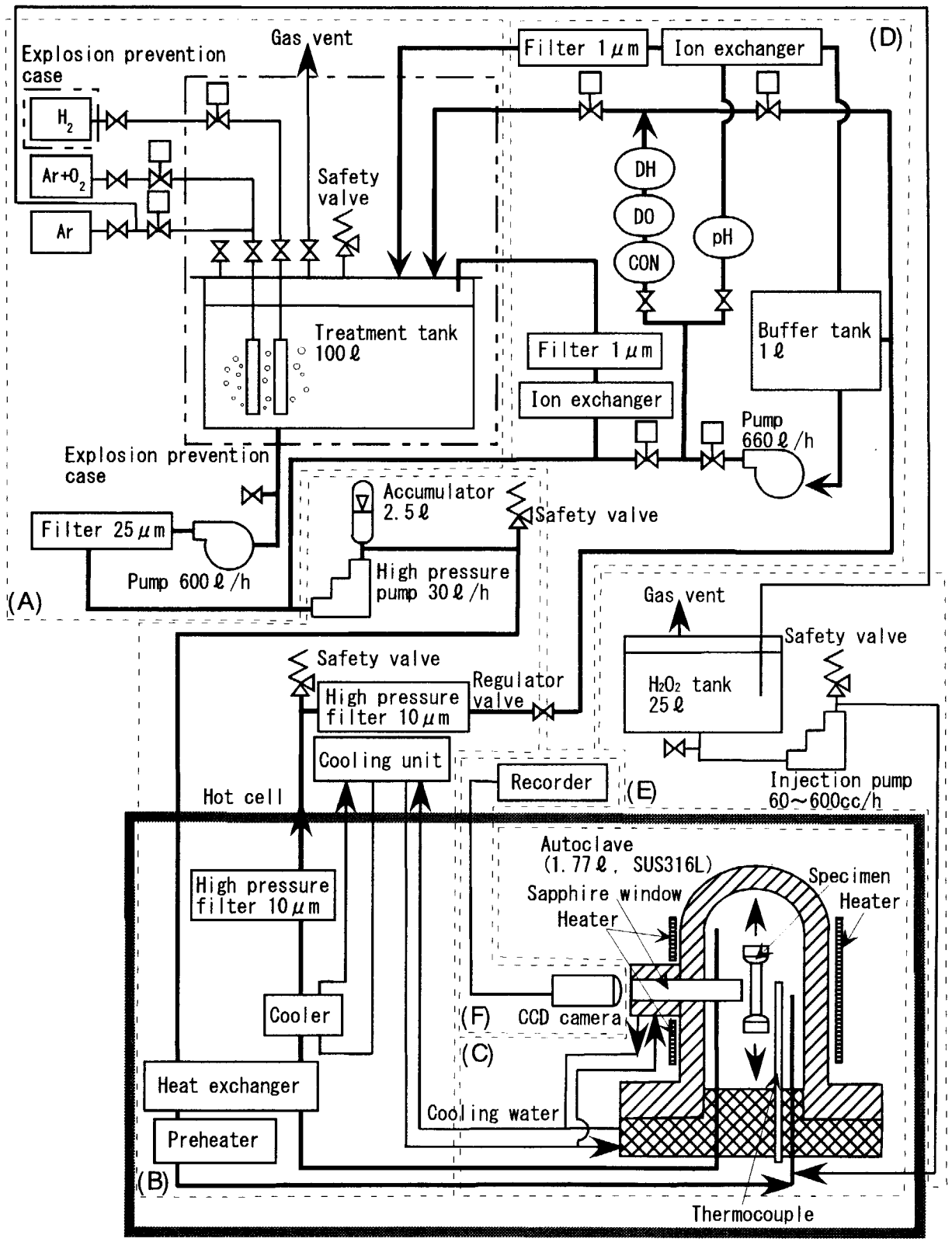


Fig.1 Schematic flow diagram of the SSRT apparatus in high temperature water for irradiated materials
(A) Water make-up system, (B) Pressurized high temperature water circulation system, (C) Tensile testing system, (D) Monitoring/purification system, (E) Hydrogen peroxide injection system and (F) Observation/recording system.

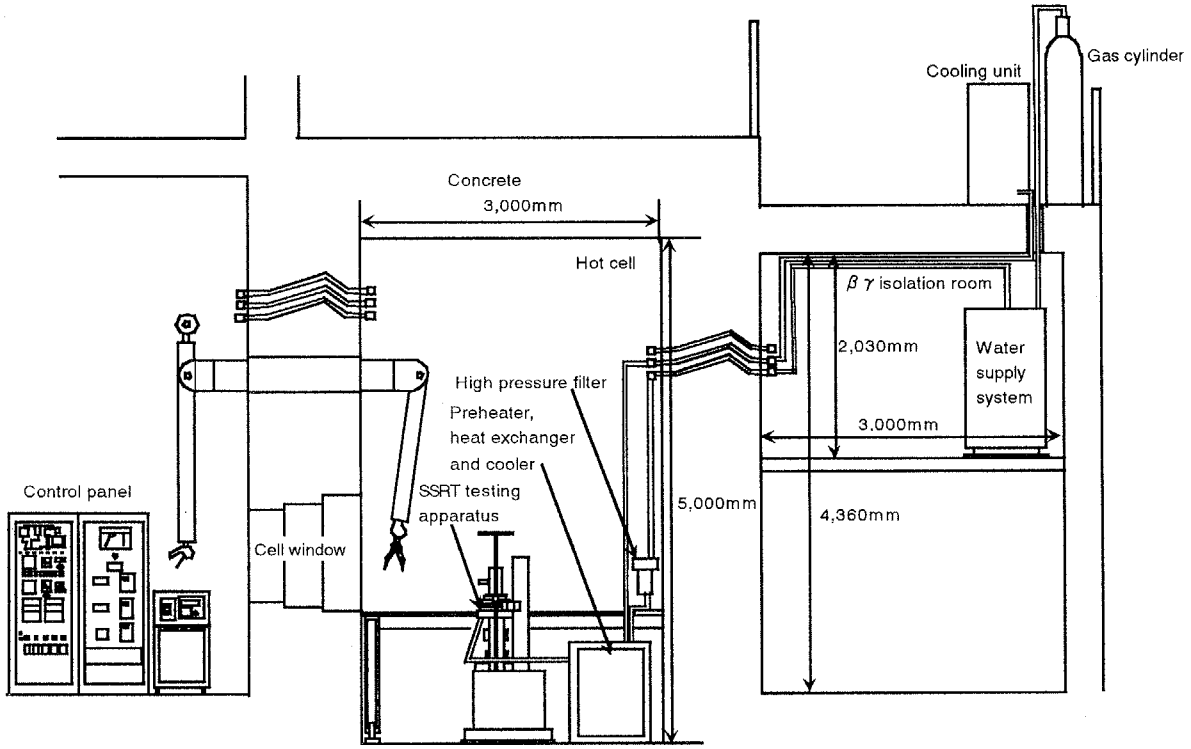


Fig. 2 Location of the SSRT facility in a hot cell.

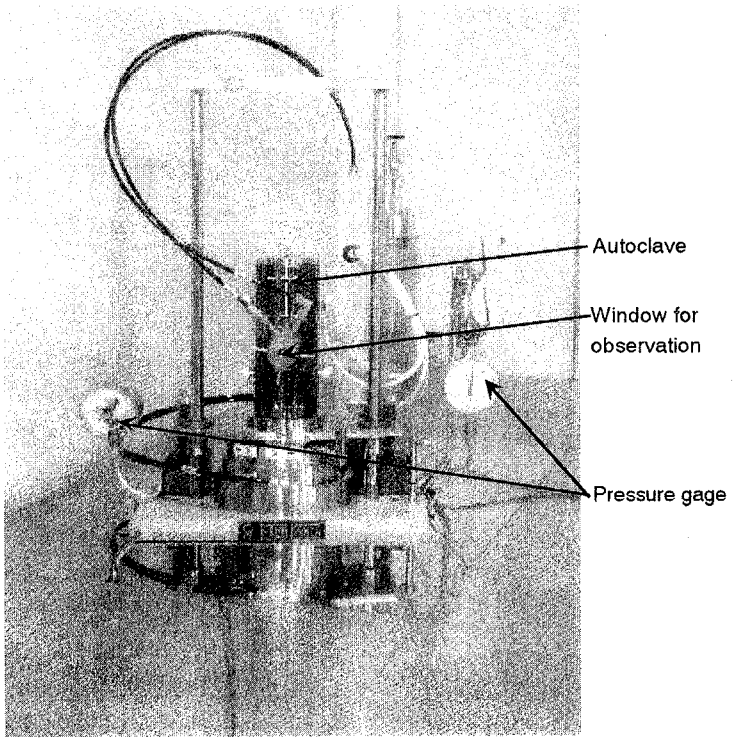


Fig. 3 Autoclave with a window for observation.

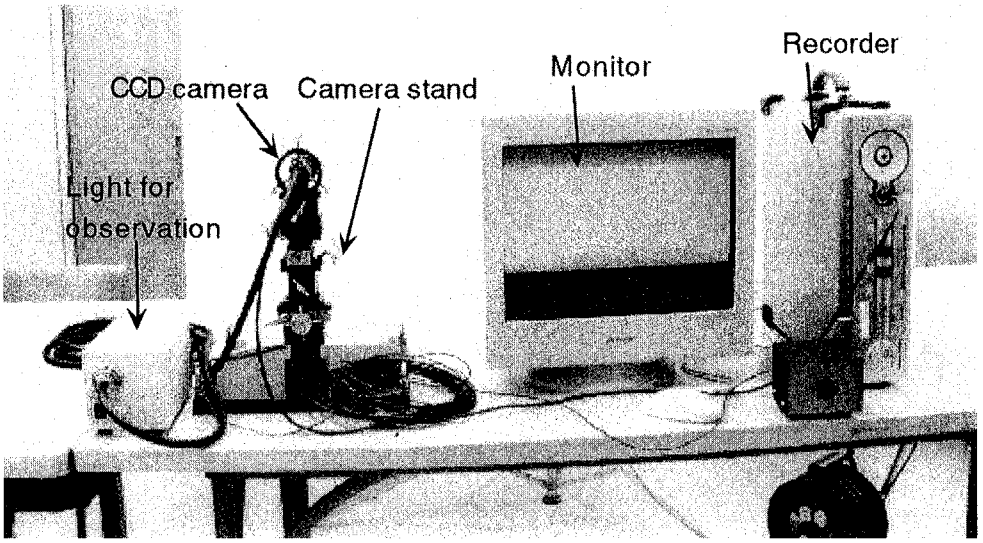


Fig. 4 Observation/recording system.

JP0350289

2.25 STATIC AND DYNAMIC CORROSION EXPERIMENTS IN LIQUID LEAD-BISMUTH

Y. Kurata*, K. Kikuchi, M. Futakawa, S. Saito and T. Sasa

Neutron Science Research Center,
Japan Atomic Energy Research Institute,
Tokai-mura, Naka-gun, Ibaraki-ken
319-1195 Japan

Abstract

Static and dynamic corrosion tests in liquid Pb-Bi eutectic were conducted to investigate applicability of metallic materials for an accelerator driven system which is being developed for transmutation of long-lived nuclear wastes. The static corrosion tests were performed in oxygen-saturated Pb-Bi at 450 and 550℃ for 3000h. The dynamic corrosion test was conducted using a liquid Pb-Bi loop where temperatures of high and low temperature parts were 450 and 400℃, and the flow rate of liquid Pb-Bi at the test section was about 1m/sec. In the static tests, the corrosion depth of F82H, Mod.9Cr-1Mo steel and JPCA after immersion at 450℃ for 3000h was 14,13 and 5 μm, respectively. The thickness of the corrosion layer decreased with increasing Cr content of steels in the static corrosion test. The corrosion depth of type 316ss at 450℃ was estimated to be about 100 μm after the test for 3000h in the Pb-Bi loop. It was also found that morphology of the interface faced to flowing Pb-Bi is different from that faced to static Pb-Bi. We observed the phenomena such as mass transfer, corrosion/erosion by flowing Pb-Bi, penetration of Pb-Bi into grain boundaries and dropping of grains in the dynamic corrosion test.

Keywords : Lead-bismuth, Static corrosion, Dynamic corrosion, Accelerator driven system, Transmutation, Loop test, Mass transfer, Liquid metal

1.Introduction

Liquid Pb-Bi is considered to be the first candidate of spallation targets and coolants of an accelerator driven system(ADS) which is currently being developed for transmutation of long-lived nuclear wastes. Because it has excellent physical and chemical properties such as high neutron yield, low neutron absorption cross section, high boiling point, low melting point and lower reaction property with water and air in comparison with Na. However, liquid Pb-Bi is more corrosive than liquid Na and corrosion research in liquid Pb-Bi is one of the key issues for development of the ADS.

Recently, corrosion study in liquid Pb-Bi has been actively conducted focussing development of the ADS[1-4]. Since new experimental data have just been obtained in several laboratories and the development of liquid metal technology is also needed for reliable experimental data, accumulation of experimental data in liquid Pb-Bi is essential to elucidate corrosion behavior in

* Corresponding author. Tel: +81-29-282-5059 Fax: +81-29-282-6489
E-mail address: ykurata@popsvr.tokai.jaeri.go.jp (Y.Kurata)

liquid Pb-Bi. In this paper, results of static corrosion test in liquid Pb-Bi and dynamic corrosion test using a liquid Pb-Bi loop are described.

2.Experimental procedure

2.1 Materials

Table Ⅰ shows chemical composition of materials used in the static corrosion test. Effects of Cr and Ni contents in steels on corrosion in liquid Pb-Bi are studied using 2.25Cr-1Mo steel, F82H (8Cr-2W steel), Mod.9Cr-1Mo steel, JPCA (14Cr-16Ni-2Mo steel), type 410ss, type 430ss and pure iron. Type 316ss shown in Table Ⅱ was used as the specimen in a liquid Pb-Bi loop.

2.2 Test method

Fig.1shows the static corrosion test equipment in liquid Pb-Bi. The retort contacting liquid Pb-Bi was made of quartz. The size of specimens used for the static corrosion test was 15 mm x 30 mm x 2mm. The surface of specimens was polished using emery papers up to #600. The test specimens were pulled out from the molten Pb-Bi at the end of the static corrosion test. The static corrosion test was performed in oxygen-saturated Pb-Bi for 3000h. Testing temperatures of the static tests were 450 and 550℃. Fig.2 shows the liquid Pb-Bi loop used for the dynamic corrosion test. The condition of the dynamic corrosion test was the following: The temperatures of high and low temperature parts of the loop were 450℃ and 400℃, respectively, and the flow rate of liquid Pb-Bi at the test section was about 1m/sec. A tube of type 316ss (outer diameter of 13.8mm and thickness of 2mm) was used as a specimen. The corrosion test in flowing Pb-Bi was performed for about 3000h(3126h). Argon gas of 99.995% purity was used as a cover gas of expansion and dump tanks.

3.Results and discussion

3.1 Static corrosion test

As a result of the static corrosion test, effect of the Cr content on corrosion properties was estimated. Characteristic of the corrosion layer at 450℃ is mainly described in this paper. Fig.3 shows optical micrographs of the cross-sections of specimens after corrosion at 450℃ for 3000h in liquid Pb-Bi. Copper was plated on the specimen surface to protect corrosion films. The corrosion film of pure iron is the thickest as shown in Fig.3(g). The order of the corrosion layer thickness at 450℃ is the following : Fe >2.25Cr-1Mo steel, F82H and Mod.9Cr-1Mo steel > 410ss, Mo > JPCA >430ss.

Corrosion films formed at 450℃ were oxides. Fig.4 shows the EPMA analysis of the cross section of F82H specimen after the static corrosion test at 450℃ for 3000h. Corrosion films of F82H, Mod.9Cr-1Mo steel and 2.25Cr-1Mo steel at 450℃ consisted of two oxide layers ; outer corrosion film composed of magnetite without appreciable Cr and inner corrosion film composed of Cr-Fe spinel oxide. Fig.5 shows the relationship between corrosion depth and Cr content in steels. The thickness of corrosion layer decreases with increasing Cr content in steels. The corrosion depth of F82H, Mod.9Cr-1Mo steel and JPCA after immersion at 450℃ for 3000h was 14, 13 and 5 μm in the static corrosion test, respectively. The corrosion layer of pure iron and 2.25Cr-1Mo steel became particularly thicker at 550℃ than that at 450℃. It seems that adding Cr, in particular, more than 12%Cr, in steels brings about improvement of corrosion resistance in liquid Pb-Bi.

3.2 Dynamic corrosion test

The test section was set at the high temperature part(450℃) of the liquid Pb-Bi loop. Type 316ss was used as the test section and components of the liquid Pb-Bi loop. Fig.6 shows the cross section and inner surface of the type 316ss tube. Type 316ss tube used as the test section was produced by a normal method. The final treatment of the tube was wash with hot acid. This treatment produces deeply dug grain boundaries as shown in this figure. Fig7 shows results of macro-observation of the high-temperature test section of the liquid Pb-Bi loop after the corrosion test for about 3000h(3126h). Pits or hollows are clearly observed on the inner surface of the type 316ss tube after the corrosion test. In particular, corrosion/erosion is observed at the portion G over wide range. The corrosion depth of type 316ss at the high temperature part was estimated to be about 100 μm after the test for 3000h.

Fig.8 shows various interface morphology of the test section after the corrosion test. Not only pits or hollows with several 10 μm depth/width but also penetration of liquid Pb-Bi into grain boundaries are observed. There are oxide films on the interface in some places. On the other hand, there are also places without appreciate oxide films on the interface. Progress of corrosion/erosion at the test section is shown in Fig. 9. The following contrast is characteristic; rough interface at the initial surface and smooth interface at the bottom of the corroded hollow. A grain boundary fissure is also recognized at the rough interface. It is considered that pits or hollows observed over wide range on the inner surface of the tube were produced by corrosion/erosion in flowing Pb-Bi. Fig.10 shows the EPMA analysis of the test section. As shown in this figure, dark islands in Pb-Bi have almost similar chemical composition to that of the 316ss metal matrix. Therefore, they are considered to be grains peeled off from the 316ss metal matrix during the corrosion in flowing Pb-Bi. As indicated in Fig. 6, the initial inner surface has deeply dug grain boundaries. Taking this fact into consideration, it is considered that the rough surface with deeply dug grain boundaries accelerates corrosion/erosion by flowing Pb-Bi, penetration of Pb-Bi into grain boundaries and dropping of grains.

Fig. 11 shows the result of EPMA analysis of the deposit at low-temperature part (400℃). Large grains of Fe-Cr steel(Cr content: approximately 12-14%) formed at the low temperature part. This fact indicates the mass transfer phenomenon where Cr, Fe and Ni dissolved at the high-temperature part deposit at the low-temperature part of the loop. It is interesting that there are dissolution of 316ss at high temperature part and deposition of large grains of ferritic Fe-Cr steel at low temperature parts.

4.Conclusions

The following conclusions were drawn from the static and dynamic corrosion experiments in liquid Pb-Bi:

1) The corrosion depth of F82H, Mod.9Cr-1Mo steel and JPCA after immersion at 450℃ for 3000h was 14,13 and 5 μm in the static corrosion test, respectively.

2) The thickness of the corrosion layer decreased with increasing Cr content of steels in the static corrosion test.

3) The corrosion depth of type 316ss at 450℃ was estimated to be about 100 μm after the test for 3000h in the Pb-Bi loop.

4) Dissolution of main elements at the high temperature part and deposition of Fe-Cr steel at the low temperature part occurred in the dynamic corrosion test.
5) We observed the phenomena such as corrosion/erosion by flowing Pb-Bi, penetration of Pb-Bi into grain boundaries and dropping of grains in the dynamic corrosion test. It is considered that the rough surface with deeply dug grain boundaries accelerates these phenomena.

References

[1] G. Mueller, G. Schumacher and F. Zimmermann, J. Nucl. Mater., 278(2000)85.
[2] G. Benamati, P. Buttol, V. Imbeni, C. Martini and G. Palombarini, J. Nucl. Mater., 279(2000)308.
[3] F.Barbier and A. Rusanov, J. Nucl. Mater., 296(2001)231.
[4] Y. Kurata, M. Futakawa, K. Kikuchi, S. Saito and T. Osugi, J. Nucl. Mater., 301(2002)28.

Table I Chemical composition of specimens for static corrosion tests (wt %)

	C	Cr	Ni	Mo	Fe	V	W
F82H	0.095	7.72	<0.02	<0.01	Bal.	0.01	1.95
Mo.9cr-1Mo steel	0.10	8.41	0.06	0.88	Bal.	0.047	<0.0005
JPCA	0.058	14.14	15.87	2.29	Bal.	0.003	0.01
410ss	0.067	12.21	0.12	0.02	Bal.	0.013	-
430ss	0.08	16.24	0.15	0.02	Bal.	0.024	-
2.25Cr-1Mo steel	0.10	2.18	0.02	0.92	Bal.	0.009	-
Fe	0.002	-	-	-	Bal.	0.001	-
Mo	0.014	-	-	Bal.	-	-	0.016

Table II Chemical composition of specimen for dynamic corrosion test (wt %)

	C	Cr	Ni	Mo	Fe	Si	Mn
316ss	0.05	16.61	11.28	2.08	Bal.	0.34	1.55

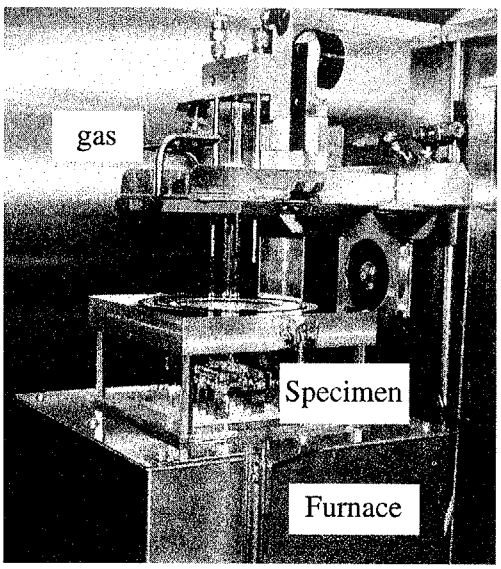


Fig.1 Static corrosion equipment in liquid Pb-Bi.

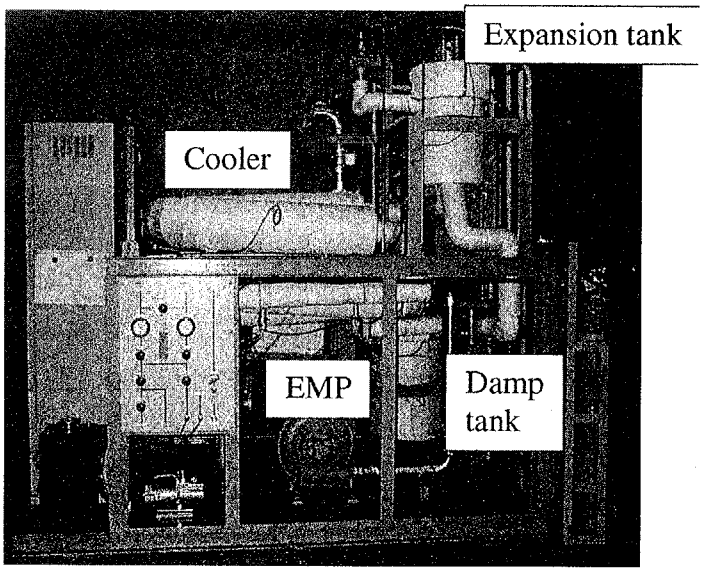


Fig.2 Liquid Pb-Bi loop.

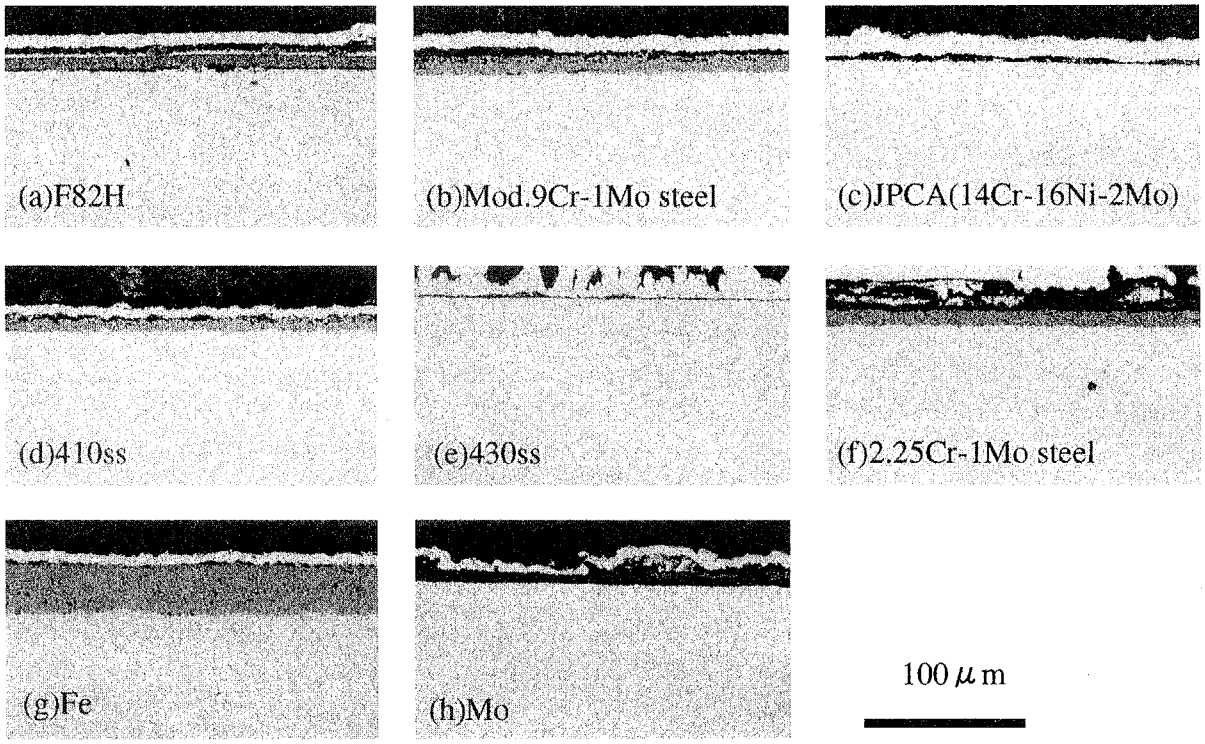


Fig.3 Optical micrographs of cross sections of specimens after the static corrosion test at 450℃ for 3000h.

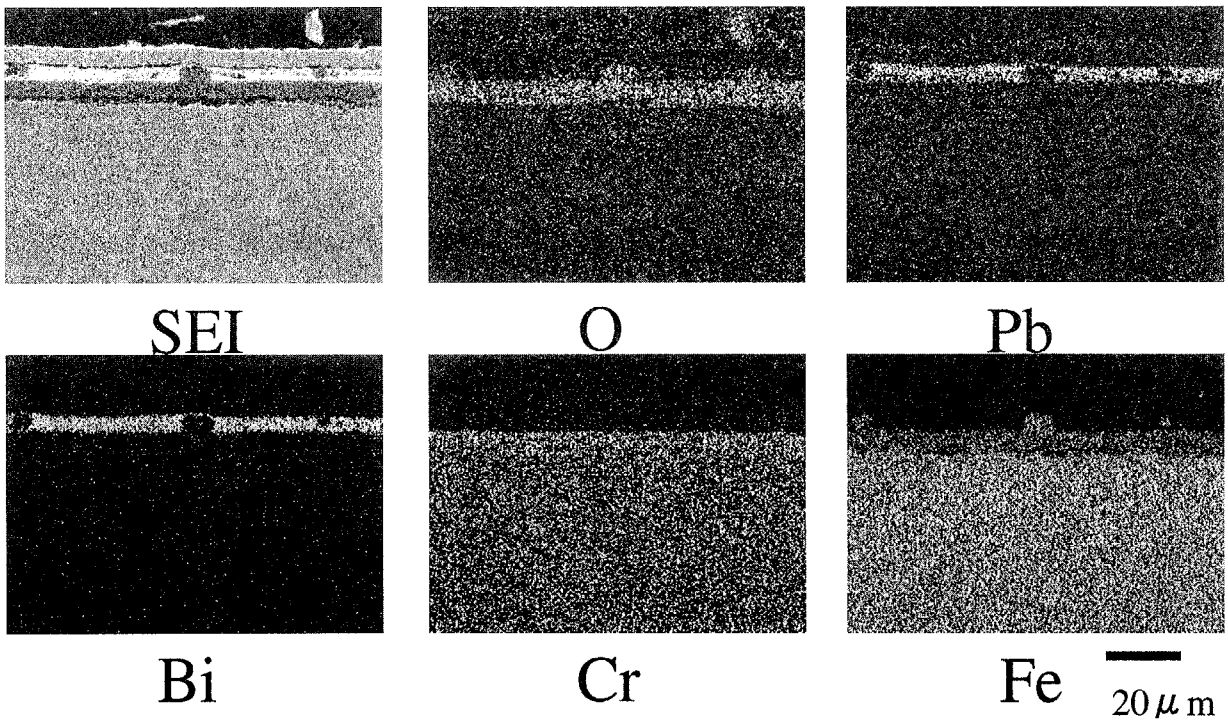


Fig.4 EPMA analysis of the cross section of F82H specimen after the static corrosion test at 450℃ for 3000h.

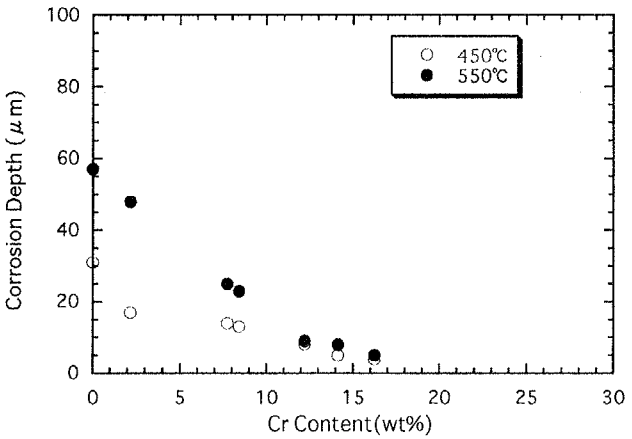
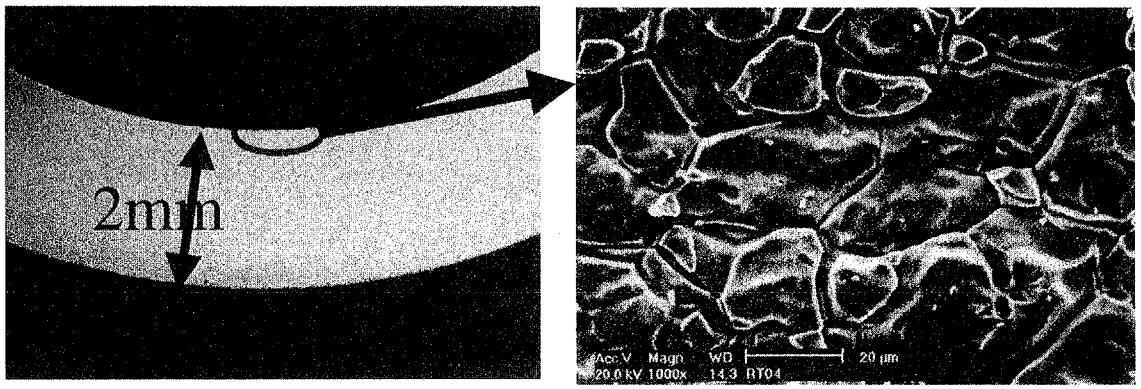


Fig.5 Corrosion depth versus Cr content in steels.



(a)Transverse section (b) SEM of inner surface

Fig.6 Cross section and inner surface of the type316ss tube specimen of liquid Pb-Bi loop.

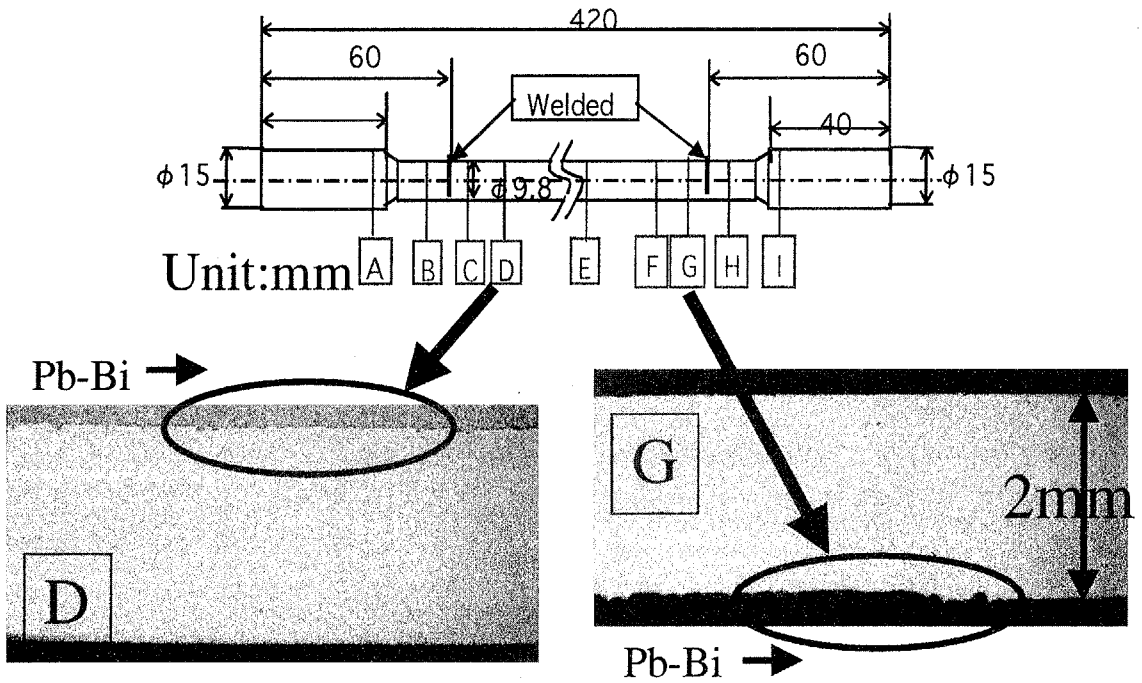


Fig.7 Shape of the test section of the liquid Pb-Bi loop and its macro-observation after the corrosion test.

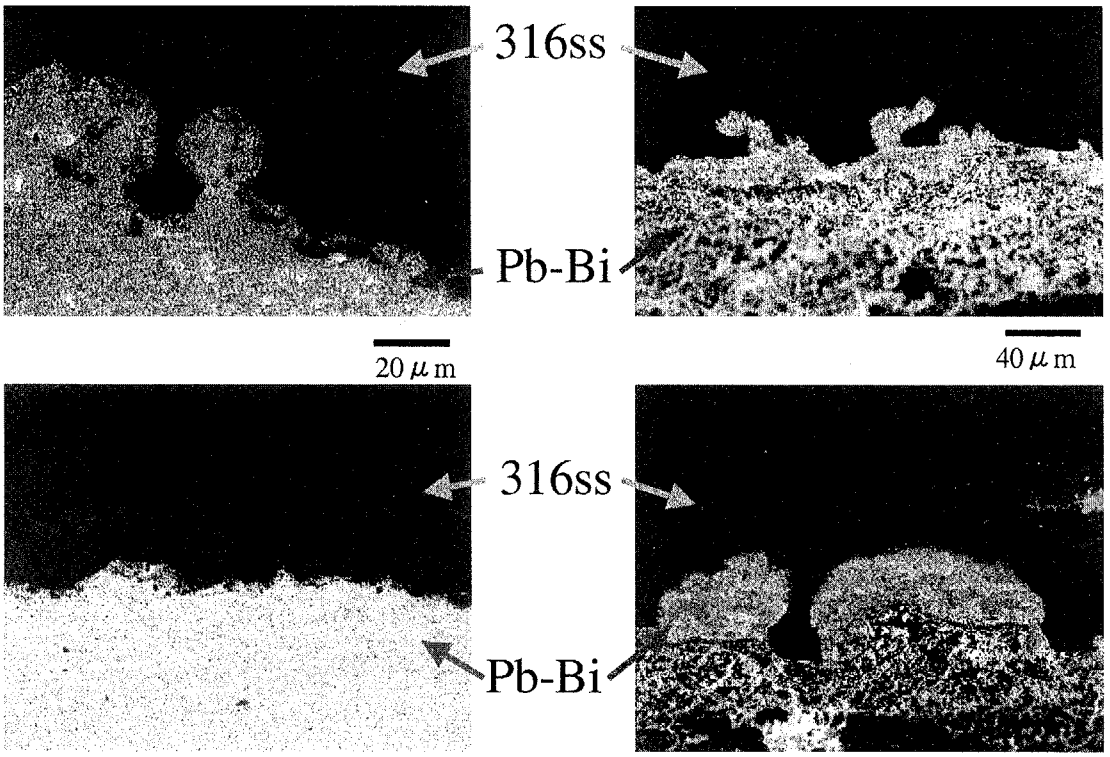


Fig.8 Various interface morphology of the test section after the corrosion test in Pb-Bi loop.

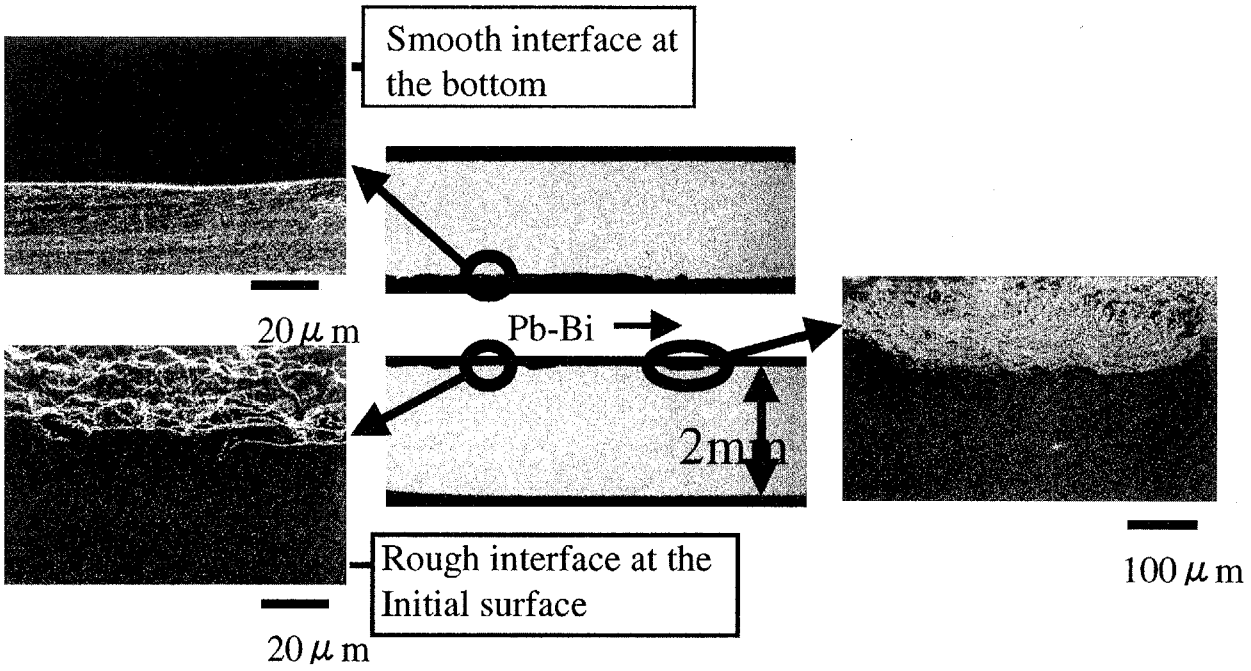


Fig.9 Progress of corrosion/erosion at the test section of the liquid Pb-Bi loop.

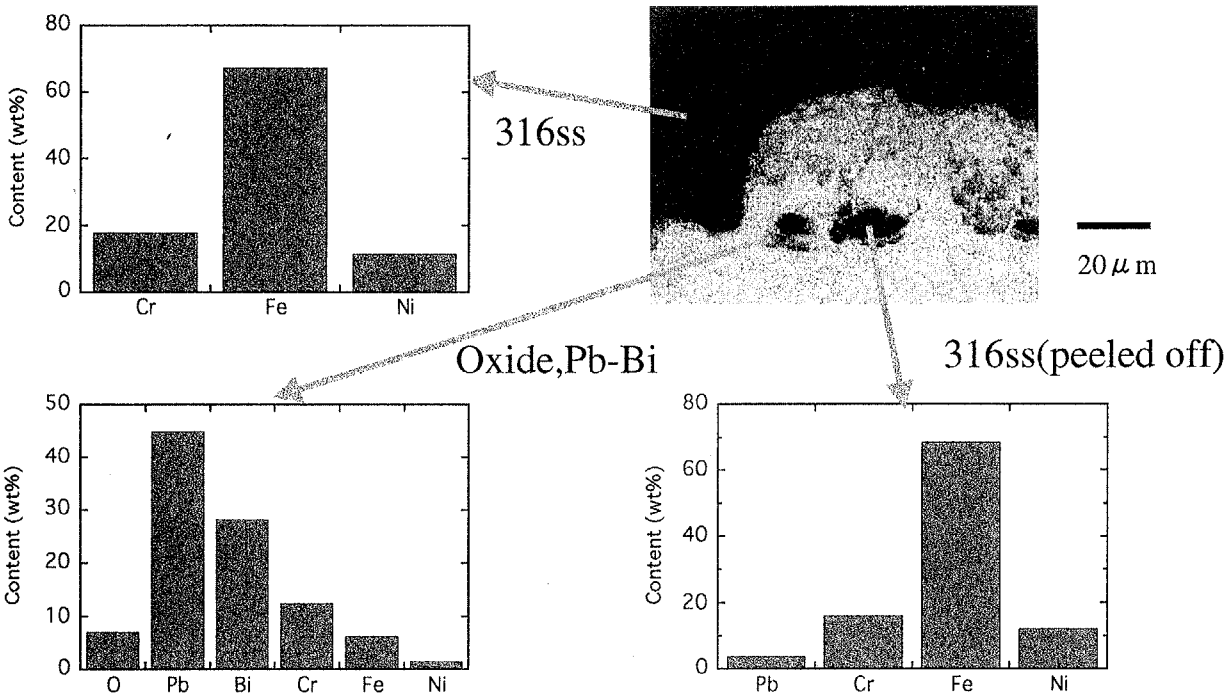


Fig.10 EPMA analysis of the high-temperature test section of the liquid Pb-Bi loop after corrosion test.

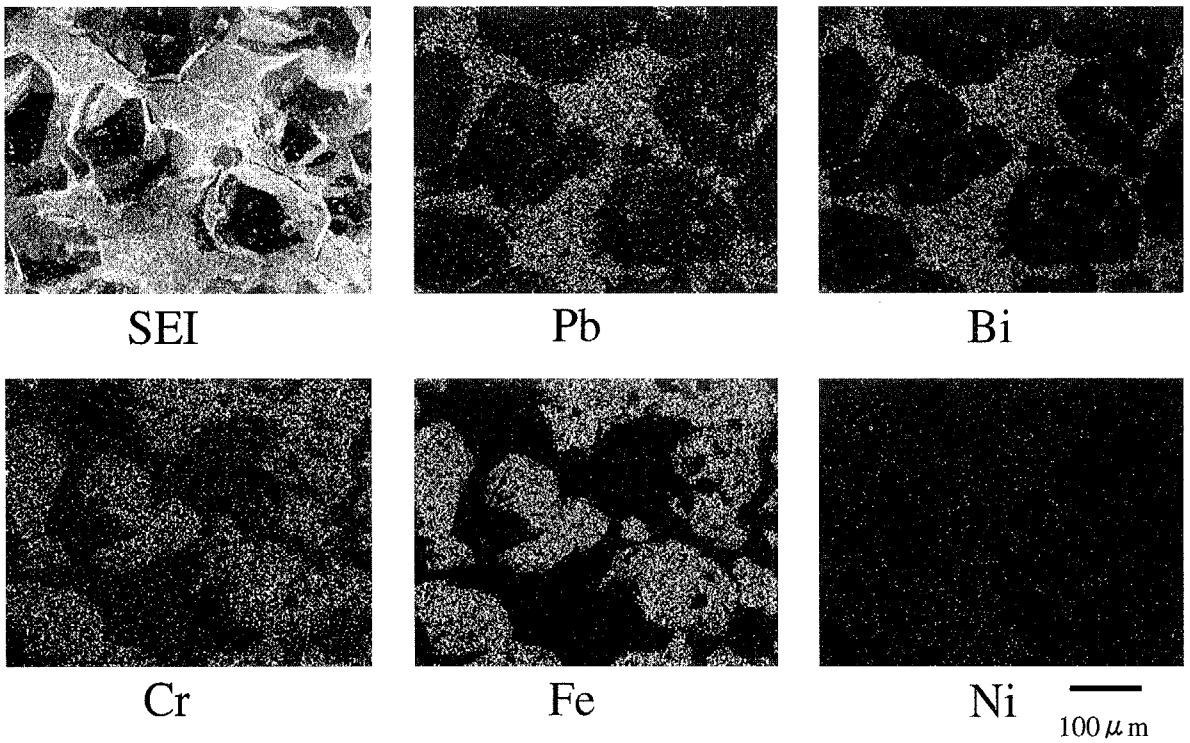


Fig.11 EPMA analysis of deposit at low-temperature part of the liquid Pb-Bi loop after corrosion test.

JP0350290

2.26 TWO-DIMENSIONAL GRAPHITE-LIKE Si_xC OBSERVED BY POLARIZATION DEPENDENCE IN THE NEAR-EDGE X-RAY ABSORPTION FINE STRUCTURE

Yuji Baba, Iwao Shimoyama and Tetsuhiro Sekiguchi
Synchrotron Radiation Research Center, Japan Atomic Energy Research Institute
Tokai-mura, Naka-gun, Ibaraki-ken, 319-1195, Japan

Abstract

Solid carbon forms mainly two kinds of local structures, i.e., three-dimensionally spread diamond-like structure and two-dimensional graphite structure. In contrast, solid silicon and silicon carbide tend to prefer only diamond structure composed of sp^3 bonds resulting in the formation of a three-dimensionally spread lattice. Recently, the theoretical calculation using an ab initio tight-binding-like method has revealed that two-dimensional graphite-like SiC layer possibly exists (M. Fuentes-Cabrera et al., Model. Simul. Mater. Sci. Eng. 7, 929 (1999)). In order to clarify whether or not such two-dimensional graphitic Si_xC layer exists, we implanted Si^+ ions in highly oriented pyrolitic graphite (HOPG), and the electronic structures localized at the silicon atoms were investigated in-situ by means of X-ray photoelectron spectroscopy (XPS) and near-edge X-ray absorption fine structure (NEXAFS) using linearly polarized synchrotron radiation. The resonance peak appeared at 1839 eV in the Si *K*-edge NEXAFS spectra for Si^+-implanted HOPG, and its energy is lower than the resonance peaks in any other Si-containing materials. The intensity of the resonance peak showed strong polarization dependence, which suggests that the final state orbitals around the Si atoms have π^*-like character. It is elucidated that the Si-C bonds produced by the Si^+-ion implantation are nearly parallel to the graphite plane, and Si_xC phase forms two-dimensionally spread graphite-like layer with sp^2 bonds.

Keywords: silicon carbide, graphite, two-dimensional layer, ion implantation, near-edge X-ray absorption fine structure, X-ray photoelectron spectroscopy, polarization dependence, synchrotron radiation

1. Introduction

Low-dimensional materials have been attracted much attention because of their unique properties, which are not observed in bulk materials [1]. Especially, recent rapid progress in semiconductor technology is accelerating the search for new two-dimensional (2D) semiconductor materials. Among numerous kinds of 2D materials investigated so for, graphite is considered to be ideal 2D layer. One sheet of graphite (graphene) is composed of six-membered aromatic rings with sp^2 bonds, and its thickness is only in the order of one atom. Newly found carbon nanotube [2] which has similar structure to graphite is also classified into the graphite family, and it has been attracted much attention as a new electric material in nanotechnology. As to the electric property, graphite has semi-metallic conductivity. Besides graphite, hexagonal boron nitride (BN) which has a similar structure to graphite is a wide-gap insulator. Therefore, if some of the carbon atoms in graphite are substituted by the other atoms, we can possibly obtain ideal 2D thin films with various electric properties from metallic phase to insulator. Theoretical [3,4] and experimental [5,6] works have recently revealed that two-dimensional carbon nitrides of graphite-like structures surely exist. Also the synthesis of hybrid nanotubes composed of boron, carbon and nitrogen has been attempted recently for the purpose of controlling electric property [7,8].

On the other hand, silicon, belonging to the same group in the periodic table as carbon, tends to form three-dimensionally spread diamond structure with sp^3 bond. If silicon atoms

are ordered in 2D layer, the interaction between the two 2D layers becomes stronger than the Van-der-Waals force [9] resulting in the formation of puckered structure [10]. Such three-dimensionally spreading character of silicon atoms makes it difficult to fabricate ultra thin layer of semiconducting Si and insulating SiO_2 in silicon technology. Although many of the organosilicon molecules having Si-Si double bonds are known [11], no stable solid phase of graphite-like silicon with sp^2 bonds has been synthesized so far. (Note that in the case of isolated molecules, benzene-like molecule composed of silicon which is called as silabenzene has recently been synthesized [12].)

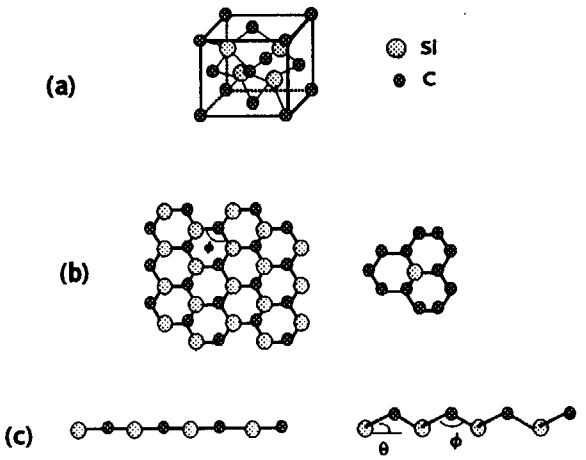


Fig.1 Schematics of structures of "real" and "imaginary" solid phases composed of silicon and carbon [10]. (a) Unit cell of real β-SiC phase of zinc-blende structure. (b) Top view of imaginary SiC phase where $\phi = 120°$. (c) Side view of monolayer of SiC phase. The puckered angle θ is the bond angle measured from the plane where a flat graphite-like sheet would be placed. For sp^3 bond, $\theta = 19.47°$ which corresponds to the tetrahedral angle $\phi = 109.47°$.

This situation also holds for the silicon carbide. There are some stable SiC phases such as α-SiC and β-SiC, all of which are composed of sp^3 bonds. The local geometry of the typical β-SiC phase of zinc-blende structure is shown in fig.1 (a). However, the theoretical study on the possible graphite-like 2D layer for SiC has recently been conducted by Fuentes-Cabrera et al. using an ab initio tight-binding-like method [10]. They calculated the stabilities of the aromatic phase of 2D monolayers of SiC. They concluded that the 2D SiC prefers to form the flat aromatic phase (fig.1(c), left) rather than puckered layer (fig.1(c), right), while Si prefers to puckered form and never forms flat aromatic phase. If the two-dimensional SiC phase does exist, we can possibly deposit ultra thin or just monolayer of semiconductor on solid surfaces. However, no experimental evidence has been reported so far as to whether or not the aromatic, flat SiC phase does exist.

In order to answer the above questions, we investigate the local electronic and geometric structures of silicon implanted in graphite. For this purpose, we chose highly oriented pyrolitic graphite (HOPG) as a starting material. We implanted low-energy Si^+ ions in HOPG, and the electronic structures localized at the silicon atoms were investigated in-situ by means of the near-edge X-ray absorption fine structure (NEXAFS) spectroscopy. The local geometric structures were also clarified by the incident angle dependencies of the NEXAFS spectra using linearly polarized synchrotron beam. X-ray photoelectron spectroscopy (XPS) was used in elucidating the core-level binding energies and surface atomic compositions.

2. Experimental

The experiments were performed at the BL-27A station of the Photon Factory in the High Energy Accelerator Research Organization (KEK-PF) employing double crystals of InSb(111) as a monochromator. The energy resolution of the monochromator was 0.85 eV at 1.84 keV (Si *K*-edge). The synchrotron beam was generated in the bending magnet, and it was linearly polarized in the horizontal direction.

The ultrahigh vacuum system (base pressure 1 x 10^{-8} Pa) consisted of a manipulator

which can rotate around the vertical axis, a hemispherical electron-energy analyzer (VSW Co. Class-100) for XPS measurements, and a cold-cathode ion-gun (OMEGATRON Co. OMI-0045CK). An HOPG single crystal of 12 mm×12 mm purchased from Advanced Ceramics Co. was used as a substrate. The orientation of HOPG was checked in the separate experiments at the BL-11A station of KEK-PF by means of the polarization-dependencies of the C *K*-edge NEXAFS spectra. For comparison, amorphous diamond-like carbon (DLC) mainly composed of sp^3 bonds with no orientation was also used as a substrate.

Tetrafluorosilane (SiF_4) gas was used as ion source. Various atomic and molecular fragment ions such as F^+, Si^+, SiF^+ and SiF_3^+ were produced by the discharge of SiF_4 gas. Therefore the mass of the ions was separated by a Wien-filter-type mass separator using orthogonal electric and magnetic fields, and only atomic Si^+ ions were bombarded on the sample. The accelerating voltage was 1 keV, and the ion flux was 1×10^{11} atoms/cm^2 · sec. The NEXAFS spectra were taken by the total electron yields, which were obtained by the sample drain current. The total electron yields were normalized by the photon flux, which was always monitored by the current of aluminum foil located in front of the sample. In order to compare the spectral features, the NEXAFS and XPS spectra were also taken for the reference materials such as β -SiC (6H-SiC) and single crystal of Si(100).

3. Results and discussion

3. 1 XPS

Figure 2 shows the XPS spectra around the Si 1s region excited by 2100-eV photons. The surface C/Si ratios of the Si^+-ion bombarded HOPG and DLC were estimated to be 0.01 on the basis of the C 1s/Si 1s peak intensity ratios considering the photoionization cross sections [13] and inelastic electron mean free paths (IMFP) of photoelectrons [14]. The chemical shift between Si(100) and SiC is 1.6 eV, which means that carbon atoms are negatively charged compared with silicon atoms. The binding energy of the Si 1s for Si^+-ion implanted DLC is almost the same as that for the SiC, which suggests that the amorphous Si_xC composed of sp^3 bonds is formed. While the Si 1s peak for Si^+-ion implanted HOPG shifts to higher binding energy by 1.3 eV than that for SiC. If the implanted silicon atoms form cluster resulting in the island structure, or if the implanted layer becomes amorphous Si_xC with only sp^3 bonds, the binding energy of implanted silicon would be close to that of the bulk silicon. The observed higher binding energy suggests that the Si^+-ion implanted HOPG forms new layer where carbon atoms are more negatively charged compared with normal SiC.

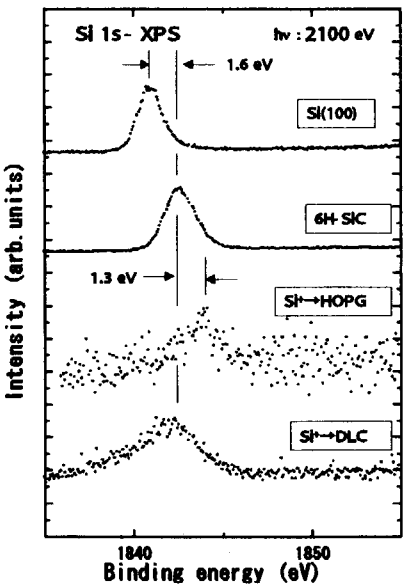


Fig.2 X-ray photoelectron spectra around Si 1s region excited by 2100-eV photons for Si(100) single crystal, 6H-SiC, Si^+-ion implanted HOPG, and Si^+-ion implanted DLC.

3. 2 NEXAFS

Figure 3 shows the NEXAFS spectra at the Si K-edge. The spectrum for the Si^+-ion implanted DLC represents a similar structure to that for 6H-SiC (see dotted bars). This

finding supports the XPS results, i.e., Si^+-ion implanted DLC forms amorphous Si_xC composed of sp^3 bonds. On the other hand, the NEXAFS spectrum for Si^+-ion implanted HOPG does not follow that for 6H-SiC, and new peaks marked A and B are observed. It is noteworthy that the energy of the peak A is around 1839 eV, and no peak is observed in such low-energy region for 6H-SiC. Also such low-energy peak has never been reported in Si *K*-edge NEXAFS spectra for any other silicon-containing compounds. In the case of carbon *K*-edge NEXAFS spectra, it has been established that the resonance peak corresponding to $1s\rightarrow\pi^*$ excitation is lower than that originating from $1s\rightarrow\sigma^*$ excitation. In fact, it was reported that the energy of the C $1s\rightarrow\pi^*$ resonance peak of graphite is lower by 10 eV than those of the C $1s\rightarrow\sigma^*$ peaks of graphite and diamond [15]. From the analogy to the carbon case, it is presumed that the peak A in fig.3 is attributed to the resonance excitation from the Si 1s to unoccupied orbitals which have π^*-like character.

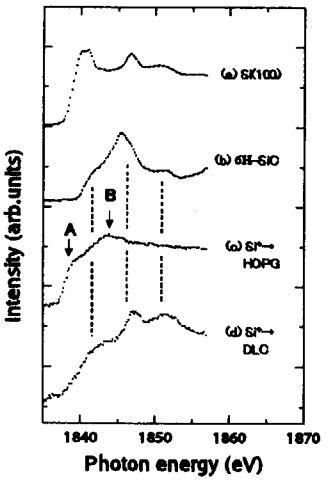


Fig.3 NEXAFS spectra at the silicon *K*-edge taken by the total electron yield for (a) Si(100) single crystal, (b) 6H-SiC, (c) Si^+-ion implanted HOPG, and (d) Si^+-ion implanted DLC.

3. 2 Polarization dependences of NEXAFS spectra

Figure 4 displays the polarization dependence of the Si *K*-edge NEXAFS spectra for the Si^+-ion implanted HOPG (a) and DLC (b) at a fluence of 7×10^{13} atoms/cm^2. The top view of the sample location is displayed in the upper small inset of each figure. In the spectra for Si^+-ion implanted HOPG, remarkable polarization dependence is observed for the peak A. The intensity of the peak A increases with the decrease in the incident angles of the synchrotron beam. On the other hand, no polarization dependence is observed in the spectra for Si^+-ion implanted DLC. The peak intensity I of the NEXAFS spectra using the synchrotron beam of electric field **E** is expressed as follows [16],

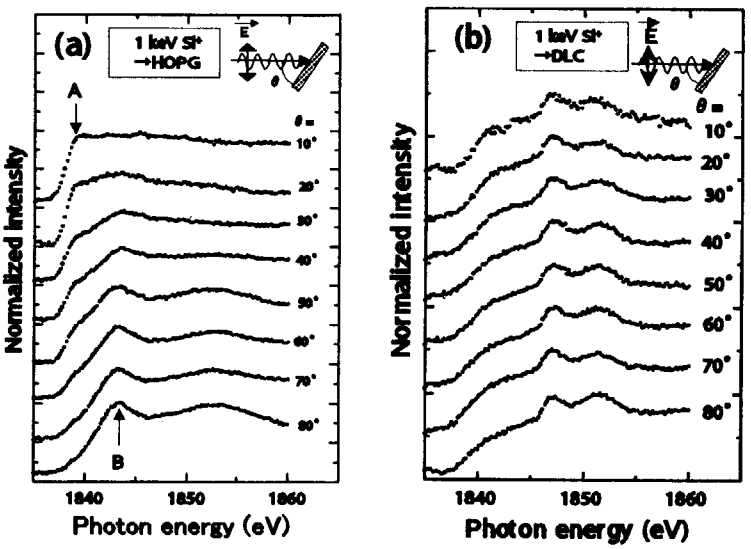


Fig.4 Polarization dependences of Si *K*-edge NEXAFS spectra for (a) Si^+-ion implanted HOPG, and (b) Si^+-ion implanted DLC. The fluence of the Si^+ ions are 7×10^{13} atoms/cm^2. The small inset shows the top view of the sample. **E** is the electric field vector of synchrotron beam and θ is the incident angle defined by the angle between sample surface and synchrotron beam.

$$I \propto |\mathbf{E} \cdot \mathbf{O}|^2 \propto \cos^2 \delta \quad (1)$$

where **O** is the direction of the final state orbital and δ is angle between **E** and **O**. If this resonance peak is due to the dangling bond located at the silicon atoms, such polarization dependences will be never observed. Considering the polarization dependence in fig.4(a), we can suppose that the final state orbitals represented by the peak A are perpendicular to the basal plane of graphite sheet, i.e., parallel to the c-axis of graphite. In order to certify this speculation, we will next discuss the angle of the orbitals and chemical bonds more quantitatively.

In figure 5(a), the intensities of the peak A are plotted as a function of the incident angle θ. (In the row spectra, the peaks A are overlapped with the higher-energy peaks. But the lower-energy sides of the peaks A show the Gaussian-like curves. Therefore we calculate the areas of the peaks A by the peak deconvolutions using Gaussian-curve fitting. The example of the curve fitting in the NEXAFS spectrum at θ=30° is shown in the small inset of fig.5(a)). The intensities of the peaks A were normalized by the total electron yields at 1860 eV for respective incident angles where no polarization dependence exists. It is seen that the intensity of the peak A monotonously decreases with the incident angle.

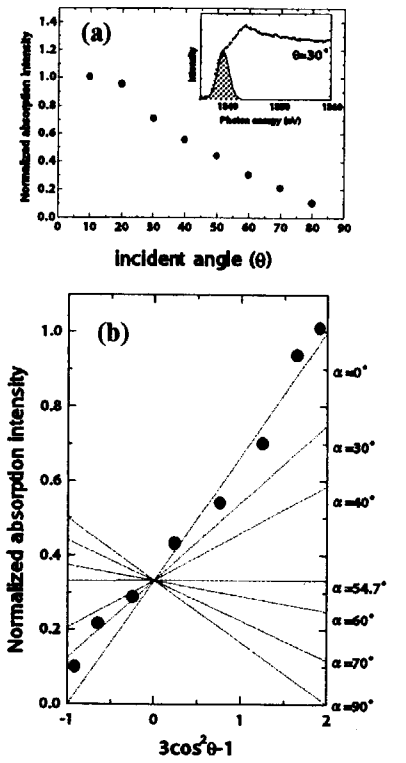


Fig.5 Normalized absorption intensities (filled circles) of the peak A in the Si *K*-edge NEXAFS spectra for Si^+-ion implanted HOPG as a function the incident angle θ. In the figure (a), the intensities are plotted as a function of θ. The small inset displays the example for the measurement of the peak intensity by Gaussian-curve fitting for the NEXAFS spectrum at θ=30°. In the figure (b), the intensities are plotted as a function of $3\cos^2\theta$-1. The dotted lines represent theoretical lines when the final state orbital of the core-to-valence resonance excitation points to the polar angle indicated in the figure.

The resonance intensity in the NEXAFS spectrum is given as

$$I(\theta) = A [P \cdot I_P + (1-P) \cdot I_V] \quad (2)$$

where I_P and I_V are the transition intensities associated with the angle-dependent matrix elements parallel and vertical, respectively, to the electric vector, θ is the incidence angle of the synchrotron beam, A is the normalization factor and P is the polarization factor [17]. The substrate used here is graphite, thus the substrate has a symmetry higher than threefold. In this case, the intensities are simply expressed as

$$I_P = (1/3) \cdot [1 + (1/2) \cdot (3\cos^2\theta - 1) \cdot (3\cos^2 \alpha - 1)] \quad (3)$$

and

$$I_V = (1/2) \cdot \sin^2 \alpha \quad (4)$$

where α is the polar angle of the final state orbitals [17]. The polarization factor of the synchrotron beam in the present experimental condition is estimated to be about 0.95 [18]. The theoretically calculated values of I for various α-values are plotted as dotted lines in fig.5(b) as a function of $3\cos^2\theta$-1. The values are normalized such that the data at $3\cos^2\theta$-1=0 are 1/3. The normalized intensities of the peaks A are plotted as filled circles in fig.5(b). At first glance, the experimental data follow the line of α=0°. This means that

the final state orbitals point to the c-axis of the graphite. It is revealed that some of the carbon atoms in graphite are substituted by the implanted silicon atoms, and the Si-C σ -bond thus produced is nearly parallel to the basal plane of the graphite sheet. The top view of the obtained structure is displayed in the right side of fig.1 (b), and the side view is virtually represented in the left side of fig.1(c).

The present results clearly reveal that the two-dimensional Si_xC layer surely exists at low Si concentration. Further research to clarify whether an aromatic SiC with stoichiometric composition shown in the left side of fig.1(b) exists or not is now in progress by synthesizing the samples at higher Si concentration and at higher temperature. The existence of two-dimensional Si_xC layer will open up a possibility of future application of the formation of ultra thin or monolayered semiconductor phase.

4. Summary

We have investigated the local electronic and geometric structures of silicon atoms implanted in HOPG by means of NEXAFS and XPS using linearly polarized synchrotron beam. In the Si *K*-edge NEXAFS spectra, the resonance peaks were observed around 1839 eV, which is lower than the energies of the resonance peaks in any other silicon-containing compounds. The intensity of these resonance peaks showed strong polarization dependence. The quantitative analysis of the polarization dependence revealed that the final-state orbitals of the resonance peak point to the c-axis of the graphite plane. On the basis of the low-energy feature and the direction of the final-state orbitals, it is concluded that the observed low-energy resonance peaks originate from the excitation from Si 1s to π^* orbitals which are perpendicular to the graphite plane. The present results show that the σ -type Si-C bonds produced by the Si^+-ion implantation are nearly parallel to the graphite plane, and the Si_xC phase forms two-dimensionally spread graphite-like layer with sp^2 bonds.

Acknowledgements

The authors would like to thank the staff of the KEK-PF for their assistance throughout the experiments.

References

[1] S. Kagoshima, T. Sanbongi, H. Nagasawa and T. Takahashi, *Low-dimensional Conductors* (Shokabo, Japan, 2000)
[2] S. Iijima and T. Ichihashi, Nature **363**, 603 (1993).
[3] A. Snis and S.F. Mater, Phys. Rev. B **60**, 10855 (1999).
[4] M.C. Santos and F. Alvalez, Phys. Rev. B **58**, 13918 (1998).
[5] I. Shimoyama, G. Wu, T. Sekiguchi and Y. Baba, Phys. Rev. B, **62**, R6053 (2000).
[6] I. Shimoyama, J. Jpn. Soc. Synchrotron Rad. Res. **15**, 12 (2001).
[7] X. Blase, J.C. Charlier, A.De Vita and R. Car, Appl. Phys. A **68**, 293 (1999).
[8] K. Suenaga, J. Surf. Sci. Soc. Jpn, **21**, 560 (2000).
[9] Y. Wang, K. Scheerschmidt and U. Gösele, Phys. Rev. B **61**, 12846 (2000).
[10] M. Fuentes-Cabrera, A. Munoz, W. Windl, A.A. Demkov and O.F. Sankey, Model. Simul. Mater. Sci. Eng. 7, 929 (1999).
[11] G. Raabe and J. Michl, Chem. Rev. **85**, 419 (1985).
[12] K. Wakita, N. Tokitoh, R. Okazaki, N. Takagi and S. Nagase, J. Am. Chem. Soc. **122**,

5648 (2000).
[13] J.M. Scofield, UCRL-51326 (1973).
[14] M.P. Seah and W.A. Dench, Surf. Interface Anal. **1**, 2 (1972).
[15] G. Comelli, J. Stöhr and C.J. Robinson, Phys. Rev. B **38**, 7511 (1988).
[16] J. Stöhr, *NEXAFS Spectroscopy* (Springer-Verlag, 1992) p.71.
[17] J. Stöhr, *NEXAFS Spectroscopy* (Springer-Verlag, 1992) p.282.
[15] H. Kitamura, Synchrotron Radiation Calculation Program for PC98, V.2.3 (1993).

JP0350291

2.27 AFM EVALUATION OF GRAIN BOUNDARY CORROSION BEHAVIOR ON ION IRRADIATED STAINLESS STEEL

Yoshiyuki Nemoto[1]*, Yukio Miwa[1], Takashi Tsukada[1] and Hirokazu Tsuji[1]

[1]Department of Nuclear Energy System, Japan Atomic Energy Research Institute

Shirakata-Shirane2-4, Tokai-mura, Naka-gun, Ibaraki 319-1195, Japan.

Abstract

Irradiation assisted stress corrosion cracking (IASCC) of austenitic stainless steel has been studied as main concern of an aging problem of light water reactor (LWR) materials. It is essential to evaluate corrosion behavior at grain boundary of irradiated materials for mechanistic understanding of IASCC. However there is no suitable technique to evaluate grain boundary corrosion behavior of irradiated materials. The objective of this work is to develop the measurement method for the grain boundary corrosion behavior of irradiated materials using atomic force microscope (AFM). Ni ion irradiation was carried out for solution annealed Fe-18Cr-12Ni alloys at about 573K. The peak damage level was estimated as 1 dpa. To study the relation between grain boundary characteristics and corrosion behavior, orientation imaging microscope (OIM^{TM}) observation was conducted. After the potentiostatic corrosion procedure, surface of the specimens was examined by AFM and OIM. Some of grain boundaries were corroded, and those were random coincidence grain boundaries. The depth of corroded region at grain boundaries was successfully evaluated by AFM in nanometer scale.

Keywords: IASCC, Stainless steel, Irradiation, TIARA, Grain boundary, Corrosion, AFM, EBSP, OIM

---

*Corresponding author ; Tel. +81-29-282-5348, Fax. +81-29-282-5349,

E-mail address: y.nemoto@popsvr.tokai.jaeri.go.jp (Y. Nemoto)

1. Introduction

Irradiation assisted stress corrosion cracking (IASCC) is considered as an important concern on plant life management of light water reactor (LWR) [1-2], and also on the design and development of international thermonuclear experimental fusion reactor (ITER) [2]. Local degradation of corrosion resistance at grain boundary is considered as one of the mechanisms of stress corrosion cracking (SCC) and IASCC. In the case of SCC, heat treatment while welding process would sensitize materials, and the passive film on grain boundary would lose corrosion resistance. Under irradiation condition, even in solution-annealed materials, radiation induced segregation (RIS) would cause corrosion resistance degradation on grain boundary, and it would lead IASCC.

In IASCC study, corrosion behavior of grain boundary after irradiation should be studied to understand crack initiation and growth. In the former studies, to evaluate grain boundary corrosion behavior of thermal sensitized materials, electrochemical potentiokinetic reactivation (EPR) method had been conducted. In the case that EPR method would be applied to irradiated materials, not only grain boundaries but also inside of grains would be corroded while the test, because irradiated materials contain precipitates and irradiation damages in its grains. For detail study about the grain boundary corrosion behavior of irradiated materials, another evaluation methods need to be developed.

The objective of this work is to develop the new experimental method to evaluate grain boundary corrosion behavior of irradiated materials using atomic force microscope (AFM). The advantages of applying AFM are that corrosion behavior can be measured in nanometer scale, and each grain boundary corrosion behavior can be measured separately. Furthermore, a combination with orientation imaging microscope (OIM^{TM}) using electron backscatter diffraction pattern (EBSP) method is expected to be useful to evaluate relation between corrosion behavior and grain boundary characteristics. Moreover, on combination with transmission electron microscope (TEM) with energy dispersed X-ray spectrometer (EDS), the influence of microstructure development and radiation induced segregation (RIS) for corrosion behavior of each grain boundary can be evaluated.

2. Specimen preparation

High purity Fe-18Cr-12Ni alloy was used for the present study. The chemical composition is given in Table I. Materials were solution annealed at 1323K for 30min, and fabricated to a disk shape, it is 3mm in diameter and 0.2mm in thickness. The surface of specimens was polished with emery paper, diamond paste and finished with electro-chemical polishing. Ni

ion irradiation was carried out for the specimens with 12MeV Ni^{3+} ion up to a fluence level of $3.8x10^{19}$ ion/m^2 at 573K respectively, using tandem accelerator at the Takasaki ion accelerators for advanced radiation application (TIARA). The peak radiation damage level was estimated as 1 dpa respectively. After irradiation, the surface of irradiated specimens was removed about 1micrometer by electro-chemical polishing, as shown as in figure 1. It was to expose the peak area of radiation damage to the surface of specimens for the following experiments.

After the surface was removed, AFM observation was conducted for the surface of an irradiated specimen. Figure 2 shows the AFM topography of it. The surface was almost flat, and no grain boundary corrosion was observed, but small gaps on grain boundaries were observed.

3. Optimization of corrosion condition

Ideal corrosion condition for exact measurements of grain boundary corrosion behavior is illustrated in figure 3. Surface should be remained flat, and only grain boundary need to be corroded a little. On the specimen surface like this, AFM measurement for grain boundary corrosion behavior is expected to be successful. Potentiostatic corrosion procedure at passivating potential was chosen for this study. On the passivating potential, passive film will be formed on the surface of stainless steel, and cover the surface and protect it. In the case that chromium (Cr) would be depleted on grain boundary by thermal sensitization or RIS, there will be no passive film formed on grain boundary, thus the grain boundary will be dissolved during the procedure. After potentiostatic corrosion procedure, the surface condition of irradiated specimens is expected to be close to ideal condition to measure grain boundary corrosion behavior. In this study, potentiostatic corrosion procedures were conducted at 150mV in 1N H_2SO_4 + 0.01mol/dm^3 KSCN solution, at 303K.

Figure 4 is the AFM topography of that un-irradiated solution annealed specimen after potentiastatic corrosion test at passivating potential for 1000sec. Grain boundary corrosion was not observed on the surface of it. Figure 5 gives the AFM topography of an ion irradiated specimen after potentiostatic corrosion procedure at passivating potential for 1000sec. Grain boundaries of this specimen were corroded. The surfaces of some grains were kept flat, but the others were corroded. For AFM measurement of grain boundary corrosion depth, surface of grains should be kept flat. From comparison of the results of an un-irradiated specimen and an irradiated specimen, it is obvious that the corrosion observed in irradiated specimen was caused by radiation effects.

Figure 6 is the AFM topography of ion irradiated specimen after a potentiostatic corrosion procedure at passivating potential for 500sec. Corrosion of the irradiated specimen corroded at passivating potential for 1000sec. was too much for AFM measurement, so the corrosion length was shorten to 500sec. for this specimen. Grain boundaries of this specimen were corroded a little, and the surfaces of grains were kept flat. It is close to ideal corrosion condition for the measurement of grain boundary corrosion behavior by AFM.

4. Evaluation of grain boundary corrosion behavior of irradiated specimens

Figure 7 shows an OIM image of the same area of figure 6. Crystallographic orientation of each grain is indicated by color. If orientation of a grain is close to (111) plane, the grain is specified blue, if it is close to (001) plane, the grain is specified red, and if it is close to (101) plane, the grain is specified green. From comparison of figure 6 and figure 7, it can be concluded that when the surface of a grain close to (111) plane, the height was gotten lower than the other grains after corrosion procedure.

AFM topography in figure 8 is the enlargement of the area indicated by box in figure 6. Line analysis was conducted along the three lines drawn in figure 8, crossing grain boundaries. Grain boundary corrosion depth was measured as about 70nm as shown as in figure 9. Figure 10 is the OIM image of the same area as figure 8, it is indicating grain boundary characteristics. Random grain boundaries are drawn in black, $\Sigma 3$ coincidence grain boundaries are drawn in red. From the comparison of figure 8 and 10, all of the grain boundaries corroded obviously were random grain boundary.

Figure 11 is higher magnification AFM topography of a random grain boundary of the irradiated specimen corroded for 500sec. The surface was covered with oxide grains. The grain boundary was corroded from interstices between oxide grains, and the depth was about 70nm.

5. Discussion

Grain boundary corrosion depth of an ion irradiated material was measured by AFM in nanometer scale. From the comparison of grain boundary corrosion behavior measured by AFM and grain boundary character evaluated by OIM, all of the grain boundaries obviously corroded were random grain boundary. It is considered that because at random grain boundary, RIS would be occurred more than at coincidence grain boundaries. RIS lead Cr depletion at grain boundaries. As the result of Cr depletion, passive film will not be formed on random grain boundary, so it was dissolved during potentiostatic corrosion procedure. To inquire this,

it is needed to measure Cr depletion behavior at the random grain boundaries by field emission gun type TEM (FE-TEM) with EDS.

In the results obtained by AFM, some of random grain boundaries were corroded as wide as about 500nm. In the former studies, Cr depletion width at grain boundary was estimated as few nanometer by FE-TEM analysis with EDS [3]. It is considered that not only Cr depletion area was corroded, but also surrounding area was corroded because of edge effect. On the other hand, some of random grain boundaries were corroded steeper as shown as in figure 11. There might be some other reasons influence to corrosion behavior, not only grain boundary characteristics. In previous studies [4-5], it is reported that grain boundary triple points are easier to corrode. In figure 8, it was observed that grain boundary triple points were more corroded than the other area, and grain boundaries corroded wider when it is close to grain boundary triple points. However, some of random grain boundaries are not corroded wider even if those are close to grain boundary triple points. For detail study, microstructure observation and chemical analysis of these grain boundaries and surrounding area by FE-TEM with EDS are needed.

6. Summary

In this work, new evaluation method using AFM for grain boundary corrosion behavior on irradiated materials was developed. Optimization of corrosion condition for the measurement of grain boundary corrosion on ion irradiated specimens was succeeded, and corrosion depth of each grain boundaries was measured by AFM in nanometer scale. The grain boundary corrosion depth was measured as 70nm, on the ion irradiated Fe-18Cr-12Ni alloy after potentiostatic corrosion procedure at passivating potential. Each grain boundary corrosion behavior was measured separately, and relation between grain boundary characteristics and corrosion behavior was evaluated by combination with OIM observation. All of grain boundaries obviously corroded were random grain boundary.

Acknowledgements

Authors greatly appreciate Dr. Hiroyasu Tanigawa, Mr. Chiaki Kato and Dr. Yoshiyuki Kaji of Japan Atomic Energy Research Institute (JAERI), and Mr. Seiichi Suzuki of TexSEM Laboratories (TSL) who helped experiments on this work.

Reference:

[1] M. Kodama, R. Katsura, J. Morisawa, S. Nishimura, S. Suzuki, K. Asano, K. Fukuya and

K. Nakata, Proc. sixth Int. Symp. on Environmental Degradation of Materials in Nuclear Power Systems - Water Reactors, TMS, **583** (1993).

[2] T. Tsukada, JAERI-Research 98-007, Japan Atomic Energy Research Institute, (1998), [in Japanese].

[3] S.M. Bruemmer, E.P. Simonen, P.M. Scott, P.L. Andresen, G.S. Was and J.L. Nelson, J. Nucl. Mater., **274** (1999), 299.

[4] T. Watanabe, Nippon Kinzoku-gakkai Kaihou, **31** vol. 2 (1992), 138, [in Japanese].

[5] G. Palumbo and K. T. Aust, Proc. Intern. Symp. on Advanced Structural Materials, Ed. by D. S. Wilkinson, Pergamon Press, (1989), 227.

Table I Chemical composition of specimen (weight %)

C	N	Si	P	S	Ti	Mn	Cr	Ni	Al	Fe
0.003	0.0014	0.01	0.001	0.0014	0.01	1.36	18.17	12.27	0.16	Bal.

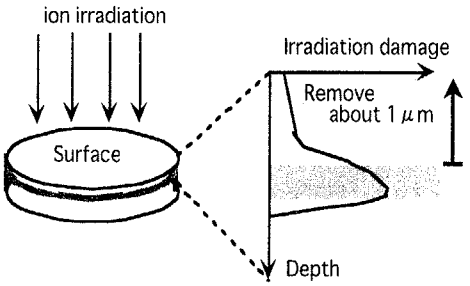


Fig.1 Remove the surface layer about 1 μm to expose peak area of radiation damage to the specimen surface.

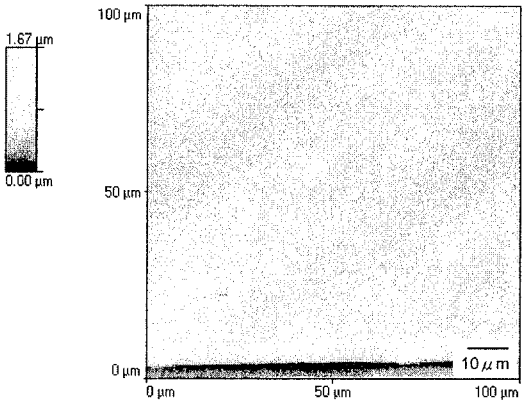


Fig.2 AFM topography of an ion irradiated specimen before corrosion test.

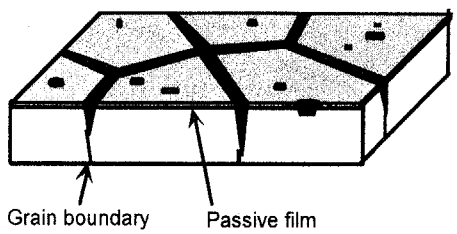


Fig. 3 Ideal surface condition for AFM measurement

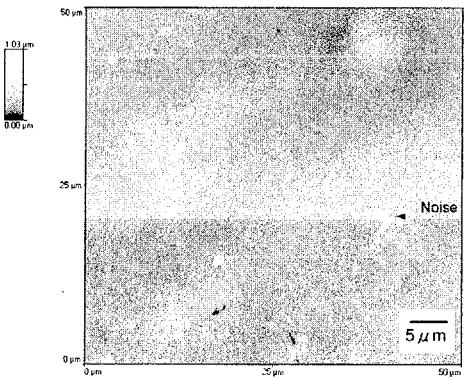


Fig.4 AFM topography of an un-irradiated solution annealed specimen after corrosion test for 1000sec.

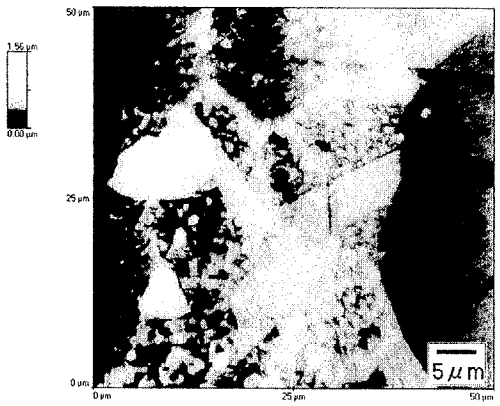


Fig.5 AFM topography of an ion irradiated specimen after corrosion test for 1000sec.

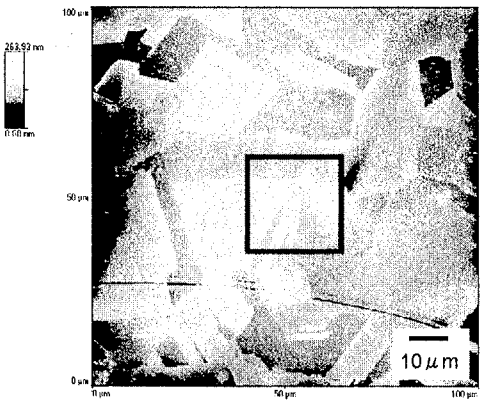


Fig.6 AFM topography of an ion irradiated specimen after corrosion test for 500sec.

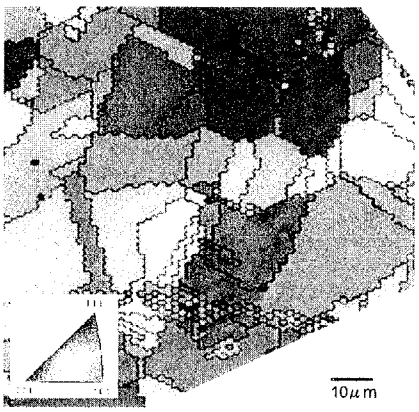


Fig.7 OIM image of an ion irradiated specimen it was corrosion tested for 500sec. It is indicating crystallographic orientation of grains on same area as in figure 6.

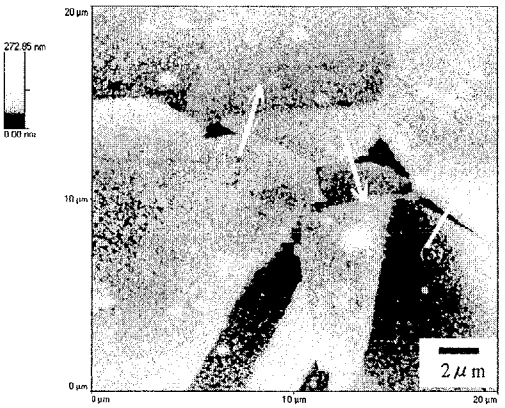


Fig.8 Enlargement of the area surrounded in figure 6.

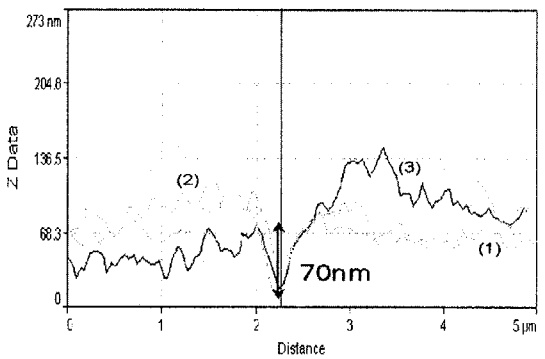


Fig.9 Results of height measurement along the lines drown in figure 8.

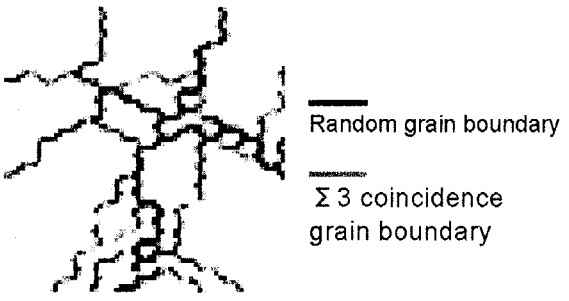


Fig. 10 OIM image of the same area as figure 8, it indicates grain boundary characters.

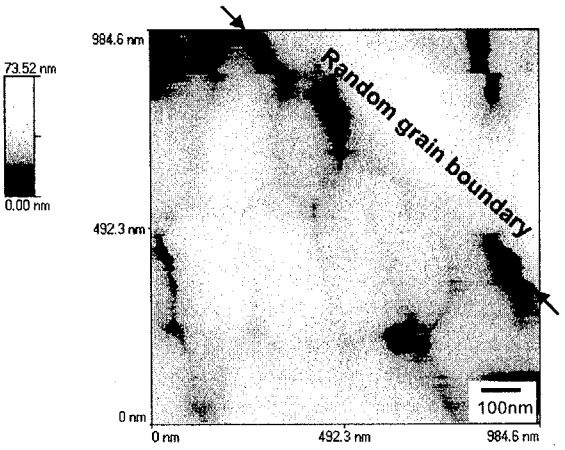


Fig.11 Higher magnification AFM topography of an ion irradiated specimen after corrosion test for 500sec.

JP0350292

2.28 Effect of Helium and Hydrogen Production on Hardness of F82H Steel Irradiated by Dual/Triple Ion Beams

Eiichi Wakai*, Tomotsugu Sawai, Hiroyasu Tanigawa, Akira Naito, Tomitsugu Taguchi and Shiro Jistukawa

Department of Materials Science, Tokai Research Establsihment, JAERI, Tokai-mura, Ibaraki 319-1195, Japan

Abstract

Effect of helium and hydrogen production on radiation-hardening of F82H irradiated by dual or triple beam condition were investigated. The specimens used were four types of ferritic martensitic steels of F82H-std (Fe-8Cr-2W-0.2V-0.04Ta-0.1C) steels tempered at 750°C for 60 minutes, 20% cold worked F82H steel, F82H tempered for 10 minutes and non-tempered F82H steels. The irradiation was performed at 450°C to 50 dpa under simultaneous dual beams of 10.5 MeV Fe^{3+} and 1.05 MeV He^{+} or triple beams of those and 380keV H^{+} ions. The ratios of He (appm)/dpa and H (appm)/dpa were 15 nad 15 (or 150) for dual and triple ion beams. The hardness of the irradiated specimens measured at room temperature using a micro indentation after the irradiations. The hardness in these F82H steels irradiated at 450°C to 18 dpa under triple beam irradiation was harder than that under dual beam irradiation. Irradiation softening and hardening under dual beams was observed in F82H steel irradiated at 450°C to 18 and 50 dpa, respectively.

Keyword: *F82H, ferritic steel, triple ion beams, dual ion beams, radiation-hardening, radiation-softening, microstructure, hardness*

*Corresponding author:
Eiichi Wakai
Department of Materials Science, Tokai Research Establsihment, JAERI,
Tokai-mura, Ibaraki 319-1195, Japan
Tel:029-282-6563, Fax:029-282-5922,
e-mail: wakai@realab01.tokai.jaeri.go.jp

1. Introduction

Low-activation ferritic/martensitic steels are candidate materials for the first wall and blanket structure of fusion reactors. The high-energy neutrons produced in the D-T fusion reaction induce displacement damage and generate gas atoms from (n, p) and (n,α) reactions in the materials. The presence of these gases may lead to degradation of mechanical properties. The effect of neutron irradiation on the tensile deformation of F82H steel has been reported[1)-3)]. Recently, the swelling of F82H and the other 7-9Cr low-activation ferritic steels irradiated at 430°C to 67 dpa in FFTF was reported by Morimura[4)]. The swelling of F82H was 0.1%, and that of the other steels was 0.1- 0.7%. Maziasz and Klueh[5)] had investigated the swelling versus helium production rate in 9Cr-1MoVNb(-0, -2Ni) and 12Cr-1MoVW(-0, -2Ni) steels irradiated at 400°C to 47 dpa, using the efficiency of helium production rate for HFIR and FFTF, and they indicated that the swelling of 0.1 to 0.4% depended on helium production. Recently, we have reported the effects of helium production and heat treatment on swelling behavior of F82H steels using ^{10}B, ^{58}Ni and ^{60}Ni doping. The irradiation was performed in the HFIR at 300 and 400°C to 51 dpa[6)]. The swelling of tempered F82H-std and F82H doped with ^{10}B irradiated at 400°C was from 0.5 to 1.2 %, while the swelling of the non-tempered F82H doped with ^{58}Ni or ^{60}Ni was less than 0.02%. At 300°C the swelling in all steels was insignificant. In the F82H+Ni, high number densities of carbides were formed in the matrix at these temperatures. The production of helium atoms enhanced the swelling of the F82H steel. However, the non-tempered treatment for the F82H+Ni remarkably suppressed the swelling. The cause of low swelling in the F82H+Ni may be due to the formation of the high density of carbides acting as sinks or the decrease in mobility of vacancies that interacted with carbon atoms in matrix.

Purpose of the present study is to investigate the effect of helium and hydrogen production on hardening and microstructures of F82H steel irradiated by dual or triple beam conditions.

2. Experimental procedure

The chemical compositions of the F82H-std steel (IEA-heat, rolling No. KG820-2, sampling position 42W-16, grain size number 3.5) used in this study are given in Table 1. The heat treatment for F82H-std specimen was firstly normalized at 1040°C for 40 minutes in a vacuum followed by air-cooling. After that the specimens were tempered at 750°C for 1 hour in a vacuum followed by air-cooling.

Table 1
Chemical compositions of the F82H steel (IEA heat) used in this study

Alloys	Cr (wt%)	C	N	P	S	Al	Si	V	Ti	Mn	Ta	W
F82H-std	7.84	0.09	0.007	0.003	0.001	0.001	0.07	0.19	0.004	0.1	0.04	1.98

Table 2
Four kinds of specimens used in this study

Specimens	Normalizing	Tempering	Cold work
F82H-std	1040℃、40min.	750℃、60min.	-
F82H-Nor	1040℃、40min.	-	-
F82H-10min-T	1040℃、40min.	750℃、10min	-
F82H-CW	1040℃、40min.	750℃、60min.	20%

In order to investigate the effect of heat treatment and gas atoms on irradiation hardening/softening and microstructural changes, four types of specimens were prepared as shown in Table 2, and they are denoted as F82H-std, F82H-Nor., F82H-10min-T, F82H-CW, respectively. The microstructures of the specimens were observed using a Hitachi HF2000 transmission electron microscope before irradiation experiments. Standard 3 mm-diameter disks cut from 0.25 mm-thickness sheet stock were irradiated in the TIARA facility. It was performed under a simultaneous dual ion irradiation with 10.5 MeV Fe^{3+} ions and1.05 MeV He^{+} ions or a simultaneous triple ion irradiation with those and 380 keV H^{+} ions. The irradiation was mainly performed to 18 or 50dpa(displacement per atoms). The peak ratios of He (appm)/dpa and H (appm)/dpa are 15 and 15 (or 150) for dual and triple beam irradiation. The peak positions of damage, helium and hydrogen ions were all about 1.75 μm, which was calculated by using SRIM97 code. During the irradiation, the temperature of the surface in all specimens was continuously measured with Nikon's thermal vision system. Indentation testing was performed on these specimens, using a Berkovich diamond indenter at a maximum load to 25mN, on an ultra micro-indentation, UMIS-2000. Micro-hardness profiles were obtained by a contact pressure evaluation method based on the procedure proposed by Oliver et al[7].

3. Results

3.1 Microstructures and hardness before irradiation

Figs. 1(a)-1(d) show the microstructures of F82H-Nor, F82H-10min-T, F82H-std, and F82H-CW specimens, respectively. Lath structure and a high density dislocation were formed in the F82H-Nor specimen and no carbides were seen as given in Fig. 1(a). In the tempered F82H for 10 minutes, carbides were formed in matrix and lath boundaries, and the dislocation density was lower than that in the F82H-Nor. In the standard of F82H specimen tempered for 60 minutes, the density of dislocations decreased, and the carbides grew. The density dislocation in F82H-CW specimen was clearly lower than that in the F82H-10min-T. Fig. 2 shows hardness of the specimens measured at room temperature using an ultra micro-indentation. The hardness of F82H-Nor was about twice of F82H-std. The hardness of F82H-CW was smaller than that of F82H-10min-T.

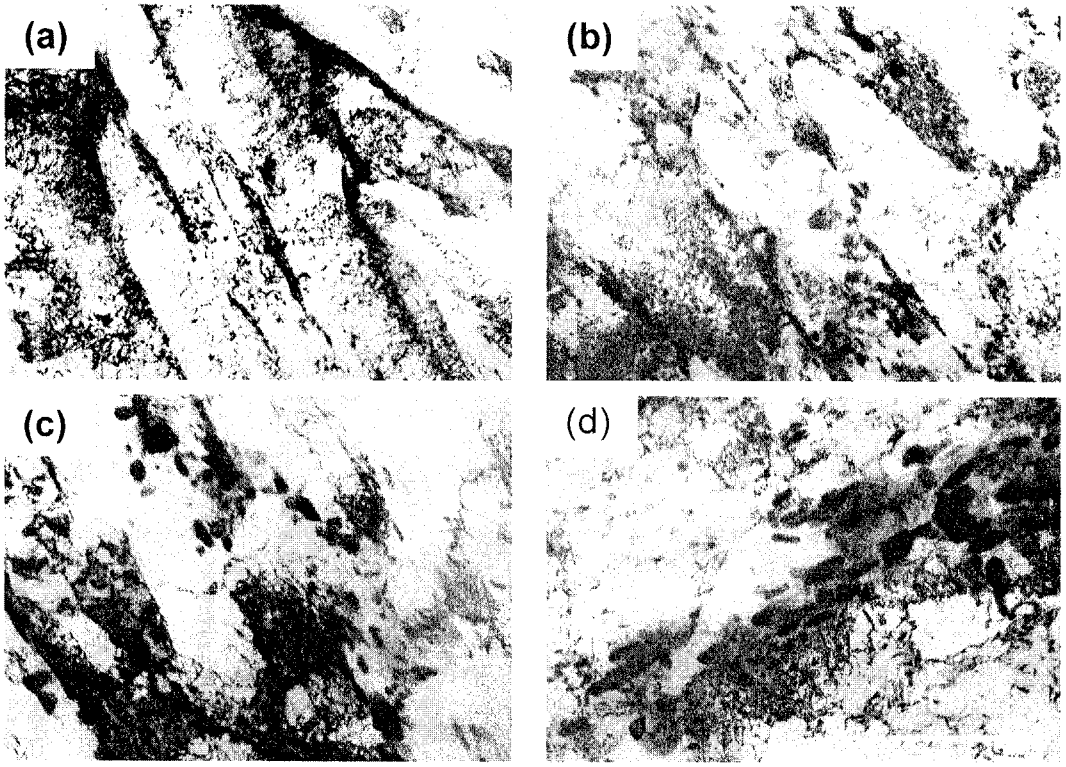


Fig. 1 Microstructures of non-tempered F82H (a), 10min-tempered F82H (b), 60min-tempered F82H-std (c), and 20%CW F82H (d) steels taken by a transmission electron microscope before irradiation

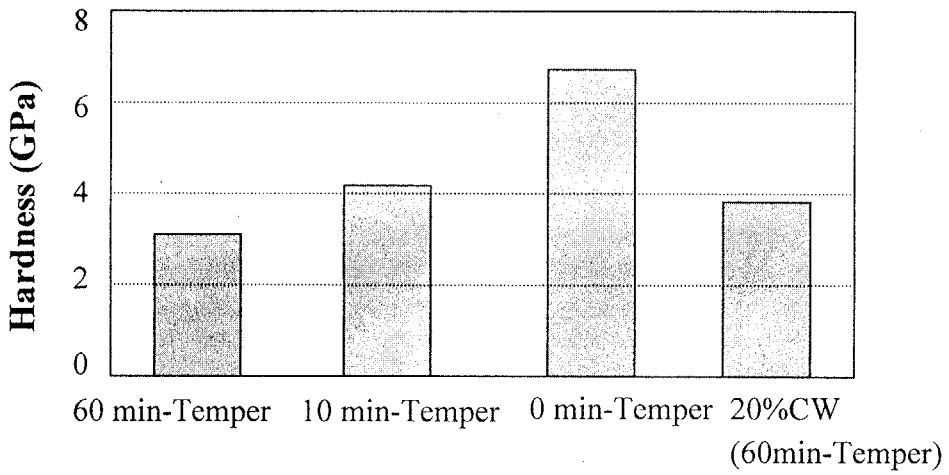


Fig. 2 Micro-hardness of 60min-tempered F82H(std), 10min-tempered F82H, non-tempered F82H, and 20%CW F82H steels measured by an ultra micro-indentation before irradiation. The tempering was performed at 750°C after the normalizing at 1040°C.

3.2 Hardness after ion irradiation

Fig. 3 shows the dose dependence of hardness measured at room temperature in the F82H-std irradiated at 450°C to 50 dpa under dual beams of Fe^{3+} and He^{+} ions. The hardness of F82H-std before irradiation was about 3.4 GPa at room temperature. A small of irradiation-hardening was observed in the specimen irradiated at 450°C to 2.3 dpa, and the hardness were tendency to be somewhat reduced at 18 dpa and again slightly increased at 50dpa. The hardness of all specimens for dose dependence is given in Fig. 4, and the changes due to the irradiation are similar to the F82H-std.

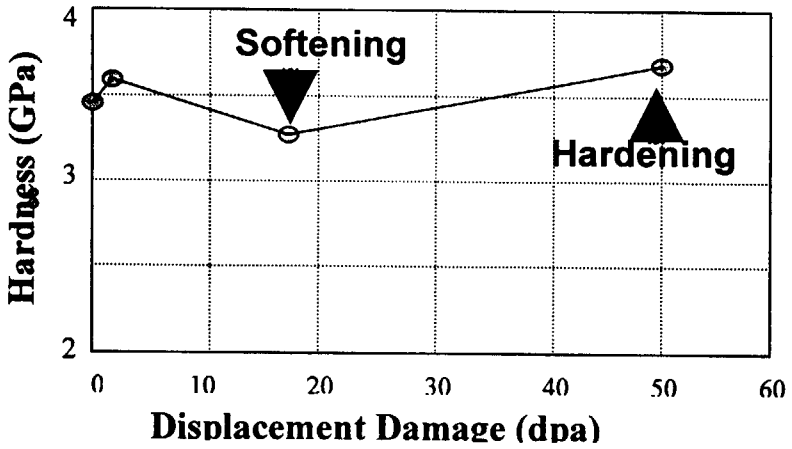


Fig.3 Dependence of hardness on irradiation dose in the F82H-std (tempered at 750°C for 60minutes) irradiated at 450°C to 50 dpa under dual ion beams of Fe^{3+} and He^{+} ions.

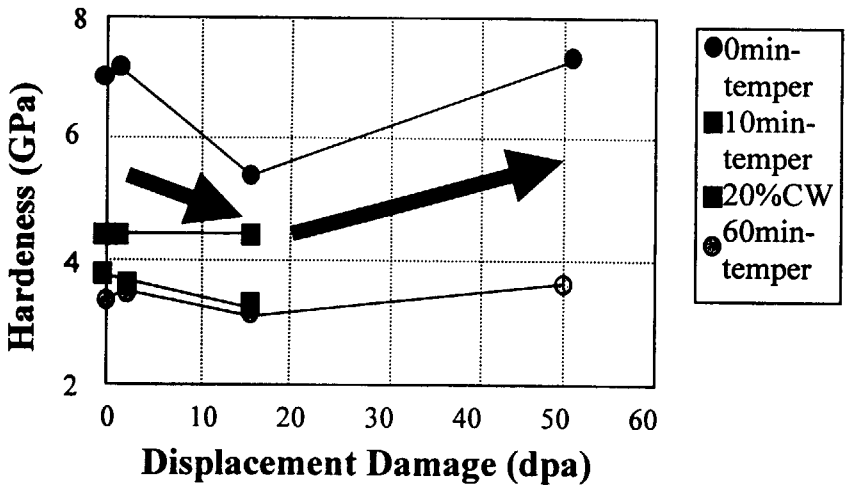


Fig.4 Hardenss of F82H-0min-tempered (as normalized), F82H-10min-temper, F82H+20%CW steels irradiated at 450°C under dual ion beams of Fe^{3+} and He^{+} ions.

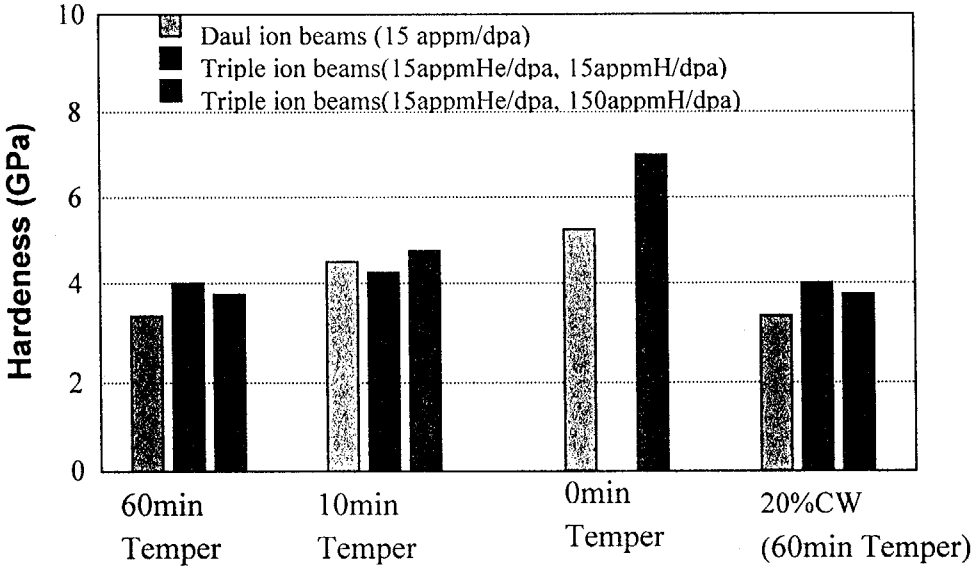


Fig. 5 Effect of triple and dual ion beams on hardness of F82H steels irradiated at 450°C to 18 dpa.

The effect of triple beam in the F82H-std and F82H-normalizing irradiated at 450°C to 18 dpa was shown in Fig. 5. In both specimens the increase of hardness in triple beam condition was larger than that in dual beam condition. Hydrogen atoms might affect somewhat on the formation and growth of cavity.

4. Discussion

As shown in Figs. 3 and 4, irradiation softening occurred at 450°C to 18 dpa, and irradiation hardening was observed to 50 dpa. The change of hardness during irradiation might to be related to microstructural evolution of defects such as dislocations, dislocation loops and cavities. It is well known that the dislocation network of cold worked stainless steels irradiated by neutrons rapidly decreases in a displacement damage about 5 to 10 dpa at even around 400°C[8]-[9]. Although the density of Frank loops increases, the total dislocation density including dislocation network and Frank loops decreases at 5 to 10 dpa. If no cavities were formed, it is expected to be reduced hardness. In ferritic martensitic steels[10], the reduction of hardness was induced by neutron irradiation of FFTF/MOTA above 430°C to 36 dpa. They have high densities of dislocation. In the F82H-std steel used in this experiment, it has a high number density of dislocations about 5×10^{14} m^{-2}. The other steels used in this study have also higher density dislocations than that of F82H-std. The situation of F82H steel irradiated at 450°C might be very similar to that of CW stainless steels, and the softening of F82H steel could be expected, because of the decrease of dislocation density induced by the irradiation. In this study, gas atoms were implanted to the specimens and many bubbles could

be formed. Bubbles and voids have barrier strength for deformation[11], and they could contribute on irradiation hardening. The swelling of F82H-std steels irradiated at 450°C to about 50 dpa under dual ion beam of Fe^{3+} and He^{+} ions has been reported by Naito et al.[12] and it is about 0.1%. The mean size and number density of cavity are about 2.5 nm and $4x10^{21}$ m^{-3}. The hardening caused by cavity formation can be estimated by using a model of Orowan's simplest expression for dispersed barrier, and the change in shear strength due to planar defects can be written as

$$\Delta\tau = \mu b(Nd)^{0.5}/\beta \qquad (1)$$

where is the shear modulus, b is the Burgers vector magnitude and is a measure of the barrier strength, and $(Nd)^{0.5}$ is the average barrier spacing where N and d are the obstacle's number density and average diameter, respectively. Taking the values of $\beta = 4$ [13], the assumptions of $\Delta\sigma_y \sim 3.1\Delta\tau$[14] and $\Delta H \sim 3\Delta\sigma_y$[15] gives $\Delta H \sim 0.34$ GPa, which is corresponds to the net hardening of the irradiated F82H-std steels, 0.3 GPa. Thus, the irradiation hardening might be appropriate to be mainly induced by the growth of cavities.

The effects of triple ion beams on hardening and swelling in BCC metals were reported[16]-[17]. According to the reference[17], the difference of irradiation hardening of ferritic steel between dual ion condition and triple beam was examined at temperatures from 80 to 350°C, it was largest at lowest temperature. In this experiment, the irradiation hardening under triple beams was slightly larger than the dual ion beams, and similar results could be obtained in this study even at high temperature of 450°C.

5. Conclusions

Effect of helium and hydrogen production on hardening of F82H irradiated by dual or triple beam condition were investigated. The irradiation was performed at 450°C to 50 dpa under simultaneous dual beams of 10.5 MeV Fe^{3+} and 1.05 MeV He^{+} or triple beams of those and 380keV H^{+} ions. The ratios of He (appm)/dpa and H (appm)/dpa were 15 nad 15 (or 150) for dual and triple ion beams. The specimens used were four types of ferritic martensitic steels of F82H-std (Fe-8Cr-2W-0.2V-0.04Ta-0.1C) steels tempered at 750°C for 60 minutes, 20% cold worked F82H steel, F82H tempered for 10 minutes and non-tempered F82H steels. The hardness measured at room temperature using a micro indentation. The results obtained as described below;

(1) Irradiation softening and hardening under dual beams was observed in F82H steel irradiated at 450°C to 18 and 50 dpa, respectively.
(2) The hardness in all F82H steels irradiated at 450°C to 18 dpa under triple beam irradiation was larger than that under dual beam irradiation.
(3) The cause of the irradiation softening and hardening might be related with microstructural evolution such as dislocations and cavities during irradiation.

Acknowledgement

The authors would like to thank members of TIARA facility in JAERI for utilization of ion beam experiment.

References

(1) K. Shiba, I. Ioka, J. P. Robertson, M. Suzuki, and A. Hishinuma, Euromat-**96**(1996), p.265.
(2) K. Shiba, A. Hishinuma, J. Nucl. Mater., 283-287(2000)474-477.
(3) F. Rowcliffe, J. P. Robertson, R. L. Klueh, K. Shiba, D. J. Alexander, M. L. Grossbeck, and S. Jitsukawa, J. Nucl. Mater., **258-263**(1998), pp. 1275-1279.
(4) T. Morimura, A. Kimura, and H. Matsui, J. Nucl. Mater., **239**(1996)118-125.
(5) P. J. Maziasz and R. L. Klueh, American Society for Testing and Materials-1046, Philadelphia, 1990, p. 35.
(6) E. Wakai, N. Hashimoto, J. P. Robertson, R.L. Klueh, K. Shiba, and S. Jistukawa: J. Nucl. Mater., 283-287(2000)799-805.
(7) W.C. Oliver, G.M. Pharr, J. Mater. Res. 7(1992)1564.
(8) S.J. Zinkle, P.J. Maziasz, and R. E. Stoller, J. Nucl. Mater., 206(1993)266-286.
(9) P.J. Maziasz, J. Nucl. Mater., 191-194(1992)701.
(10) A. Kohyama, Y. Kohno, K. Asakura, H. Kayano, J. Nucl. Mater., 212-215(1994)684-689.
(11) G.E. Lucas, J. Nucl. Mater., 206(1993)287-305.
(12) A. Naito, E. Wakai, T. Sawai, and S. Jitsukawa, presented in MRS meeting, 2000, in Boston, in USA.
(13) J. M. Martin, Micro-mechanism in Particle-Hardened Alloys, Cambridge University, Cambridge, 1980.
(14) R.E. Stroller, Effects of Radiation on Materials, ASTM STP 1270, ASTM, Philadelphia, 1996, pp. 25-58.
(15) U. F. Kocks, Metall. Trans. 1(1970)1121.
(16) S. Yonamine, T. Iwai, Y. Arai, N. Sekinura, A. Naito, Y. Miwa and S. Hamada, J. Nucl. Mater., in press.
(17) G.E. Lucas, G. R. Odette, R. Maiti and J. W. Sheckherd, Influence of Radiation on Materials Properties, ASTM STP 956, ASTM, Philadelphia,1987, pp. 379-394.

JP0350293

2.29 SINTERING AND POLYTYPE TRANSFORMATION OF SiC BY AlB_2 ADDITION

Hidehiko Tanaka[1], Takefumi Mitsuhashi[1], Dong-Woo Shin[2], and Sam-Shik Park[2],
[1]National Institute for Materials Science,
1-1 Namiki, Tsukuba-shi, Ibaraki-ken 305-0044 Japan
E-mail address:TANAKA.Hidehiko@nims.go.jp
[2]Gyeongsang National University, Chinju, Kyoung-nam 660-701 Korea

Abstract

In order to develop the industrial process for SiC materials in the nuclear environment, the sintering behaviors of SiC powders were investigated. α(6H)- and β(3C)-SiC powders were sintered with AlB_2 and C additives. α-SiC powder could be sintered to almost full density at 1900°C. This temperature is 250°C lower than that by the conventional sintering method that uses B and C additives. Al atoms solved form the additive into SiC grains and stabilized 4H polytype, which caused transformation of 6H to 4H. It was also observed that anisotropic grain growth occurred and fracture toughness of the sintered SiC increased with the aspect ratio of grains. β-SiC powder needed slightly higher temperature than α-SiC powder to complete sintering. β-SiC transformed from 3C to 6H and 4H and exhibited exaggerated grain growth.

Keywards: Silicon carbide, Sintering, AlB_2 additive, Transformation, Grain growth, Fracture toughness, Aspect ratio.

1. Introduction

SiC sintered materials have very high strength at high temperature and they have very high tribological performance [1]. SiC fine powders are sintered by the addition of B and C [2] in the industry. To sinter SiC with these additives very high temperature about 2150°C is required. In order to develop new sintering method that enabled to easily sinter SiC powder, much work has been done.

The work so far focused mainly on searching for the new sintering additives. We have intensively investigated the effective additives for the sintering of SiC, and have found that Al-B-C compounds, AlB_2 and C for instance, are very effective additives [3]. When Al-B-C compounds are added in SiC powder, they form liquid phase having the composition of $Al_8B_4C_7$ [4]. With this liquid SiC powders can be sintered at lower temperature. We have also found that SiC powders behave anisotropic grain growth during sintering by the Al-B-C compounds. The sintered SiC with anisotropic grain morphology, i.e. high aspect ratio of grains, increases its fracture toughness.

In this paper, we report low temperature sintering behavior of α-powder with AlB_2 and C additive, microstructural evolution and fracture toughness of sintered SiC. The

sintering behavior of β-SiC powder is also reported comparing with that of α-SiC powder.

2. Experimental procedure

Starting materials were α(6H)-SiC fine powder (UD A-1, Showa Denko Co., Tokyo), β(3C)-SiC(Beta-rumdum ultrafine, Ibiden Co., Gifu), AlB_2 (Kojundo Chemical Co., Saitama) and C from a phenolic resin (J-325. Dainippon Ink Co., Tokyo). Two SiC powders were mixed with AlB_2 and C in SiC ball mills with ethanol medium, subsequently dried and sieved. They were compacted by CIP at 200 MPa, and sintered in a carbon resistance furnace (402E/7 dilatometer, Netzch Co., Germany) at 1800 to 2150°C.

The amounts of polytypes in the sintered specimens were determined by X-ray diffraction analysis using the profile fitting method [5]. The microstructures of the specimens were observed by SEM. The mean grain size and the mean aspect ratio of grain shape were measured with an image analyzing apparatus. The elastic moduli were determined by the pulse echo method, and fracture toughness was measured by the indentation fracture method.

3. Results and discussion

3.1 Sintering behavior of α-SiC powder

The specimen names, the contents of additives and sintering densities at each sintering temperature are listed in Table I. The specimens with small amount of additives, i.e. 0.67 mass% AlB_2 and 2 mass% C, sintered to almost full density (>95%TD) at over 1900°C and those with 1.34 and 2.70 mass% AlB_2 and 2 mass% C could sintered to >95%TD at 1850°C. These results show that AlB_2 and C additives are very effective. Considering that the conventional sintering method needs 2150°C to complete densification of SiC powder with B and C, it is said that low temperature sintering could be achieved by AlB_2 and C additives. When the amount of AlB_2 additive was 5.40 mass%, the density of the specimens did not reach >90 %TD. In these specimens exaggerated grain growth occurred and retarded densification at the early stage of sintering.

The typical microstructure is shown in Fig.1. It is usually observed that the sintered α-SiC with B and C additives consits of equi-axis grains, i.e., isotropic polyhedral grains. On the contrary, by AlB_2 and C additives SiC powders grew into rod- or plate-shaped grains.

Table I Contents of additives in starting powders and sintering densities

Sample No.	Contents of AlB_2, C and 6H-SiC powder (mass %)			Sintering Temperatures(°C) and relative densities of sintered SiC(masst%)					
	AlB_2	C	6H-SiC	1800	1850	1900	1975	2000	2150
SC-1	0.67	2.00	97.33	87.2	94.6	98.0		98.8	99.9[G]
SC-2	1.34	2.00	96.66	90.7	96.0	97.2		98.9	97.9[G]
SC-3	2.70	2.00	95.30	90.2	96.5	97.4	97.8, 97.6*		96.7[G]
SC-4	5.40	2.00	92.60	79.3	80.2	81.8[G]	85.4[G]		86.1[G]

Holding time at the maximum temperature is 30min., or *0 min.
[G] The sintered 6H-SiC exhibited large grain growth.

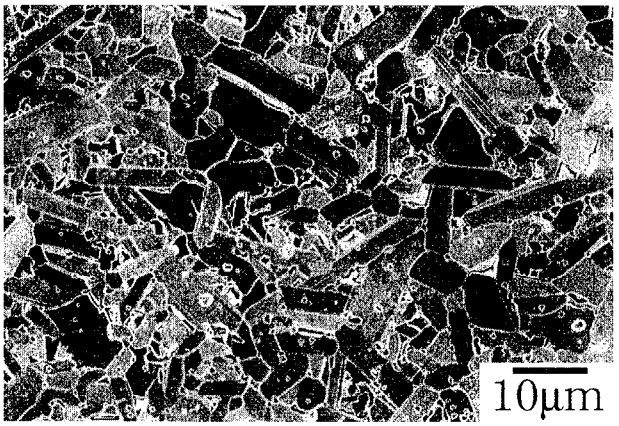


Fig.1 Typical grain shape of specimen SC-3 sintered at 1975°C.

3.2 Phase transformation of sintered α-SiC

The phase transformation of the sintered SiC specimens is shown in Table II. The starting powders were mostly single phase of 6H. 6H was stable at around 2000°C, and usually did not transform. SiC grains with AlB_2, however, behaved polytype transformation from 6H to 4H when the amount of additive was large and the sintering temperature was high. As Al solution into SiC crystals stabilizes 4H polytype [6], the transformation seems to have been accelerated by Al solution.

Table II Polytype contents in the starting α-SiC powder and sintered SiC specimens.

Sample No.	Sintering Temps.(°C) and Times(min)		Polytype contents(%) 4H	6H	15R
6H-Starting powder			2	98	0
SC-1a	2000	30	4	92	4
SC-2a	2000	30	9	86	5
SC-3b	2150	30	30	67	3
SC-3c	1975	30	10	89	1
SC-3d	1975	0	7	93	0
SC-4c	1975	30	4	85	11

The letters "a, b, c and d" appended after the sample No.s indicate the differences in sintering temperatures.

3.3 Fracture toughness and microstructure of sintered α-SiC

The microstractural parameters and fracture toughness are listed in Table III. From the table it was found that the fracture toughness, K_{IC}, increased with the aspect ration of grains. The plate- or rod-shaped grains favored mechanical properties of the sintered SiC materials. Toughening by rod-shaped grains has been analyzed by the grain bridging mechanism. From the theory the apparent fracture energy, K_A^2, is expressed as follows [5]:

$$K_A^2=T_0^2+(\pi/6)^{1/3}E\tau\varepsilon^2\alpha^{5/3}G \quad (1)$$

Where T_0^2 is intrinsic fracture energy of materials, E, τ and ε are Young modulus, frictional stress and bridging rapture strain of pull-out grain, respectively. α and G are the aspect ratio and the grain size. Eq.1 1 indicates that the fracture toughness very much depends on these two parameters. The sintered SiC specimens had high toughness in proportion to the aspect ratio and the size of grains.

Table III Grain sizes, aspect ratios, Vicker's hardnesses, Young's moduli and fracture toughnesses of sintered 6H-SiC specimens.

Sample	Microstructural parameters		Mechanical properties		
No.	GS(μm)	α	HV5	E(GPa)	K_{IC}(MPam$^{1/2}$)
SC-1a	1.7	1.6	2254	430	3.6 ± 0.3
SC-2a	2.5	1.9	2144	440	3.9 ± 0.2
SC-3b	6.1	2.6	1936	405	4.3 ± 0.2
SC-3c	3.4	1.9	2061	443	4.2 ± 0.3
SC-3d	3.1	1.8	2109	415	4.1 ± 0.2
SC-4c	4.4	2.1	890	277	---
SC-B*	1.3	1.7	2560	442	3.0 ± 0.2

GS: Mean grain sizes, α: Mean aspect ratios, HV5: Vicker's hardnesses by 5 kg loading, E: Young's moduli, K_{IC}: Fracture toughnesses by IF method, *sintered with B and C.

3.4 Sintering behavior of β-SiC powder

β-SiC powders were sintered as the same manner as α-SiC powder. The results are summarized in Fig.2. In the figure, the contour lines of equi-density of sintered α- and β-SiC are drawn along with that of α-SiC. β-SiC powders were slightly harder to sinter and required about 50°C higher temperature than α-SiC to complete sintering. The sintered β-SiC exhibited exaggerated grain growth when it contained large amount of additives and the sintering temperatures were higher than 2000°C. β-SiC powders easily transformed to 6H and 4H by the grain growth, because it was not stable at the sintering temperature.

4. Summary

α- and β-SiC powders were sintered with AlB_2 and C additives at 1800~2150°C. Both of powders could be sintered about 1900°C. This sintering temperature was 250°C lower than that of the conventional sintering method with B and C additives. Low temperature sintering could be possible with AlB_2 and C additives.

Grains in the sintered SiC became elongated shape, and its aspect ratio and grain size increased with the sintering temperature. The large aspect ratio of grains seems to increase fracture toughness by the grain bridging mechanism.

β-SiC powder was slightly harder to sinter than α-SiC. This was due to thermally unstable nature of 3C polytype at sintering temperature. β-SiC grains exhibited transformation of 3C to 6H and 4H, and exaggerated grain growth at >2000°C.

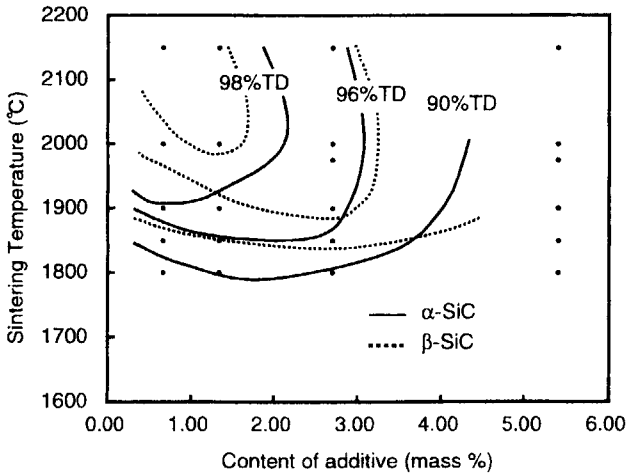


Fig.2 Relation among sintering densities, temperatures and amounts of AlB_2 additive.

References

[1] H.Suzuki, K.Iseki and H.Tanaka, *Advanced Silicon Carbide Ceramics* (Uchida-Rokakuho Publ. Co., Tokyo Japan 2001).

[2] S.Prochazka, *Special Ceramics vo.l6* (British Ceramic Association, Stoke-on Trent UK 1975) pp171.

[3] H.Tanaka and Y.Zhow, J. Mater. Res., **14**, 518 (1999).

[4] Y.Inomata and H.Tanaka, J. Ceram. Soc., Japan, **88**, 353 (1980).

[5] H.Tanaka and N.Iyi, J. Am. Ceram. Soc., **78**, 1223 (1995).

[6] Yo Tajima and W.D.kingery, J. Am. Ceram. Soc., **65**, C27 (1982).

JP0350294

2.30 ELLIPSOMETRY STUDIES ON NITROGENATED DIAMOND-LIKE CARBON (DLC) THIN FILMS PRODUCED BY RF MAGNETRON SPUTTERING.

P.R.Vinod[1*], H.Kakiuchi [1], T.Terai [1], A.N.Itakura [2], M.Kitajima [2]
[1] Department of Quantum Engineering and Systems Science, The University of Tokyo, 7-3-1 Hongo, Bunkyo-ku, Tokyo 113-8656, Japan.
[2] National Institute for Materials Science, 1-2-1 Sengen, Tsukuba shi, Ibaraki 305-0047, Japan

Abstract

Nitrogen doped Diamond-like carbon thin films were deposited on n-Si and SiO_2 substrates by rf magnetron sputtering using pure graphite (99.999%) as the target material and mixtures of Ar, N_2 and H_2 for plasma generation. The dependence of structural and optical properties on nitrogen content was investigated using XPS, Raman spectroscopy, FT-IR spectroscopy, and Ellipsometry studies. It was found that as the nitrogen content was increased in the plasma, sp^2 bonding favored. Also it was observed that oxygen contamination increased with nitrogen content. Typical C-H stretching modes connected with diamond-like carbon could be seen in FT-IR spectra. The I_D and I_G bands were well defined and it was observed that as nitrogen content increased I_G band was enhanced. Ellipsometry studies revealed that the optical constants like refractive index (n) and extinction co-efficient (k) increased with increase in nitrogen content as well as substrate temperature.
Keywords: Diamond-like Carbon, Anti-Reflection, Ellipsometry, Refractive Index, Extinction Co-efficient.

1 Introduction

DLC is an amorphous material mainly comprising of sp^2 and sp^3 bonded carbon atoms. Due to its unique properties such as hardness, chemical inertness, good mechanical adhesion, high dielectric strength, tunable refractive index, etc. it has applications in various fields [1]. These DLC films can be prepared by a lot of techniques. However all these techniques use hydrocarbons for generating plasma. Here we employ rf magnetron sputtering and the plasma gas is a mixture of argon, nitrogen and hydrogen. These films have a complicated network of carbon atoms of different hybridized states [2] with hydrogen included in atomic and molecular form. The main aim of this study is to determine the possibility of application of DLC coating (doped with nitrogen) as a good anti-reflection coating for solar cells, thereby increasing the efficiency of these cells.

2 Experimental :

Here in our study rf magnetron sputtering technique was employed to produce DLC films. The rf (13.56MHz) power was 100w. Pure graphite (99.999%) was used as target and the

---

Corresponding Author. Tel : +81-90-4439-1968 Fax : +81-3-3945-5213
Email Address : vinod@starling.t.u-tokyo.ac.jp

deposition was carried out on n-Si and SiO_2 substrates (8x8 mm^2, 0.5mm thick). The plasma gas comprised of different concentrations of nitrogen and hydrogen along with argon. The target was at a distance of 4cm from the substrate. The total working gas pressure was 1Pa and deposition time was 0.5, 1 and 2 hour. Deposition was carried out for different substrate temperature (50, 100, 150, and 200^0c) under same plasma conditions to understand the effect of substrate temperature on properties of these films. The deposited films were then subjected to various surface studies to understand bonding nature of these of films. Optical studies were also carried out to exploit the optical properties of these films. XPS studies were done to estimate the concentration of relative elements present in the films. Raman and FT-IR spectroscopic studies were done to understand the chemical nature of these films. The primary optical constants such as refractive index (n) and extinction co-efficient (k) were determined using laser ellipsometry.

3 Results and Discussion:

The deposited films were subjected to these characterization techniques to understand the properties of these films.

3.1 XPS Analysis:

Typical C1s and N1s spectra was seen by XPS studies. To check the bonding states of C in the a-C:H:N films, the C1s peak was de convoluted with 4 Gaussian bands [3,4]. On comparing the de convoluted peaks for different samples the following features were observed: sp^2CN bonding was favored as nitrogen content in the plasma increased. The oxygen contamination was found to increase as nitrogen content in the plasma increased. It was observed that carbon was present in graphitic form as well as diamond-like form. In a similar manner, the N1s peak was deconvoluted using three Gaussian bands.

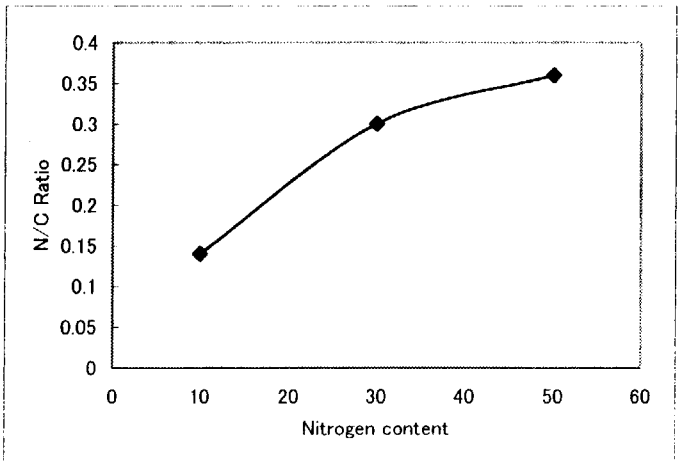


Fig 1. N/C Ratio as a function of nitrogen content in the plasma.

The N/C ratio of the films deposited at different nitrogen plasma conditions were obtained from the integral areas of C1s and N1s peak using the photo-ionization cross-section of each element [5]. The N/C ratio increased with increase in nitrogen content in the plasma. N/C ratios were 0.14, 0.3, and 0.36 for the plasmas containing 10%, 30%, and 50% nitrogen respectively as shown in figure 1.

3.2 Auger Electron Spectroscopy:

AES spectra revealed that pure a-C:H films contained almost no nitrogen. It was found that nitrogen content in the films increased as nitrogen in the plasma increased. For the same composition it was observed that nitrogen content increased with increase in substrate temperature. Deposition time had no much influence on nitrogen content. Only films deposited on SiO_2 showed Si peaks, because of higher adhesion of films on to n-Si substrates rather than SiO_2.

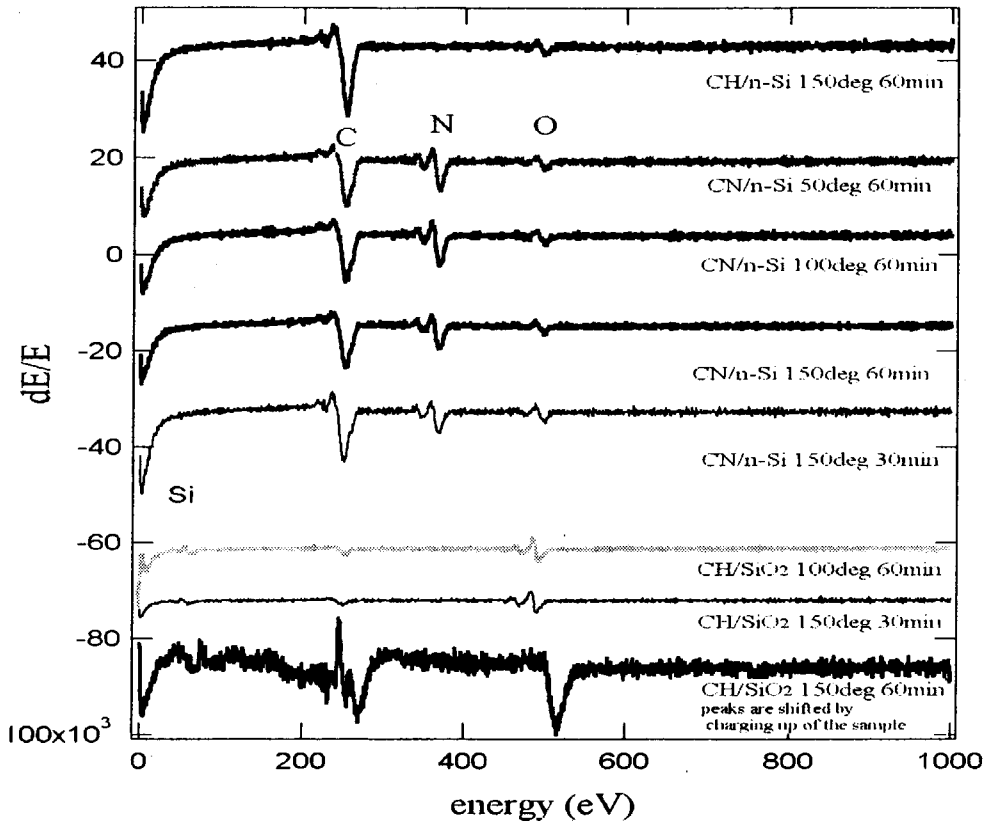
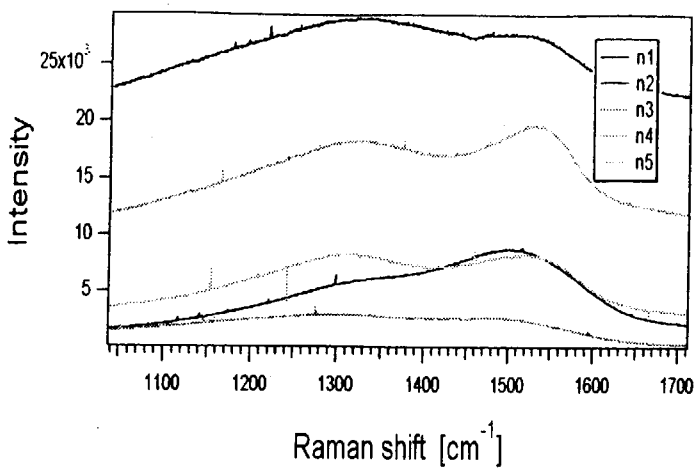


Fig 2. AES Spectra of a-C:H:N films deposited at different plasma conditions.

3.2 Raman Spectroscopy

Raman spectroscopic studies were done to get an idea about the I_D and I_G bands for these films. Typical Raman spectra for these films is shown in fig2. It was observed that as nitrogen content increases the I_G band was enhanced. This implied that the structure was becoming more and more graphitic implying that more sp^2 bonding was favored.



n1---CN/n-Si, 150^0; n2---CH/ SiO_2, 150^0; n3---CH/ SiO_2, 150^0;
n4—CN/ SiO_2, 150^0; n5---CH/n-Si, 100^0
Fig2. Raman spectra of a-C:H:N films of various composition.

In case of pure a-C:H films the I_D/I_G ratio was less than one. It was observed that the I_D/I_G ratio increased with increase in substrate temperature.

3.3 FT-IR Spectroscopy

The infra-red absorption spectra are shown in fig4. It consists of a broad band at 1000-1600cm^{-1}; C≡N stretching at 2100-2250 cm^{-1}; C-H stretching mode at 2800-3000 cm^{-1}; N-H stretching mode at 2800-3000 cm^{-1}.

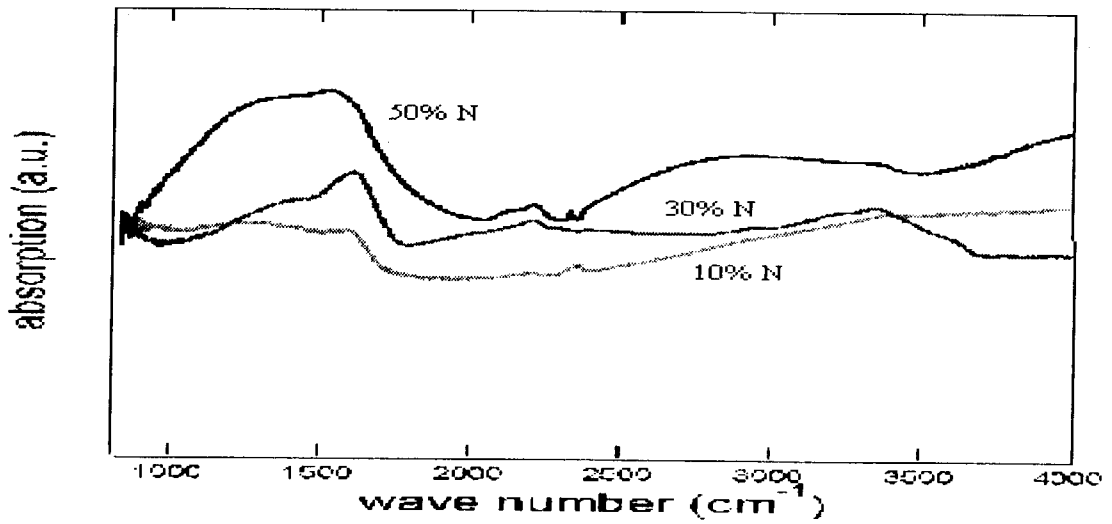


Fig 2 . FT-IR Absorption spectra of a-C:H:N films deposited at 3 different Nitrogen content in the plasma.

The broad band at 1000-1600 cm^{-1} shown in fig.3 is attributed to carbon matrix of nitrogen atoms. This band can be deconvoluted to 2 bands which are quite similar to I_D and I_G bands found in Raman spectroscopy [6]. The one located near 1400-1600 cm^{-1} is due to the presence of large sp^2 domains while the other near 1250-1400 cm^{-1} is due to sp^3 domains [7].

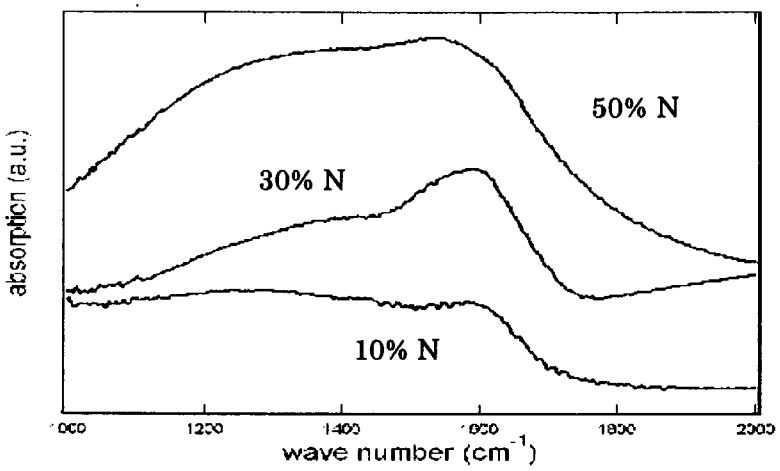
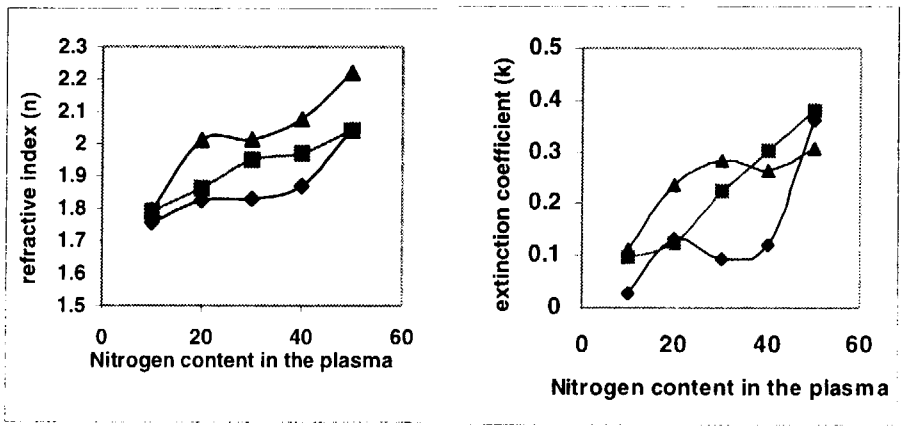


Fig 3. FT-IR Absorption band at 1000-1600cm^{-1} for DLC films of various nitrogen content.

Peak shift is observed as nitrogen content in the plasma increases. The band at 1400-1600 cm^{-1} is found to increase as nitrogen content increases and this implies that sp^2 CN bonding is favored and this corresponds to the results stated earlier.

C≡N stretching modes were found at 2100-2250 cm^{-1} and N-H stretching modes were found at 3200-3500 cm^{-1} according to assignment in molecules [8]. The peak height of CN bonding was found to be enhanced as nitrogen content increases. The absorption band at 2800-3000 cm^{-1} is identified with C-H stretching vibration, which is attributed to diamond-like carbon film [9,10]. As nitrogen content increased this peak was found to be de enhanced showing that the bonding was more likely to graphitic than diamond-like structure.

3.4 Ellipsometry



◆ $T_s = 50^0C$ ■ $T_s = 150^0C$ ▲ $T_s = 200^0C$

Fig3a. Variation of refractive index (n) as a function of nitrogen content

Fig3b. Variation of extinction coefficient (k) as a function of nitrogen content

In order to understand the optical properties of these films the samples were subjected to

ellipsometry measurements. He-Ne laser was used at a fixed angle of incidence of 70 to determine the main optical constants like refractive index (n) and extinction coefficient (k). Fig 5a and 5b shows the variation of refractive index and extinction coefficient as a function of nitrogen content. It was observed that as nitrogen content increased the values of n and k increased and a similar trend was observed with increase in substrate temperature.

In order for a film to exhibit good anti-reflection property, it should have minimum reflectance and this is attained if the following condition is satisfied. The refractive index (n_f) of the film should be equal to the square root of the refractive index (n_s) of the substrate [11]. Here we found that 30%N_2 content sample has n = 1.97 which is the required one for a Si substrate whose refractive index is 3.88. It was observed from ellipsometry that 30% nitrogen content sample had some good anti-reflection property.

4 Conclusion

Nitrogenated Diamond-like carbon (DLC) thin films were deposited on n-Si and SiO_2 substrates at different conditions. From XPS studies it is observed that the carbon is present in both graphitic and diamond-like structure. It is observed that nitrogen content greatly favored sp^2 bonding. Increase in nitrogen content led to oxygen contamination. AES studies revealed that DLC films were less adherent to SiO_2 than Si substrates. It was also observed that Nitrogen concentration in the films was independent of deposition time. On the other hand nitrogen content in these films increased with substrate temperature. Raman and FT-IR spectroscopic studies proved the existence of hydrogen and nitrogen inside the film. Various typical stretching modes were observed. Typical I_D and I_G bands were also found. I_D/I_G ratio increased as substrate temperature increased. Typical C-H stretching attributed to DLC structure was found and this proves that the carbon is present in DLC form also. Ellipsometry studies revealed that the optical constants such as refractive index and extinction co-efficient could be altered by suitably changing the nitrogen content and substrate temperature. Both n and k were found to increase with increase in nitrogen content and substrate temperature.

5 References

1. Robert. E. Clausing et al Diamond and Diamond-like films coatings, NATO ASI Series.
2. J.K. Walters et al Phys. Rev. B 50 (1994) 8931.
3. J.H. Scofield, Journal of Electron Spectroscopy and Related Phenomena, 8(1976) 129-137.
4. C. Jama, et al Surface Coatings Technology 116-119 (1999) 59-64.
5. Sebastino Trusso et al Thin Solid Films 355-356 (1999) 219-222.
6. J.H.Kaufman, et al Phys. Rev. B 39 (1989) 13053.
7. X.A. Zhao, et al Applied Phys. Lett. 66 (1995) 58.
8. Jianhua Ju, et al Journal of Non-Crystalline Solids 278 (2000) 213-217.
9. Nobuki Mutsukura, et al Thin Solid Films 349 (1999) 115-119.
10. N.A. Sanchez, et al Thin Solid Films 373 (2000) 247-250.
11. K. Vedam, optical characterization of Real surfaces and Thin films, Physics of Thin Films Vol. 19, Harcourt Publishers (1995).

JP0350295

2.31 CHANGE IN PROPERTIES OF $Bi_2Sr_2CaCu_2O_{8+x}$ SINGLE CRYSTALS DUE TO NEUTRON IRRADIATION FOLLOWED BY THERMAL ANNEALING

Toshiki Shitamichi[1*], Makito Nakano[1], Kouji Ogikubo[1], Takayuki Terai[1],
Michio Yamawaki[1], and Taiji Hoshiya[2],
[1]Depertmant of Quantum Engineering and System Science, The University of Tokyo,7-3-1 Hongo, Bunkyo-ku, Tokyo, 113-8656, Japan
[2]Tokai Reserch Establishment, Japan Atomic Erergy Reserch Institute, 2-4 Shirakata-Shirane, Tokai-mura, Ibaraki 319-1195, Japan

Abstract

Change in pinning properties of $Bi_2Sr_2CaCu_2O_{8+x}$(Bi-2212) single crystals due to fast neutron irradiation followed by thermal annealing is reported. At the fluence of $5\times10^{18}cm^{-2}$, the J_c and U_0^* decreased due to excess irradiation and increased to thermal annealing after irradiation. For the specimen annealed at 673K, J_c and U_0^* at 20K and 40K increased as annealing time increased up to 24h. On the other hand, for specimen annealed at 1073K, they increased up to 1h or 3h and then decreased. These results indicate a difference in the change of the defect structure due to the thermal annealing.

Keywords:Bi-2212; Neutron irradiation; Thermal annealing; Pinning center

1.Introduction

Particle beam irradiation is one of the most effective methods to introduce strong pinning centers into high-T_c superconductors. In perticular, fast neutron irradiation can introduce defects as pinning centers in all area materials. The thermal annealing treatment after fast neutron irradiation can change the size and the density of the defects in the materials. In some cases, this method is quite effective for critical current *Jc* enhancement, because superconducting properties, including J_c and apparent pinning energy U_0^*, are strongly affected by the defect structure in the

*Corresponding author. Tel and Fax: +81-3-5841-7420
*E-mail address:*toshiki@starling.q.t.u-tokyo.ac.jp (T.Shitamichi)

materials. In this study, the superconducting property change of of Bi-2212 single crystals due to neutron irradiation followed by thermal annealing was invenstigated

2.Experimantal

The Bi-2212 single crystal specimens were prepared by the floating-zone method. The size was $1\times1\times0.05mm^3$(c-axis). The specimens sealed in quartz capsules of 10^{-4} Pa were irradiated isotropically with neutrons (>1MeV) using JMTR (Japan Materials Testing Reactor) at JAERI (Japan Atomic Energy Reserch Institute). The irradiation temperature was room temperature (<313K). The fluence was $1\times10^{16}cm^{-2}$, $1\times10^{17}cm^{-2}$, $2\times10^{17}cm^{-2}$, $6\times10^{17}cm^{-2}$, $1\times10^{18}cm^{-2}$, $2.8\times10^{18}cm^{-2}$, $5\times10^{18}cm^{-2}$. After irradiation, the specimens were annealed in air at 673K or at 1073K for 1-24 hours. Magnetization hysteresis curves were measured with a vibrating sample magnetometer (V.S.M.) at 5K, 20K, 40K and 60K as a function of applied magnetic field parallel to the c-axis. The critical current J_c in a-b plane was caluculated from the magnetization hysteresis curves using the expanded Beam's model[1]. On the other hand, magnetic relaxation measurement was carried out for the specimens before and after annealing with the V.S.M. at 20K and 40K with the applied magnetic field of 0.01T parallel to the c-axis of the specimens. The apparent pinning energy U_0^* was obtaind from the magnetic relaxation curves using the Anderson-Kim model at 20K[2]. At 40K logarithmic relaxation rate α [3] was caluculated instead of U_0^*

3.Result and discussion

The dependences of critical current density J_c on neutron irradiation are shown in Fig.1. J_c change similarly depend on the fluence. J_c increased from the initial value before irradiation due to the irradiation of radiation-induced defect clusters. Jc took a maximum value around the fluence of $6\times10^{17}cm^{-2}$ and decreased in the excess fluence region.

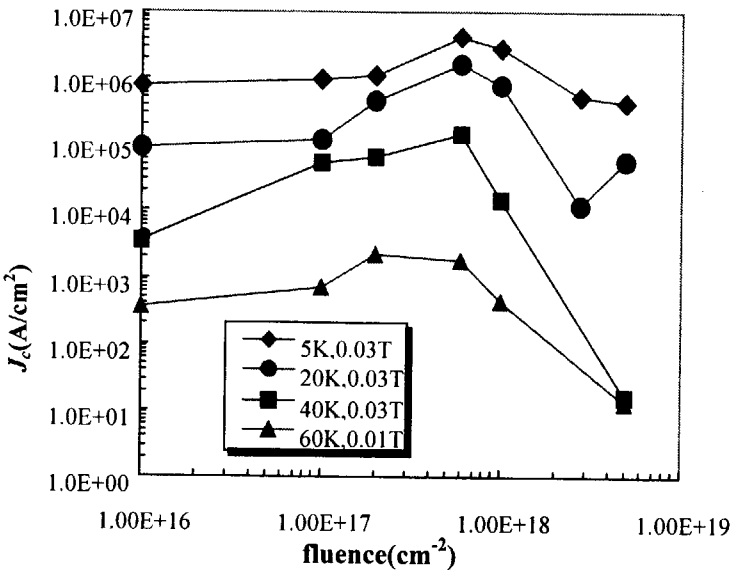


Fig.1 The dependence of J_c on neutron

The dependence of J_c on annealing time is shown in Fig.2 and 3. In the low fluence and at the optimum fluence, J_c once increased by neutron irradiation and then decreased by thermal annealing in almost all the conditions. This is that the size of defect clusters is smaller than the most effective pin, and annealing makes it less effective. At the excess fluence, J_c once decreased by too much neutron irradiation and recoverd by thermal annealing in the almost all the conditions. For long annealing time, J_c keeps the higher value 673K annealed specimens while J_c 1073K annealed ones decreased slightly.

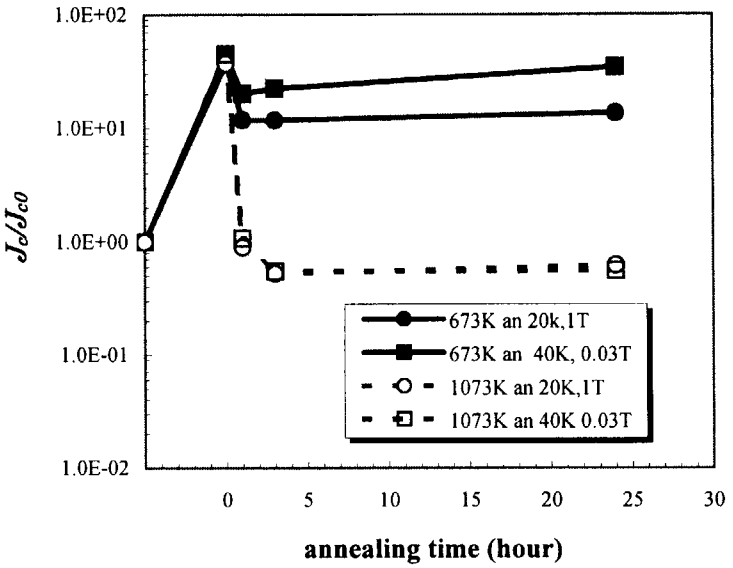


Fig.2 The dependence of J_c on annealing time (6×10^{17}cm^{-2} 1T for 20K, 0.03T for 40K)

Fig.4 and 5 show the dependence of U_0^* and α on annealing time. At 20K, Jc and U_0^* change similarly depending on the annealing time. At 40K, Jc was larger for the specimen annealed at 673K than for the one annealed at 1073K, while α was larger for the latter than for the former. This means that complex defects formed by annealing at 1073K act as stronger pinning centers at 40K but the number is small.

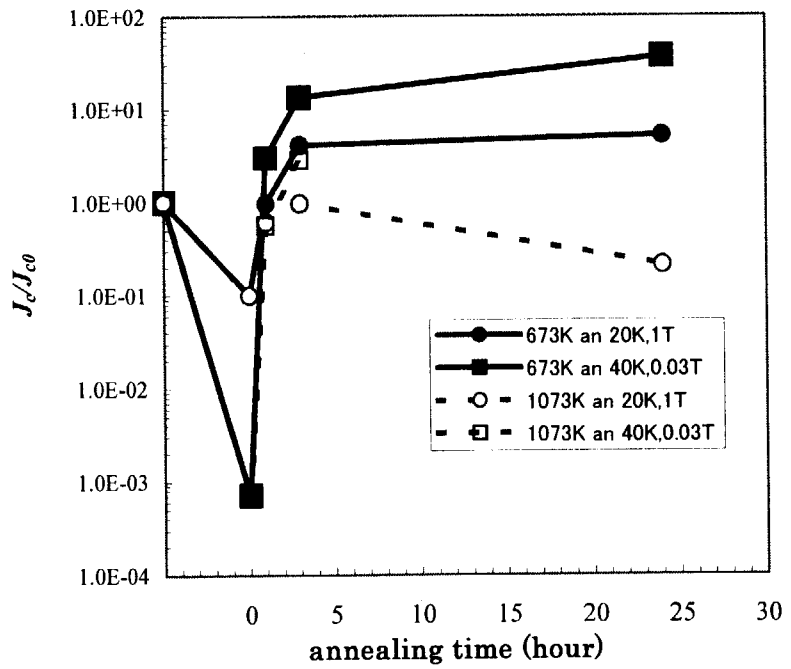


Fig.3 The dependence of *Jc* on annealing time (5×10^{18}cm^{-2} 1T for 20K, 0.03T for 40K)

Fig.6 shows a schematic drawing on the change of defect structure due to irradiation and annealing. When an original specimen (a) is irradiated with an optimum fluence (b), J_c,U_0^* and α increase the most. This means that defects due to neutron irradiation act as pinning centers very well. Irradiated more fluence (c), J_c,U_0^* and α decrease remarkably. This

is caused by the reduction of superconducting region because of a lot of defects overlapping. Complex defects are formed due to lomg time annealing 673K (d) and J_c U_0^* and α increase. Because of low temperature annealing, only oxygen atoms can move and the other atoms consisting of Bi-2212 cannot move, which means that only the defects coming from oxygen atoms recover. On the other hand, short time annealing at 1073K causes complex defect formation (e) and J_c,U_0^* and α increase. These defects act as strong pinning centers at 40K. Finally many defects dissapear (f) and J_c,U_0^* and α decrease with annealing time because almost all the defects recover at such a high temperature.

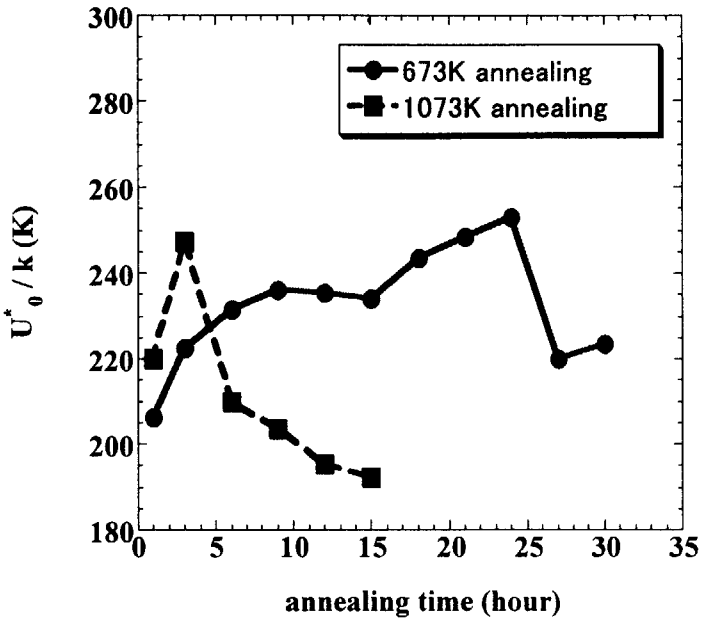


Fig.4 The dependence of U_0^* on annealing time

4.Summery

(1)By irradiation with fast neutron, *Jc* increased up to around the fluence of 6×10^{17}n/cm^2 and then decreased in the excess fluence region.

(2)In the low fluence and at the optimum fluence, J_C decreased by thermal annealing due to the size of defect clusters. On the other hand, at the excess fluence, J_C increased in the first 3 h. By longer time annealing, J_C annealed specimens decreased slightly for 1073K, but J_C annealed one keeps the higher value for 673K. (3)At excess fluence, U_0^* and α are dependent on measurement temperature, annealing time and annealing temperature. Even though *Jc* increased by thermal annealing, neither the U_0^* nor α always increased.

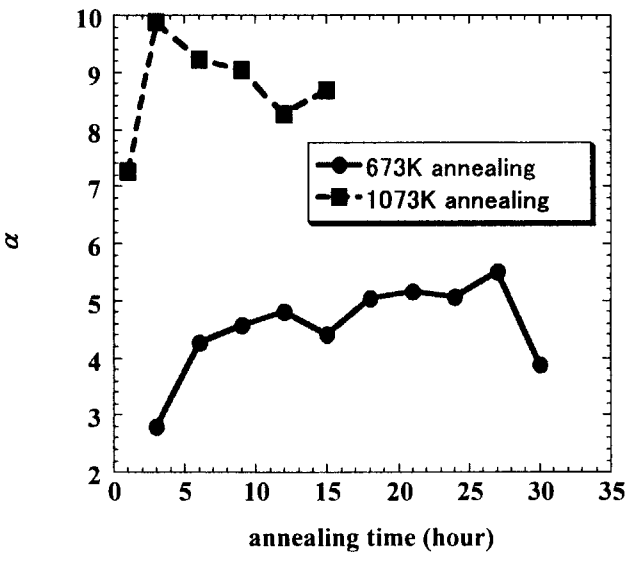


Fig.5 The dependence of α on anenaling time

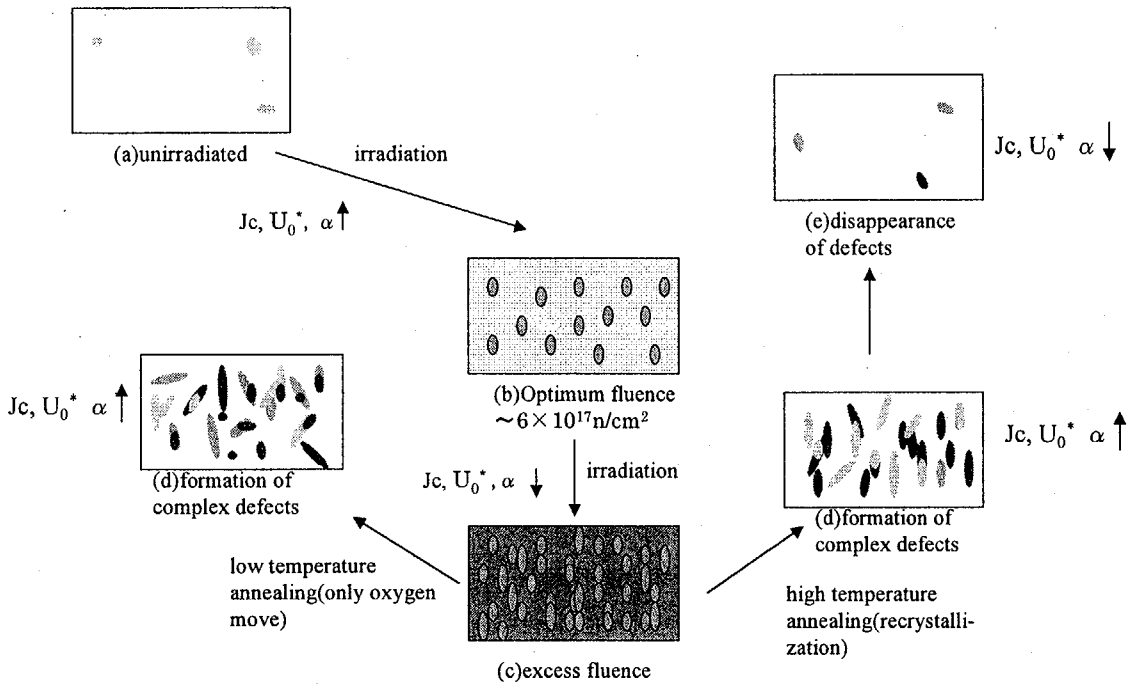


Fig.6 The schematic drawing of defects atructure by irradiated and annealing

<reference>

[1] E.M.Gyorgy *et al.*, Appl. Phys. Lett. **55** (1989) 283.

[2] P.W.Anderson and Y.B.Kim, Rev. Mod. Phys. **36** (1964) 39

[3] C.W.Hagen and R.Griessen, Phys. Rev. Lett. **62** (1989) 2857

JP0350296

2.32 DIFFERENCE IN LOW ENERGY PLASMA EXCITATION AND CHEMICAL REACTIVITY OF RARE GASES

Hiroaki Ogawa and Kiyoshi Kiuchi

Japan Atomic Energy Research Institute, Department of Nuclear Energy System
2-4 Shirakata Shirane, Tokai-mura, Ibaraki-ken, 319-1195 Japan

Abstract

The gas release behavior of heavy rare gases such as Xe and Kr formed as major fission products in fuel pellets plays an important role on the reliability of fuel claddings due to increase the internal pressure. To clarify the chemical characteristics of rare gases is useful to inhibit the gas release and to improve the radioactive waste management and to the industrial application. On this study, the chemical reactivity was examined using the low energy plasma excitation techniques and oxidation in oxygen atmosphere. Two types of RF sources of the induced couple and static capacity types were used as the low energy plasma source. The electron density in plasma of rare gases was dependent on the binding energy of each gas. The large difference in electron densities among rare gases was typically observed in the induced couple type plasma, because of the high production yield at wall surfaces covered with low energy electrons. It was suggested that the chemical compounds were formed in the condensed atmosphere as fuels tubes.

Keywords: Rare gases, Chemical reaction, Low energy plasma excitation, plasma-wall interaction, Electron density, Electron temperature

1. Introduction

Radioactive heavy rare gases like xenon and krypton are formed as major fission products with the high abundance dependent on the burn-up ratio. The reliability of light-water reactor fuel elements is affected with the release behavior of these gases produced in oxide fuels [1-7]. The accumulation of these gases into a gap between cladding and fuels decreases the thermal conductivity and enhances the fuel temperature [1-7]. The extra gas release from oxide fuels would be enhanced vice-versa. Therefore, the chemical form and thermodynamic stability of heavy rare gases like xenon in oxide fuels is very important for understanding the gas release mechanism. Although, Xe and Kr are considered to rare gases elements with the closed shell with the high chemical stability, the chemical reactivity under heavy neutron irradiation like fuel elements would be controlled with the excitation behavior accompanied with radiochemical effects. Generally, the excitation cross-section on these rare gases has the maximum yield at low energy electrons with a few ten eV lower than the ionization yield [8-11]. The flux of low energy electrons is proportional to the flux of particles with the high energy. Electrons in relation to excitations are formed mainly by three mechanisms, namely, Compton scattering, electrons pair formation and photo-excitations. On the other hand, the formation of chemical compounds between heavy rare gases like xenon and fluorine was already reported [12-17]. The ionization energy of heavy rare gases elements is nearly equal to that of oxygen. It is expected to the high chemical reactivity between excited rare gases and oxygen in oxide fuels atmosphere under heavy irradiation. Moreover, the effective means for chemically stabilizing heavy rare gases is very important with respect to

the waste management for minimizing the radioactive gas release from nuclear power plants.

On the present study, the chemical reactivity of heavy rare gases like xenon exited under heavy irradiation was examined with the low energy plasma excitation method by using devices driven two types of RF excitation sources.

2. Experimental Methods

The experimental system is consist of the main chamber, RF generator unit, plasma diagnostic system, gas analysis system, gas inlet system and vacuum exhaust system as illustrated in Fig.1. The RF source for generating the plasma operated at 13.56MHz. The maximum output power is 300W. The RF plasma discharges were used two types, namely, a capacitive coupling (CC.) type for an opened plasma and an induced coupling (IC.) type for a closed plasma. The plasma discharge on the CC. type is generated between two electrodes with 20 cm in diameter. The electrode potential is possible to control by changing the applied voltage at upper side electrode. On the IC. type, a discharge tube was made of a pyrex glass with 25cm in length and 2cm in diameter. The diameter is very small because of enhancing an interaction between the plasma with a wall. The electrode is a coil with 10cm in length and 10cm in diameter with five reels. It is made of a copper tube with 1/4-inch. Those electrodes are cooled by flowing water at 293K.

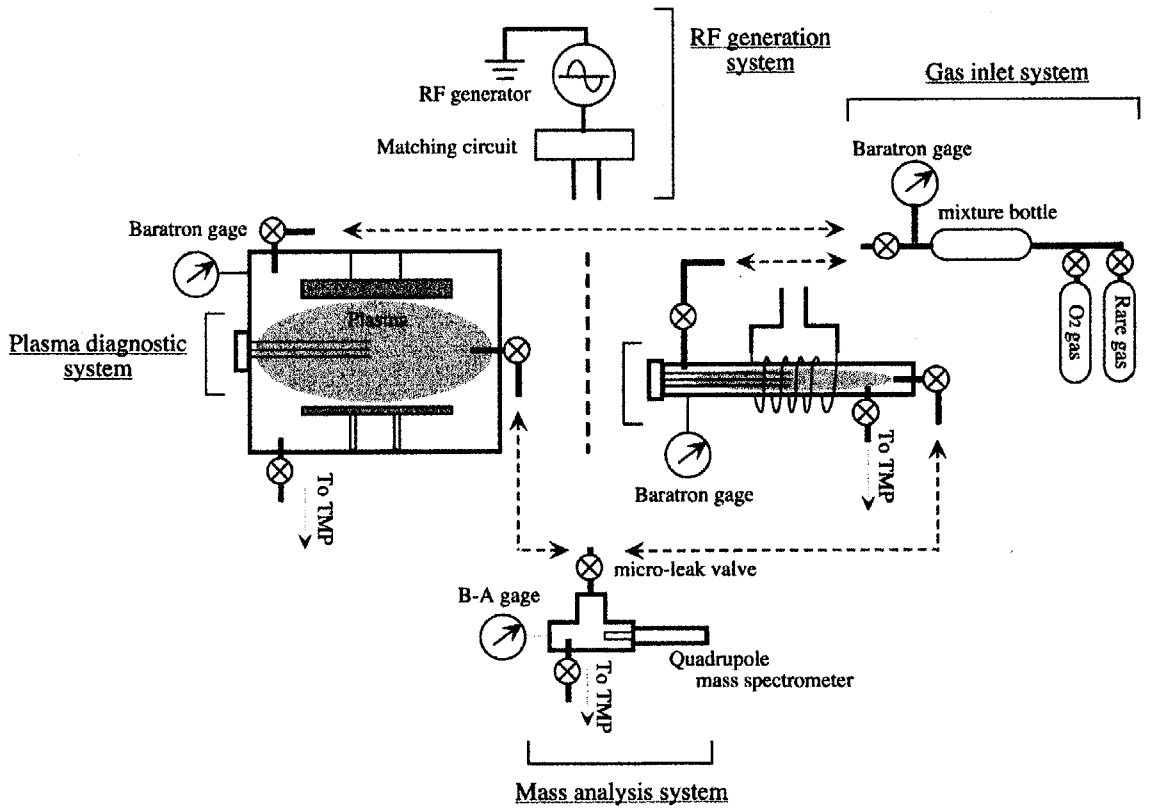


Fig.1 The experimental apparatus used in the low energy plasma excitation tests.

The triple-probe method was used in the plasma diagnostic technique as illustrated in Fig.2 [18-20]. The probe is made of tungsten wire with a 0.75mm in diameter. Each wire is covered with a ceramic insulator, except for 1mm in length at the tip, and is set at 4mm far in distance. The chemical composition of gases was analyzed by a quadrupole mass spectrometer with the mass range from 0 to 400amu. The experimental conditions are summarized in Table 1.

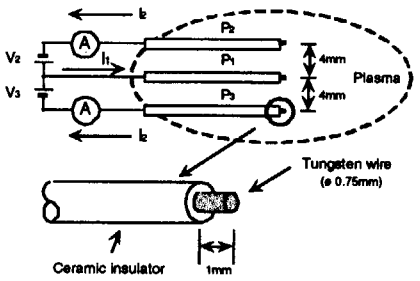


Fig.2 The schematic diagram of the triple-probe method used in the plasma inspection.

Table 1 Test conditions for exciting rare gases by RF discharge.

Experimental method	CC. Type	IC. Type
Rare gases elements	He, Ne, Ar, Kr, Xe	
RF output power / W	10 ~ 100	
Pressure range / Pa	0.1 ~ 10	10 ~ 1000

On the plasma diagnosis, the electron density (n_e) and the electron temperature (kT_e) were evaluated with data obtained by the triple-probe method. The electron temperature is calculated with a following equation:

$$\frac{I_1+I_2}{I_1+I_3}=\frac{1-\exp(-eV_{d2}/kT_e)}{1-\exp(-eV_{d3}/kT_e)} \qquad (I_1=I_2+I_3) \tag{1}$$

where k is the Boltzmann constant, T_e is the temperature (K), V_{d2} and V_{d3} are the externally applied voltages to the probes P_2 and P_3 with reference to the probe P_1, respectively. I_2 and I_3 are probe current of the P_2 and P_3, respectively.

The electron density is given by the measured ion current as the following equation;

$$I_i=\frac{I_3-I_2\exp(-e\Delta V/kT_e)}{1-\exp(-e\Delta V/kT_e)} \qquad (\Delta V=V_{d3}-V_{d2}) \tag{2}$$

$$I_i=0.61n_e e\left(\frac{kT_e}{m_i}\right)^{1/2}S \tag{3}$$

where I_i is the ion current, n_e, e, mi and S are the electron density, charge, mass and surface area of the probe, respectively.

The electron density and temperature were measured at the center of plasma.
As a result of the mass analysis of the gas, N_2 contamination into the system from air might neglect.

3. Experimental Results

3.1 Evaluation of fission products and chemical compounds of heavy rare gases

The mass fraction of major representative fission products calculated by ORIGEN-II is shown in Fig.3, by supposing 45GWd/t of 4.5% enriched fuels. Xenon is a heavy rare gas with the highest abundance in the fission products. The release rate of xenon from oxide fuels into a gap is enhanced by the growth of zirconium oxide with the low thermal conductivity [1-7]. It means the important role of the oxide surface temperature on xenon gas release. Xenon in the high burn-up fuels is accumulated in the rim layer at out side of fuels. The behavior of xenon on the RIA (reaction induced accident), the existence in the critical temperature for gas release is expected. The fuel temperature would be increased with both effects of xenon gas release and thickening of oxide film with the low thermal conductivity. Therefore, the chemical form of xenon and the decomposition temperature of it are important roles on the reliability of fuel cladding.

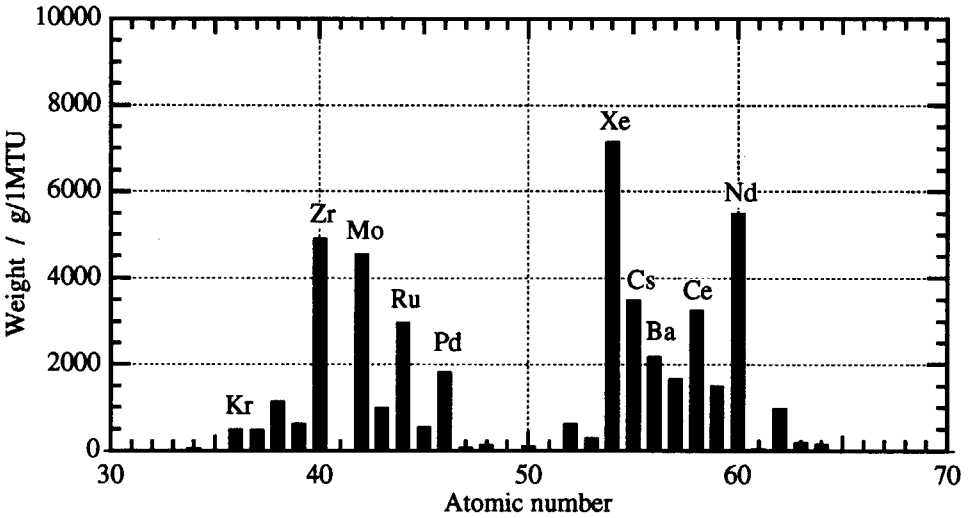


Fig.3 The mass fraction of the fission products calculated by ORIGEN-II.

On the other hand, the formation of chemical compounds between heavy rare gases with reactants and the high electro-negativity elements such as halogen and oxygen has been reported[12-17]. The typical compounds have already obtained by laboratory means as shown in Table 2.

Table 2 The known stable chemical compounds of rare gases elements.

Elements	Xe	Kr	Ar , Ne , He
Oxide	XeO_3 , XeO_4 , etc.	----------	----------
Fluoride	XeF_2 , XeF_4 , XeF_6 , etc.	KrF_2	----------
Mix compound	$XeOF_4$, XeO_2F_2 , XeO_3F_2 , etc.	----------	----------

At least, the chemically stable compounds were obtained in Xe and Kr without any additional excitation techniques. These facts are encouraged to the difference in the chemical reactivity among rare gases elements under heavy irradiation. Especially, heavy rare gases elements such as Xe and Kr are suggested to be easy to from the excited species in low temperature plasma expected in the condensed phases on heat transfer surfaces such as fuel claddings.

3.2 Analysis of plasma discharge driven by the CC. type.

The effect of rare gases pressure on the electron density in plasma was plotted in Fig.4 within 0.1 to 10Pa at the RF output power of 100W. Heavy rare gases like Xe and Kr with the low ionization energy show the stable plasma excitation over a wide pressure range. The electron density of Kr and Xe plasmas has the peak intensity around 1Pa. On the other hand, the electron density in He, Ne and Ar plasmas with the high ionization energy tends to increase toward the low vacuum side. However, the discharge is localized into near electrodes. Therefore, the stable uniform plasma by the RF discharge is obtained in heavy rare gases with the low ionization energy.

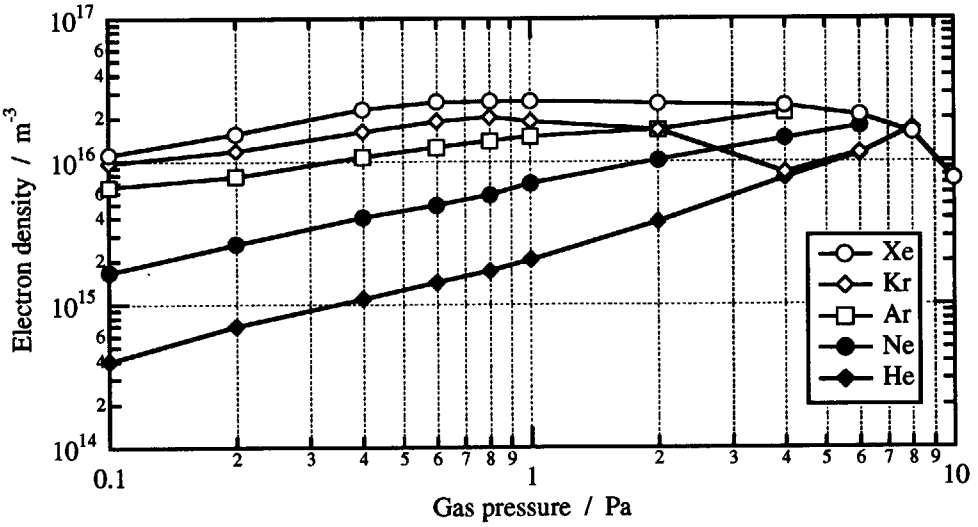


Fig.4 Effect of gas pressure on the electron density in rare gases plasmas excited by the CC. type.

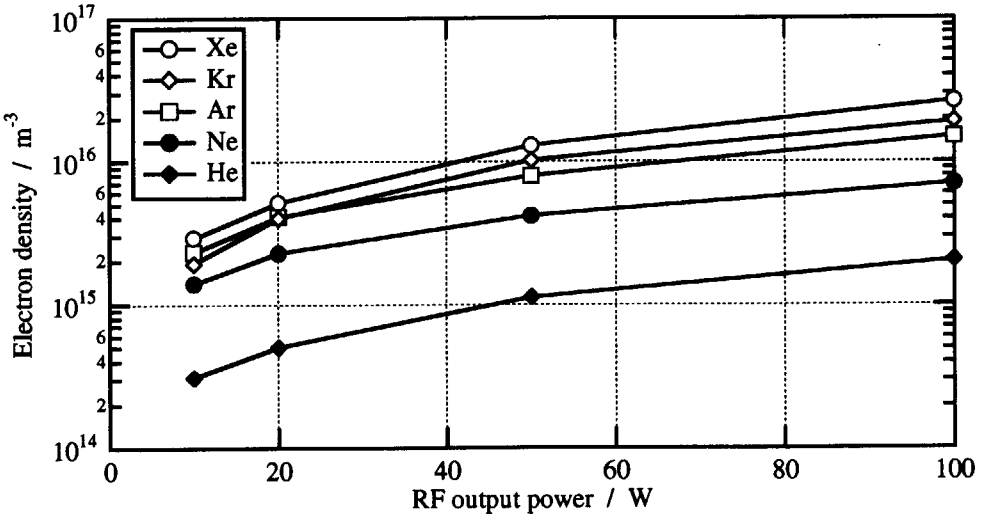


Fig.5 The effect of RF output power dependency on the electron density of rare gases obtained by on the CC. type test.

The effect of the RF output power on the electron density at 1Pa is plotted in Fig.5. The electron density of each rare gas increases lineally with increasing the RF output power. The

electron density of xenon plasma with the lowest ionization energy showed the maximum value. The relationship between the electron density and the electron temperature is shown in Fig.6. The temperature of electrons with the low density increased with increasing the ionization energy. It is clear that the excitation in RF plasma is easy to heavy rare gases such as Xe with the low ionization energy.

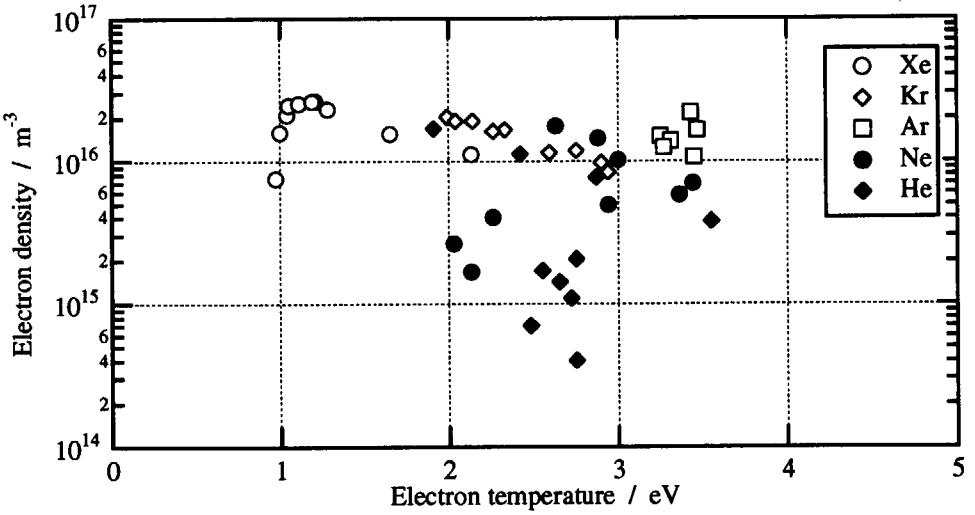


Fig.6 The Relationship between the electron density and the electron temperature obtained by the CC. type test.

3.3 Analyses of plasma discharge driven by the IC. type.

The effect of rare gas pressure on the electron density in plasma was plotted in Fig.7 within 10 to 1000Pa at the RF output power of 100W.

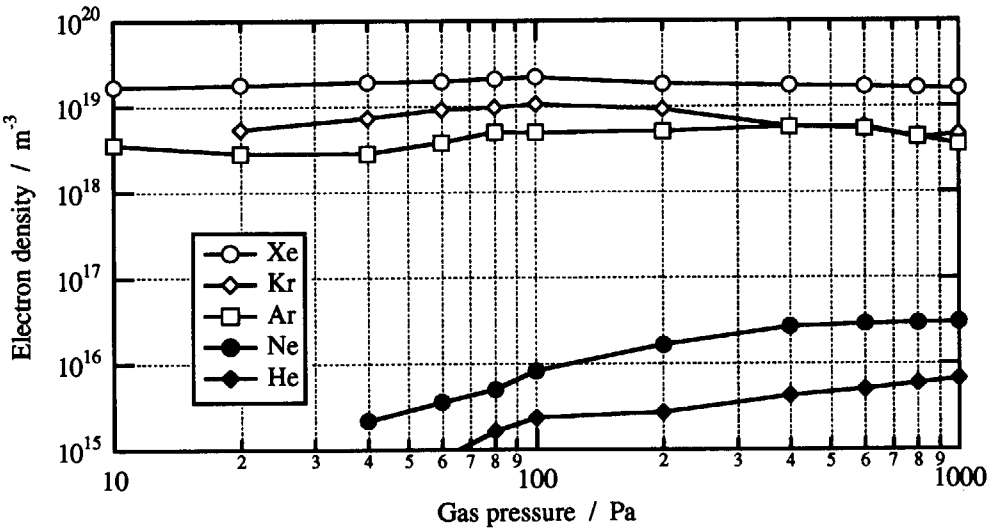


Fig.7 The gas pressure dependency of the electron density for rare gases obtained by the IC. type test.

The range of gas pressure for obtaining the stable discharge is different from that of the CC.

type due to the difference in plasma devices as illustrated in Fig.1. On this discharge method enhanced the interaction between the plasma with the wall, even if the same input energy of 100W, the electron density of Xe, Kr, and Ar increased markedly comparing with that of Ne and He. The electron density showed the peak value around 100Pa. As shown in Fig.8, the electron density in each rare gases plasma increased lineally with increasing the RF output power as same as that of the CC. type. The relationship between the electron density and electron temperature is shown in Fig.9. It is suggested that the remarkable difference in the excitation mechanism between heavy rare gases groups (Xe, Kr and Ar) and light rare gases (Ne and He) groups.

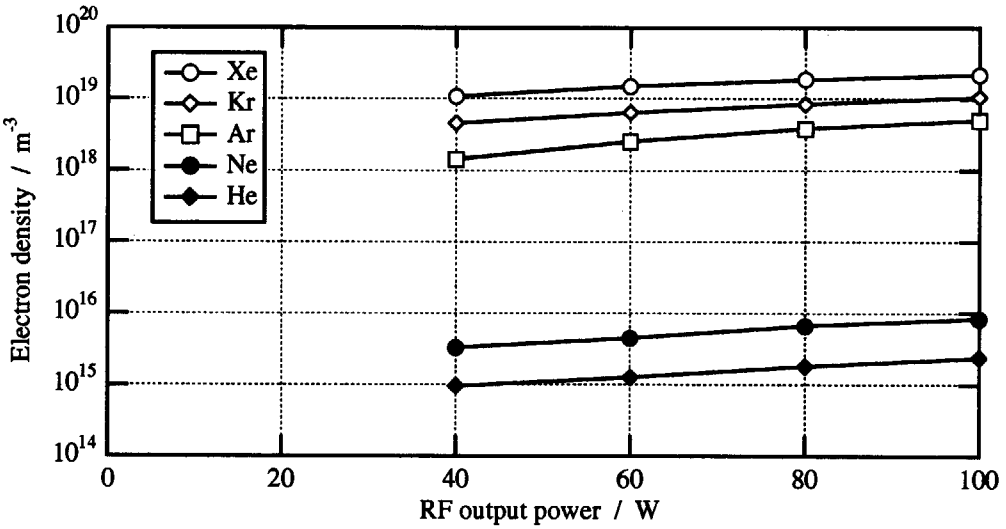


Fig.8 The effect of RF output power dependency on the electron density of rare gases obtained by the IC. type test.

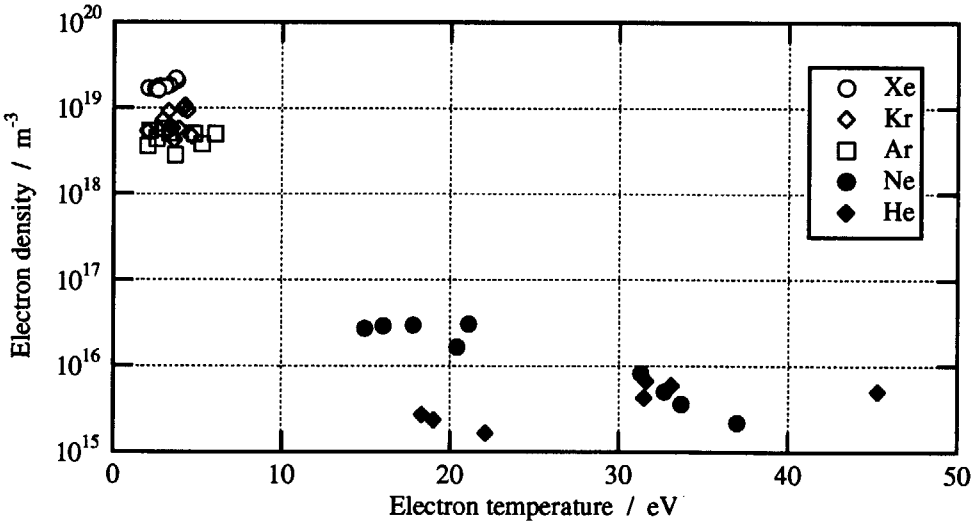


Fig.9 The relationship between the electron density and the electron temperature obtained by the IC. type test.

4. Discussions

The excitation behavior of each rare gas was evaluated by using two different types of RF plasma device. One is the CC. type with the opened plasma space discharged between two electrodes. The other is the closed plasma space discharged in a pyrex tube by outside reeled coil. The essential difference in both devices is the effect of plasma –wall interactions. The difference in relationships between the electron density and the ionization energy of each rare gas at the RF input power of 100W is compared in Fig.10. Heavy rare gases groups (Xe, Kr and Ar) with the low ionization energy shows the remarkable large difference between two devices. On the other hand, the difference in the electron density between two devices of light rare gases groups (Ne and He) with the high ionization energy is small. On the IC. type, the input energy in He and Ne plasmas is consumed for increasing the electron temperature (Fig.9). It is interpreted with the role of the wall surface on the excitation of plasma.

The cross sections for the excitation as function of the electron temperature is shown in Fig.11 based on other reports [8-11]. The average electron temperature of a few eV in rare gases plasma excited in the CC. type device is almost coincident with that of the medium peak cross section. At the closed plasma space such as the IC. type, the excitation would be accelerated with interactions between electrons and adsorbed gases on the pyrex glass wall. It is expected that the adsorption of heavy rare gases groups (Xe, Kr and Ar) on the wall with the high chemical reactivity are more easier than that of light rare gases groups (Ne and He) with the low chemical reactivity. The major excitation in the IC. type between two groups of rare gases would be dominated with the plasma-wall interactions. The high adsorption energy would be expected in heavy rare gases elements derived from the high chemical reactivity. These phenomena are expected in the formation of the chemical compound such as fluorides and mix-oxides. Already, the existence of these compounds of Xe and Kr has been proved. In the nuclear fuels, the chemical interaction among the excited species in the condensed phases under high pressure would be accelerated by heavy irradiation. A large amount of heavy rare gases such as Xe would be expected to form the chemical compound between the excited species of oxygen with the high electro-negativity.

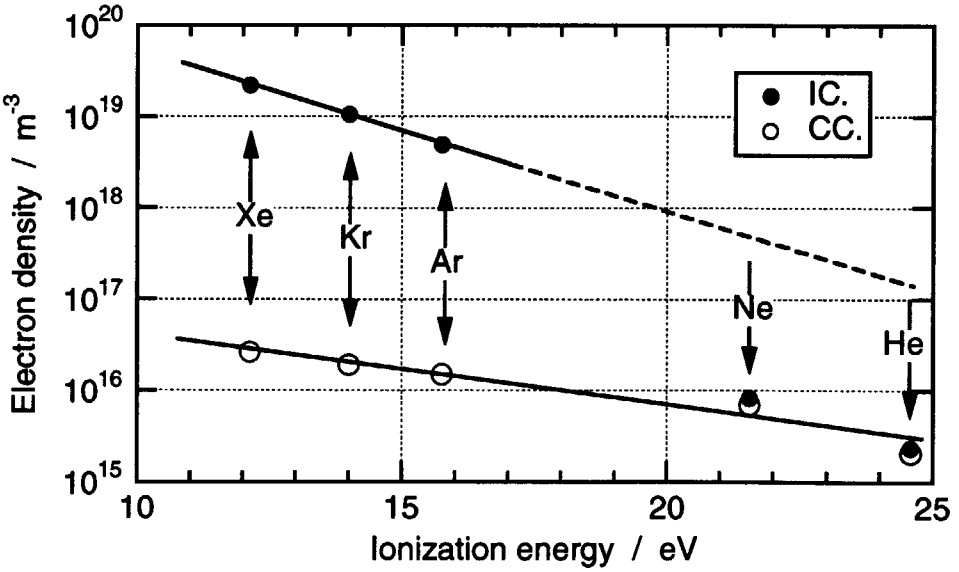


Fig.10 Difference in relationships between electron densities and the ionization energy obtained in both CC. type and IC. type tests.

5. Conclusions

The chemical reactivity of heavy rare gases like xenon was examined fundamentally for understanding the gas release mechanism as fission products in nuclear oxide fuel elements under heavy irradiation and for searching the adequate waste management method as radioactive wastes. The electron density in low energy plasma was examined in two types of RF devices, namely, the IC. type and CC. type. The excitation behavior in mono-rare gases of He, Ne, Ar, Kr and Xe was examined as functions of gases pressure and RF input energy. The results are summarized as follows:

1. The surface temperature of oxide fuels is one of the important factors on the gas release of radioactive heavy elements like xenon contained in fission products. The chemical form and stability of these gases have an important role on the gas release mechanism.
2. The electron density of heavy rare gases like xenon has the highest excitation yield in a wide pressure range under the low energy plasma discharge. The electron density increases with proportional to the RF input power at 100Pa at the maximum yield on the IC. type.
3. The electron density in the low energy plasma is dependent on the ionization energy of each rare gas.
4. The markedly high excitation efficiency is seen in Xe, Kr, Ar in the IC. type devices with the effect of plasma-wall interactions. It is interpreted with the excitation of adsorbed heavy rare gases on the wall by the low energy electrons with the high excitation yield.

Acknowledgments

The authors would like to thank I. Ioka and K. Fukaya for the some of the technical support. We acknowledge financial support from Japan Science and Technology Corporation (as representative T. Ooyama, H. Sekine and R. Kato et al.).

References

[1] P. E. MacDonard, High Efficiency Nuclear Fuel Program, DOE/NE-50, INEEL, ANL (1998).
[2] P. Blanpain, et al., Recent Results from the in Reactor MOX Fuel Performance in France and Improvement Program, ANS Topical Meeting, Portland, Oregon (1997).
[3] S. Doi, et al., High Burn-up Mox Fuel and Fuel Rod Design Improvement, ibid.
[4] K. Asahi, et al., Irradiation and Post Irradiation Testing Program of BWR MOX Fuel Rods, ANS Topical Meeting, West Palm Beach, F1 (1994).
[5] J. N. Morgan, et al., Siemens' Experience with Large Scale Mixed Oxide Fuel Assembly Insertion in Light Water Reactors, ibid.
[6] G. R. Klip, et al., Proc. ANS-ENS Int. Topical Meeting on LWR fuel Performance, vol.2 (1991) 730.
[7] T. Mitsugi, et al., Behavior of MOX Fuel Irradiated in a Thermal Reactor, ANS Topical Meeting, Portland Oregon (1997).
[8] M. Hayashi, J. Phys., D15 (1982) 1411.
[9] M. Hayashi, J. Phys., D16 (1983) 581.
[10] M. Hayashi, J. Phys., D16 (1983) 591.
[11] Y. Nakamura and M. Kurachi, J. Phys., D21 (1988) 718.
[12] H. H. Claassen, H. Selig and J. G. Malm, J. Amer. Soc., 84 (1962) 3593.
[13] R. Hoppe, W. Dahne, H. Mattauch and K. M. Rodder, Angew. Chem., 74 (1962) 903.
[14] R. Hoppe, H. Mattauch K. M. Rodder and W. Dahne, Z. anorg. Allgem. Chem., 324 (1963) 214.
[15] S. Reichman and F. Schreiner, J. Chem. Phys., 51 (1969) 2355.

[16] R. D. Burbank and G. R. Jones, J. Amer. Chem. Soc., 96 (1974) 43.
[17] H. F. Mark, D. F. Othmer, C. G. Overberger and G. T. Seaborg, Kirk-Othmer ENCYCLOPEDIA OF CHEMICAL TECHNOLOGY third edition, vol.12 (1980) 288-297.
[18] T. Okuda and K. Yamamoto, J. Appl. Phys., 31 (1960) 158.
[19] Sin-Li Chen and T. Sekiguchi, J. Appl. Phys., 36 (1965) 2363.
[20] Sin-Li Chen, J. Appl. Phys., 42 (1971) 406.

JP0350297

JAERI－Conf 2003－001

2.33 CORROSION OF TYPE 304L STAINLESS STEEL IN BOILING DILUTE NEPTUNIUM NITRATE SOLUTION

Takafumi Motooka* and Kiyoshi Kiuchi
Tokai Research Establishment, Japan Atomic Energy Research Institute
Tokai-mura, Naka-gun, Ibaraki-ken 319-1195

Abstract

Corrosion of type 304L stainless steel in nitric acid solution containing neptunium was studied under immersion and heat-transfer condition. Corrosion rates of stainless steel were obtained by the weight loss measurement and the quantitative analysis of metallic ions dissolved in solution. The surface morphology was observed by scanning electron microscopy. The corrosion acceleration mechanism was investigated by polarization measurement and spectrophotometry. The corrosion rate in boiling 9M nitric acid was accelerated by addition of neptunium. The corrosion of stainless steel was promoted under heat-transfer condition compared to immersion condition. In polarization measurements, the cathodic current was increased by addition of neptunium. Spectrophotometric measurements showed the oxidization of neptunium in boiling nitric acid. It was suggested that the accelerated corrosion in nitric acid solution containing neptunium was caused by re-oxidation of neptunium.

Keywords: corrosion, neptunium, stainless steel, redox potential, heat-transfer, immersion, nitric acid

1. Introduction

In a previous investigation of corrosion in nitric acid,[1] it is possible to artificially simulate the corrosion environment under actual operation conditions by equalizing the redox tendency of the test solution. On the basis of this hypothesis, non-radioactive ion, vanadium ion (VO_2^+), was simulated in nitric acid solutions instead of radioactive ion, neptunium ion (NpO_2^{2+}). The redox potential between VO_2^+ and VO^{2+} is 1.004 V (V *vs.* NHE) and the redox potential between NpO_2^{2+} and NpO_2^+ is 1.149 V.[2] From the fact that redox potential of neptunium is slightly higher than that of vanadium, it imagines that neptunium nitrate causes slightly higher acceleration than vanadium nitrate in the corrosion of 304L SS in nitric acid.

In this study to verify the corrosiveness of neptunium ions in nitric acid, the corrosion of 304L SS under heat-transfer and immersion condition was examined by weight loss and polarization measurements and spectrophotometry. We have also attempted to establish corrosion mechanism in nitric acid solution containing neptunium.

2. Experimental Procedures

2.1 Material

A 304L SS plate was used in this test (Table I). Test specimens for corrosion tests were cut from it and finely polished. Test solutions were Solution A (9M HNO_3), Solution B (9M HNO_3 + 3.8mM ^{237}Np) and Solution C (9M HNO_3 + 3.8mM VO_2^+). Purity of ^{237}Np used in this study was checked by γ-ray spectrometry. The valence states of neptunium were Np(IV), (V), and (VI). Their ratios were unknown.

* Corresponding author. Tel : +81-29-282-5399 Fax : +81-282-5864
E-mail address : motooka@popsvr.tokai.jaeri.go.jp

Table I Chemical composition of type 304L SS (wt%)

C	Si	Mn	P	S	Cu	Ni	Cr	Mo	N
0.011	0.34	1.71	0.013	0.001	0.02	10.81	19.01	0.03	0.038

2.2 Corrosion Tests

Corrosion test were conduct for a total of 930 hours in the above three test solutions. The solutions were renewed every 310 hours in immersion and heat transfer corrosion tests. Both tests were conducted with a thermostatted glass cell under a boiling condition (at 341K) at a pressure of 16 kPa. The ratio of solution volume to surface area of specimen was about 18 mL/cm^2. The heat-flux in heat-conducting specimen was maintained 60 kW/m^2 during tests. The corrosion rate in immersion tests was obtained by the weight loss measurement of specimens by use of an electric balance. The corrosion rate in heat-transfer tests was calculated from the quantitative analysis of metallic ions (Fe, Cr and Ni) dissolved in test solutions by inductively coupled plasma arc emission spectrometry. Surface morphology of specimens was observed by scanning electron microscopy (SEM).

2.3 Polarization Measurement

Anodic and cathodic polarization measurements of specimens in each test solution were conducted with a glass three electrodes cell at 293K using a Solartron 1285A potentiostat/galvanostat. Potential was measured by a Ag/AgCl reference electrode.

2.4 Photospectrometry

A Hitachi U-3400 photo-spectrometer with a spectral range from 190 to 2600 nm was used. The solution in the reference compartment was 9M HNO_3.

3. Results

3.1 Corrosion Rates and SEM Observation

Figure 1 shows the corrosion rate of type 304L SS in nitric acid. The corrosion rate was increasing with test time under heat transfer condition. Under heat-transfer condition, the corrosion rate at 930 hours was about six times higher in the neptunium nitrate solution than in pure 9M HNO_3. Under immersion condition, the corrosion rate at 930 hours was about sixteen times higher in the neptunium nitrate solution than in 9M HNO_3. The corrosiveness of neptunium is slightly weak compared to vanadium in both conditions.

Figure 2 shows the surface morphology of tested specimens under heat transfer condition. Grain-boundary was preferentially attacked.

3.2 Polarization Measurement

Figure 3 shows polarization curves and corrosion potentials at 293K. The corrosion potential shifted toward nobler region by addition of neptunium or vanadium. The corrosion potential was 0.964 V (V *vs.* NHE) in pure 9M HNO_3, 0.988 V in vanadium nitrate solution, and 0.994 V in neptunium nitrate solution, respectively.

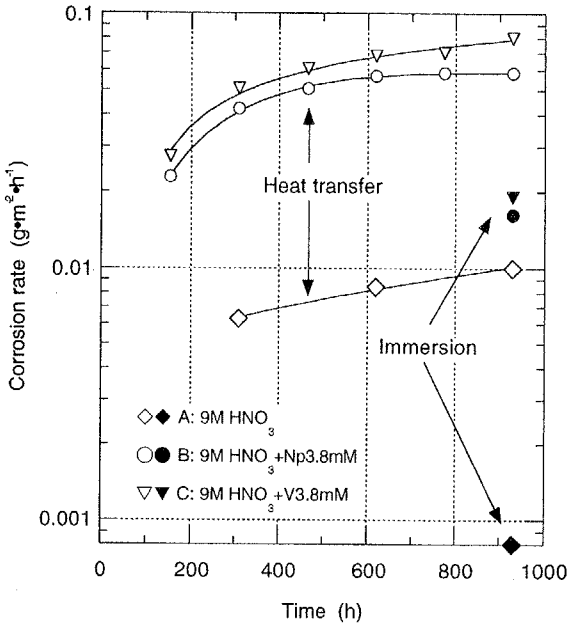


Fig.1 Corrosion rates of type 304L SS in test solutions.
Open: heat transfer, Closed: immersion condition

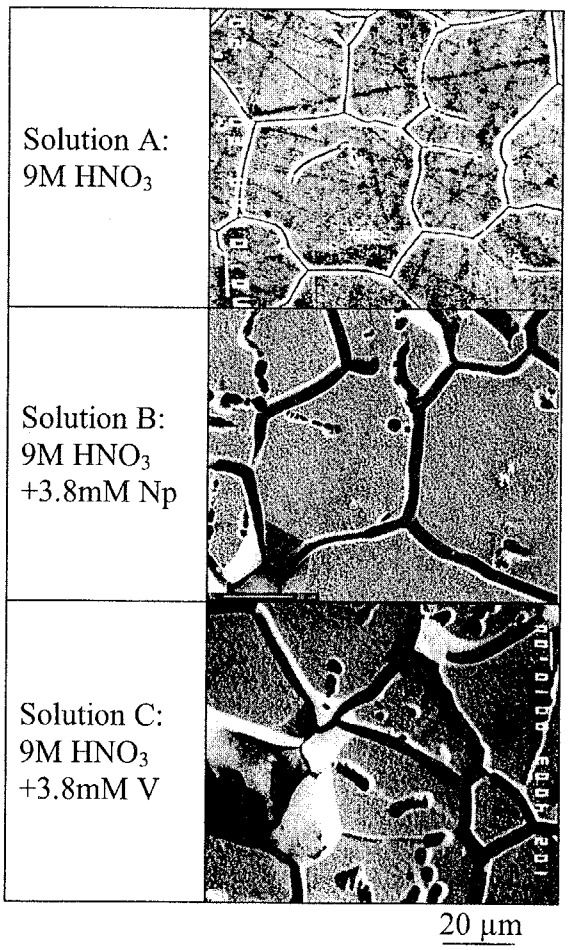


Fig.2 SEM photographs of type 304L SS tested under heat transfer condition.

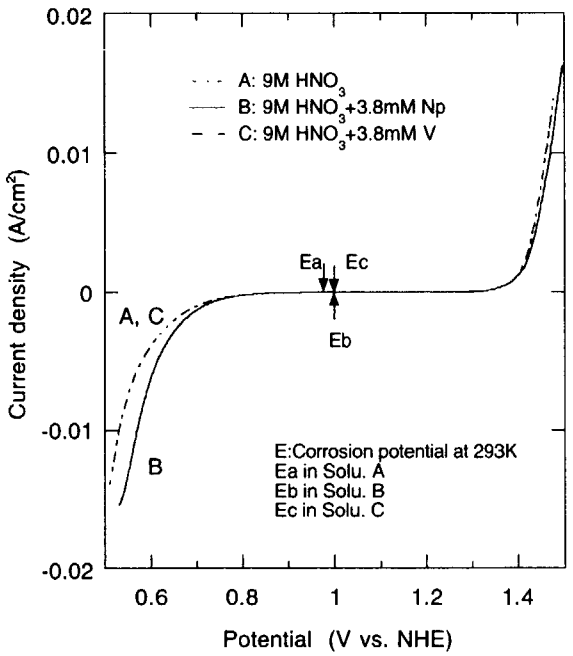


Fig.3 Polarization curves of type 304L SS in test solutions at room temperature.

3.3 Absorption Spectrum of Np

The absorption spectrum of neptunium in the initial nitric acid solution and in the solution after testing is shown in Fig.4. Np(V) shows a absorption peak at 1100 nm, Np(VI) at 550 and 1225 nm, and Np(IV) at 700 and 800 nm.[3] Neptunium existed in the tetra-, penta- and hexa-valent states. Np(IV) in nitric acid was oxidized to Np(V) or Np(VI) in corrosion tests, because the absorbance assigned to Np(VI) and Np(V) increased and the absorbance due to Np(IV) decreased after corrosion tests.

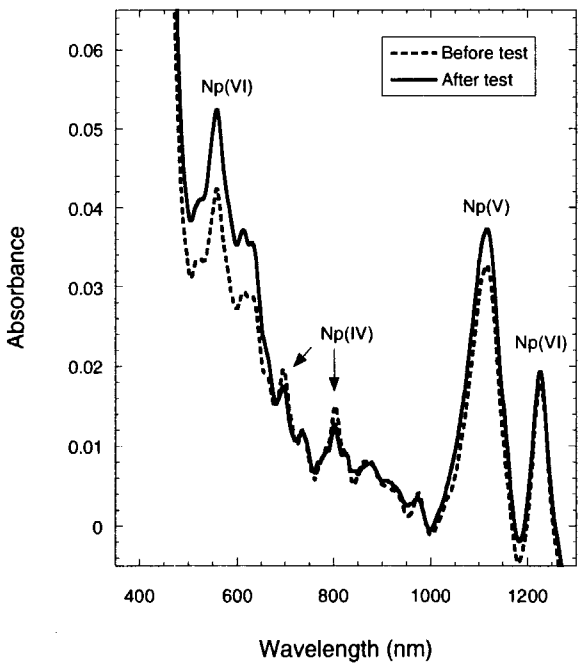


Fig. 4 Absorption spectrum of 3.8mM Np in 9M HNO_3 before and after corrosion test.

4. Discussion

The redox potential of nitric acid is given as follows:[2)]

$$3H^{+}+NO_3^{-}+2e^{-} = HNO_2+H_2O \quad (2)$$

$$E = E_0+(RT/2F)ln(\{[H^{+}]^3[NO_3^{-}]/[HNO_2]\}) \quad (3)$$

where E_0=0.934 V (V *vs.* NHE).

Vanadium with the redox potential of VO_2^{+} /VO^{2+}, E_0=1.004 V, is known to accelerate corrosion rate of stainless steel in boiling nitric acid solution.[4)] In the corrosion process, vanadium ion keeps on existing in the highest oxidation state, and is responsible for accelerating the corrosion rate of stainless steel.[4)]

As the redox potential of neptunium NpO_2^{2+}/NpO_2^{+} with E_0=1.149 V is low compared with those of the other corrosive ions like Cr(VI), Ru(III) and Ce(IV) [$HCrO_4^{-}$/Cr^{3+}, E_0=1.350 V; Ru_2O_3/Ru^{2+}, E_0=1.304 V; $Ce(OH)^{3+}$/Ce^{3+}, E_0=1.715 V], it is not likely that neptunium causes an acceleration in corrosion rate of type 304L SS. The effect of neptunium on the acceleration corrosion is able to explain in terms of the decrease of cathodic over-voltage. The cathodic current in the neptunium nitrate solution is higher than that in pure nitric acid solution as shown in Fig.4. This cathodic current increase suggests that NpO_2^{2+} is reduced to NpO_2^{+} on the surface of specimen. NpO_2^{+} produced on the surface of specimen is oxidized instantaneously to NpO_2^{2+} in the neptunium nitrate solution and consequently electrons are continuously consumed on the surface of specimen to lead to the acceleration of corrosion.

As the simulation result by REACT code[5)], it indicates the tendency that the higher is the acidity the faster is the oxidation, and the phenomenon that almost all Np(V) is oxidized to Np(VI) and the amount of Np(V) is negligible in steady state. As can be seen in Fig.4, the absorbance of Np(V) and Np(VI) increased after corrosion test. This phenomenon indicates re-oxidation of Np(V) which is produced by anodic reaction of stainless steel in corrosion process. When Np(VI) is consumed in corrosion process, it causes oxidation of stainless steel such as Fe to Fe(II) and reduction of Np(VI) to Np(V) as shown in Fig.4. This will lead to the presence of absorption peak of Np(V) after corrosion test. The absorption spectrum indicated good agreement on the above hypothesis. Figure 5 shows the schematic model for the corrosion mechanism of stainless steels in neptunium nitrate solution.

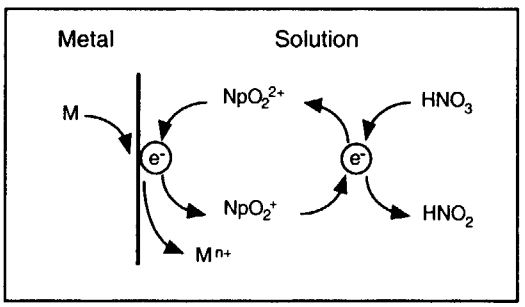


Fig.5 Model for the corrosion mechanism of stainless steel in neptunium nitrate solution.

5. Conclusions

Corrosion tests of type 304L SS in boiling neptunium nitrate solution were conducted under immersion and heat-transfer condition. After the tests, the weight loss measurement and the quantitative analysis of metallic ions were conducted to evaluate the corrosion rates. The surface morphology was observed by SEM. The valence of neptunium was analyzed by photospectrometery. Following results were obtained:

(1) The corrosion rate of stainless steel was accelerated by addition of neptunium in nitric acid solution. Preferential intergranular corrosion attack was observed. The corrosion was promoted under heat-transfer condition compared to immersion condition.
(2) In polarization measurements, the cathodic current was increased by addition of neptunium.
(3) The absorption spectrum suggested that the re-oxidation of neptunium is one of the controlling factors on the corrosion in neptunium nitrate solution.

References

[1] M. Okubo, M. Shintani, H. Ishimaru, *et al.*, "Demonstration tests on corrosion resistance of equipments for spent fuel reprocessing process," SFEN-RECOD 86, p.1181 (1994)
[2] M. Pourbaix, *Atlas of Electrochemical Equilibria in Aqueous Solutions*, Pergamon Press, Oxford, (1966)
[3] H. A. Friedman and L. M. Toth, "Adsoprption spectra of Np(III), (IV), (V) and (VI) in nitric acid," *J. Inorg. Nucl. Chem.*, **42**, 1347 (1980)
[4] A. B. McIntosh and T. E. Evans, *Proc. 2nd Int. Conf. on the Peaceful Uses of Atomic Energy*, P/30 U.K., p.206 (1958)
[5] S. Tachimori, "Numerical simulation for chemical reactions of actinide elements in aqueous nitric acid solution," *J. Nucl. Sci. Technol.*, **28**[3], 218 (1991)

JP0350298

2.34 EFFECT OF TRIPLE ION BEAM IRRADIATION ON MECHANICAL PROPERTIES OF HIGH CHROMIUM AUSTENITIC STAINLESS STEEL

Ikuo Ioka[1]*, Masatoshi Futakawa[1], Yoshiyasu Nanjyo[1], Kiyoshi Kiuchi[1], Yuji Kuroda[2] and Takefumi Anegawa[3]

[1]Japan Atomic Energy Research Institute, Department of Nuclear Energy System
2-4 Shirakata Shirane, Tokai-mura, Ibaraki-ken, 319-1195 Japan
[2]The Japan Atomic Power Company, , Research and Development Department
6-1, 1-chome, Ohtemachi, Chiyoda-ku, Tokyo, 100-0004 Japan
[3]Tokyo Electric Power Company, Nuclear Power Engineering Department
1-3 Uchisaiwai-cho, 1-choume, Chiyoda-ku, Tokyo, 100-0011 Japan

Abstract

A high-chromium austenitic stainless steel has been developed for an advanced fuel cladding tube considering waterside corrosion and irradiation embrittlement. The candidate material was irradiated in triple ion (Ni, He, H) beam modes at 573K up to 50dpa to simulate irradiation damage by neutron and transmutation product. The change in hardness of the very shallow surface layer of the irradiated specimen was estimated from the slope of load/depth-depth curve which is in direct proportion to the apparent hardness of the specimen. Besides, the Swift's power low constitutive equation ($\sigma=A(\varepsilon_0+\varepsilon)^n$, A: strength coefficient, ε_0: equivalent strain by cold rolling, n: strain hardening exponent) of the damaged parts was derived from the indentation test combined with an inverse analysis using a finite element method (FEM). For comparison, Type304 stainless steel was investigated as well. Though both Type304SS and candidate material were also hardened by ion irradiation, the increase in apparent hardness of the candidate material was smaller than that of Type304SS. The yield stress and uniform elongation were estimated from the calculated constitutive equation by FEM inverse analysis. The irradiation hardening of the candidate material by irradiation can be expected to be lower than that of Type304SS.

Keywords: High-chromium austenitic stainless steel, Cladding tube, LWR, Ultra high burnup, Ion irradiation, Constitutive equation, Finite element method, Hardness, Mechanical properties, Indentation test

1. Introduction

The ultra-high burnup of LWR is considered to be an important technology for establishing nuclear power plants as one of the most promising future energy system in point view of reducing radioactive wastes and electrical cost. Cladding materials with the excellent long performance under heavy irradiation would be required to these developments. The high chromium austenitic stainless steels(25Cr-35Ni-0.2Ti UHP)[1] were selected as one of candidates that is possible to made by the present engineering technologies. And, there are many practical irradiation data as fuel cladding tubes made of austenitic stainless steels in LWRs and LMFBRs. Many fuel cladding tubes made of austenitic stainless had been suffered

* Corresponding author, Tel:+81-29-282-6385 Fax:+81-29-282-6489.
E-mail adderess: ioka@popsvr.tokai.jaeri.go.jp (I.Ioka)

from environmental cracking along with longitudinal in early BWR and PWR plants[2-5]. Moreover, the uniform elongation of Type 304SS and 316SS was rapidly decreased with increasing neutron dose[6-8] at the practical temperature range (473-673K). Therefore, it is important to suppress environmental cracking and ductility loss on the high chromium austenitic alloys for cladding tubes. A triple ion beam facility at JAERI was used for simulating the effect of irradiation on the mechanical properties of the candidate material. However, the ion irradiated area is limited to the very shallow surface layer (<2μm depth) so that the irradiation damage is distributed around the thin layer. A indentation technique was applied to examine the ion irradiation effect on the mechanical properties of the thin layer[9].

In this study, the change in apparent hardness of the very shallow surface layer of the irradiated material was calculated from the slope of load/depth-depth curve which is in direct proportion to the appearance hardness of the material. Besides, the Swift's power low constitutive equation ($\sigma=A(\varepsilon_0+\varepsilon)^n$, A: strength coefficient, ε_0: equivalent strain by cold rolling, n: strain hardening exponent) of the damaged parts was derived from the microindentation test combined with an inverse analysis[10] using a finite element method (FEM). The material properties of the candidate material were compared with that of Type 304SS after ion irradiation to evaluate the irradiation hardening characteristics of the candidate material.

2. Experimental procedure

2.1 Material

The chemical composition of candidate material is 25Cr-35Ni-Ti UHP with high austenite stability at irradiation temperature as shown in Table I. It was melted using cold crucible induction melting (CCIM) for attaining ultra high purity of which total impurities is less than 100ppm. The billet was prepared by hot forging after solution annealed at 1373K for one hour and water cooled. The cladding tube with 11.3mm in outer diameter, 0.4mm in thickness and 1000mm in length was produced by incorporating the thermo-mechanical treatment so-called SAR (abbreviated the strained, aged and recrystallized)[11]. The treatment consists of 65% cold-worked, aged at 873K for 15hours and recrystallized at 1048K for 10hours. The interstitial solutes such as C, N, and O are stabilized in intra-grains as uniformly distributed fine precipitates. Finally, 7% cold-worked was conducted to the cladding tube for getting the sufficient tensile strength and for stretching. Type 304SS tubes were also used as a reference of stainless steel cladding tubes in the past commercial use of LWRs. The reference is the same Type 304SS cladding tubes made for fuel elements used in 'Mutsu'. The final thermal history is 8% cold-worked after solution annealed.

Table 1 Chemical Composition of the Material Tested in Weight Percent (%).

Materials	Fe	C	Si	Mn	P	S	Cr	Ni	Ti	N	O	Co
25Cr-35Ni-Ti UHP	bal.	0.0013	<0.005	0.001	0.001	0.0009	24.55	34.99	0.18	0.0014	0.0011	
Type 304SS	bal.	0.063	0.49	1.45	0.016	0.012	18.72	10.27				0.03

The specimens for ion irradiation were cut into 3mm diameter by the slurry drill from cladding tubes and then the bulge of the specimen was removed by polishing precisely. The surface of the specimen was finally electro-chemically polished. The specimens were irradiated using triple ion beam accelerator equipped in the TIARA at Takasaki site of JAERI. The irradiation condition was selected based on the condition calculated with computer simulation by assuming 100Gwd/t(MOX) on ABWRs. The dose rate, helium by (n, α) and hydrogen by (n, p) were adjusted by the ion irradiation of 12MeV Ni^{3+}, 1.1MeV He^+ and 380keV H^+ at 573K corresponding to cladding surface temperature. The Ni^{3+}, He^+, and H^+ ion beams were generated by Tandem accelerator, Single-ended accelerator and Ion implanter respectively. More detailed description of the triple ion beam facility is given elsewhere[12].

For triple ion beam irradiation, the beams were applied simultaneously. The Ni^{3+} ion produces displacement damage in the surface layer of the specimen. The He^{+} and H^{+} ions simulate the effect of He generation during Ni(n, α) and the effect of H generation during Ni(n, p), respectively.

The SRIM97 code was used to calculate the implanted ion distribution and the displacement dose as a function of depth from the specimen surface. The calculation results are shown in Fig.1. Fig.1(a) represents the displacement damage in dpa by Ni^{3+} as a function of depth from the surface. The displacement damage by He^{+} and H^{+} ions is disregarded, because they are small. The peak dose is about 110dpa around 2μm. The He^{+} and H^{+} ions were implanted in depth ranges from 1.0 to 1.5μm using energy degraders with aluminum foil. Fig.1(b) shows the distribution of the implanted Ni^{3+}, He^{+} and H^{+} ions in the specimen as a function of depth. The peak of Ni^{3+} ion (2.8at%) occurs about 2μm. The He^{+} and H^{+} ions in the implanted range were 100-150 appmHe and 1000-1600 appmH, respectively. The implanted He^{+} and H^{+} ions were controlled to neglect the effect of implanted Ni^{3+} ions. The ratios of helium and hydrogen concentrations to dpa (appm/dpa) were about 2-3 appmHe/dpa and 20-30 appmH/dpa for simulating 100Gwd/t(MOX) on ABWRs condition. The damage rate was about $1.6x10^{-3}$ dpa/s.

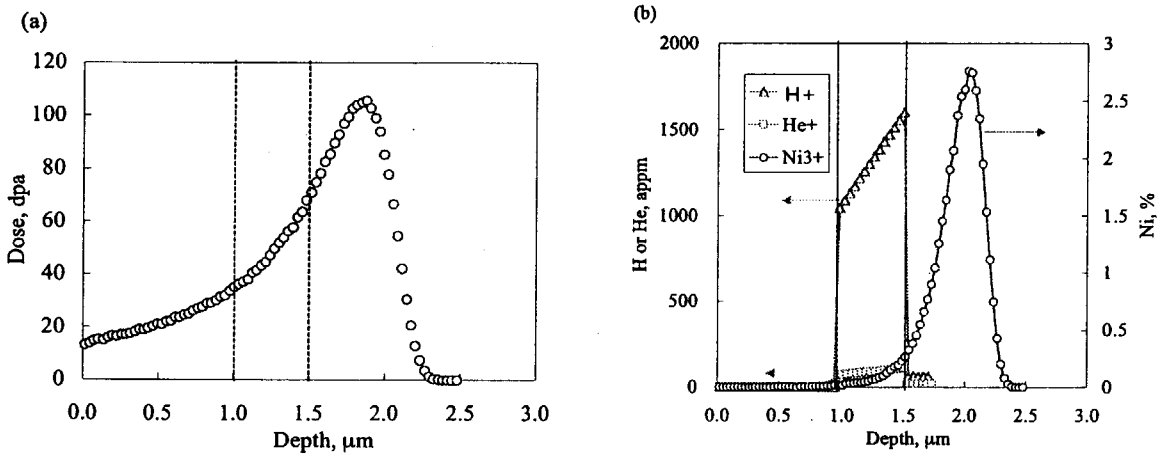


Fig.1 Depth profiles of (a) displacement damage by nickel and (b) nickel, hydrogen and helium concentrations in the specimen irradiated by triple beams

2.2 Indentation test

The indentation tests were carried out on the polished surfaces of specimens at room temperature. Two types of indenters were used for the indentation test. One is the Berkovich indenter for measuring the apparent hardness, the other is the conical indenter that has a hemispherical apex with radius of 1.2μm for deriving the constitutive equation. A testing machine, DUH-201 (Shimazu Co, Japan), was used for it. During loading and unloading, the load and indent depth were continuously measured with a resolution of 19.6μN and 1 nm, respectively. A load was imposed through the indenter on the specimen's surface with loading rate of 2.7mN/s, held for 1s, and then removed. The maximum load of 100mN was chosen not to be affected by the size effect manly due to the roughness of the indenter apex and the roughness of the specimen surface, as taking both the indentation depth and the radius of the indenter apex into account.

2.3 Identification of constitutive equation

The inverse analysis was carried out using an explicit FEM code, LS-DYNA, which

enables us to robustly analyze a large deformation accompanying with contacting behavior. In the analysis, the indenter and specimen were treated as axisymmetric two-dimensional bodies to take calculative efficiency into account. The modeled indenters were perfectly rigid. The contact interface between the specimen and the indenter was assumed to be frictionless, because the frictional force induced with friction coefficient up to 0.3 had few effects on the load-depth relationship. The mesh size is given to be sufficiently fine to keep accuracy: the minimum element size around the apex contacting zone was 0.05μm. The total number of the elements used in the model was 1509. The loading rate in the calculation was small enough to neglect an inertia effect as a static condition.

The constitutive equation of the material installed into the model was assumed to be a simple power-law which is generally believed to be applicable to normal metallic materials as follows:

$$\sigma = E\varepsilon \qquad \sigma \le \sigma_y \tag{1}$$

$$\sigma = A(\varepsilon_0 + \varepsilon)^n \tag{2}$$

$$\varepsilon_0 = (\sigma_y / A)^{1/n} - (\sigma_y / E) \qquad \sigma > \sigma_y \tag{3}$$

where, σ is true stress, ε true strain, E Young's modulus, σ_y yield stress, A work hardening coefficient and n work hardening exponent. Hereafter, we have to identify the following material constants; σ_y, A and n through the inverse analysis on the load-depth, L-D, curve.

The flow chart of the identification with inverse analysis is illustrated in Fig. 2. Here, **C** and **E** are determinants of material constants and estimated errors of material constants. **Z** and **Y** are determinants of experimental and calculated values on L and dL/dD. **R** is determinant of error in measuring systems. S_{max} is the maximum number of steps in the divided L-D curve. **H** is $\partial \mathbf{Y}/\partial \mathbf{C}$. The procedure of the inverse analysis is as follows.

1) $\mathbf{C_0}$, $\mathbf{E_0}$, **R** and S_{max} are input as initial values.
2) $\mathbf{Z_s}$ of L and dL/dD at step S is input.
3) $\mathbf{Y_s}$ of L and dL/dD at step S is calculated by FEM code.
4) The estimated values on **C** and **E** are given by the following equation of Kalman filter using each value, $\mathbf{C_s}$, $\mathbf{E_s}$, $\mathbf{Y_s}$, $\mathbf{H_s}$ and **R** at step S,

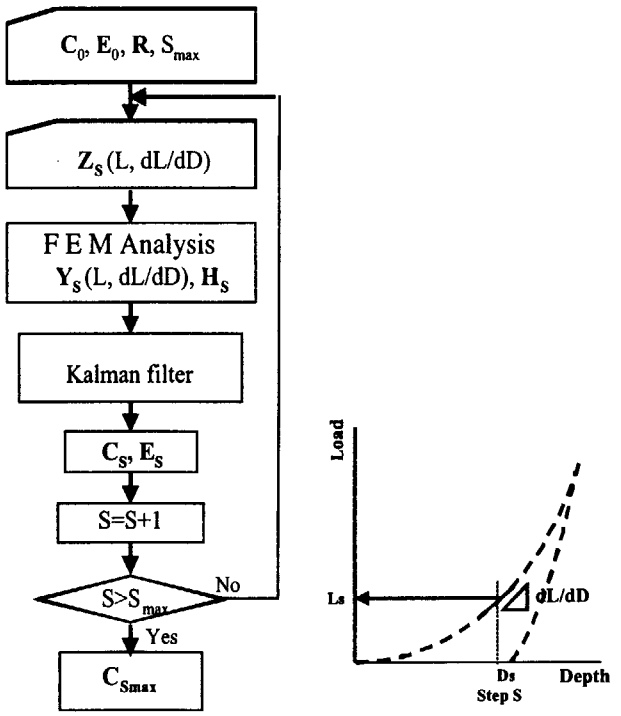


Fig.2 Flow chart for identification of material constants

$$\mathbf{C_S} = \mathbf{C_{S-1}} + \mathbf{E_S H_S R^{-1}}\left(\mathbf{Z_S} - \mathbf{Y_S}\right) \tag{4}$$

$$\mathbf{E_S} = \left(\mathbf{E_{S-1}}^{-1} + \mathbf{H_S}^{T}\mathbf{R^{-1}H_S}\right)^{-1} \tag{5}$$

5) Go back to 2) and repeat the process up to S_{max}. Finally we can obtain the optimal values C_{Smax} estimated at final step S_{max}.

3. Results and discussion

3.1 Hardness

The relationships between load and depth obtained by the indentation test of 25Cr-35Ni-Ti UHP and Type 304SS were expressed as the L/D-D curves, as shown in Fig.3. Each data point is an average from five indentations. The measured curves of the unirradiated(solid line) and triple ion irradiated(dotted line) specimens are plotted together. The curves were fitted with **L/D=a+bD**, where **D** is a depth (μm) from the surface, **L** is the load(gf) at that depth, and **a** and **b** are constant. In particular, the value of **b** is in direct proportion to the appearance hardness of the material[13]. The initial stage up to around 0.1μm in each curve should be neglected because this part of the curve is very dependent on surface roughness of the specimen and the roundness of indenter's tip shape, regardless of the change of the material property. The slope of the ion irradiated curve is higher than that of the unirradiated curve up to a depth of 0.4μm. It means that the ion irradiated layer (about 2μm) affects the L/D-D response of the ion irradiated specimen up to 0.4μm depth.

Figure 4 shows the relative ratio of appearance hardness for the irradiated specimens normalized to it of original specimens. The irradiation defects such as black dots, loops, and bubbles are considered to be strongly relation to the irradiation hardening and ductility loss. The irradiation hardening of 25Cr-35Ni-Ti UHP is expected to be lower than that of Type 304SS from fig.4.

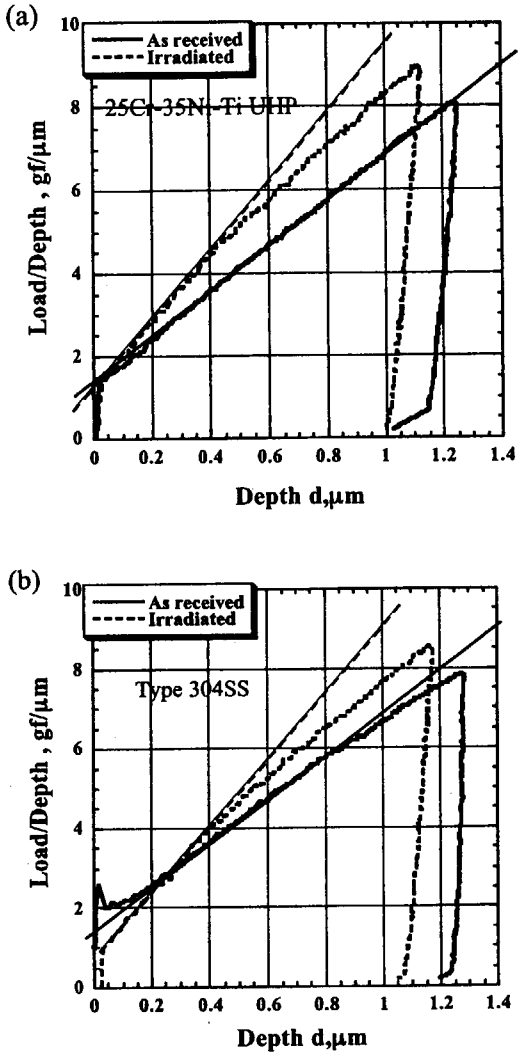


Fig.3 load/depth-depth (L/D-D) curves of 25Cr-35Ni-Ti UHP and type 304

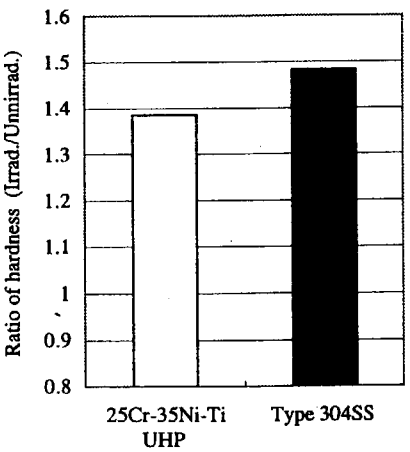


Fig.4 Relative ratio of hardness for specimens irradiated 50dpa by triple ion beams to it of original specimens at 278K

3.2 Constitutive equation

Figure 5 shows the L-D curves measured using the conical indenter, and the calculated results using material constants in Eqs (1)-(3) identified according to the method with the inverse

analysis on the L-D curve. Regardless of the materials, the calculated L-D curves agree with the experimental ones well. The material constants estimated from the inverse analyses on the L-D curves of 25Cr-35Ni-Ti UHP and Type 304SS are summarized Table 2. Increase in yield stress of Type 304SS was bigger than that of the 25Cr-35Ni-Ti UHP. It is well known that a hardness can be related to a yield stress. The result is in fairly good agreement with the change in apparent hardness as shown in Fig.4. The change in the value of A is same in both specimens by ion irradiation. The value of n corresponds to the uniform deformation of the material. After ion irradiation, the decrease in n of Type 304SS was bigger than that of 25Cr-35Ni-Ti UHP. So, it seems that the ductility loss of Type 304SS by ion irradiation is larger than that of 25Cr-35Ni-Ti UHP. As a result, the irradiation hardening of the candidate is expected to be lower than that of Type 304SS from Fig.4 and the estimated material constants.

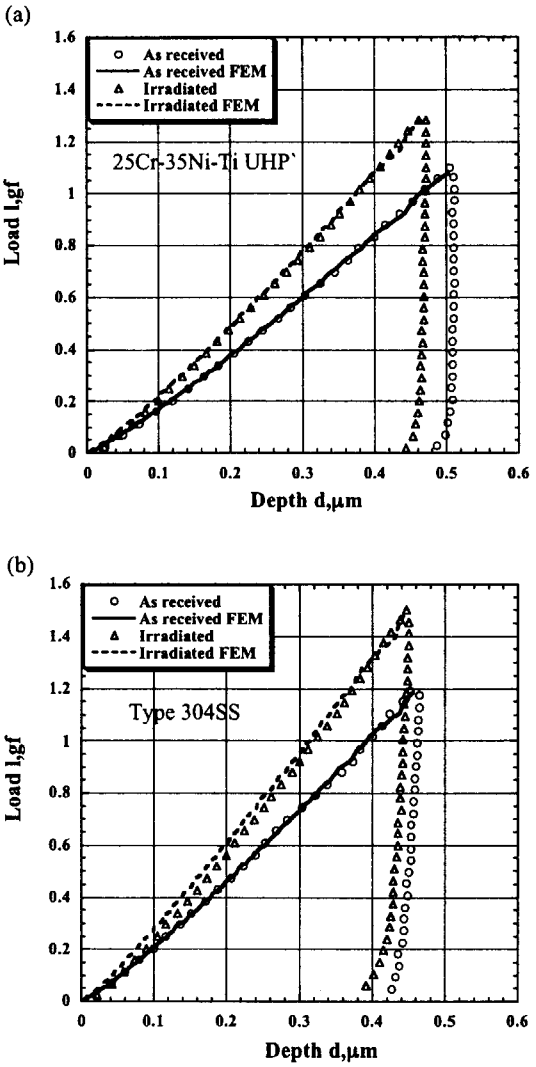


Fig.5 L-D curves measured using the conical indenter, and the calculated results by the inverse analysis

4. Conclusions

The mechanical properties of the ion irradiated material which is a candidate for ultra-high burnup fuel cladding was examined using the novel technology used the indentation technique combined with numerical calculation.

(1) The apparent hardness of Type 304SS was higher than that of the candidate after ion irradiation.

(2) The constants in the constitutive equation for the ion irradiated thin layer were determined by the inverse analyses with Kalman filter.

(3) The mechanical properties of the irradiated thin layer was deduced using the obtained constitutive equation.

(4) Increase in yield stress of Type 304SS was bigger than that of the candidate. The result is in fairly good agreement with the result of apparent hardness.

Table 2 The material constants estimated from the inverse analyses on the L-D curves of 25Cr-35Ni-Ti UHP and Type 304SS

		σ_y, MPa	A, MPa	n
Type 304SS	Unirrad.	213	1464	0.29
	Irrad.	528	1564	0.23
	Irrad./Unirrad.	2.45	1.07	0.79
25Cr-35Ni-Ti UHP	Unirrad.	191	1397	0.36
	Irrad.	411	1492	0.33
	Irrad./Unirrad.	2.15	1.07	0.92

Acknowledgements

The authors would like to thank Mr. K.Tachibana and T.Suzuki of JAERI for the experiment, and also thank to Dr. M.Fujiwara of KOBELCO Co. for preparation of the specimens.

References

[1] K.Kiuchi, I.Ioka, M.Takizawa, and S.Wada, "Development of Advanced Cladding Materials for Burnup Extension", IAEA TCM Reports on Technical and Economic Limit to Fuel Burnup Extension", Argentina(1999).

[2] T.J.Pashos, "Experience with Stainless Steel as a Fuel Clad Material in Water-Cooled Power Reactors," APED-4260(1963).R.DUCAN, "Stainless Steel Failure Investigation Program,"GEAP-5530(1968).

[3] I.Miller, "European Operating Experience," Joint Topical Meeting on Commercial Nuclear Fuel Technology Today," 75-CAN/ANS-100(1975).

[4] V.Pasupathi and P.Lingensmith, "Investigation of Stainless Steel Clad Fuel Rod Failures and Fuel Performance in Connecticut Yankee Reactor," EPRI NP-2119(1981).

[5] D.R.Harries, "Neutron Irradiation-Induced Embrittlement in Type 316 and Other Austenitic Steels and Alloys," Journal of Nuclear Materials, 82, 2(1979).

[6] M.L.Grossbeck, K.Ehrkich and C.Wassilew, "An Assessment of Tensile, Irradiation Creep, Creep Rupture and Fatigue Behavior in Austenitic Stainless Steels with Emphasis on Spectral Effects", Journal of Nuclear Materials, 174, 264(1990).

[7] J.P.Robertson, I.Ioka, A.F.Rowcliffe, M.L.Grossbeck and S.Jitsukawa, "Temperature Dependence of the Deformation Behavior of Type 316 Stainless Steel After Low Temperature Neutron Irradiation", Effects of Radiation on Materials: 18th International Symposium , ASTM STP 1325, 671, R.K.Nanstad,

[8] M.L.Hamilton, F.A.Garner and A.S.Kumar, Eds., American Society for Testing and Materials, West Conshohocken, PA, USA(1999).

[9] I.Ioka, M.Futakawa and T.Wakui, "Mechanical characterization on ion irradiated thin surface layer by nanoindentation technique with inverse analysis", 7th Inter. Conf. on Nucl. Eng., Tokyo, Apr.19-23, ICONE-7095(1999).

[10] M.Futakawa, T.Wakui, Ytanabe and I.Ioka, "Stress-Strain Relationship Evaluated by Inverse Analysis on Indentation Load-Depth Curve".

[11] K.Kiuchi, M.Kikuchi and K.Kondo, "A New Type of Low Temperature Sensitization of Austenitic Stainless Steels Enhanced with Defect-Solute Interactions", Journal of Nuclear Materials, 179-181, 481(1991).

[12] TIARA GROUPE, "JAERI TIARA Annual Report (1992); April 1991-March 1992, "JAERI-M-93-047(1993).

[13] H.Takahashi et al., "Development of evaluation techniques for small specimens", Atomic Energy Society of Japan, (1992)84.

This is a blank page.

国際単位系 (SI) と換算表

表 1　SI基本単位および補助単位

量	名称	記号
長さ	メートル	m
質量	キログラム	kg
時間	秒	s
電流	アンペア	A
熱力学温度	ケルビン	K
物質量	モル	mol
光度	カンデラ	cd
平面角	ラジアン	rad
立体角	ステラジアン	sr

表 2　SIと併用される単位

名称	記号
分，時，日	min，h，d
度，分，秒	°，′，″
リットル	l，L
トン	t
電子ボルト	eV
原子質量単位	u

1 eV = 1.60218 × 10^{-19} J

1 u = 1.66054 × 10^{-27} kg

表 3　固有の名称をもつSI組立単位

量	名称	記号	他のSI単位による表現
周波数	ヘルツ	Hz	s^{-1}
力	ニュートン	N	$m \cdot kg/s^2$
圧力，応力	パスカル	Pa	N/m^2
エネルギー，仕事，熱量	ジュール	J	N·m
工率，放射束	ワット	W	J/s
電気量，電荷	クーロン	C	A·s
電位，電圧，起電力	ボルト	V	W/A
静電容量	ファラド	F	C/V
電気抵抗	オーム	Ω	V/A
コンダクタンス	ジーメンス	S	A/V
磁束	ウェーバ	Wb	V·s
磁束密度	テスラ	T	Wb/m^2
インダクタンス	ヘンリー	H	Wb/A
セルシウス温度	セルシウス度	℃	
光束	ルーメン	lm	cd·sr
照度	ルクス	lx	lm/m^2
放射能	ベクレル	Bq	s^{-1}
吸収線量	グレイ	Gy	J/kg
線量当量	シーベルト	Sv	J/kg

表 4　SIと共に暫定的に維持される単位

名称	記号
オングストローム	Å
バーン	b
バール	bar
ガル	Gal
キュリー	Ci
レントゲン	R
ラド	rad
レム	rem

1 Å = 0.1 nm = 10^{-10} m

1 b = 100 fm^2 = 10^{-28} m^2

1 bar = 0.1 MPa = 10^5 Pa

1 Gal = 1 cm/s^2 = 10^{-2} m/s^2

1 Ci = 3.7 × 10^{10} Bq

1 R = 2.58 × 10^{-4} C/kg

1 rad = 1 cGy = 10^{-2} Gy

1 rem = 1 cSv = 10^{-2} Sv

表 5　SI接頭語

倍数	接頭語	記号
10^{18}	エクサ	E
10^{15}	ペタ	P
10^{12}	テラ	T
10^{9}	ギガ	G
10^{6}	メガ	M
10^{3}	キロ	k
10^{2}	ヘクト	h
10^{1}	デカ	da
10^{-1}	デシ	d
10^{-2}	センチ	c
10^{-3}	ミリ	m
10^{-6}	マイクロ	μ
10^{-9}	ナノ	n
10^{-12}	ピコ	p
10^{-15}	フェムト	f
10^{-18}	アト	a

（注）

1. 表1－5は「国際単位系」第5版，国際度量衡局 1985年刊行による。ただし，1 eVおよび1 uの値はCODATAの1986年推奨値によった。
2. 表4には海里，ノット，アール，ヘクタールも含まれているが日常の単位なのでここでは省略した。
3. barは，JISでは流体の圧力を表わす場合に限り表2のカテゴリーに分類されている。
4. EC閣僚理事会指令ではbar，barnおよび「血圧の単位」mmHgを表2のカテゴリーに入れている。

換　算　表

力	N(=10^5 dyn)	kgf	lbf
	1	0.101972	0.224809
	9.80665	1	2.20462
	4.44822	0.453592	1

粘　度　1 Pa·s(N·s/m^2) = 10 P(ポアズ)(g/(cm·s))

動粘度　1 m^2/s = 10^4 St(ストークス)(cm^2/s)

圧力	MPa(=10 bar)	kgf/cm^2	atm	mmHg(Torr)	lbf/in^2(psi)
	1	10.1972	9.86923	7.50062 × 10^3	145.038
	0.0980665	1	0.967841	735.559	14.2233
	0.101325	1.03323	1	760	14.6959
	1.33322 × 10^{-4}	1.35951 × 10^{-3}	1.31579 × 10^{-3}	1	1.93368 × 10^{-2}
	6.89476 × 10^{-3}	7.03070 × 10^{-2}	6.80460 × 10^{-2}	51.7149	1

エネルギー・仕事・熱量	J(=10^7 erg)	kgf·m	kW·h	cal(計量法)	Btu	ft·lbf	eV
	1	0.101972	2.77778 × 10^{-7}	0.238889	9.47813 × 10^{-4}	0.737562	6.24150 × 10^{18}
	9.80665	1	2.72407 × 10^{-6}	2.34270	9.29487 × 10^{-3}	7.23301	6.12082 × 10^{19}
	3.6 × 10^6	3.67098 × 10^5	1	8.59999 × 10^5	3412.13	2.65522 × 10^6	2.24694 × 10^{25}
	4.18605	0.426858	1.16279 × 10^{-6}	1	3.96759 × 10^{-3}	3.08747	2.61272 × 10^{19}
	1055.06	107.586	2.93072 × 10^{-4}	252.042	1	778.172	6.58515 × 10^{21}
	1.35582	0.138255	3.76616 × 10^{-7}	0.323890	1.28506 × 10^{-3}	1	8.46233 × 10^{18}
	1.60218 × 10^{-19}	1.63377 × 10^{-20}	4.45050 × 10^{-26}	3.82743 × 10^{-20}	1.51857 × 10^{-22}	1.18171 × 10^{-19}	1

1 cal = 4.18605 J（計量法）

= 4.184 J　（熱化学）

= 4.1855 J（15 °C）

= 4.1868 J（国際蒸気表）

仕事率　1 PS（仏馬力）

= 75 kgf·m/s

= 735.499 W

放射能	Bq	Ci
	1	2.70270 × 10^{-11}
	3.7 × 10^{10}	1

吸収線量	Gy	rad
	1	100
	0.01	1

照射線量	C/kg	R
	1	3876
	2.58 × 10^{-4}	1

線量当量	Sv	rem
	1	100
	0.01	1

（86年12月26日現在）

Proceedings of the 3rd International Symposium on Material Chemistry in Nuclear Environment (MATERIAL CHEMISTRY'02 MC'02) March 13-15, 2002, Tsukuba

古紙配合率100%
白色度70%再生紙を使用しています